

Transactions of the ASME®

HEAT TRANSFER DIVISION

Chair, G. P. PETERSON
Vice Chair, W. A. FIVELAND
Past Chair, O. A. PLUMB
Secretary, J. H. KIM
Treasurer, L. C. WITTE
Technical Editor, J. R. HOWELL (2000)

Associate Technical Editors,

P. S. AYYASWAMY (2000)

C. BECKERMANN (2001)

R. D. BOYD (1999)

B. T. F. CHUNG (2001)

R. W. DOUGLASS (2000)

J.-C. HAN (2000)

D. A. KAMINSKI (2001)

M. KAVIANY (1999)

R. L. MAHAJAN (2001)

A. MAJUMDAR (2001)

M. P. MENGUC (2000)

T. TONG (1999)

D. A. ZUMBRUNNEN (2001)

BOARD ON COMMUNICATIONS

Chairman and Vice President
R. K. SHAH

OFFICERS OF THE ASME

President, W. M. PHILLIPS

Executive Director,

D. L. BELDEN

Treasurer,

J. A. MASON

PUBLISHING STAFF

Managing Director, Engineering

CHARLES W. BEARDSLEY

Director, Technical Publishing

PHILIP DI VIETRO

Managing Editor, Technical Publishing

CYNTHIA B. CLARK

Managing Editor, Transactions

CORNELIA MONAHAN

Production Coordinator

JUDITH SIERANT

Production Assistant

MARISOL ANDINO

Transactions of the ASME, Journal of Heat Transfer (ISSN 0022-1481) is published quarterly (Feb., May, Aug., Nov.) for \$240.00 per year by The American Society of Mechanical Engineers, Three Park Avenue, New York, NY 10016.

Periodicals postage paid at New York, NY and additional mailing offices. POSTMASTER: Send address changes to Transactions of the ASME, Journal of Heat Transfer, c/o THE AMERICAN SOCIETY OF MECHANICAL ENGINEERS, 22 Law Drive, Box 2300, Fairfield, NJ 07007-2300.

CHANGES OF ADDRESS must be received at Society headquarters seven weeks before they are to be effective.

Please send old label and new address. PRICES: To members, \$40.00, annually; to nonmembers, \$240.00. Add \$40.00 for postage to countries outside the United States and Canada.

STATEMENT from By-Laws. The Society shall not be responsible for statements or opinions advanced in papers or printed in its publications (B7.1, Para. 3). COPYRIGHT © 1999 by The American Society of Mechanical Engineers.

Authorization to photocopy material for internal or personal use under circumstances not falling within the fair use provisions of the Copyright Act is granted by ASME to libraries and other users registered with the Copyright Clearance Center (CCC) Transactional Reporting Service provided that the base fee of \$3.00 per article is paid directly to CCC, 222 Rosewood Drive, Danvers, MA 01923. Request for special permission or bulk copying should be addressed to Reprints/Permission Department. INDEXED by Applied Mechanics Reviews and Engineering Information, Inc. Canadian Goods & Services Tax Registration #126148048.

Journal of Heat Transfer

Published Quarterly by The American Society of Mechanical Engineers

VOLUME 121 • NUMBER 2 • MAY 1999

TECHNICAL PAPERS

Analytical and Experimental Techniques

253 Numerical Modeling of Conjugate Heat Transfer on Complex Geometries With Diagonal Cartesian Method, Part I: Methods
W. L. Lin, K. D. Carlson, and C.-J. Chen

261 Numerical Modeling of Conjugate Heat Transfer on Complex Geometries With Diagonal Cartesian Method, Part II: Applications
K. D. Carlson, W. L. Lin, and C.-J. Chen

Properties and Property Measurements

268 Recovery of Temperature and Species Concentration Profiles in Flames Using Low-Resolution Infrared Spectroscopy
F. Yousefian, M. Sakami, and M. Lallemand

280 Measuring Thermal Conductivity of Fluids Containing Oxide Nanoparticles
S. Lee, S. U.-S. Choi, S. Li, and J. A. Eastman

Conduction Heat Transfer

290 Higher-Order Sensitivity of Heat Conduction Problems to Random Data Using the Spectral Stochastic Finite Element Method
R. Ghanem

300 A Sequential Gradient Method for the Inverse Heat Conduction Problem (IHCP)
K. J. Dowding and J. V. Beck

Forced Convection

307 Swirling Effects on Laminarization of Gas Flow in a Strongly Heated Tube
S. Torii and W.-J. Yang

314 Numerical Investigation of Flow Field and Heat Transfer in Cross-Corrugated Ducts
H. Blomerius, C. Hölsken, and N. K. Mitra

322 Turbulent Heat Transport in a Perturbed Channel Flow
C. U. Buice and J. K. Eaton


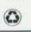
326 An Experimental Study on Forced Convection Heat Transfer From Flush-Mounted Discrete Heat Sources
C. P. Tso, G. P. Xu, and K. W. Tou

Jets, Wakes, and Impingement

333 Experimental and Numerical Studies of Heat Transfer From a Liquid Bath due to an Impinging Gas Jet
F. Qian, B. Farouk, R. Mutharasan, and N. Macken

341 Local and Instantaneous Heat Transfer Characteristics of Arrays of Pulsating Jets
H. S. Sherif and D. A. Zumbrunnen

(Contents continued on Outside Back Cover)

This journal is printed on acid-free paper, which exceeds the ANSI Z39.48-1992 specification for permanence of paper and library materials. ™
 85% recycled content, including 10% post-consumer fibers.

(Contents continued)

Natural Mixed Convection

- 349 Analysis of Combined Forced and Free Flow in a Vertical Channel With Viscous Dissipation and Isothermal-Isoflux Boundary Conditions
A. Barletta

Radiative Transfer

- 357 Radiative Heat Transfer in Periodic Geometries Using a Finite Volume Scheme
S. R. Mathur and J. Y. Murthy

Boiling and Condensation

- 365 Nucleate Boiling Heat Transfer of Binary Mixtures at Low to Moderate Heat Fluxes
R. J. Benjamin and A. R. Balakrishnan
- 376 Nucleate Pool Boiling on Ribbed Surfaces With Micro-Roughness at Low and Moderate Heat Flux
S.-S. Hsieh, C.-J. Weng, and J.-J. Chiou
- 386 Heat Transfer Behavior on Small Horizontal Heaters During Pool Boiling of FC-72
T. D. Rule and J. Kim
- 394 Assessment of CHF Enhancement Mechanisms in a Curved, Rectangular Channel Subjected to Concave Heating
J. C. Sturgis and I. Mudawar
- 405 Condensation of Downward-Flowing Zeotropic Mixture HCFC-123/HFC-134a on a Staggered Bundle of Horizontal Low-Finned Tubes
H. Honda, H. Takamatsu, and N. Takata

Combustion

- 413 The Measurement of Transient Two-Dimensional Profiles of Velocity and Fuel Concentration Over Liquids
A. Ito, A. Narumi, T. Konishi, G. Tashtoush, K. Saito, and C. J. Cremers

Phase Change and Multiphase Heat Transfer

- 420 Effect of Combined Particle-Phase Diffusivity and Viscosity on the Compressible Boundary Layer of a Particulate Suspension Over a Flat Plate
A. J. Chamkha
- 430 An Experimental Investigation Into the Effects of Grain Transport on Columnar to Equiaxed Transition During Dendritic Alloy Solidification
J. W. Gao and C. Y. Wang

Heat Pipes

- 438 Temperature Response of Heat Transport in a Micro Heat Pipe
G. P. Peterson and H. B. Ma

Porous Media, Particles, and Droplets

- 446 Heat Transfer of Sprays of Large Water Drops Impacting on High Temperature Surfaces
T. L. Cox and S. C. Yao

Heat Transfer in Manufacturing

- 451 Mass, Momentum, and Energy Transport in a Molten Pool When Welding Dissimilar Metals
F. K. Chung and P. S. Wei

TECHNICAL NOTES

- 462 A Boundary Element Method for the Solution of a Class of Steady-State Problems for Anisotropic Media
D. L. Clements and W. S. Budhi
- 466 The Effective Thermal Conductivity of High Porosity Fibrous Metal Foams
V. V. Calmidi and R. L. Mahajan
- 471 Dimensional Analysis in Heat Transfer
T. M. Dalton and M. R. D. Davies

(Contents continued on Inside Back Cover)

(Contents continued)

- 473 Comparative Analysis of Different Models for the Turbulent Prandtl Number
M. C. Silva, L. C. De Lima, and R. F. Miranda
- 478 Transient Thermal Analysis of a Translucent Thermal Barrier Coating on a Metal Wall
R. Siegel
- 481 Inverse Analysis of Radiative Heat Transfer Systems
M. R. Jones
- 484 Relative Stability of Boiling on a Flat Plate: Effects of Heater Orientation
W. W. Lin, J. C. Yang, and D. J. Lee
- 486 Pool Evaporation of Decane Into an Enclosed Gas Space Undergoing Thermal Convection
J. P. Burelbach, M. Epstein, and H. K. Fauske
- 488 Effects of Surface Tension and Binary Diffusion on Pool Boiling of Dilute Solutions: An
Experimental Assessment
S. G. Kandlikar and L. Alves
- 493 Heat Transfer Studies During Solidification of PCM Inside an Internally Finned Tube
R. Velraj and R. V. Seeniraj
- 497 Heat Conduction From Spheroids
R. S. Alassar
- 500 A Theoretical Study, With Experimental Verification, of the Temperature-Dependent
Viscosity Effect on the Forced Convection Through a Porous Medium Channel
D. A. Nield, D. C. Porneala, and J. L. Lage

ANNOUNCEMENTS AND SPECIAL NOTES

- 279 Change of Address Form
- 289 8th International Symposium on Transport Phenomena and Dynamics of Rotating
Machinery—First Announcement and Call for Papers
- 299 Visualization of Thermal Phenomena—Call for Photographs
- 429 Periodicals on ASMENET
- 504 Information for Authors

W. L. Lin¹
Mem. ASME.

K. D. Carlson²
Assoc. Mem. ASME.

C.-J. Chen³
Dean of Engineering and
Professor of Mechanical Engineering,
e-mail: cjchen@eng.fsu.edu
Fellow ASME.

Department of Mechanical Engineering,
College of Engineering,
Florida A&M University and Florida
State University,
2525 Pottsdamer Street,
Tallahassee, FL 32310

Numerical Modeling of Conjugate Heat Transfer on Complex Geometries With Diagonal Cartesian Method, Part I: Methods

In this study, a diagonal Cartesian method for thermal analysis is developed for simulation of conjugate heat transfer over complex boundaries. This method uses diagonal line segments in addition to Cartesian line segments to approximate complex boundaries in Cartesian coordinates. The velocity fields are also modeled using the diagonal Cartesian method. The transport equations are discretized with the finite analytic (FA) method. The current work is validated by simulating a rotated lid-driven cavity flow with conjugate heat transfer, and accurate results are obtained.

1 Introduction

Many heat transfer simulations in use today are capable of computing only one mode of heat transfer. That is, if conduction in a solid is being calculated, convection is used as a boundary condition, with either the surface temperature or the heat transfer coefficient h assumed to be known (and usually constant). Likewise, if fluid convection is being calculated, either the surface temperature or the heat flux is assumed known (and again, usually constant). In many engineering applications, however, these interface quantities are unknown and/or variable. To simulate these problems accurately requires simultaneous solution of heat transfer in the solid and fluid domains, i.e., conjugate heat transfer analysis.

Mori et al. (1974, 1976) found analytical solutions for conjugate heat transfer in fully developed laminar flow between stationary parallel plates and in a circular tube. Cao and Faghri (1991, 1992) solved conjugate forced convection in an axisymmetric pipe that was enclosed in a phase-change material (PCM) energy storage module, for both laminar and turbulent flows. Ray and Srinivasan (1992) developed a simulation for conjugate laminar mixed convection in a shrouded array of electronic components. By assuming the flow was hydrodynamically and thermally fully developed in one direction, the problem was reduced to a two-dimensional problem. A similar approach was taken by Weisberg and Bau (1992) to perform a numerical study of conjugate laminar forced convection in microchannels utilized as heat exchangers for electronic cooling. Conjugate heat transfer in channel flow over an array of integrated circuits (IC's) mounted along one wall of the channel was studied numerically by Wang and Saulnier (1993). The problem was modeled as two-dimensional, with four IC's in the solution domain. The simulation was performed for laminar flow with $Re = 1300$. Using air as the working fluid, a parametric study was performed by varying the conductivity of the circuit

board (PCB) materials and the IC materials. It was found that the thermal field was much more sensitive to the PCB conductivity than it was to the IC conductivity. Finally, the current authors (Lin et al., 1997; Carlson et al., 1997) modeled conjugate heat transfer in a compact heat exchanger with regular (i.e., Cartesian-oriented) fins. The analysis showed that assuming the heat exchanger walls and fins have a constant temperature (as opposed to using conjugate heat transfer analysis) results in an overprediction of the heat transfer by five to eight percent for Reynolds numbers between 50 and 500.

Notice that all the research mentioned above includes relatively simple geometries. Very few conjugate heat transfer analyses have been performed involving truly complex geometries. In order to simulate incompressible flows over complex geometries, the diagonal Cartesian method was developed by the current authors (Lin et al., 1998). A structured Cartesian grid is used to retain the simplicity of a Cartesian coordinate system. Complex boundaries are approximated using both Cartesian grid lines and diagonal line segments. An enlarged control volume method is introduced to ensure mass conservation and to treat pressure boundary conditions on complex boundaries. Conservation of momentum and energy are enforced with the finite analytic (FA) method, using nine-point and five-point FA elements (Chen et al., 1981, 1984; Lin et al., 1998).

In this paper, the diagonal Cartesian method is used to simulate conjugate heat transfer involving complex geometries. Part I of the paper describes the diagonal Cartesian method for thermal analysis, and its verification. Application of this method to the design and analysis of a compact heat exchanger with complex fins is given in Part II of this paper.

2 Formulation of the Problem

The fluid is assumed to be an incompressible Newtonian fluid with constant properties, and there is no heat generation in the solid or fluid domains. With these assumptions, the equations that govern laminar fluid flow and conjugate heat transfer are as follows.

Fluid domain:

$$u_x + v_y = 0 \quad (1)$$

$$u_t + uu_x + vv_y = -p_x + \frac{1}{Re} (u_{xx} + u_{yy}) \quad (2)$$

¹ Currently Postdoctoral Research Associate, National Center for Supercomputing Applications (NCSA), University of Illinois at Urbana-Champaign (UIUC), Urbana, IL 61801.

² Currently at the Department of Mechanical Engineering, The University of Iowa, Iowa City, IA 52242.

³ To whom correspondence should be addressed.

Contributed by the Heat Transfer Division for publication in the JOURNAL OF HEAT TRANSFER. Manuscript received by the Heat Transfer Division, June 25, 1998; revision received, Jan. 22, 1999. Keywords: Cavities, Computational, Conduction, Conjugate, Convection, Flow, Fluids, Forced Convection, Geometry, Heat Transfer, Interface, Laminar, Modeling, Numerical Methods. Associate Technical Editor: R. Dougllass.

$$v_t + uv_x + vv_y = -p_y + \frac{1}{\text{Re}} (u_{xx} + v_{yy}) \quad (3)$$

$$\theta_t + u\theta_x + v\theta_y = \frac{1}{\text{Pe}} (\theta_{xx} + \theta_{yy}) \quad (4)$$

Solid domain:

$$\theta_t = \frac{\alpha_s}{\alpha_f} \frac{1}{\text{Pe}} (\theta_{xx} + \theta_{yy}) \quad (5)$$

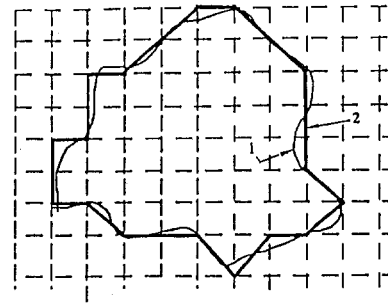
where the variables for time, space, velocity, pressure, and temperature have been nondimensionalized by the characteristic time L/U_{ref} , characteristic length L , characteristic velocity U_{ref} , characteristic dynamic pressure ρU_{ref}^2 , and characteristic temperature difference ΔT . The Reynolds number is defined as $\text{Re} = U_{\text{ref}} L / \nu$, where ν is the kinematic viscosity of the fluid. The Peclet number is defined as $\text{Pe} = \text{Re} \text{Pr}$, where Pr is the Prandtl number of the fluid. α_s and α_f are the thermal diffusivities of the solid and fluid, respectively. The Dirichlet velocity boundary condition is

$$\mathbf{v} = \mathbf{v}_{bc} \quad (6)$$

where \mathbf{v}_{bc} is the dimensionless boundary velocity vector. The temperature boundary condition at the computational (outer) boundary can be specified as either a given temperature or a given heat flux. The temperature boundary condition at solid/fluid interfaces (inner boundaries) is the conservation of energy flux, given as

$$(\theta_n)|_{\text{fluid}} = \frac{k_s}{k_f} (\theta_n)|_{\text{solid}} \quad (7)$$

where k_f and k_s are the fluid and solid thermal conductivities, and n is the direction normal to the interface. Enforcement of this interface temperature boundary condition provides the necessary coupling between the solid and fluid domains to simulate conjugate heat transfer.



1 – Original Geometry
2 – Approximated Geometry

Fig. 1 Diagonal Cartesian approximation of complex boundaries

3 Diagonal Cartesian Method for Complex Geometries

The diagonal Cartesian method is utilized to approximate complex geometries and to simulate incompressible fluid flows over complex boundaries. As shown in Fig. 1, complex geometries are approximated by both Cartesian grid lines and diagonal line segments. The conservation of mass and momentum on complex boundaries is enforced by the enlarged control volume method, which is described in detail in Lin et al. (1998). It is found that the diagonal Cartesian method can provide an accurate simulation of incompressible flow over complex boundaries.

3.1 Discretization of Governing Equations. The momentum and energy equations given in Eqs. (2)–(5) are discretized using the FA method (Chen et al., 1981, 1984). This yields

$$u_p = \alpha_p \sum_{nb=1}^m (C_{nb} u_{nb}) + (1 - \alpha_p) u_p^0 - \alpha_p S_p^u \left(\frac{\partial p}{\partial x} \right) \quad (8)$$

Nomenclature

C = finite analytic coefficients
 D^* , D_w^* = source term of pressure equation
 L = characteristic length of domain
 Nu = local Nusselt number $\text{Nu} = hL/k_f$
 $\overline{\text{Nu}}$ = average Nusselt number
 Pe = Peclet number $\text{Pe} = \text{Re} \text{Pr}$
 Pr = Prandtl number $\text{Pr} = \nu/\alpha_f$
 Re = Reynolds number $\text{Re} = U_{\text{ref}} L / \nu$
 S_{gen} = energy generation term for temperature equation
 T = dimensional temperature
 U_{ref} = characteristic velocity
 a^p, a^E, a^W, a^N, a^S = coefficients of pressure equation
 c_s, c_f = specific heats of the solid and fluid, respectively
 h = heat transfer coefficient
 k_s, k_f = thermal conductivities of the solid and fluid, respectively
 n = direction normal to the solid/fluid interface

p = dimensionless pressure
 q'' = heat flux
 q_{hs} = energy generation per unit volume
 r_s, r_f = weighting factors for wall temperature equations
 t = dimensionless time
 u, v = dimensionless velocities in x and y directions
 \mathbf{v} = dimensionless velocity vector
 \mathbf{v}_{bc} = dimensionless velocity vector at boundaries
 x, y = dimensionless Cartesian coordinates

Greek

α_p = coefficients for the discretized momentum equations
 α_s, α_f = thermal diffusivities of the solid and fluid, respectively
 Δt = dimensionless time step size
 ΔT = characteristic temperature difference
 $\Delta x, \Delta y$ = grid intervals in x and y directions

ν = kinematic viscosity of fluid
 ρ = density of fluid
 τ = dimensional time
 θ = dimensionless temperature
 $\theta_{b,ex}$ = dimensionless bulk exit temperature

Superscripts

0 = variables at previous time step
 $*$ = pseudo-variables
 P, E, W, N, S = central node and four neighboring nodes
 e, w, n, s = cell surface positions of a smaller control volume

Subscripts

f, s, P, E, W, N, S = fluid or solid value
 NE, NW, SE, SW = central node and eight neighboring nodes
 e, w, n, s = cell surface positions of a smaller control volume

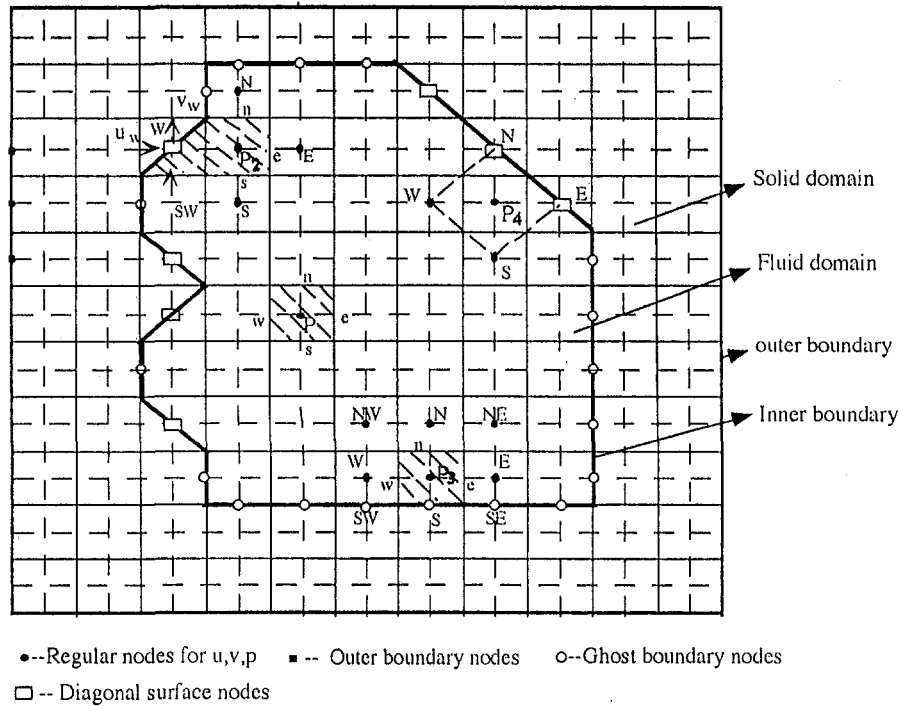


Fig. 2 Conservation of mass and momentum on complex boundaries

$$v_p = \alpha_p \sum_{nb=1}^m (C_{nb} v_{nb}) + (1 - \alpha_p) v_p^0 - \alpha_p S_p^v \left(\frac{\partial p}{\partial y} \right) \quad (9)$$

where

$$\alpha_p = \frac{1}{1 + (C_p \text{Re}/\tau)} \quad (10)$$

$$S_p^u = S_p^v = C_p \text{Re} \quad (11)$$

and

$$\theta_p = \alpha_p \sum_{nb=1}^m (C_{nb} \theta_{nb}) + (1 - \alpha_p) \theta_p^0 \quad (12)$$

where fluid domain:

$$\alpha_p = \frac{1}{1 + (C_p \text{Pe}/\tau)} \quad (13)$$

solid domain:

$$\alpha_p = \frac{1}{1 + \left(C_p \frac{\alpha_f}{\alpha_s} \text{Pe}/\tau \right)} \quad (14)$$

u_p^0 , v_p^0 , and θ_p^0 are values at node P from the previous time step, and C_{nb} and C_p are the FA coefficients (Chen et al., 1981, 1984). $m = 8$ for regular nodes (nodes which are not on or adjacent to diagonal boundaries) such as node P_3 in the lower part of Fig. 2, and $m = 4$ for nodes adjacent to diagonal surfaces, such as node P_4 . Detailed analysis of the accuracy of the FA method is given in Chen et al. (1981, 1984).

3.2 Ghost Boundary Nodes and Enlarged Control Volume Method. Conservation of mass in the fluid region is achieved with a pressure equation that uses control volumes such as the cross-hatched regions shown in Fig. 2. These control volumes are denoted using the lowercase letters n , s , e , and w to distinguish

them from the nodes that make up the FA elements, denoted with uppercase letters in Fig. 2. Details of the treatment of the pressure equation for regular geometries are given in Lin et al. (1997). For fluid nodes adjacent to diagonal surfaces, mass conservation is enforced on an enlarged trapezoidal control volume such as the one shown for node P_2 in Fig. 2. From the principle of mass conservation over this enlarged control volume, the following pressure equation is obtained (Lin et al., 1998):

$$a^p P_{P_2} = a^e P_e + a^w P_w + a^N P_N + a^S P_s - (D^* + D_w^*) \quad (15)$$

where

$$D^* = \frac{U_e^* - U_w}{\Delta x_i} + \frac{V_n^* - V_s^*}{\Delta y_j} \quad (16)$$

$$D_w^* = \frac{V_w - V_{sw}}{\Delta x_i \Delta y_j} \Delta x_{i-1} \quad (17)$$

The related coefficients and parameters are given in Lin et al. (1998).

Conjugate heat transfer analysis for regular boundaries requires the introduction of ghost boundary nodes such as nodes SW , S , and SE shown for node P_3 in the lower part of Fig. 2. This is necessary because there are no actual computational nodes on regular interfaces (in Fig. 2, the computational nodes lie at the intersections of the dashed lines). Ghost nodes are introduced using the interface temperature boundary condition given in Eq. (7) to relate the temperatures at the ghost nodes to the temperatures of the computational nodes directly above and below the ghost nodes. This results in the following discretized temperature equation, which includes only actual computational nodes:

$$\theta_p = \frac{\alpha_p}{(1 - \alpha_p r_f C_s)} [C_{NW} \theta_{NW} + C_N \theta_N + C_{NE} \theta_{NE} + (C_w + r_f C_{SW}) \theta_w + (C_e + r_f C_{SE}) \theta_e + r_s C_{SW} \theta_{SW} + r_s C_s \theta_s + r_s C_{SE} \theta_{SE}] + \frac{(1 - \alpha_p)}{(1 - \alpha_p r_f C_s)} \theta_p^0 \quad (18)$$

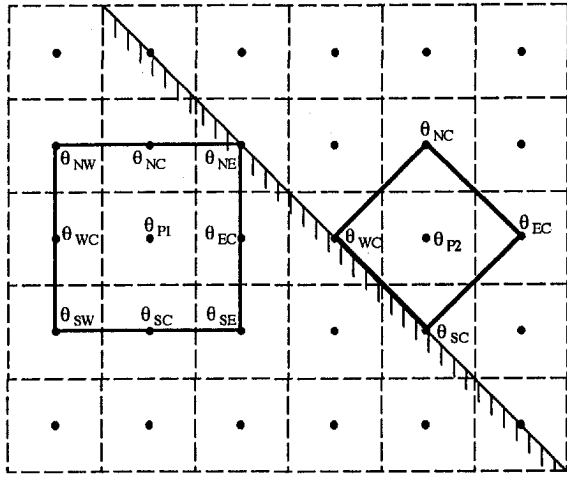


Fig. 3 Nodes near a complex boundary

The corresponding coefficients and a detailed analysis are given in Carlson et al. (1997).

4 Conjugate Heat Transfer for Complex Boundaries

Conjugate heat transfer at regular boundaries has been modeled with the ghost boundary node method just described, and simulation of incompressible flow over complex boundaries has been achieved with the diagonal Cartesian method (Lin et al., 1998). This section describes the treatment of conjugate heat transfer at complex (i.e., diagonal) boundaries.

Consider two nodes, $P1$ and $P2$, which are close to the complex boundary shown in Fig. 3. Node $P1$ is diagonally adjacent to the complex boundary. However, it is still possible to form a homogeneous nine-point FA element around this node, so a nine-point FA element is used. Node $P2$ is horizontally and vertically adjacent to the complex boundary. It is not possible to form a homogeneous nine-point FA element around nodes which are horizontally or vertically adjacent to a complex boundary, so a five-point FA element is employed here instead of a nine-point FA element. Notice that, unlike regular boundaries formed with Cartesian line segments, boundaries formed with diagonal segments pass through the computational nodes. Because of this, no additional work is required to compute wall temperatures, since those values are computed at the neighboring nodes (WC and SC , in this example).

The final situation that must be addressed is the computation of temperature for nodes that lie on diagonal boundaries, such as those shown in Fig. 4. The equation for the temperature at interface nodes such as node P in Fig. 4(a) can be derived directly from the interface temperature boundary condition. This will be referred to as the boundary condition method. For a uniform grid such as in Fig. 4(a), finite differencing can be used to discretize the interface temperature boundary condition (Eq. (7)) at node P , which gives

$$\frac{\theta_{NE} - \theta_P}{d} = \frac{k_s \theta_P - \theta_{SW}}{k_f d} \quad (19)$$

where d is the dimensionless distance from node NE to P and from P to SW . This can be simplified to

$$\theta_P = C_{SW} \theta_{SW} + C_{NE} \theta_{NE} \quad (20)$$

where

$$C_{SW} = \frac{k_s}{k_s + k_f} \quad (21)$$

$$C_{NE} = \frac{k_f}{k_s + k_f} \quad (22)$$

It is important to note that Eq. (20) requires a uniform grid. The discretization of the interface temperature boundary condition for a nonuniform grid (see Fig. 4(b)) is much more complicated than for a uniform grid. Additional calculations and programming are required, such as determining between which pair of points the normal passes. For example, θ_{nf} could lie between nodes NE and EC or between NC and NE , depending on the local grid spacing. Additionally, interpolation must be employed to find θ_{nf} and θ_{ns} .

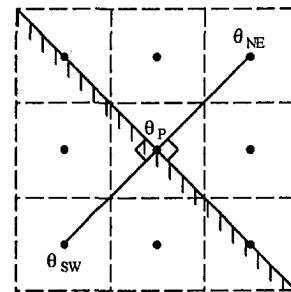
In an attempt to overcome these complications, a second approach was investigated. In this approach, which will be referred to as the control volume method, the temperature at node P is related to the temperatures of its neighbors through an energy balance. Consider the nonuniform grid shown in Fig. 5(a). Performing an energy balance on the cell containing P (shown in Fig. 5(b)) results in

$$q''_i \Delta X_i + q''_w \Delta Y_j - q''_n \Delta X_i - q''_e \Delta Y_j + \frac{1}{2} \Delta X_i \Delta Y_j q_{hs} = \frac{1}{2} (\rho_s c_s + \rho_f c_f) \Delta X_i \Delta Y_j \frac{dT_P}{d\tau} \quad (23)$$

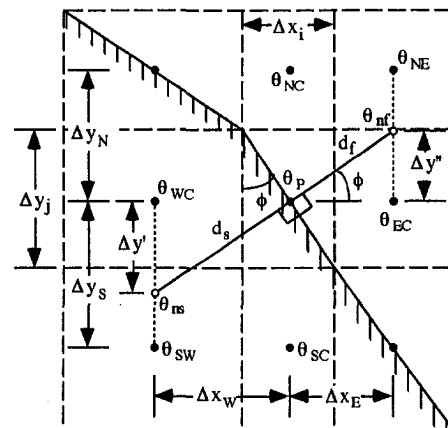
where the q'' values are the heat fluxes through each cell face and q_{hs} is the energy generation per unit volume in the solid. Neglecting convection, the heat flux can be written as

$$q'' = -k \frac{\partial T}{\partial n} \quad (24)$$

where n is the direction normal to the cell face. Discretizing Eq. (24) with finite differencing, substituting the result into Eq. (23) and nondimensionalizing with the characteristic quantities L , U_{ref} , ΔT , and $\Delta \tau$ yields



(a) uniform grid



(b) non-uniform grid

Fig. 4 The boundary condition method

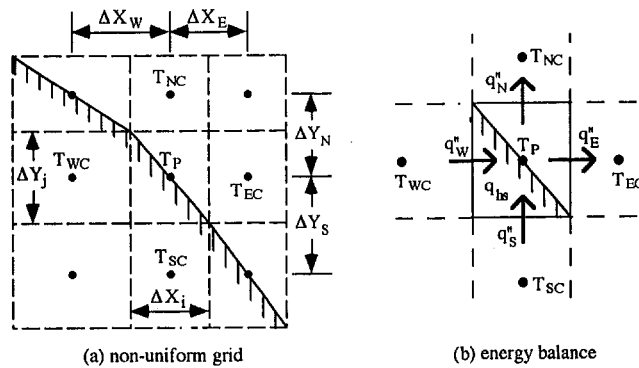


Fig. 5 The control volume method

$$\begin{aligned} & \frac{k_s}{k_f} \left[\frac{\theta_{SC} - \theta_P}{\Delta y_s} \right] \Delta x_i + \frac{k_s}{k_f} \left[\frac{\theta_{WC} - \theta_P}{\Delta x_w} \right] \Delta y_j - \left[\frac{\theta_P - \theta_{NC}}{\Delta y_N} \right] \Delta x_i \\ & - \left[\frac{\theta_P - \theta_{EC}}{\Delta x_E} \right] \Delta y_j + \frac{L^2 \Delta x_i \Delta y_j q_{hs}}{2k_f \Delta T} \\ & = \frac{\Delta x_i \Delta y_j Pe}{2\Delta t} \left(\frac{\rho_s c_s}{\rho_f c_f} + 1 \right) (\theta_P - \theta_P^0). \end{aligned} \quad (25)$$

Solving this expression for θ_P gives

$$\theta_P = \frac{1}{C_P} [C_{SC}\theta_{SC} + C_{WC}\theta_{WC} + C_{NC}\theta_{NC} + C_{EC}\theta_{EC} + S_{gen} + M\theta_P^0] \quad (26)$$

where

$$C_{SC} = \frac{k_s \Delta x_i}{k_f \Delta y_s} \quad (27)$$

$$C_{WC} = \frac{k_s \Delta y_j}{k_f \Delta x_w} \quad (28)$$

$$C_{NC} = \frac{\Delta x_i}{\Delta y_N} \quad (29)$$

$$C_{EC} = \frac{\Delta y_j}{\Delta x_E} \quad (30)$$

$$C_P = C_{SC} + C_{NC} + C_{WC} + C_{EC} + M \quad (31)$$

$$S_{gen} = \frac{L^2 \Delta x_i \Delta y_j q_{hs}}{2k_f \Delta T} \quad (32)$$

$$M = \frac{\Delta x_i \Delta y_j Pe}{2\Delta t} \left(\frac{\rho_s c_s}{\rho_f c_f} + 1 \right). \quad (33)$$

Implementation of the control volume method (Eq. (26)) is the same for both uniform and nonuniform grids, which makes it easier to program and more robust than the boundary condition method (Eq. (20)). Notice that although the control volume method does not directly use the interface temperature boundary condition given in Eq. (7), the energy balance from which it derives does account for the two different materials within the control volume. Finally, the control volume method neglects convection, but convection is minimal very close to interfaces, and this error should decrease as the grid size decreases.

The boundary condition and control volume methods were compared by computing conjugate heat transfer for a rotated lid-driven cavity flow (see Section 6 for details) with $Re = 100$, $Pr = 1$ and $K = k_s/k_f = 2$. Figure 6 shows the local Nusselt number curves along the heated moving wall computed using both methods. Both of these solutions were computed on a 100×100

uniform grid, which includes 56×56 nodes in the fluid domain. These curves are compared to the curve obtained from solving the same problem for a regular (unrotated) cavity on a 49×49 grid (39×39 in the fluid). The two methods produce a very similar curve, with the boundary condition method being slightly more accurate than the control volume method. This problem was also solved for $K = 20$ and 2000 . As K increases, the difference between the boundary condition and control volume results decreases slightly. It is seen, then, that there is little difference in the results produced by these two methods. Because of its simplicity and robustness, the control volume method is utilized in the present simulation.

As a final note, it is worth mentioning that a nonstaggered grid is employed in this work, so the temperature and velocity components for each node are computed at the same location. Because of this, the momentum and energy equations are discretized over the same set of FA elements. Therefore, the boundary treatments discussed in this section for nodes near solid/fluid interfaces also apply to the solution of the momentum equations. In fact, application to the momentum equations is simpler, because while the interface temperature is unknown and requires special treatment, the velocity of the interface is a known quantity which can be directly used in the solution.

5 Numerical Solution Procedure

The two-dimensional simulation developed in this work numerically solves the discretized pressure and transport equations using a modified version of a PISO/SIMPLEC scheme (Pressure-Implicit with Splitting of Operators (Issa, 1986), Semi-Implicit Method for Pressure-Linked Equations—Consistent (Doormaal and Raithby, 1984)). The computational procedure is as follows:

- 1 Specify the initial conditions for the velocity, pressure, and temperature fields.
- 2 Calculate the FA coefficients for velocity in Eqs. (8) and (9).
- 3 Solve the momentum equations (Eqs. (8) and (9)) implicitly for u and v with an ADI (Alternating Direction Implicit) algorithm, using the pressure field from the previous time step.
- 4 Return to Step 2 until convergent velocities are obtained.
- 5 Update the FA coefficients.
- 6 Solve the pressure equation (such as Eq. (15)) implicitly with the ADI algorithm.
- 7 Update the velocities explicitly using Eqs. (8) and (9).
- 8 Return to Step 5 until both the pressure and velocity fields are converged.
- 9 Using the converged velocity field for the current time step, calculate the FA coefficients for temperature in Eq. (12) or (18).
- 10 Solve Eq. (12) or (18) implicitly for the temperature field with the ADI algorithm.
- 11 Repeat the above step until a convergent temperature field is obtained.

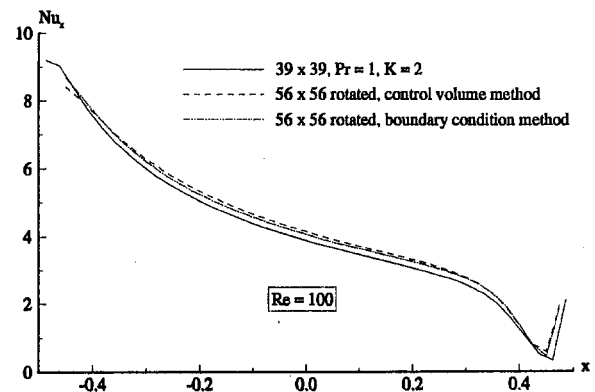


Fig. 6 Local Nusselt number curves along the heated cavity wall

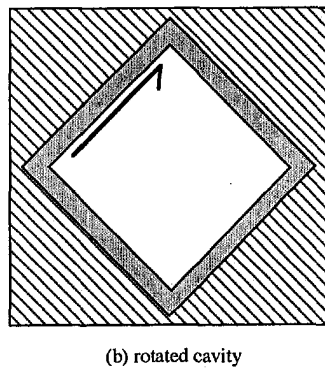
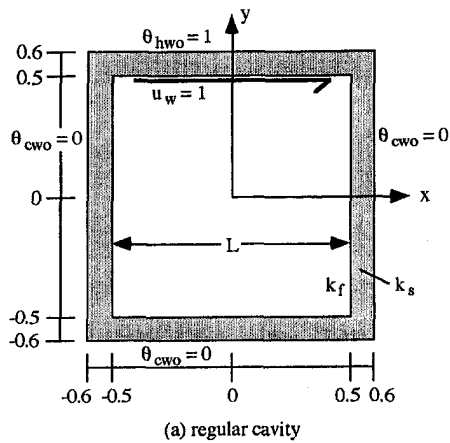


Fig. 7 Regular and rotated thick-walled lid-driven cavities

12 Return to Step 2 for the next time-step.

Notice that for steady-state problems, the temperature field is computed after the converged steady-state velocity and pressure fields are obtained. Since the velocity field does not change throughout the computation of the temperature field, the energy equation is linear. The solution of the energy equation for a steady-state temperature field reduces to solving a linear partial differential equation with constant coefficients. Thus, the computation is very stable, and a large time-step size can be used to march toward the desired steady-state solution. In the steady-state simulations performed in this work, a time-step size of $\Delta t = 10^{30}$ is used to ensure that the solution proceeds to steady-state as rapidly as possible.

Convergence is determined by computing the residuals Δp_{\max} , Δu_{\max} , Δv_{\max} , and $\Delta \theta_{\max}$, which are defined as the maximum difference (over all points in the computational domain) between the values of that variable computed at the present and previous iterations. Unless otherwise stated, the pressure, velocity, and temperature fields are considered convergent when Δp_{\max} is less than 10^{-4} and Δu_{\max} , Δv_{\max} , and $\Delta \theta_{\max}$ are less than 10^{-5} . All computations were performed on a SGI Indigo2 workstation, which has a 200 MHz R4400 processor.

6 Verification of Conjugate Heat Transfer Over Complex Boundaries

The verification of the diagonal Cartesian method for the modeling of velocity and pressure fields in flows with complex boundaries was shown in detail by Lin et al. (1998). The verification of the diagonal Cartesian method for temperature fields is achieved in the present section through the simulation of conjugate heat transfer in a thick-walled lid-driven cavity flow.

Burggraf (1966) and Chen et al. (1981) solved for convective heat transfer inside a lid-driven cavity with given wall (solid/fluid

interface) temperatures. To formulate a cavity problem involving conjugate heat transfer, the walls of the cavity are given a finite thickness and thermal conductivity, as shown in Fig. 7. The cavity consists of three stationary walls and one wall which is moving with a dimensionless velocity of one. The outer surfaces of the stationary walls have a dimensionless temperature of zero, and the outer surface of the moving wall has a dimensionless temperature of one. The moving wall causes the fluid inside the cavity to rotate, and the fluid exchanges heat with all four cavity walls. The effects of varying thermal conditions are studied by solving the problem for Reynolds number $Re = 100$ with Prandtl numbers $Pr = 0.1$ and 1 , and conductivity ratios $K = k_s/k_f = 2, 20, 2000$ and ∞ (only convection). In order to validate the simulation of conjugate heat transfer for complex geometries, this conjugate cavity problem is solved both as shown in Fig. 7(a) (regular cavity), and rotated by 45 degrees as shown in Fig. 7(b) (rotated cavity). The results from the regular cavity, which has only rectilinear boundaries, are used as a benchmark for comparison with the rotated cavity results.

It should be noted that the choice to rotate the cavity by 45 degrees, which aligns the cavity boundaries exactly with the diagonal lines utilized by the diagonal Cartesian method, was a deliberate choice. The ability of the diagonal Cartesian method to model arbitrary geometries was demonstrated by Lin (1997) and Lin et al. (1998) using (among other geometries) a lid-driven cavity that was rotated by 30 degrees. The conjugate heat transfer model used for regular (i.e., Cartesian) geometries was validated by Bravo (1991). The purpose of the arrangement used here is to evaluate the accuracy of the conjugate heat transfer model utilized for complex (i.e., diagonal) boundaries. By aligning the cavity with the diagonal grid lines, it is possible to remove the error in the solution due to the boundary approximation, which means any error in the solution is due to the complex conjugate heat transfer model. In addition, the cavity rotated by 45 degrees has only diagonal boundaries (as opposed to a combination of diagonal and regular line segments, which would result from rotation by any other angle), and as such it serves as a rigorous test of the complex boundary conjugate heat transfer model.

For the rotated cavity, grid independence of the $Re = 100$ flow field was established by computing the velocity and pressure fields for three different grids: 64×64 , 76×76 and 100×100 . These grid sizes are deceptively large, because the solution domain for the rotated cavity has many nodes which are outside both the fluid and the cavity walls, and are therefore inactive (see Fig. 7(b)). The actual number of nodes used is considerably smaller. For example, the 64×64 grid has 43×43 nodes in the fluid and cavity walls (total number of active nodes), with 35×35 nodes in the fluid. The time steps necessary for a converged solution were $\Delta t = 0.08, 0.05$, and 0.025 for the $64 \times 64, 76 \times 76$, and 100×100 grids, respectively. As in the regular cavity, these problems were run to a dimensionless time of 40. The CPU times required for

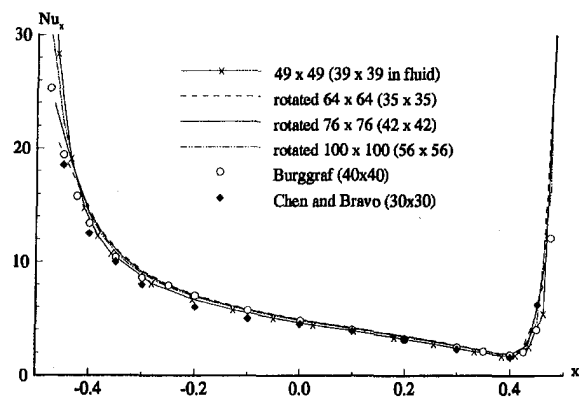


Fig. 8 Local Nusselt numbers along the heated wall for $Re = 100$, $Pr = 1$

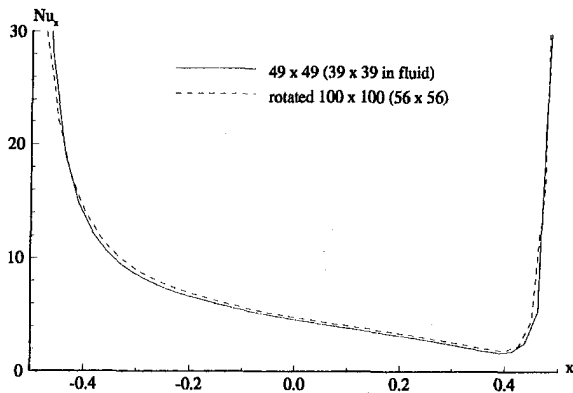


Fig. 9 Comparison of regular and rotated cavity Nusselt number curves

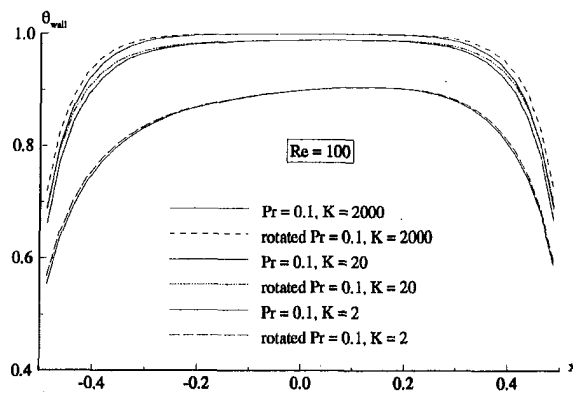


Fig. 11 Comparison of heated wall temperatures for $Pr = 0.1$

these simulations were 4700 seconds, 10,500 seconds, and 35,100 seconds.

To establish temperature field grid independence, the case of $Pr = 1, K = \infty$ was solved for each grid. The local Nusselt number curves along the heated wall for each of these grids are shown in Fig. 8 (the calculation of the Nusselt number is described in Part II of this paper). The results agree well with those of Burggraf (1966) and Chen et al. (1981). As the grid is refined, these curves move closer to the curve obtained for the regular cavity. For the sake of clarity, Fig. 9 displays only the 49×49 regular cavity curve and the 100×100 rotated cavity curve. The 100×100 grid results agree well with the 49×49 regular grid curve, so the 100×100 grid was selected for the rotated cavity computations.

The temperature fields were then computed for $Pr = 0.1$ and 1,

$K = 2, 20, 2000,$ and ∞ using the 100×100 grid. The isotherms for the different conductivity ratios with $Pr = 1$ are shown in Fig. 10. These isothermal plots are qualitatively very similar to the corresponding regular cavity results (see Carlson (1997) for more detail). The $Pr = 0.1$ isotherms also agree well with the corresponding regular cavity results.

A comparison of the heated wall temperature (inner surface) for the regular and rotated cavities with $Pr = 0.1$ is shown in Fig. 11. The agreement between the regular and rotated results is excellent in the middle of the wall. Near the wall ends, the rotated cavity wall temperatures are slightly higher than the regular cavity values, but still show good agreement.

Figure 12 compares the local Nusselt number curves of the regular and rotated cavities for the different cases being studied. The regular and rotated cavity results agree well with each other,

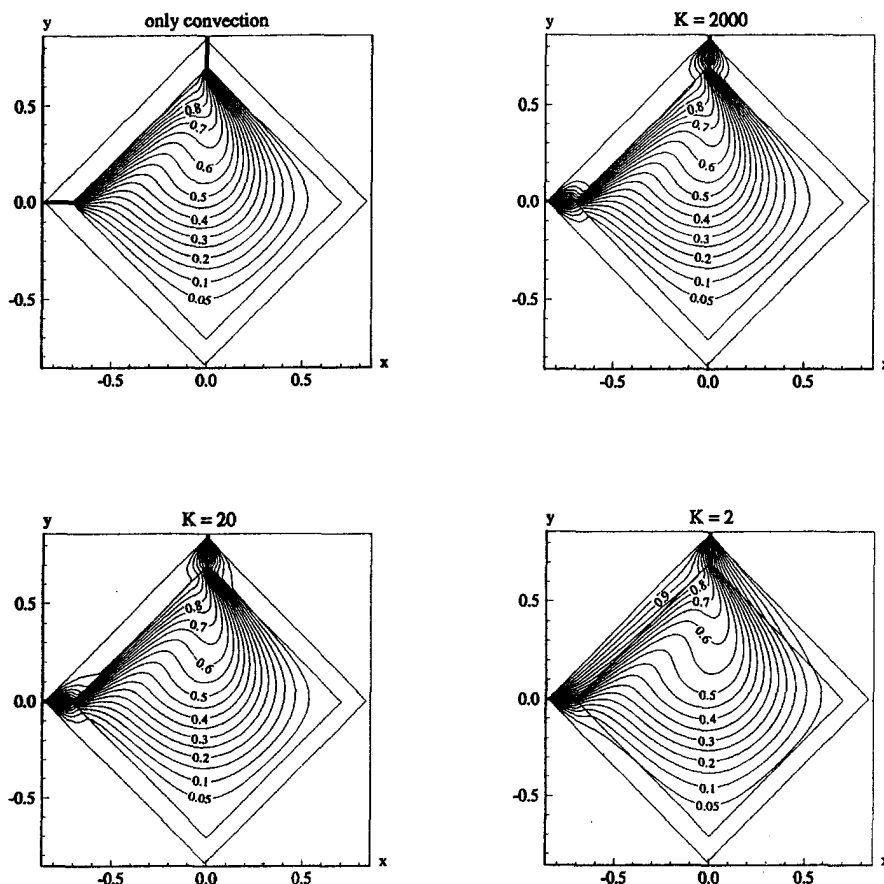


Fig. 10 Isothermal plots for the rotated cavity with $Re = 100, Pr = 1$

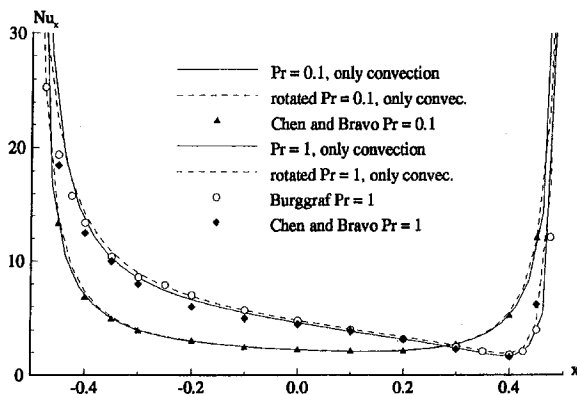


Fig. 12 Local Nusselt number comparison for convection only, $Re = 100$

and with the numerical results of other researchers. All of these cases show good agreement between the regular and rotated results.

7 Conclusions

This paper presents a diagonal Cartesian method for thermal analysis. The boundary condition and control volume methods are proposed for conjugate heat transfer over complex boundaries. It is verified that the conjugate heat transfer model used in the present simulation is valid for complex as well as regular geometries. The good agreement between the present results and those of other researchers demonstrates that, even for the extreme example of a rotated cavity where all the boundaries are complex (diagonal), accurate conjugate heat transfer results can be computed for complex geometries on a Cartesian grid. This method is applied to the design and analysis of a compact heat exchanger in Part II of this paper.

Acknowledgments

The authors would like to thank SCRI (Supercomputer Computations Research Institute) at Florida State University, and NCSA (National Center for Supercomputing Applications) at UIUC (University of Illinois at Urbana-Champaign) for the use of computer facilities in this research. The authors would also like to thank the United States Department of Energy for their support of this research through the Computational Science Graduate Fellowship Program.

References

- Bravo, R. H., 1991, "Development of the Three-Dimensional Finite Analytic Method for the Simulation of Fluid Flow and Conjugate Heat Transfer," Ph.D. thesis, Department of Mechanical Engineering, The University of Iowa.
- Burggraf, O. R., 1966, "Analytical and Numerical Studies of the Structure of Steady Separated Flows," *Journal of Fluid Mechanics*, Vol. 24, pp. 113–151.
- Cao, Y., and Faghri, A., 1991, "Performance Characteristics of a Thermal Energy Storage Module: A Transient PCM/Forced Convection Conjugate Analysis," *International Journal of Heat and Mass Transfer*, Vol. 34, No. 1, pp. 93–101.
- Cao, Y., and Faghri, A., 1992, "A Study of Thermal Energy Storage System With Conjugate Turbulent Forced Convection," *ASME JOURNAL OF HEAT TRANSFER* Vol. 114, pp. 1019–1027.
- Carlson, K. D., 1997, "Numerical Simulation of Fluid Flow and Conjugate Heat Transfer for Complex Geometries," Ph.D. thesis, Department of Mechanical Engineering, Florida State University.
- Carlson, K. D., Lin, W. L., and Chen, C. J., 1997, "Pressure Boundary Conditions of Incompressible Fluid Flows with Conjugate Heat Transfer on Non-staggered Grids, Part II: Applications," *Numerical Heat Transfer, Part A*, Vol. 32, pp. 481–501.
- Chen, C. J., Naseri-Neshat, H., and Ho, K. S., 1981, "Finite-Analytic Numerical Solution of Heat Transfer in Two-Dimensional Cavity Flow," *Numerical Heat Transfer, Part B*, Vol. 4, pp. 179–197.
- Chen, C. J., and Chen, H. C., 1984, "Development of Finite Analytic Method for Unsteady Three Dimensional Navier-Stokes Equations," *Journal of Computational Physics*, Vol. 53, No. 2, pp. 209–226.
- Doormaal, J. P., and Raithby, G. D., 1984, "Enhancements of the SIMPLE Method for Predicting Incompressible Fluid Flows," *Numerical Heat Transfer, Part B*, Vol. 7, pp. 147–163.
- Ghia, U., Ghia, K. N., and Shin, C. T., 1982, "High-Re Solutions for Incompressible Flow Using the Navier-Stokes Equations and a Multigrid Method," *Journal of Computational Physics*, Vol. 48, pp. 387–411.
- Issa, R. I., 1986, "Solution of the Implicitly Discretized Fluid Flow Equations by Operator-Splitting," *Journal of Computational Physics*, Vol. 62, pp. 40–65.
- Lin, W. L., 1997, "Diagonal Cartesian Method for Modeling of Flows over Complex Boundaries," Ph.D. thesis, Department of Mechanical Engineering, Florida State University.
- Lin, W. L., Carlson, K. D., and Chen, C. J., 1997, "Pressure Boundary Conditions of Incompressible Fluid Flows with Conjugate Heat Transfer on Non-staggered Grids, Part I: Methods," *Numerical Heat Transfer, Part A*, Vol. 32, pp. 459–479.
- Lin, W. L., Carlson, K. D., and Chen, C. J., 1998, "Diagonal Cartesian Method for Modeling of Incompressible Flows over Complex Boundaries," *Numerical Heat Transfer, Part B*, Vol. 33, pp. 181–213.
- Mori, S., Sakaribara, M., and Tanimoto, A., 1974, "Steady Heat Transfer to Laminar Flow in Circular Tube with Conduction in the Tube Wall," *Heat Transfer—Japanese Research*, Vol. 3, pp. 37–46.
- Mori, S., Shinke, T., and Sakaribara, M., 1976, "Steady Heat Transfer to Laminar Flow Between Parallel Plates with Conduction in Wall," *Heat Transfer—Japanese Research*, Vol. 5, pp. 17–25.
- Ray, S., and Srinivasan, J., 1992, "Analysis of Conjugate Laminar Mixed Convection Cooling in a Shrouded Array of Electronic Components," *International Journal of Heat and Mass Transfer*, Vol. 35, No. 4, pp. 815–822.
- Wang, H. Y., and Saulnier, J. B., 1993, "A Sensitivity Study of Material Properties for Coupled Convective-Conductive Heat Transfer Generated in an Electronic Equipment," *International Journal of Heat and Mass Transfer*, Vol. 36, No. 15, pp. 3831–3839.
- Weisberg, A., and Bau, H. H., 1992, "Analysis of Microchannels for Integrated Cooling," *International Journal of Heat and Mass Transfer*, Vol. 35, No. 10, pp. 2465–2474.

K. D. Carlson¹
Assoc. Mem. ASME

W. L. Lin²
Mem. ASME

C.-J. Chen³
Dean of Engineering and
Professor of Mechanical Engineering,
e-mail: cjchen@eng.fsu.edu
Fellow ASME

Department of Mechanical Engineering,
College of Engineering,
Florida A&M University and Florida
State University,
2525 Pottsdamer Street,
Tallahassee, FL 32310

Numerical Modeling of Conjugate Heat Transfer on Complex Geometries With Diagonal Cartesian Method, Part II: Applications

Part I of this study discusses the diagonal Cartesian method for temperature analysis. The application of this method to the analysis of flow and conjugate heat transfer in a compact heat exchanger is given in Part II. In addition to a regular (i.e., Cartesian-oriented) fin arrangement, two complex fin arrangements are modeled using the diagonal Cartesian method. The pressure drop and heat transfer characteristics of the different configurations are compared. It is found that enhanced heat transfer and reduced pressure drop can be obtained with the modified fin arrangements for this compact heat exchanger.

1 Introduction

Finned heat exchangers are devices commonly used in the electronics and computer industries to remove heat from a device. For applications with limited space, compact heat exchangers are frequently used. Flow in compact heat exchangers is often designed to be laminar. This is beneficial because laminar flow causes a smaller pressure drop across the heat exchanger compared to turbulent flow, and hence decreases power consumption. In addition, less noise is generated. However, less mixing of the fluid occurs in laminar flow, which decreases the heat transfer to the fluid. A common method for enhancing heat transfer is to add fins which are staggered in the streamwise direction. An example of this is shown in Fig. 1. Adding fins enhances the fluid mixing, enlarges the contact area over which heat transfer can occur, and increases the time it takes the fluid to meander through the heat exchanger. All of these changes augment heat transfer. The trade-off in adding fins is an increase in the pressure drop across the heat exchanger. It is important to optimize this trade-off using an accurate conjugate heat transfer analysis of the compact heat exchanger.

Bravo and Chen (1989) performed a numerical study on a short heat exchanger such as the one shown in Fig. 1. The overall dimensions of their heat exchanger were $5L \times 2L$, with wall and fin thicknesses of $0.125L$. They considered a heat exchanger without fins, one with one pair of fins and one with two pairs of fins. The fin heights used were $0.5L$, L , and $1.5L$. The study was done for Prandtl numbers of 0.7 (air) and 4 (water), and Reynolds numbers 100, 150, 300, and 500. Bravo and Chen found that increasing the Prandtl number or the Reynolds number increased the average Nusselt number (and hence the heat transfer). Additionally, increasing the number of fins or the fin height resulted in an increase in the Nusselt number and an associated increase in the

pressure drop across the heat exchanger. However, the increase in the pressure drop was several orders of magnitude larger than the increase in the heat transfer. The same conclusions were reached by Kelkar and Patankar (1987), in a similar study of the periodic fully developed region of a longer staggered fin heat exchanger. Of the different geometries studied, Bravo and Chen (1989) concluded that possibly the most efficient design (significant heat transfer augmentation with minimal increase in pressure drop) was the one shown in Fig. 1.

The study of Bravo and Chen (1989) assumed that the wall and fin temperatures were constant. In other words, the thermal conductivity of the fins and walls was considered to be infinite. However, examining the fins in Fig. 1, one expects that the fin temperature should decrease near the tip, since the fin conductivity is finite. The current authors (Carlson et al., 1997) investigated the conjugate effects of fin and wall conduction on heat transfer to the fluid flowing through the compact heat exchanger shown in Fig. 1. It was found that the constant wall temperature assumption overpredicts the heat transfer for the compact heat exchanger by five to eight percent when Re is between 50 and 500.

The finned heat exchanger increases the bulk fluid temperature at the heat exchanger exit by 70–450 percent when compared with the same heat exchanger without fins. However, the pressure drop for the finned heat exchanger is considerably larger than for the finless heat exchanger. This may be acceptable if the power required to overcome the additional pressure drop is inexpensive, or if augmentation of heat transfer in a limited amount of space is necessary. If this type of heat exchanger is to be employed in such applications, it would be beneficial to optimize the geometry in order to maximize the heat transfer and minimize the pressure drop. It was found (Carlson et al., 1997; Carlson, 1997) that there is very little heat transfer on the downstream side of the fins and on the wall above the heat exchanger entrance (i.e., in the large recirculation zones). It is also evident that the heat transfer will increase if the fin temperatures can be kept higher near the fin tips. One way to achieve this is to redesign the heat exchanger so that the fins are wider at the base and taper toward the fin tips. This design change will increase the amount of highly conductive material for heat to move through as it progresses toward the fin tips, and should increase the fin tip temperatures. The wider fin bases should also reduce the size of the recirculation zones, which will bring more rapidly moving fluid into contact with the fins and walls, thus increasing the heat transfer.

Two modified heat exchanger geometries which take these

¹ Currently at the Department of Mechanical Engineering, The University of Iowa, Iowa City, IA 52242.

² Currently Postdoctoral Research Associate, National Center for Supercomputing Applications (NCSA), University of Illinois at Urbana-Champaign (UIUC), Urbana, IL 61801.

³ To whom correspondence should be addressed.

Contributed by the Heat Transfer Division for publication in the JOURNAL OF HEAT TRANSFER. Manuscript received by the Heat Transfer Division, June 25, 1998; revision received, Jan. 22, 1999. Keywords: Computational, Conduction, Conjugate, Convection, Finned Surfaces, Flow, Fluids, Forced Convection, Geometry, Heat Transfer, Heat Exchangers, Interface, Laminar, Modeling, Numerical Methods. Associate Technical Editor: R. Douglas.

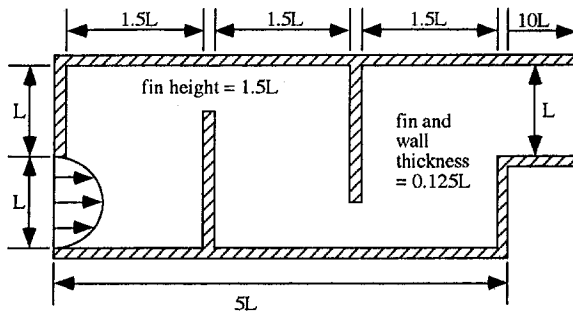


Fig. 1 Compact heat exchanger with staggered fins

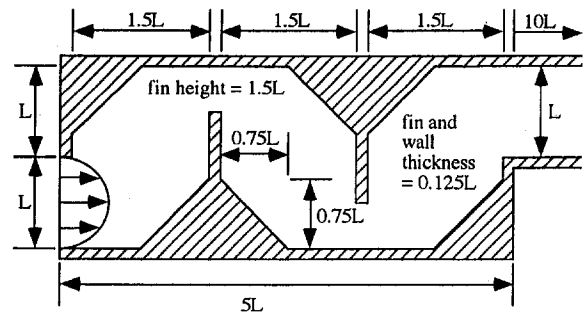


Fig. 2 Complex fin heat exchanger C1

points into consideration are studied here. The first modified geometry is shown in Fig. 2. In this complex fin heat exchanger (which will be referred to as C1), the regular fins are modified so they begin to taper to a wider base half way down the fin. The geometry directly above the entrance and below the exit of the heat exchanger are modified in a similar manner. The second complex fin heat exchanger (C2) is shown in Fig. 3. In this heat exchanger, the fins begin to taper at the fin tips instead of in the middle as in C1. Again, the areas above the entrance and below the exit are modified as well. The surfaces in C1 that are neither vertical nor horizontal are all 45-deg angles, which allows them to be modeled exactly with the diagonal Cartesian method. The corresponding surfaces in C2 are not 45-deg angles, so this geometry must be approximated. Conjugate heat transfer and pressure drop will be analyzed for these two geometries, and compared with results for the heat exchanger in Fig. 1 and a finless heat exchanger.

2 Formulation of the Problem and Numerical Approach

The fluid is assumed to be an incompressible Newtonian fluid with constant properties, and there is no heat generation in the solid or fluid domains. With these assumptions, the equations which govern laminar fluid flow and conjugate heat transfer are as follows:

fluid domain:

$$u_x + v_y = 0 \quad (1)$$

$$u_t + uu_x + vv_y = -p_x + \frac{1}{\text{Re}} (u_{xx} + u_{yy}) \quad (2)$$

$$v_t + uv_x + vv_y = -p_y + \frac{1}{\text{Re}} (v_{xx} + v_{yy}) \quad (3)$$

solid domain:

$$\theta_t = \frac{\alpha_s}{\alpha_f} \frac{1}{\text{Pe}} (\theta_{xx} + \theta_{yy}) \quad (5)$$

where the variables for time, space, velocity, pressure, and temperature have been nondimensionalized by the characteristic time L/U_{ref} , characteristic length L , characteristic velocity U_{ref} , characteristic dynamic pressure ρU_{ref}^2 and characteristic temperature difference ΔT . The Reynolds number is defined as $\text{Re} = U_{\text{ref}} L / \nu$. The Dirichlet velocity boundary condition $\mathbf{v} = \mathbf{v}_{bc}$ is applied at the walls. The temperature boundary condition at the computational (outer) boundary can be specified as either a given temperature or a given heat flux. The temperature boundary condition at the

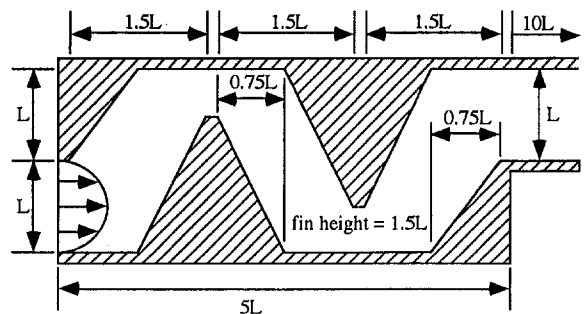


Fig. 3 Complex fin heat exchanger C2

Nomenclature

AND = dimensional average normal distance
 C_{pr} = pressure coefficient
 $E1$ = total length error
 $E2$ = dimensionless average normal distance
 LA, LO = total length of the original and approximated contours
 LD = characteristic length of the computational domain
 L = characteristic length
 Nu = local Nusselt number $\text{Nu} = hL/k_f$
 $\bar{\text{Nu}}$ = average Nusselt number
 P = dimensional pressure
 Pe = Peclet number $\text{Pe} = \text{Re} \text{Pr}$

Pr = Prandtl number $\text{Pr} = \nu/\alpha_f$
 Re = Reynolds number $\text{Re} = U_{\text{ref}} L / \nu$
 T = dimensional temperature
 U_{ref} = characteristic velocity
 h = convective heat transfer coefficient
 k_s, k_f = thermal conductivities of the solid and fluid, respectively
 n = direction normal to the solid/fluid interface
 p = dimensionless pressure
 t = dimensionless time
 u, v = dimensionless velocities in x and y -directions
 \mathbf{v} = dimensionless velocity vector
 \mathbf{v}_{bc} = dimensionless velocity vector at boundaries

x, y = dimensionless Cartesian coordinates

Greek

α_s, α_f = thermal diffusivities of the solid and fluid, respectively
 ΔT = characteristic temperature difference
 ν = kinematic viscosity of fluid
 ρ = density of fluid
 θ = dimensionless temperature
 $\theta_{b,ex}$ = dimensionless bulk exit temperature

Subscripts

f, s = fluid or solid value

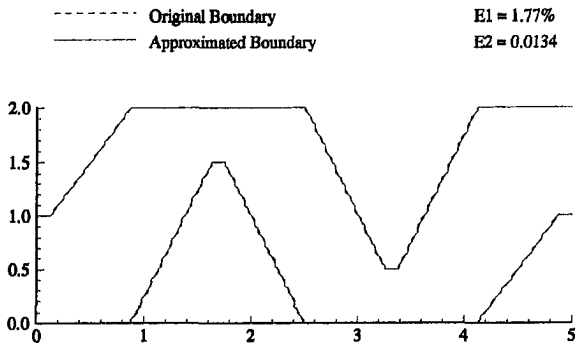


Fig. 4 Geometric approximation of heat exchanger C2

solid/fluid interface (inner boundary) is the conservation of energy flux, given as

$$(\theta_n)|_{\text{fluid}} = \frac{k_s}{k_f} (\theta_n)|_{\text{solid}} \quad (6)$$

where k_f and k_s are the fluid and solid thermal conductivities, and n is the direction normal to the interface. Enforcement of this interface temperature boundary condition provides the necessary coupling between the solid and fluid domains to simulate conjugate heat transfer.

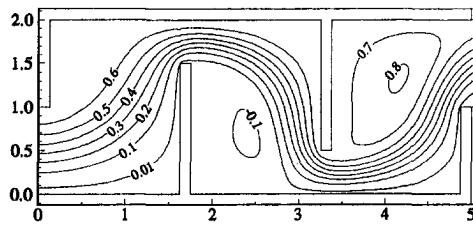
The diagonal Cartesian method (Lin et al., 1998) is used for the current simulation of flow and conjugate heat transfer in a compact heat exchanger. A structured grid is utilized for the sake of simplicity. The method approximates complex boundaries using both Cartesian grid lines and diagonal line segments. A corre-

sponding automatic and problem-independent grid generation method was formulated for complex geometries. A pressure boundary condition was also developed to enforce mass conservation near complex boundaries (Lin et al., 1998). The method, based on cell-centered nodes on a nonstaggered grid, uses ghost boundary nodes and boundary velocity information to avoid specification of pressure values on the boundaries. For complex boundaries, an enlarged control volume method is used for the conservation of momentum and the treatment of pressure boundary conditions at diagonal surface nodes (Lin et al., 1998). The governing equations given above are discretized with the finite analytic method (Chen et al., 1981, 1984), using nine-point and five-point elements. A modified version of a PISO/SIMPLEC scheme (Pressure-Implicit with Splitting of Operators (Issa, 1986), Semi-Implicit Method for Pressure-Linked Equations—Consistent (Doormaal and Raithby, 1984)), is used to solve the discretized transport equations. The residual for a particular variable is the maximum difference (over all points in the computational domain) between the values of that variable computed at the present and previous iterations.

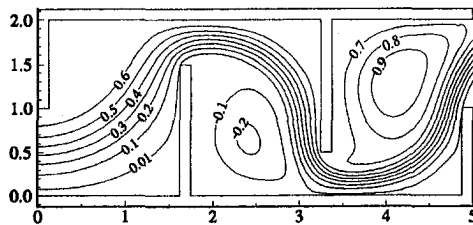
3 Approximation of Complex Boundaries and Other Computational Details

Figure 4 shows the original and approximated surfaces of heat exchanger C2. The total length error $E1 = 1.8$ percent and the dimensionless average normal distance $E2 = 0.013$. The total length error $E1$ and the average normal distance $E2$ are defined in the following equations (Lin et al., 1998):

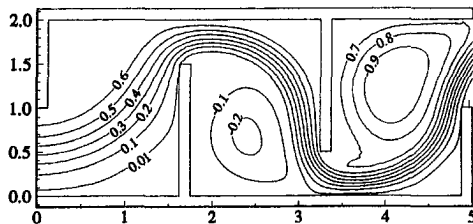
$$E1 = \frac{|LO - LA|}{LO} \times 100 \text{ percent} \quad (7)$$



(a) Re = 50

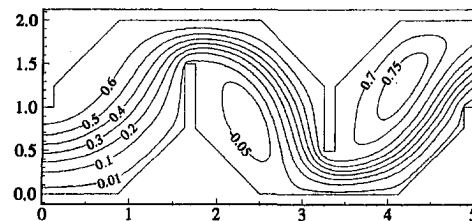


(b) Re = 200

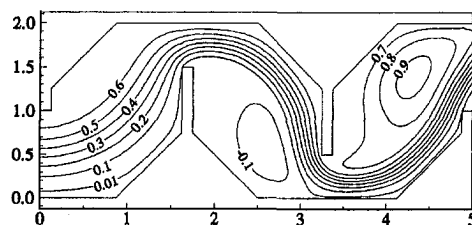


(c) Re = 500

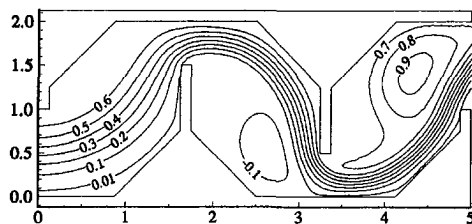
Fig. 5 Streamline plots for regular fin heat exchanger



(a) Re = 50



(b) Re = 200



(c) Re = 500

Fig. 6 Streamline plots for heat exchanger C1

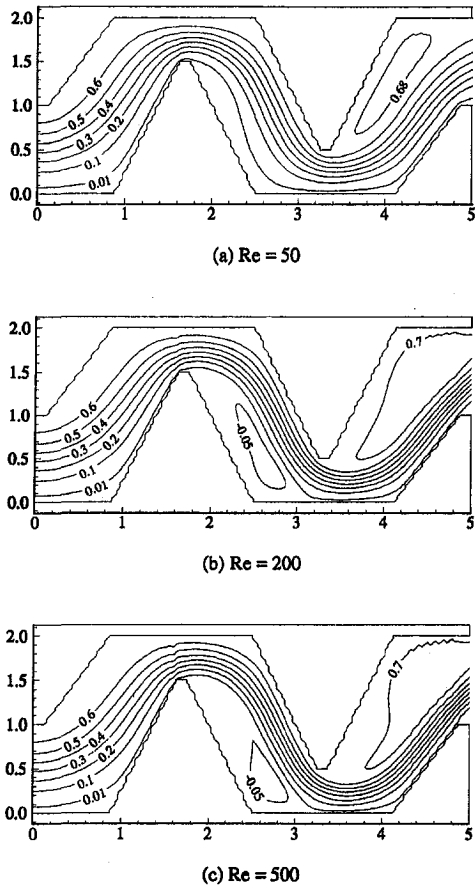


Fig. 7 Streamline plots for heat exchanger C2

$$E2 = \frac{AND}{LD} \quad (8)$$

where LO and LA are the total length of the original contour and the approximated one, respectively. AND is the dimensional average normal distance, and LD is the characteristic length of the computational domain. The detailed definition and calculation of LO , LA , LD , and AND are given by Lin et al. (1998). Based on these numbers and a visual inspection of Fig. 4, this is a good approximation of the complex surfaces.

This study investigates the conjugate effects of fin and wall conduction on heat transfer to the fluid flowing through the compact heat exchangers shown in Figs. 2 and 3. The inlet flow has a parabolic velocity profile with a maximum dimensionless velocity

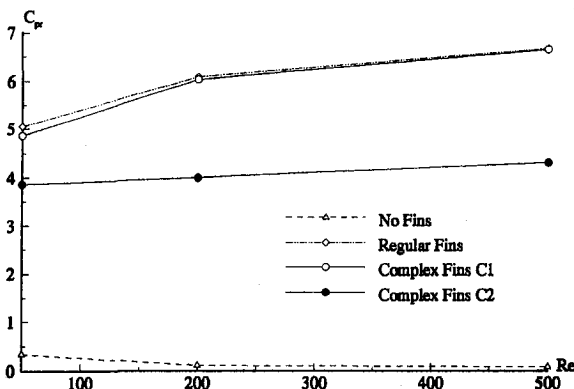


Fig. 8 Pressure coefficient comparison for different heat exchangers

$u_{max} = 1.0$ (i.e., the characteristic velocity is $U_{ref} = U_{max}$) and a uniform dimensionless temperature $\theta = 0.0$. The temperature of the outer wall of the heat exchanger is held constant at $\theta = 1.0$. The dimensionless temperature θ is defined as $\theta = (T - T_{in}) / (T_w - T_{in})$, where T_{in} is the inlet temperature and T_w is the constant outer wall temperature.

The outlet channel extends a length $10L$ downstream of the heat exchanger, and the outlet boundary conditions are taken as fully developed at the end of this channel. In fact, the problem was initially solved with outlet channel lengths from $5L$ to $15L$. The length of the outlet channel did not significantly affect the flow or temperature fields within the heat exchanger, so the $10L$ outlet channel was selected. The walls of the outlet channel are insulated. The material selected for the heat exchanger is aluminum ($k_s = 273$ W/m-K), and the working fluid used in this study is water ($Pr = 4.0$, $k_f = 0.63$ W/m-K), giving a conductivity ratio $K = k_s/k_f = 376$. The Reynolds numbers used in this study are $Re = 50, 200$, and 500 , where Re is based on the inlet height L and the maximum inlet velocity U_{max} .

The pressure drop across the heat exchanger is characterized by the pressure coefficient C_{pr} defined as

$$C_{pr} = \frac{P_{in} - P_{ex}}{\rho U_{ref}^2} = p_{in} - p_{ex} = \Delta p \quad (9)$$

where P_{in} and P_{ex} are the average pressures across the heat exchanger inlet and exit, respectively.

The Nusselt number is used in this study to compare heat transfer characteristics. The local Nusselt number is defined as

$$Nu = \frac{hL}{k_f} \quad (10)$$

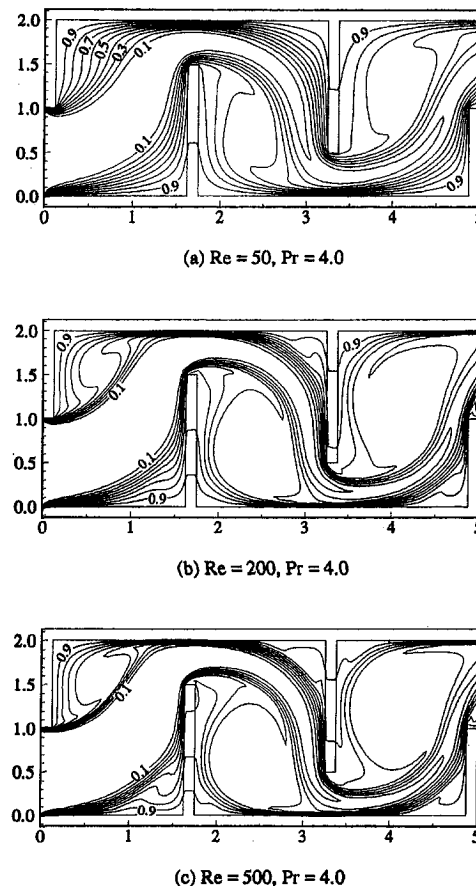


Fig. 9 Isotherms for regular fin heat exchanger, $\Delta\theta = 0.1$

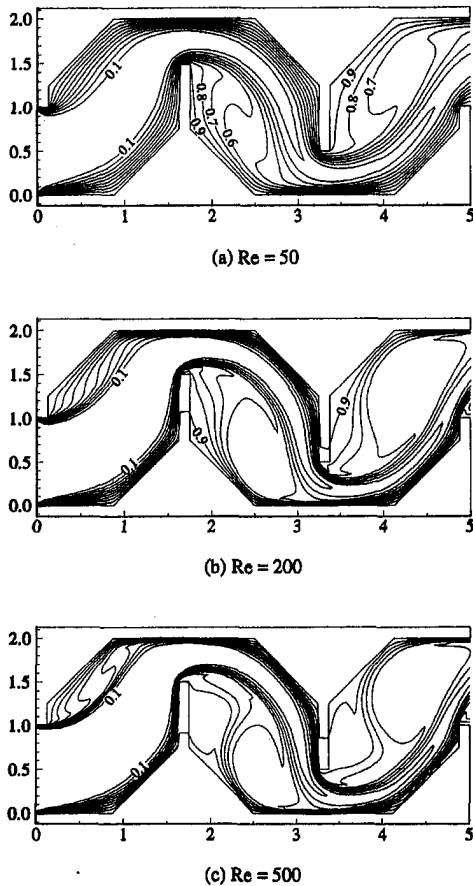


Fig. 10 Isotherms for heat exchanger C1, $\Delta\theta = 0.1$

where h is the convective heat transfer coefficient. h can be found from the following definition of the heat flux on the fluid side of the solid/fluid interface:

$$q'' = k_f \left. \frac{\partial T}{\partial N} \right|_{\text{interface}} = h(T_w - T_{in}) \quad (11)$$

Solving Eq. (11) for h , using this expression for h in Eq. (10) and nondimensionalizing gives

$$\text{Nu} = \frac{hL}{k_f} = \frac{\left. \frac{\partial T}{\partial N} \right|_{\text{interface}} L}{(T_w - T_{in})} = \left. \frac{\partial \theta}{\partial n} \right|_{\text{interface}} \quad (12)$$

where $n = N/L$ is the direction normal to the interface. The average Nusselt number is given by

$$\overline{\text{Nu}} = \frac{\int_A \text{Nu} dA}{\int_A dA} \quad (13)$$

where the area A in this equation is the total surface area (including the fin area) inside the heat exchanger. $\overline{\text{Nu}}$ is essentially the average Nusselt number per unit area, and is thus a measure of the overall heat transfer efficiency of the heat exchanger.

A 196×74 grid was utilized in this study, with a uniform grid

in the heat exchanger and a grid that is uniform in the y -direction and stretched in the x -direction in the outlet channel. To ensure steady-state, the $\text{Re} = 50$ and 200 cases were run to a dimensionless time $t = 30$, and the $\text{Re} = 500$ case was run to $t = 50$. Grid independence and determination of a steady-state time are detailed in Carlson et al. (1997). Time-step sizes $\Delta t = 0.05$, 0.0375 , and 0.025 were used for the $\text{Re} = 50$, 200 , and 500 cases to obtain a converged solution. Once the convergent flow fields were obtained, conjugate heat transfer was simulated in C1 and C2. The temperature convergence criterion for all three flows was met in 26 or fewer iterations for C1 and in 39 or fewer iterations for C2. The total CPU times required to compute the flow and temperature fields were in the range of 15,000 to 30,000 seconds, except for the $\text{Re} = 500$ cases, which required about 40,000 seconds to compute because they were run to $t = 50$ and had the smallest time step size. All computations were performed on an SGI Indigo2 workstation, which has a 200 MHz R4400 processor.

4 Conjugate Heat Transfer With Complex Fins

For the sake of reference, Fig. 5 shows the streamline plots for the three Reynolds number flows through the regular fin heat exchanger studied by Carlson et al. (1997). Figure 6 shows the same plots for heat exchanger C1. The main flow streamlines in these two figures are actually very similar, except that the recirculation zones are smaller in Fig. 6. This is due to the additional aluminum at the base of the fins, above the entrance and below the exit. The streamline plots for the flows through C2 are given in Fig. 7. Note that the recirculation zones are even smaller than those in C1 due to the reduction in channel width. For $\text{Re} = 50$, in fact, very little recirculation exists in C2. The main flow streamlines in C1 and C2 look similar for corresponding Reynolds numbers. However, the vertical portions of the fins in C1 force the flow to

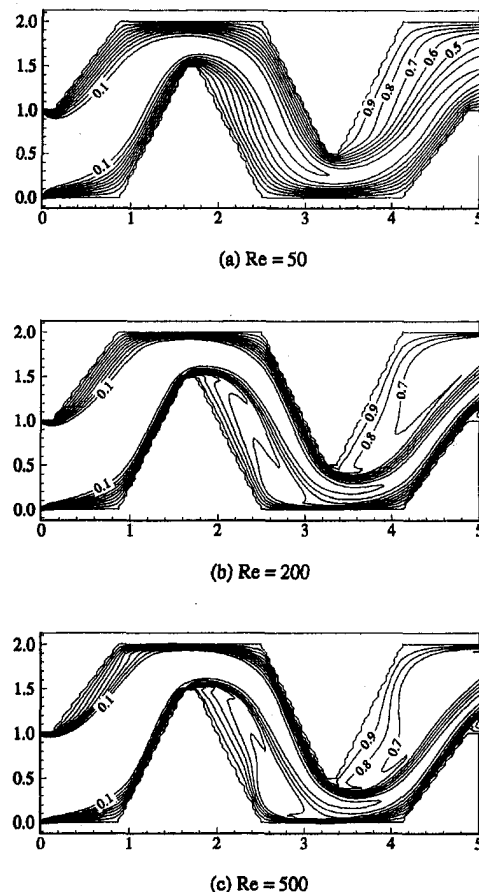
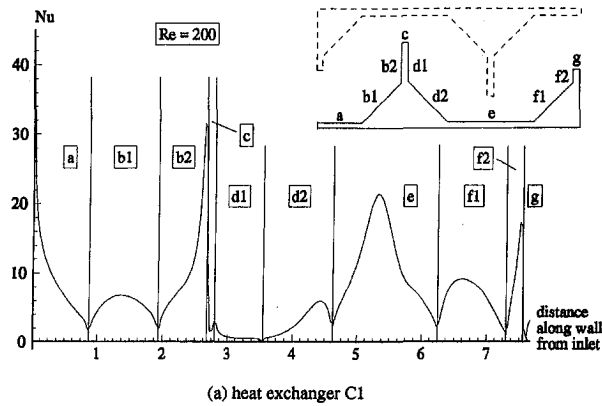
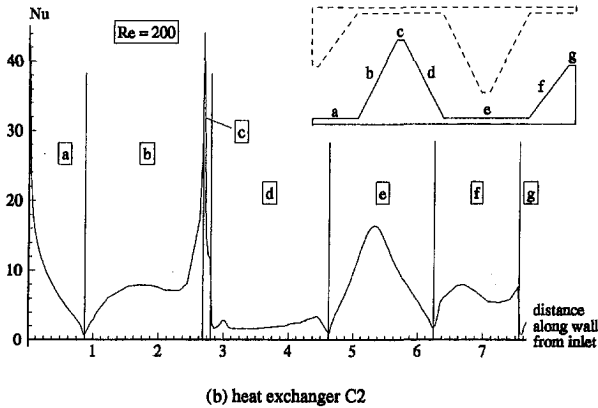


Fig. 11 Isotherms for heat exchanger C2, $\Delta\theta = 0.1$



(a) heat exchanger C1



(b) heat exchanger C2

Fig. 12 Lower wall local Nusselt number values for C1 and C2

impinge on the opposing walls rather directly, while the angled fins in C2 allow the flow to take a less winding path. The fluctuations in the streamlines in Fig. 6 are the result of numerical integration, not a physical phenomenon.

The pressure coefficients computed for the three different Reynolds number flows through C1 and C2 are compared to the regular fin heat exchanger and the finless heat exchanger in Fig. 8. The pressure coefficient in C1 is slightly lower than that found in the regular fin heat exchanger for $Re = 50$, but as the Reynolds number increases, the pressure coefficients for the two heat exchangers seem to converge to the same value. The similarity in C_{pr} between C1 and the regular fin heat exchanger is not surprising, considering the similarity of the main flow streams in these two heat exchangers. The pressure coefficient in C2 is significantly lower for all three Reynolds numbers. It appears that fins tapered all the way to the tip provide a shorter, smoother flow path than regular fins or the fins in C1.

The isotherms for the regular fin heat exchanger, heat exchanger C1 and heat exchanger C2 are presented in Figs. 9, 10, and 11, respectively. Notice that the temperatures near the fin tips in both C1 and C2 are indeed higher than for the regular fin heat exchanger. In fact, the fins in C2 are essentially isothermal for all three Reynolds numbers because of the large amount of highly conductive aluminum used in these fins. Also, the isotherms near the heat exchanger surfaces in C1 and C2 are packed more closely together, indicating higher temperature gradients than were found with regular fins. Both higher fin tip temperatures and higher thermal gradients in the fluid near the aluminum surfaces will improve heat transfer to the fluid.

The local Nusselt numbers along the walls of C1 and C2 for $Re = 200$ are shown in Figs. 12 (bottom walls) and 14 (top walls). The same plots for the regular fin heat exchanger are shown in Figs. 13 (bottom wall) and 15 (top wall). Comparing Figs. 12 and 13, it is seen that the local Nusselt number profiles for the regular

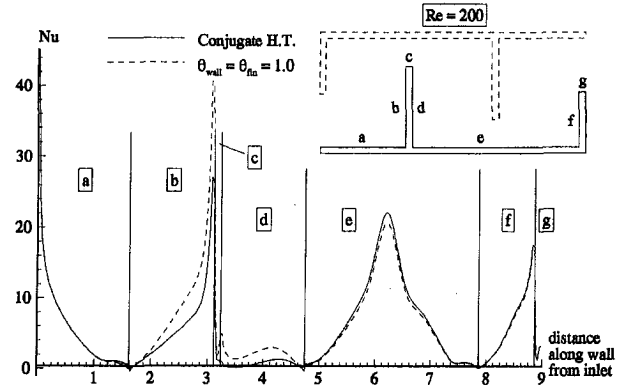
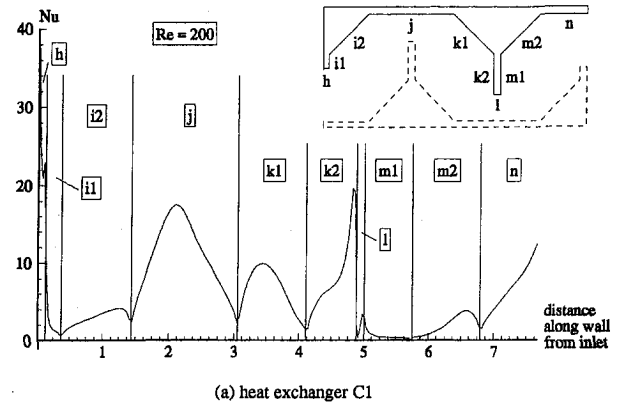
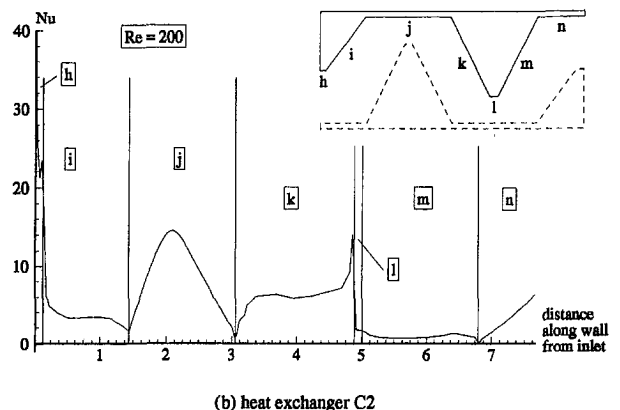


Fig. 13 Lower wall local Nusselt number values for regular fin heat exchanger

fin heat exchanger, C1 and C2 are all similar. However, there are several areas in C1 and C2 that have a higher local Nusselt number than in the regular fin heat exchanger, such as the left half of b1 and f1 in heat exchanger C1 and the left half of b and f in heat exchanger C2. Also, the higher fin tip temperatures in C1 and C2 cause an increase in the local Nusselt number near the fin tip compared to the regular fin value. The local Nusselt number in region e of C1 is larger than in region e of C2, which is probably the result of C1 forcing the flow stream more directly into the wall at e. This will increase the temperature gradient and hence the heat transfer. If Fig. 14 is compared to Fig. 15, these same trends are evident in corresponding regions of the upper walls. Larger values of the local Nusselt number in several areas of C1 and C2 indicate that the heat transfer efficiency in these heat exchangers should be higher than for the regular fin design.



(a) heat exchanger C1



(b) heat exchanger C2

Fig. 14 Upper wall local Nusselt number values for C1 and C2

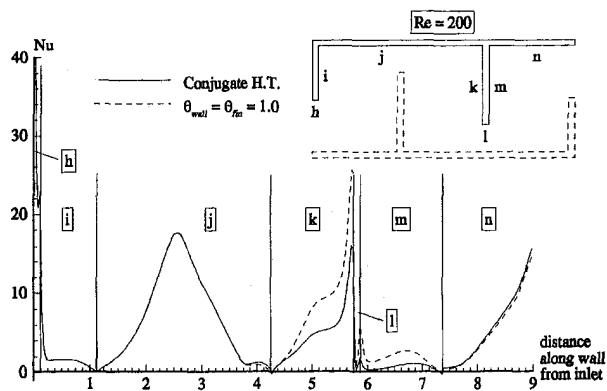


Fig. 15 Upper wall local Nusselt number values for regular fin heat exchanger

The average Nusselt numbers for C1, C2, the regular fin and finless heat exchangers are shown as a function of Reynolds number in Fig. 16. It is seen that for $Re = 50$, C1 and C2 have about the same efficiency, and both are more efficient than the regular fin and finless heat exchangers. As Re increases, C1 becomes more efficient than C2, but C2 is still more efficient than the regular fin heat exchanger.

Figure 17 compares the exit bulk temperatures of the different heat exchangers. It is seen that C1 produces an exit bulk temperature slightly higher than the regular fin heat exchanger. The exit temperatures of C2 are lower than that of the regular fin heat exchanger and C1, but still considerably higher than the exit temperatures generated in the finless heat exchanger.

5 Conclusions

The results presented in this part of the paper indicate that heat exchanger C1 increases the heat transfer compared to the regular fin heat exchanger, incurring about the same pressure drop. C2, on the other hand, has comparable heat transfer characteristics, but the pressure drop is much lower than in the regular fin heat exchanger or in C1. For Reynolds numbers around 50, C2 seems to be the best choice, transferring slightly less heat than C1 and the regular fin heat exchanger, but with a much smaller pressure drop. For

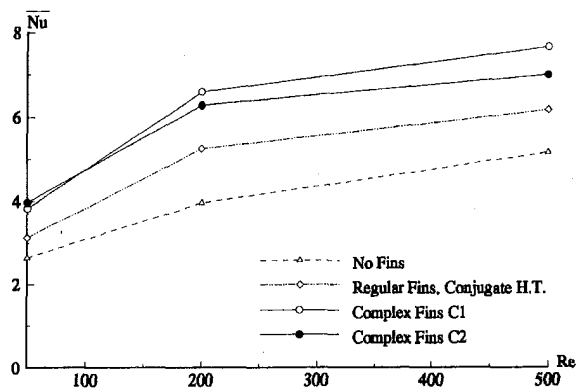


Fig. 16 Average Nusselt numbers for the heat exchangers studied

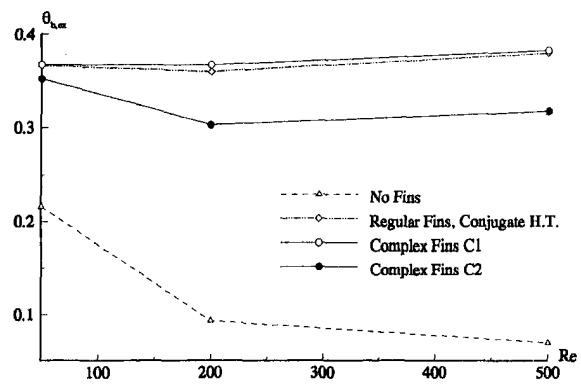


Fig. 17 Exit bulk temperatures for the heat exchangers studied

larger Reynolds numbers, the choice of heat exchanger depends on the situation. If the cost of the power required to overcome the pressure drop is a concern, then C2 is the best choice. If the maximum amount of heat transfer is desired, then C1 is appropriate.

Acknowledgments

The authors would like to thank SCRI (Supercomputer Computations Research Institute) at Florida State University, and NCSA (National Center for Supercomputing Applications) at UIUC (University of Illinois at Urbana-Champaign) for the use of computer facilities in this research. The authors would also like to thank the United States Department of Energy for their support of this research through the Computational Science Graduate Fellowship Program.

References

Bravo, R. H., and Chen, C. J., 1989, "Heat Flow Characteristics of a Finned Heat Exchanger," *Heat Transfer in Convective Flows*, ASME HTD-Vol. 107, ASME, New York, pp. 25-30.

Carlson, K. D., 1997, "Numerical Simulation of Fluid Flow and Conjugate Heat Transfer for Complex Geometries," Ph.D. thesis, Department of Mechanical Engineering, Florida State University.

Carlson, K. D., Lin, W. L., and Chen, C. J., 1997, "Pressure Boundary Conditions of Incompressible Fluid Flows with Conjugate Heat Transfer on Non-staggered Grids, Part II: Applications," *Numerical Heat Transfer, Part A*, Vol. 32, pp. 481-501.

Chen, C. J., Naseri-Neshat, H., and Ho, K. S., 1981, "Finite-Analytic Numerical Solution of Heat Transfer in Two-Dimensional Cavity Flow," *Numerical Heat Transfer, Part B*, Vol. 4, pp. 179-197.

Chen, C. J., and Chen, H. C., 1984, "Development of Finite Analytic Method for Unsteady Three Dimensional Navier-Stokes Equations," *Journal of Computational Physics*, Vol. 53, No. 2, pp. 209-226.

Doormaal, J. P., and Raithby, G. D., 1984, "Enhancements of the SIMPLE Method for Predicting Incompressible Fluid Flows," *Numerical Heat Transfer, Part B*, Vol. 7, pp. 147-163.

Issa, R. I., 1986, "Solution of the Implicitly Discretized Fluid Flow Equations by Operator-Splitting," *Journal of Computational Physics*, Vol. 62, pp. 40-65.

Kelkar, K. M., and Patankar, S. V., 1987, "Numerical Prediction of Flow and Heat Transfer in a Parallel Plate Channel With Staggered Fins," *ASME JOURNAL OF HEAT TRANSFER*, Vol. 109, pp. 25-30.

Lin, W. L., Carlson, K. D., and Chen, C. J., 1997, "Pressure Boundary Conditions of Incompressible Fluid Flows with Conjugate Heat Transfer on Non-staggered Grids, Part I: Methods," *Numerical Heat Transfer, Part A*, Vol. 32, pp. 459-479.

Lin, W. L., Carlson, K. D., and Chen, C. J., 1998, "Diagonal Cartesian Method for Modeling of Incompressible Flows over Complex Boundaries," *Numerical Heat Transfer, Part B*, Vol. 33, pp. 181-213.

Recovery of Temperature and Species Concentration Profiles in Flames Using Low-Resolution Infrared Spectroscopy

F. Yousefian
Engineer, Researcher

M. Sakami
Département des Sciences Appliquées,
Université du Québec à Chicoutimi,
Quebec, G7H 2B1
Canada

M. Lallemand
Laboratoire d'Etudes Thermiques
(U.M.R. 6608 C.N.R.S.),
ENSMA,
86960 Poitiers-Futuroscope,
France
e-mail: lallemand@banzai.univ-poitiers.fr

The temperature and species distributions in semi-transparent gaseous axisymmetric objects are retrieved by carrying out the inversion of their directional low-resolution spectral transmission and/or spectral emission in the infrared by using methods based on the solution of the radiative transfer equation. The validity domains of the hypothesis on which the low resolution inversion methods are based are discussed by comparison with the corresponding exact radiative properties generated by line-by-line descriptions. A propane-air laminar premixed flame is experimentally studied. The infrared data are collected for the (ν_3) band of CO_2 , either by a directional scanning (at a fixed frequency) or by a frequency scanning (in a fixed direction). Depending on the data acquisition methods, two different reconstruction techniques are used. For spatial scanning, a generalized Abel transformation or the regularized Murio's method, is utilized. For spectral scanning the recovered results are carried out by the Chahine-Smith method. For both techniques, profile reconstructions are worked out accounting for a spectral data bank based on the narrow statistical band model. Finally, thermal and CO_2 concentration mappings of the premixed flame are presented.

Introduction

Diagnostics of hot gases, flames, and plasmas from spectroscopic statements can be conducted either in high resolution by means of tunable laser diodes, or in low resolution by working with infrared Fourier transform spectrometers. As the high-temperature gas flows of interest are rather nonisothermal, for both techniques the obtained values (temperatures and species concentrations) are averaged over the experimental line of sight and are dependent on the spatial resolution. Using inverse radiative analysis, which is based on the solution of the radiative transfer equation (RTE), recoveries of steady temperatures and species distributions in semi-transparent media (STM) are feasible in high resolution, (Yousefian and Lallemand, 1997), as well as in low resolution, by collecting emission and absorption data as a function of a control parameter which can be either directional or spectral.

As this paper deals with the low-resolution techniques, only corresponding references will be quoted here, (for a general survey see Lallemand and Soufiani (1995)). Zhang and Cheng (1986) have determined the temperature profile of axisymmetric combustion-gas from low-resolution emission/transmission infrared data. Hall and Bonczyk (1990) have used a similar technique to reconstruct the absorption coefficient and temperature profiles in ethylene and iso-octane sooting flames. Markham et al. (1990) have used FTIR emission/transmission spectroscopy for measurements of particle concentration and temperature. A species and temperature tomographic reconstruction based on FTIR emission and transmission spectra has been developed for a sooting diffusion flame by Best et al. (1991). The case of axisymmetric propane-air flames was solved by Sakami and Lallemand (1993, 1994). Menguc and Dutta (1994) have proposed a tomographic re-

construction technique for the determination of the extinction and scattering distribution in axisymmetric media. Li and Ozisik (1994) have used an optimization technique for the source profiles reconstruction in plane parallel and cylindrical STM from directional radiative properties. Recently, Char and Yeh (1996) have determined by emission the temperature for an open propane flame.

The present study concerns reconstruction techniques for laminar premixed propane-air flames, based on low-resolution experimental emission and/or transmission data, collected from a Fourier Transform infrared spectrometer in the (ν_3) band of CO_2 (at 2295 cm^{-1}) for limited optical thickness. Two retrieval techniques are used:

- 1 the solution of the coupled absorption/emission problem, in which data stems from a wide band spectrum by spatially scanning the semi-transparent object over a set of lines of sight. Once the CO_2 absorption coefficient profile is retrieved by a generalized Abel transformation, as well as, a conjugate-adjoint gradient method, the CO_2 concentration profiles and the temperature profiles of the flame, can be recovered, leading to its thermal cartography;
- 2 the combination of the Chahine and the Smith spectral methods exploiting only emission data measurements for a set of discrete frequencies spanning the 2390 cm^{-1} band of CO_2 , which offers the benefit of observing the flame on a single line of sight.

For these problems, the range of validity of the various hypothesis made (on which the large band inversion methods rest on) are examined and discussed in the framework of a data bank based on the narrow statistical band model.

Radiative Analysis

Monochromatic Absorption and Emission of an Axisymmetric Semi-Transparent Medium. Let us consider an axi-

Contributed by the Heat Transfer Division for publication in the JOURNAL OF HEAT TRANSFER. Manuscript received by the Heat Transfer Division, Jan. 5, 1998; revision received Oct. 1, 1998. Keywords: Heat Transfer. Associate Technical Editor: P. Menguc.

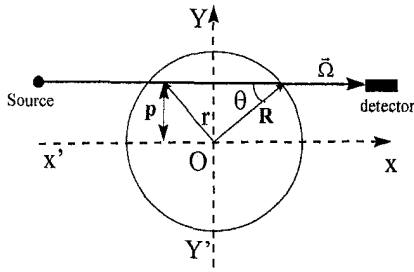


Fig. 1 Geometry in a cross section of the axisymmetric flame

symmetric emitting-absorbing, but nonscattering, medium (Fig. 1). In each cross section a temperature distribution $T(r)$, and a CO_2 molar fraction distribution $x_{\text{CO}_2}(r)$ are set up. For any point external to the medium, in the specified line of sight Ω (orthogonal to the symmetry axis of the object), one can observe the projections of both the outgoing emission and the transmitted radiation. Let $I_\nu(p)$ be the spectral intensity associated to the position p of the line of sight Ω with respect to the axis $X'OX$ and $t_\nu(p)$ be the corresponding transmittivity of the object. In a nonuniform medium the local specific intensity $I_\nu(s, p)$ which is a function of position and direction is solution of the radiative transfer equation (RTE) which can be expressed for a medium of unit refractive index as follows:

$$\frac{dI_\nu(s, p)}{ds} + \kappa_\nu(s)I_\nu(s, p) = \kappa_\nu(s)I_\nu^0[T(s)], \quad (1)$$

$\kappa_\nu(s)$ being the spectral absorption coefficient at a position s and $I_\nu^0[T(s)]$ being the intensity of blackbody radiation at the local temperature (the Planck's function). For an axisymmetric medium at local thermodynamic equilibrium, the outgoing spectral emission intensity associated to the projection parameter p , is given by

$$I_\nu^{\text{out}}(p) = 2\sqrt{t_\nu(p)} \left\{ \int_p^R \frac{\kappa_\nu(r)I_\nu^0[T(r)]r}{\sqrt{r^2 - p^2}} \times \cosh \left[\int_p^r \frac{\kappa_\nu(r')r'dr'}{\sqrt{r'^2 - p^2}} \right] dr \right\} \quad (2)$$

where R is an arbitrary working radius, while the transmittivity $t_\nu(p)$ is related to the absorption profile by the Abel equation

$$\text{Log } t_\nu(p) = \left[-2 \int_p^R \frac{\kappa_\nu(r)}{\sqrt{r^2 - p^2}} r dr \right]. \quad (3)$$

From an experimental point of view since the propane-air flame measurements were carried out by means of a Fourier transform infrared spectrometer of limited resolution (ranging from 1 to 10 cm^{-1}), the measured quantities are the low-resolution intensity $\bar{I}_\nu(p)$ leaving the object and its transmittivity $\bar{t}_\nu(p)$. According to Eqs. (2) and (3) the integrated transmittivity and integrated emission over a frequency interval $\Delta\nu$, centered on the frequency ν_i , are, respectively,

$$\begin{aligned} \bar{I}_{\nu_i}(p) &\equiv \frac{1}{\Delta\nu} \int_{\Delta\nu} I_\nu(p) d\nu \\ &= \frac{1}{\Delta\nu} \int_{\Delta\nu} \left[\exp \left(-2 \int_p^R \frac{\kappa_\nu(r)}{\sqrt{r^2 - p^2}} r dr \right) \right] d\nu \quad (4) \end{aligned}$$

$$\begin{aligned} \bar{I}_{\nu_i}(p) &\equiv \frac{1}{\Delta\nu} \int_{\Delta\nu} I_\nu^{\text{out}}(p) d\nu \\ &= \frac{1}{\Delta\nu} \int_{\Delta\nu} 2\sqrt{t_\nu(p)} \left\{ \int_p^R \frac{\kappa_\nu(r)I_\nu^0[T(r)]r}{\sqrt{r^2 - p^2}} \right. \\ &\quad \left. \times \cosh \left[\int_p^r \frac{\kappa_\nu(r')r'dr'}{\sqrt{r'^2 - p^2}} \right] dr \right\} d\nu. \quad (5) \end{aligned}$$

Validity of the Spectroscopic Large Band Approximation.

The proposed inversion methods rest on the replacement of Eqs. (4)–(5) by the following expressions:

$$\bar{I}_{\nu_i}(p) = \exp \left(-2 \int_p^R \frac{\bar{\kappa}_{\nu_i}(r)}{\sqrt{r^2 - p^2}} r dr \right) \quad (6)$$

$$\begin{aligned} \bar{I}_{\nu_i}(p) &= 2\sqrt{\bar{t}_{\nu_i}(p)} \left\{ \int_p^R \frac{\bar{\kappa}_{\nu_i}(r)I_{\nu_i}^0[T(r)]r}{\sqrt{r^2 - p^2}} \right. \\ &\quad \left. \times \cosh \left[\int_p^r \frac{\bar{\kappa}_{\nu_i}(r')r'dr'}{\sqrt{r'^2 - p^2}} \right] dr \right\}, \quad (7) \end{aligned}$$

$\bar{\kappa}_{\nu_i}(r)$ being the mean absorption coefficient over the spectral domain $\Delta\nu$ at the frequency ν_i ; defined as

$$\bar{\kappa}_{\nu_i}(r) = \frac{1}{\Delta\nu} \int_{\Delta\nu} \kappa_\nu(r) d\nu \quad (8)$$

and $\bar{t}_{\nu_i}(p)$ being the mean spectral transmittivity given by

$$\bar{t}_{\nu_i}(p) = \frac{1}{\Delta\nu} \int_{\Delta\nu} \exp \left(- \int_0^{s(p)} \kappa_\nu ds \right) d\nu. \quad (9)$$

Depending on the spectral resolution of the measurements, exploitation of formulae (4)–(5) or (6)–(7) might lead to different retrieved results and it is of primary interest to specify the range of validity for the assumptions: $\bar{I}_{\nu_i}(\kappa) = t_\nu(\bar{\kappa}_{\nu_i})$ and $\bar{I}_{\nu_i}(p) = I_\nu(p, \bar{\kappa}_{\nu_i}, \bar{t}_{\nu_i})$.

The Synthetic Spectra Generation. The mean absorption coefficient corresponding to a given temperature T , a total pressure P and a molar fraction x_{CO_2} can be expressed as

$$\bar{\kappa}(P, T) = \bar{\kappa}(P = 1 \text{ atm}, T) P x_{\text{CO}_2} \quad (10)$$

accordingly the optical thickness is defined as

$$\tau = P \int_0^d \bar{\kappa}[T(s)] x(s)_{\text{CO}_2} ds. \quad (11)$$

We have reconstituted for CO_2 , in a spectral range of 25 cm^{-1} near 2295 cm^{-1} , a pseudo line-by-line spectra and compared the exact average transmittivity $\bar{t}_\nu(\kappa)$ given by Eq. (9) over band widths of 0.1 up to 25 cm^{-1} , with the corresponding transmittivities $t_\nu(\bar{\kappa})$ calculated from the mean absorption coefficient $\bar{\kappa}$ coming from the synthetic spectrum. In doing this, we have used the data bank of EM2C Laboratory (Soufiani and Taine, 1994) founded upon the narrow statistical band model (NSBM) and the exponential tailed model of Malkmus.

One considers N lines covering the spectral interval $\Delta\nu$, if $\bar{\delta}$ denotes the mean space between two lines at temperature T , $N = \Delta\nu/\bar{\delta}$. All lines are assumed to be (1) of Lorentzian profile

$$f(\nu - \nu_l) = \frac{1}{\pi} \frac{\gamma_l}{\gamma_l^2 + (\nu - \nu_l)^2} \quad (12)$$

where γ_l represents the line midheight half-width of line l , and (2) of same average half-width $\bar{\gamma}$,

$$\bar{\gamma} = \frac{1}{N} \sum_{l=1}^N \gamma_l. \quad (13)$$

The temperature dependence of $\bar{\gamma}$ is taken into account according to the expression

$$\bar{\gamma} = 0.07 \frac{P}{P_s} \left(\frac{T_s}{T} \right)^{0.7} \quad (14)$$

where P_s denotes the standard pressure at 1 atm and T_s is a reference temperature.

Accordingly, the absorption coefficient of the line centered at the frequency, ν_l , will be written as

$$\kappa(\nu - \nu_l) = \frac{1}{\pi} \frac{S_l \bar{\gamma}}{\bar{\gamma}^2 + (\nu - \nu_l)^2}, \quad (15)$$

S_l being the intensity associated with each line l . The S_l are distributed according to the Malkmus probability distribution function

$$P(S) = \frac{1}{S \ln R_m} (e^{-S/S_m} - e^{-R_m S/S_m}), \quad (16)$$

the two constants S_m and R_m being defined bellow.

The synthetic spectrum is generated by the following procedure. For a defined temperature and pressure and a given set of band parameters \bar{k} and $1/\delta$, taken from the EM2C data bank (do not confuse \bar{k} and $\bar{\kappa}$ as defined by Eq. (8)), values of the S_m and R_m are given, according to Rivière (1994), by

$$S_m = \pi \bar{k} \delta \quad (17)$$

and

$$\ln R_m = \pi \frac{\bar{\delta}}{\delta}, \quad (18)$$

where $1/\delta$ is the reciprocal of the mean space between the lines (active or inactive, thus temperature independent) in the complete physical spectrum in the domain $\Delta\nu$ as given by Soufiani (1995). A $P(S)$ value is randomly chosen in the interval $[0, 1]$, then by inverting Eq. (16) and using Eq. (15) a possible single line is constructed and is randomly distributed in the domain $\Delta\nu$. This process, repeated N times, would generate a pseudo line-by-line spectrum covering the interval of frequency $\Delta\nu$.

A mean absorption coefficient $\bar{\kappa}_\nu$, is defined in place of Eq. (8), as

$$\bar{\kappa} = \frac{1}{N\delta} \sum_{l=1}^N S_l \quad (19)$$

if $|\bar{k}_\nu - \bar{\kappa}_\nu|/\bar{k}_\nu > 10^{-2}$, the generated spectrum will be rejected and the process will be repeated until \bar{k}_ν and $\bar{\kappa}_\nu$ will be in a preselected agreement.

In Figs. 2(a)–(b) typical results are shown for a spectral region of 25 cm^{-1} centered on the frequency 2375 cm^{-1} of two isothermal columns of CO_2 corresponding to $T = 700 \text{ K}$ with $N = 583$ and $T = 1900 \text{ K}$ with $N = 5142$. The very different dynamics of these two spectra should be noted.

According to the above procedure the errors due to the large band approximation have been carried out for both the transmission and the emission case for a simulated non-isothermal flame on the basis of the NSBM and the simple Curtis-Godson approximation. A flame of radius 2 cm is considered in a cross section of which are set up linear temperature profiles, $T(r)(\text{K}) = 700 r(\text{cm}) + 600$, and concentration profiles in CO_2 , $x_{\text{CO}_2} = 1.r(\text{cm})$. The results are illustrated in Fig. 3(a)–(b) as a function of the optical thickness (Eq. (11)). One can observe an optimum accuracy for a resolution of $\Delta\nu = 4 \text{ cm}^{-1}$ with a relative error in transmission, as well as in emission, less than

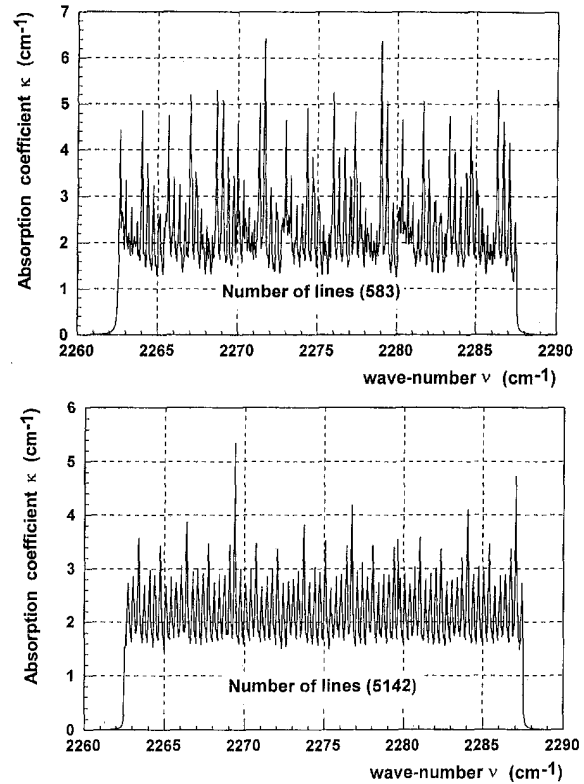


Fig. 2 Examples of synthetic spectra of CO_2 in the range $2263\text{--}2288 \text{ cm}^{-1}$ $T = 700 \text{ K}$ (Top) and $T = 1900 \text{ K}$ (bottom)

one percent up to $\tau = 0.5$. Thus, in the following experimental study, our investigations will be limited up to this optical thickness value for the premixed flames.

Spatial Scanning: Absorption, Temperature, and Concentration Profiles in Hot Gases by the Abel Transformation

The Inversion Techniques. By writing Eq. (3) as $W_\nu(p) = \text{Log} [I_\nu(p)]$, the mean absorption coefficient $\bar{\kappa}_\nu(r)$ can be immediately obtained from the Abel inversion formulae:

$$\bar{\kappa}_\nu(r) = -\frac{1}{\pi} \int_r^R \frac{[W_\nu(p)]'}{\sqrt{p^2 - r^2}} dp \quad (20)$$

where $[W(p)]'$ denotes the derivative of the low resolution measured quantity $W_\nu(p)$.

Once the absorption profile is obtained, by inverting the emission data $M_\nu(p) = I_\nu^{\text{out}}(p)/2\sqrt{I_\nu(p)}$, the temperature profile can be retrieved by another Abel inversion of Eq. (7), as

$$\bar{\kappa}_\nu(r) I_\nu^{\text{out}}(r) = -\frac{1}{\pi} \int_r^R \frac{[M_\nu(p)]'}{\sqrt{p^2 - r^2}} \cosh \int_p^R \frac{\bar{\kappa}_\nu(r') r' dr'}{\sqrt{r'^2 - p^2}} dp. \quad (21)$$

The $\bar{\kappa}_{\text{CO}_2}(r)$ and the $T(r)$ being determined in a cross section, the concentration profile of x_{CO_2} is carried out by means of Eq. (10) where we have taken $\bar{\kappa}_\nu(P = 1 \text{ atm}, T(r)) = \bar{k}_\nu[P = 1 \text{ atm}, T(r)]$ from the EM2C data bank at pressure $P = 1 \text{ atm}$ and at the local temperature $T(r)$.

Methods of Resolution. The Abel inversion in Eqs. (20)–(21) is a classic ill-posed problem. Among the resolution methods one can enumerate the direct calculation of Eqs. (20)–(21), the expansion in terms of orthogonal functions (Jacobi's polynomials) (Simonneau, 1993), the Fourier-Bessel-Candel

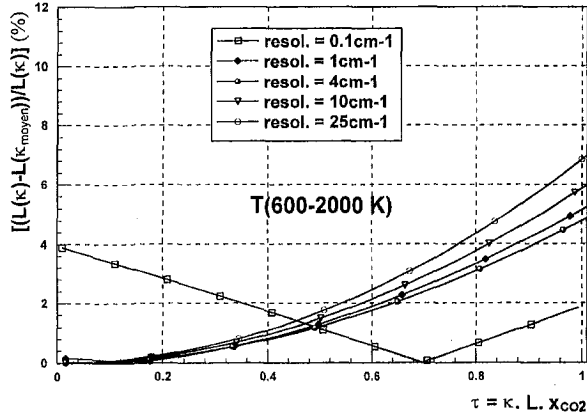
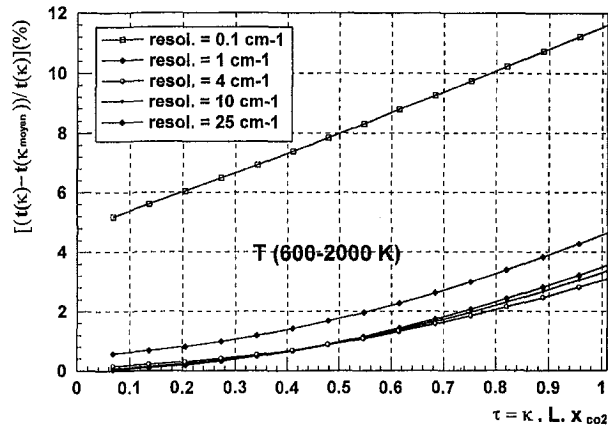


Fig. 3 Validation of large band assumption for CO₂; relative error in transmission (top) and relative error in emission (bottom)

transformation (Candel, 1981), the mollification method (Murio, 1993), the conjugate gradient method applied to the regulated problem of the operator, and its adjoint (Sakami, 1994).

Restitution by the Jacobi Polynomials. In the Simonneau method, the function to be reconstructed is expanded on the basis of Jacobi polynomials $K_n(y)$, as follows:

$$\bar{\kappa}_\nu(y) = \sum_{n=0}^{N_s} C_n K_n(y), \quad (22)$$

N_s being the number of terms of the sum (depending on the number of measurements available and their accuracy). The coefficients C_n are expressed in terms of the discrete experimental data. The simple recurrence law of the orthogonal polynomials $K_n(y)$ facilitates the calculation of the C_n coefficients.

Restitution by the Conjugate Gradient Method Applied to the Operator and its Adjoint. By a uniform space discretization of the integrals in Eqs. (6)–(7), each direct problem of transmission or emission can be reformulated in finite dimensions as (Murio, 1993)

$$\mathbf{A}f = g \quad (23)$$

where \mathbf{A} is an operator (not necessarily linear), f is the unknown vector, and g is the measured vector, i.e., $W_\nu(p)$ in transmission and $M_\nu(p)$ in the emission case. In transmission the matrix elements are

$$a_{ij}(p) = a_{ij}(ih) = \int_{jh}^{(j+1)h} \frac{2}{\sqrt{r^2 - (ih)^2}} r dr \quad j \geq i$$

$$a_{ij}(p) = 0 \quad j < i,$$

and in emission

$$a_{ij}(p) = a_{ij}(ih) = \int_{jh}^{(j+1)h} \frac{2I_i^0(r)}{\sqrt{r^2 - (ih)^2}} \cosh \int_{jh}^r \frac{\kappa(r') r' dr'}{\sqrt{r^2 - (ih)^2}} \quad j \geq i$$

$$a_{ij}(p) = 0 \quad j < i.$$

It has been shown by Murio (1993), on the basis of the Fredholm alternative, that resolution of Eq. (23) is equivalent to the coupled problem

$$\mathbf{A}f = g$$

$$\mathbf{A}^*h = 0 \quad (24)$$

where \mathbf{A}^* is the adjoint of operator \mathbf{A} and h is an adjoint function. One way to stabilize the problem (23) is to use a regularization procedure, that leads to the equivalent problem

$$\mathbf{A}f - \sqrt{\alpha}h = g$$

$$\mathbf{A}^*h + \sqrt{\alpha}f = 0, \quad (25)$$

where α is a regularization parameter. Under that statement, problem (25) can be properly worked out by means of an iterative procedure

$$\mathbf{A}f_n^\alpha - g = \sqrt{\alpha}h_n^\alpha$$

$$n = 0, 1, 2, \dots$$

$$f_{n+1}^\alpha = f_n^\alpha - \beta_n[(\alpha f_n^\alpha + \mathbf{A}^*(\sqrt{\alpha}h_n^\alpha))]. \quad (26)$$

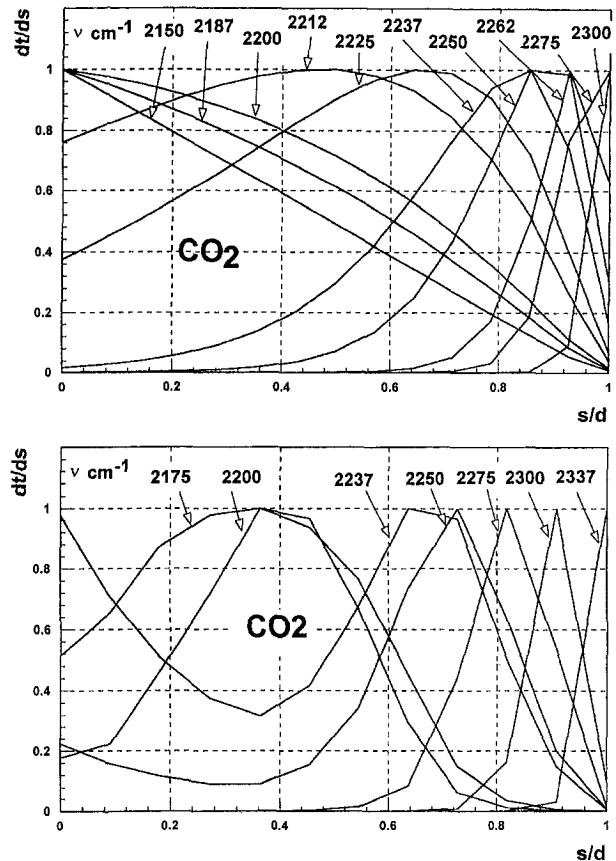


Fig. 4 Normalized kernels for a plane parallel slab of CO₂; isothermal slab (top): (with $T(s) = 900$ K; $x_{\text{CO}_2}(s) = 1$), and nonisothermal slab (bottom) ($T(s) = 1200 \exp[-5s^2] + 400$; $x_{\text{CO}_2}(s) = 0.25 \exp[-50s^2] + 0.07$)

Following Murio (1993) in Eq. (26), β_n is a real number determined at each iteration by the conjugate gradient algorithm.

$$\bar{\tau}_i = \exp\left(-\frac{\bar{W}_i}{\delta_i}\right). \quad (30)$$

Spectral Scanning: The Chahine-Smith Method

In its original version, the Chahine algorithm is a method using a very large spectral band (Chahine, 1972) for reconstructing temperature profiles from the emission in a fixed direction of observation coming from a semi-transparent, nonhomogeneous gaseous slab. The infrared emission of a plane parallel semi-transparent medium (an atmosphere, a flame or a glass bath . . .) of thickness d , can be observed remotely in a specified line of sight at low resolution for N frequency channels of the emission band centered on frequency ν_i ($i = 1 \dots N$).

Expression of the Low-Resolution Outgoing Emission Intensity. Along the normal direction of a STM slab with non-emitting and nonreflecting boundaries, the integral solution of the RTE in terms of the curvilinear abscissa, s , in the spectral interval $\Delta\nu$ yields

$$\begin{aligned} \bar{I}_i^{\text{out}} = \frac{1}{\Delta\nu} \int_{\Delta\nu} \left(\int_0^d \kappa(s) I^\circ[T(s)] \right. \\ \left. \times \left[\exp - \int_s^d \kappa(s') ds' \right] ds \right) d\nu. \end{aligned} \quad (27)$$

After (1) interchanging the space and the spectral integration, (2) assuming the constancy for the Planck's function in the interval $\Delta\nu$, and (3) introducing the space derivative for the transmittivity given by Eq. (9), Eq. (27) becomes

$$\bar{I}_i^{\text{out}} = \int_0^d I_i^\circ[T(s)] \frac{\partial \bar{\tau}_i}{\partial s} ds \quad i = 1 \dots N \quad (28)$$

or by an integration by parts

$$\bar{I}_i^{\text{out}} = \int_0^d \bar{\tau}_i \frac{\partial I_i^\circ[T(s)]}{\partial s} ds \quad i = 1 \dots N \quad (29)$$

where the transmittivity $\bar{\tau}_i(s)$ is expressed by the Curtis-Godson approximation.

Transmittivity Calculation. For a nonhomogeneous gaseous column of combustion gas the mean transmittivity corresponding to channel i can be calculated from the Curtis-Godson approximation:

The mean equivalent width of the column has been expressed by the averaged parameters \bar{k}_i and $\bar{\delta}_i$ entering the narrow statistical band

$$\frac{\bar{W}_i(d)}{\delta_i} = \frac{\bar{\beta}_i}{\pi} \left(\sqrt{1 + \frac{2\pi\bar{k}_i}{\bar{\beta}_i}} - 1 \right) \quad (31)$$

where

$$\bar{k}_i = P \int_0^d \bar{k}_i(s) x_{\text{CO}_2}(s) ds, \quad (32)$$

(P denoting the total pressure),

$$\bar{\beta}_i = P \int_0^d \bar{k}_i(s) x_{\text{CO}_2}(s) \bar{\beta}_i(s) ds \quad (33)$$

$$\bar{\beta}_i(s) = \frac{2\pi\bar{\gamma}(s)}{\delta_i}. \quad (34)$$

As for the Lorentz mean width $\bar{\gamma}$ (following Soufiani and Taine (1997)), it is assumed to be independent on the considered position in the spectrum, and is given by

$$\begin{aligned} \bar{\gamma}_{\text{CO}_2}(s) = \frac{P}{P_s} \left(\frac{T_s}{T} \right)^{0.7} [0.07 x_{\text{CO}_2} \\ + 0.0058(1 - x_{\text{CO}_2} - x_{\text{H}_2\text{O}}) + 0.1 x_{\text{H}_2\text{O}}] \end{aligned} \quad (35)$$

where $P_s = 1$ atm and $T_s = 296$ K and $x_{\text{H}_2\text{O}}$ is the mole molar fraction of H_2O .

Figures 4(a)–(b) show, calculated from the data bank for the CO_2 (2375 cm^{-1}) band, representations of the kernels $K(i, s)$ in Eq. (28), namely,

$$K(i, s) \equiv \frac{\partial \bar{\tau}_i}{\partial s} = \bar{k}_i \exp(-\bar{k}_i s) \quad (36)$$

for different channels as a function of the position along a diameter of the flame, (a) for a thermally homogeneous plane parallel slab (with $T(s) = 900$ K; $x_{\text{CO}_2}(s) = 1$) and (b) in presence of variable concentration and temperature profiles ($T(s)(\text{K}) = 1200 \exp[-5s^2] + 400$; $x_{\text{CO}_2}(s) = 0.25$

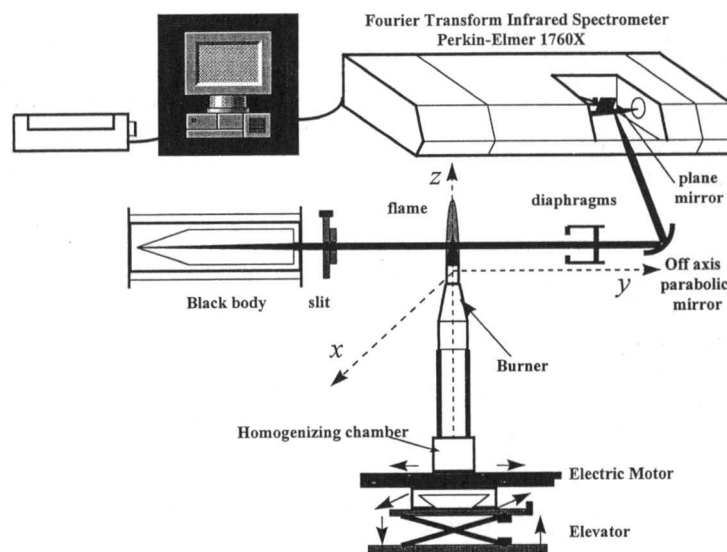


Fig. 5 The experimental setup

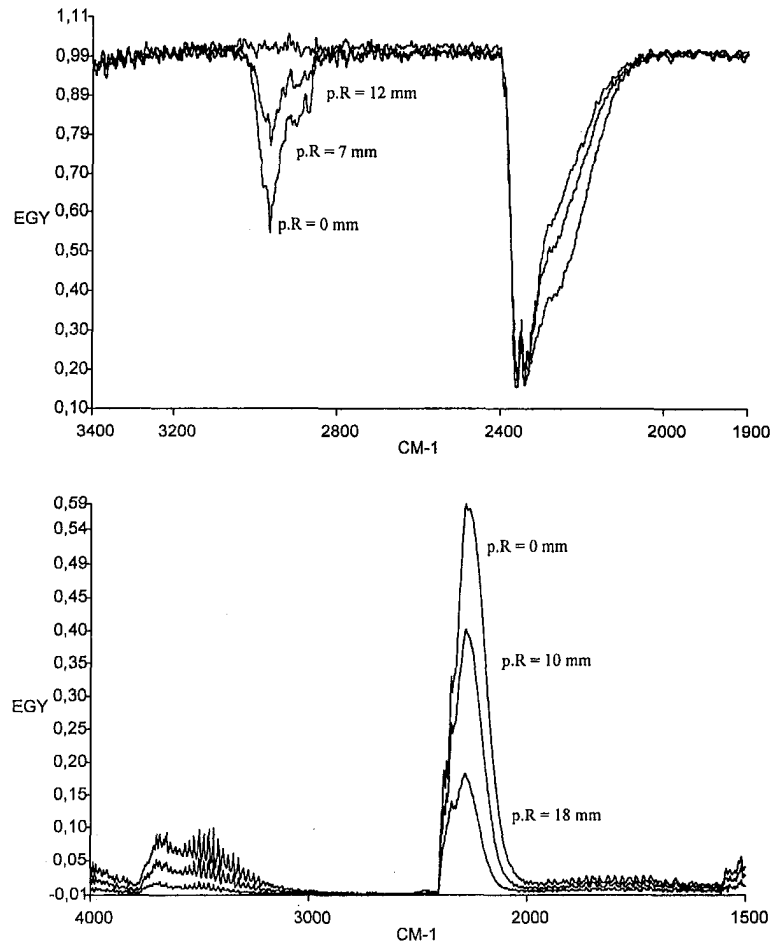


Fig. 6 Flame spectra for different position parameters p , transmission (top) and apparent emission (bottom)

$\exp[-50s^2] + 0.07$). One can note that for each of the channels there exists a maximum associated with a sounding depth, from which the main part of the emission is radiated. However, in thermally nonhomogenous flow, the maximum of each kernel is temperature dependent and, as a consequence, not accurately located when an iterative procedure is used for finding the two unknown functions $\kappa(s)$ and $T(s)$.

Restitution of Temperature Profiles by the Chahine Method. The Chahine method is an iterative process in which the basic integral equations, Eqs. (28), can be rewritten as

$$\bar{T}_i^{\text{out}} = \int_0^d \frac{\bar{T}_i^{\text{mes}}}{\bar{T}_i^{\text{out}}} I_i^{\circ}[T^n(s)] \left[\frac{\partial \bar{T}_i}{\partial s} \right]^n ds \quad i = 1 \dots N \quad (37)$$

where \bar{T}_i^{mes} is the integrated outgoing intensity associated to the channel i and \bar{T}_i^{out} the corresponding intensity calculated by Eqs. (29)–(34) for the temperature profiles at the iteration n . At the convergence of the process Eq. (37) looks like the original Eq. (28) involving the relaxation scheme for each channel:

$$I_i^{\circ}(T_i^{n+1}) = \frac{\bar{T}_i^{\text{mes}}}{\bar{T}_i^{\text{out}}} I_i^{\circ}(T_i^n) \quad i = 1 \dots N. \quad (38)$$

Equation (38) leads to the local temperature at the particular position s_i :

$$T_i^{n+1}(s_i) = \frac{C_1}{\nu_i \text{Log} \left[1 - \Gamma_{ni}^n \left\{ 1 - \exp\left(\frac{C_2}{\nu_i T_i^n(s_i)}\right) \right\} \right]}, \quad (39)$$

C_1 and C_2 being the two fundamental radiation constants. The knowledge of the finite number, N , of local temperatures in Eq. (39) yields the temperature distribution throughout the STM thickness.

The Smith Method for the Concentration Profiles. The set of Eqs. (29) can be written in the alternative iterative form

$$\bar{T}_i^{\text{mes}} - \bar{T}_i^{\text{out}} = \int_0^d [\bar{T}_i^{n+1}(s) - \bar{T}_i^n(s)] \frac{\partial I_i^{\circ}(s)}{\partial s} ds \quad i = 1 \dots N. \quad (40)$$

Let us introduce the integrated concentration of CO_2 along the geometrical path

$$u(s) = P \int_0^s x_{\text{CO}_2}(s') ds'. \quad (41)$$

A Taylor expansion of the transmittivity yields

$$I_i^{\text{mes}} - I_i^{\text{out}}(d) = \int_0^d [u^{n+1}(s) - u^n(s)] \left(\frac{\partial \bar{T}_i}{\partial u} \right)^n \frac{\partial I_i^{\circ}(s)}{\partial s} ds. \quad (42)$$

By assuming the ratio $u^{n+1}(s)/u^n(s)$ being independent of the abscissa, s , and by letting

$$S^n = \int_0^d [u^n(s)] \left(\frac{\partial \bar{T}_i}{\partial u} \right)^n \frac{\partial I_i^{\circ}(s)}{\partial s} ds \quad (43)$$

from Eq. (42), one has

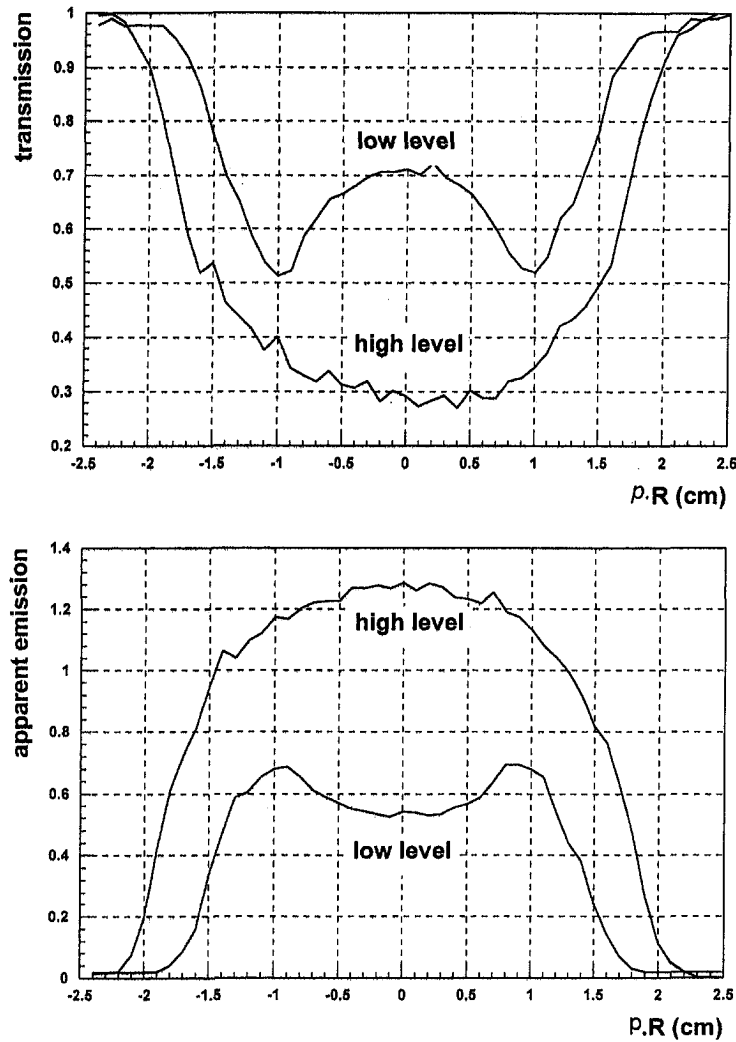


Fig. 7 Transmission (top) and apparent emission (bottom) of the propane-air flame at 2375 cm^{-1}

$$u^{n+1}(s) = u^n \frac{(I_i^{\text{mes}}(d) - I_i^{\text{out}})}{S^n} + u^n. \quad (44)$$

By taking the derivative of Eq. (44) and according to Eq. (42), one gets

$$x_{\text{CO}_2}^{n+1}(s) = \left(\frac{\partial u}{\partial s} \right)^{n+1} = \frac{(I_i^{\text{mes}}(d) - I_i^{\text{out}}(d))}{S(u^n)} x_{\text{CO}_2}^n(s) + x_{\text{CO}_2}^n(s), \quad (45)$$

that is the iterative relationship which should be fulfilled by the molar fraction distribution of CO_2 .

Application to a Premixed Flame

Presented here are some applications of the exposed methods to retrieve temperature and CO_2 distributions in a premixed flame of propane-air studied by the transmission/emission techniques, namely space scanning and spectral scanning. The experimental data were acquired by low resolution FTIR measurements. As previously discussed, the apparatus was tuned at a resolution of 4 cm^{-1} and the optical thickness of the flame was $\tau < 0.5$.

The Mapping of Temperature and Species in an Axisymmetric Premixed Flame.

The Experimental Setup. The experimental device shown in Fig. 5 is composed of four parts: the burner, the system of displacement, the black body source, and various optical components.

(a) *The burner.* It is a 30-cm high, 4-cm diameter brass tube filled with a honey comb material in order to laminarize the gas flow, and fitted with a conical ending such that the base of the flame has a 2-cm diameter. At the bottom, the gases (99 percent pure propane and air) are mixed in a homogenizing chamber. Two flowmeters enable the measurements of the fuel-to-air ratio of the mixture. Flow rates were adjusted to maintain the flame in a laminar regime. During all experiments the corresponding equivalence ratio ρ , defined as the ratio of molar fraction fuel/molar fraction comburant for the mixture and the stoichiometry, respectively, was $\rho = 0.92$.

(b) *The displacement system.* The burner is mounted on an electronically driven microframe supported by an elevator. Thus displacements in the three dimensions are allowed; the lateral movements of translation are recorded in the memory of the FTIR spectrometer.

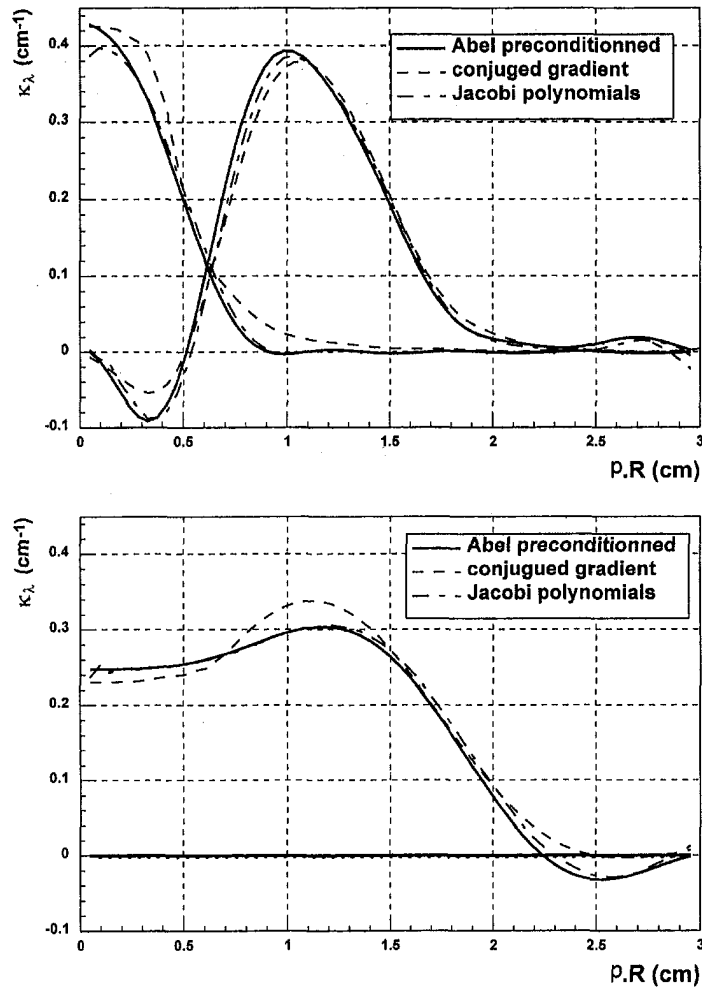


Fig. 8 Recovered CO₂ absorption profiles in a premixed flame, 15 mm level (top) and 40 mm level (bottom)

(c) *The black body source.* It is a 150-mm long, 14-mm diameter furnace fitted with a conical extremity. Its temperature is uniform over only half of its length. A radiative modeling of the cavity's emission at the working reference temperature, $T_{ref} = 1300 \text{ K} \pm 5 \text{ K}$, gives for its total emissivity a value of 0.95. Consequently, all the intensity measurements have been corrected according to this value.

(d) *The optical system.* Several pin holes (of diameters 2 and 3 mm) determine a fixed line of sight. By translating repeatedly the flame in an horizontal plane, a set of emission or transmission measurements is acquired. The vertical displacement allows the study of the flame for different heights. The spatial resolution is defined by a 1-mm slit placed in front of the source. Radiation from the black body or from the flame was directed to a FTIR spectrometer by means of a parabolic off-axis mirror, followed by a plane mirror close to the spectrometer entrance. The FTIR spectrometer (Perkin Elmer 1760X) is equipped with a triglycide sulfate (TGS) detector. It was verified that the detector exhibits a linear response with respect to the incident radiation flux.

Experimental Transmission and Emission Measurements. For a given position of the line of sight with respect to the flame's axis of symmetry, the transmittivity and the emission measurements are carried out according to the following three steps:

- recording the emission spectrum ($S_{1\nu}$) of the black body source alone at the reference temperature T_{ref} ,

- recording of the emission spectrum of the flame ($S_{2\nu}$) alone by putting a shutter in front of the black body, and
- recording of the black body's emission across the flame ($S_{3\nu}$).

The measured spectral transmittivity is

$$t_\nu = \frac{S_{3\nu} - S_{2\nu}}{S_{1\nu}} \quad (46)$$

and the apparent emission is

$$\epsilon_1 = \frac{S_{2\nu}}{S_{1\nu}} \quad (47)$$

The estimated error on quantities obtained from Eqs. (46)–(47) is ± 1.5 percent at the minimum transmission frequency (respectively, maximum emission frequency).

Typical transmission and emission spectra of the flame taken at the position of 15 mm above the burner's end are displayed in Figs. 6(a)–(b). They were calculated from Eqs. (46)–(47) in the spectral range $1900\text{--}3400 \text{ cm}^{-1}$ for three different lines of sight (p). In the transmission spectrum one can see the propane band and the (ν_3) band of CO₂ band ($4.3 \mu\text{m}$). One should especially note the increase of the width of the band with respect to the normal conditions. In the emission spectrum the sensitivity in magnitude with the directions p is manifested for the CO₂ band at a higher rate than that of the water band. Accordingly, in both emission and transmission the measure-

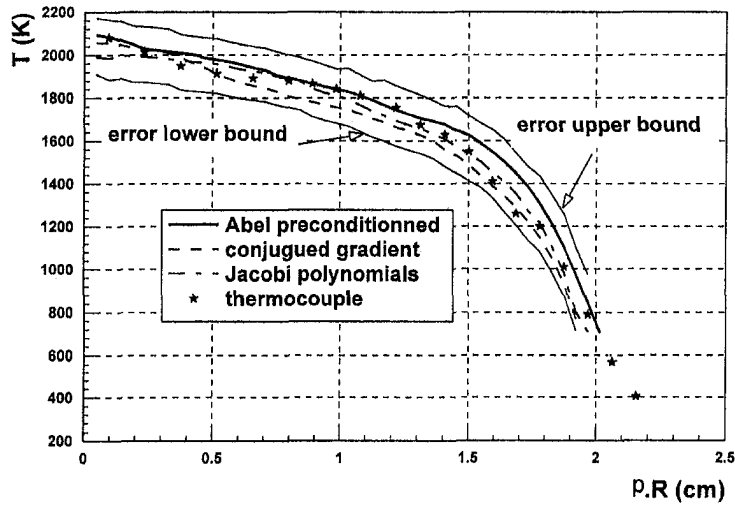
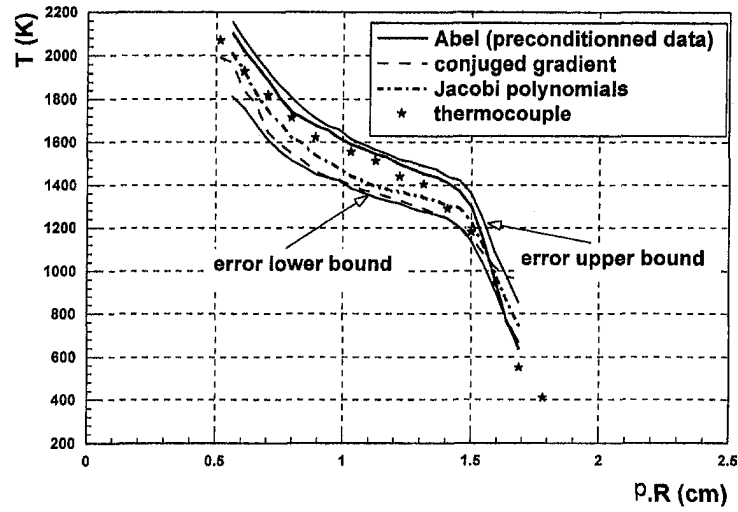


Fig. 9 Recovered temperature profiles in a premixed flame, low level (top) and high level (bottom)

ment have been performed at the specified frequencies 2375 cm^{-1} for CO_2 and 2980 cm^{-1} for propane. Primary experimental transmission and emission diagrams of the flame as a function of the displacement parameter p of the

(ν_3) CO_2 band are drawn in Figs. 7(a)–(b) for two vertical positions situated at 15 mm and 40 mm above the burner. In each level, 64 equally distributed p values were selected. Before the mathematical inversions, the experimental data sets were

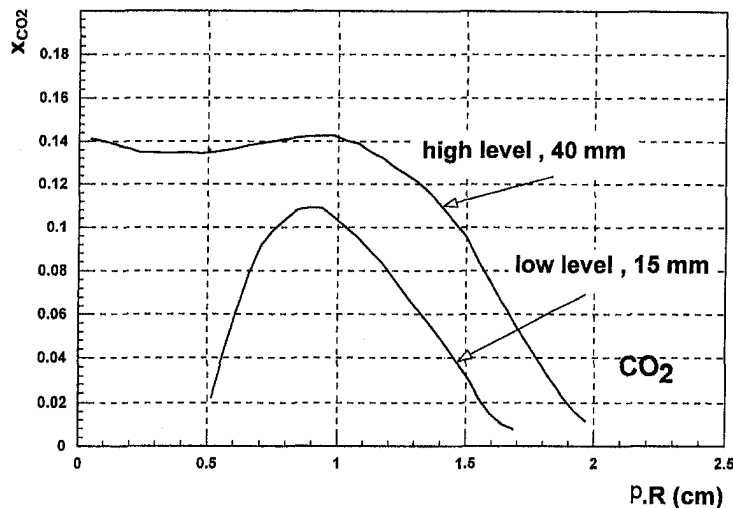


Fig. 10 Recovered CO_2 concentration profiles

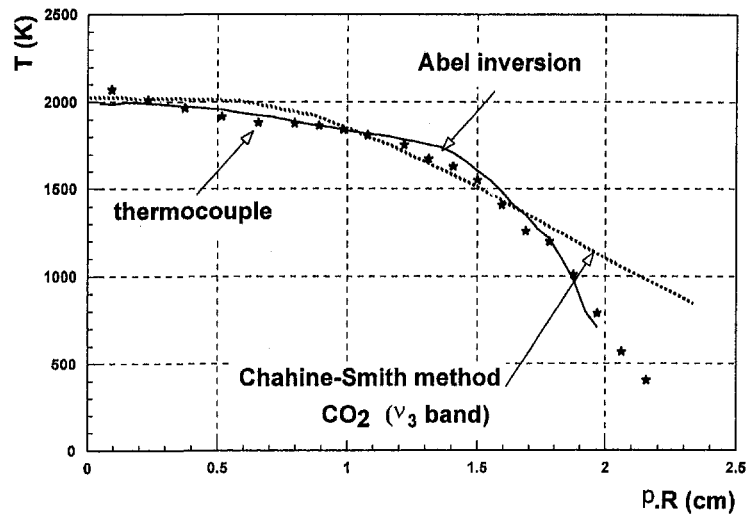


Fig. 11 Temperature profiles retrieved for the flame at 35 mm from the burner bottom

preconditioned in two steps, (1) by symmetrization with respect to the p parameter by using the Connes's method (Connes, 1961) and (2) by filtering out noisy data by a Fourier analysis (Sakami, 1994).

Results of Inversions

Inversion of the Space Scanning Measurements.

Absorption Profile Recoveries. Resolution of Eq. (20) for the set of experimental directional transmittivity results leads to the absorption coefficient profiles of CO_2 and propane. These results are retrieved by the preconditioned Abel transform, the Abel-Simonneau method, and the conjugate gradient method and reproduced in Fig. 8(a)–(b) for the low and the high observation's position of the flame, respectively. In the case of the regularization method results are obtained with the parameter $\alpha = 0.28$. In the Simonneau method the number of expansion terms was $N_s = 35$.

Temperature Profile Recoveries. Once absorption profiles are known for each altitude they can be introduced in the emission expressed by Eq. (21), then by means of a second Abel inversion, the unknown function $I_v^0(r)$ is obtained. The resulting temperature distributions for the experimental flame are shown in Figs. 9(a)–(b), (a) at 15 mm above the burner's end, and (b) at a 40-mm height that is situated 10 mm above the cone shaped flame's tip, so, in a complete burning gas zone. Represented also in Fig. 9 are thermocouple measurements (carried out with a 50- μm diameter 6–30 Pt/PtRh, corrected for radiative exchanges and conductive losses). They are situated between the conjugate gradient method results and those of the Simonneau inversion method.

Carbon Dioxide Concentration Distributions. Concentration profiles of CO_2 corresponding to the $\bar{\kappa}_{\text{CO}_2}(r)$ and $T(r)$ profiles in the flame, retrieved in Figs. 8 and 9, are presented in Fig. 10.

These results can be valuably compared with those predicted by the propane-air combustion thermodynamic model for the experimental equivalence ratio of $\rho = 0.92$. Indeed, the adiabatic temperature was found equal to 2160 K and the corresponding CO_2 concentration equal to 0.11, as computed by the Quatuor code (Heuzé et al., 1987).

Accuracy on the Retrieved Distributions by the Abel Inversions. The errors in the emission and transmission measurements are evaluated to be ± 1.5 percent. They involve an error of

± 2 percent on the physical model. Accordingly, by a simulation (Eqs. (20)–(21)) the uncertainties introduced in the temperature reconstruction process are evaluated in the extreme unfavorable case to be ± 7 percent near the symmetry axis and ± 11 percent toward the flame edge, as for the CO_2 distribution the error is ± 9 percent on the axis and ± 14 percent for the edge.

The Chahine-Smith Method. In the Chahine-Smith method a set of 12 frequency channels belonging to the (ν_3) band of CO_2 was selected between 2175 to 2375 cm^{-1} with a resolution of 12.5 cm^{-1} . The following iterative process is used:

- 1 select initial $T^0(r)$ and $x_{\text{CO}_2}^0(r)$ profiles from a priori information,
- 2 calculate for each channel, i , the kernel in Eq. (36), and evaluate the positions of the maxima, $\bar{\kappa}(T^0, x^0)$ being evaluated with reference to the EM2C data bank for the first chosen profiles,
- 3 for each channel, i , for fixed $x_{\text{CO}_2}^0$, calculate by the relaxation Eqs. (38)–(39) a first local temperature $T^1(z_i)$ associated to the position z_i ; then smooth the obtained temperature profiles by a polynomial approximation, $T^1(z)$,
- 4 calculate the updated averaged transmittivities by Eq. (30),
- 5 for each channel, i , use the Smith procedure, Eq. (45), to obtain the local concentration profiles $x_{\text{CO}_2}^1(z_i)$, (constraints to the condition $x_{\text{CO}_2}^1 < 1$) and fit it with a polynomial approximation $x_{\text{CO}_2}^1(z)$,
- 6 calculate the updated averaged transmittivity $\bar{\tau}_i(T^1, x_{\text{CO}_2}^1)$ by Eq. (30),
- 7 calculate the outgoing intensity $I_i^+(d)$ by Eq. (29) and calculate the residu $\Delta = \|I_i^+(d) - I_i^-(d)\|$,
- 8 if $\Delta > \epsilon$ return to step 2 until the error $\Delta \approx$ experimental noise.

By sounding the premixed flame in an axial plane and using this procedure, the temperature profile is retrieved. The results are illustrated in Fig. 11 for the altitude 35 mm above the burner bottom and compared with the previous ones coming from the Abel inversion.

Accuracy of the Chahine-Smith Inversion. The convergence of the procedure and the accuracy of the method depends on the sensitivity coefficients $dI_i^+(d)/dT(s)$ and $dI_i^+(d)/dx(s)$. Since the local temperature sensitivity coefficient is ten times higher than the local concentration one, the iteration procedure first converges in temperature, and then in concentration profile

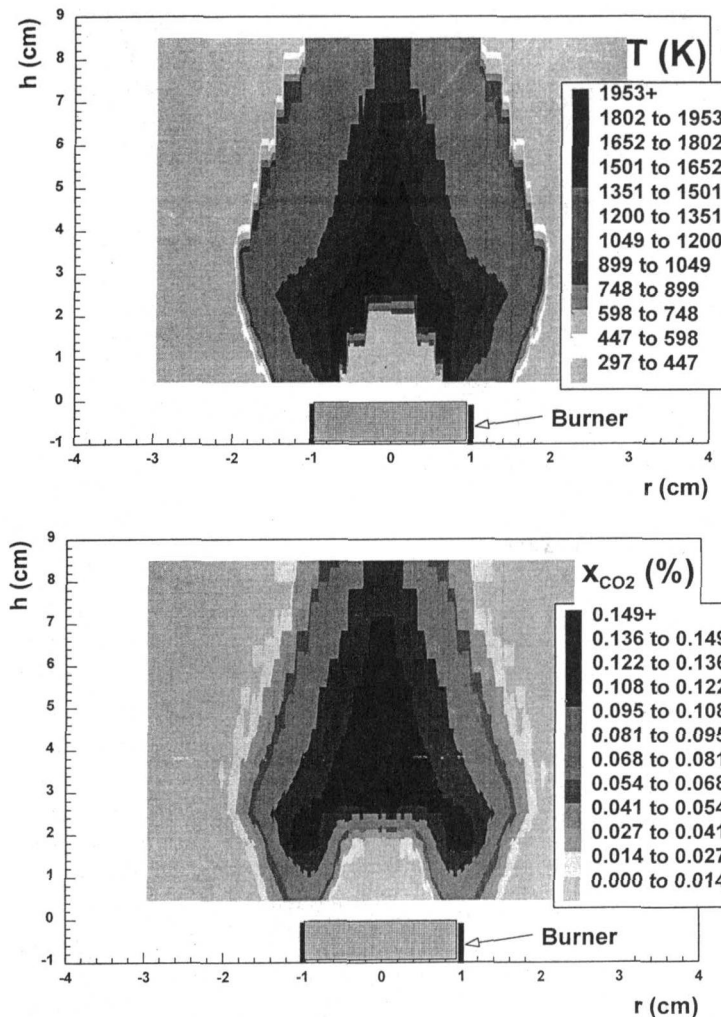


Fig. 12 (a) Temperature mapping; (b) CO₂ mapping

(Yousefian, 1998). As a consequence, the accuracy in concentration determination is quite poor especially in the presence of strong gradients as already pointed out by Zhang and Cheng (1986).

Thermal and Species Mapping of the Premixed Flame.

Seven cross sections of the flame were experimentally explored by the emission/transmission and the Abel method of inversion. By interpolation of these results temperature and concentration mappings have been produced and presented in Figs. 12.

Conclusion

Temperature and species concentration structures in an axisymmetric laminar flame have been reconstructed at low resolution, separately, by means of emission/transmission space scanning and by spectral scanning. The data collected in the infrared ν_3 band of CO₂ were inverted by two different techniques. The Abel reconstruction technique is very effective for media of limited optical thickness in the validity range of which the recovered temperature fields are in agreement with those measured directly by conventional thermocouple sounding. On the other hand, the Chahine-Smith method of inversion used for emission data gives only poor results when associated with the statistical narrow band model mean parameters. Thus its handling advantages, requiring only spectral scanning in a single line of sight, are offset by less accurate results and less adaptability when high temperature and stiff concentration gradients are present, as is the case near the flame front.

As for nonaxisymmetric STM, an extension of the low-resolution spectral experimental technique by spatial scanning, associated with the two-dimensional Radon transform, could be able to provide absorption and temperature tomographies by the two-dimensional projection technique as already developed by Sakami and Lallemand (1993) with simulated data.

Acknowledgments

The authors gratefully acknowledge Dr. A. Soufiani for helpful discussions and the communication of the EM2C data bank.

References

- Best, P.E., Chien, P.L., Carangelo, R.M., Solomon, P.R., Danchak, M., and Ilovici, I., 1991, "Tomographic Reconstruction of FT-IR Emission and Transmission Spectra in a Sooting Laminar Diffusion Flame. Species Concentration and Temperatures," *Combustion and Flame*, Vol. 85, pp. 309–318.
- Candel, S.M., 1981, "An Algorithm for the Fourier-Bessel Transform," *Computer Physics Communication*, Vol. 23, pp. 343–351.
- Chahine, M.T., 1972, "A General Relaxation Method for Inverse Solution of the Full Radiation Transfer Equation," *J. Atm. Sciences*, Vol. 29, pp. 741–747.
- Char, J.M., and Yeh, J.H., 1996, "The Measurement of Open Propane Flame Temperature Using Infrared Technique," *J. Quant. Spectrosc. Radiat. Transfer*, Vol. 56, pp. 133–144.
- Chen, F.P., and Goulard, R., 1976, "Some Aspects of Optical Pollutant Measurement Systems for Jet Engine Exhaust Flows," AIAA Paper, 76-108, 14th Aerospace Sciences Meeting, Washington, DC.
- Connes, J.R., 1961, "Recherches sur la Spectroscopie par Transformation de Fourier," *Revue d'Optique*, Vol. 2, pp. 45–79.
- Hall, R.J., and Bonczyk, P.A., 1990, "Sooting Flame Thermometry Using Emission/Absorption Tomography," *Applied Optics*, Vol. 29, No. 31, pp. 4590–4598.

- Huezé, O., Presles, H.N., and Bauer, P., 1987, "Quatuor: A thermochemical Code for Computing Thermodynamic Properties of Detonation and Combustion Products," *Congrès International de Pyrotechnie Spatiale*, June 8–12, Jean-les-Pins, France, p. 87.
- Hughey, B.J., and Santavicca, D.A., 1982, "A comparison of techniques for reconstruction axisymmetric reacting flow fields from absorption measurements," *Com. Sci. and Tech.*, Vol. 29, pp. 167–190.
- Lallemand, M., and Soufiani, A., 1995, "Mesures de Temperature dans les Milieux Semi-Transparents," *Rev. Gen. Therm.*, Vol. 34, pp. 69–85.
- Li, H.Y., 1994, "Estimation of the Temperature Profile in a Cylindrical Medium by Inverse Analysis," *J. Quant. Spectrosc. Radiat. Transfer*, Vol. 52, pp. 755–764.
- Markham, J.R., Zhang, Y.P., Carangelo, R.M., and Solomon, P.R., 1990, "FT-IR Emission/Transmission Tomography of a Coal Flame," *23th Symposium (Int.) on Combustion*, The Combustion Institute, pp. 1869–1875.
- Murio, D.A., 1993, *The Mollification Method and the Numerical Solution of Ill-Posed Problems*, John Wiley and Sons, New York.
- Mengüç, M.P., and Dutta, P., 1994, "Scattering Tomography and its Application to Sooting Diffusion Flames," *ASME JOURNAL OF HEAT TRANSFER*, Vol. 116, pp. 144–151.
- Rivière, P., 1994, "Modélisation des Propriétés Radiatives de la Vapeur d'Eau à Haute Température. Application à la Signature Infrarouge," thesis, Ecole Centrale Paris.
- Sakami, M., and Lallemand, M., 1995, "Retrieval of Absorption and Temperature Profiles in a Premixed Flame by Inverse Radiative Methods," *First International Symposium Radiative Heat Transfer*, Pinar Mengüç, ed., Kusadasi, Turkey, Aug. 13–18, Begell House, New York, pp. 555–576.
- Sakami, M., and Lallemand, M., 1993, "Retrieval of Absorption and Temperature Profiles in Axisymmetric and Non-Axisymmetric Emitting-Absorbing Media by Inverse Radiative Methods, Inverse Problems in Engineering, Theory and Practice," *The First Conference in a Series on Inverse Problems in Engineering*, Palm Coast, FL, pp. 259–266.
- Sakami, M., 1994, "Application des Méthodes Inverses à la Métrologie Thermique par Spectrométrie Infrarouge," thesis, Université de Poitiers.
- Simmonneau, E., Varela, A.M., and Munoz-Tunon, C., 1993, "Spectral Inversion of the Generalized Abel Integral Transform," *J. Quant. Spectrosc. Radiat. Transfer*, Vol. 49, No. 2, pp. 149–156.
- Smith, W.L., 1970, "Iterative Solution of the Radiative Transfer Equation for the Temperature and Absorption Gas Profile of an Atmosphere," *Appl. Opt.*, Vol. 9, pp. 1993–1999.
- Soufiani, A., and Taine, J., 1995, "High Temperature Statistical Narrow Band Parameters for H₂O, CO₂ and CO, and Correlated k , ck parameters," Laboratoire (EM2C), Ecole Centrale Paris.
- Soufiani, A., and Taine, J., 1997, "High Temperature Gas Radiative Property Parameters of Statistical Narrow-Band Model for H₂O, CO₂ and CO and Correlated- k Model for H₂O and CO," *Int. J. Heat Mass Transf.* Vol. 40, pp. 987–991.
- Soufiani, A., 1995, private communication.
- Yousefian, F., and Lallemand, M., 1996, "Temperature and Concentration Profiles Using Infrared Data by Inverse Radiative Analysis. Application to Premixed Flames," *Inverse Problems in Engineering, Theory and Practice. The 2nd Conference in a Series on Inverse Problems in Engineering*, Le Croisic, France, June 9–14.
- Yousefian, F., and Lallemand, M., 1997, "Inverse Radiative Analysis of High Resolution Infrared Emission Data for Temperature and Species Profiles Recoveries in Axisymmetric Semi-transparent Media," *J. Quant. Spectrosc. Radiat. Transfer*, to appear.
- Yousefian, F., 1998, "Application des Techniques Radiatives Inverses à la Métrologie Thermique par Voie Spectroscopique Infrarouge," thesis, Université de Poitiers.
- Zhang, J.Q., and Cheng, J.S., 1986, "Determination of the Temperature Profile of Axisymmetric Combustion-Gas Flow from Infrared Spectral Measurements," *Combustion and Flame*, Vol. 65, pp. 163–176.

S. Lee

Department of Mechanical Engineering,
Kyonggi University,
Suwon, Kyonggi-Do Korea
e-mail: shinpyo@kuic.kyonggi.ac.kr

S. U.-S. Choi

Energy Technology Division,
e-mail: choi@anl.gov
Mem. ASME

S. Li

Materials Science Division

J. A. Eastman

Materials Science Division

Argonne National Laboratory,
Argonne, IL 60439

Measuring Thermal Conductivity of Fluids Containing Oxide Nanoparticles

Oxide nanofluids were produced and their thermal conductivities were measured by a transient hot-wire method. The experimental results show that these nanofluids, containing a small amount of nanoparticles, have substantially higher thermal conductivities than the same liquids without nanoparticles. Comparisons between experiments and the Hamilton and Crosser model show that the model can predict the thermal conductivity of nanofluids containing large agglomerated Al_2O_3 particles. However, the model appears to be inadequate for nanofluids containing CuO particles. This suggests that not only particle shape but size is considered to be dominant in enhancing the thermal conductivity of nanofluids.

1 Introduction

Traditional heat transfer fluids, such as water, oil, and ethylene glycol mixture are inherently poor heat transfer fluids. There is a strong need to develop advanced heat transfer fluids, with significantly higher thermal conductivities and improved heat transfer characteristics than are presently available. Despite considerable previous research and development focusing on industrial heat transfer requirements, major improvements in heat transfer capabilities have been held back because of a fundamental limit in the thermal conductivity of conventional fluids.

It is well known that metals in solid form have thermal conductivities that are higher than those of fluids by orders of magnitude. For example, the thermal conductivity of copper at room temperature is about 700 times greater than that of water and about 3000 times greater than that of engine oil (Touloukian and Ho, 1970). Even oxides such as alumina (Al_2O_3), which are good thermal insulators compared to metals such as copper, have thermal conductivities more than an order-of-magnitude larger than water. Therefore, fluids containing suspended solid particles are expected to display significantly enhanced thermal conductivities relative to those of conventional heat transfer fluids.

In fact, numerous theoretical and experimental studies of the effective thermal conductivity of suspensions that contain solid particles have been conducted since Maxwell's theoretical work was published more than 100 years ago (Maxwell, 1881). However, all of the studies on thermal conductivity of suspensions have been confined to those produced with millimeter or micrometer-sized particles. Until now, researchers had no way to prevent solid particles from eventually settling out of suspension. The lack of stability of suspensions that involve coarse-grained particles is undoubtedly a primary reason why fluids with dispersed coarse-grained particles have not been previously commercialized.

We are on the verge of a new scientific and technological era, the standard of which is the nanometer (billionths of a meter). Initially sustained by progress in miniaturization, this new development has helped form a highly interdisciplinary science and engineering community. Nanotechnology is expected to have ap-

plications in a number of areas, including biotechnology, nano-electronic devices, scientific instruments, and transportation (Ashley, 1994; Rohrer, 1996).

Modern nanotechnology provides great opportunities to process and produce materials with average crystallite sizes below 50 nm. Recognizing an opportunity to apply this emerging nanotechnology to established thermal energy engineering, Argonne has developed the concept of a new class of heat transfer fluids called "nanofluids," which transfer heat more efficiently than conventional fluids (Choi, 1995). Nanofluids are engineered by suspending ultrafine metallic or nonmetallic particles of nanometer dimensions in traditional heat transfer fluids such as water, engine oil, and ethylene glycol.

Argonne has already produced nanofluids and conducted proof-of-concept tests (Eastman et al., 1997). In particular, it was demonstrated that oxide nanoparticles, such as Al_2O_3 and CuO , have excellent dispersion properties in water, oil, and ethylene glycol and form stable suspensions (i.e., significant settling does not occur in static suspensions even after weeks or months).

Nanofluids are expected to exhibit superior properties relative to those of conventional heat transfer fluids and fluids containing micrometer-sized particles. Because heat transfer takes place at the surface of the particle, it is desirable to use particles with a large total surface area. The surface-area-to-volume ratio is 1000 times larger for particles with a 10-nm diameter than for particles with a 10- μm diameter. The much larger surface areas of nanoparticles relative to those of conventional particles should not only improve heat transfer capabilities, but also increase the stability of the suspensions. Nanoparticles offer extremely large total surface areas and therefore have great potential for application in heat transfer.

The use of the conventional millimeter and micrometer-sized particles in heat transfer fluids in practical devices is greatly limited by the tendency of such particles to settle rapidly and to clog mini and microchannels. However, nanoparticles appear to be ideally suited for applications in which fluids flow through small passages, because the nanoparticles are stable and small enough not to clog flow passages. This will open the possibility of using nanoparticles in microchannels for many envisioned applications. Successful employment of nanofluids will support the current trend toward component miniaturization by enabling the design of smaller and lighter heat exchanger systems. One such application is in the next generation of cooling systems for mirrors and

Contributed by the Heat Transfer Division for publication in the JOURNAL OF HEAT TRANSFER. Manuscript received by the Heat Transfer Division, July 7, 1998; revision received, Jan. 25, 1999. Keywords: Conduction, Enhancement, Heat Transfer, Nanoscale, Two-Phase. Associate Technical Editor: A. Majumdar.

monochromators in high-intensity X-ray sources such as Argonne's Advanced Photon Source. Because the X-ray beam creates tremendous heat, cooling rates of 2000–3000 W/cm² must be achievable. An advanced cooling process that employs microchannels with nanofluids could provide more efficient cooling than any existing approach (Lee and Choi, 1996).

Another advantage of nanofluids over conventional suspensions of coarse-grained particles in fluid systems is in their expected improved abrasion-related properties. Because coarse-grained particles are relatively large, and thus have significant mass, they can abrade surfaces that they contact. This results in shortened lifetimes of such components as water pumps and bearings. In contrast, the small sizes and masses of nanoparticles would impart little kinetic energy in collisions with component surfaces and thus would be expected to produce little or no damage. A recent paper (Hu and Dong, 1998) shows that titanium oxide nanoparticles in oil, unlike conventional particles, reduce the friction coefficient and increase resistance to wear. Therefore, it is possible that nanoparticles would actually improve the lubricating properties of heat transfer fluids.

The primary objective of the present study is to investigate experimentally the thermal conductivity behavior of oxide nanofluids with low particle concentrations (1–5 vol.%).

2 Production and Characterization of Nanofluids

Nanofluids are produced by dispersing nanometer-scale solid particles into liquids such as water, ethylene glycol, or oils. Modern fabrication technology provides great opportunities to process materials at micrometer and nanometer scales. "Nanostructured" or "nanocrystalline" materials are comprised of individual crystallites that are typically <50 nm in size. Bulk materials formed by the consolidation of large numbers of nanocrystallites often exhibit greatly modified properties compared to those of conventional coarser-grained materials (for a review, see Gleiter, 1989). The change in behavior is due to the large fraction of atoms in a nanostructured material that are located within only a few atomic spacings of one or more crystallite surfaces (called "grain boundaries" in a bulk consolidated nanostructured material). Nonconsolidated nanocrystalline powders also show modified properties due to their large free surface areas (e.g., catalytic activity is enhanced significantly using nanocrystalline powders).

Much progress has been made recently in the processing of nanocrystalline materials. Current nanocrystalline materials technology can produce large quantities of powders with average particle sizes in the 10–100 nm range. Several processing routes can be used to produce nanocrystalline materials, such as gas-condensation, mechanical attrition, or chemical precipitation techniques (for a review of the many possible processing techniques, see Gleiter (1989)). Gas-condensation processing (Granqvist and Buhrman, 1976; Kimoto et al., 1963), which was used in the current experiments, is the most common method used currently in laboratory production of nanostructured materials.

Briefly, gas-condensation processing involves the vaporization of metallic or nonmetallic precursor species in the presence of a controlled gas pressure (typically a few Torr of an inert gas such as helium). Collisions between the vapor and the inert gas result in the condensation of nanometer-sized particles of the precursor material, which are then collected and used in either powder or bulk consolidated form. Advantages of gas-condensation over

Table 1 Average particle diameters

	CuO	Al ₂ O ₃
Number-weighted particle diameter (nm)	18.6 ± 0.6	24.4 ± 1.0
Area-weighted particle diameter (nm)	23.6 ± 1.0	38.4 ± 2.0

other processing techniques include the ability to produce particles under cleaner conditions. For example, chemical techniques often result in undesirable surface coatings on particles.

If powders are produced by gas condensation, some agglomeration of individual particles occurs. It is well known, however, that these agglomerates require little energy to fracture into smaller constituents, and thus it is possible that even agglomerated nanocrystalline powders can be successfully dispersed into fluids and result in good properties.

In this study, oxide nanofluids were produced by a two-step method, in which first oxide nanoparticles are prepared, followed by a second step in which the powders are dispersed into the base fluids in a mixing chamber. Al₂O₃ and CuO nanoparticles produced by gas condensation (Nanophase Technologies Corp., Burr Ridge, IL) were used as the oxide nanoparticles, and were dispersed in water or ethylene glycol. A polyethylene container (3.78 L) was used as a mixing chamber and was shaken thoroughly to ensure a homogeneous suspension.

Nanoparticles were characterized before and after dispersion in liquids. Characterization of particle size before dispersion in liquids was carried out using transmission electron microscopy techniques. Both CuO and Al₂O₃ particles exhibited a log-normal size distribution, as expected for particles produced by the gas-condensation process. The particle distributions were fit to a log-normal function and both number and area-weighted values were determined for the average particle diameters. The number-weighted size distribution weights all particles equally. The area-weighted size distribution weights the particles according to their surface areas. Hence, the area weighting will emphasize larger particles more than small ones. Since heat transfer is a surface phenomena, the area-weighted average is expected to produce the more relevant values. The values that come from the fits are shown in Table 1.

One interesting and important thing is that we observe the CuO particles to be smaller than the Al₂O₃ particles, which is consistent with our observation in this study that CuO-nanofluids exhibit better thermal conductivity values than Al₂O₃-nanofluids.

Transmission electron microscopy of nanoparticles distilled from nanofluid solutions was used to characterize the effects of solutions on agglomeration behavior. Transmission electron micrographs showing the particle size and morphologies of agglomerated Al₂O₃ and CuO powders are seen in Fig. 1. It can be seen that both Al₂O₃ and CuO nanoparticles agglomerate to form much larger particles than individual grains before dispersion. Some agglomerates are as large as 100 nm. In addition to CuO exhibiting a smaller grain size than Al₂O₃, the CuO agglomerate sizes are smaller than those of Al₂O₃. No attempt was made to break up the agglomerated nanoparticles because even agglomerated nanoparticles were successfully dispersed into liquids and formed stable suspensions.

To verify systematically the effects of volume fraction and conductivities of solid phase and liquid on the thermal conductivity

Nomenclature

a = radius
 g = Euler's constant
 k = thermal conductivity
 K = thermal diffusivity
 n = shape factor
 q = electric power

R = resistance
 t = time
 T = temperature
 α = particle volume fraction
 δT = temperature difference
 ψ = sphericity

Subscripts

p = particle
 o = base fluid
 ref = reference temperature

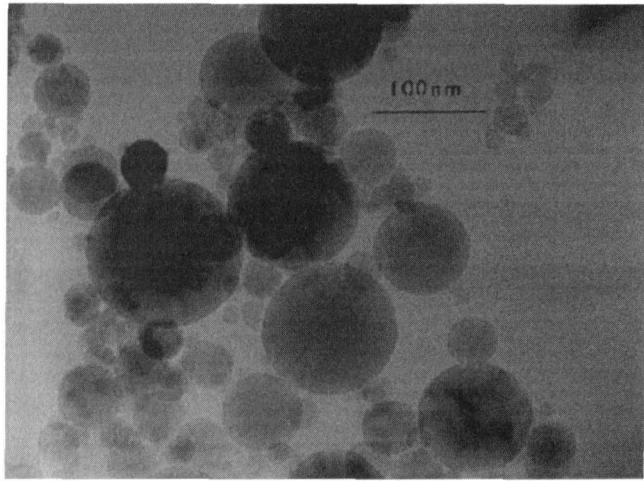


Fig. 1(a)

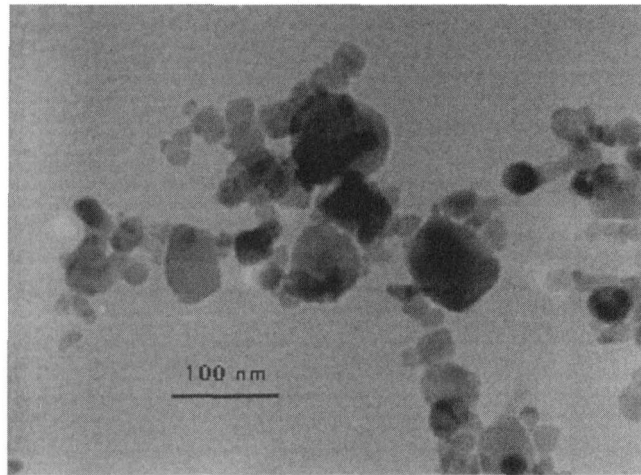


Fig. 1(b)

Fig. 1 Transmission electron micrographs showing the particle size and morphology of the agglomerated (a) Al_2O_3 and (b) CuO powders used in this study

ity of nanofluids, four oxide nanofluids with different volume fractions were produced. These four systems consisted of CuO in water, CuO in ethylene glycol, Al_2O_3 in water, and Al_2O_3 in ethylene glycol, with particle loadings up to a maximum of 5 vol. %.

3 Experiments

To measure the thermal conductivity of nanofluids, we used a transient hot-wire method. Because our nanofluids are electrically conductive, this caused difficulty in applying the ordinary transient hot-wire technique. A new hot-wire cell and electrical system have been designed for our experiment according to the method proposed by Nagasaka and Nagashima (1981).

3.1 Transient Hot-Wire Method. In this study, a transient hot-wire method has been adopted because recent advances in electronic techniques have helped to establish this method as one of the most accurate ways to determine fluid thermal conductivity. The advantage of this method lies first in its almost complete elimination of the effects of natural convection, whose unwanted presence presents problems for measurements made with a steady-state apparatus. In addition, the method is very fast relative to steady-state techniques.

The major expositions of both theory and application of the

transient hot-wire method were made by Kestin and Wakeham (1978), Roder (1981), and Johns et al. (1988). A hot-wire system involves a wire suspended symmetrically in a liquid in a vertical cylindrical container. The wire serves both as heating element and as thermometer. Almost without exception, platinum is the wire of choice.

The mathematical model that one attempts to approximate is that of an infinite-line source of heat suspended vertically in an infinite medium. The method is called transient because the power is applied abruptly and briefly. The working equation is based on a specific solution of Fourier's law and can be found in standard text (Carslaw and Jaeger, 1959):

$$T(t) - T_{\text{ref}} = \frac{q}{4\pi k} \ln \left(\frac{4K}{a^2 C} t \right), \quad (1)$$

where $T(t)$ is the temperature of the wire in the fluid at time t , T_{ref} is the temperature of the cell, q is the applied electric power, k is the thermal conductivity, K is the thermal diffusivity of the fluid, a is the radius of the wire, and $\ln C = g$, where g is Euler's constant.

The relationship given by Eq. (1) implies a straight line for a plot of δT versus $\ln(t)$. In practice, systematic deviations occur at both short and long times. However, for each experimental measurement, there is a range of times over which Eq. (1) is valid, that is, the relationship between δT and $\ln(t)$ is linear. The slope of the δT versus $\ln(t)$ relationship is obtained over the valid range, i.e., between times t_1 and t_2 , and, using the applied power, we calculated thermal conductivity from

$$k = \frac{q}{4\pi(T_2 - T_1)} \ln \left(\frac{t_2}{t_1} \right), \quad (2)$$

where $T_2 - T_1$ is the temperature rise of the wire between times t_1 and t_2 . From the temperature coefficient of the wire's resistance, the temperature rise of the wire can be determined by the change in its electrical resistance as the experiment progresses.

Despite the advantages of the transient hot-wire method, it is impossible to measure the thermal conductivity of electrically conducting fluids because current flows through the liquids, the heat generation of the wire becomes ambiguous, and polarization occurs on the wire's surface. This method is thus normally restricted to electrically nonconducting fluids such as noble gases and organic liquids.

Only a few attempts have thus far been made to expand the transient hot-wire method to measure electrically conducting liquids. Nagasaka and Nagashima (1981) used a platinum wire (diameter = 40 μm) coated with a thin electrical insulation layer (thickness = 7.5 μm) to measure the thermal conductivity of an NaCl solution, and they analyzed the effects on the thermal conductivity measurement due to this thin insulation layer. Because nanofluids are likely to be electrically conducting (metallic nanoparticles and the suspending fluid such as water are electrically conducting materials), the ordinary transient hot-wire technique cannot be used. Therefore, Nagasaka and Nagashima's method has been adopted in this experiment.

3.2 Experimental Apparatus and Procedure. A transient hot-wire cell was designed and constructed specifically for the measurement of the thermal conductivities of nanofluids. The experimental apparatus and the electrical circuit used in this study are shown schematically in Fig. 2. In the Wheatstone bridge, R_w is the resistance of the hot wire, R_1 is a 1 k Ω potentiometer, R_2 is a 1 k Ω resistor, R_3 is a 15 Ω resistor, and R_4 is a 20 Ω dummy resistor used to stabilize the DC power supply. Adjusting the resistance of the potentiometer R_1 allows the offset voltage from the Wheatstone bridge to be canceled out and thus the high-voltage gain of the analog-to-digital (A/D) converter can be used.

Platinum is used for the hot wire because its resistance/temperature relationship is well known over a wide temperature range. In the resistance thermometer grade of Pt wire, the wire

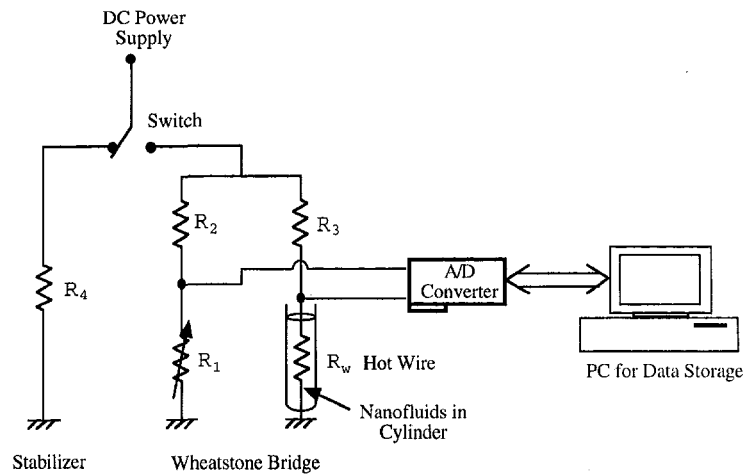


Fig. 2 Schematic diagram of transient hot-wire apparatus for measuring thermal conductivities of nanofluids (A/D = analog-to-digital)

diameters available are 25.4 μm , 50.8 μm , and 76.2 μm . A 76.2- μm diameter Pt wire was used because the other two wires were too fragile to be coated with electrical insulation, and we believed that the ratios of wire diameter to thickness of the insulation layer were too low for the other two wires. The wire was welded to rigid copper supporters, with one side of a supporter connected to a rubber string so the wire tension could be adjusted to hold the wire straight.

The wire and welded spots were coated with an epoxy adhesive which has excellent electrical insulation and heat conduction. The thickness of the coating on the wire is estimated to be less than 10 μm . Because the specific resistance of the 76.2 μm wire is low, a very long wire (the length is 180 mm, and the resistance at 20°C is 4.594 Ω) was used to provide the high resistance required for a hot-wire sensor. We did not use a two-wire compensation system (Roder, 1981) to eliminate effects due to axial conduction at both ends of the wire because identical geometry of the welded points and diameter of the coated hot wires cannot be guaranteed. Instead, the long hot wire (wire length-to-diameter ratio is ≈ 2300) was used as a hot-wire sensor to minimize end conduction loss. A 500 mL polypropylene cylinder with inner diameter of 50 mm and length of 340 mm was used as the nanofluid container; the outside of the cylinder is thermally insulated with glass fiber. The hot-wire sensor system is located at the center of the cylinder and the alignment to the direction of gravity is adjusted by the string system described above.

Switching the power supply from R_4 to the Wheatstone bridge initiates the voltage change in the hot wire, and this varying voltage over time is recorded by the A/D converter with resolution of 1.53 mV at a sampling rate of ten times per second (compared to Nagasaka and Nagashima's six times per second for NaCl solution). From this measured voltage variation and Ohm's law applied to the electric circuit shown in Fig. 2, the resistance change of the wire and the heating current through the wire can be calculated. Finally, the temperature variation of the wire can be calculated by the temperature-resistance relationship of the Pt wire. A value of 0.0039092/°C (Bentley, 1984) has been used for the resistance temperature coefficient of the Pt wire. A linear curve-fit of the experimental data in the log scale was performed by using a commercial software.

4 Results and Discussion

4.1 Calibration With Base Fluids. The base fluids used in this study as the suspending liquids are deionized water and ethylene glycol. To establish the accuracy of our thermal conductivity measurements, calibration experiments were performed for

water and ethylene glycol in the temperature range of 290 K to 310 K and at atmospheric pressure.

Typical temperature rises of the wire in water or ethylene glycol are shown in Fig. 3. Thirty data points from 3 to 6 s were used to calculate the slope of the temperature rise. We can see that while the electric power applied to the wire for water and ethylene glycol is the same, the slopes of the temperature rises are different, which means that the thermal conductivities of water and ethylene glycol are different, as expected. Because the thermal conductivity of water is greater than that of ethylene glycol, the slope for water is lower than that for ethylene glycol.

Figure 4 shows the measured thermal conductivities derived from Fig. (3) using Eq. (2), along with literature data for water and ethylene glycol (Touloukian and Ho, 1970). To determine the uncertainty in the thermal conductivity measurement, we used Eq. (2) as the data reduction equation and performed an uncertainty analysis based on the presentations of Abernethy et al. (1985) and Coleman and Steele (1989). The applied electric power was measured with an uncertainty of 0.26 percent and the wire temperature variation with time was measured with an uncertainty of 1.4 percent. The uncertainty in the thermal conductivity for water at 304 K was 1.43 percent. The calibration data in Fig. 4 show that our thermal conductivity measurement system and procedure is accurate to 1.5 percent in the temperature range tested, which is in excellent agreement with the results of the uncertainty analysis. Because the enhanced thermal conductivity of nanofluids is expected to be >1.5 percent of the base fluids at the minimum volume fraction of 0.01, this accuracy is considered adequate for quantitatively determining the thermal conductivity of nanofluids.

4.2 Measurement of Thermal Conductivity of Al_2O_3 and CuO Nanofluids. The thermal conductivity measurements were made at room temperature and no attempt was made to maintain the temperature of nanofluids at a constant temperature because the fluctuations of the room temperature in the laboratory were very small.

Figure 5 shows the measured thermal conductivity of four oxide nanofluids as a function of nanoparticle volume fraction. The results show that nanofluids, containing only a small amount of nanoparticles, have substantially higher thermal conductivities than the same liquids without nanoparticles. For the copper oxide/ethylene glycol system, thermal conductivity can be enhanced by more than 20 percent at a volume fraction of 0.04 (4 vol.%).

Our experimental results clearly show that the thermal conductivity ratios increase almost linearly with volume fraction, but with different rates of increase for each system. The present experimental data also show that the thermal conductivity of nanofluids depends on the thermal conductivities of both the base fluids and

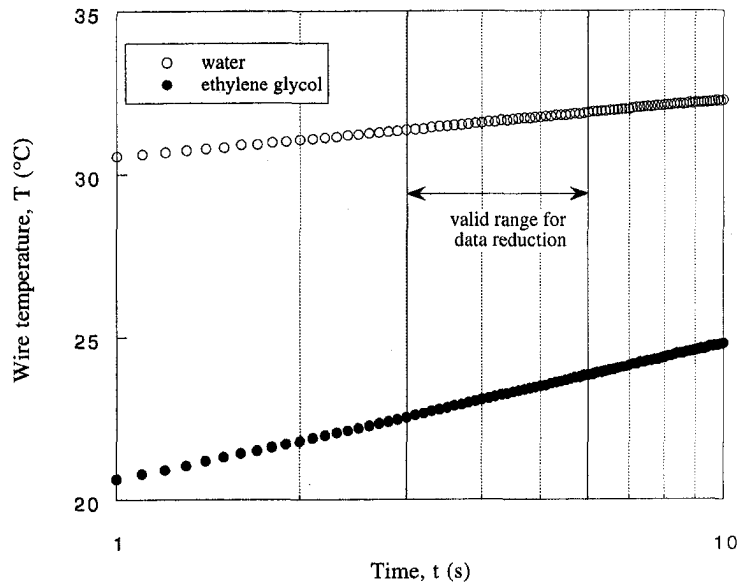


Fig. 3 Typical temperature rises versus logarithm of time

particles. For nanofluids using the same nanoparticles, the conductivity ratio increases of ethylene glycol nanofluid systems are always higher than those of water nanofluid systems. For nanofluids using the same liquid, the conductivity ratio of the CuO system is always higher than that of the Al_2O_3 system. We believe that CuO results in better thermal conductivity values than Al_2O_3 primarily because the CuO particles are smaller than the Al_2O_3 particles as shown in Table 1. In addition, it is possible that the processing of the CuO nanoparticles could have resulted in incomplete oxidation, which would then be manifested by the presence of a small amount of unreacted high thermal conductivity Cu being present in addition to the CuO.

4.3 Comparison With Hamilton and Crosser Model. Because of the absence of a theory for the thermal conductivity of nanofluids, an existing model for the solid/liquid system has been used to compare the predicted values with the measured thermal conductivity of nanofluids. Maxwell's model shows that the effective

thermal conductivity of suspensions containing spherical particles increases with the volume fraction of the solid particles. For nonspherical particles, it is known that the thermal conductivity of suspensions depends not only on the volume fraction of the particles, but also on the shape of the dispersed particles.

Hamilton and Crosser (1962) developed an elaborate model for the effective thermal conductivity of two-component mixtures as a function of the conductivity of the pure materials, the composition of the mixture, and the shape of the dispersed particles. The conductivity of two-component mixtures can be calculated as follows:

$$k = k_0 \left[\frac{k_p + (n-1)k_0 - (n-1)\alpha(k_0 - k_p)}{k_p + (n-1)k_0 + \alpha(k_0 - k_p)} \right] \quad (3)$$

where k is the mixture thermal conductivity, k_0 is the liquid thermal conductivity, k_p is the thermal conductivity of solid par-

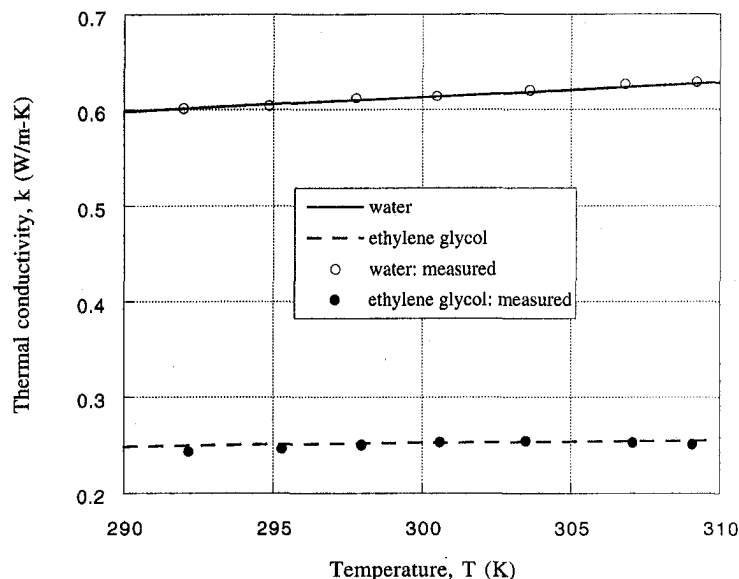


Fig. 4 Validation of present transient hot-wire method measuring thermal conductivity of base fluids; water, ethylene glycol

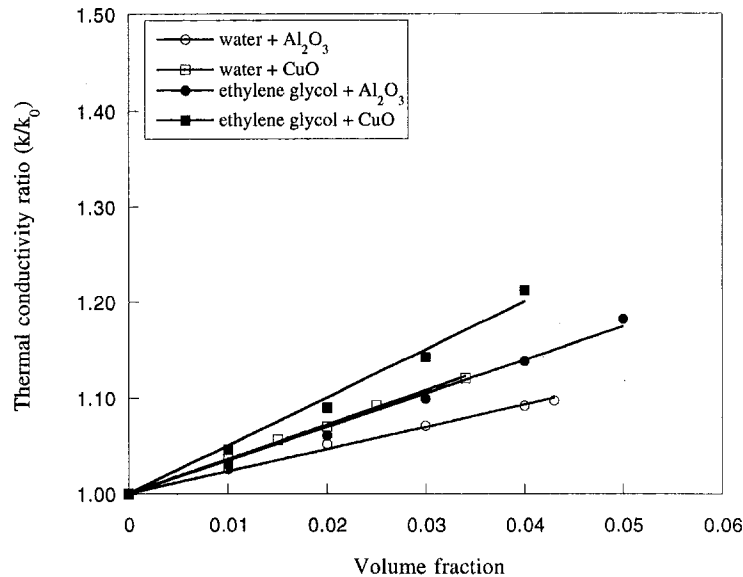


Fig. 5 Enhanced thermal conductivity of oxide nanofluids system

ticles, α is the particle volume fraction, and n is the empirical shape factor given by

$$n = 3/\Psi, \quad (4)$$

where Ψ is sphericity, defined as the ratio of the surface area of a sphere (with a volume equal to that of the particle) to the surface area of the particle. This model shows that nonspherical shapes will increase conductivity above that of spheres.

Although Eq. (3) is highly nonlinear, if the thermal conductivity ratio of solid phase to liquid phase, $k_p/k_0 \gg 1$ and the volume fraction is low, Eq. (3) can be linearized as follows:

$$k/k_0 \approx 1 + n\alpha. \quad (5)$$

Applying the Hamilton and Crosser model to aluminum oxide and copper oxide nanoparticles in water and ethylene glycol, we estimated the thermal conductivity ratios for two values of n (6 for cylinders and 3 for spheres). The present experimental thermal conductivities of oxide nanofluids are compared with the predicted results of Hamilton and Cross using Eq. (3). Comparisons of increase of the thermal conductivity ratios predicted by the Hamilton-Crosser model with results from the present experiments are shown in Fig. 6(a) for water/Al₂O₃ nanofluids, Fig. 6(b) for ethylene glycol/Al₂O₃ nanofluids, Fig. 6(c) for water/CuO nanofluids, and Fig. 6(d) for ethylene glycol/CuO nanofluids.

For Al₂O₃ nanofluids, it is seen from Fig. 6(a) and Fig. 6(b) that the predicted thermal conductivity ratios for spheres ($n = 3$) are in good agreement with the present experiments. This is consistent with the TEM micrographs which show that Al₂O₃ particles are quite close to perfect spheres. The thermal conductivity of Al₂O₃ nanofluids can be predicted satisfactorily by the Hamilton-Crosser model because these nanofluids contain large agglomerated spherical particles.

Figures 6(c) and 6(d) show the measured thermal conductivity of nanofluids containing CuO, along with the model predictions. It is seen that the agreement between the present experiments and model predictions is not good. The measured thermal conductivity ratios for CuO nanofluids are substantially larger than the Hamilton-Crosser model predictions. It is possible that a small quantity of metallic Cu in the CuO material used in these experiments increased the thermal conductivity of CuO nanofluids.

In the Hamilton-Crosser model, the thermal conductivity of suspensions depends strongly on particle shape when the ratio of the conductivities of the two phases k_p/k_0 is high as shown in Fig. 6(a–b) for alumina. When $k_p/k_0 = 0(1)$, particle shape is not

significant in enhancing the thermal conductivity of nanofluids, as shown in Fig. 6(c–d) for CuO with $k_p/k_0 < 4$.

4.4 Comparison With Experiments of Masuda et al. To our knowledge no experimental studies have been carried out on the thermal conductivity of CuO nanofluids. Direct comparison between the present experimental data and those of other investigators is possible only for water/Al₂O₃ nanofluids. Recently, Masuda et al. (1993) showed experimentally that Al₂O₃ particles at a volume fraction of 4.3 percent can increase the thermal conductivity of water by 30 percent.

For comparison, their experimental data and present work for water/Al₂O₃ nanofluids are shown in Fig. 7. The thermal conductivity ratios in our present experiments are lower than those of Masuda et al. by more than 20%. This is not surprising, since the mean diameter of Al₂O₃ particles used in the experiments of Masuda et al. is 13 nm, which in the present experiments is 38 nm. Because surface-area-to-volume ratio is three times larger for particles with a 13-nm diameter than for particles with a 38 nm diameter, a greater improvement in effective thermal conductivity is expected.

Another reason for the significant differences is that Masuda et al. used the electrostatic repulsion technique and a high-speed shearing disperser (up to $\approx 20,000$ r/min). These techniques might change the morphology of the nanoparticles, which was emphasized in the Hamilton-Crosser model as a shape factor n . Mainly because we did not use such techniques, nanoparticles in our systems were agglomerated and thus became larger and more spherical than those used by Masuda et al. In fact, Fig. 7 clearly shows that the measured data by Masuda et al. agree better with the estimated thermal conductivity from the Hamilton and Crosser model, assuming the shape factor of $n = 6$ (cylinders), and that our data agree better with the model predictions with the shape factor of $n = 3$ (spheres). However, it is important to note that even the model profile for nonspherical particles begins to diverge from the experimental data of Masuda et al. at a very low volume fraction. This strongly suggests that not only particle shape but also size is considered to be dominant in enhancing the thermal conductivity of nanofluids. Therefore, it is reasonable to expect that the model will fail to predict the thermal conductivity of nanofluids containing particles smaller than 13 nm.

Because heat transfer between the particles and the fluid takes place at the particle-fluid interface, our expectation is that if we have more interfacial area, then we would expect heat transfer to

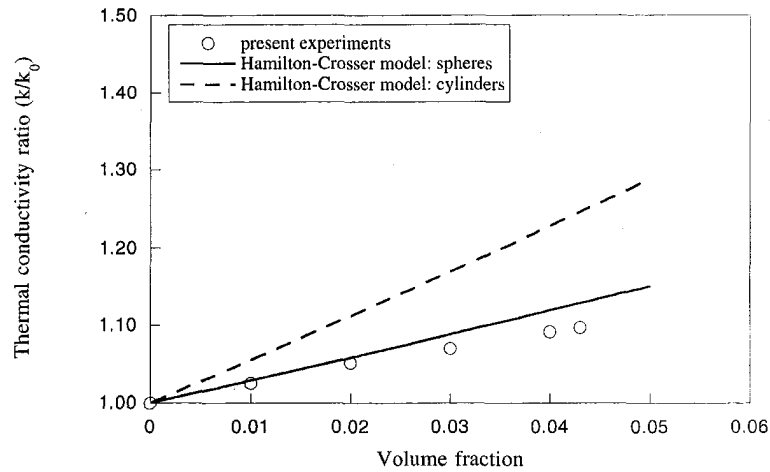


Fig. 6(a)

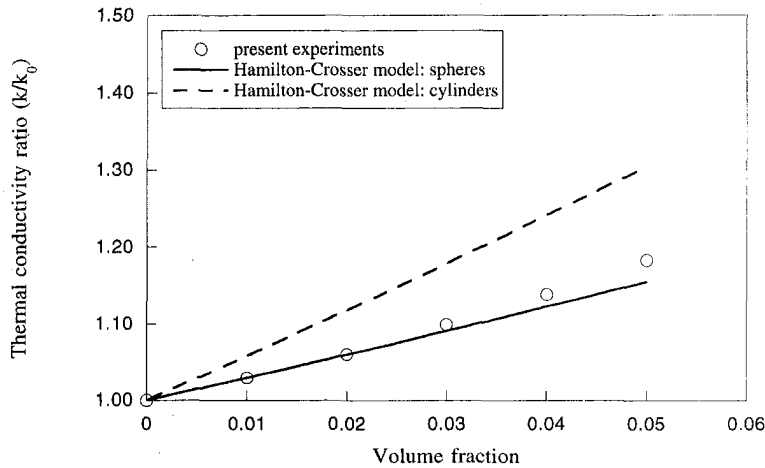


Fig. 6(b)

Fig. 6 Comparison of increase of thermal conductivity ratio between Hamilton-Crosser model and present experiment (a) water/ Al_2O_3 nanofluids, (b) ethylene glycol/ Al_2O_3 nanofluids, (c) water/ CuO nanofluids, and (d) ethylene glycol/ CuO nanofluids

be more efficient and thus quicker. If the behavior was just a simple rule of mixtures, where all that matter is the volume of particles, then particle surface area wouldn't matter. However, our thermal conductivity data indicate this not to be the case. Therefore, it is desirable to use particles with a large-surface-area-to-volume ratio. Previous theoretical work by Hamilton and Crosser (1962) focused on the possible effects of increasing particle surface area by controlling particle shapes to be nonspherical. However, improvement in surface area per particle volume attainable by this strategy is limited. As particle size decreases, the surface area of the particle decreases as the square of the length dimension, while the volume decreases as the cube of the length dimension. Because of this "square/cube law," the surface-area-to-volume ratio of nanoparticles is three orders of magnitude greater than that of microparticles. Therefore, a much more dramatic improvement in effective thermal conductivity is expected as a result of decreasing the particle size than can be obtained by altering the particle shapes of larger particles. Because all previous studies of the thermal conductivity of suspensions have been confined to those containing millimeter or micrometer-sized particles, existing models appear to be inadequate for nanofluids containing particles as small as 10 nm.

It is well known that, in the microscale regime, the thermal conductivity of a thin film material is much less than its bulk value, due to the scattering of the primary carriers of energy (phonon and/or electron) at its boundary (Flik and Tien, 1990; Majumdar, 1998). For electrical insulators such as the oxide materials of

interest in the present study, the phonon mean-free path can be estimated using an equation that Debye derived (Geiger and Poirier, 1973). Calculations show that for oxides such as Al_2O_3 , the estimated phonon mean-free path is comparable to the particle sizes we used. Therefore, the intrinsic thermal conductivity of oxide nanoparticles may be reduced compared to bulk oxides due to the size effect. Supporting this idea, the thermal conductivity of yttria-stabilized zirconia (YSZ) thin films with controlled nanocrystalline grain sizes was recently measured (Soyez et al., 1998). At room temperature, approximately a factor of two reduction in thermal conductivity of 10-nm grain-sized YSZ compared to that of the bulk material is seen.

All existing theories, models, and correlations for thermal conductivity (Maxwell, 1873; Hamilton and Crosser, 1962; Hashin and Shtrikman, 1962; Jeffrey, 1973; Jackson, 1975; Davis, 1986; Bonnecaze and Brady, 1991; Lu and Lin, 1996) were developed for fluids with relatively large particles and are very limited and often contradictory when applied to fluids containing nanoparticles because, in these theories, the effective thermal conductivity of liquid/particle suspensions depends only on the volume fraction and shape of the suspended particles, not on particle size.

There is a large body of literature that addresses the effect of the boundary resistance between the particle and the fluid on the thermal conductivity of composites and suspensions (Benveniste, 1987; Chiew and Glandt, 1987; Concalves and Kolodziej, 1993; Auriault and Ene, 1994; Ni et al., 1997). However,

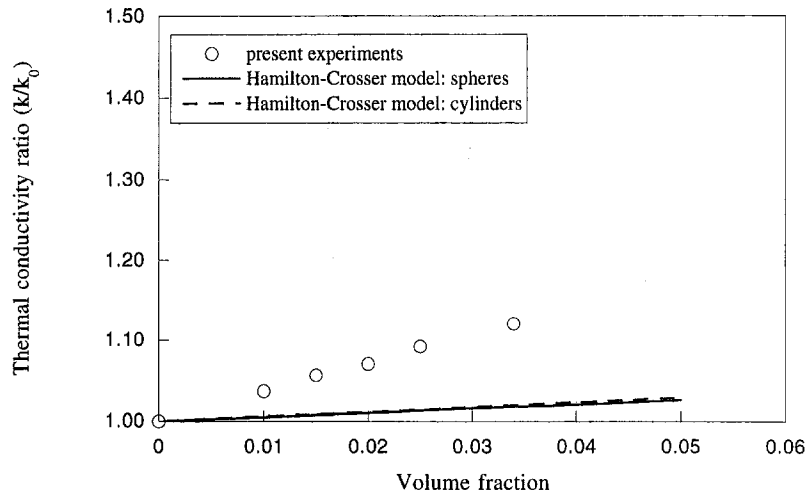


Fig. 6(c)

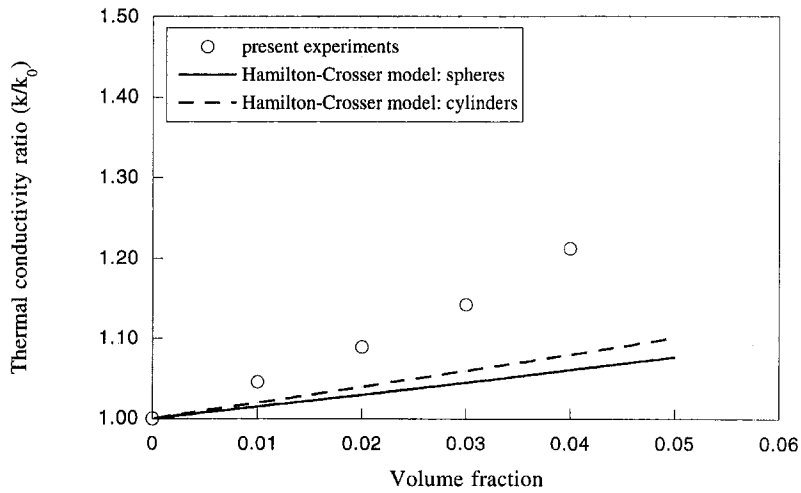


Fig. 6(d)

these models predict decreased thermal conductivity of nanofluids due to increased surface boundary resistance when particle size decreases. Comparison of our Al_2O_3 in water results with those of Masuda et al. (1993) clearly indicate that the effective conductivity for this system increases with decreasing particle

size, in contrast to the predictions based on boundary resistance. Also, these models are confined to conventional suspensions containing millimeter or micrometer-sized particles. Nanofluids appear to be quite different from conventional suspensions. The much larger surface areas of nanophase powders relative to

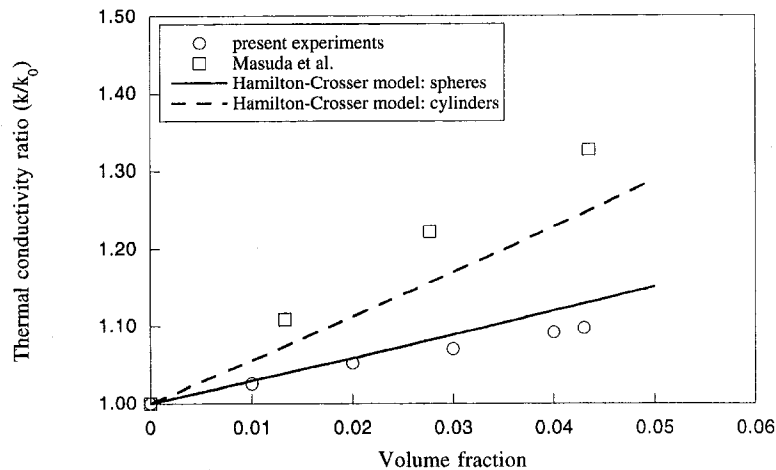


Fig. 7 Comparison of present experimental thermal conductivity ratios with experiments of Masuda et al. and model predictions for water/ Al_2O_3 nanofluids

those of conventional powders not only markedly improve conduction heat transfer capabilities, but also increase the stability of suspensions. Only recently have nanoparticles of 50 nm or less become available to investigators. We need to develop a more comprehensive theory in the future to explain the behavior of nanofluids. It appears that the thermal conductivity of nanofluids is very much surface area and structure dependent. Any new models of nanofluid thermal conductivity should include the surface area and structure dependent behavior as well as the size effect and boundary resistance.

5 Conclusions and Future Research Plan

To experimentally investigate the thermal conductivity behavior of dilute nanofluids, we measured the thermal conductivity of four oxide nanofluids (Al_2O_3 in water, Al_2O_3 in ethylene glycol, CuO in water, and CuO in ethylene glycol) by a transient hot-wire method.

The present experimental results show that nanofluids, containing only a small amount of nanoparticles, have substantially higher thermal conductivities than the same liquids without nanoparticles. For the copper oxide/ethylene glycol system, thermal conductivity can be enhanced by more than 20 percent at a volume fraction of 0.04 (4 vol.%). In the low-volume fraction range tested (up to 0.05), the thermal conductivity ratios increase almost linearly with volume fraction, but with different rates of increase for each system. The present experimental data also show that the thermal conductivity of nanofluids depends on the thermal conductivities of both the base fluids and particles: For nanofluids using the same nanoparticles, the conductivity ratio increases of ethylene glycol nanofluid systems are always higher than those of water nanofluid systems; For nanofluids using the same liquid, the conductivity ratio of the CuO system is always higher than that of the Al_2O_3 system.

Comparisons between the measured thermal conductivity of nanofluids and the predicted values of a model developed by Hamilton and Crosser (1962) were made. The Hamilton-Crosser model is capable of predicting the thermal conductivity of nanofluids containing large agglomerated Al_2O_3 particles. However, the model appears to be inadequate for nanofluids containing CuO particles. Further work is required to clarify the reasons for this discrepancy.

To clearly understand the mechanisms of thermal conductivity enhancement of nanofluids, further research is needed. One of the major differences between experimental data and the theoretical model is that the rate of increase of thermal conductivity depends strongly on particle size. Therefore, not only the effect of particle shape, which was considered by Hamilton and Crosser (1978), but more importantly, the effect of particle size should be investigated. We need to develop a more comprehensive theory in the future to explain the complex behavior of nanofluids.

In our study, the thermal conductivity of stationary nanofluids was considered. Several investigators have reported augmentation of the effective thermal conductivity of suspensions with millimeter-sized polystyrene particles under laminar flow (Ahuja 1975; Sohn and Chen 1981). Therefore, we expect that the effective thermal conductivity of nanofluids under flow conditions might be higher than that seen in the present experimental results. Hence, heat transfer tests to assess the thermal performance of nanofluids under controlled flow conditions are currently being conducted.

Acknowledgments

This work was supported by the U.S. Department of Energy, BES-DMS under Contract W-31-109-Eng-38, and by a grant from Argonne National Laboratory's Coordinating Council for Science and Technology.

References

Abernethy, R. B., Benedict, R. P., and Dowdell, R. B., 1985, "ASME Measurement Uncertainty," *ASME Journal of Fluids Engineering*, Vol. 107, pp. 161–164.

- Ahuja, A. S., 1975, "Augmentation of Heat Transport in Laminar Flow of Polystyrene Suspensions. I. Experiments and Results," *J. Appl. Phys.*, Vol. 46, No. 8, pp. 3408–3416.
- Ashley, S., 1994, "Small-scale Structure Yields Big Property Payoffs," *Mechanical Engineering*, Vol. 116, No. 2, pp. 52–57.
- Auriault, J.-L., and Ene, H. I., 1994, "Macroscopic Modelling of Heat Transfer in Composites with Interfacial Thermal Barrier," *Int. J. Heat Mass Transfer*, Vol. 37, No. 18, pp. 2885–2892.
- Bentley, J. P., 1984, "Temperature Sensor Characteristics and Measurement System Design," *J. Phys. E: Sci. Instrum.*, Vol. 17, pp. 430–439.
- Benveniste, Y., 1987, "Effective Thermal Conductivity of Composites with a Thermal Contact Resistance between the Constituents," *J. Appl. Phys.*, Vol. 61, No. 16, pp. 2840–2843.
- Bonnecaze, R. R., and Brady, J. F., 1991, "The Effective Conductivity of Random Suspensions of Spherical Particles," *Proc. R. Soc. Lond.*, Vol. A432, pp. 445–465.
- Carslaw, H. S., and Jaeger, J. C., 1959, *Conduction of Heat in Solids*, 2nd Ed., Oxford University Press, New York, p. 510.
- Chiew, Y. C., and Glandt, E. D., 1987, "Effective Conductivity of Dispersions: The Effect of Resistance at the Particle Surfaces," *Chem. Eng. Sci.*, Vol. 42, No. 11, pp. 2677–2685.
- Choi, U. S., 1995, "Enhancing Thermal Conductivity of Fluids with Nanoparticles," *Developments and Applications of Non-Newtonian Flows*, D. A. Siginer and H. P. Wang, eds., FED-Vol. 231/MD-Vol. 66, ASME, New York, pp. 99–105.
- Coleman, H. W., and Steele, W. G., 1989, *Experimentation and Uncertainty Analysis for Engineers*, John Wiley and Sons, New York.
- Concalves, L. C. C., and Kolodziej, J. A., 1993, "Determination of Effective Thermal Conductivity in Fibrous Composites with Imperfect Thermal Contact between Constituents," *Int. Comm. Heat Mass Transfer*, Vol. 20, pp. 111–121.
- Davis, R. H., 1986, "The Effective Thermal Conductivity of a Composite Material with Spherical Inclusions," *International Journal of Thermophysics*, Vol. 7, No. 3, pp. 609–620.
- Eastman, J. A., Choi, U. S., Li, S., Thompson, L. J., and Lee, S., 1997, "Enhanced Thermal Conductivity through the Development of Nanofluids," *Proceedings of the Symposium on Nanophase and Nanocomposite Materials II*, Vol. 457, Materials Research Society, Boston, pp. 3–11.
- Flik, M. I., and Tien, C. L., 1990, "Size Effect on the Thermal Conductivity of High- T_c Thin-Film Superconductors," *ASME JOURNAL OF HEAT TRANSFER*, Vol. 112, pp. 872–881.
- Geiger, G. H., and Poirier, D. R., 1973, *Transport Phenomena in Metallurgy*, Addison-Wesley, Reading, MA, p. 190.
- Gleiter, H., 1989, "Nanocrystalline Materials," *Prog. Mater. Sci.*, Vol. 33, pp. 223–315.
- Granqvist, C. G., and Buhrman, R. A., 1976, "Ultrafine Metal Particles," *J. Appl. Phys.*, Vol. 47, p. 2200.
- Hamilton, R. L., and Crosser, O. K., 1962, "Thermal Conductivity of Heterogeneous Two-Component Systems," *I & EC Fundamentals*, Vol. 1, No. 3, pp. 187–191.
- Hashin, Z., and Shtrikman, S., 1962, "A Variational Approach to the Theory of the Effective Magnetic Permeability of Multiphase Materials," *J. Appl. Phys.*, Vol. 33, No. 10, pp. 3125–3131.
- Hu, Z. S., and Dong, J. X., 1998, "Study on Antiwear and Reducing Friction Additive of Nanometer Titanium Oxide," *WEAR*, Vol. 216, pp. 92–96.
- Jackson, D. J., 1975, *Classical Electrodynamics*, 2nd Ed., John Wiley and Sons, London.
- Jeffrey, D. J., 1973, "Conduction Through a Random Suspension of Spheres," *Proc. R. Soc. Lond.*, Vol. A335, pp. 355–367.
- Johns, A. I., Scott, A. C., Watson, J. T. R., and Ferguson, D., 1988, "Measurement of the Thermal Conductivity of Gases by the Transient Hot Wire Method," *Phil. Trans. R. Soc. Lond.*, Vol. A325, pp. 295–356.
- Kestin, J., and Wakeham, W. A., 1978, "A Contribution to the Theory of the Transient Hot-wire Technique for Thermal Conductivity Measurement," *Physica*, Vol. 92A, pp. 102–116.
- Kimoto, K., Kamilaya, Y., Nonoyama, M., and Uyeda, R., 1963, "An Electron Microscope Study on Fine Metal Particles Prepared by Evaporation in Argon Gas at Low Pressure," *Jpn. J. Appl. Phys.*, Vol. 2, p. 702.
- Lee, S. P., and Choi, U. S., 1996, "Application of Metallic Nanoparticle Suspensions in Advanced Cooling Systems," *Recent Advances in Solids/Structures and Application of Metallic Materials*, Y. Kwon, D. Davis, and H. Chung, eds., PVP-Vol. 342/MD-Vol. 72, ASME, New York, pp. 227–234.
- Lu, S., and Lin, H., 1996, "Effective Conductivity of Composites Containing Aligned Spherical Inclusions of Finite Conductivity," *J. Appl. Phys.*, Vol. 79, No. 9, pp. 6761–6769.
- Majumdar, A., 1998, "Microscale Energy Transport in Solids," *Microscale Energy Transport*, C. L. Tien, A. Majumdar, and F. Gerner, eds., Taylor & Francis, Washington, DC.
- Masuda, H., Ebata, A., Teramae, K., and Hishinuma, N., 1993, "Alteration of Thermal Conductivity and Viscosity of Liquid by Dispersing Ultra-fine Particles (Dispersion of $\gamma\text{-Al}_2\text{O}_3$, SiO_2 , and TiO_2 Ultra-fine particles)," *Netsu Bussei (Japan)*, Vol. 4, No. 4, pp. 227–233.
- Maxwell, J. C., 1881, "A Treatise on Electricity and Magnetism," 2nd Ed., Vol. 1, Clarendon Press, Oxford, U.K., p. 435.
- Nagasaka, Y., and Nagashima, A., 1981, "Absolute Measurement of the Thermal Conductivity of Electrically Conducting Liquids by the Transient Hot-wire Method," *J. Phys. E: Sci. Instrum.*, Vol. 14, pp. 1435–1440.
- Ni, F., Gu, G. Q., and Chen, K. M., 1997, "Effective Thermal Conductivity of Nonlinear Composite Media with Contact Resistance," *Int. J. Heat Mass Transfer*, Vol. 40, pp. 943–949.

Roder, H. M., 1981, "A Transient Hot Wire Thermal Conductivity Apparatus for Fluids," *Journal of Research of the National Bureau of Standards*, Vol. 86, No. 5, pp. 457-493.

Rohrer, H., 1996, "The Nanoworld: Chances and Challenges," *Microelectronic Engineering*, Vol. 32, No. 1-4, pp. 5-14.

Sohn, C. W., and Chen, M. M., 1981, "Microconvective Thermal Conductivity in

Dispersed Two-Phase Mixtures as Observed in a Low Velocity Couette Flow Experiment," *ASME JOURNAL OF HEAT TRANSFER*, Vol. 103, pp. 47-51.

Soyez, G., Eastman, J. A., DiMelfi, R. J., and Thompson, L. J., 1998, private communication.

Touloukian, Y. S., and Ho, C. Y., eds., 1970 to 1977, *Thermal Properties of Matter, The TPRC Data Series*, Plenum Press, New York.

Higher-Order Sensitivity of Heat Conduction Problems to Random Data Using the Spectral Stochastic Finite Element Method

R. Ghanem

The Johns Hopkins University,
Baltimore, MD 21218

The spectral formulation of the stochastic finite element method is applied to the problem of heat conduction in a random medium. Specifically, the conductivity of the medium, as well as its heat capacity are treated as uncorrelated random processes with spatial random fluctuations. This paper introduces the basic concepts of the spectral stochastic finite element method using a simple one-dimensional heat conduction examples. The implementation of the method is demonstrated for both Gaussian and log-normal material properties. Moreover, the case of the material properties being modeled as random variables is presented as a simple digression of the formulation for the stochastic process case. Both Gaussian and log-normal models for the material properties are treated.

1 Introduction

Mathematical models of physical systems, be they in the form of partial differential equations, or in some other algorithmic form, are essentially abstract representations of our observations regarding these systems. One important usage of these models derives from their ability to predict the behavior of the systems in response to their environment, and thus allow for the mitigation against extreme conditions under which these systems may fail to fulfill their intended function. With the recent technological advances in materials and computational science, the expected accuracy of these models is being continually pushed to its limits. The engineering of materials at the nanoscale level, for example, requires tolerances that are vanishingly small. Also, given the capabilities of today's computers, and even more so the extrapolation of these capabilities into the near future, ever more sophisticated models of physical systems can be solved numerically, thus providing higher accuracy on the behavior of these systems and significantly extending their operational boundaries.

It is therefore clear that the drive for more accurate models is justified both by the need for the added accuracy from such models as well as by the ability to solve numerically the corresponding complex equations. One way to achieve this higher accuracy is to improve the fidelity of the parameters of the analytical model. In many cases, the accuracy in estimating these parameters can indeed be tightly controlled. The high costs associated with such a control, however, makes it very desirable to be able to assess a priori the sensitivity of the predictions with respect to specific parameters, so as to guide future experimental investigations according to a rational cost effective strategy.

In this paper, the above sensitivities are investigated by casting the problem in a probabilistic context, thus providing a rigorous framework in which to characterize the uncertainties in the data, to propagate them through the mathematical model, and to study their effect on predicted field variables. A number

of papers and books have been devoted to analyzing the propagation of uncertainty as described above (Fadale and Emery, 1994; Beck et al., 1985). The framework set forth in this paper views the random nature of the problem as contributing a new dimension to the problem along which approximation techniques, such as the weighted residual method, are applied. The details of this technique have been published elsewhere (Ghanem and Spanas, 1991; Schueller, 1997), and a brief review is included here for the sake of completeness.

In this paper a random medium property, such as thermal conductivity, will be expanded according to

$$\mathbf{k}(\mathbf{x}, \theta) = \sum_i \xi_i(\theta) \mathbf{k}_i(\mathbf{x}), \quad (1)$$

where θ denotes the random dimension, \mathbf{k}_i represents a deterministic function representing a component of the fluctuation of the property \mathbf{k} , while ξ_i represents the random magnitude of this function and hence its random contribution to the overall property. These functions can be viewed as representing the components of the random fluctuation at various scales, and will therefore be referred to as the scales of fluctuation. Clearly, the probabilistic structure of the random variables $\xi_i(\theta)$ depends on that of $\mathbf{k}(\mathbf{x}, \theta)$. These variables will follow a Gaussian distribution if and only if the quantity $\mathbf{k}(\mathbf{x}, \theta)$ being represented is itself Gaussian, otherwise their probabilistic character is not easily characterized in closed form. Both the property and its various scales are global quantities and depend on the spatial position \mathbf{x} ; they can also be multivariate quantities. The random medium, acting as a nonlinear filter, will couple the uncertainties from the various scales. The particular case of a random variable can be obtained as a specific digression of the foregoing to the case where the scales of fluctuation are constant over the range of their argument, and $\mathbf{k}(\mathbf{x}, \theta)$ is therefore independent of \mathbf{x} . Although most material properties are more accurately described as stochastic processes with spatially random fluctuations, in many cases it may prove more efficient, or consistent with the available data, to model them as random variables. The unification of the treatment for both cases is convenient as it permits a continuous transition from one case to the other while quantifying the change in the prediction. The solution sought in this paper, in the form of the temperature $T(\mathbf{x}, t, \theta)$

Contributed by the Heat Transfer Division for publication in the JOURNAL OF HEAT TRANSFER. Manuscript received by the Heat Transfer Division, May 22, 1997; final revision, Sept. 2, 1998. Keywords: Conduction, Modeling and Scaling, Numerical Methods. Associate Technical Editor: S. Ramadhyani.

throughout the domain, is a multidimensional nonlinear function of the set $\{\xi_i\}$ and will be assumed to have the following generic form:

$$T(\mathbf{x}, t, \theta) \equiv T(\{\xi_i(\theta)\}) = \sum_{i=0}^{\infty} T_i(\mathbf{x}, t) \psi_i(\theta), \quad (2)$$

where $\{T_i(\mathbf{x}, t)\}$ are deterministic quantities to be calculated, and $\{\psi_i(\theta)\}$ is a basis in the space of random variables. This basis will be taken to be the set of multidimensional Hermite polynomials in the quantities $\{\xi_i(\theta)\}$. This basis will be referred to as the polynomial chaos (Weiner, 1938). The Monte Carlo simulation procedure is a special case of the above representation, with

$$\psi_i(\theta) = \delta(\theta - \theta_i), \quad (3)$$

where θ_i is a particular outcome, and δ denotes Dirac's delta function. In this case, the stochastic process can be viewed as being equal to the collection of its realizations, and the summation in Eq. (2) should be viewed as a formal summation. In this case, the nonlinear filter action of the medium is eliminated by virtue of the property of the delta functions. Higher-order interactions between the various scales are therefore nonexistent in this case, and the scales associated with a Monte Carlo simulation are independent. This is as expected, since in this case, these scales represent independent realizations of the random property of the medium. It is clear, therefore, that Monte Carlo simulation provides a collocation approximation along the random dimension. This paper will present the framework that generalizes this concept. Of course, for the approximation associated with Eq. (3), the deterministic quantities $T_i(\mathbf{x}, t)$ represent individual realizations of the solution process that are associated with the random abscissa θ_i . Moreover, in a Monte Carlo setting, the equations for $T_i(\mathbf{x}, t)$ are uncoupled. More generally, the equations for the $T_i(\mathbf{x}, t)$ will be coupled, and they must be solved for simultaneously, thus requiring additional computational effort. However the number of terms required in the series representation will depend on the particular basis chosen. A balance can thus be reached between the size of the final system and the level of coupling between its components (Ghanem, 1998).

In addition to providing insight into the propagation of uncertainty with respect to scales of fluctuation of the random material properties, a format of the solution as given by Eq. (2) has an important appeal. Specifically, having distilled the uncertainty out of the spatial dimension through a representation that is reminiscent of the method of separation of variables, it becomes possible to perform a number of analytical operations on the solution process. These may be needed to determine, among others, the optimal sampling locations for both material properties and field variable. The details of these calculations, however, are not pursued further in this paper since the emphasis here is on developing the framework for characterizing the solution process itself.

In the next section, the discretization of random processes in terms of a finite number of random variables is presented. Emphasis is placed on two expansions, namely the Karhunen-Loeve and the polynomial chaos expansions.

In the next section, random variables and stochastic processes are briefly reviewed with emphasis on their representation in computationally tractable forms. Following that, the nondimensional equations governing heat conduction in a randomly heterogeneous medium are reviewed. Next, the discretization with respect to the spatial variables is implemented via the finite elements formalism, resulting in a set of nonlinear ordinary differential equations with respect to the time variable. In view of the randomness of the material properties of the material, the unknowns at this stage consist of vectors of random variables representing the temperature at the nodes. After that, the Karhunen-Loeve and the polynomial chaos expansions are used to obtain an ordinary differential equation with deterministic coefficients. Finally, the formalism is exemplified by its application to a one-dimensional problem, and the significance of the results is discussed.

2 Representation of Random Variables and Stochastic Processes

The development presented in this paper hinges on the definition of random variables as *measurable functions* from the space of elementary events to the real line. As functions, approximation theory, as developed for deterministic functions, will be

Nomenclature

a_{i_1, \dots, i_k} = coefficient in polynomial chaos expansion	\mathbf{H} = derivatives of the shape functions	$\delta(\cdot)$ = Dirac's delta function
\mathbf{a}_{ij} = nondimensional conductance tensor	L = length of domain	$\psi_i(\theta)$ = orthogonal polynomials in $\{\xi_i\}$
\mathbf{C} = global capacitance matrix	N, N_c, N_k = number of terms included in various expansions	λ_i = eigenvalue of the covariance kernel
\mathbf{C}_i = global capacitance matrix derived from the i th term in Karhunen-Loeve expansion	$R_{kk}(\mathbf{x}, \mathbf{y})$ = covariance function of $k(\mathbf{x})$	$\phi_i(\mathbf{x})$ = eigenfunction of the covariance kernel
$\mathbf{C}_i^{(e)}$ = elemental matrix associated with matrix \mathbf{C}_i	\mathbf{q} = flux vector	Ω = spatial domain of definition of the problem
c = heat capacity	q_b = boundary flux	$\partial\Omega_1$ = spatial domain boundary with essential boundary conditions
\bar{c} = mean of c	\mathbf{T} = nodal temperatures	$\partial\Omega_2$ = spatial domain boundary with natural boundary conditions
d = nondimensional heat capacity	\mathbf{T}_i = i th component of the nodal temperatures	$\pi(\cdot)$ = symmetric permutation of its arguments
\mathbf{K} = global conductance matrix	$T(\mathbf{x}, t, \theta)$ = random temperature at point \mathbf{x} and time t	θ = index on space of random events
\mathbf{K}_i = global conductance matrix derived from the i th term in Karhunen-Loeve expansion	T_0 = initial temperature	$\xi_i(\theta)$ = uncorrelated random variables
$\mathbf{k}(\mathbf{x}, \theta)$ = random thermal conductivity at location \mathbf{x}	\dot{T} = time derivative of T	ξ = nondimensional spatial coordinate
$\mathbf{k}_i(\mathbf{x})$ = i th scale of fluctuation of $k(\mathbf{x}, \theta)$	T^+ = nondimensional temperature	
$\bar{k}(\mathbf{x})$ = mean of k	t^+ = nondimensional time	
	α = nondimensional thermal property = \bar{k}_{11}/\bar{c}	
	$\Gamma_n(\xi_{i_1}, \dots, \xi_{i_n})$ = polynomial chaos of order n	

applied to random variables. The main question to be addressed, already raised in the Introduction, is the characterization of the solution to a physical problem where some parameters of the model have been modeled as stochastic processes. The answer to this question lies in the realization that in the deterministic finite element method, as well as most other numerical analysis techniques, a solution to a deterministic problem is known once its projection on a basis in an appropriate function space has been evaluated. It often happens, in deterministic analysis, that the coefficients in such a representation have an immediate physical meaning, which distracts from the mathematical significance of the solution. Carrying this argument over to the case involving stochastic processes, the solution to the problem will be identified with its projection on a set of appropriately chosen basis functions. A random variable, will thus be viewed as a function of a single variable, θ , that indexes the space of elementary events. A stochastic process or field, k , being defined as a space-indexed (or time-indexed) collection of random variables is then formally a function of $n + 1$ variables where n is the physical dimension of the space over which each realization of the process is defined. This dimension generally refers to either space or time, spatial stochastic processes being the subject of this paper. As already mentioned in the Introduction, Monte Carlo simulation can be viewed as a collocation along this θ dimension. Other approximations along this dimension are possible, and are explored in this section. This theoretical development is consistent with the identification of the space of second-order random variables as a Hilbert space with the inner product on it defined as the mathematical expectation operation (Loeve, 1977). Second-order random variables are those random variables with finite variance, they are mathematically similar to deterministic functions with finite energy.

2.1 Karhunen-Loeve Expansion. The Karhunen-Loeve expansion (Loeve, 1977) of a stochastic process $k(\mathbf{x}, \theta)$, is based on the spectral expansion of its covariance function $R_{kk}(\mathbf{x}, \mathbf{y})$. Here, \mathbf{x} and \mathbf{y} are used to denote spatial coordinates, while the argument θ indicates the random nature of the corresponding quantity. When the process has been discretized over space, a covariance matrix is obtained that represents the correlation between the various members of the resulting discretized vector. The covariance function being symmetrical and positive definite, by definition, has all its eigenfunctions mutually orthogonal, and they form a complete set spanning the function space to which $k(\mathbf{x}, \theta)$ belongs. It can be shown that if this deterministic set is used to represent the process $k(\mathbf{x}, \theta)$, then the random coefficients used in the expansion are also orthogonal. The expansion then takes the following form:

$$k(\mathbf{x}, \theta) = \bar{k}(\mathbf{x}) + \sum_{i=1}^{\infty} \sqrt{\lambda_i} \xi_i(\theta) \phi_i(\mathbf{x}), \quad (4)$$

where $\bar{k}(\mathbf{x})$ denotes the mean of the stochastic process, and $\{\xi_i(\theta)\}$ forms a set of orthogonal random variables. Furthermore, $\{\phi_i(\mathbf{x})\}$ are the eigenfunctions and $\{\lambda_i\}$ are the eigenvalues, of the covariance kernel, and can be evaluated as the solution to the following integral equation:

$$\int_{\Omega} R_{kk}(\mathbf{x}, \mathbf{y}) \phi_i(\mathbf{y}) d\mathbf{y} = \lambda_i \phi_i(\mathbf{x}), \quad (5)$$

where Ω denotes the spatial domain over which the process $k(\mathbf{x}, \theta)$ is defined. The most important aspect of this spectral representation is that the spatial random fluctuations have been decomposed into a set of deterministic functions in the spatial variables multiplying random coefficients that are independent of these variables. If the random process being expanded, $k(\mathbf{x}, \theta)$, is gaussian, then the random variables $\{\xi_i\}$ form an orthogonal Gaussian vector. The Karhunen-Loeve expansion is mean-square convergent irrespective of the probabilistic structure of the process being expanded, provided it has a finite

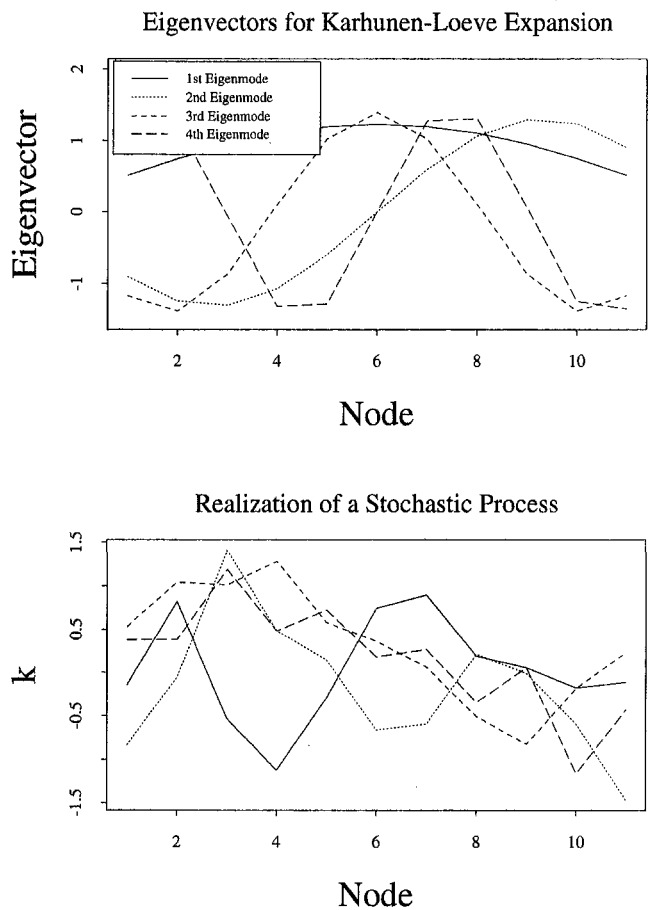


Fig. 1 Eigenvectors and realizations for correlation length = 0.2

variance (Loeve, 1977). The closer a process is to white noise, the more terms are required in its expansion, while at the other limit, a random variable can be represented by a single term. In physical systems, it can be expected that material properties vary smoothly at the scales of interest in most applications, and therefore only few terms in the Karhunen-Loeve expansion can capture most of the uncertainty in the process. Clearly, the more accuracy is required from the predictions of a certain model, the more terms should be included in the Karhunen-Loeve series representing its data. This expansion represents a rational procedure for optimally truncating a discrete representation of a stochastic process which minimizes the lost information. Figure 1 shows a one-dimensional stochastic process with a very small correlation length along with its first four scales of fluctuation (the functions $\phi_i(\mathbf{x})$). Since the eigenfunctions are normalized, the eigenvalues reflect the contribution of each of the scales to the overall process. Given the intrinsic symmetry and positive-definiteness of the covariance function these eigenvalues decay monotonically. Figure 2 shows similar data for a stochastic process having a very large correlation length. Note that in this case, only the first eigenvector contributes significantly to the overall process. Given the almost constant amplitude of this eigenvector, realizations of the process are almost constant over the spatial extent of the domain. Also shown in both of these figures are corresponding realizations of the stochastic processes simulated according to the Karhunen-Loeve representation.

2.2 Polynomial Chaos Expansion. The covariance function of the solution process is not known a priori, and hence the Karhunen-Loeve expansion cannot be used to represent it. Since the solution process is a function of the material properties, nodal temperatures, $T(\theta)$, can be formally expressed as some nonlinear functional of the set $\{\xi_i(\theta)\}$ used to represent

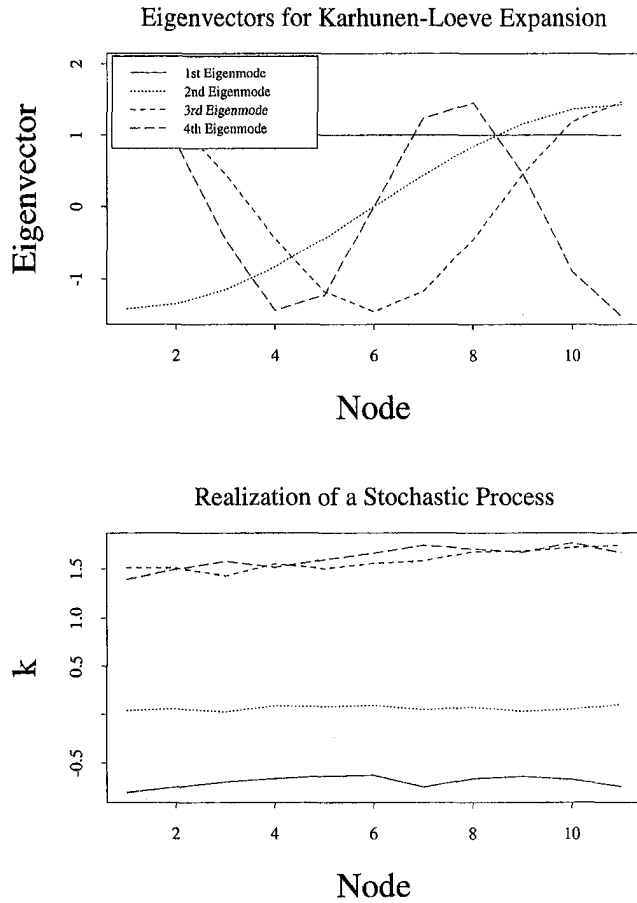


Fig. 2 Eigenvectors and realizations for correlation length = 100

the material stochasticity. It has been shown (Cameron and Martin, 1947) that this functional dependence can be expanded in terms of polynomials in Gaussian random variables, referred to as polynomial chaoses. Namely,

$$T(\theta) = a_0 \Gamma_0 + \sum_{i_1=1}^{\infty} a_{i_1} \Gamma_1(\xi_{i_1}(\theta)) + \sum_{i_1=1}^{\infty} \sum_{i_2=1}^{i_1} a_{i_1 i_2} \Gamma_2(\xi_{i_1}(\theta), \xi_{i_2}(\theta)) + \dots \quad (6)$$

In this equation, the symbol $\Gamma_n(\xi_{i_1}, \dots, \xi_{i_n})$ denotes the polynomial chaos (Wiener, 1938; Kallianpur, 1980) of order n in the variables $(\xi_{i_1}, \dots, \xi_{i_n})$. These are generalizations of the multidimensional Hermite polynomials to the case where the independent variables are functions measurable with respect to the Wiener measure. In general, the n th-order polynomial chaos can be expressed as

$$\Gamma_n(\xi_1(\theta), \dots, \xi_n(\theta)) = \begin{cases} \sum_{\substack{r=n \\ r \text{ even}}}^0 (-1)^r \sum_{\pi(i_1, \dots, i_n)} \prod_{k=1}^r \xi_{i_k}(\theta) \prod_{l=r+1}^n \xi_{i_l}(\theta) & n \text{ even} \\ \sum_{\substack{r=n \\ r \text{ even}}}^0 (-1)^{r-1} \sum_{\pi(i_1, \dots, i_n)} \prod_{k=1}^r \xi_{i_k}(\theta) \prod_{l=r+1}^n \xi_{i_l}(\theta) & n \text{ odd} \end{cases} \quad (7)$$

where $\pi(\cdot)$ denotes a permutation of its arguments, and the sum is over all such permutations such that the sets $\{\xi_{i_1}, \dots, \xi_{i_r}\}$ is modified by the permutation. Introducing a one-to-one

mapping to a set with ordered indices denoted by $\{\psi_i(\theta)\}$ and truncating the polynomial chaos expansion after the p th term, Eq. (6) can be rewritten as

$$T(\theta) = \sum_{j=0}^p T_j \psi_j(\theta). \quad (8)$$

These polynomials are orthogonal in the sense that their inner product $\langle \psi_j \psi_k \rangle$, which is defined as the statistical average of their product, is equal to zero for $j \neq k$. Moreover, they can be shown to form a complete basis in the space of second-order random variables. A complete probabilistic characterization of the process $T(\theta)$ is obtained once the deterministic coefficients T_j have been calculated. A given truncated series can be refined along the random dimension either by adding more random variables to the set $\{\xi_i\}$ or by increasing the maximum order of polynomials included in the polynomial chaos expansion. The first refinement takes into account higher frequency random fluctuations of the underlying stochastic process. Although the present paper addresses spatial processes, these random fluctuations can be either temporal or spatial depending, respectively, on whether the process extends over time or space. The second refinement captures strong nonlinear dependence of the solution process on this underlying process. It should be noted at this point that the polynomial chaos expansion can be used to represent, in addition to the solution process, stochastic processes that model non-Gaussian material properties. The processes representing the material properties are thus expressed as the output of a nonlinear system to a Gaussian input.

3 Governing Equations

Since it will be assumed in the foregoing that the material properties of the medium are spatially varying, it will be necessary to carefully develop the nondimensional form of the heat conduction equations. The heat equation for a spatially varying medium is given by

$$c \frac{\partial T}{\partial t} - \nabla \cdot \mathbf{k} \nabla T = 0, \quad \mathbf{x} \in \Omega \quad (9)$$

subjected to the following initial and boundary conditions:

$$T(0, \mathbf{x}) = T_0, \quad T(t, \mathbf{x}) = T_b, \quad \mathbf{x} \in \partial\Omega_1, \\ -\mathbf{k} \frac{\partial T}{\partial n} = q_b, \quad \mathbf{x} \in \partial\Omega_2. \quad (10)$$

In these equations, Ω denotes the spatial domain of definition of the problem, $\partial\Omega_1$ denotes a subset of its boundary along which essential boundary conditions are applied, while $\partial\Omega_2$ denotes that portion of the boundary along which natural conditions are applied, and \mathbf{x} denotes a spatial coordinate. Moreover, \mathbf{k} and c denote, respectively, the conductivity tensor and the volumetric heat capacity of the medium which will be assumed to be spatially varying random process. Let

$$\mathbf{k} = [\mathbf{k}_{ij}] = \bar{k}_{11} [\mathbf{a}_{ij}] \quad (11)$$

where \mathbf{a} is an anisotropy tensor, equal to the identity tensor for a homogeneous and isotropic material, and \bar{k}_{11} denotes the mean of the conductivity tensor in direction 11. Moreover, introducing the following nondimensional space and time variables

$$\zeta = \frac{\mathbf{x}}{L}, \quad t^+ = \frac{\alpha t}{L^2}, \quad T^+ = \frac{T - T_0}{q_b L / \bar{k}_{11}}, \\ \alpha = \frac{\bar{k}_{11}}{c}, \quad d = \frac{c}{\bar{c}}, \quad (12)$$

where L is some representative spatial scale, results in the final form of the governing equation,

$$d \frac{\partial T^+}{\partial t^+} - \nabla \cdot \mathbf{a} \nabla T^+ = 0. \quad (13)$$

The initial and boundary conditions associated with the new nondimensional variables are given by

$$T^+(0, \boldsymbol{\zeta}) = 0, \quad T^+(t, \boldsymbol{\zeta}) = \frac{T_b - T_0}{q_b L / \bar{k}_{11}}, \quad \boldsymbol{\zeta} \in \partial\Omega_1, \\ -\mathbf{a} \frac{\partial T^+}{\partial n} = 1, \quad \boldsymbol{\zeta} \in \partial\Omega_2. \quad (14)$$

Following the presentation in the previous section above, the conductivity tensor and the volumetric heat capacity can be expanded according to

$$d(\boldsymbol{\zeta}) = 1 + \sum_{i=1}^{N_c} \xi_i d_i(\boldsymbol{\zeta}) = \sum_{i=0}^{N_c} \xi_i d_i(\boldsymbol{\zeta}), \quad (15)$$

and

$$\mathbf{a}(\boldsymbol{\zeta}) = \mathbf{I} + \sum_{i=1}^{N_k} \xi_i \mathbf{a}_i(\boldsymbol{\zeta}) = \sum_{i=0}^{N_k} \xi_i \mathbf{a}_i(\boldsymbol{\zeta}). \quad (16)$$

It should be noted here that since the processes \mathbf{a} and d are assumed to be independent, the random variables ξ_i appearing in their respective expansions are also independent. Thus, denoting

$$N = N_c + N_k, \quad (17)$$

the above expansions can be rewritten as

$$d(\boldsymbol{\zeta}) = 1 + \sum_{i=1}^N \xi_i d_i(\boldsymbol{\zeta}), \quad d_i = 0, \quad i > N_c, \quad (18)$$

and

$$\mathbf{a}(\boldsymbol{\zeta}) = \mathbf{I} + \sum_{i=1}^N \xi_i \mathbf{a}_i(\boldsymbol{\zeta}), \quad \mathbf{a}_i = 0, \quad i \leq N_c. \quad (19)$$

Substituting these two expansions into the governing equation yields

$$\left(1 + \sum_{i=1}^N \xi_i d_i(\boldsymbol{\zeta})\right) \frac{\partial T^+}{\partial t^+} - \nabla \cdot \left(1 + \sum_{i=1}^N \xi_i \mathbf{a}_i(\boldsymbol{\zeta})\right) \nabla T^+ = 0. \quad (20)$$

In the spirit of the finite element method, this last equation is projected onto a basis consisting of test functions, taken here to be the set of local polynomials in the spatial variables $\boldsymbol{\zeta}$. Following that with the traditional Galerkin projection results in the following algebraic equation for the nodal temperatures:

$$\sum_{i=0}^N \xi_i \mathbf{C}_i \dot{\mathbf{T}} + \sum_{i=0}^N \xi_i \mathbf{K}_i \mathbf{T} = \mathbf{q}, \quad (21)$$

where the matrices \mathbf{C}_i and \mathbf{K}_i are obtained by assembling the elemental matrices given by

$$\mathbf{C}_i^{(e)} = \int_{\Omega^{(e)}} d_i(\boldsymbol{\zeta}) \mathbf{H}(\boldsymbol{\zeta}) \mathbf{H}^T(\boldsymbol{\zeta}) d\boldsymbol{\zeta}, \quad (22)$$

and

$$\mathbf{K}_i^{(e)} = \int_{\Omega^{(e)}} \nabla \mathbf{H}^T(\boldsymbol{\zeta}) \mathbf{a}_i(\boldsymbol{\zeta}) \nabla \mathbf{H}(\boldsymbol{\zeta}) d\boldsymbol{\zeta}, \quad (23)$$

and the right-hand side vector is obtained by assembling the following elemental vectors:

$$\mathbf{q}^{(e)} = \int_{\partial\Omega^{(e)}} \mathbf{H}(\boldsymbol{\zeta}) d(\partial\Omega). \quad (24)$$

Here, the matrices \mathbf{H} consist of derivatives of the shape functions. For the problem at hand, bilinear shape functions are adequate and will be used in the numerical example. The essential boundary conditions can then be implemented according to standard finite element procedures, assuming they are to be

imposed with probability one. For each realization of the random variables ξ_i , the above equations can be solved for a corresponding realization of the temperature \mathbf{T} throughout the domain. It should be noted that the element-level matrices $\mathbf{C}_i^{(e)}$ and $\mathbf{K}_i^{(e)}$ appearing above are given by expressions that are analogous to the elemental matrices in deterministic finite elements. The only distinction being in the fact that the material properties used in computing the i th matrix are given by the i th scale of fluctuation of the material property as given by $d_i(\boldsymbol{\zeta})$ or $\mathbf{a}_i(\boldsymbol{\zeta})$.

Next, a procedure is developed that implements the concepts developed in the previous section. Specifically, the temperature field \mathbf{T} is represented as

$$\mathbf{T} = \sum_{j=0}^M \psi_j \mathbf{T}_j, \quad (25)$$

and a framework is developed for evaluating the deterministic coefficients \mathbf{T}_j in this expansion. Substituting this expansion in Eq. (21) above yields

$$\sum_{j=0}^M \sum_{i=0}^N \xi_i \psi_j \mathbf{C}_i \dot{\mathbf{T}}_j + \sum_{j=0}^M \sum_{i=0}^N \xi_i \psi_j \mathbf{K}_i \mathbf{T}_j = \mathbf{q}. \quad (26)$$

Multiplying this last equation by each of the ψ_k and taking the ensemble average results in the following equation:

$$\sum_{j=0}^M \sum_{i=0}^N \langle \xi_i \psi_j \psi_k \rangle \mathbf{C}_i \dot{\mathbf{T}}_j + \sum_{j=0}^M \sum_{i=0}^N \langle \xi_i \psi_j \psi_k \rangle \mathbf{K}_i \mathbf{T}_j = \langle \mathbf{q} \psi_k \rangle, \\ k = 1, \dots, M. \quad (27)$$

This last procedure is mathematically equivalent to forcing the error in the approximation for the temperature to be orthogonal to the approximating space as defined by the basis $\{\psi_i\}$. Finally, denoting $\langle \xi_i \psi_j \psi_k \rangle$ by d_{ijk} , and $\langle \mathbf{q} \psi_k \rangle$ by \mathbf{q}_k , this last equation becomes

$$\sum_{j=0}^M \sum_{i=0}^N d_{ijk} \mathbf{C}_i \dot{\mathbf{T}}_j + \sum_{j=0}^M \sum_{i=0}^N d_{ijk} \mathbf{K}_i \mathbf{T}_j = \mathbf{q}_k, \quad k = 1, \dots, M. \quad (28)$$

This is a linear system of deterministic equations that can be solved for the unknown coefficients \mathbf{T}_j . Values for the coefficients d_{ijk} can be calculated ahead of time and tabulated. Clearly, this system of equations has dimension $M \times N$ -degrees of-Freedom where N -degrees of-Freedom is the number of deterministic degrees-of-freedom in the system, and is therefore much more computationally intensive to solve than the deterministic problem. However, efficient customized algorithms have been developed (Ghanem and Kruger, 1996) that take into consideration the fact that all submatrices \mathbf{C}_i and \mathbf{K}_i have the same nonzero structure as their deterministic counterparts, thus significantly reducing the storage requirements for the problem. Advantage can also be drawn from the observation that a lower-order solution (say with a smaller value of M) provides a good approximation to a higher-order solution. This property is a consequence of the spectral nature of the polynomial chaos expansion. Its immediate benefit is achieved when implemented with an iterative linear solver whereby the availability of a good initial guess is crucial for the accelerated convergence of the iterations. Efficiency gains of two orders of magnitudes have been achieved by capitalizing on the above observations (Ghanem and Kruger, 1996). For a first-order expansion, the number of equations that needs to be assembled is equal to the number of terms in the Karhunen-Loeve expansion. This is similar, in terms of computational effort, to the perturbation approach, with the added benefit, however, of the ability to expand to higher-order expansions in a convergent and consistent manner and without the need to compute higher-order derivatives.

Once the coefficients in the expansion of the solution process have been evaluated, the variance of the solution can be readily obtained. Noting that the polynomial chaos basis is orthogonal,

a simple expression for the covariance matrix of the solution process is given by

$$\mathbf{R}_{TT} = \sum_{i=1}^N \mathbf{T}_i \mathbf{T}_i^T \langle \psi_i^2 \rangle. \quad (29)$$

The variance of the solution at any nodal point is then obtained as the diagonal elements of \mathbf{R}_{TT} . Of course, additional information is contained in the expansion coefficients \mathbf{T}_i , beyond this second-order characterization. Indeed, a complete probabilistic characterization is condensed in these coefficients. Simulated realizations of the solution can be simply obtained by generating a set of random variables ξ_i from which the polynomial chaoses are formed and used in the expansion of the temperature field. The coefficients of the first-order expansion (those multiplying the first-order polynomials, $\xi_1, \xi_2, \xi_3, \xi_4$) can be viewed as the first-order sensitivity coefficients similar to those obtained from a perturbation-based analysis of the problem (Fadale and Emery, 1994).

The framework presented in the previous sections is now applied to a simple example. Consider a one-dimensional domain defined over $\zeta \in [0, 1]$, with both random heat capacity and random conductivity. Assume each of these two random quantities to be specified, in a probabilistic sense, by its mean value and its correlation function. Note that in the case of a random variable, this mean value would be a constant, and the correlation function would be equal to the variance of the random variable. The covariance function used in the numerical examples is the exponential function having the form,

$$R_{kk}(x, y) = \sigma_k^2 e^{-|x-y|/b}, \quad (30)$$

where σ_k denotes the standard deviation of k and b its correlation length. The two random processes can then be represented in the following form:

$$\mathbf{C} = \bar{\mathbf{C}} + \xi_1 \mathbf{C}_1, \quad (31)$$

and

$$\mathbf{K} = \bar{\mathbf{K}} + \xi_1 \mathbf{K}_1 + \xi_2 \mathbf{K}_2 + \xi_3 \mathbf{K}_3, \quad (32)$$

where the random variables ξ_i appearing in both expansions are orthogonal. The inclusion of two terms in the representation of the heat capacity reflects the hypothesis that it varies slowly over space, while the inclusion of four terms in the representation for the conductivity corresponds to the hypothesis that this property varies more significantly over space. Figures 1 and 2 show examples of two such processes. In order to combine both expansions in the same computational framework, it is expedient to rewrite them as follows:

$$\mathbf{C} = \bar{\mathbf{C}} + \xi_1 \mathbf{0} + \xi_2 \mathbf{0} + \xi_3 \mathbf{0} + \xi_4 \mathbf{C}_4 = \sum_{i=0}^4 \xi_i \mathbf{C}_i, \quad (33)$$

and

$$\mathbf{K} = \bar{\mathbf{K}} + \xi_1 \mathbf{K}_1 + \xi_2 \mathbf{K}_2 + \xi_3 \mathbf{K}_3 + \xi_4 \mathbf{0} = \sum_{i=0}^4 \xi_i \mathbf{K}_i. \quad (34)$$

Moreover, an expansion of the temperature field as given by Eq. (6) will be sought. This has the form

$$\begin{aligned} \mathbf{T} &= \bar{\mathbf{T}} + \xi_1 \mathbf{T}_1 + \xi_2 \mathbf{T}_2 + \xi_3 \mathbf{T}_3 + \xi_4 \mathbf{T}_4 + (\xi_1^2 - 1) \mathbf{T}_5 \\ &\quad + (\xi_1 \xi_2) \mathbf{T}_6 + (\xi_1 \xi_3) \mathbf{T}_7 + (\xi_1 \xi_4) \mathbf{T}_8 + (\xi_2^2 - 1) \mathbf{T}_9 \\ &\quad + (\xi_2 \xi_3) \mathbf{T}_{10} + (\xi_2 \xi_4) \mathbf{T}_{11} + (\xi_3^2 - 1) \mathbf{T}_{12} + (\xi_3 \xi_4) \mathbf{T}_{13} \\ &\quad + (\xi_4^2 - 1) \mathbf{T}_{14} + (\xi_1^3 - 3\xi_1) \mathbf{T}_{15} + (\xi_4^3 - 3\xi_4) \mathbf{T}_{34} \\ &= \sum_{i=0}^{15} \psi_i \mathbf{T}_i + \psi_{34} \mathbf{T}_{34}. \end{aligned} \quad (35)$$

This expansion includes all the second-order terms plus two third-order terms in the four variables ξ_i defining the material

properties, and thus serves as an approximation of the temperature field as a surface in the space defined by these variables (recall that $\xi_0 \equiv 1$ and is thus not considered as one of the basic variables). The indexing on the coefficients in all the above expansions is compatible with a four-dimensional expansion. For lower-dimensional expansion, the same indexing can still be used with only the coefficients referencing the active ξ_i variables not equal to zero. For higher-order expansions, on the other hand, the indexing scheme must be modified in order to insert the polynomials with respect to the new variables at their appropriate location. The expansion given by Eq. (35) can be shown to be a mean-square convergent for any stochastic process with finite variance (Ghanem and Spanos, 1991). The significance of the various terms in Eq. (35) is of great relevance in applications. In particular, to the extent that each ξ_i represents the contribution of the i th scale of fluctuation of a specific material property, the coefficients of the first-order terms in the expansion of the temperature field (i.e., those terms multiplying the first-order polynomials), represent the first-order sensitivity of the temperature with respect to those scales. More accurate estimates of these sensitivity coefficients, however, can be obtained by including the effects of the higher-order terms, according to the chain rule, resulting in the following equation:

$$\frac{\partial \mathbf{T}}{\partial \xi_i} = \sum_{j=0}^{14} \frac{\partial \psi_j}{\partial \xi_i} \cdot \mathbf{T}_j. \quad (36)$$

The first-order sensitivity of the temperature with respect to the overall property is obtained by adding the contribution from all scales making up that property, resulting in

$$\frac{\partial \mathbf{T}(t, \theta)}{\partial \mathbf{a}(t, \theta)} = \sum_{j=0}^{14} \sum_{i=0}^{14} \frac{\partial \gamma_j}{\partial \xi_i} \mathbf{T}_j(t) \phi_i^T(t, \theta). \quad (37)$$

The resolution of the sensitivity at the levels of individual scales, however, is of great significance in itself. Indeed, it permits the identification of the significant scales of the property, thus indicating a preferred strategy for the experimental estimation of that property. Specifically, through a judicious spacing of measurements along a specimen, a specific scale of fluctuation of the material property can be evaluated. The higher-order terms in the expansion can be used to refine the estimated values of these sensitivities to within target accuracy.

4 Non-Gaussian Material Properties

There is ample evidence that many material properties cannot formally be modeled as Gaussian processes. This observation is consistent with the fact that most material properties are strictly positive. Notwithstanding its simplicity, the Gaussian model becomes physically unacceptable when the coefficient of variation of the material property gets above 0.2. For these values of the coefficient of variation, the Gaussian model stipulates the occurrence of negative values for the material properties with a non-negligible probability. For these situations, non-Gaussian models have to be adopted. Consistent with the series representation of general stochastic processes adopted in this paper, non-Gaussian processes are represented as orthogonal polynomials in a Gaussian process.

Thus, assuming that both thermal conductivity k , and heat capacity, c , are modeled as non-Gaussian processes, the expansions in Eqs. (33) and (34) would be replaced by the following expansions:

$$\begin{aligned} \mathbf{C} &= \bar{\mathbf{C}} + \xi_1 \mathbf{0} + \xi_2 \mathbf{0} + \xi_3 \mathbf{0} + \xi_4 \mathbf{C}_4 + (\xi_1^2 - 1) \mathbf{0} + (\xi_1 \xi_2) \mathbf{0} \\ &\quad + (\xi_1 \xi_3) \mathbf{0} + (\xi_1 \xi_4) \mathbf{0} + (\xi_2^2 - 1) \mathbf{0} + (\xi_2 \xi_3) \mathbf{0} \\ &\quad + (\xi_2 \xi_4) \mathbf{0} + (\xi_3^2 - 1) \mathbf{0} + (\xi_3 \xi_4) \mathbf{0} + (\xi_4^2 - 1) \mathbf{C}_{14} \\ &= \sum_{i=0}^{14} \psi_i \mathbf{C}_i, \end{aligned} \quad (38)$$

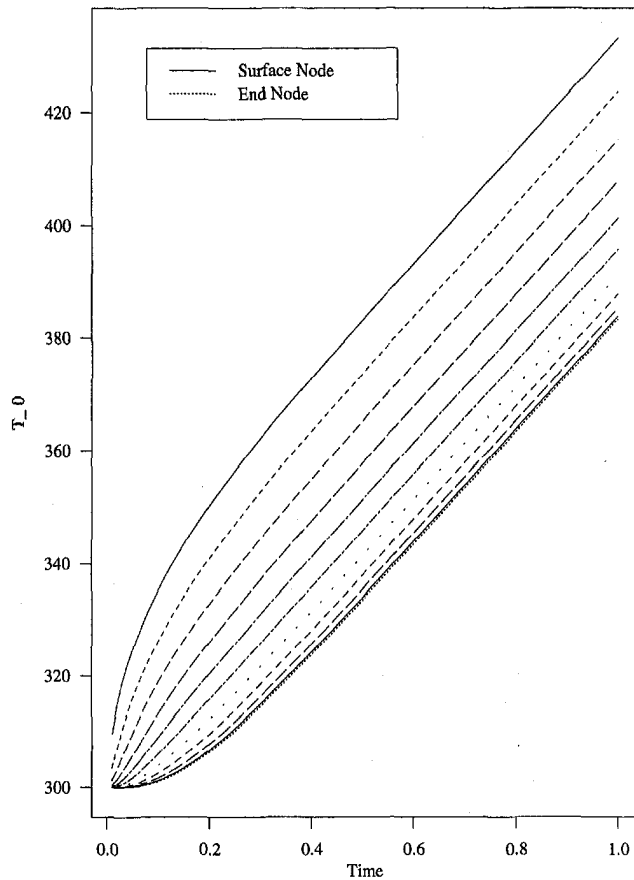


Fig. 3 Coefficients in the expansion of temperature. Solution using mean values of the parameters.

and

$$\begin{aligned} \mathbf{K} = & \bar{\mathbf{K}} + \xi_1 \mathbf{K}_1 + \xi_2 \mathbf{K}_2 + \xi_3 \mathbf{K}_3 + \xi_4 \mathbf{0} + (\xi_1^2 - 1) \mathbf{K}_5 \\ & + (\xi_1 \xi_2) \mathbf{K}_6 + (\xi_1 \xi_3) \mathbf{K}_7 + (\xi_1 \xi_4) \mathbf{K}_8 + (\xi_2^2 - 1) \mathbf{K}_9 \\ & + (\xi_2 \xi_3) \mathbf{K}_{10} + (\xi_2 \xi_4) \mathbf{K}_{11} + (\xi_3^2 - 1) \mathbf{K}_{12} \\ & + (\xi_3 \xi_4) \mathbf{K}_{13} + (\xi_4^2 - 1) \mathbf{0} = \sum_{i=0}^{14} \psi_i \mathbf{K}_i. \quad (39) \end{aligned}$$

The expansion for the temperature field remains unchanged. It is important to note that the deterministic coefficient appearing in the above expansions for the material properties must be determined based on the probabilistic characteristics of the data. This involves regressing the data on a polynomial of independent normalized Gaussian variables. Analytical expressions for the important case of a lognormal process have been obtained (Ghanem, 1999). The importance of the log-normal case stems from the restriction of such processes to assuming positive values. For small values of the coefficient of variation, log-normal processes are similar to some Gaussian process. This similarity rapidly diminishes as the coefficient of variation increases. Obviously for the non-Gaussian case, the coefficients d_{ijk} is equal to $\langle \psi_i \psi_j \psi_k \rangle$. This coefficients can be readily evaluated and tabulated using any of the readily available symbolic manipulation packages such as Macsyma or Mathematica.

5 Numerical Example

The method described above is now exemplified by its application to a simple problem. Consider a one-dimensional domain of unit length subjected to a constant heat flux specified by its nondimensional magnitude, $q_b L / \bar{k} = 1^\circ\text{C}$, at one end and per-

fectly insulated at the other end. Here \bar{k} denotes the statistical mean of the thermal conductivity. Let the initial temperature of the domain be at 300°C . The spatial domain is divided into a uniform mesh of ten elements. Figure 3 shows the evolution with time of the temperature at various nodal points in the domain under the assumption of a homogeneous medium having thermal properties equal to the average values. Figure 4 shows the results associated with the thermal conductivity and the heat capacity having both a Gaussian probability density function and a coefficient of variation equal to 0.4. The subscript on the temperature in this figure refers to the expansion given in Eq. (35). Comparing the coefficients \mathbf{T}_1 and \mathbf{T}_4 , it is clear that the temperature distribution throughout the domain is much more sensitive to variations in the heat capacity than to variations in the conductivity. It should be noted, however, that the uncertainty in the value of the heat capacity is likely to be much smaller than the uncertainty in the value of thermal conductivity. It has also been observed that treating the heat capacity as a deterministic quantity does not affect significantly the computed values of the coefficients associated with an uncertain hydraulic conductivity, thus leading to the conclusion that the two quantities can be uncoupled in an uncertainty analysis. Moreover, for larger values of the coefficient of variation of the heat capacity, second-order effects, as captured by the coefficients \mathbf{T}_{15} and \mathbf{T}_{34} , have the same order of magnitude as the first order sensitivity coefficient, \mathbf{T}_4 .

Figure 5 shows results associated with the conductivity having a log-normal distribution with coefficient of variation equal to 0.4. It is clear from comparing this figure to the previous one that assumptions regarding the probabilistic character (Gaussian versus log-normal) have a significant impact on the predicted level of uncertainty in the temperature variation over time. Note

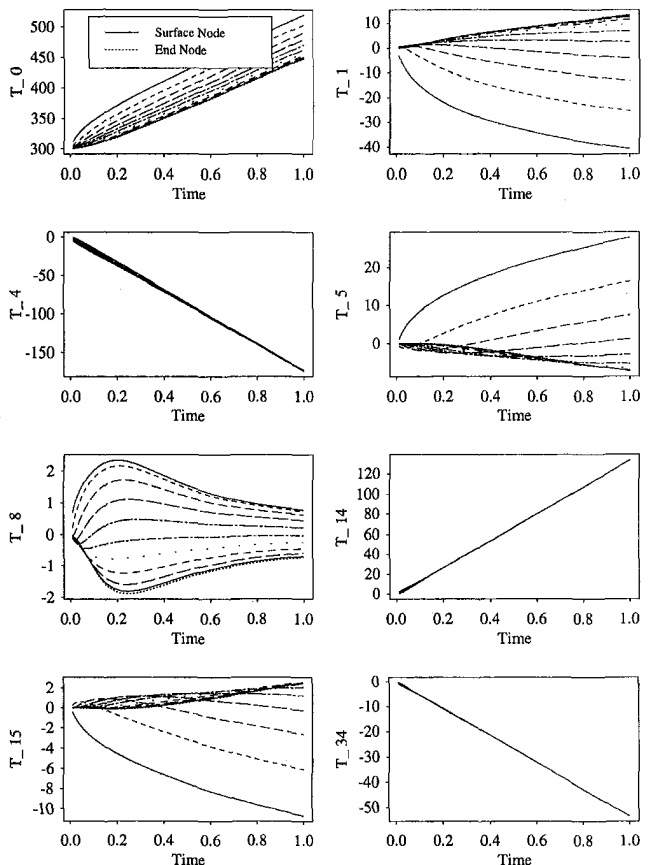


Fig. 4 Coefficients in the expansion of temperature. Gaussian conductivity and heat capacity; COV conductivity = 0.4; COV heat capacity = 0.4; correlation length = 100; one term in Karhunen-Loeve expansion.

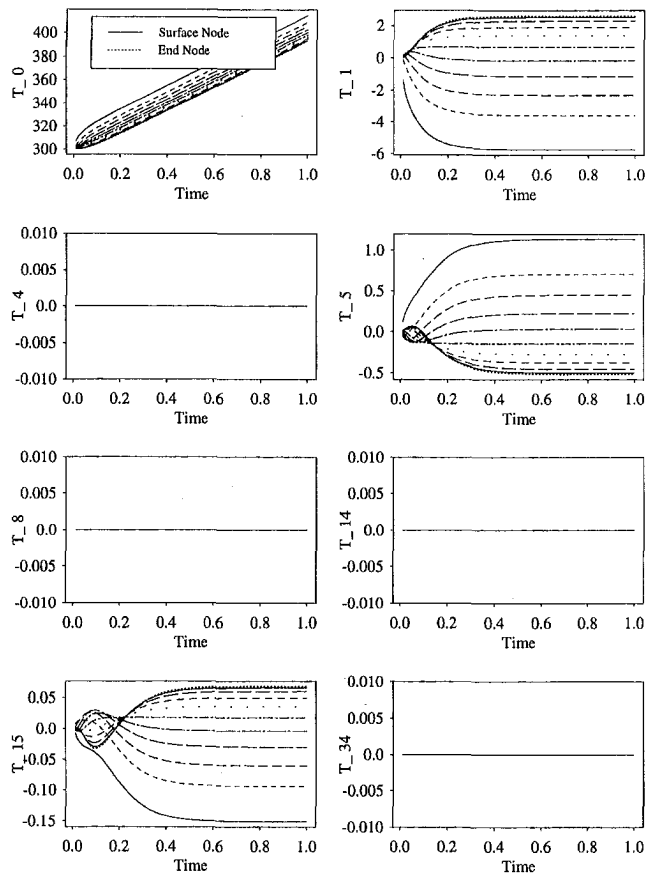


Fig. 5 Coefficients in the expansion of temperature. Lognormal conductivity; COV conductivity = 0.4; COV heat capacity = 0; correlation length = 100; one term in Karhunen-Loeve expansion.

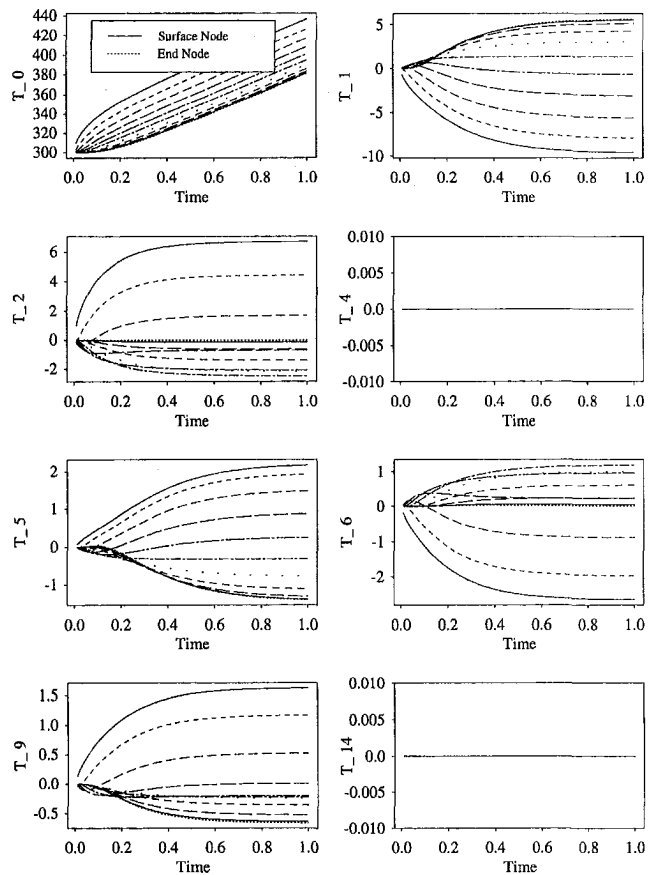


Fig. 6 Coefficients in the expansion of temperature. Gaussian conductivity process; COV conductivity = 0.4; correlation length = 0.2; two terms in Karhunen-Loeve expansion.

that even the mean temperature field, as described by T_0 is significantly affected by whether the conductivity is assumed to be Gaussian or log-normal. It has been observed, following a parametric study, that the effect of non-Gaussian material randomness increases substantially with the level of random fluctuations as described by the coefficient of variation. In Fig. 5, the heat capacity is assumed to be deterministic and the correlation length of the process is assumed to be equal to 100 times the spatial extent of the problem. In this limit of large correlation length, the conductivity can be treated as random variable, and is therefore made to depend on a single ξ_i . Since it is not Gaussian, however, it is developed as a polynomial in this gaussian variable, and three terms are used in expanding it (four terms in Eq. (39) including the mean). This corresponds to the terms K_0, K_1, K_5, K_{15} in Eq. (39) being nonzero. Since the heat capacity is taken to be deterministic in this case, the coefficients corresponding to it in the expansion of the temperature field are equal to zero, as demonstrated in the figure.

In all the above results, the correlation length of the conductivity process is taken to be very large (100) and a single term is included in its expansion. Figure 6 shows results similar to those in Fig. 4 except now the correlation length of the conductivity process is taken equal to 0.2, and two terms are included in the expansion of the process. These results correspond to the case of a Gaussian conductivity process. The terms multiplying the polynomials in ξ_1 and ξ_2 are now activated. The first-order sensitivity, captured by the terms multiplying ξ_1 and ξ_2 , is now resolved with respect to each of these scales. Given the short correlation length used in this example, the contribution from the two scales is of the same order of magnitude. These scales of fluctuation represent the frequencies of fluctuation of the data at which the contributions to the overall property are uncor-

related. It is clear from these results that the sensitivity of the temperature field with respect to the uncertainties in the conductivity depends greatly on these scales of fluctuation.

Figures 7 and 8 show the standard deviation of the temperature along the domain. This was obtained as the diagonal elements of the covariance matrix R_{TT} as indicated in Eq. (29), with the four plots in each of these figures referring to a different upper limit on the summation in that equation. Figure 7 refers to the case with standard deviation and correlation length of thermal

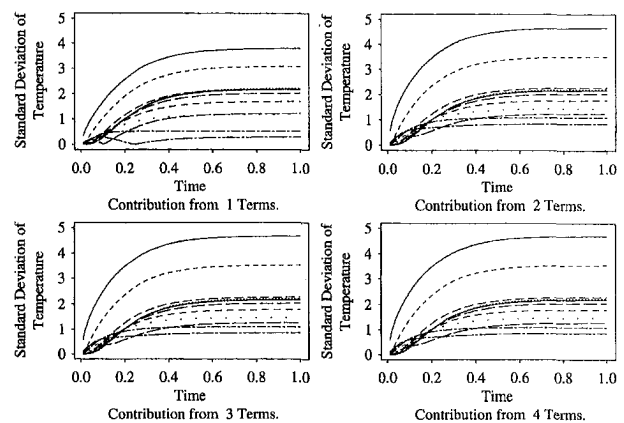


Fig. 7 Standard deviation of the solution. Gaussian conductivity process; COV conductivity = 0.4; correlation length = 100; one term in Karhunen-Loeve expansion.

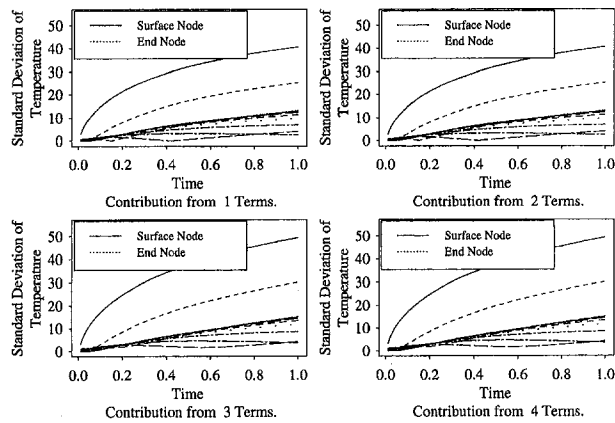


Fig. 8 Standard deviation of the solution. Gaussian conductivity process; COV conductivity = 0.4; correlation length = 0.2; two terms in Karhunen-Loeve expansion.

conductivity equal to 0.4 and 100, respectively, while Fig. 8 refers to the case where these values are, respectively, equal to 0.4 and 0.2. This information has typically been used to assess the usefulness of model predictions in the presence of uncertainty. Large standard deviations of the solution process are usually indicative of low reliability of the results. It is clear from comparing Figs. 7 and 8 that the latter case, corresponding to a spatially varying material property, predicts significantly larger standard deviation (and thus statistical scatter) in the temperature field. In light of the unavoidable spatial variability of thermal conductivity in most materials, either due to manufacturing variability, or to microscopic variation in environmental conditions, this observation suggests that novel procedures for data collecting should be developed in order to better assess this variability.

Finally, Figs. 9 and 10 show the results associated with a Monte Carlo simulation of the problem. These figures show results obtained from one 100-realization Monte Carlo simulation, together with results from two 1000-realization simulations, as well as the results obtained from the polynomial chaos expansion described in this paper. Results are shown for two cases featuring different levels of correlation in the hydraulic conductivity process. It is clear that the results obtained from a Monte Carlo simulation, even one with 1000 realizations, are fairly unreliable as they do not converge in a consistent fashion. Convergence of the estimates obtained from the proposed method, on the other hand, can be assessed, albeit not formally, by comparing the contribution of successive terms in the expansion

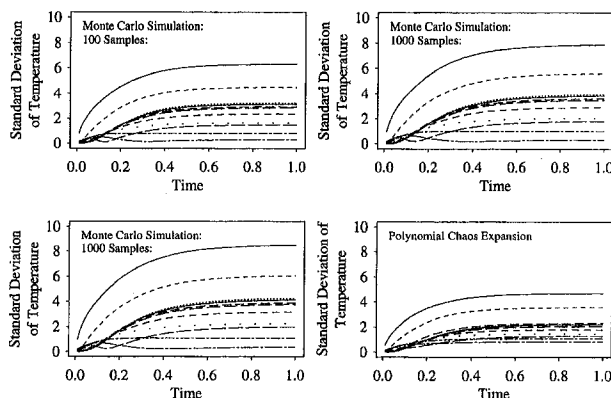


Fig. 9 Standard deviation of the solution. Gaussian conductivity process; COV conductivity = 0.4; correlation length = 100; two terms in Karhunen-Loeve expansion.

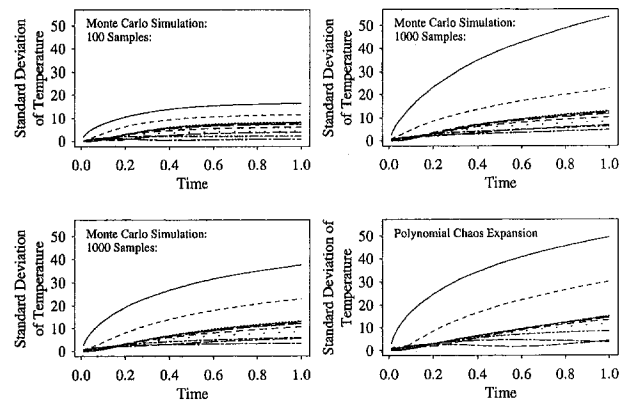


Fig. 10 Standard deviation of the solution. Gaussian conductivity process; COV conductivity = 0.4; correlation length = 0.2; two terms in Karhunen-Loeve expansion.

to the standard deviation of the solution. It is thus clear from Figs. 7 and 8 that contributions beyond those from the second-order terms have a small effect on the overall standard deviation. It should be noted, however, that in addition to providing reliable estimates to the second-order statistics, as demonstrated here, the representation of the solution in the polynomial chaos expansion permits the efficient simulation of realizations of the solution, thus permitting the rapid estimation of probabilities of extreme events.

6 Conclusion

A method has been presented that is capable of addressing, in great generality heat conduction problems involving random media. The method is based on treating the random aspect of the problem as a new dimension along which a spectral expansion is carried out. The method has been exemplified by its application to a simple problem. Material properties modeled as stochastic processes are handled just as easily as those modeled as random variables, and multiple heterogeneities can be included simultaneously. Moreover, the method is not restricted in its applicability to Gaussian material properties. This method, however, results in an extended system of equations that is larger than the associated deterministic finite element system. This increase in size is commensurate with the addition of a new dimension to the problem, and should be viewed as the cost of added resolution. Indeed, instead of lumping it into its average value, the data is resolved according to its frequency of occurrence (probabilistic model), and this frequency is being propagated through the mechanics of the problem in order to infer about the frequency of occurrence of the temperature field. Techniques have been developed that capitalize on the peculiar structure of the final large matrix (Ghanem and Kruger, 1996). This peculiarity stems from the fact that each of its submatrices has an identical nonzero structure. It has been observed from the results presented in this paper that the level of predicted uncertainty in the computed solution process depends greatly on whether the material properties are modeled as stochastic processes or random variables.

An important value of the procedure presented in this paper is that it provides the solution in the form of a convergent expansion, thus a reliable characterization for the propagation of uncertainty from the thermal properties values to the predicted values of the temperature can be obtained.

References

- Beck, J., Blackwell, B., and St. Clair, C., 1985, *Inverse Heat Conduction: Ill-Posed Problems*, John Wiley and Sons, New York.
- Cameron, R., and Martin, W., 1947, "The Orthogonal Development of Nonlinear Functionals in Series of Fourier-Hermite Functionals," *Ann. Math.*, Vol. 48, pp. 385-395.

- Fadale, T. D., and Emery, A. F., 1994, "Transient Effects of Uncertainties on the Sensitivities of Temperatures and Heat Fluxes Using Stochastic Finite Elements," *ASME JOURNAL OF HEAT TRANSFER*, Vol. 116, pp. 808–814.
- Ghanem, R., 1998, "Hybrid Stochastic Finite Elements: Coupling of Spectral Expansions With Monte Carlo Simulations," *ASME Journal of Applied Mechanics*, Vol. 65, pp. 1004–1009.
- Ghanem, R., 1999, "Nonlinear Gaussian Spectrum of Log-Normal Stochastic Processes and Variables," *ASME Journal of Applied Mechanics*, accepted for publication.
- Ghanem, R., and Kruger, R., 1996, "Numerical Solution of Spectral Stochastic Finite Element Systems," *Computer Methods in Applied Mechanics and Engineering*, Vol. 129, pp. 289–303.
- Ghanem, R., and Spanos, P., 1991, *Stochastic Finite Elements: A Spectral Approach*, Springer-Verlag, New York.
- Kallianapur, G., 1980, *Stochastic Filtering Theory*, Springer-Verlag, Berlin.
- Loeve, M., 1977, *Probability Theory*, 4th Ed., Springer-Verlag, New York.
- Schueller, G. I., 1997, "State-of-Art Report on Computational Stochastic Mechanics," *Probabilistic Engineering Mechanics*, Vol. 12, No. 4, pp. 197–321.
- Spanos, P. D., and Ghanem, R., 1989, "Stochastic Finite Element Expansion for Random Media," *Journal of Engineering Mechanics Division, ASCE*, Vol. 115, No. 5, pp. 1035–1053.
- Wiener, N., 1938, "The Homogeneous Chaos," *Amer. J. Math.*, Vol. 60, pp. 897–936.
-

A Sequential Gradient Method for the Inverse Heat Conduction Problem (IHCP)

K. J. Dowding¹
Assoc. Mem. ASME

J. V. Beck

Department of Mechanical Engineering,
Michigan State University,
East Lansing, MI 48824

A sequential-in-time implementation is proposed for a conjugate gradient method using an adjoint equation approach to solve the inverse heat conduction problem (IHCP). Because the IHCP is generally ill-posed, Tikhonov regularization is included to stabilize the solution and allow for the inclusion of prior information. Aspects of the sequential gradient method are discussed and examined. Simulated one and two-dimensional test cases are evaluated to study the sequential implementation. Numerical solutions are obtained using a finite difference procedure. Results indicate the sequential implementation has accuracy comparable to the standard whole-domain solution, but in certain cases requires significantly more computational time. Benefits of the on-line nature of a sequential method may outweigh the additional computational requirements. Methods to improve the computational requirements, which make the method competitive with a whole domain solution, are given.

1 Introduction

Estimating the conditions at the surface of a heat-conducting body from internal measurements is typically called the inverse heat conduction problem (IHCP). Inverse describes this type of conduction problem because conditions at the boundary or surface of a body are estimated using internal measurements. A direct conduction problem, by contrast, uses conditions specified on the boundary to compute the internal temperature. While the direct problem is generally a well-posed problem, the inverse problem tends to be ill-posed and very sensitive to measurement errors (Beck et al., 1985). A sequential method to solve the IHCP is discussed in this paper. The focus is on multidimensional problems.

Many methods applied to solve the one-dimensional IHCP have been extended for the multidimensional problem. Function specification and gradient methods have received the most attention. Function specification specifies a functional form for the heat flux over a future interval (Beck et al., 1985). Specifying a functional form over the future interval provides regularization to stabilize the ill-conditioned problem (Lamm, 1995). In conjunction with specifying a functional form, function specification solves the problem in a sequential (on-time) manner.

Several researchers have investigated the two-dimensional application of the function specification method. It was applied to estimate spatially and time-varying convective heat transfer coefficients (Osman and Beck, 1989, 1990), and surface heat flux (Osman et al., 1997). A boundary element method was coupled with function specification to investigate multidimensional problems by Zabaras and Liu (1988). Hsu et al. (1992) applied a finite element method to solve the general two-dimensional problem with inverse methods similar to function specification.

Gradient methods, which typically apply a conjugate gradient iterative scheme, use iterative or Tikhonov regularization to stabilize the solution and solve the multidimensional problem. Most researchers use an adjoint equation approach coupled with the conjugate gradient search method. Iterative regularization (Alifanov, 1994; Alifanov et al., 1996) depends on the slowness or

"viscosity" of the solution and use the iteration index as the regularization parameter. Several papers use iterative regularization (see Alifanov and Kerov (1981) and Alifanov and Egorov (1985)). Additional investigations using gradient methods, but not iterative regularization, are given in Zabaras and Yang (1996), Reinhardt (1996a, b), and Jarny et al. (1991).

Function specification and gradient methods are powerful approaches to solve the multidimensional IHCP. An advantage of the function specification method is that the problem retains the causal nature, represented with a Volterra operator (Lamm, 1995). This allows a sequential solution and implementation in an on-line procedure with possible savings in computational time and memory. Gradient methods are typically applied on the whole time domain, not taking advantage of the causal nature of the problem. The demonstrated success of gradient methods, with the efficiency and on-line capabilities of a sequential implementation, suggest a sequential implementation of a gradient method would be a powerful combination. A method that sequentially implements a gradient scheme, using an adjoint equation approach, is proposed and to be developed; additional stability is introduced by including Tikhonov regularization. The method is anticipated to benefit by not requiring a prescribed functional form, which is particularly useful for the computational aspects of a sequential implementation. Other researchers who have proposed a sequential implementation are Reinhardt and Hao (1996a, b) and Artyukhin and Gedzhadze (1994); however, past implementations have addressed the one-dimensional problem with a limited investigation of the method. This paper addresses the one and two-dimensional problems for the sequential implementation. Although applying the sequential gradient method to linear one-dimensional problems is probably not needed or recommended, addressing the one-dimensional problem provides valuable insight to the proposed sequential gradient method. This is the first known two-dimensional implementation of a sequential gradient method. Issues related to the influence of the number of future time steps and the computational requirements for a sequential implementation are important and studied in this paper.

The next section develops the multidimensional IHCP. Section 3 outlines the sequential implementation of the inverse solution. The numerical solution of the IHCP and potential benefits of the sequential gradient method are discussed in Section 4. Results using the sequential gradient method are presented in Section 5, including suggested improvements in the sequential method. Conclusions are given in the final section.

¹ Present address: Sandia National Laboratories, Thermal Science Department, Albuquerque, NM 87185-0835.

Contributed by the Heat Transfer Division for publication in the JOURNAL OF HEAT TRANSFER. Manuscript received by the Heat Transfer Division, July 9, 1997; revision received, Dec. 8, 1998. Keywords: Conduction, Numerical Methods, Transient and Unsteady Heat Transfer. Associate Technical Editor: R. Boyd.

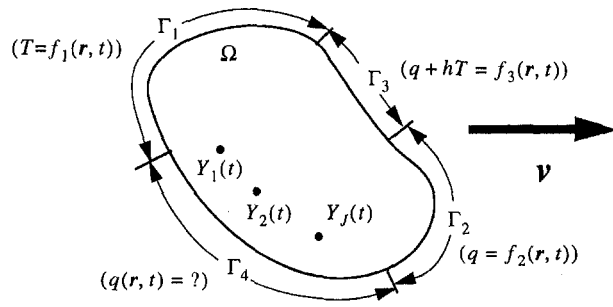


Fig. 1 Schematic of multidimensional general IHCP

2 Problem Statement of the Multidimensional IHCP

A schematic of the general multidimensional IHCP is shown in Fig. 1. In the analysis that follows, the conduction problem is assumed linear, i.e., thermal properties do not depend on temperature. Extending the gradient methods for nonlinear problems is discussed in Artyukhin (1996) and Loulou et al. (1996). For the proposed sequential implementation, it is possible to temporarily linearize a nonlinear problem, and consider it linear (discussed in Section 4.2). Assuming the thermal properties are independent of temperature, the problem is mathematically formulated as follows:

$$\nabla \cdot (k(\mathbf{r})\nabla T(\mathbf{r}, t)) = \rho C(\mathbf{r}) \left[\frac{\partial}{\partial t} T(\mathbf{r}, t) + \mathbf{v} \cdot \nabla T(\mathbf{r}, t) \right], \quad \begin{matrix} (\mathbf{r}) \text{ in } \Omega \\ (t_0 < t \leq t_f) \end{matrix} \quad (1)$$

$$-k_i \frac{\partial}{\partial \hat{\mathbf{n}}} T(\mathbf{r}, t) + h_i T(\mathbf{r}, t) = f_i(\mathbf{r}, t), \quad \begin{matrix} (\mathbf{r}) \text{ on } \Gamma_i, (i = 1, 2, 3) \\ (t_0 < t \leq t_f) \end{matrix} \quad (2a)$$

$$-k(\mathbf{r}) \frac{\partial}{\partial \hat{\mathbf{n}}} T(\mathbf{r}, t) = q(\mathbf{r}, t), \quad \begin{matrix} (\mathbf{r}) \text{ on } \Gamma_4 \\ (t_0 < t \leq t_f) \end{matrix} \quad (2b)$$

$$T(\mathbf{r}, t_0) = T_0(\mathbf{r}). \quad (2c)$$

The thermal conductivity and volumetric heat capacity are $k(\mathbf{r})$ and $\rho C(\mathbf{r})$. The spatial domain Ω is moving at a constant velocity of \mathbf{v} and the symbols Γ_i ($i = 1, 2, 3, 4$) represent segments of the domain boundary. The outward pointing normal vector is denoted $\hat{\mathbf{n}}$. Functions $f_1(\mathbf{r}, t)$, $f_2(\mathbf{r}, t)$, $f_3(\mathbf{r}, t)$, and $T_0(\mathbf{r})$ are assumed known. Boundary coefficients k_i and h_i are specified to form the different possible boundary conditions, i.e., $k_1 = 0$ and $h_1 = 1$ specifies a temperature boundary condition (first kind), $k_2 = k(\mathbf{r})$ and $h_2 = 0$ a flux condition (second kind), $k_3 = k(\mathbf{r})$ and $h_3 = h(\mathbf{r})$ a convective condition (third kind). Surface Γ_4 has the unknown heat flux $q(\mathbf{r}, t)$. Excess information of transient temperature measurements exists within the body (or at the surface of the body) at locations $(\mathbf{r} = \mathbf{d}_j)$ $j = 1, \dots, J$. These measured temperatures are denoted

$$Y(\mathbf{d}_j, t_k) = Y_j(t_k), \quad (3)$$

and are available at discrete times t_k , $t_0 < t_k \leq t_f$, $k = 1, 2, \dots, M^*$. The analysis is developed for measurements being at discrete locations but continuous on time. It is straightforward to consider the case of discrete time.

The objective is to estimate $q(\mathbf{r}, t)$ using the measured temperatures. Hence, the heat flux $q(\mathbf{r}, t)$ is estimated such that the calculated temperatures match the measured temperatures, $T(\mathbf{d}_j, t; q) = Y_j(t)$, where $T(\mathbf{d}_j, t; q)$ is the solution of Eqs. (1) and (2). Due to the ill-conditioned nature of this problem, the matching is accomplished in a least-squares sense by minimizing the function

$$J(q) = \underbrace{\frac{1}{2} \sum_{j=1}^J \int_{t_0}^{t_f} [T(\mathbf{d}_j, t; q) - Y_j(t)]^2 dt}_{J_S} + \underbrace{\frac{1}{2} \alpha_T \int_{t_0}^{t_f} \int_{\Gamma_4} [q(\mathbf{r}, t) - q_{\text{pri}}(\mathbf{r}, t)]^2 d\mathbf{r} dt}_{J_R}. \quad (4)$$

Nomenclature

a, b = dimension of two-dimensional simulated case, m
 C = specific heat, J/kgC
 \mathbf{d}_j = location for temperature sensor j , m
 e_j = temperature residual sensor j , °C
 E = function space
 f_i = nonhomogeneous term for boundary surface, Γ_i
 h = convection coefficient, $W/(m^2°C)$
 h_i = boundary condition coefficient
 I = number of components retained in sequential implementation
 J = objective function, °C² sec
 J_S = sum-of-squares term in objective function, °C² sec
 J_R = regularization (Tikhonov) term in objective function, °C² sec
 k = thermal conductivity, $W/m°C$
 k_i = boundary condition coefficient
 L = length, m

L_2 = function space of all "square integrable" functions
 M = number of temporal components for estimated heat flux on Γ_4
 M^* = number of discrete time steps
 $\hat{\mathbf{n}}$ = outward pointing unit normal vector
 p = number of parameters
 p^n = search direction, °C²/(W/m²)m
 P = number of spatial components for heat flux on Γ_4
 q = heat flux, W/m^2
 \hat{q}, \hat{q}_e = estimated heat flux, estimated heat flux with measurement errors, W/m^2
 q_{pri} = prior information for heat flux, W/m^2
 q_{est} = stored flux for sequential solution, W/m^2
 \mathbf{r} = two-dimensional coordinate vector, m
 r = number of future time steps
 S_V = temperature error, °C

t, t_0, t_f = time, initial time, final time, sec
 T, T_0 = temperature, initial temperature, °C
 \mathbf{v} = velocity vector, m/s
 Y = measured temperature, °C
 α_T = Tikhonov regularization parameter, $(°C/(W/m^2))^2 1/m$
 Γ_i = boundary surface i for domain Ω
 δ = expected temperature noise, °C sec
 Δq = update to heat flux, W/m^2
 Δt = time step, sec
 ϵ = convergence tolerance
 ρ = density, kg/m^3
 σ = standard deviation of temperature noise, °C
 $\hat{\sigma}_{S_e}$ = estimated error in heat flux, random measurement errors, °C
 τ = relaxation parameter
 Ω = two-dimensional domain

For the last term in Eq. (4), J_R serves as regularization (assuming that $q(\mathbf{r}, t) \in L_2$ on $\Gamma_4 \times (t_0, t_f)$) to stabilize the ill-conditioned problem. It allows for prior information to be included, where $q_{\text{pri}}(\mathbf{r}, t)$ is assumed known, but could possibly be zero. Regularization of this form is similar to zeroth-order Tikhonov regularization (Tikhonov and Arsenin, 1977).

Schemes to minimize $J(q)$ in Eq. (4), which use iterative search methods such as steepest descent or conjugate gradient, require the gradient of $J(q)$. Methods to compute this gradient depend on the function space where $q(\mathbf{r}, t)$ is assumed to reside. Two possibilities are a *finite-dimensional* space and an *infinite-dimensional* space. For the infinite dimensional problem a priori information is not required concerning the (unknown) function $q(\mathbf{r}, t)$. However, computation of the gradient requires solving two additional problems, which are the adjoint and sensitivity problems. For the special case when a priori information is available (or assumed) concerning the function, the problem is considered finite dimensional and standard differential calculus can be used to compute the gradient.

The approach considered here is the more general infinite-dimensional problem. The heat flux is assumed to be in the function space E on $\Gamma_4 \times (t_0, t_f)$. One possible choice for the function space is $E = L_2$, all square integrable functions on $\Gamma_4 \times (t_0, t_f)$. In this case the scalar product is defined by

$$\langle Z_1, Z_2 \rangle_{L_2} = \int_{t_0}^{t_f} \int_{\Gamma_4} Z_1(\mathbf{r}, t) Z_2(\mathbf{r}, t) d\mathbf{r} dt \quad (5)$$

for functions $Z_1(\mathbf{r}, t)$ and $Z_2(\mathbf{r}, t)$. The associated norm of function $Z_1(\mathbf{r}, t)$ is

$$\|Z_1\|_{L_2}^2 = \int_{t_0}^{t_f} \int_{\Gamma_4} |Z_1(\mathbf{r}, t)|^2 d\mathbf{r} dt. \quad (6)$$

See Jarny et al. (1991) for other possible function spaces. The analysis is developed assuming the more general infinite-dimensional function space. The solution for a finite-dimensional space can be obtained as a special case of the more general solution (Dowding, 1997).

3 Inverse Solution

The formulation for the inverse estimation of the surface heat flux is discussed. A conjugate gradient search method is used with an adjoint equation to estimate the surface heat flux. Although the solution is implemented in a sequential manner, the equations are similar to a whole domain solution. However, the solution is applied sequentially over a subset of the time domain. The details to derive the describing equations are not given in this paper due to space limitation. Jarny et al. (1991) provide an excellent reference to derive the describing equations for a gradient method to solve the multi-dimensional IHCP.

The unknown surface heat flux is estimated using an iterative search method

$$q^{n+1}(\mathbf{r}, t) = q^n(\mathbf{r}, t) + \Delta q(\mathbf{r}, t), \quad (\mathbf{r}) \text{ on } \Gamma_4. \quad (7)$$

The correction to the heat flux is

$$\Delta q(\mathbf{r}, t) = -\rho^n p^n(\mathbf{r}, t), \quad (\mathbf{r}) \text{ on } \Gamma_4 \quad (8)$$

where p^n is the search direction and ρ^n is a (positive) scalar step size. For the steepest descent method the search direction is

$$p^n(\mathbf{r}, t) = \nabla J(\mathbf{r}, t, q^n). \quad (9)$$

(It is actually the negative of the gradient, but the negative sign is incorporated in Eq. (8).) The conjugate gradient method, which typically converges more quickly, uses the history of the search direction to improve the current direction. Computation of the search direction requires the gradient ∇J of the objective function

J . To calculate the gradient an adjoint problem is derived. In addition to the adjoint problem, the sensitivity problem is needed to compute the step size ρ^n in the given direction p^n . The solution of three problems is required for the inverse solution. The three problems represent the direct, adjoint, and sensitivity problems. (See Dowding (1997) for derivation of the three problems.) Discussion of the sequential implementation is given next.

A sequential procedure is used to apply the gradient method over subsets of the time interval. The whole time domain $t_0 < t \leq t_f$ is uniformly discretized, $t = m\Delta t \equiv t_m$, $m = 1, 2, \dots, M^*$, where Δt is the time-step and $M^* = (t_f - t_0)/\Delta t$. Heat flux is estimated for $M = M^* - r + (I - 1)$ discrete intervals, where r is the number of future steps and I is the number of components retained. Assuming that the function $q(\mathbf{r}, t)$ is known for times $t \leq t_{m-1}$, the unknown heat flux over r -future time-steps, $t_{m-1} < t \leq t_{m+r-1}$ is estimated. Equations for the whole domain implementation are identical in form to those for the sequential implementation. These equations are solved sequentially over the time interval $t_{m-1} < t \leq t_{m+r-1}$ progressing over the whole time domain. On each sequential interval, information from the previous interval is used to specify initial conditions or guesses. After the inverse solution converges the estimated heat flux from the current sequential interval is retained, which is typically the estimates at only the first time-step. However, estimates from more than the first time-step can be retained. The time interval is shifted by the number of retained estimates and the process is repeated. After the final sequential interval the residual principle is applied to insure the correct regularization magnitude is used

$$J_S(q^n) = \sum_{j=1}^J \int_{t_0}^{t_f} [T(\mathbf{d}_j, q^n) - Y_j(t)]^2 dt \approx \tau \delta^2 \quad (10)$$

where δ^2 is the expected noise or error in the problem and $\tau \geq 1$ is a relaxation parameter. In this investigation the relaxation parameter is one.

4 Numerical Solution of the IHCP

This section discusses the benefits and advantages of a sequential implementation for solving the IHCP. Because these advantages are closely related to the numerical solution, the numerical method to solve the IHCP is briefly discussed first.

4.1 Numerical Solution. A numerical solution for the two-dimensional IHCP is developed using a finite control volume (FCV) approach to derive finite difference equations. Numerically solving the IHCP using a gradient method and adjoint equation approach requires solving three partial differential equations representing the direct, adjoint, and sensitivity problems. Fortunately, the describing differential equations are similar for the three problems and numerical computations required for one problem apply for the other problems.

The numerical solution is developed for the two-dimensional problem using an alternating direction implicit (ADI) scheme. A one-dimensional solution is obtained as a special case. The FCV equations for the direct problem are represented as a two step solution

$$[K_1]\{T^{n+1/2}\} = \{D^n\} \quad (11)$$

$$[K_2]\{T^{n+1}\} = \{E^{n+1/2}\} \quad (12)$$

where $[K_1]$ and $[K_2]$ are the standard FCV tridiagonal matrices, $\{T^n\}$ is a vector of unknown temperatures (sensitivity or adjoint) for time n , and $\{D^n\}$ and $\{E^{n+1/2}\}$ are vectors of known information for the respective time-steps. The two sets of equations represent the two steps of an ADI scheme. Other numerical methods, such as finite element, can also be applied to discretize the three problems.

All three problems, direct, adjoint, and sensitivity, require solv-

ing a set of equations similar to those shown in Eqs. (11) and (12). When convection is not present ($v = 0$), the matrices ($[K_1]$ and $[K_2]$) are identical for the three problems. The adjoint problem has different matrices when convection is included. Computation of the matrices is done only one time for constant thermal properties, i.e., a linear problem. Furthermore, when solving the tridiagonal set of equations, computational savings are possible for the linear problem. This is true for a whole domain as well as sequential solution. However, for nonlinear problems it is possible to temporarily linearize during a sequential solution and benefit from the computational savings associated with linear problems. Aspects of this procedure are discussed below.

4.2 Benefits of a Sequential Solution for the IHCP. The benefits of applying a sequential solution for the IHCP are discussed. Several supporting reasons for a sequential solution are discussed. Although not all reasons are investigated in this paper, nor verified, it suggests the possibility of growth for a sequential gradient method.

1 A sequential method can be implemented in an “on-line” or “real-time” mode. For example, in monitoring the surface heating during the flight of a space vehicle, data can be collected for a short period then the surface heat flux can be computed in “real-time.”

2 For nonlinear problems, due to temperature-dependent thermal properties or other temperature-dependent coefficients in the differential equation, the sequential method permits temporarily linearizing the problem. This is an important point because it is not possible when solving on the whole time domain. Since the problem is solved on the shorter sequential interval, it is valid to assume that the temperature-dependent quantity is constant during the sequential interval (r -future time steps). The validity of the assumption depends on the degree of nonlinearity in the problem. In most applications the nonlinear term(s) is not known with sufficient accuracy to justify accounting for the nonlinearity during the temperature change in a sequential interval. To linearize, thermal properties and temperature-dependent variables are evaluated at the initial temperature distribution of the sequential interval. The matrices $[K_1]$ and $[K_2]$ are formulated only at the beginning of each sequential interval. Conversely, in the whole domain approach the matrices are reformulated periodically during the (transient) solution depending on the degree of nonlinearity. Every iteration in the inverse solution requires reformulating the matrices for a whole domain solution. In addition, during the sequential solution Eqs. (11) and (12) will have similar left-hand sides and by saving the decomposition when solving the set of simultaneous equations, computational savings are possible.

3 The magnitude of the Tikhonov regularization parameter can be adjusted in a sequential implementation. Again, this is not restricted to the sequential implementation, but is more practical to implement in a sequential method because current solution information is available to select the magnitude of the Tikhonov parameter. Adjusting the Tikhonov parameter permits a more accurate estimate of rapidly changing functions with less bias incurred in the estimation. (In this paper the Tikhonov parameter is not considered to vary with time.)

4 Additional heat flux components can be retained in a sequential implementation. This is an advantage compared to a standard function specification solution (Beck et al., 1985), because additional bias is not introduced with the function specification approximation. More components from the solution over a sequential interval may therefore be retained, depending on the choice of r and associated experimental conditions.

5 In the gradient formulation of the IHCP only the three noted problems (direct, sensitivity, and adjoint) are solved, albeit iteratively. The size and number of problems does not depend on the spatial representation of the unknown heat flux. The function specification method, in contrast, is required to solve a direct problem and several sensitivity problems (Osman et al., 1997), the number of which depends on the spatial representation of the unknown heat flux. (Both methods require assumptions about the

transient representation of the heat flux and are equally influenced by this choice.) Computational load for the (sequential) gradient method may be less influenced by the spatial representation of the heat flux than the function specification method. The iteration required for a gradient method may offset some of the computational difference with the function specification method. When this point is coupled with the temporary linearization that is possible with the sequential method (point 2), it provides potential to solve nonlinear multidimensional problems efficiently.

5 Results and Discussion

Several one and two-dimensional test cases are evaluated to study the sequential gradient method (SGM). It is compared with the standard whole-domain gradient method (GM) to provide a reference. The GM is chosen for comparison to understand how the sequential implementation influences the gradient method. Beck et al. (1996) has shown using experimental data that similar results are obtained with a variety of methods (Tikhonov regularization, iterative regularization, and function specification). In all cases the residual principle is applied to select the proper magnitude of the Tikhonov regularization. Cases with “exact” data and data corrupted with measurement errors are studied. Specific results are not shown for the one-dimensional cases, but observations are briefly discussed and a reference is given. Results are shown for the two-dimensional case with measurement errors.

Although the sequential gradient method is not recommended for one-dimensional problems, three standard one-dimensional test cases were studied. The cases provide insight to the transient response of the method (Dowding, 1997). The one-dimensional test cases indicated (1) the accuracy in the estimated heat flux for the SGM is comparable to the GM and improves as r increases, (2) the SGM requires more computational time than the GM, and computational time increases with r , (3) there is a minimum allowable r -value, (4) GM and SGM are insensitive to the specified initial guess, and (5) the use of the sequential function specification gradient method (SFGSM), i.e., holding the heat flux constant over the sequential interval, improves the computational requirements compared to SGM, making it competitive with the GM. The insight gained from the one-dimensional results are that there are two possibilities to make the SGM competitive, in terms of accuracy and computational time, with a whole-domain implementation. First, the sequential interval is lengthened by making the number of future time steps larger—essentially making the method more like the GM. The second approach, which is more appealing, is to maintain the heat function constant over the sequential interval. These insights are carried forward to study the two-dimensional cases, which is the intended use of the method.

A rectangular domain of dimensions $[0, a] \times [0, b]$ is studied for two-dimensional simulated cases. One bounding surface of the two-dimensional body is assumed to have an unknown heat flux. All other surfaces are insulated. Furthermore, constant thermal properties and a uniform initial temperature are assumed. The dimensionless groups of interest for this geometry are $a/b = 2$ and $kl/\rho C = 1$. Measurements are available at 11 equally spaced locations ($x^+ = x/a = 0.0, 0.1 \dots, 1.0$) beneath the surface of unknown heat flux at a depth of $y^+ = y/b = 0.1$. The dimensionless time-step (Fourier number) based on the sensor depth is $\Delta t_e^+ = (kl/\rho C)\Delta t/(0.1)^2 = 0.06$, which represents a difficult case; 200 time-steps are considered in the analysis. Unless mentioned otherwise, no prior information is used ($q_{pri} = 0$).

A test case which is triangular on space, and undergoes a step on time, is analyzed. Numerical conditions are 21 nodes in the y -direction and 11 in the x -direction. Data were assumed at 200 time-steps and 11 spatial components of the heat flux are estimated; 2200 total heat flux components are estimated. Estimation of the heat flux with measurement errors is shown in Fig. 2 for a whole domain solution and Fig. 3 shows a sequential solution with $r = 6$. The two solutions are quite different; whereas the whole domain solution is relatively smooth, the sequential solution has a

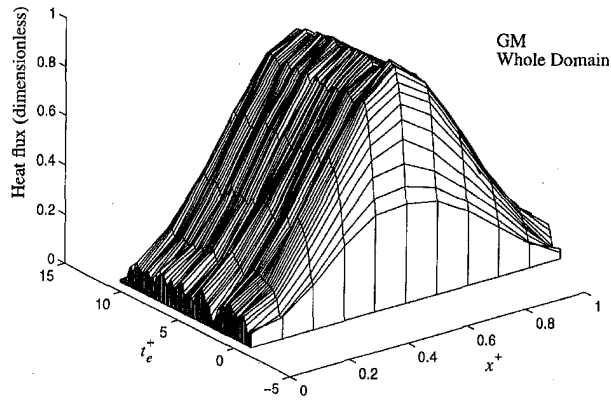


Fig. 2 Estimated surface heat flux for triangular test case using data corrupted with measurement errors ($\sigma = 0.0018^\circ\text{C}$). Whole domain solution, ($q_{pri} = 0$).

significantly larger variability. It is not clear if the variability of the SGM estimated heat flux is larger on time or on space. The sequential results are certainly unacceptable in comparison to the whole domain solution for $r = 6$.

Analysis of the triangular test cases with measurement errors is presented in Table 1. The table lists the solution method and analysis domain, with the number of future time-steps and number of components retained on time in the first three columns. Column four gives the magnitude of the Tikhonov parameter. The number of iterations, both total and average per sequential interval, are given in columns five and six. Computational time is listed in column seven. The errors in the sum-of-squares temperature and estimated heat flux are shown in columns eight and nine,

$$S_Y = \left\{ \frac{1}{J(M-1)} \sum_{j=1}^J \sum_{i=1}^M [T(\mathbf{d}_j, t_i) - Y_j(t_i)]^2 \right\}^{1/2} \quad (13)$$

$$\hat{\sigma}_{s_e} = \left\{ \frac{1}{P(M-1)} \sum_{k=1}^P \sum_{i=1}^M [q(\mathbf{r}_k, t_i) - \hat{q}_e(\mathbf{r}_k, t_i)]^2 \right\}^{1/2} \quad (14)$$

The poor performance of the sequential approach for small r -values is attributed to two related factors. The first factor is that the sequential implementation is more ill-posed than the whole-domain solution. Since the sequential solution solves over a shorter time domain, the effect of measurement errors is more significant and results in a more ill-conditioned problem than the whole-domain problem. Examining Table 1 shows that, even though the sequential problem is more ill-posed, the magnitude of the Tik-

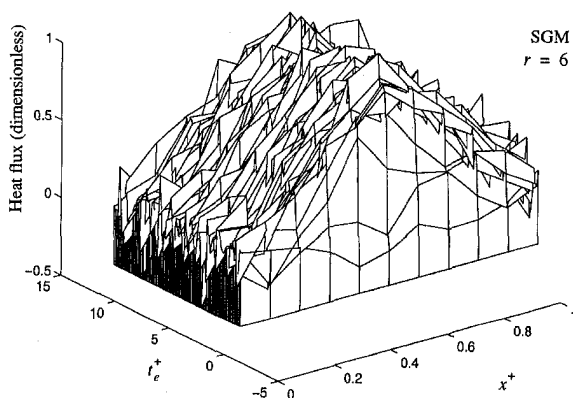


Fig. 3 Estimated surface heat flux for triangular test case using data corrupted with measurement errors ($\sigma = 0.0018^\circ\text{C}$). Sequential solution with $r = 6$, ($q_{pri} = 0$).

Table 1 Estimation results for two-dimensional IHCP with simulated data corrupted with random errors*

Method	Analysis domain		Tikhonov α_T	Iterations		Comp time (sec)	S_Y ($^\circ\text{C}$)	$\hat{\sigma}_{s_e}$ W/m^2
	r	I		total	per seq int			
GM	all	all	1.70 E-03	9	-	31.8	1.82 E-03	8.57 E-02
SGM	6	1	2.20 E-04	764	4.0	77.8	1.81 E-03	1.36 E-01
SGM	8	1	4.50 E-04	758	4.0	96.0	1.80 E-03	1.02 E-01
SGM	10	1	7.00 E-04	746	4.0	119.0	1.80 E-03	9.19 E-02
SGM	15	1	1.25 E-03	718	4.0	173.7	1.80 E-03	8.65 E-02
SGM	20	1	1.50 E-03	759	4.3	246.9	1.80 E-03	7.53 E-02
SGM	20	10	1.20 E-03	90	5	30.8	1.80 E-03	8.51 E-02
SFSGM	6	1	5.00 E-05	767	4.0	77.1	1.81 E-03	1.57 E-01
SFSGM	8	1	8.30 E-05	769	4.1	96.3	1.80 E-03	1.12 E-01
SFSGM	10	1	1.1 E-04	761	4.1	120.2	1.80 E-03	9.71 E-02
SFSGM	15	1	9.50 E-05	693	3.8	167.2	1.87 E-03	8.97 E-02
SGM ¹	6	1	1.40 E-03	396	2.1	37.6	1.80 E-03	1.16 E-01
SGM ¹	8	1	3.50 E-03	391	2.0	50.1	1.80 E-03	1.02 E-01
SGM ¹	20	10	3.00 E-03	59	3.2	19.4	1.82 E-03	8.21 E-02

* Prior information used for solution

honor parameter in column four is decreased compared to the whole domain solution (except at large r -values). Decreasing the Tikhonov parameter is contradictory to stabilizing a more ill-conditioned problem. However, to obtain the required magnitude in the sum-of-squares function, S_Y , the Tikhonov parameter must be decreased. The reason for this outcome (decreasing α_T for SGM) is the second factor in the poor performance of the sequential implementation. It is the difficulty of estimating values near the end of the sequential interval which influences the early values. Because the values near the end of the time region are biased, the regularization parameter must be decreased to provide the inverse solution "flexibility" to obtain the proper magnitude of the sum-of-squares function S_Y . Although decreasing the Tikhonov parameter reduces the temperature sum-of-squares, it results in an increase in the variability of the estimated heat flux $\hat{\sigma}_{s_e}$, which is demonstrated in Fig. 3.

In contrast to the one-dimensional solution, maintaining the heat flux constant over the sequential analysis interval does not improve the two-dimensional results. See method SFSGM in Table 1. In the two-dimensional solution, maintaining the heat flux constant over the sequential interval does not work because the additional stability introduced by the approximation requires a reduction in the Tikhonov parameter to obtain the desired sum-of-squares. The reduction in α_T in turn increases the variability in the estimated heat flux. The computational time and mean-squared error are not improved for SFSGM.

The sequential gradient method is shown to perform poorly for small magnitudes of r , which are in the range that would typically be used for function specification. The estimated results are improved as the number of future time-steps is increased. Figure 4 demonstrates that the effect at the end of the interval is reduced by lengthening the sequential interval. At $r = 15$ and 20 the mean-squared error in Table 1 is +1 percent and -12 percent different than the mean-squared error of the whole domain estimation, respectively. The improved accuracy in the estimated heat flux using larger r -values is at the cost of a significantly increased computational requirement. Sequential solutions (SGM) for larger magnitudes of r require 500–800 percent (depending on r) more computational time than the whole domain solution. Computational time increases proportional to the increase in r . However, in some cases the potential benefits of an on-line (real time) method may outweigh the increased computational time.

As demonstrated, lengthening the sequential interval by increasing the number of future time steps improves the mean-squared error in the estimated heat flux (see Table 1 and Figs. 4). Length-

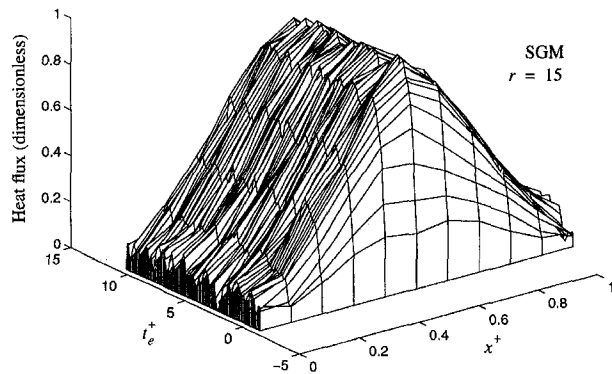


Fig. 4 Estimated surface heat flux for triangular test case using data corrupted with measurement errors ($\sigma = 0.0018^\circ\text{C}$). Sequential solution with $r = 15$, ($q_{\text{pri}} = 0$)

ening the sequential interval is also shown to increase the computational time in Table 1. An advantage of the SGM, compared to the SFGM, is that functional constraints are not imposed on the solution. Consequently more than one component may be retained for a sequential interval and the computational time can be reduced by having fewer sequential intervals. For example, when retaining ten components for the triangular heat flux with $r = 20$, the computational time is reduced to 30.8 seconds, which is only three percent greater than the whole domain computational time. The mean-squared error for this case, shown in the final column of Table 1, is within one percent of the whole domain error; the mean-squared has increased 14 percent compared to retaining only one component for $r = 20$. Although lengthening the sequential interval and retaining more components on time improves the computational aspects, the process may reduce the likelihood that nonlinear problems can be temporarily linearized. Since larger sequential intervals are considered, it may be less likely that changes in thermal properties, due to the temperature variation during the sequential interval, are negligible. This is an important potential advantage of the sequential method. The validity of this assumption will depend on the magnitude of nonlinearity in the problem. The computational costs to solve the nonlinear problem may increase more dramatically for the GM compared to the SGM for reason outlined previously. Retaining only one component for the SGM may be appropriate, and computationally competitive, in the nonlinear case.

Another improvement for the sequential implementation is suggested. A characteristic noticed for the one-dimensional problem, and two-dimensional test cases with measurement errors, is that the Tikhonov parameter decreases for the sequential problem, compared to its magnitude for the whole-domain solution. The decrease in the Tikhonov parameter is more pronounced at smaller r -values and approaches the magnitude of the whole domain solution as r is increased. A smaller Tikhonov parameter is not expected for the sequential solution because the problem is more ill-posed. It is the sequential implementation that forces the Tikhonov parameter to be reduced, at least for small r -values. Since the sequential solution is solved on the shorter time interval, the zeroth-order Tikhonov regularization is more influential. The sensitivity (or in this case adjoint function) is not as significant, particularly for r -values beyond four to five time-steps from the end of the interval, which represents a dimensionless time of 0.3. The nature of zeroth-order regularization is to bias or “drive” the estimates towards zero to reduce their variability. Consequently, to obtain the desired temperature sum-of-squares, the Tikhonov parameter must be decreased so as not to “drive” the estimates towards zero. As r is increased to be farther away from this region, the sensitivity (or adjoint function) is larger, and the regularization affects the solution less.

When solving in a sequential manner, however, there is additional information available concerning the heat flux. The heat flux

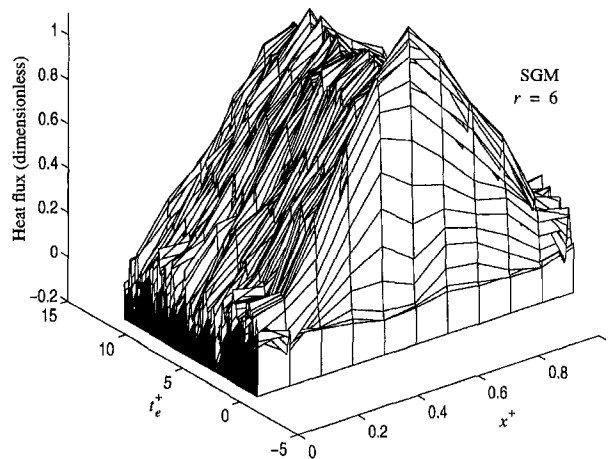


Fig. 5 Estimated surface heat flux for triangular test case using data corrupted with measurement errors ($\sigma = 0.0018^\circ\text{C}$). Sequential solution with $r = 6$ using prior information.

need not be “driven” towards zero with the zeroth-order regularization, instead it can be confined using the concept of prior information. The prior information for the heat flux is specified from converged values at the previous sequential interval. The initial estimate for the sequential interval, which is specified from the converged estimates at the previous sequential interval, are set identically to be the prior information. The prior information is seen to enter the solution as $q_{\text{pri}}(\mathbf{r}, t)$ in Eq. (4), which is the Tikhonov regularization term in the sum-of-squares function. Hence, instead of penalizing estimates that are different from zero, it penalizes estimates that are different from those estimated during the previous sequential interval. For components that are far enough away from the end of the sequential interval the prior information has little influence. Near the end of the sequential interval, however, the prior information is more influential and helps control components in this region. The use of prior information is shown to significantly reduce the computational time and allow smaller values of r .

The results using prior information are given near the bottom of Table 1. As shown in the table, by using the initial estimate as prior information, the sequential method is improved compared to no prior information. Figure 5 shows the estimated triangular heat flux for $r = 6$. Compared to the estimated flux without prior information (see Fig. 3) results are significantly smoother. For $r = 6$ the mean-square error is reduced by 15 percent, and the computational time is reduced by half with prior information. For larger magnitudes of r using prior information the mean-squared error is comparable, while computational time is approximately one-half its former value without prior information. Notice that the magnitude of the Tikhonov parameter is greater when using prior information, but because it penalizes changes from the prior information (estimates at previous sequential interval), it does not bias the estimates as significantly. Prior information allows for smaller r -values to be considered and reduces computational time by requiring fewer iterations.

This investigation has shown that the SGM (and GM) have inherent bias near the end of a time interval that increases the difficulty of estimating components near the end of the interval. (It is well understood to be difficult to estimate components near the end of a time interval for the IHCP. It is for this reason that successful methods use future information.) The option suggested to reduce this effect for the sequential solution lengthened the interval and retained more components. Retaining additional components requires selecting three parameters, the Tikhonov parameter (α_T), number of future time-steps (r), and the number of retained components (J). Having to select three parameters is a disadvantage of the SGM method. In a sequential solution, however, the number of components retained could be built into the

algorithm by specifying an expected level of noise, which is also needed to select the Tikhonov parameter. The use of prior information is shown to reduce the computational requirements and may eliminate the need to retain additional components.

The potential advantages of an SGM are the capability of temporarily linearizing to solve nonlinear problems and the efficiency in addressing multidimensional cases. Results of this investigation have shown that given data for which the time interval is specified, the whole-domain gradient method is as good, or superior to, the sequential gradient method. The nonlinear multidimensional problem may show a different outcome. Furthermore, though comparing the SGM to the whole-domain solution provides a basis for the new method, in the future a comparison with other sequential methods is needed. These future comparisons will help establish the SGM's benefit as a tool for solving the IHCP.

6 Conclusions

A sequential gradient method was developed to solve the IHCP. Several one and two-dimensional cases using simulated measurements were investigated to characterize the sequential method. A sequential implementation permits an on-line or real-time analysis. A comparison between the sequential method and a whole-domain solution was made to provide a reference. Although in certain cases the sequential method required more computational time than the whole-domain method, the benefits of the sequential method may outweigh its costs. Ways to improve the computational requirements of the sequential method were suggested.

The characteristic nature of the gradient/adjoint method at the end of a time interval, coupled with the effect of zeroth-order Tikhonov regularization, reduced the performance of the sequential implementation when compared to its whole-domain counterpart. Retaining more than one component to reduce the number of sequential solutions and using prior information both improved the sequential solution. Though prior information allowed shorter sequential intervals to be considered, the gradient/adjoint method did not adapt well computationally to a sequential implementation. However, these observations are based on investigating linear problems. Results indicate that given data for a linear problem over a specified time interval, the whole-domain approach is better than a sequential solution. To some extent this indicates the efficiency of the whole-domain gradient method. With the benefits noted for the gradient/adjoint methods when considering multidimensional cases, and the linearization possible with a sequential implementation, the sequential implementation of the gradient/adjoint method is promising for addressing nonlinear problems.

Acknowledgments

This research was partially supported by the Research Excellence Fund of the State of Michigan through the Composite Materials and Structures Center at Michigan State University.

References

- Alifanov, O. M., Artyukhin, E. A., and Romyantsev, S. V., 1996, *Extreme Methods for Solving Ill-Posed Problems with Applications to Inverse Heat Transfer Problems*, Begell House, New York.
- Alifanov, O. M., 1994, *Inverse Heat Transfer Problems*, Springer-Verlag, New York.
- Alifanov, O. M., and Egorov, Yu. V., 1985, "Algorithms and Results of Solving the Inverse Heat Conduction Problem in a Two-Dimensional Formulation," *Journal of Engineering Physics*, Vol. 48, No. 4, pp. 489–496.
- Alifanov, O. M., and Kerov, N. V., 1981, "Determination of External Thermal Load Parameters by Solving the Two-Dimensional Inverse Heat Conduction Problem," *Journal of Engineering Physics*, Vol. 41, No. 4, pp. 1049–1053.
- Artyukhin, E. A., and Gedzhadze, I. Yu., 1994, "Sequential Regularization Solution of a Boundary Inverse Heat Conduction Problem," 2nd Joint Russian-America Workshop on Inverse Problems in Engineering, Aug., St. Petersburg, Russia.
- Artyukhin, E. A., 1996, "Account for Smoothness when Estimating Temperature-Dependent Thermophysical Characteristics," *Proceedings of the Second International Conference on Inverse Problems in Engineering: Theory and Practice*, D. Delaunay, K. Woodbury, and M. Raynaud, eds., ASME Engineering Foundation, New York.
- Beck, J. V., Blackwell, B., and St. Clair, C. R., 1985, *Inverse Heat Conduction*, John Wiley and Sons, New York.
- Beck, J. V., Blackwell, B., and Haji-Sheikh, A., 1996, "Comparison of Some Inverse Heat Conduction Methods Using Experimental Data," *International Journal of Heat and Mass Transfer*, Vol. 39, No. 17, pp. 3649–3657.
- Dowding, K. J., 1997, "Multi-Dimensional Estimation of Thermal Properties and Surface Heat Flux Using Experimental Data and a Sequential Gradient Method," Ph.D. Dissertation, Michigan State University, East Lansing, MI.
- Hsu, T., Sun, N., Chen, G., and Gong, Z., 1992, "Finite Element Formulation for Two-Dimensional Inverse Heat Conduction Analysis," *ASME JOURNAL OF HEAT TRANSFER*, Vol. 114, pp. 553–557.
- Jarny, Y., Ozisik, M. N., and Bardon, J. P., 1991, "A General Optimization Method using Adjoint Equation for Solving Multi-Dimensional Inverse Heat Conduction," *International Journal of Heat and Mass Transfer*, Vol. 34, No. 11, pp. 2911–2919.
- Lamm, P. K., 1995, "Future-Sequential Regularization Methods for Ill-Posed Volterra Equations: Applications to the Inverse Heat Conduction Problem," *J. Math. Analysis and Applications*, Vol. 195, pp. 469–494.
- Loulou, T., Artyukhin, E. A., and Bardon, J. P., 1996, "Estimation of the Time-Dependent Thermal Contact Resistance at the Mold-Casting Interface," *Proceedings of the Second International Conference on Inverse Problems in Engineering: Theory and Practice*, eds. D. Delaunay, K. Woodbury, and M. Raynaud, eds., ASME Engineering Foundation, New York.
- Osman, A. M., Dowding, K. J., and Beck, J. V., 1997, "Numerical Solution of the General Two-Dimensional Inverse Heat Conduction Problem (IHCP)," *ASME JOURNAL OF HEAT TRANSFER*, Vol. 119, pp. 38–45.
- Osman, A. M., and Beck, J. V., 1990, "Investigation of Transient Heat Transfer Coefficients in Quenching Experiments," *ASME JOURNAL OF HEAT TRANSFER*, Vol. 112, pp. 843–848.
- Osman, A. M., and Beck, J. V., 1989, "Nonlinear Inverse Problem for the Estimation of Time-and-Space Dependent Heat Transfer Coefficients," *Journal of Thermophysics and Heat Transfer*, Vol. 3, No. 2, pp. 146–152.
- Reinhardt, H. J., and Hao, N. H., 1996a, "A Sequential Conjugate Gradient Method for the Stable Numerical Solution to Inverse Heat Conduction Problems," *Inverse Problems*, Vol. 2, pp. 263–272.
- Reinhardt, H. J., and Hao, N. H., 1996b, "On the Numerical Solution of Inverse Heat Conduction Problems by Gradient Methods," *Proceedings of the Second International Conference on Inverse Problems in Engineering: Theory and Practice*, eds. D. Delaunay, K. Woodbury, and M. Raynaud, eds., ASME Engineering Foundation, New York.
- Tikhonov, A. N., and Arsenin, V. Y., 1977, *Solutions of Ill-Posed Problems*, Winston and Sons, Washington DC.
- Zabaras, N., and Yang, G., 1996, "Inverse Design and Control of Microstructural Development in Solidification Processes with Natural Convection," *Proceedings of the 31st National Heat Transfer Conference*, Vol. 1, Houston, TX, 3–6 Aug. 3–6, V. Prasad et al., eds., ASME, New York, pp. 1–8.
- Zabaras, N., and Liu, J., 1988, "An Analysis of Two-Dimensional Linear Inverse Heat Transfer Problems Using an Integral Method," *Numerical Heat Transfer*, Vol. 13, pp. 527–533.

Swirling Effects on Laminarization of Gas Flow in a Strongly Heated Tube

S. Torii

Associate Professor,
Department of Mechanical Engineering,
Kogoshima University,
1-21-40 Korimoto,
Kagoshima 890, Japan
e-mail: torii@mech.kagoshima-u.ac.jp
Mem. ASME

W.-J. Yang

Professor,
Department of Mechanical Engineering
and Applied Mechanics,
University of Michigan,
Ann Arbor, MI 48109
e-mail: wuyang@engin.umich.edu
Fellow ASME

A numerical study is performed to investigate thermal transport phenomena in a process of laminarization from a turbulent flow in a strongly heated circular tube in coaxial rotation. The k - ε turbulence and t^2 - ε , heat transfer models are employed to determine the turbulent viscosity and eddy diffusivity for heat, respectively. The governing boundary layer equations are discretized by means of a control-volume finite difference technique and numerically solved using a marching procedure. When the tube is at rest, it is disclosed that: (i) when laminarization occurs, the streamwise velocity gradient at the wall is diminished along the flow, resulting in a substantial reduction in the turbulent kinetic energy over the whole tube cross section, (ii) the attenuation causes a deterioration in heat transfer performance, and (iii) simultaneously, both the turbulent heat flux and temperature variance diminish over the whole tube cross section in the flow direction. However, the presence of tube rotation contributes to the promotion of laminarization of gas flow. The mechanism is that a reduction in the velocity gradient induced by tube rotation suppresses the production of turbulent kinetic energy, resulting in an amplification in laminarizing the flow process.

Introduction

When a gas in a channel is heated with very high heat flux, the flow may possibly be laminarized, that is, a transition from turbulent to laminar flows occurs at a higher Reynolds number than the usual critical value, i.e., $Re = 2300$. This phenomenon is called laminarization. Both the criteria for its occurrence and the heat transfer characteristics have been reported by several investigators (for example, Bankston, 1970; Coon and Perkins, 1970; McEligot et al., 1970; Perkins et al., 1973; Mori and Watanabe, 1979; Ogawa et al., 1982). Kawamura (1979), Torii et al. (1990), and Fujii et al. (1991) analyzed laminarization phenomena by means of k - kL , k - ε , and k - kL - $\bar{u}\bar{v}$ models, respectively. In order to obtain detailed information on the flow and thermal fields, Torii et al. (1993) and Torii and Yang (1997) investigated the transport phenomena in the strongly heated circular tube flows by means of a Reynolds stress turbulence model and a two-equation heat transfer model, respectively.

The problems of fluid flow and heat transfer in axially rotating pipes are encountered in the inlet part of fluid machinery, rotating heat exchangers, and cooling systems of rotors. When a fluid enters a pipe rotating around the axis, the tangential force induced by rotation produces a fluid swirl, a flow pattern unseen in a stationary pipe. Numerical and experimental investigations on the flow phenomena are available in the literature (for example, Murakami and Kikuyama, 1980; Kikuyama et al., 1983; Weigand and Beer, 1990). However, to the authors' knowledge, no experimental data has been presented on flow and thermal characteristics such as turbulence quantities in an axially rotating pipe heated with a high heat flux at low Reynolds number. The reason is difficulties in measuring turbulent quantities in strongly heated flows in an axially rotating pipe. Although numerical simulation provides detailed information on the transport phenomena, the existing theoretical studies are periled by the assumption of constant properties in the governing equations. Thus it fails to yield crucial information on thermal and fluid flow transport characteristics in the

axially rotating pipe gas flow with high heat flux, because the coolant in rotating machinery, particularly in a high-temperature gas turbine, is under high flux heating.

In the present study, a combination of the k - ε model for velocity field and the t^2 - ε model for thermal field is applied to analyze gas flows in an axially rotating pipe with high heat flux. This is motivated by the following findings: (i) the calculated values of both the friction factor and the Nusselt number in a slightly heated pipe are in excellent agreement with correlations in the higher Reynolds number region of over 3000, (ii) the predicted transition Reynolds number is approximately 2200, (iii) the k - ε - t^2 - ε model can predict laminarizing flows in a stationary pipe with uniform high heat flux, (iv) the application of the k - ε model to an isothermal swirling flow in an axially rotating pipe yields a substantial reduction in the friction coefficient together with an increase in the velocity ratio, and (v) the streamwise velocity profile in an axially rotating pipe gradually forms a parabolic shape along the downstream flow direction, indicating a reverse transition stage from turbulent to laminar flow (Torii et al., 1990; Torii and Yang, 1995a, 1997). An emphasis is placed on effects of axial rotation of a pipe on flow and thermal fields, including turbulent kinetic energy, velocity and temperature profiles, turbulent heat flux, and temperature variance.

Governing Equations and Numerical Scheme

A turbulent flow in a strongly heated circular tube is analyzed using cylindrical coordinates, as shown in Fig. 1. In such a system, the dependence of gas properties on temperature, especially change in the gas density must be taken into account according to Schlichting (1985). Here, the governing equations are derived based on the assumption of the incompressible fluid. This is because an incompressibility can be assumed if the fluctuating components of velocity and density are sufficiently smaller than the corresponding time-averaged values and the boundary layer approximation can be applied to these equations (Schlichting, 1985). Based on the derivation process as suggested in Schlichting (1985), steady two-dimensional governing equations, under the boundary layer approximation, can be expressed as follows:

Continuity Equation:

Contributed by the Heat Transfer Division for publication in the JOURNAL OF HEAT TRANSFER. Manuscript received by the Heat Transfer Division, May 20, 1998; revision received, Nov. 6, 1998. Keywords: Forced Convection, Heat Transfer, High Temperature, Turbulence. Associate Technical Editor: R. Dougllass.

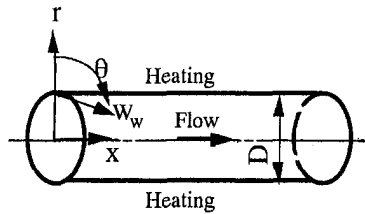


Fig. 1 A schematic of physical system and coordinate.

$$\frac{\partial(\bar{\rho}U)}{\partial x} + \frac{1}{r} \frac{\partial(r\bar{\rho}\hat{V})}{\partial r} = 0 \quad (1)$$

Momentum Equations:

x-direction:

$$\bar{\rho}U \frac{\partial U}{\partial x} + \bar{\rho}\hat{V} \frac{\partial U}{\partial r} = -\frac{dP}{dx} + \frac{1}{r} \frac{\partial}{\partial r} \left(r\mu \frac{\partial U}{\partial r} - r\bar{\rho}u\bar{v} \right) \quad (2)$$

r-direction

$$\frac{W^2}{r} = \frac{1}{\bar{\rho}} \frac{\partial P}{\partial r} \quad (3)$$

theta-direction:

$$\bar{\rho}U \frac{\partial W}{\partial x} + \bar{\rho}\hat{V} \frac{\partial W}{\partial r} + \frac{VW}{r} = \frac{1}{r^2} \frac{\partial}{\partial r} \left\{ r^3 \mu \frac{\partial}{\partial r} \left(\frac{W}{r} \right) - \bar{\rho}r^2 \bar{v}w \right\} \quad (4)$$

Energy Equation:

$$c_p \bar{\rho}U \frac{\partial T}{\partial x} + c_p \bar{\rho}\hat{V} \frac{\partial T}{\partial r} = \frac{1}{r} \frac{\partial}{\partial r} \left(r\lambda \frac{\partial T}{\partial r} - rc_p \bar{\rho}v\bar{t} \right) \quad (5)$$

Note that $\bar{\rho}U$ and $\bar{\rho}\hat{V}$ result from the derivation process (Schlichting, 1985) and they are obtained by conservation of mass. Here, the body force term in the momentum equation has been neglected, because in a small diameter tube, the buoyancy parameter, Gr/Re_m^2 , would be less than 0.1 resulting in forced convection dominating (Torii and Yang, 1997).

The Reynolds stresses $-\bar{\rho}u\bar{v}$ and $-\bar{\rho}v\bar{w}$ in Eqs. (2) and (4) are obtained using the Boussinesq approximation as.

$$-\bar{\rho}u\bar{v} = \mu_t \frac{\partial U}{\partial r} \quad (6)$$

and

Table 1 Empirical constants and model functions in the k - ε turbulence model

C_μ	C_1	C_2	C_3	α_k	α_ε	f_1	f_2	f_μ
0.09	1.44	1.9	$1 - 0.06 Ri^{0.5}$	1.0	1.3	$1 + 0.28 \exp\left(-\frac{Ri}{25}\right)$	$1 - 0.3 \exp(-Ri^2)$	$\left(1 - \exp\left(-\frac{Ri}{26.5}\right)\right)^2$

$$-\bar{\rho}v\bar{w} = \mu_t r \frac{\partial}{\partial r} \left(\frac{W}{r} \right) \quad (7)$$

respectively. Here, the turbulent viscosity μ_t can be expressed in terms of the turbulent kinetic energy k and its dissipation rate ε , with the use of Kolmogorov-Prandtl relation (Rodi, 1982), as

$$\mu_t = \bar{\rho} C_\mu f_\mu \frac{k^2}{\varepsilon} \quad (8)$$

The quantities C_μ and f_μ are a model constant and a model function, respectively. Torii et al. (1990) developed a low Reynolds number version of the k - ε turbulence model which is capable of reproducing both the transition from turbulent to laminar flows in a slightly heated pipe and the laminarization phenomena in the strongly heated pipe. Both transport equations read

$$\bar{\rho}U \frac{\partial k}{\partial x} + \bar{\rho}\hat{V} \frac{\partial k}{\partial r} = \frac{1}{r} \frac{\partial}{\partial r} \left\{ r \left(\frac{\mu_t}{\sigma_k} + \mu \right) \frac{\partial k}{\partial r} \right\} + \mu_t \left[\left(\frac{\partial U}{\partial r} \right)^2 + \left\{ r \frac{\partial}{\partial r} \left(\frac{W}{r} \right) \right\}^2 \right] - \bar{\rho}\varepsilon - 2\mu \left(\frac{\partial \sqrt{k}}{\partial r} \right)^2 \quad (9)$$

$$\bar{\rho}U \frac{\partial \varepsilon}{\partial x} + \bar{\rho}\hat{V} \frac{\partial \varepsilon}{\partial r} = \frac{1}{r} \frac{\partial}{\partial r} \left\{ r \left(\frac{\mu_t}{\sigma_\varepsilon} + \mu \right) \frac{\partial \varepsilon}{\partial r} \right\} + C_\varepsilon f_1 \bar{\rho} \frac{\varepsilon}{k} \mu_t \left[\left(\frac{\partial U}{\partial r} \right)^2 + \left\{ r \frac{\partial}{\partial r} \left(\frac{W}{r} \right) \right\}^2 \right] - C_2 C_\varepsilon f_2 \frac{\varepsilon^2}{k} + \nu \mu_t (1 - f_\mu) \left(\frac{\partial^2 U}{\partial r^2} \right)^2 \quad (10)$$

The empirical constants and model functions in Eqs. (8), (9), and (10) are summarized in Table 1.

Using the turbulent thermal conductivity λ_t , the turbulent heat flux $-c_p \bar{\rho}v\bar{t}$ in Eq. (5) can be expressed in the following simple gradient form:

$$-c_p \bar{\rho}v\bar{t} = \lambda_t \frac{\partial T}{\partial r} \quad (11)$$

Nagano and Kim (1988) expressed the turbulent thermal conductivity λ_t in terms of the temperature variance, \bar{t}^2 , the dissipation rate of temperature fluctuations, ε_t , k , and ε , as

Nomenclature

D = diameter, m
 f = friction coefficient, $-D(dP/dx)/(2\rho u_m^2)$
 G = average mass flux of gas flow, kg/(m²s)
 N = velocity ratio, W_w/u_m
 Pr_t = turbulent Prandtl number
 q_w = heat flux, W/m²
 q_{in}^+ = dimensionless heat flux parameter, $q_w/(Gc_p T)_{in}$
 Re = Reynolds number, $u_m D/\nu$
 Ri = Richardson number, Eq. (18)
 St = Stanton number, $q_w/(\rho c_p u_m (T_w - T_b))$
 t^* = friction temperature, $q_w/(\rho c_p u^*)$, K

t^2 = temperature variance, K²
 U, V, W = time-averaged velocity components in axial, radial, and tangential directions, respectively, m/s
 \hat{V} = instantaneous velocity component in radial direction, $V + v$, m/s
 u_m = mean velocity over tube cross section
 u, v, w = fluctuating velocity components in axial, radial, and tangential directions, respectively, m/s

u^* = friction velocity, $\sqrt{\tau_w/\rho}$, m/s
 W_w = tangential velocity on the wall, m/s
 y = distance from wall, m
 y^+ = dimensionless distance, $u^* y/\nu$

Greek Letters

α_t = turbulent thermal diffusivity, m²/s
 θ^+ = dimensionless temperature, $\theta^+ = (T - T_c)/(T_w - T_c)$

Table 2 Empirical constants and model functions in the \bar{t}^2 - ε_t heat transfer model

C_λ	C_{P1}	C_{P2}	σ_h	σ_ϕ	C_{D1}	C_{D2}	f_{P1}	f_{P2}	f_{D1}	f_{D2}	f_λ
0.11	1.80	0.72	1.0	1.0	2.20	0.80	1.0	1.0	1.0	1.0	$\{1 - \exp(-\frac{f_{Pr}}{30.5} 2 St y^*)\}^2$

$$\lambda_t = c_p \bar{\rho} C_\lambda f_\lambda k \sqrt{\frac{\bar{t}^2}{\varepsilon_t}}, \quad (12)$$

where C_λ is a model constant and f_λ is a model function. The two-equation heat transfer model developed by Nagano and Kim (1988) is modified by Torii and Yang (1997) in order to reproduce the thermal transport characteristics in the turbulent-to-laminar transition region in a slightly heated pipe. This modified transport equations for \bar{t}^2 and ε_t are expressed as

$$\bar{\rho} U \frac{\partial \bar{t}^2}{\partial r} + \bar{\rho} \bar{V} \frac{\partial \bar{t}^2}{\partial r} = \frac{1}{r} \frac{\partial}{\partial r} \left\{ r \left(\frac{\lambda_t}{c_p \sigma_h} + \frac{\lambda}{c_p} \right) \frac{\partial \bar{t}^2}{\partial r} \right\} + \frac{2\lambda_t}{c_p} \left(\frac{\partial T}{\partial r} \right)^2 - 2\rho \varepsilon_t - 2 \frac{\lambda}{c_p} \left(\frac{\partial \sqrt{\bar{t}^2}}{\partial r} \right)^2 \quad (13)$$

$$\bar{\rho} U \frac{\partial \varepsilon_t}{\partial x} + \bar{\rho} \bar{V} \frac{\partial \varepsilon_t}{\partial r} = \frac{1}{r} \frac{\partial}{\partial r} \left\{ r \left(\frac{\lambda_t}{c_p \sigma_\phi} + \frac{\lambda}{c_p} \right) \frac{\partial \varepsilon_t}{\partial r} \right\} + C_{P1} f_{P1} \frac{\lambda_t \varepsilon}{c_p k} \left(\frac{\partial T}{\partial r} \right)^2 + C_{P2} f_{P2} \mu_t \frac{\varepsilon_t}{k} \left[\left(\frac{\partial U}{\partial r} \right)^2 + \left\{ \frac{1}{r} \frac{\partial}{\partial r} \left(\frac{W}{r} \right) \right\}^2 \right] - C_{D1} f_{D1} \rho \frac{\varepsilon_t^2}{\bar{t}^2} - C_{D2} f_{D2} \rho \frac{\varepsilon \varepsilon_t}{k} + \frac{\alpha \lambda_t}{c_p} (1 - f_\lambda) \left(\frac{\partial^2 T}{\partial r^2} \right)^2, \quad (14)$$

respectively. The empirical constants and model functions in Eqs. (12), (13), and (14) are summarized in Table 2. In the present study, k - ε - \bar{t}^2 - ε_t model was employed to investigate the mechanism of transport phenomena, because the k - ε - \bar{t}^2 - ε_t model can predict the laminarizing flow in the strongly heated stationary pipe than the other model employed for comparison (Torii and Yang, 1997).

Hirai et al. (1986) reported that if the standard k - ε model is applied to an axially rotating pipe flow, there would be no distinction between the calculated streamwise velocity distributions with and without rotation and turbulence suppression of a swirling flow by the centrifugal force (so-called laminarization phenomena) would not occur. This is attributed to a linear radial profile of the tangential velocity, as pointed out by Kawamura and Mishima (1991) and Torii and Yang (1995a). In order to predict swirling flow phenomena in an axially rotating pipe, it is necessary to prescribe the swirl velocity profile. Kikuyama et al. (1983) conducted an experimental study and found that both the Reynolds number and rotation rate do not affect the radial profiles of the time-averaged tangential velocity at different axial locations. Experimental results led Weigand and Beer (1990) to propose that the universal tangential profile is dependent on the radial location and the axial distance from the inlet. They derived the experimental correlation as

$$W = W_w \left(\frac{r}{D/2} \right)^{(2+f(z^*))}, \quad (15)$$

where

$$f(z^*) = \frac{1}{z^*} + 9.5e^{-0.019z^*}. \quad (16)$$

In the present study, Eq. (15) is employed to replace Eq. (4) in determining the tangential velocity. This is because the developing and fully developed flows in the axially rotating pipe are precisely predicted using the modified k - ε turbulence model in which Eq. (15) was employed to determine the tangential velocity (Torii and Yang, 1995a, b), that is, the model can reproduce suppression of turbulence by rotation. It should be noted that the experimental correlation of the tangential velocity, which takes into account the acceleration of gas expansion due to heating, must be used to investigate heat and fluid flow in a strongly heated pipe rotating around the axis. It is assumed that a substantial change in the streamwise velocity is induced by the acceleration effect of gas expansion rather than by that of the tangential velocity.

In analyzing the fluid flow and thermal transport in a slightly heated axially rotating pipe, Torii and Yang (1995a, b) modified a k - ε turbulence model proposed by Torii et al. (1990) to determine swirling effects. By adjusting C_3 in the dissipation term of the turbulence dissipation rate equation, they proposed a model function containing the Richardson number, Ri, as

$$C_3 = 1 - 0.06 Ri^{0.5}, \quad (17)$$

where

$$Ri = \frac{k^2 W^0 (rW)}{\varepsilon^2 r^2 \frac{\partial r}{\partial r}}. \quad (18)$$

The same model function is employed to include swirling effects.

No attempt is made to reduce the governing equations into dimensionless form, because no simplification is achieved by doing so. A set of governing equations are solved using the control volume finite difference procedure developed by Patankar (1980). A power-law variation is used in the interpolation of the dependent variables. Since all turbulent quantities as well as the time-averaged streamwise velocity vary rapidly in the near-wall region, the size of nonuniform cross stream grids is increased with a geometric ratio from the wall towards the center line. The maximum control volume size near the center line is always kept less than three percent of the tube radius. In order to ensure the accuracy and validity of calculated results, at least two control volumes are positioned in the viscous sublayer, i.e., $y^+ < 5$. Throughout numerical calculations, the number of control volumes is properly selected between 62 and 98 over the cross section of the circular tube to obtain a grid-independent solution. This result becomes clearer in the following section. It yields a convergence in numerical results obtained using different grid spacings. The discretized equations are solved in the downstream direction beginning at the inlet following the marching procedure (for the parabolic equations). The same algorithm was successfully used in the prediction of developing pipe flows (Kawamura, 1979; Torii et al., 1990; Fujii et al., 1991; Torii and Yang, 1995b). The maximum step-size in the streamwise direction is limited to five times the minimum size in the radial direction of the control volume. At each axial location, the thermal properties for each control volume are determined from the axial pressure and temperature using a numerical code of reference (PROPATH, 1987).

Only one-half of the pipe cross section is treated in solving the above governing equations in view of symmetry in the fluid flow. The hydrodynamically fully developed isothermal flow in a stationary pipe is assumed at the starting point of the heating section. The following boundary conditions are used at the wall:

$$r = 0 \text{ (center line): } \frac{\partial U}{\partial r} = W = \frac{\partial k}{\partial r} = \frac{\partial \varepsilon}{\partial r} = \frac{\partial T}{\partial r} = \frac{\partial \bar{t}^2}{\partial r} = \frac{\partial \varepsilon_t}{\partial r} = 0$$

$$r = D/2 \text{ (wall): } U = k = \varepsilon = \bar{t}^2 = \varepsilon_t = 0, W = W_w$$

$$\frac{\partial T}{\partial r} = \frac{q_w}{\lambda_w} \text{ (constant heat flux).}$$

Computations are proceeded in the following order.

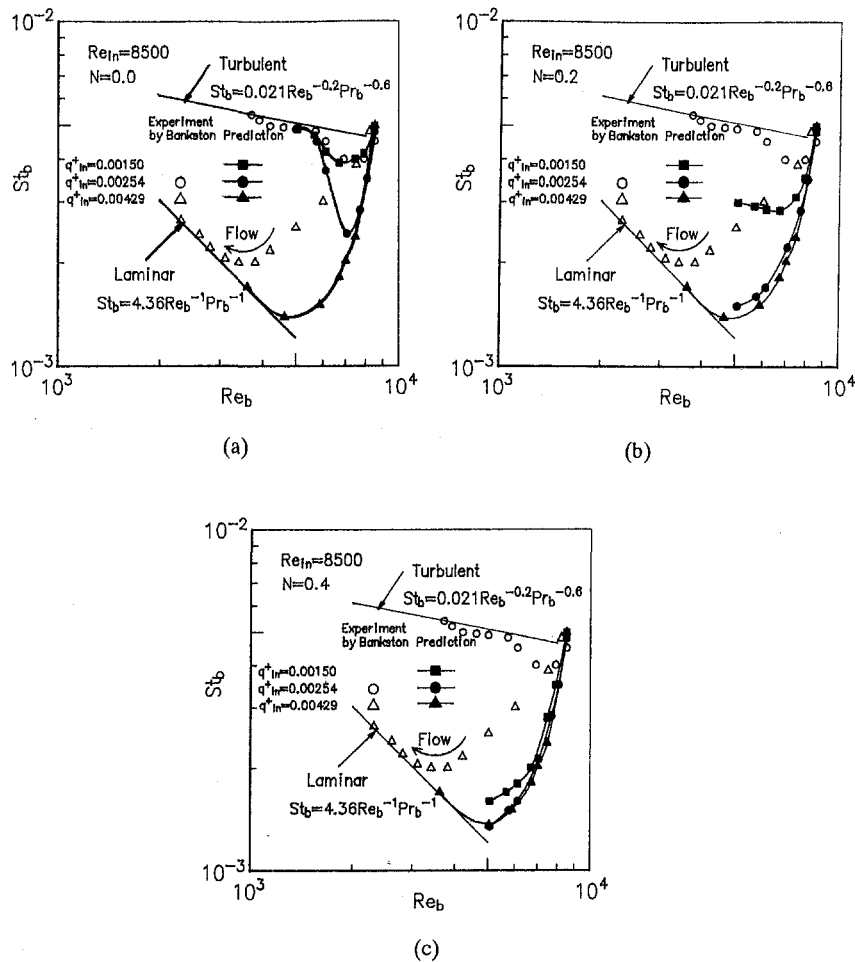


Fig. 2 Variations of predicted local Stanton number St_b with Reynolds number Re_b as a function of nondimensional heat flux q_{in}^+ for (a) $N = 0.0$, (b) $N = 0.2$, and (c) $N = 0.4$.

1 Assume initial values for U , W , k , ε , T , \bar{t}^2 , and ε_r , and assign a constant axial pressure gradient. Note that computations are initiated with the values of U , k , and ε in the hydrodynamically fully developed isothermal flow in the stationary circular tube.

2 Solve the equations for U , k , ε , T , \bar{t}^2 and ε_r and obtain W at an axial location using Eq. (15).

3 Repeat step 2 until the criterion of convergence is satisfied, which is set at

$$\max \left| \frac{\phi^M - \phi^{M-1}}{\phi_{\max}^{M-1}} \right| < 10^{-4} \quad (19)$$

for all the variables $\phi(U, k, \varepsilon, T, \bar{t}^2, \text{ and } \varepsilon_r)$. The superscripts M and $M-1$ in Eq. (19) indicate two successive iterations, while the subscript "max" refers to a maximum value over the entire field of iterations.

4 Calculate new values of U , k , ε , T , \bar{t}^2 , and ε_r by correcting the axial pressure gradient.

5 Repeat steps 2–4 until the conservation of the streamwise flow rate is satisfied under the criterion

$$\left| \frac{\iint U_{cp} r d\theta dr - \iint U_{in} r d\theta dr}{\iint U_{in} r d\theta dr} \right| \leq 10^{-5}. \quad (20)$$

Evaluate the convergent values of U , k , ε , T , \bar{t}^2 , and ε_r . Here, U_{cp} is the axial velocity under the correction process and U_{in} is that at the inlet of the circular tube.

6 Repeat steps 2–5 until x reaches the desired length, i.e., a location $150D$ downstream from the inlet.

The nondimensional heat flux parameter, q_{in}^+ , represents the heat flux at the tube wall. The dimensionless parameters are $q_{in}^+ < 0.005$; inlet Reynolds number (i.e., Reynolds number at the onset of heating) $Re_{in} = 8,500$; velocity ratio of wall velocity to inlet bulk velocity $N = 0.0 \sim 1.0$; inlet gas (nitrogen) temperature $T_{in} = 273$ K; Prandtl number of inlet gas $Pr = 0.72$. Numerical computations were performed on a NEC personal computer (32 bit).

Results and Discussion

Figure 2 illustrates the variation of local heat transfer coefficients in a strongly heated gas flow in the form of Stanton number St_b versus Reynolds number Re_b , with q_{in}^+ as the parameter. Numerical results (solid symbols) are compared with the experimental data (hollow symbols) of Bankston (1970). No experimental data are presented for $q_{in}^+ = 0.0015$. The uncertainty in the measured heat transfer coefficients strongly depends on the accuracy of local heat flux and inner wall temperature. That is, each test section was individually calibrated by determining the local resistivity of the tube wall and the local effective heat-exchange coefficient between the outer wall of the tube and the environment. The inner wall temperature of the tube was estimated using the mea-

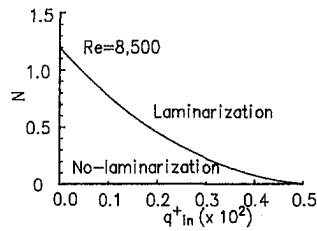


Fig. 3 Laminarization map on $N - q_{in}^+$ plot.

sured outside wall temperature, taking into account both the radial and axial conduction (including the effects of temperature-dependent thermal conductivity, electrical resistivity, and the diameter of the tube) and radiation from the outer surface of the tube. These effects were also considered in the determination of local heat fluxes by Bankston (1970). Figures 2(a), (b), and (c) correspond to the velocity ratios, N of 0.0, 0.2, and 0.4, respectively. $N = 0.0$ refers to stationary case (i.e., Bankston's experiment). The inlet bulk Reynolds number is fixed at 8500. Both the Dittus-Boelter's turbulent heat transfer correlation and the Stanton number for laminar flow heat transfer under the constant wall heat flux condition are superimposed in the figure by solid straight lines. In Fig. 2, a reduction in the bulk Reynolds number signifies a change in the streamwise location, because the bulk Reynolds number decreases from the inlet with the axial distance resulting from an increase in the molecular viscosity by heating. Here, the bulk Reynolds number, Re_b , is determined using the mean velocity at the axial location and the viscosity at the mean temperature at the same location, in which both values are obtained by averaging the local streamwise velocity and temperature over the whole pipe cross section, respectively. It is observed in Fig. 2(a) that at $q_{in}^+ = 0.00254$ indicated by hollow circle, the measured Stanton numbers decrease first in the inlet region due to the thermal entrance effect, followed by an upturn, approaching the turbulent correlation further downstream. This implies that no laminarization will occur. The streamwise variation of the local Stanton number is reproduced by the turbulence model employed here, although it overestimates an attenuation in the heat performance in the initial stage. On the contrary, for $q_{in}^+ = 0.00429$, the experimental Stanton numbers depart from the turbulent correlation toward the laminar case as the flow goes downstream until the Reynolds number is much lower. The substantial reduction in St_b is attributed to the occurrence of laminarization. Though a remarkable reduction in the Stanton number along the flow is predicted by the turbulence model, it cannot precisely reproduce the corresponding experimental data. Here, discrepancy between the experimental data and the numerical results, as seen in Fig. 2(a), is to be due to the accuracy of the $r^2-\varepsilon$ model as mentioned in literature (Torii and Yang, 1997). Figure 2(b) for $N = 0.2$ shows a substantial reduction in the local Stanton numbers even in the case of $q_{in}^+ = 0.00254$. This trend is intensified with an increase in the pipe rotation, as seen in Fig. 2(c) for $N = 0.4$. The local Stanton numbers are substantially diminished at a lower heating level ($q_{in}^+ = 0.0015$). Figure 3 is a laminarization map on a plot of the velocity ratio, N , versus the heat flux parameter, q_{in}^+ for $Re = 8500$. It defines the laminarization zone and nonlaminarization zone, i.e., turbulent flow. Bankston (1970) pointed out that the occurrence of the laminarization is evidenced by a substantial reduction of the local Stanton numbers along the flow. Note that the heating level q_{in}^+ in Fig. 3 is in agreement with the criterion of laminarization in the strongly heated pipe without rotation (Ogawa et al., 1982). As the velocity ratio N increases, laminarization takes place even at a lower heating q_{in}^+ whose level does cause the laminarizing flow in the stationary pipe. In other words, an axial rotation of the pipe with high flux heating induces a deterioration in heat transfer performance, although the same rotation level causes no laminarization in the

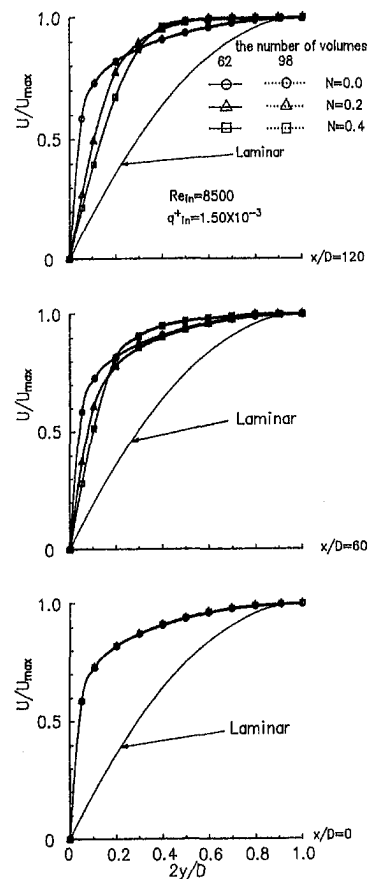


Fig. 4 Effects of velocity ratio N on the distribution of time-averaged streamwise velocity U/U_{max} in an axially rotating pipe at three different axial locations, $x/D = 0, 60,$ and 120 , for $Re_{in} = 8,500$ and $q_{in}^+ = 1.50 \times 10^{-3}$.

axially rotating pipe in the absence of heating. That is, the presence of pipe rotation contributes to the promotion of laminarization of gas flow in the heated pipe.

An attempt is made to explore the effects of pipe rotation on the flow and thermal fields, i.e., turbulent kinetic energy, velocity and temperature profiles, turbulent heat flux and temperature variance. Numerical results are obtained at $q_{in}^+ = 0.0015$ for no laminarization in a stationary pipe. Figure 4 illustrates the effects of the velocity ratio N on the radial distributions of the time-averaged streamwise velocity U/U_{max} at three different axial locations $x/D = 0, 60,$ and 120 . The velocity U is normalized by the maximum value U_{max} at each axial location. The laminar flow profile is superimposed in the figure as a solid line for comparison. There is only a slight change in the velocity profile even if the number of control volumes is set between 62 and 98. Therefore, no appreciable difference appears between the numerical results with different grid spacing. At $N = 0.0$, the velocity gradient at the wall is slightly diminished along the flow. This reduction of the velocity gradient is intensified with an increase in N . The corresponding variation of the turbulent kinetic energy along the flow is illustrated in Fig. 5. Here, the turbulent kinetic energy k is normalized by a square of the wall friction velocity at the onset of heating u_{in}^{*2} . One observes that the turbulent kinetic energy level at $N = 0.2$ is slightly suppressed over the whole tube cross section along the flow in the presence of pipe rotation. The corresponding profile at $x/D = 120$ is similar to that at $N = 1.0$ for the slightly heated swirling flow (Torii and Yang, 1995a). This implies that the reduction in the turbulent kinetic energy is caused by the slight pipe rotation if the flow is heated with high heat flux, whose level induces no laminarization in the stationary pipe. The reduction is amplified with an increase in the rotation speed, in accordance with

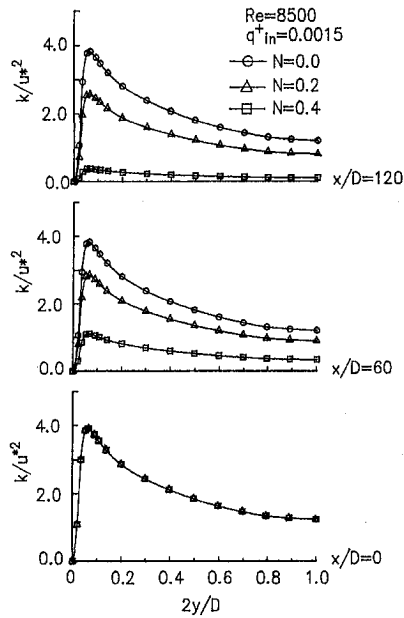


Fig. 5 Effects of velocity ratio N on the distribution of turbulent kinetic energy k/u_*^2 in an axially rotating pipe at three different axial locations, $x/D = 0, 60,$ and 120 , for $Re_m = 8500$ and $q_{in}^+ = 0.015$.

the variation of the streamwise velocity distribution in Fig. 4, because the production of the turbulent kinetic energy is affected by the streamwise velocity gradient as shown in Eq. (9). For

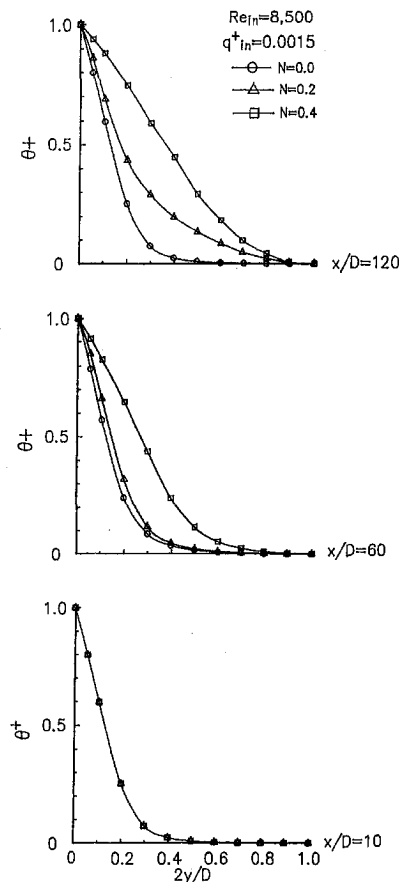


Fig. 6 Effects of velocity ratio N on the distribution of time-averaged temperature in an axially rotating pipe with three different axial locations, $x/D = 10, 60,$ and 120 , for $Re_m = 8500$ and $q_{in}^+ = 0.0015$.

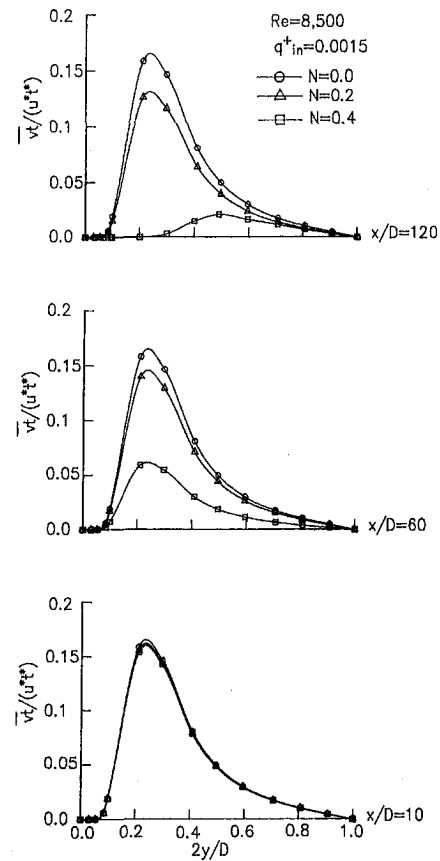


Fig. 7 Effects of velocity ratio N on the distribution of turbulent heat flux $\overline{v_t}/(u_*t^*)$ in an axially rotating pipe at three different axial locations, $x/D = 10, 60,$ and 120 , for $Re_m = 8500$ and $q_{in}^+ = 0.0015$.

reference, a substantial attenuation in the turbulent kinetic energy at $N = 0.4$ and $x/D = 120$ as seen in Fig. 5, was larger than that at $N = 2.0$ for the axially rotation pipe flow with lower flux heating (Torii and Yang, 1995a). Note that although the production of the turbulent kinetic energy is also caused by the change in the tangential velocity, there is no effect due to heating, because the tangential velocity is automatically determined by Eq. (15), as mentioned previously. If the tangential velocity is also affected by the acceleration of gas expansion due to heating, its presence yields an attenuation in the turbulent kinetic energy.

Figure 6 depicts the effects of N on the time-averaged temperature profile θ^+ at $x/D = 10, 60,$ and 120 . It is observed that the temperature gradient at the wall slightly decreases along the flow. An increase in the pipe rotation promotes a decrease in the temperature gradient along the flow. Figure 7 illustrates the predicted change in the turbulent heat flux profiles at the three different axial locations. Here, the turbulent heat flux $\overline{v_t}$ is divided by the product of the friction temperature, t^* , and the friction velocity, u^* , at each axial location. A slight change in the turbulent heat flux profile from $N = 0.0$ to 0.2 is seen in the flow direction, while a substantial attenuation occurs from $N = 0.2$ to 0.4 over the whole pipe cross section, in accordance with a variation of the time-averaged temperature distribution, causing a deterioration of heat transfer performance, as seen in Fig. 2. Figure 8 depicts the radial distribution of the temperature variance, $\overline{t^2}$, in the thermal field at the three different axial locations. Here, the temperature variance $\overline{t^2}$ is divided by the square of the friction temperature, t^{*2} , at each axial location. The production of $\overline{t^2}$, at $N = 0.0$ and 0.2 , is slightly suppressed over the whole pipe cross section in the flow direction. In contrast, at $N = 0.4$, the y-directional reduction in $\overline{t^2}$ is significantly intensified at $N = 0.4$, with its peak

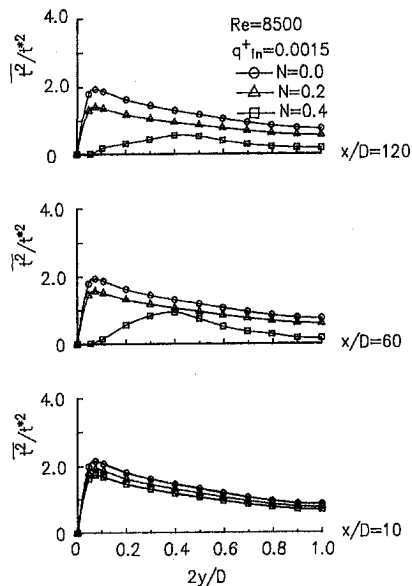


Fig. 8 Effects of velocity ratio N on the distribution of temperature variance $\overline{t^2}/\overline{t^2}$ in an axially rotating pipe at three different axial locations, $x/D = 10, 60,$ and 120 , for $Re_{in} = 8500$ and $q_{in}^+ = 0.0015$.

shifting toward the tube center and attenuated along the flow direction. Since the eddy diffusivity concept (Eq. (11)) is employed to determine the turbulent heat flux, $-c_p \overline{\rho v t}$, in Eq. (5), λ_t is directly related to k , ε , $\overline{t^2}$, and ε_t , as depicted in Eq. (12). Hence, reductions in the turbulent kinetic energy and the temperature variance result in an attenuation of the Stanton number, as shown in Fig. 2.

In summary, under a uniform heat flux heating, the streamwise variations of the turbulent kinetic energy, velocity, and temperature profiles, turbulent heat flux, and temperature variance during laminarization in a rotating pipe are similar to those in a stationary pipe with strong heating and low Reynolds number flow.

Summary

A $\overline{t^2}$ - ε_t heat transfer model and a k - ε turbulence model have been employed to numerically investigate fluid flow and heat transfer in a strongly heated pipe in the presence of the pipe rotation. The study has concluded that,

1 in a lower heat flux case in which no laminarization occurs in a stationary pipe flow, pipe rotation causes a substantial reduction of the local Stanton number. The deterioration of local heat transfer performance is intensified with an increase in the rotational speed. In other words, an increase in tube rotation results in an augmentation in laminarization in a gas flow.

2 when laminarization takes place, the velocity gradient in the vicinity of the tube wall is suppressed along the flow, resulting in a substantial attenuation in the turbulent kinetic energy over the entire tube cross section. In addition, both the temperature variance and the turbulent heat flux are diminished over the whole tube cross section in the flow direction, causing in a decrease in the time-averaged temperature gradient at the wall.

3 consequently, the turbulent heat flux is diminished with a decrease in both the turbulent kinetic energy and the temperature variance over the pipe cross section, resulting in the deterioration of heat transfer performance.

4 reductions in both the velocity and temperature gradients induced by pipe rotation suppress both the turbulent kinetic energy and temperature variance, resulting in an amplification in laminarizing the flow process.

References

- Bankston, C. A., 1970, "The Transition from Turbulent to Laminar Gas Flow in a Heated Pipe," *Trans. ASME Ser. C*, Vol. 92, No. 4, pp. 569–579.
- Coon, C. W. and Perkins, H. C., 1970, "Transition from the Turbulent to the Laminar Regime for Internal Convective Flow with Large Property Variations," *Trans. ASME Ser. C*, Vol. 92, No. 3, pp. 506–512.
- Fujii, S., Akino, N., Hishida, M., Kawamura, H., and Sanokawa, K., 1991, "Numerical Studies on Laminarization of Heated Turbulent Gas Flow in Annular Duct," *J. Atomic Energy Soc. Jpn.*, Vol. 33, No. 12, pp. 1180–1190 (in Japanese).
- Hirai, S., Takagi, T., and Matumoto, M., 1986, "Prediction of the Laminarization Phenomena in Turbulent Swirling Flows," *Trans. JSME*, Vol. 52, No. 476, B, pp. 1608–1616 (in Japanese).
- Kawamura, H., 1979, "Prediction of Strongly Heated Turbulent Flow of Gas in a Circular Tube Using a Two-Equation Model of Turbulence," *Trans. Jpn. Soc. Mech. Eng.*, Vol. 45, No. 395, B, pp. 1038–1046 (in Japanese).
- Kawamura, H. and Mishima, T., 1991, "Numerical Prediction of Turbulent Swirling Flow in a Rotating Pipe by a Two-Equation Model of Turbulence (Fully Developed Swirling Flow)," *Trans. JSME*, Vol. 57, No. 536, B, pp. 1251–1256 (in Japanese).
- Kikuyama, K., Murakami, M., and Nishibori, K., 1983, "Development of Three-Dimensional Turbulent Boundary Layer in an Axially Rotating Pipe," *ASME Journal of Fluids Engineering*, Vol. 105, pp. 154–160.
- McEligot, D. M., Coon, C. M., and Perkins, H. C., 1970, "Relaminarization in Tubes," *J. Heat & Mass Transfer*, Vol. 13, No. 2, pp. 431–433.
- Mori, Y. and Watanabe, K., 1979, "Reduction in Heated Transfer Performance Due to High Heat Flux," *Trans. Jpn. Soc. Mech. Eng.*, Vol. 45, No. 397, B, pp. 1343–1353 (in Japanese).
- Murakami, M. and Kikuyama, K., 1980, "Turbulent Flow in Axially Rotating Pipes," *ASME Journal of Fluids Engineering*, Vol. 102, pp. 97–103.
- Nagano, Y. and Kim, C., 1988, "A Two-Equation Model for Heat Transport in Wall Turbulent Shear Flows," *ASME JOURNAL OF HEAT TRANSFER*, Vol. 110, pp. 583–589.
- Ogawa, M., Kawamura, H., Takizuka, T., and Akino, N., 1982, "Experimental on Laminarization of Strongly Heated Gas Flow in Vertical Circular Tube," *J. Atomic Energy Soc. Jpn.*, Vol. 24, No. 1, pp. 60–67 (in Japanese).
- Patankar, S. V., 1980, *Numerical Heat Transfer and Fluid Flow*, Hemisphere, Washington, DC.
- Perkins, K. R., Schade, K. W., and McEligot, D. M., 1973, "Heated Laminarizing Gas Flow in a Square Duct," *J. Heat and Mass Transfer*, Vol. 16, No. 3, pp. 897–916.
- Propath Group, 1987, "Propath: a Program Package for Thermophysical Property," Version 4.1, (in Japanese).
- Rodi, W., 1982, "Examples of Turbulence Models for Incompressible Flows," *AIAA J.*, Vol. 20, pp. 872–879.
- Torii, S., Shimizu, A., Hasegawa, S., and Higasa, M., 1990, "Laminarization of Strongly Heated Gas Flows in a Circular Tube (Numerical Analysis by Means of a Modified k - ε Model)," *JSME Int. J.*, Ser. II, Vol. 33, No. 33, pp. 538–547.
- Torii, S., Shimizu, A., and Hasegawa, S., 1993, "Numerical Analysis of Laminarizing Tube Flows by Means of a Reynolds Stress Turbulence Model," *Heat Transfer-Japanese Research*, Vol. 22, No. 2, pp. 154–170.
- Torii, S. and Yang, W.-J., 1995a, "Numerical Prediction on Fully Developed Turbulent Swirling Flows in an Axially Rotating Pipe by Means of a Modified k - ε Turbulence Model," *J. Numerical Methods for Heat and Fluid Flow*, Vol. 5, No. 2, pp. 175–183.
- Torii, S., and Yang, W.-J., 1995b, "A Numerical Analysis on Flow and Heat Transfer in the Entrance Region of an Axially Rotating Pipe," *Int. J. Rotating Machinery*, Vol. 2, No. 2, pp. 123–129.
- Torii, S. and Yang, W.-J., 1997, "Laminarization of Turbulent Gas Flows inside a Strongly Heated Tube," *Int. J. Heat Mass Transfer*, Vol. 40, No. 13, pp. 3105–3117.
- Weigand, B., and Beer, H., 1990, "Fluid Flow and Heat Transfer in an Axially Rotating Pipe: The Rotational Entrance," *The Third Int. Symp. on Transport Phenomena, Dynamics and Design of Rotating Machinery*, Vol. 1, pp. 439–454.

Numerical Investigation of Flow Field and Heat Transfer in Cross-Corrugated Ducts

H. Blomerius

C. Hölsken

N. K. Mitra¹

Institut für Thermo- und Fluidodynamik
Ruhr-Universität,
D-44780 Bochum, Germany

Flow field and heat transfer in sine-wave crossed-corrugated ducts have been investigated by numerical solution of the Navier-Stokes and energy equations in the laminar and transitional flow regime between $Re = 170$ and 2000 . The ratio of the corrugation wave length λ^ to amplitude a^* has been varied between 7 and 10 . The angle of the corrugation of the neighboring plates has been kept fixed at 45 deg. Results show that the critical Reynolds number for self-sustained flow oscillations is about 240 . For Reynolds numbers larger than 1000 , the Nusselt number and the friction factor are nearly independent of the dimensionless wavelength. Computational results compare well with available experimental results.*

1 Introduction

Regenerative and recuperative plate heat exchangers consist often of stacked corrugated plates. The orientation of the corrugation between neighbouring plates is nonaligned (Fig. 1). Multitude contact points between the plates lead to high compressive strength of the heat exchangers. The corrugations give structural stability even at low material thickness of the plates and produce highly complex flow structure which determines the thermal performance and the flow loss of the heat exchanger.

The performance of plate heat exchangers with sinusoidal corrugation characterized by the ratio of the wavelength λ and the amplitude a and the angle of inclination of corrugations of neighboring plates has been experimentally investigated by Okada et al. (1972), Focke et al. (1985, 1985), Gaiser et al. (1990, 1994), Ciofalo et al. (1996) and Stasiek et al. (1994), and Muley and Manglik (1997), who called the geometry chevron plates. The geometrical parameters were varied in the ranges of $3.5 < \lambda^*/a^* < 14.25$ and $0 < \varphi < 90$ deg. Stasiek et al. (1996) reported also numerical investigations for periodic boundary conditions and entry flows. They used the commercial code Flow3D to solve steady laminar and turbulent flow equations in the Reynolds number range between $Re_{dh} = 1000$ and $10,000$. Here Re_{dh} is based on the hydraulic diameter $dh^* = 4V^*/A^*$ where V^* and A^* are the volume and the surface, respectively. They computed laminar flow for Re_{dh} up to 3000 and for turbulent flows they used different turbulence models and a large eddy simulation and compared their results of local and overall heat transfer with experimental data obtained from thermochromic liquid crystal measurements. The best agreement with experimental local Nusselt numbers was given by the large eddy simulation for $Re_{dh} \geq 4000$ and by the low Reynolds number $k-\epsilon$ model at lower Re . They used a coarse mesh of 32^3 grids for all wave lengths λ^*/a^* and for all flow models except for the standard $k-\epsilon$ model for which they used 24^3 grids. The influence of the grid width and grid nonorthogonality were not ascertained.

Both experimental and numerical investigations show that heat transfer and pressure drop depend strongly on the dimensionless corrugation wavelength λ^*/a^* and on the inclination angle φ . The results can be summarized as follows:

Smaller λ^*/a^* leads to higher heat transfer and pressure loss. At $\varphi = 90$ deg heat transfer reaches nearly the same minimum for all λ^*/a^* . The maximum heat transfer and pressure loss are obtained at about the same φ . For $\varphi > 50$ deg the Nu distributions for different λ^*/a^* tend to merge together. Numerical results of Ciofalo et al. (1996) agree qualitatively with experiments of Focke et al. (1985) and Gaiser (1990), but show quantitative deviation of 40 percent and 25 percent in friction factor and Nusselt number respectively. Muley and Manglik (1997) reported experimental Nu and f in a heat exchanger consisting of mixed chevron plates with $\varphi = 30$ deg and 60 deg in the Reynolds number range of $2-6000$ and Pr range of $2.4-4.5$ and $130-220$. They found transition at $Re \approx 500$ and the Nu is proportional to $Re^{1/2}$ and $Re^{0.76}$ in laminar and turbulent regimes, respectively.

For small inclination angles ($\varphi < 30$ deg) the fluid primarily follows the main stream direction in zig-zag patterns and that for larger angles ($\varphi > 60$ deg) the fluid follows along the furrows between the corrugations of the plates. At $\varphi \approx 45$ deg the flow structure is more complex since both types of fluid trajectories are equally prominent (see Fig. 2). Focke et al. (1985) identified $\varphi = 45$ deg as the inclination angle which produces the largest driving force that generates swirl in the flow in the furrows. The angle $\varphi = 45$ deg is interesting for cross-flow plate heat exchangers since this angle guarantees the same flow patterns for both fluids.

Up to now no investigation of the flow structure evolution as a function of Reynolds number has been performed. Furthermore, the effect of flow oscillation and the transition to turbulence on heat transfer is unknown. This requires knowledge of the complete time dependent flow and temperature fields.

The aim of this work is to examine numerically flow structure and its effect on heat transfer in cross-corrugated ducts at an inclination angle of $\varphi = 45$ deg. Furthermore parametric investigations in order to shed light on the transition of the flow in dependence of the Reynolds number and the influence of the unsteady and transitional flow structure on the heat transfer and pressure loss have also been carried out.

The Reynolds number based on the hydraulic diameter Re_{dh} is

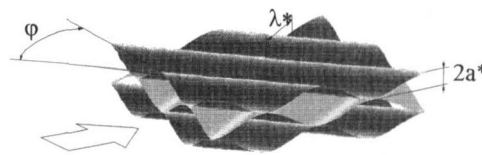


Fig. 1 Cross-corrugated plates for heat exchangers. φ : inclination angle; λ^* : wavelength of corrugation; a^* : amplitude of corrugation.

¹To whom correspondence should be addressed. e-mail: mitra@vtp.ruhr-uni-bochum.de.

Contributed by the Heat Transfer Division for publication in the JOURNAL OF HEAT TRANSFER. Manuscript received by the Heat Transfer Division, June 4, 1997; revision received, Aug. 27, 1998. Keywords: Flow Instability, Flow Separation, Forced Convection, Heat Exchangers, Numerical Methods. Associate Technical Editor: J.-C. Han.

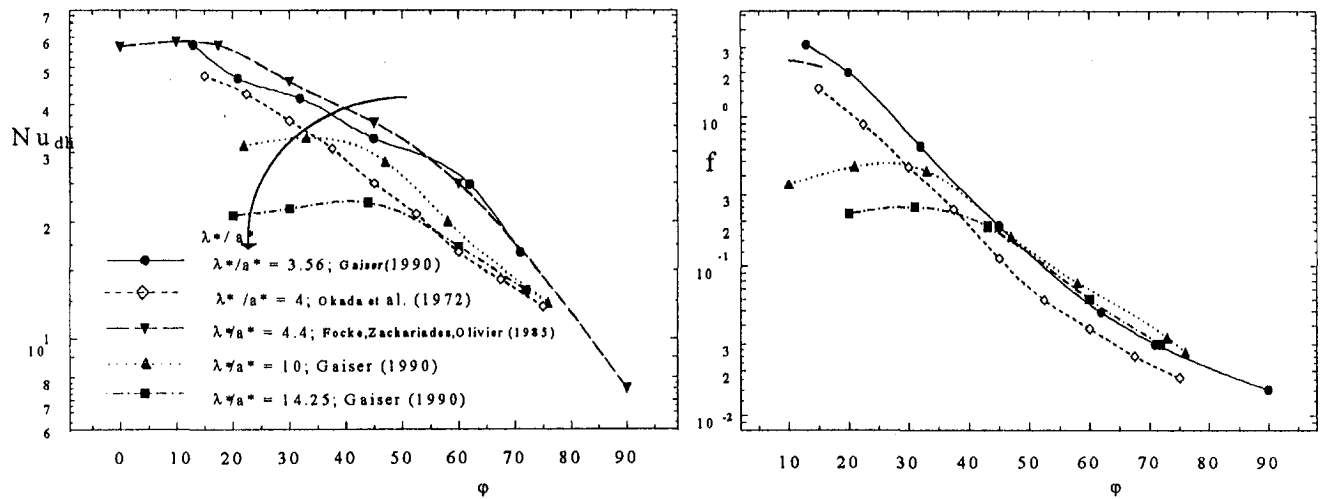


Fig. 2 Experimental and numerical data for Nusselt numbers and friction factors of various authors at $Re_{dh} = 2000$. Solid symbols: experimental data; empty symbols: numerical data.

varied from 150 to 2000. Two wavelengths $\lambda^*/a^* = 7$ ($dh^*/H^* = 1.697$) and $\lambda^*/a^* = 9$ ($dh^*/H^* = 1.797$) are examined since these wave lengths are typical in application (see Gaiser, 1990). An investigation for $\lambda^*/a^* = 10$ ($dh^*/H^* = 1.83$) and $Re_{dh} = 2000$ has been performed in order to validate the numerical results against experiments of Gaiser (1990). The flow medium is air with $Pr = 0.7$.

2 Computational Model and Method of Solution

The flow in the corrugated duct with identical repetitive elements is geometry dominated and will be eventually periodically fully developed (see Patanker et al., 1977). A periodical element of the duct, shown in Fig. 3, is chosen as the computational domain. For this element periodic boundary conditions are assumed at the

Nomenclature

A^* = surface area (m^2)	Greek Letters	$Re_H = \bar{u}^*H^*/\nu^*$ = Reynolds number based on channel height H
a^* = corrugation amplitude (m)	β_j^i = co-factor of $\partial x_i/\partial \xi_j$ in the transformation matrix	Pr = Prandtl number
B^* = channel width (m)	φ = angle between corrugation and main stream direction	Superscript
dh^* = hydraulic diameter (m)	ξ_1, ξ_2, ξ_3 = curvilinear coordinates	* = dimensional quantity
f^* = frequency (s^{-1})	λ^* = wavelength of corrugation (m)	- = averaged
h^* = coefficient for convective heat transfer ($Wm^{-2}K$)	θ = dimensionless temperature	Subscript
H^* = average channel height (m)	γ = ratio of mass flow in main and lateral directions	0 = first cell
J = Jacobi determinant of the transformation matrix	ν^* = kinematic viscosity ($m^2 s^{-1}$)	B = bulk
k^* = thermal conductivity ($Wm^{-1}K^{-1}$)	ρ^* = density ($kg m^{-3}$)	i, j, k, m = indices of vector/matrix components
L^* = channel length (m)	Dimensionless Parameters	in = inlet
p^* = pressure (Nm^{-2})	$f = (\Delta p^*/(\rho^*l^*2\bar{u}^{*2}))(dh^*/4L^*)$ = apparent friction factor	l = low
T^* = temperature (K)	$G = (Nu/Nu_0)/(ff_0)^{1/3}$ = goodness factor	le = left
t^* = time (s)	$Nu_{dh} = h^*dh^*/k^*$ = Nusselt number	out = outlet
\bar{u}^* = span averaged main velocity (ms^{-1})	$S = f^*H^*/\bar{u}^*$ = Strouhal number	per = periodic
\mathbf{v}^* = velocity vector	$Re_{dh} = \bar{u}^*dh^*/\nu^*$ = Reynolds number based on the hydraulic diameter	P = periodic length
V^* = Volume (m^3)		ri = right
u^*, v^*, w^* = velocity components in the x, y (ms^{-1}) and z -direction, respectively		ref = reference
x = vector of Cartesian components		u = up
(x, y, z) = Cartesian coordinates		W = wall
x_1, x_2, x_3 = Cartesian coordinates		

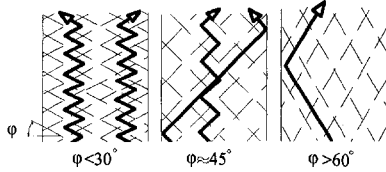


Fig. 3 Flow patterns in cross-corrugated structures for different angles of inclination

entrance and exit and at the sides. The length and the breadth of the computational domain are $L^* = B^* = 2\lambda^* \sin 45^\circ$.

The dimensionless constant property conservation equations on a generalized curvilinear coordinate system are

Continuity:

$$\frac{\partial U_i}{\partial \xi_i} = 0; \quad (1)$$

Navier-Stokes:

$$\frac{\partial u_k}{\partial t} + \frac{\partial}{\partial \xi_i} \left\{ U_i u_k - \frac{1}{J \text{Re}_H} \left(B_j^i \frac{\partial u_k}{\partial \xi_j} + \beta_j^i \omega_k^j \right) \right\} + \frac{\partial}{\partial \xi_j} (\beta_j^i p) = 0; \quad (2)$$

Energy:

$$\frac{\partial T}{\partial t} + \frac{\partial}{\partial \xi_i} \left(U_i T - \frac{1}{J \text{Re}_H \text{Pr}} B_j^i \frac{\partial T}{\partial \xi_j} \right) = 0; \quad (3)$$

with

$$U_i = u_j \beta_j^i; \quad B_j^i = \beta_m^i \beta_m^j; \quad \omega_k^j = \frac{\partial u_j}{\partial \xi_m} \beta_k^m; \quad i, j, k, m = 1, 2, 3.$$

The Einstein summation convention is adopted. ξ_1, ξ_2, ξ_3 are curvilinear coordinates and u_1, u_2, u_3 are the Cartesian velocity components. β_j^i are co-factors of $\partial x_i / \partial \xi_j$ in the Jacobian J .

The constant density fluid model is exact for liquids and approximate for gas flows. The cross-sectional flow area can change by 100 percent, although for the case of larger area, the fluid can move in lateral direction. In typical plate heat exchanger applications the velocity is small (≤ 3 m/s). Hence, for gas flows, the effect of velocity on the gas density is negligible. The effect of temperature on density depends on the temperature range of operation and can be neglected if the temperature change is less than ten percent.

All lengths are made dimensionless by the channel height $H^* = 2a^*$ (Fig. 3) and the velocities by the mean channel velocity. The

temperature is made dimensionless by the bulk temperature of the inlet $T_{b,in}^*$ and a periodic temperature Θ is defined with the constant wall temperature and the bulk temperature, respectively.

$$x_i = \frac{x_i^*}{H^*} \quad u_i = \frac{u_i^*}{\bar{u}^*} \quad T = \frac{T^*}{T_{b,in}^*} \quad p = \frac{p^* - p_{ref}^*}{\rho^* \bar{u}^{*2}} \quad t = \frac{t^* \bar{u}^*}{H^*}$$

$$\Theta = \frac{T - T_w}{T_b - T_w}$$

The pressure is split into the pressure gradient β which can be related to f and into the periodic pressure p_{per} .

$$p(\dot{x}, t) = -\beta(t)x_1 + p_{per}(\dot{x}, t) \quad (4)$$

The pressure gradient β is determined during computation from the mass conservation.

The following boundary conditions are used at the inlet and exit

$$\phi_{in} = \phi(\xi_{1,0}, \xi_2, \xi_3, t) = \phi(\xi_{1,0} + L_p, \xi_2, \xi_3, t) = \phi_{out}$$

$$\frac{\partial \phi(\xi_{1,0})}{\partial \xi_i} = \frac{\partial \phi(\xi_{1,0} + L_p)}{\partial \xi_i} \quad (5)$$

and on the lateral boundaries

$$\phi_{ri} = \phi(\xi_1, \xi_{2,0}, \xi_3, t) = \phi(\xi_1, \xi_{2,0} + B_p, \xi_3, t) = \phi_{le}$$

$$\frac{\partial \phi(\xi_{2,0})}{\partial \xi_i} = \frac{\partial \phi(\xi_{2,0} + B_p)}{\partial \xi_i} \quad (6)$$

where $\phi = \{u_i, p_{per}, \Theta\}$. On the solid walls we used

$$\phi(\xi_{3,1}) = \phi(\xi_{3,n}) = 0 \quad (7)$$

for $\phi = \{u_i, \Theta\}$.

The gradient conditions in Eqs. (5) and (6) are not mandatory but allow faster convergence.

The nondimensional length and breadth of the computational domain are $L = B = \lambda^* / \sqrt{2} a^*$. An algebraic grid-generation technique was employed to generate boundary conforming grids for three-dimensional ducts. In subsequent flow computations no computational problem was confronted because of the stiffness of the algebraically grids, so further smoothing by an elliptic grid generation technique is avoided.

First, all grid point locations on the top and the bottom wall of the duct were selected. The topography of the corrugated surface is given by

$$x_3(x_1, x_2) = a \sin(b(x_1 \pm x_2)). \quad (8)$$

In the interior of the domain the grid points are interpolated along straight lines connecting the corresponding top and bottom grid points (Fig. 4(a)). In order to avoid grid cells with zero thickness

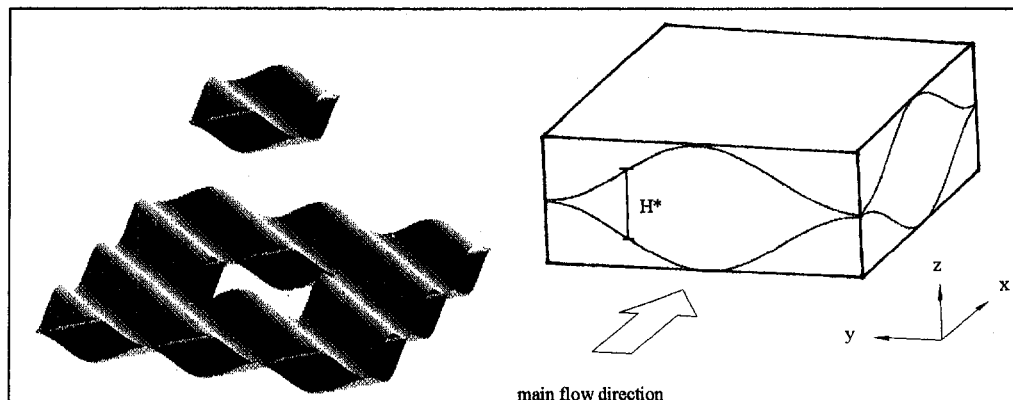


Fig. 4 A characteristic element of the heat exchanger is chosen for the numerical modeling

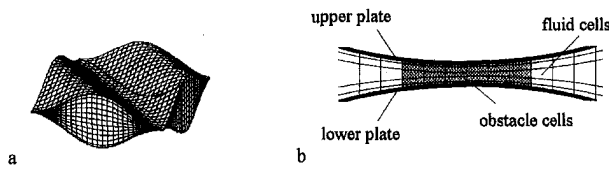


Fig. 5 Grid points in the interior of the computational domain are interpolated along straight lines (a); treatment of the contact points between the upper and lower plates (b)

in the z -direction the upper and the lower corrugation plates are not allowed to touch each other. To realize the contact points between the upper and the lower plates the small region around the contact points (see Fig. 4(b)) is described by obstacle cells. Velocities in these cells are taken equal to zero and the temperature is set equal to the plate temperature. This geometrical modeling brings slight change in flow physics.

The basic equations have been solved by the time-marching pressure-based finite volume numerical code FIVO, developed by the group of the senior author (see Kost et al. (1992) and Grosse-Gorgemann (1995). FIVO uses SIMPLEX (see van Doormaal and

Raithby, 1984), for pressure correction. The code corresponds to the direct simulation of Navier-Stokes equations without turbulence model. Following a deferred-correction approach, the convective fluxes I_c are split into an implicit part, expressed through the first-order accurate upwind difference scheme (UD) and an explicit part containing the difference between the second order accurate central differencing scheme (CD) and the first-order upwind approximations.

$$I_c = I_c^{UD} + \delta(I_c^{CD} - I_c^{UD}) \quad (9)$$

The factor δ was chosen to be 0.95. The diffusive terms are approximated by central differences. First-order forward time discretization was used to approximate the time gradients. FIVO is for transition studies not completely appropriate. However, using small time steps one can extract good quantitative results. The resulting set of algebraic equations was solved using the SIP-algorithm of Stone (1968). Depending on λ^*/a^* , 80,000 to 150,000 grid points were used to discretize the computational domain. Time-marching calculations were stopped when either a steady or a periodic flow was found, or in case of aperiodic solutions when average values of Nusselt number and friction factor became approximately constant.

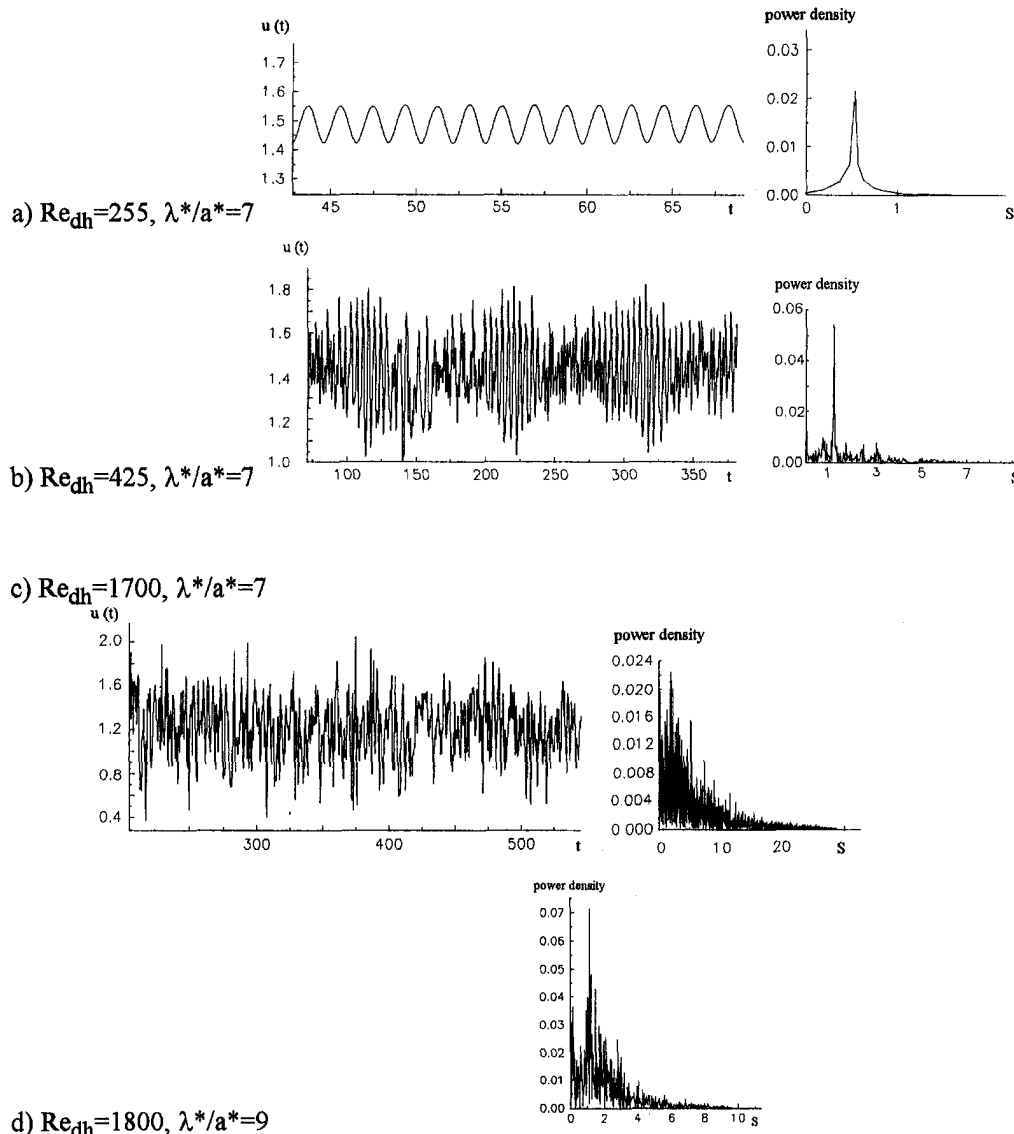


Fig. 6 Time dependency of streamwise velocity (left side) and frequency spectrum (right side). Position of the reference point: $x^*/H^* = 4$, $y^*/H^* = 4$, $z^*/H^* = 0.5$.

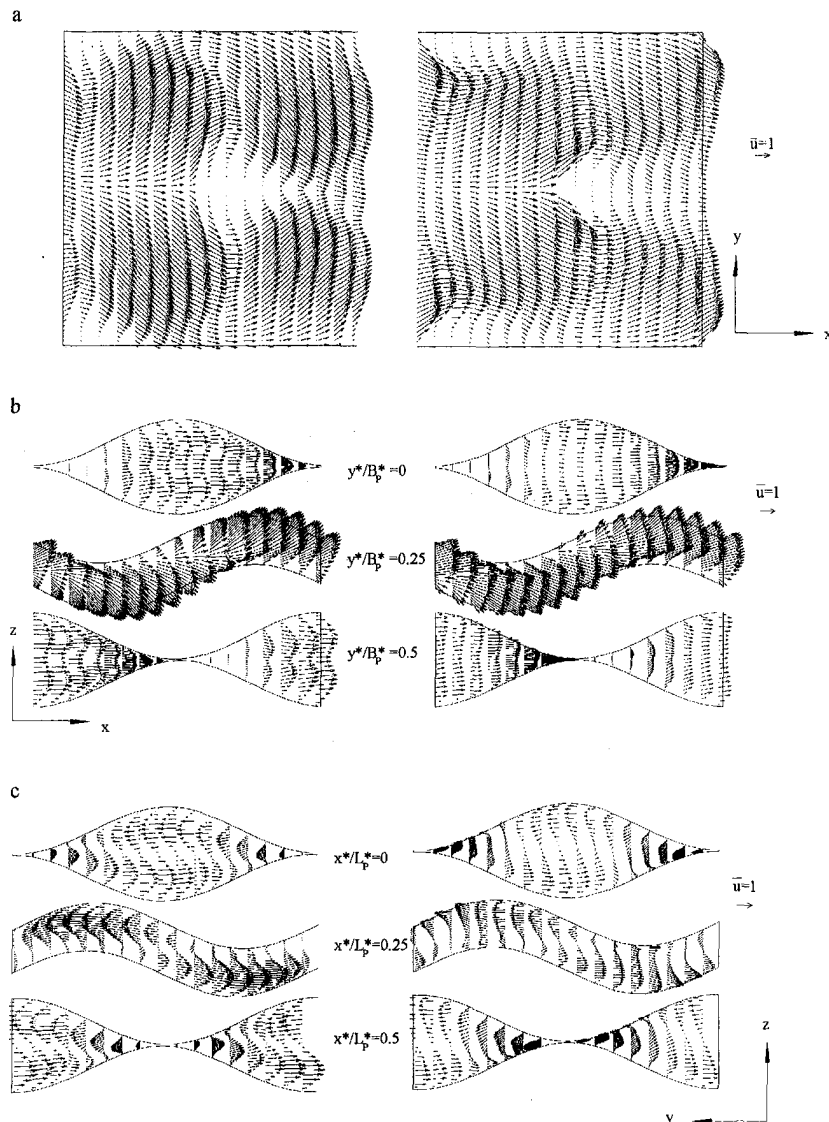


Fig. 7 Velocity vectors for $\lambda^*/a^* = 9$; $Re_{dh} = 180$ (left side) and $Re_{dh} = 1800$, time averaged (right side). (a) Midplane ($z = H$), (b) streamwise velocity, and (c) secondary velocity.

Three equidistant set of grids (0.1, 0.05, and 0.025) in the flow and spanwise directions and 0.05, 0.025, and 0.0125 in the normal direction have been tried to determine the grid dependence of the results. From the extrapolated grid-independent result the maximum deviation (for the coarse grid) of the average Nu and f were 1.4 percent and 0.35 percent for $Re_{dh} = 200$ and 10.2 percent and 6.9 percent for $Re_{dh} = 1500$, respectively. We chose the coarse grid for further computations. The time step Δt could be chosen from the stability condition. We used $\Delta t = 0.005$ which is roughly 25 percent of the Δt given by the stability condition. Strouhal numbers computed with $\Delta t = 0.005$ and $\Delta t = 0.001$ for a periodic flow case showed negligible (<3 percent difference). All computations were performed on a IBM RS 6000 3BT workstation. CPU-times of about 15 hours for a steady-state solution and up to 350 hours for periodic or aperiodic flows were required.

3 Results and Discussion

3.1 Flow and Temperature Field. Steady flow solutions were obtained for $Re_{dh} = 170$, $\lambda^*/a^* = 7$ ($dh^*/H^* = 1.697$) and $Re_{dh} = 180$, $\lambda^*/a^* = 9$ ($dh^*/H^* = 1.797$). With increasing Re the solutions bifurcated from steady to time-periodic self-sustained oscillatory flows. The exact Reynolds number of transition from steady to periodic flow was not determined due to the

requirement of large computational times. However, it was found that this transition Re_{dh} lies between 170 and 255 for $\lambda^*/a^* = 7$ and between 180 and 270 for $\lambda^*/a^* = 9$. The time series of the u -component at a point ($x^*/H^* = 4$, $y^*/H^* = 4$, $z^*/H^* = 0.5$) in the computational domain for $\lambda^*/a^* = 7$ and $Re_{dh} = 255$, 425, and 1700, were recorded and Fourier analyzed. For $Re_{dh} = 255$ a periodic flow with a single dominant frequency with a Strouhal number $S = 0.5$ appeared. For $Re_{dh} = 425$ the dominant Strouhal number was 1.3. For $Re_{dh} = 1700$ no dominant Strouhal number could be detected and the flow was aperiodic. With increasing Re the amplitudes of fluctuations also grew. At $Re_{dh} = 1700$ the flow could be considered turbulent.

Comparing the time-dependent behavior of the two wavelengths with various Reynolds numbers we found that the transition to turbulence for the larger wavelengths occurred at higher Reynolds numbers. Even at $Re_{dh} = 1800$ ($\lambda^*/a^* = 9$) a few dominating frequencies can be detected and the range of the frequency spectrum is smaller than that of the geometry with the wavelength $\lambda^*/a^* = 7$. We should mention that the grid-independent transition Re may be slightly different from our results which, however, show the correct trend.

The plots of streamwise and secondary velocities (see Fig. 5 for $Re_{dh} = 1800$) indicated considerably different flow structures for

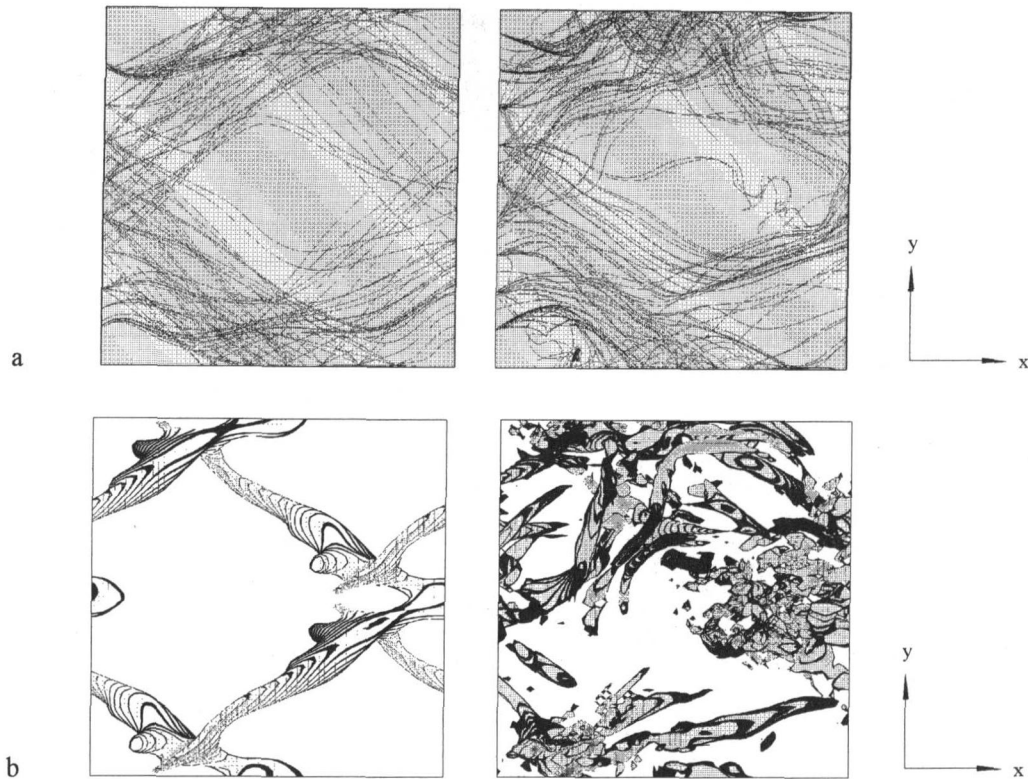


Fig. 8 $\lambda^*/a^* = 9$; $\text{Re}_{dh} = 180$ (left) and $\text{Re}_{dh} = 1800$ (right). (a) Instantaneous pathlines, (b) shaded areas show zones of large vorticity.

the two Reynolds numbers 180 and 1800. However, the secondary and streamwise velocities were of the same order of magnitude for both Re. The plot of secondary velocities for $\text{Re}_{dh} = 180$ at $x^*/L_p^* = 0$ showed a stable shear layer in the midplane of the duct between the two streams following the furrows. In contrast an extensive vortex led to considerable mixing between these streams at $\text{Re}_{dh} = 1800$. The maximum velocities were nearly twice the average streamwise velocity.

Three-dimensional pathline maps (not shown here) show different flow phenomena. The major part of the flow followed the valleys of corrugations of upper and lower walls at 45 deg to the main flow direction while a minor part of the flow followed the main flow direction, crossing the crests of the corrugations. Comparing the two pathline maps for $\text{Re}_{dh} = 180$ and $\text{Re}_{dh} = 1800$ we noticed that at the higher Reynolds number interactions between the streams in the valleys led to stronger mixing of the flow.

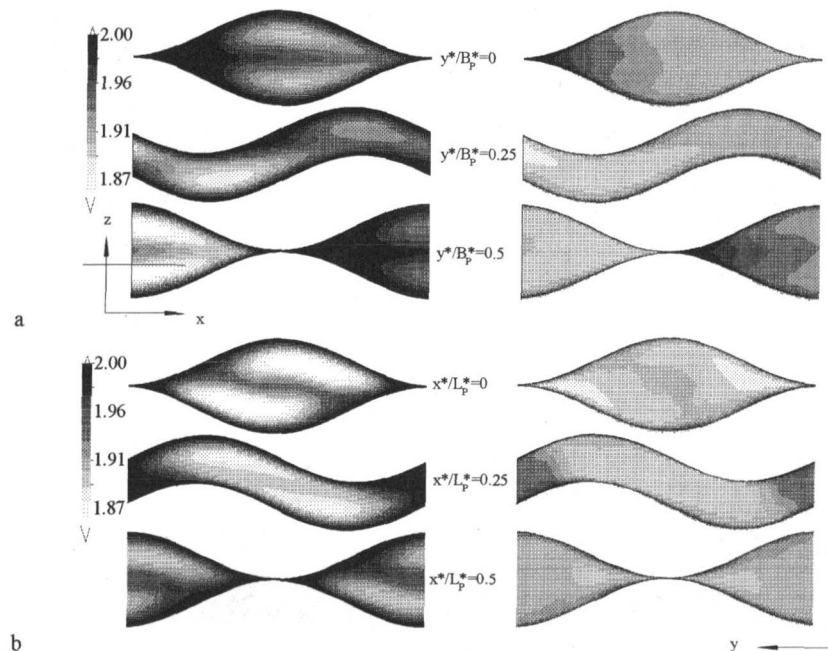


Fig. 9 Temperature fields, $\lambda^*/a^* = 9$; $\text{Re}_{dh} = 180$ (left side) and $\text{Re}_{dh} = 1800$, time averaged (right side). (a) Section at $y = \text{constant}$ and (b) section at $x = \text{constant}$.

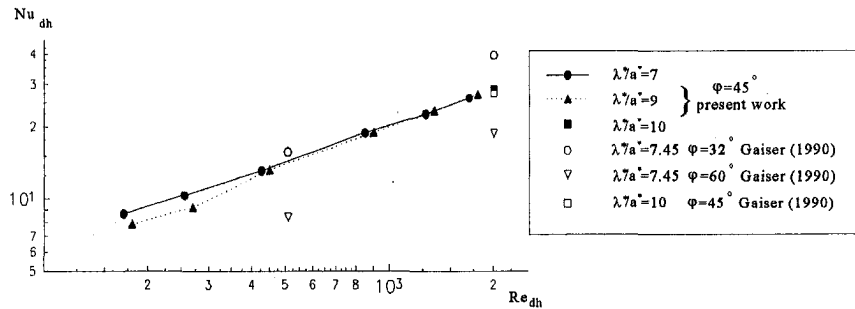


Fig. 10 Overall Nusselt numbers over Reynolds number

To investigate whether the ratio of the mass flux fraction in the main flow direction to the lateral direction depends on the Re we computed γ ,

$$\gamma = \frac{\int_{A_{in}} u_1(\xi_{1,0}, \xi_2, \xi_3) dA}{\int_{A_{side}} |u_2(\xi_1, \xi_{2,0}, \xi_3)| dA}, \quad (10)$$

and found that γ is independent of Re and but depends strongly on λ^*/a^* changing from 1.20 for $\lambda^*/a^* = 7$ to 1.45 for $\lambda^*/a^* = 9$.

At $Re_{dh} = 180$ we noticed a swirling motion in the furrows induced by perpendicular flow direction in the furrows of the upper and the lower corrugation. In contrast to the instantaneous disordered structures at $Re_{dh} = 1800$ the distribution at $Re_{dh} = 180$ appeared quite orderly.

At $Re_{dh} = 180$ the temperature field was found sharply split into two regions, divided by a stable shear layer. Only little mixing occurred between the flows in the opposite furrows of the corrugations. At $Re_{dh} = 1800$ (see Fig. 6) turbulent interactions of the flows in the opposite furrows led to a more homogenous temperature distribution over the whole cross section. The fluid temperature was found to increase while passing through the duct. In the wake region behind the contact points the fluid had nearly the same temperature as the wall. This wake region was much more extended for $Re_{dh} = 180$ because of the poor mixing of the fluid and consequent low heat transfer in this region.

3.2 Heat Transfer and Flow Loss. Heat transfer and flow loss are characterized by the Nusselt number

$$Nu = \left. \frac{\partial \Theta}{\partial \xi_2} \right|_{\xi_2=0} \frac{dh^*}{2a^*} \quad (11)$$

and the apparent friction factor, respectively,

$$f = \beta \frac{dh^*}{2L^*}. \quad (12)$$

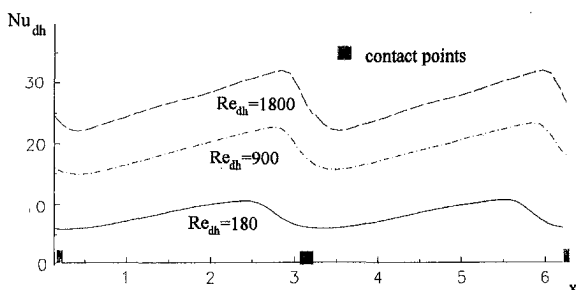


Fig. 11 Spanwise-averaged Nusselt number distribution. $\lambda^*/a^* = 9$.

The Nu was also averaged on the surface.

Figure 7 shows the average Nusselt number as a function of Reynolds number for different λ^*/a^* . Experimental results of Gaiser (1990) have also been plotted for comparison. The Nusselt number increases with increasing Reynolds number in the range $0 \leq Re_{dh} \leq 2000$. For $Re_{dh} > 500$ the influence of the wavelength on Nusselt number can be neglected. At lower Reynolds numbers the Nusselt numbers for the larger wavelength are lower. This can be attributed to the delay in transition to turbulence for the larger wavelength compared with the shorter wavelength. The computations for $\lambda^*/a^* = 10$ and Reynolds number of 2000 show agreement within five percent with the experiments of Gaiser (1990) for $\phi \approx 45$ deg.

The spanwise averaged Nusselt numbers for different Reynolds numbers are shown in Fig. 8. Obviously the heat transfer upstream and downstream of the contact points dominates the Nusselt number distribution. The periodic Nusselt numbers reach maximum values shortly upstream of the contact points. These maxima are shifted slightly downstream with increasing Reynolds numbers. The difference between maximum and minimum values also increases with the Reynolds number.

Figure 9 shows the time-average apparent friction factor against Reynolds number. The difference between friction factors of the two wavelengths vanishes like the overall Nusselt number at higher Reynolds numbers. The computed friction factor for $\lambda^*/a^* = 10$ at $Re_{dh} = 2000$ deviates from measurements of Gaiser (1990) by about eight percent. The measured Nu for mixed chevron plates ($\beta = 30$ deg/60 deg) by Muley and Manglik (1997) are 17 at $Re_{dh} = 1000$ and 8.4 at $Re_{dh} = 400$ compared to our computations of 19, 8, and 12. The corresponding f at $Re_{dh} = 1000$ is 0.45, compared to ours at 0.25. The difference is caused by the geometry. The trend of larger Nu and smaller f with $\beta = 45$ deg/45 deg, than with $\beta = 30$ deg/60 deg, is correct (see the reference cited by Muley and Manglik, 1997).

Figure 10 depicts the goodness factor $G = (Nu/Nu_0)/(ff_0)^{1/3}$ where the subscript 0 stands for the plane channel value. G is independent of λ^*/a^* for $Re_{dh} \geq 500$, and it monotonically increases and becomes larger than 1 for $Re_{dh} \geq 1000$.

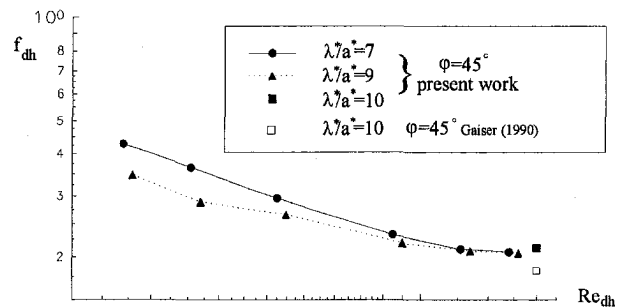


Fig. 12 Time-averaged friction factors

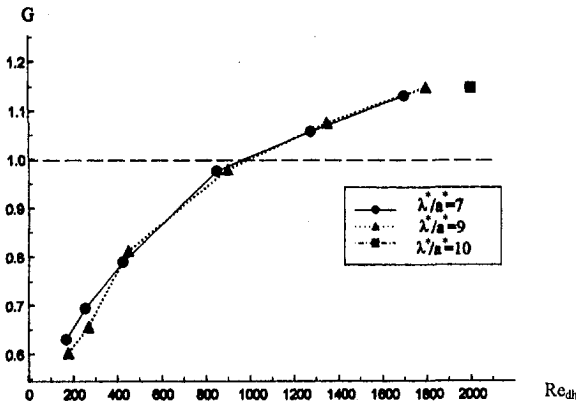


Fig. 13 Goodness factor G over Reynolds number for different λ^*/a^*

4 Conclusions

Numerical simulations of flow in cross-corrugated 45-degree-oriented ducts show that self-sustained oscillations occur in the range of $Re_{dh} = 170$ to $Re_{dh} = 270$ for $\lambda^*/a^* = 7$ and $\lambda^*/a^* = 9$. With increasing Reynolds number the flow tends to become chaotic. The flow structure changes dramatically with increasing Reynolds number. The strong mixing effects between the fluid streams in opposite furrows of the duct at high Reynolds numbers cause an improvement of heat transfer and an increase of pressure drop. Transition to turbulence takes place at a smaller Re for the shorter wavelength. Comparisons of numerical results with available experimental data show good agreement. The goodness factor becomes larger than 1 at higher (>1000) Reynolds numbers.

Acknowledgments

We thank Prof. M. Fiebig for his interest in this work and the Associate Editor, Prof. J. C. Han, for the patience and his excellent suggestions in restructuring this paper.

References

- Ciofalo, M., Stasiek, J., and Collins, M. W., 1996, "Investigation of Flow and Heat Transfer in Corrugated Passages—II. Numerical Simulations," *Int. J. Heat Mass Transfer*, Vol. 4, pp. 165–192.
- Focke, W. W., Zachariades, J., and Olivier, I., 1985, "The Effect of the Corrugation Inclination Angle on Thermohydraulic Performance of Plate Heat Exchangers," *Int. J. Heat Mass Transfer*, Vol. 28, No. 8, pp. 1469–1479.
- Focke, W. W., 1985, "Asymmetrically Corrugated Plate Heat Exchangers," *Int. Comm. Heat Mass Transfer*, Vol. 12, pp. 67–77.
- Gaiser, G., 1990, "Strömungs- und Transportvorgänge in gewellten Strukturen." Inst. für chem. Verfahrenstechnik der Universität Stuttgart, Dr. Ing. dissertation.
- Gaiser, G., and Kotke, V., 1990, "Effects of Corrugation Parameters on Local and Integral Heat Transfer in Plate Heat Exchangers and Regenerators," *Proc. 9th Int. Heat Transfer Conference*, Jerusalem, Vol. 5, pp. 85–90.
- Gaiser, G., 1994, "Effects of Local Heat and Mass Transfer on the Design of Corrugated Catalytic Structures," *Proc. 10th Int. Transfer Conference*, Brighton, Vol. 5, pp. 261–266.
- Grosse-Gorgemann, A., 1995, "Numerische Untersuchungen der laminaren oszillierenden Strömung und des Wärmeübergangs in Kanälen mit rippenförmigen Einbauten." Dr.-Ing. Diss., Ruhr-Universität Bochum.
- Kost, A., Bai, L., Mitra, N. K., and Fiebig, M., 1992, "Calculation Procedure for Unsteady Incompressible 3-D-Flows in Arbitrary Shaped Domains," *Notes of Numerical Fluid Mechanics*, Vol. 35, Hirschel, ed., Vieweg Verlag, pp. 269–278.
- Muley, A., and Manglik, R. M., 1997, "Enhanced Heat Transfer Characteristics of Single-Phase Flows in a Plate Heat Exchanger With Mixed Chevron Plates," *J. Enhanced Heat Transfer*, Vol. 4, pp. 187–201.
- Patancker, S. V., Liu, C. H., and Sparrow, E. M., 1977, "Fully Developed Flow and Heat Transfer in Ducts Having Streamwise Periodic Variations of Cross-Sectional Area," *ASME JOURNAL OF HEAT TRANSFER*, Vol. 99, pp. 180–186.
- Okada, K., Ono, M., Tomimura, T., Okuma, T., Konno, H., Ohtani, S., 1972, "Design and Heat Transfer Characteristics of New Plate Heat Exchangers," *Heat Transfer-Japanese Research*, Vol. 1, No. 1.
- Stasiek, J., Ciofalo, M., Smith, I. K., and Collins, M. W., 1994, "Experimental and Analytical Studies of Fluid Flow and Heat Transfer Across Corrugated-Undulated Heat Exchanger Surfaces," *Proc. 10th Int. Heat Transfer Conference*, Brighton, Vol. 6, pp. 103–109.
- Stasiek, J., Collins, M. W., Ciofalo, M., and Chew, P. E., 1996, "Investigation of Flow and Heat Transfer in Corrugated Passages—I. Experimental Results," *Int. J. Heat Mass Transfer*, Vol. 39, No. 1, pp. 149–192.
- Stone, H. L., 1968, "Iterative Solution of Implicit Approximations of Multidimensional Partial Differential Equations," *SIAM J. Numerical Analysis* 5, pp. 530–558.
- Van Doormaal, J. P., and Raithby, G. D., 1984, "Enhancement of the SIMPLE-Method for Predicting Incompressible Fluid Flows," *Numerical Heat Transfer*, Vol. 7, pp. 147–163.

Turbulent Heat Transport in a Perturbed Channel Flow

C. U. Buice¹

J. K. Eaton
Fellow ASME

Department of Mechanical Engineering,
Stanford University,
Stanford, CA 94305

The recovering boundary layer downstream of a separation bubble is known to have a highly perturbed turbulence structure which creates difficulty for turbulence models. The present experiment addressed the effect of this perturbed structure on turbulent heat transport. The turbulent diffusion of heat downstream of a heated wire was measured in a perturbed channel flow and compared to that in a simple, fully developed channel flow. The turbulent diffusivity of heat was found to be more than 20 times larger in the perturbed flow. The turbulent Prandtl number increased to 1.7, showing that the turbulent eddy viscosity was affected even more strongly than the eddy thermal diffusivity. This result corroborates previous work showing that boundary layer disturbances generally have a stronger effect on the eddy viscosity, rendering prescribed turbulent Prandtl number models ineffective in perturbed flows.

Introduction

Perturbed turbulent boundary layers are wall-bounded shear layers which have recently undergone a change in boundary condition such as the wall roughness, pressure gradient, or wall curvature. The turbulence statistics and eddy structure are not in equilibrium with the mean flow in perturbed boundary layers. That is, the turbulence properties are different than they would be if the same mean flow profile was maintained for an extended distance. An important subclass of perturbed boundary layers is the recovery region downstream of a separation zone where the turbulence remains out of equilibrium with the mean flow for at least 50 boundary layer thicknesses downstream of reattachment (Bradshaw and Wong, 1972). This is because some fraction of the large eddies in the separated shear layer pass nearly unchanged through the reattachment zone and decay very slowly in the recovering boundary layer (c.f. Prouchick and Kline, 1983). Those separated shear layer eddies are generated by the Kelvin-Helmholtz instability and are substantially different in character than typical eddies encountered in an attached boundary layer. While the mean velocity profile recovers quickly to a nearly normal state, the turbulence statistics remain disturbed for a large distance downstream.

The fluid mechanics of boundary layers recovering from separation have been studied extensively because of difficulties they cause for turbulence models. The effect of the nonequilibrium turbulent eddies on turbulent heat transport is not as well known. Usually turbulent heat transport is represented in models using a turbulent Prandtl number formulation in which the turbulent heat flux is proportional to the Reynolds shear stress. However, there is no evidence that turbulent heat transport reacts in the same way to perturbations as the turbulent shear stress. Ayala et al. (1997) measured the turbulent heat flux in an adverse pressure gradient boundary layer and found that increases in the turbulent shear stress above zero-pressure-gradient levels were proportionally larger than increases in the turbulent heat flux. Elkins and Eaton (1997) studied heat transport in a three-dimensional boundary layer in which the turbulent shear stress was reduced by the presence of crossflow. They found that the turbulent heat transport was not as strongly affected so that the turbulent Prandtl number was reduced by the imposition of crossflow. The recovering boundary layer downstream of separation is more severely per-

turbed than the examples above, so one might expect more drastic effects on the turbulent Prandtl number.

The present study was conducted in a two-dimensional turbulent channel flow downstream of a stalled planar diffuser with the geometry shown in Fig. 1. The channel flow upstream of the diffuser was fully developed, and downstream of the separation zone the mean profiles recovered rapidly back towards fully developed channel flow. However, the turbulence profiles remained highly disturbed as will be shown below. Turbulent heat transport was studied in this recovering channel flow by making measurements in the spreading thermal wake of a fine heated wire stretched across the span of the tunnel. These measurements were compared to similar data we acquired in an unperturbed fully developed channel flow at the same Reynolds number. The objectives were to measure the rate of turbulent diffusion of the heated wake to determine the effect of the nonequilibrium eddies in the flow and to determine if this effect could be captured by a turbulent Prandtl number model.

Apparatus and Techniques

The experiments were performed in a blower-driven wind tunnel with a test-section geometry as illustrated in Fig. 1. Details of the facility are described in Buice and Eaton (1997). Upstream elements included honeycomb, 3 screens, and a 41:1 contraction to insure uniform flow at the entrance to the channel flow development section. The development section had a channel height (H) of 15 mm, a span of 610 mm and a length of 1.65 m (110 channel heights) insuring two-dimensional fully developed conditions at the inlet of the diffuser. The stalled diffuser was a 4.7:1 asymmetric expansion which produced a separation bubble extending from a mean separation point at $x/H = 7$ to a mean reattachment point at $x/H = 29$, eight inlet channel heights downstream of the diffuser exit. Thin splitter plates were used to remove the end wall boundary layers in order to obtain two-dimensional flow in the diffuser and the downstream channel. The splitter plates were located $4.7H$ from each end wall and ran from a point $6H$ upstream of the diffuser inlet to the end of the test section. The main section of interest for the present work was the downstream channel which had a channel height h of 70.5 mm, a span of 470 mm, and a length of 840 mm. The tunnel was operated under closed-loop speed control to give a channel flow Reynolds number $U_c h / \nu$ of 20,000.

A second fully developed channel flow facility was used to obtain data for the unperturbed case at the same Reynolds number. This was the vertical channel flow facility described in detail by Kulick et al. (1994). The facility had a channel height of 40 mm, a span of 457 mm, and a development length of 5.2 m ($130h$)

¹ Present address: Genomic Instrumentation Services, Redwood City, CA.

Contributed by the Heat Transfer Division for publication in the JOURNAL OF HEAT TRANSFER. Manuscript received by the Heat Transfer Division, Apr. 16, 1998; revision received, Jan. 12, 1999. Keywords: Forced Convection, Heat Transfer, Reattachment, Turbulent. Associate Technical Editor: R. Dougllass.

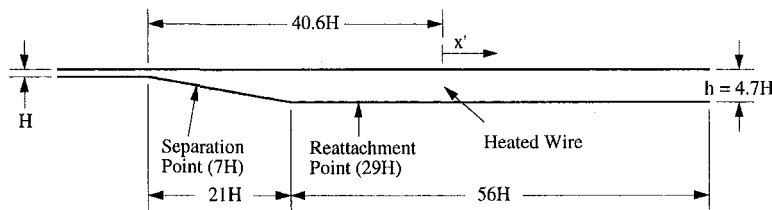


Fig. 1 Test section geometry

upstream of the measurement section. Detailed data presented in Kulick et al. (1993) demonstrate that this flow is fully developed in all turbulence quantities and produces measurements in good agreement with previous results.

In each experiment, a 0.2-mm diameter Nichrome wire was stretched across the span of the channel on the centerline. A 1.7 A DC current ran through the wire dissipating 35 W over 8 inches of wire length. Temperature profiles were measured downstream of the wire using a traversing type K thermocouple probe positioned using a computer-driven traverse. The thermocouple was fabricated from 36 gage wire (0.13 mm diameter) with a junction bead approximately 0.5 mm in diameter. The thermocouple was mounted in a 1.6-mm OD stainless-steel tube with the bead protruding approximately 3 mm from the end of the tube. The probe was aligned with the flow direction to prevent thermal conduction along the tube which could affect the temperature readings. The thermocouple was connected differentially with a reference thermocouple located in the freestream upstream of the heated wire. At each measurement point, 400 voltage samples were acquired using a Fluke 8842 digital multimeter giving a statistical uncertainty of 0.01 C. A complete uncertainty analysis including instrumentation and calibration uncertainty yields an overall uncertainty estimate of 0.04 C for the differential temperature measurements.

Mean velocity and turbulence intensity measurements reported here were measured using a TSI Model 1218 single hotwire probe operated by a high performance hotwire bridge developed by Watmuff (1994). Standard setup and calibration procedures were used (see Buice and Eaton, 1997) for details. The uncertainty in the mean velocity and turbulence intensity were estimated to be two percent and four percent, respectively, taking into account both statistical and calibration uncertainties. The Reynolds shear stress needed for calculation of the turbulent Prandtl number was measured using a TSI Model 1243 cross-wire probe operated with two of the Watmuff hotwire bridges. The probe was modified from the original TSI design to reduce the wire spacing to 0.35 mm. The probe was strung with 2.5 μm Platinum plated Tungsten wire with copper plated ends to obtain an active region l/d of 200. A homemade sample-and-hold circuit was used for simultaneous sampling of the two channels. Measurement and calibration procedures were the same as reported in Anderson and Eaton (1987). The uncertainty in the shear stress was estimated at ten percent following Anderson's analysis.

Experimental Results

Figure 2 shows the mean velocity profiles measured at three streamwise stations in the recovering channel flow. The upstream

profile was measured slightly upstream of the position of the heated nichrome wire. This profile shows some remaining distortion from the region of flow separation. The mean profile is recovering very rapidly as evidenced by the downstream profiles, which appear much like fully developed channel flow with a broad region of nearly constant velocity in the central region of the channel. Streamwise turbulence intensity profiles measured at the same stations (Fig. 3) show similar trends. All three profiles show a broad region of nearly constant turbulence intensity, although the upstream profile shows slightly more disturbance. There is a striking difference between the recovering channel flow data and the baseline fully developed channel flow data measured in the upstream channel. This level of disturbance is characteristic of boundary layers recovering from separation. The mean profile recovers very quickly to show only mild variation from the standard mean profile while the turbulence remains highly perturbed and out of equilibrium with the mean flow.

Figure 4 shows the temperature profiles measured downstream of the heated wire in the reference fully developed channel flow. Here, x'/h is the distance downstream of the wire normalized by the channel width and the temperature is normalized by the maximum in each profile. Applying Taylor's theory of turbulent dispersion of a passive scalar to a flow of uniform mean velocity, one expects the temperature profiles to take on a Gaussian form. Gaussian fits to each profile are shown in Fig. 4. The measurements closely match the Gaussian profiles except for the outer edge of the farthest downstream profile. This indicates that the central region of the reference channel flow behaves very much like a region of homogeneous turbulence with uniform mean velocity.

Figure 5 shows the temperature profiles measured in the perturbed channel flow. The most obvious feature is the much more rapid turbulent diffusion in the perturbed case. By the second profile, the thermal wake has reached the walls of the channel and the wall has been heated to a temperature above the upstream reference temperature. This results in a distinctly non-Gaussian profile downstream of $x'/h = 1.19$. Another feature of the plots is that the central peak in the temperature profile is not on the channel centerline. This is because the flow streamlines at the position of the heated wire are directed slightly towards the lower wall ($y = 0$) as the velocity deficit evident in the first profile in Fig. 2 recovers.

Gaussian curves were fit to the data in order to estimate the turbulent diffusivity. However, for this case, the least-squares fitting routine used only the central ten points of each profile where the mean flow and turbulence are reasonably homogeneous. The

Nomenclature

H = height of upstream channel, 15 mm	U_b = bulk average velocity	α_t = turbulent diffusivity of heat
h = height of downstream channel, 70.5 mm	u'_{rms} = standard deviation of fluctuating streamwise velocity	ν = molecular kinematic viscosity
Pr_t = turbulent Prandtl number, ν_t/α_t	x = streamwise coordinate	ν_t = turbulent kinematic viscosity
T = temperature	x' = streamwise coordinate measured from position of heated wire	σ = standard deviation of a Gaussian curve
T_o = maximum temperature in a profile	y = wall normal coordinate	θ = temperature difference, $T - T_{freestream}$
U = mean streamwise velocity		

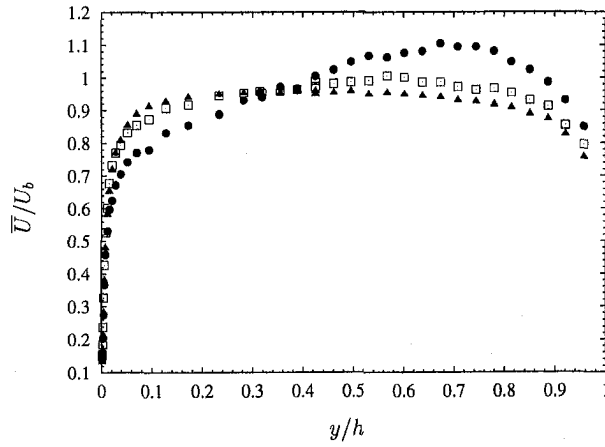


Fig. 2 Mean velocity profiles surrounding the heated wire: ●, $x'/h = -0.16$; □, $x'/h = 1.28$; ▲, $x'/h = 2.72$

temperature profiles match the Gaussian curves quite well in this central region. The standard deviations of the Gaussian curves are plotted in Fig. 6, which shows the enormous difference in turbulent diffusivity between the perturbed flow and the reference channel flow. For reasons discussed below, the square of the standard deviation is actually plotted.

Analysis of the Results

The temperature profiles can be used to estimate the turbulent diffusivity of heat and thus the turbulent Prandtl number using a simple analysis. Assuming a uniform mean velocity U , a uniform turbulent diffusivity of heat α_t , and negligible molecular diffusivity of heat in the central region of the channel, we can write an energy equation:

$$U \frac{\partial T}{\partial x} - \alpha_t \frac{\partial^2 T}{\partial y^2} = 0. \quad (1)$$

The solution of this equation gives a Gaussian temperature profile:

$$T(y) = T_o \exp\left[-\frac{1}{2}\left(\frac{y}{\sigma}\right)^2\right] \quad (2)$$

where T_o and σ are functions of x . Integration of Eq. (2) from $-\infty$ to $+\infty$ gives the starting impulse I , and therefore T_o :

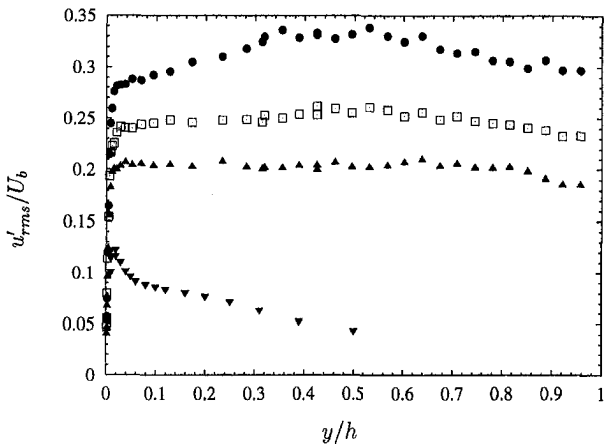


Fig. 3 Streamwise turbulence intensity profiles surrounding the heated wire compared with fully developed profile from inlet channel: ●, $x'/h = -0.16$; □, $x'/h = 1.28$; ▲, $x'/h = 2.72$; ▽, fully developed turbulent channel flow

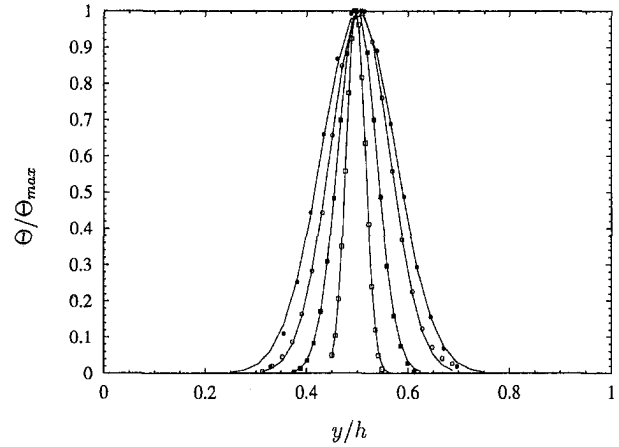


Fig. 4 Temperature profiles downstream of point source in fully developed turbulent channel flow: □, $x'/h = 0.47$; ■, $x'/h = 1.19$; ○, $x'/h = 1.91$; ●, $x'/h = 2.63$.

$$T_o = \frac{I}{\sqrt{2\pi}\sigma}. \quad (3)$$

Substituting Eq. (3) into Eq. (2) and taking the derivative gives

$$\sigma \frac{\partial \sigma}{\partial x} = \frac{\alpha_t}{U}. \quad (4)$$

Finally, integration of Eq. (4) with x and normalization by the channel width h results in a simple relationship between σ and α_t :

$$\left(\frac{\sigma}{h}\right)^2 = \frac{2\alpha_t}{Uh} \left(\frac{x}{h} + \frac{x_o}{h}\right). \quad (5)$$

Plots of $(\sigma/h)^2$ versus x/h for the two cases are shown in Fig. 6 and show the linear relationship expected. The thermal diffusivity α_t/Uh was estimated by fitting a straight line to the four data points using a least squares procedure. The resulting value was $\alpha_t/Uh = 0.027 \pm 0.0021$ for the perturbed channel and $\alpha_t/Uh = 0.0012 \pm 5.7 \times 10^{-5}$ for the reference channel flow. Thus, the turbulent diffusivity is more than 20 times greater in the perturbed channel flow. The uncertainty was evaluated considering uncertainties in the average temperatures, the Gaussian fits to the profiles, and the linear fit, all at 95 percent confidence level. The relative uncertainty for the perturbed case was higher

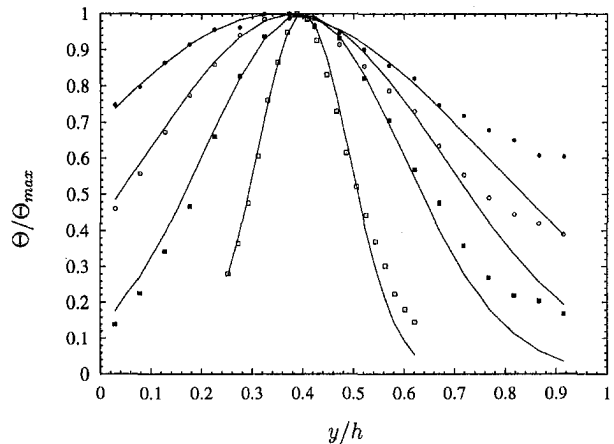


Fig. 5 Temperature profiles downstream of point source in recovering turbulent channel flow: □, $x'/h = 0.47$; ■, $x'/h = 1.19$; ○, $x'/h = 1.91$; ●, $x'/h = 2.63$

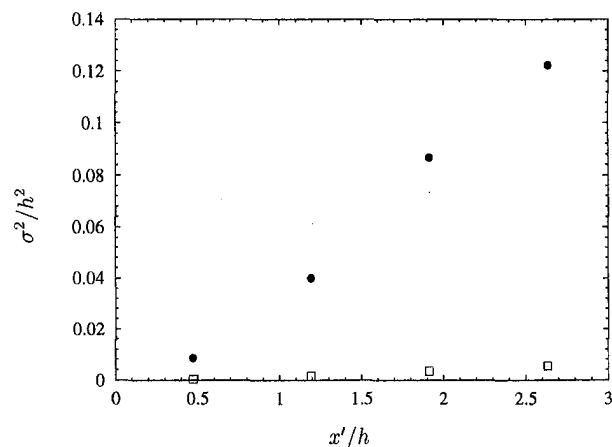


Fig. 6 Standard deviation of Gaussian curve fits: ●, recovering channel flow; □, fully developed turbulent channel flow

because the more rapid diffusion produced a much lower temperature thermal wake.

While the uncertainty in this analysis is fairly large, the magnitude of the change shows that the perturbed flow has a dramatically increased thermal diffusivity. An important issue then, is how this increased diffusivity can be modeled. Turbulence models normally calculate the turbulent heat transport using a turbulent Prandtl number formulation. The turbulent diffusivity of momentum (the eddy viscosity) is calculated directly from the turbulence model, then the diffusivity of heat is estimated using a prescribed turbulent Prandtl number defined as

$$\text{Pr}_t = \frac{\nu_t}{\alpha_t}$$

Typical values of Pr_t for turbulent boundary layers are around 0.9. Recent work by Ayala et al. (1997) found values of Pr_t ranging from 0.8 to 1.0 in a zero-pressure-gradient boundary layer, but higher values up to 1.25 in an adverse-pressure-gradient boundary layer.

Evaluation of the eddy viscosity is difficult in the present flow because both the turbulent shear stress and the mean velocity gradient are zero at the channel centerline. A reasonable assumption is that the eddy viscosity is constant in the central region of the channel, so it was estimated using data for $0.15 < y/h < 0.35$ ($0.3 < y/\delta < 0.7$, where δ is the channel half height). This averaging region avoided the logarithmic region near the wall and the region of negligible shear stress near the channel centerline. The mean velocity gradient was calculated using second-order central differences then smoothed using a five-point filter. The measured Reynolds shear stress values were used directly for the perturbed channel flow. For the reference channel flow, the shear stress was calculated directly from the pressure gradient. The average eddy viscosity for the perturbed channel flow was $\nu_t/Uh = 0.047 \pm 0.009$ at 95 percent confidence. The large uncertainty is due to the uncertainty of the shear stress measurements and the relatively small velocity gradients. For the reference channel, the normalized eddy viscosity average was 0.0011 ± 0.00013 . In this case, the relative uncertainty is smaller because the shear stress is known more accurately.

As with the thermal diffusivity, the eddy viscosity is very much greater in the perturbed channel flow than the reference channel. This very large eddy viscosity is responsible for the rapid recovery of the velocity deficit downstream of reattachment. The changes in ν_t are even larger than the changes in α_t . For the reference channel flow the estimated turbulent Prandtl number is 0.92 ± 0.12 at 95 percent confidence. The estimated uncertainty in this measurement is large, but the good agreement with previous results lends some confidence to the present technique. The turbulent Prandtl number for the perturbed channel flow was 1.7 ± 0.36 . Despite the large relative uncertainty, it is clear that the perturbed channel flow has a much larger turbulent Prandtl number. As has been found in other flows, perturbing the turbulence structure causes greater increases in the eddy viscosity than the turbulent thermal diffusivity.

Conclusions

We have examined thermal diffusion in a perturbed channel flow as compared to a reference fully developed channel flow. The thermal diffusivity is increased by approximately a factor of 20 by the turbulence in the recovery region downstream of a separation zone. This demonstrates that the turbulence is far out of equilibrium with the mean flow which rapidly recovers to a nearly fully developed profile. The turbulent eddy viscosity is affected even more strongly by the nonequilibrium eddies than the heat transport. The turbulent Prandtl number is increased by nearly a factor of two. This corroborates a similar observation by Ayala et al. in an adverse pressure gradient boundary layer.

In another study of heat transport in nonstandard boundary layers, Elkins and Eaton (1997) measured the turbulent Prandtl number in the three dimensional boundary layer on a rotating disk using direct measurements of the turbulent heat flux. Boundary layer three dimensionality suppresses the turbulent shear stresses and reduces the eddy viscosity. Elkins and Eaton found that the turbulent heat flux was not suppressed as much as the turbulent shear stress resulting in turbulent Prandtl numbers lower than conventional boundary layers. This suggests a general trend that boundary layer disturbances have a greater effect on the turbulent momentum transport than the turbulent heat transport.

References

- Ayala, A., White, B. R., and Bagheri, N., 1997, "Turbulent Prandtl number measurements in adverse pressure gradient equilibrium boundary layers," *Proceedings of the 2nd International Symposium on Turbulence, Heat and Mass Transfer*, June, Delft University Press, Delft, The Netherlands.
- Bradshaw, P., and Wong, F. Y. F., 1972, "The reattachment and relaxation of a turbulent shear layer," *Journal of Fluid Mechanics*, Vol. 52, pp. 113–135.
- Buice, C. U., and Eaton, J. K., 1997, "Experimental investigation of flow through an axisymmetric plane diffuser," Report TSD-107, Thermosciences Division, Department of Mechanical Engineering, Stanford University, Stanford, CA.
- Elkins, C. J., and Eaton, J. K., 1997, "Turbulent heat flux measurements on a rotating disk," *Proceedings of the 11th Symposium on Turbulent Shear Flows*, Grenoble, Institut National Polytechnique de Grenoble, pp. 8–13; 8–18.
- Kulick, J. D., Fessler, J. R., and Eaton, J. K., 1993, "On the interactions between particles and turbulence in a fully-developed channel flow in air," Report MD-66, Thermosciences Division, Department of Mechanical Engineering, Stanford University, Stanford, CA.
- Kulick, J. D., Fessler, J. R., and Eaton, J. K., 1994, "Particle response and turbulence modification in fully developed channel flow," *Journal of Fluid Mechanics*, Vol. 277, pp. 109–134.
- Pronchick, S. W., and Kline, S. J., 1983, "An experimental investigation of the structure of a turbulent reattaching flow behind a backward facing step," Report MD-42, Thermosciences Division, Department of Mechanical Engineering, Stanford University, Stanford, CA.

An Experimental Study on Forced Convection Heat Transfer From Flush-Mounted Discrete Heat Sources

C. P. Tso

Associate Professor,
Mem. ASME.

G. P. Xu

Graduate Student

K. W. Tou

Associate Professor,
Mem. ASME.

School of Mechanical
and Production Engineering,
Nanyang Technological University,
Nanyang Avenue,
Singapore 639798

Experiments have been performed using water to determine the single-phase forced convection heat transfer from in-line four simulated electronic chips, which are flush-mounted to one wall of a vertical rectangular channel. The effects of the most influential geometric parameters on heat transfer including chip number, and channel height are tested. The channel height is varied over values of 0.5, 0.7, and 1.0 times the heat source length. The heat flux is set at the three values of 5 W/cm², 10 W/cm², and 20 W/cm², and the Reynolds number based on the heat source length ranges from 6×10^2 to 8×10^4 . Transition Reynolds numbers are deduced from the heat transfer data. The experimental results indicate that the heat transfer coefficient is affected strongly by the number of chips and the Reynolds number and weakly by the channel height. Finally, the present results from liquid-cooling are compared with other results from air-cooling, and Prandtl number scaling between air and water is investigated.

Introduction

The rapid advances in the computer industry have resulted in an increased need for reliable and efficient cooling technologies. Present trends in microelectronics indicate that circuit densities on a single silicon chip will continue to increase and more chips will be packed in closer proximity on multichip modules. Since almost all of the electrical energy consumed by these devices appears as heat, the power density must be dissipated by the chip and modules in order to maintain the chip temperature to below 85°C. As it is becoming increasingly difficult to rely on air-cooling to remove the cooling load, liquid-cooling is considered, and it may be the only practical method for maintaining reasonable component temperatures in high power chips.

Forced convection heat transfer, from a single heat source and from an in-line four-row array of 12 heat sources flush-mounted to one wall of a horizontal rectangular channel, were studied by Incropera et al. (1986) and Mahaney et al. (1990), for Reynolds number ranges of $1000 < Re_D < 14000$ and $40 < Re_D < 3200$, respectively. Two fluids, water and FC-77, were considered, and it was found that the upstream thermal boundary affected that of downstream. Tests were conducted using a single heat source flush-mounted to one wall of a vertical rectangular channel by Mudawar and Maddox (1989), with FC-72 as the coolant. Although the slopes of the correlations obtained by Mudawar and Maddox (1989) and those by Incropera et al. (1986) are almost identical, the data of the former was approximately 37 percent higher than the latter. Gersey and Mudawar (1992, 1993) used FC-72 on a series of nine in-line simulated chips in a flow channel to ascertain the effects of orientation angle, channel height, and protruding height, and found that the upstream thermal boundary had no effect on that of downstream; and channel height, protruding height, and orientation angle had little effect on the heat transfer data.

Experiments were performed to determine the effects of Reynolds number, channel height, streamwise and spanwise spacings on

the convective heat transfer coefficients for water cooling with 5×6 arrays of heated protruding elements by Garimella and Eibeck (1990, 1991). The Nusselt number was shown to be enhanced by staggering the elements, and by decreasing the channel height, as well as by increasing the streamwise and spanwise spacings between elements. Heindel et al. (1992) studied flow of water and FC-77 over an in-line 1×10 array of discrete heat sources located on the bottom wall of an horizontal flow channel. Recently, Garimella and Schlitz (1995) have focused on heat transfer from a single flush-mounted and protruding heat source in an array of 5×5 elements using FC-77 and water.

Based on the literature survey, there are many data bases and correlations about single-phase heat transfer in flush-mounted heat sources for liquid-cooling, but they are inconsistent with each other because of different geometrical parameters and working fluids. For an array of flush-mounted heat sources, the effect of upstream thermal boundary layer on that of downstream needs to be confirmed, as indicated by the results of Incropera et al. (1986) being inconsistent with those of Gersey and Mudawar (1992). The effect of channel height on heat transfer have not been studied for flush-mounted heat sources, although this effect had been investigated for protruding elements by Gersey and Mudawar (1993) and by Garimella and Eibeck (1990).

The objective of this study is to measure convective heat transfer from a linear array of flush-mounted heat sources in a vertical up-flow channel. Water was used to simulate the dielectric liquids in the present experiment. The dimensions of the simulated chips were held constant while the height of the channel was varied. Heat transfer coefficients were obtained over a range of flow rates encompassing the single-phase laminar forced convection and turbulent forced convection regimes.

Experimental Apparatus and Procedure

The experiments were conducted in a closed-loop liquid-cooling flow facility with a vertical up-flow, plexiglass test section as shown in Fig. 1. The flow loop consisted of a reservoir, pump, heat exchanger, filter, rotameter, and flow channel. The temperature at the test-section inlet is maintained constant by means of the heat exchanger and the immersion heater in the reservoir, and was measured just prior to the test section by a K-type thermocouple. A converging section and a flow straightener which has a series of

Contributed by the Heat Transfer Division for publication in the JOURNAL OF HEAT TRANSFER. Manuscript received by the Heat Transfer Division, Oct. 7, 1996; revision received, Dec. 21, 1998. Keywords: Direct-Contact Heat Transfer, Electronic Equipment, Forced Convection. Associate Technical Editor: S. Ramadhyani.

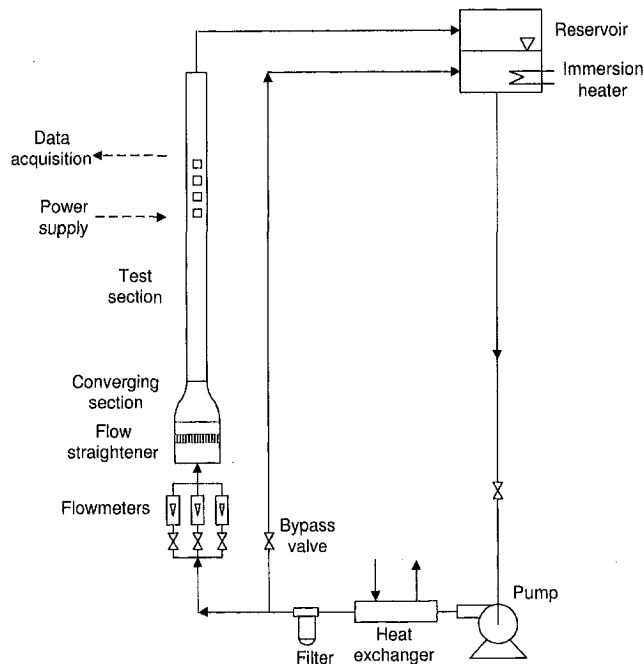


Fig. 1 Schematic of the liquid cooling test facility

screens and honeycomb ensure a uniform flow at upstream of the test section. The first chip was located 680 mm downstream of the channel inlet, providing a minimum hydrodynamic entry length of 50 hydraulic diameters. To improve the accuracy of reading, three rotameters with different ranges were used to measure the flow rate.

A detailed view of the multichip module is provided in Fig. 2. The surfaces of the chips were mounted flush in a teflon substrate module, the chips are positioned in the center of the channel wall with a spacing of 5.0 mm between the edges of the chip and the channel side walls. The channel heights were varied to three values. Each chip was fabricated from oxygen-free copper such that the cross-sectional dimensions of the chip surface in contact with the liquid are 10.0×10.0 mm. Four film resistive heaters were installed in series with each chip and adjusted so that each film resistor dissipated the same power. With the voltage across each chip being same, one voltage transducer and four current transducers were used to calculate the power dissipation of each chip. The resistors were attached with thermally conducting epoxy to the underside of the copper blocks.

Two K-type thermocouples, located 2 mm upstream and down-

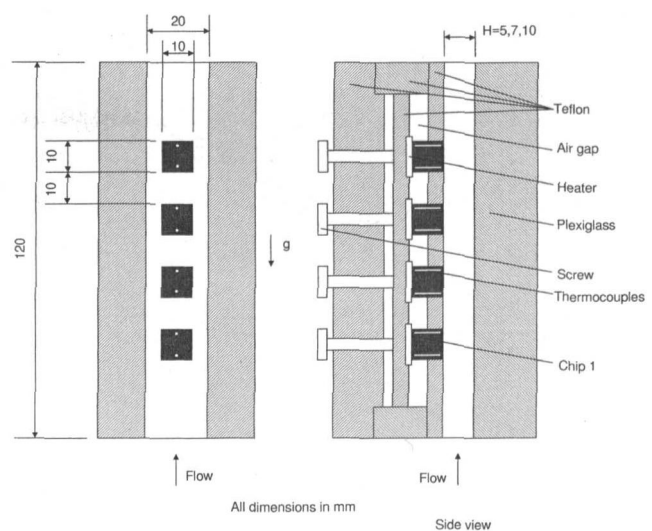


Fig. 2 Multichip module

stream of the chip, respectively, were embedded along the chip centerline in the flow direction at a depth of 0.5 mm underneath the chip surface and aligned along the chip centerline. Before measurements were recorded, the wall temperatures of the simulated chips were allowed to reach steady state, typically in ten minutes, after the power level and flow rate were set. Average of the two surface temperatures yielded the mean surface temperature.

Data were reduced in terms of an average Nusselt number for simulated chip number i

$$Nu_{i,c} = \frac{h_i L}{k} = \frac{Q_c L}{A(\bar{T}_i - T_{in})k} \quad (1)$$

for which the chip length and surface area are $L = 10$ mm and $A = 100$ mm². All thermophysical properties are evaluated at the fluid inlet temperature, except for the viscosity μ_w , which is evaluated at the chip surface temperature. The corrected heat dissipation rate Q_c , which represents the heat transferred to the fluid directly through the chip surface, has accounted for substrate conduction losses, which is of the order of less than five percent of the total heat dissipated by the heater.

All experiments with water were performed in a vertical up-flow channel over heat source length-based Reynolds number in the range from $6.2 \times 10^2 < Re_L < 7.7 \times 10^4$ ($8.2 \times 10^2 < Re_D < 6.2 \times 10^4$) for an inlet temperature of $T_{in} \approx 25^\circ\text{C}$, and for heat fluxes of 5, 10, and 20 W/cm². An estimation of the uncertainty in

Nomenclature

A = heat source surface area, m²
 B = protruding height, m
 C, C_1 = coefficients in correlations
 D = channel hydraulic diameter, m
 h = heat transfer coefficient, W/m² K
 H = channel height, m
 k = thermal conductivity, W/m K
 L = length of heat source, m
 m = exponent of Reynolds number
 n = exponent of Prandtl number
 Nu_L = Nusselt number based on length of heat source = hL/k
 Pe_L = Peclet number based on length of heat source = $Re_L Pr$

Pr = Prandtl number
 Q_c = corrected heat dissipation rate, W
 q'' = heat flux, W/m²
 Re_D = Reynolds number based on channel hydraulic diameter = UD/ν
 Re_L = Reynolds number based on length of heat source = UL/ν
 S_x = streamwise spacing between heat sources, m
 \bar{T} = average of surface temperatures, °C
 T_{in} = inlet temperature, °C

U = mean inlet velocity, m/s
 μ = dynamic viscosity, N s/m²
 ρ = density, kg/m³
 ν = kinematic viscosity, m²/s

Subscripts

cal = calculated
 exp = experimental
 i = chip number index, $i = 1, 2, 3, 4$
 m = channel entrance condition
 w = wall of heat source

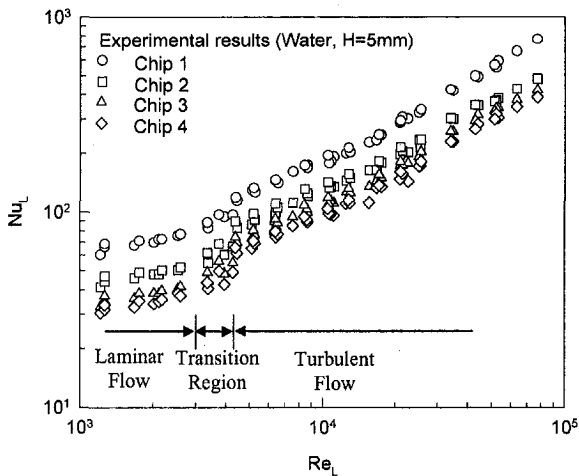


Fig. 3 Nusselt number as a function of Reynolds number

the experimental data was made using standard techniques for single-sample measurements (Kline and McClintock, 1953). The propagation of the uncertainties into the dimensionless parameters was then determined. This study revealed uncertainties in Re_L , Re_D , and Nu_L to be less than 3.5, 3.5, and 10.0 percent, respectively. These values are based on the assumption of negligible uncertainty in the relevant fluid properties.

Results and Discussions

Effects of Number of Chips. Baseline tests were first conducted with flush-mounted heat sources with $L = 10$ mm, $H/L = 0.5$. The Nusselt number is shown in Fig. 3 as a function of Reynolds number based on heat source length for the four chips. As seen in this figure, there is a drop in the heat transfer coefficient as the chip number increases. It is found that the Nusselt numbers of the second chip are about 70 percent of those of the first chip. This also conveys the fact that as the chip number increases, the differences between Nusselt number for the two neighboring chips become smaller. From an examination of all the data from this study, it is deduced that the heat transfer coefficient can be considered to have reached a chip-number-independent, fully developed value by the fourth chip for all test runs, since there is little change in values between the third and fourth chips.

The attainment of fully developed condition downstream of three to four rows was also observed by Incropera et al. (1986) in turbulent flow, Mahaney et al. (1990) in laminar flow, and Garimella and Eibeck (1990) in laminar flow for liquid-cooling. However, Gersey and Mudawar (1992) found that the row number had no effect on single-phase heat transfer coefficient for nine in-line simulated microelectronic chips using FC-72, with the chips having similar heat transfer coefficients.

Effects of Reynolds Number. Three distinct regimes can be identified in Fig. 3, indicating a transition from laminar to turbulent flow. Transition occurs at a Reynolds number, based on heat source length, of approximately 3000, and the flow is fully turbulent when $Re_L > 4300$. If Reynolds number is defined in terms of hydraulic diameter D , $Re_D = UD/\nu$, the transition Reynolds number is about 2400. It is well known that the critical Reynolds number in a pipe or duct flow in which transition from laminar to turbulent flow begins is about 2300, and the flow is fully turbulent for $Re_D > 4000$ (Incropera and DeWitt, 1985). Similar results of laminar flow and laminar/transition flow characteristics were obtained by Incropera et al. (1986) from dye injection studies, with $Re_D < 4000$ in a rectangular channel. It was also observed by Garimella and Schlitz (1995) with $Re_D < 3900$.

The input power seems to have little effect on the heat transfer

coefficient, the difference of heat transfer coefficient among these heat fluxes (5 W/cm^2 , 10 W/cm^2 and 20 W/cm^2) are less than six percent. When the input power increases, the wall temperature increases as the flow rate and inlet temperature are fixed, so the viscosity of the liquid at the wall decreases.

The Nusselt number data of laminar flow including transition region versus Peclet number based on the length of heat sources are shown in Fig. 4. For flow in a duct or between parallel plates with a fully developed laminar velocity profile, it may be shown that

$$Nu_L = C_1 Pe_L^{1/3} \quad (2)$$

where $Pe_L = Re_L Pr$. Experimental forced convection results of laminar flow for all four chips fall along this theoretical slope. The reduction of heat transfer with chip number results from thermal boundary layer development due to upstream heating. The ordinate values of the horizontal asymptotes corresponding to the constant C_1 is shown in Table 1.

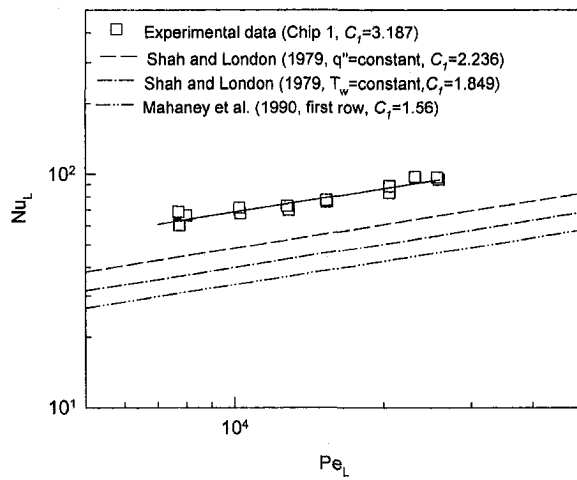
For parallel plate ducts, laminar flow and heat transfer have been analyzed in detail by Shah and London (1978). The more convenient approximate equations have the recommended form of Eq. (2) for thermally developing and hydrodynamically developed flow, with the boundary conditions of uniform peripheral wall temperature and of constant wall heat flux, respectively.

Comparing the experimental data with the analytical results for parallel plate ducts, about 30 percent underprediction of the data by using the solution of constant flux for the first chip is attributed to the fact the heat source length is short; the thermal boundary layer is very thin and has more characteristics of a thermal entry region and has a high heat transfer coefficient. With the thermal boundary layer developing, the data for Chip 2 and Chip 3 agree well with the analytical solutions of constant heat flux and constant temperature, respectively. The reduction in heat transfer coefficient with chip number indicates that the thermal boundary layer is becoming thicker and fully developed forced convection conditions are being approached by time the Chip 4 is reached.

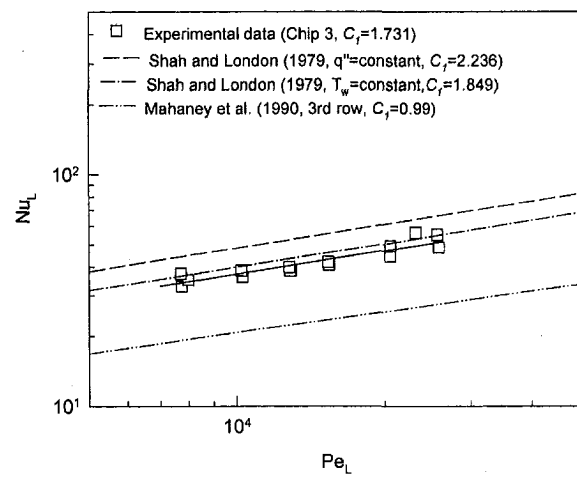
The similar trend in heat transfer characteristics caused by the row number in laminar flow was also obtained by Mahaney et al. (1990) for water-cooling of a rectangular channel with discrete heat sources. Although the same exponent of the Peclet number can correlate their data very well, the values of the heat transfer coefficients in the present study are about 80 percent higher than those obtained by Mahaney et al. for all rows. It may be due to the fact that a different geometry was used in their study. Their data were obtained from a four-row in-line array of 12 square heat sources, 12.7×12.7 mm, with streamwise spacing and spanwise spacing between heat sources 3.18 mm. Thus the ratio of streamwise spacing to the heat source length was 0.25. The ratio of streamwise spacing to the heat source length is 1.0 in the present study, and is four times that in their study. The heat transfer coefficient increases with increasing streamwise spacing. The effects of streamwise spacing between heat sources on heat transfer were found by Garimella and Eibeck (1990) in an array of protruding heat sources for water cooling, and also by Lehmann and Wirtz (1985) from an in-line rectangular rib for air-cooling.

To compare with previous work, the correlation of the experimental data obtained from an in-line 1×10 array of discrete heat sources, flush-mounted to protruding substrate by Heindel et al. (1992) using water and FC-77 as working fluid, is also shown in Fig. 4(d) for heater 10. It can be seen that the difference in the heat transfer coefficient between the fourth chip in the present study and heater 10 in the study of Heindel et al. (1992) is about 15 percent.

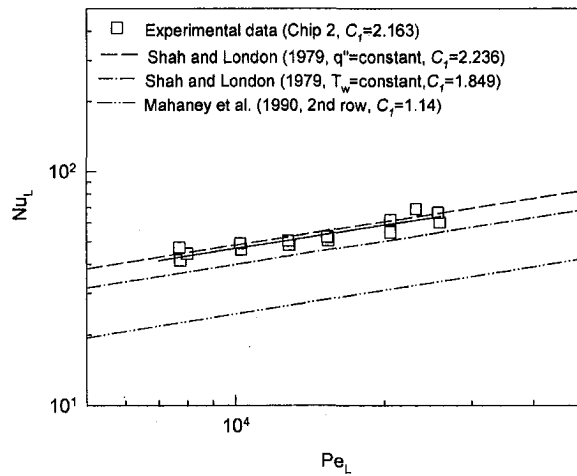
Effects of Channel Height. Three distinct regimes can also be identified for both channel heights of 7 mm and 10 mm, including laminar flow, transition region, and turbulent flow. The transition Reynolds number based on heat source length are different for the channel height 5 mm, 7 mm, 10 mm. The transition Reynolds number increases with channel height decreasing, but the Reynolds



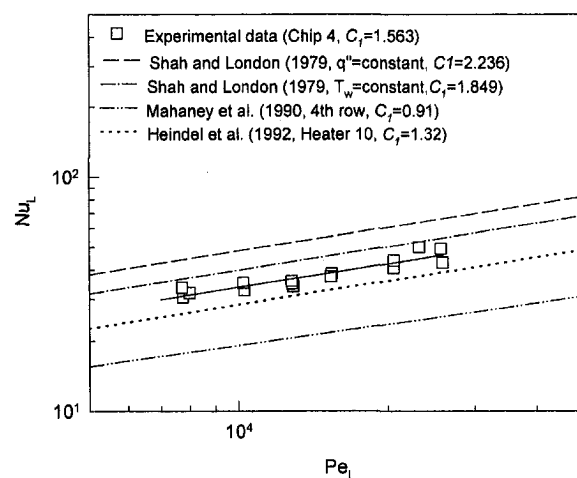
(a) Chip 1



(c) Chip 3



(b) Chip 2



(d) Chip 4

Fig. 4 Nusselt numbers of each chip as a function of Peclet number for laminar forced convection

number based on hydraulic diameter are similar, as shown in Table 2. When $Re_D \leq 2400$ the flow is laminar, and when $Re_D \geq 3400$ the flow is turbulent for three different channel heights. This result suggests that the Reynolds number based on hydraulic diameter may be more appropriately used to determine the existence of laminar or turbulent flow, rather than the Reynolds number based on heat source length, since the hydrodynamics correspond to that of internal flow.

To show the effects of channel height on the heat transfer characteristics clearly, the modified Nusselt number of each chip for three different channel heights are shown together in Fig. 5. It can be seen that the data overlap at the same Re_L and the channel height has little effect on the heat transfer for flush-mounted heat sources in the test range of $0.5 < (H/L) < 1.0$ when $Re_L > 4300$. The data are different between Re_L of about 1700 and 4300, and it may be due to the fact that the flow characteristics are different. For example, fully turbulent flow exists for channel height 10 mm at $Re_L = 2800$, but the flow is laminar for a channel height of 5 mm, so that the heat transfer coefficient at channel height 10 mm is slight higher than that at channel height 5 mm. Similar results on the effect of channel height for protruding heat

sources on heat transfer have been obtained by Gersey and Mudawar (1993).

The effects of channel height on heat transfer for flush-mounted heat sources have not been studied experimentally before, but have been studied numerically for a single flush-mounted heat source by Incropera et al. (1986). They found that the ratio of the channel height to the heat source length had little effect on heat transfer, and correlated the numerical results with the exponent of 0.11 for the (L/H) term. It is important to note, however, that the channel height H or hydraulic diameter D was used in the Reynolds number definition, and the heat transfer increased as the channel height decreased for a constant Re_H or Re_D . This trend was also observed by Lehman and Wirtz (1985) and Garimella and Eibeck

Table 1 Constants of Eq. (2) for laminar flow

	Chip 1	Chip 2	Chip 3	Chip 4
C_1	3.187	2.163	1.731	1.563
Average Deviation (%)	3.79	4.89	5.04	4.61

Table 2 Transition Reynolds number for different channel heights

H/L	Laminar flow			Fully turbulent flow		
	0.5	0.7	1.0	0.5	0.7	1.0
Re_L	● 3000	● 2300	● 1700	● 4300	● 3050	● 2540
Re_D	● 2400	● 2385	● 2267	● 3440	● 3163	● 3386

(1990), where the Reynolds number was based on H , and by McEntire and Webb (1990), where the Reynolds number was based on D .

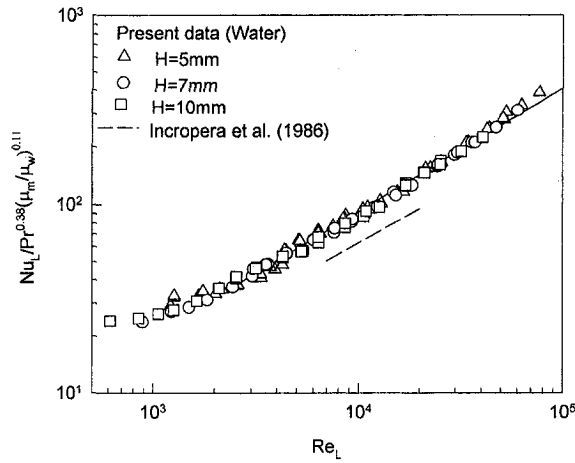
The effects of the row number on the heat transfer for channel height 7 mm and 10 mm are similar to that of channel height 5 mm. The heat transfer coefficients decrease as the chip number increases, and the fully developed condition is achieved after the third chip. The effects of heat flux on the heat transfer for these two channel heights are the same as those for channel height 5 mm.

Correlations. There are several characteristic lengths such as heat source length, channel height, and hydraulic diameter, which

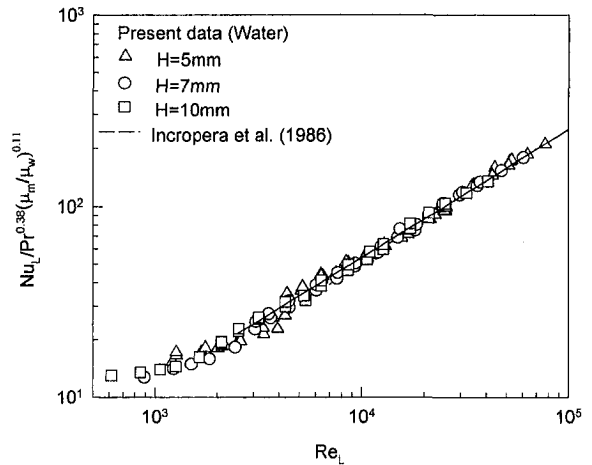
can be used to correlate the heat transfer data for electronics cooling. The results from this study of channel height effects suggest that the heat source length should be used as the characteristic length in the definitions of Nusselt and Reynolds numbers because thermal conditions are more representative of external flow for flush-mounted heat sources, although hydrodynamic conditions correspond to those of internal flow.

The systematic experimental data obtained in this study are used for development of a general empirical heat transfer correlation in the following form:

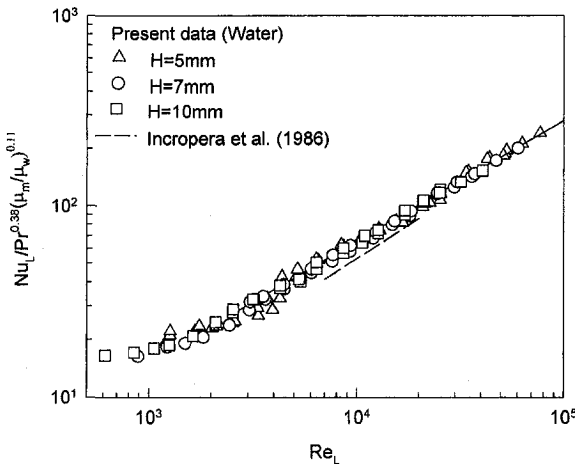
$$Nu_L = C Re_L^m Pr^{0.38} (\mu_m/\mu_w)^{0.11} \quad (3)$$



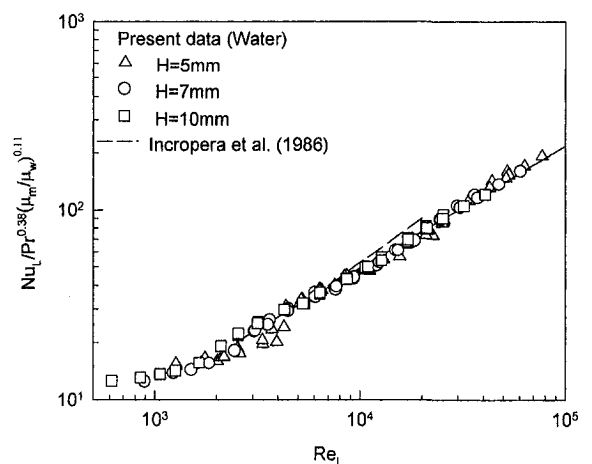
(a) Chip 1



(c) Chip 3



(b) Chip 2



(d) Chip 4

Fig. 5 Effect of channel height on heat transfer coefficient for each chip

Table 3 Constants of Eq. (3) for turbulent flow at different channel heights

	C	m	Average Deviation (%)			Number of data		
			$H = 5$	$H = 7$	$H = 10$	$H = 5$	$H = 7$	$H = 10$
Chip 1	0.231	0.649	4.67	2.56	4.64	40	26	24
Chip 2	0.189	0.634	3.75	2.30	3.07	40	26	24
Chip 3	0.115	0.668	4.08	2.44	3.15	40	26	24
Chip 4	0.126	0.648	4.68	2.68	3.41	40	26	24

where both the Nusselt number and the Reynolds number are based on heat source length and fluid properties are calculated at the inlet temperature. A value of 0.38 was used as the exponent of the Prandtl number as suggested by Incropera et al. (1986) since the exponent could not be correlated within the limited Prandtl number range of the study. The ratio of the viscosity evaluated at the inlet temperature to the viscosity evaluated at the wall temperature is used to correlate the experimental data as suggested in the literature (Kays and Crawford, 1993) to account for the strong temperature dependence of viscosity. The values of C and m are obtained by the least-square fit and presented in Table 3 for turbulent flow and Table 4 for laminar flow including the transition region. The deviations between the experimental data and prediction are less than five percent for turbulent flow and nine percent for laminar flow. The data of laminar flow for all channel heights are correlated well with the exponents of Reynolds number near the value of 0.33 which is used in the correlation of laminar flow in a duct.

The experimental data and the correlations for the four in-line simulated chips are compared in Fig. 5 with the predictions of Incropera et al. (Eq. (13) in that paper). It should be noted that the hydraulic diameter D is used as the characteristic length for Reynolds number in their correlations. Here Re_c is used instead of Re_D to compare with the present data, and so the coefficient C in their correlations needs to be recalculated. In the figures, for the first row, the slopes of correlations are almost identical, but the present data are approximately 40 percent higher than their correlation, and are about 100 percent higher than their correlation if Re_D were used in the correlation. The difference between the present results and their results decreases as the row number increases, and is less than ten percent at the third and fourth rows. It is observed that the effect of the row number on heat transfer in the present studies is stronger than those obtained by Incropera et al. (1986).

Comparison With Air-Cooling Studies. The liquid-cooling results of the present study are compared with several air-cooling studies in the literature as shown in Fig. 6 and Fig. 7 for laminar flow and turbulent flow, respectively. The correlations proposed in the literature cannot be used directly in the comparisons since the scale length used in the Reynolds number is different. The comparisons made here are based on the heat source length as the scale length. Experimental data from the present study in the comparisons are those that approximate the geometry, flow, and thermal conditions of the other studies as closely as possible.

The Nusselt numbers in laminar forced-convection for the flush-mounted heat sources from the present study are contrasted with

that of McEntire and Webb in Fig. 6 for investigating scaling between air and water. For this purpose, the same form of Eq. (2) is used to modify the correlation from McEntire and Webb (Eq. (9) and Fig. 4 in that paper). Their geometry is very close to that in the present study, as indicated in Fig. 6. Peclet number scaling based on the heat source length provides good agreement between the present result and that of McEntire and Webb, with only about five percent deviation in the fourth heat source for laminar forced-convection. Although only fully developed heat transfer coefficients in the fourth heat source are compared, the differences between present results and their data for the other three heat sources are less than 20 percent.

For the turbulent flow, however, there is no database found for heat transfer coefficients of flush-mounted heat sources in air-cooling. The results of Lehmann and Wirtz (Eq. (23) in that paper) for similar geometry with lower protruding height are compared with the present results in turbulent forced-convection as shown in Fig. 7. The heat transfer coefficient data of the first chip from present studies is chosen for comparison, because the fully developed flow and developing thermal conditions in the first chip is very close to that of Lehmann and Wirtz. In their studies, 12 ribs were mounted on a rectangular channel, with only the 11th rib heated to ensure the fully developed flow and developing thermal conditions. It is found that the present results from flush-mounted heat sources agree well with the results from protruded heat sources with low protruding height of air-cooling when the exponent of 0.33 for the Prandtl number was chosen. It is suggested that the database from air-cooling of electronic elements can be used to predict direct liquid-cooling heat transfer performance in the similar geometry as lacking of experimental data for liquid-cooling.

Conclusions

The results of our experimental study imply the following conclusions.

1 Upstream thermal boundary affects that of downstream, with the heat transfer coefficients decreasing as the chip number increases, but may reach a chip-number-independent, fully developed value by the fourth chip, as shown by the result that there is little change in values between the third and the fourth chips.

2 There are three distinct heat transfer regions associated with the Reynolds number range of the experiments. The regions include laminar, transition from laminar to turbulent, and turbulent. Although the transition Reynolds number based on

Table 4 Constants of Eq. (3) for laminar flow at different channel heights

	C	m	Average Deviation (%)			Number of data		
			$H = 5$	$H = 7$	$H = 10$	$H = 5$	$H = 7$	$H = 10$
Chip 1	1.920	0.381	3.46	6.66	4.13	15	5	6
Chip 2	1.448	0.365	4.46	7.10	4.11	15	5	6
Chip 3	0.987	0.384	4.38	8.37	5.00	15	5	6
Chip 4	1.321	0.336	4.21	3.99	4.45	15	5	6

the heat source length decreases as the channel height increases, the Reynolds number based on the hydraulic diameter is similar for all the channel heights. This result suggests that the Reynolds number based on the hydraulic diameter should be used to determine the existence of laminar or turbulent flow rather than the Reynolds number based on heat source length, since the hydrodynamics correspond to internal channel flow.

3 The channel height has little effect on the Nusselt number based on the heat source length. This suggests that the thermal conditions are more representative of external flow for the range of H/L from 0.5 to 1.0 in this study, and the heat source length used as the characteristic length in the definition of Nusselt and Reynolds numbers is better than other length scales, even though the hydrodynamic conditions correspond to those of internal flow.

4 The heat transfer coefficients for all four chips fall along one-third of the theoretical slope of Pe_L for laminar forced-convection, and are found to be about proportional to $Re_L^{0.65}$ for turbulent forced-convection.

5 Results from the present study agree well with results from the literature for air-cooling of heat sources of similar geometry when Peclet numbers are used to correlate data in laminar flow and Nusselt numbers are normalized against the Prandtl number in turbulent flow. This suggests that data from air-cooling may be used to predict the heat transfer characteristic of liquid-cooling for similar geometry if the Prandtl number scaling is considered.

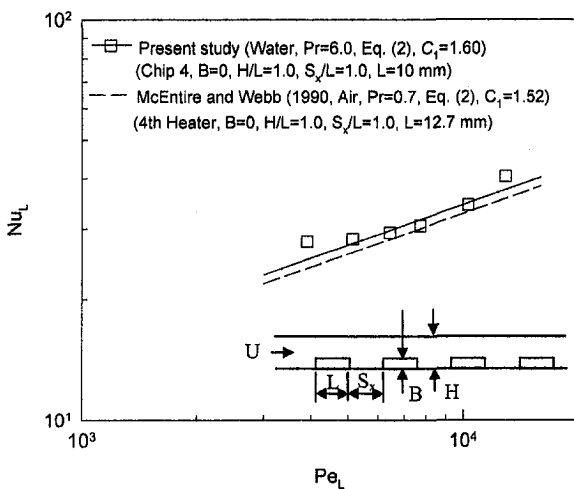


Fig. 6 Comparison of present study with air cooling study of McEntire and Webb (1990) for laminar forced convection

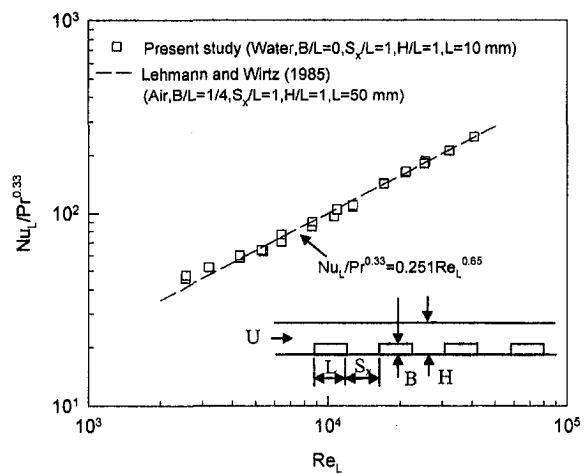


Fig. 7 Comparison of present study with air cooling study of Lehmann and Wirtz (1985) for turbulent forced convection

References

- Garimella, S. V., and Eibeck, P. A., 1990, "Heat transfer characteristics of an array of protruding elements in single phase forced convection," *Int. J. Heat Mass Transfer*, Vol. 33, pp. 2659–2669.
- Garimella, S. V., and Eibeck, P. A., 1991, "Effect of spanwise spacing on the heat transfer from an array of protruding elements in forced convection," *Int. J. Heat Mass Transfer*, Vol. 34, pp. 2427–2430.
- Garimella, S. V., and Schlitz, D. J., 1995, "Heat Transfer Enhancement in Narrow Channels Using Two and Three-Dimensional Mixing Devices," *ASME JOURNAL OF HEAT TRANSFER*, Vol. 117, pp. 590–596.
- Gersey, C. O., and Mudawar, I., 1992, "Effects of orientation on critical heat flux from chip arrays during flow boiling," *Advances in Electronic Packaging*, Vol. 1, T. C. William and A. Hiroyuki, eds., ASME, New York, pp. 123–134.
- Gersey, C. O., and Mudawar, I., 1993, "Nucleate Boiling and Critical Heat Flux From Protruded Chip Arrays During Flow Boiling," *ASME Journal of Electronic Packaging*, Vol. 115, pp. 78–88.
- Heindel, T. J., Incropera, F. P., and Ramadhyani, S. R., 1992, "Liquid Immersion Cooling of a Longitudinal Array of Discrete Heat Sources in Protruding Substrates: 1—Single-Phase Forced Convection," *ASME Journal of Electronic Packaging*, Vol. 114, pp. 55–62.
- Incropera, F. P., and DeWitt, D. P., 1985, *Fundamentals of Heat and Mass Transfer*, 2nd Ed., John Wiley and Sons, New York.
- Incropera, F. P., Kerby, J. S., Moffatt, D. F., and Ramadhyani, S., 1986, "Convection heat transfer from discrete heat sources in a rectangular channel," *Int. J. Heat Mass Transfer*, Vol. 29, pp. 1051–1058.
- Kays, W. M., and Crawford, M. C., 1993, *Convective Heat and Mass Transfer*, 3rd ed., McGraw-Hill, New York.
- Kline, R. W., and McClintock, F. A., 1953, "Describing uncertainties in single-sample experiments," *Mech. Engng.*, Vol. 75, pp. 3–8.
- Lehmann, G. L., and Wirtz, R. A., 1985, "The effect of variations in stream-wise spacing and length on convection from surface mounted rectangular components," *Heat Transfer in Electronic Equipment-1985*, HTD-Vol. 48, ASME, New York, pp. 39–48.
- Mahaney, H. V., Incropera, F. P., and Ramadhyani, S., 1990, "Comparison of predicted and measured mixed convection heat transfer from an array of discrete sources in a horizontal rectangular channel," *Int. J. Heat Mass Transfer*, Vol. 33, pp. 1233–1245.
- McEntire, A. B., and Webb, B. W., 1990, "Local forced convective heat transfer from protruding and flush-mounted two-dimensional discrete heat sources," *Int. J. Heat Mass Transfer*, Vol. 33, pp. 1233–1245.
- Mudawar, I., and Maddox, D. E., 1989, "Enhancement of critical heat flux from high power microelectronic heat sources in a flow channel," *Heat Transfer in Electronics-1989*, R. K. Shah, ed., HTD-Vol. 111, ASME, New York, pp. 51–58.
- Shah, R. K., and London, A. L., 1978, "Laminar flow forced convection in ducts," *Advances in Heat Transfer*, Supplement No. 1, Academic Press, New York.

F. Qian
Department of Mechanical Engineering and
Mechanics

B. Farouk
Department of Engineering Mechanics and
Mechanics,
Fellow ASME

R. Mutharasan
Department of Chemical Engineering
Drexel University,
Philadelphia, PA 19104

N. Macken
Department of Engineering,
Swarthmore College,
Swarthmore, PA 19081
Fellow ASME

Experimental and Numerical Studies of Heat Transfer From a Liquid Bath due to an Impinging Gas Jet

There have been extensive heat transfer studies of impinging gas jets on solid surfaces, but few on impinging gas jets on a liquid bath. In this paper, air-jet-induced transport in a heated liquid bath is considered. Two different liquids having widely different Prandtl numbers (silicone oil and a molten metal alloy, Amalloy-203®) were used as bath liquids. Both numerical calculations and experimental measurements were carried out to characterize the jet-induced flow and heat transfer in the liquid bath. The numerical model developed considers the interaction of the jet flow and the liquid bath circulation. The mixing and thermal behavior of the heated bath were determined as functions of the air-jet characteristics (inlet temperature, Reynolds number) and the bath liquid properties (liquid Prandtl number and a "bath Grashof number").

Introduction

An impinging gas jet on a liquid surface is found in many industrial systems. In electric arc furnaces and in welding processes, a highly energetic gas jet impinges on a liquid bath/pool. In many metal processing operations, a gas jet (top-blown) is used to carry out alloying and purification operations. A fundamental understanding of the interaction of a gas jet and a liquid bath can provide important insights into process behavior, resulting in improved efficiency in such systems. Previous heat transfer studies of impinging gas jets were mainly focused on gas jet/solid surface interactions (Martin, 1977). A single gas jet or an array of such jets, impinging normally on a surface, have been used to achieve enhanced coefficients for convective cooling, heating, or drying. Huang and El-Genk (1994) have reviewed the past work in this area. Although most of the investigators considered flat surfaces, some investigators considered curved solid surfaces as well. Hrycak (1982), for example, studied the heat transfer of a gas jet impinging on a concave hemispherical plate. It was found that the total heat transfer from a concave surface is higher than that from a flat surface because of the larger surface area for the same diameter. There have been several experimental investigations of the fluid mechanics of gas-jet/liquid bath and liquid-jet/liquid bath interaction. For example, Maatsch (1962) and Banks and Chandrasekhara (1963) performed experiments with an air jet impinging on a liquid bath and Cheslak et al. (1969) conducted measurements of liquid surface deformation for a gas jet impinging on water and fast setting cement. Wakelin (1966) observed the interactions between air and CO₂ jets on the surfaces of water and mercury. Olmstead and Raynor (1963) studied the depression of an infinite liquid surface by an incompressible liquid jet. In their study, a conformal mapping method and finite Hilbert transforms were used to formulate the problem as a nonlinear singular integral equation. The study was limited to small angle depressions in the liquid surface and a two-dimensional potential jet. Banks and Bhavamani (1965) studied the phenomenon of a liquid jet impinging normally on the surface of a heavier immiscible liquid. In essence, the work was continuation of the earlier work (and Banks

and Chandrasekhara, 1963) which involved an air jet impinging on a water surface. An analytical model was presented which related the velocity of the jet in the neighborhood of the interface to the depth of cavity created by the jet. The effect of interfacial tension was taken into account. Specifically an oil jet impinging on water and a water jet impinging on carbon tetrachloride were studied. Cavity depths and cavity lip-heights were measured with a vertical-traverse telescope mounted close to the test basin. In a later study, gas phase mass transfer on top-blown liquid surfaces was reported by Dai and Warner (1992). Studies of gas phase mass transfer between top-blown gas jets and liquid surfaces in the non-splashing mode were carried out using room temperature processes: absorption of ammonia from an ammonia-air jet into hydrochloric acid solution and evaporation of water with a single and multiple air jet(s). The effects of jet dynamic conditions and geometric factors of the systems on the mass transfer were studied.

The bath circulation and jet/bath interaction have also recently been studied both numerically and computationally for an air/water model (Qian et al., 1996). The velocity fields in the gas and liquid regions were computed and the predicted deformed interface was compared with experimental measurements. The predicted deformed liquid surface profiles were also compared with the relation given by Cheslak et al. (1969). The heat transfer that occurs between an air jet and a silicone oil liquid bath was also reported recently (Qian et al., 1995). Good agreements between the measured and predicted temperature distributions in the liquid bath was demonstrated. Both the model predictions and the experimental measurements showed that the cooling effect increased with high jet flows.

An air-jet-induced transport in a heated liquid bath is considered in the present paper. The overall objective of the research project was to provide fundamental understanding of the jet impingement flow and heat transfer induced in the heated liquid bath. Both computational and experimental studies were carried out to quantify the interfacial transport and dynamics along with bulk flows in the liquid bath and the jet. Two different substances having widely different Prandtl numbers (silicone oil and a molten metal alloy, Amalloy-203®) were used as the bath liquid. The mixing and thermal behavior of the heated bath were determined as functions of the air jet characteristics (Reynolds number) and bath liquid properties (liquid Prandtl number and a bath Grashof number). The numerical calculations considered the jet flow as well as the shear and buoyancy-induced flows in the liquid bath. An iterative nu-

Contributed by the Heat Transfer Division for publication in the JOURNAL OF HEAT TRANSFER and presented at '96 IMECE. Manuscript received by the Heat Transfer Division, Mar. 13, 1998; revision received, Dec. 2, 1998. Keywords: Heat Transfer, Impingement, Interface, Jets, Two-Phase. Associate Technical Editor: J. Howell.

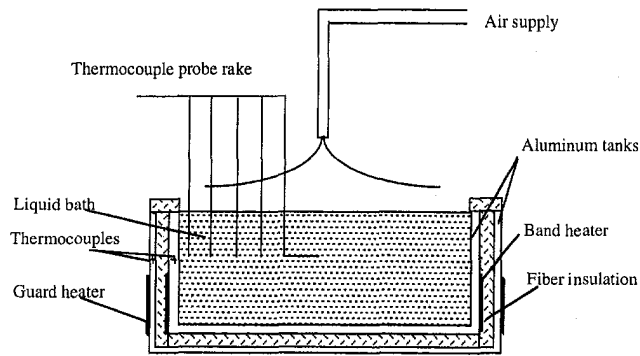


Fig. 1 Schematic of the experimental facility

merical scheme was developed such that the deformed liquid surface was predicted simultaneously along with the jet flow field and the flow field in the liquid bath. The measurements were carried out for varying jet Reynolds numbers ($0 < Re < 10,800$) where the volumetric flow rate was varied ($0\text{--}5.1 \text{ SCMH}^1$). The nozzle diameter and the distance from the nozzle exit to the undisturbed liquid surface was held constant for all cases reported. For the temperature range considered in this study (heated bath), the Prandtl number range of the bath liquids ranged from 0.093 to 910. For the heating conditions considered, the "bath Grashof number" (defined in a later section) ranged from 900 to 3000 for the silicone oil and 3×10^6 to 8×10^6 for the molten metal alloy.

Experimental Set-up

The experimental apparatus is shown in Fig. 1. An axisymmetric gas jet was considered along with a cylindrical liquid bath. The gas jet has sufficient momentum to indent the liquid surface. The induced flow in the liquid bath is driven by the shear stress along the interface. As in Dai and Warner (1992), only the nonsplashing mode was considered in the present study. The liquid was held in a thick-walled metallic (aluminum) cylindrical vessel. A band heater was used to heat the bath liquid. The bath (inner) diameter is 18.0 cm and the depth is 5.0 cm. The vessel was surrounded by ceramic insulation. The vessel and the insulation were placed

Table 1 Experimental parameters for air and the liquids

(a) Air-jet characteristics		
Jet diameter	1.2 cm	
Jet height	5.0 cm	
Volumetric flow (at 25°C)	0.0–5.1 SCMH	
Reynolds number (at 25°C)	0–10,800	
(b) Liquid properties at 110°C		
	Silicone oil	Amalloy-203®
Density	900 kg/m ³	9850 kg/m ³
Viscosity	0.096 N s/m ²	0.01 N s/m ²
Specific heat	1.47 kJ/kg °C	0.15 kJ/kg °C
Thermal conductivity	0.155 W/m °C	16.2 W/m °C
Coefficient of thermal expansion	$0.23 \times 10^{-3}/K$	$0.36 \times 10^{-4}/K$
Prandtl number	910	.093

inside another container which was also equipped with a band (guard) heater. To prevent heat transfer from the lip of the aluminum bath, a layer (1.0 cm thick) of ceramic insulation was placed along the rim of the vessel, flush with the inner wall (see Fig. 1). The thick aluminum wall of the vessel and the presence of the ceramic insulation and the outer vessel resulted in a nearly isothermal boundary condition for the bath wall (for both the side and the bottom walls) with a maximum variation in temperature of ± 5 percent about the mean value. Thermocouples were used to determine the local and bulk temperature in the fluid as well as the wall temperatures. The air jet (at ambient temperature) impinges on the liquid bath. Heat transfer data were collected to characterize the process and determine the overall heat transfer coefficient U_{avg} . These measurements were then compared with the computational model (described in the next section) predictions. A summary of the gas jet and the bath liquid parameters is given in Table 1.

Numerical Model

A computational fluid dynamic model was developed for solving the gas-phase and liquid-phase flow and temperature fields along with the interface profile prediction. The following assumptions are made in the model:

- 1 The gas jet and liquid bath are axisymmetric.

¹ Standard cubic meters per hour.

Nomenclature

A = exposed liquid surface area
 $b(r)$ = top boundary function for the curved computational domain
 c_1 = liquid bath specific heat
 $c_1\text{--}c_3$ = geometric relations between coordinate systems
 d_j = diameter of the jet nozzle
 $f(r)$ = bottom boundary function for the curved computational domain
 g = acceleration due to gravity
 Gr' = Grashof number for the bath ($Gr' = g\beta(T_w - T_\infty)H_l^3/\nu_l^2$)
 $h(r)$ = heat transfer coefficient
 H_l = undisturbed liquid bath depth
 J = Jacobian of the inverse coordinate transformation
 k_l = bath liquid thermal conductivity
 k_g = jet gas thermal conductivity
 Nu = interfacial Nusselt number ($Nu = U_{avg}d_j/k_l$)

$q(r)$ = heat transfer per unit area
 Q = total heat transfer
 Pr = bath liquid Prandtl number ($Pr = \mu_l c_p / k_l$)
 R = radius of the vessel
 r = radial coordinate
 Re = jet Reynolds number, ($Re = V_j d_j / \nu_g$)
 S = source term in the governing equation
 T = temperature
 T_b = average liquid bath temperature
 T_j = gas jet-exit temperature
 T_s = gas-liquid interface temperature
 T_w = bath wall temperature
 T_∞ = ambient temperature
 u = radial component of velocity
 U = contravariant velocity in ξ -direction
 U_{avg} = overall heat transfer coefficient at the interface

v = axial component of velocity
 V = contravariant velocity in η -direction
 V_j = average jet velocity at nozzle exit
 z = vertical coordinate

Greek Symbols

ξ, η = axes of curvilinear coordinates
 Γ = generalized diffusion coefficient
 ϕ = generalized dependent variable
 ν_g = gas kinematic viscosity
 ν_l = liquid kinematic viscosity
 μ_l = liquid absolute viscosity
 β = coefficient of thermal expansion of liquid

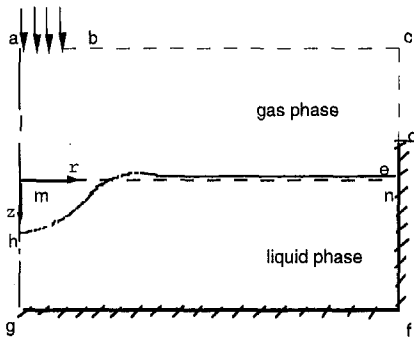


Fig. 2 Schematic of the computational domain for the gas and liquid phases

2 The deformation of the liquid surface is caused by the static pressure of the jet at the local liquid surface.

3 The effects of surface tension and shear stress on the interface shape are assumed negligible.

4 An unbroken liquid surface (nonsplashing mode) is considered in this analysis. This assumption is valid for moderately high speed jets.

The studies by Cheslak et al. (1969) and our past experiments (1996) confirm the validity of the above assumptions. The computational domains for the gas and the liquid phases are shown in Fig. 2. Only one-half of the flow domain (see Fig. 1) needs to be considered for calculation purposes due to symmetry. The gas and liquid phases are divided initially by the undisturbed liquid surface "mn." The liquid surface is deformed by the impinging jet and the final liquid surface is shown by the line "he" in Fig. 2.

The Navier-Stokes equations along with a low Reynolds number $k-\epsilon$ turbulence model (Abe et al., 1994) and the energy equation are used to describe the turbulent impinging gas jet. The liquid-phase flow is considered to be laminar and is also described by the Navier-Stokes equations. Both the gas jet and the liquid pool are treated as incompressible fluids. In the $r-z$ coordinates, the steady-state form of the governing differential equations for momentum, turbulent kinetic energy, and dissipation rate of turbulence can be cast into a general form as

$$\frac{1}{r} \frac{\partial}{\partial r} (r \rho u \phi) + \frac{\partial \rho v \phi}{\partial z} = \frac{1}{r} \frac{\partial}{\partial r} \left(\Gamma r \frac{\partial \phi}{\partial r} \right) + \frac{\partial}{\partial z} \left(\Gamma \frac{\partial \phi}{\partial z} \right) + S \quad (1)$$

where ϕ is a generalized dependent variable (representing u , radial velocity; v , axial velocity; T , temperature; k , turbulent kinetic energy; and ϵ , dissipation rate of turbulence). In the above equation, Γ is a general diffusion coefficient and S is a source term corresponding to each dependent variable (Qian, 1996). For the liquid phase, the generalized variable ϕ only represents the u , v , and T variables.

The turbulence model (Abe et al., 1994) uses the Kolmogorov velocity scale instead of the friction velocity to account for the near wall and low Reynolds number effects. The Kolmogorov velocity scale does not become zero either at the separating nor at the reattaching points in contrast to the friction velocity. Besides this major modification of the model functions, Abe et al. reevaluated the turbulence model constants in the transport equations for the turbulent energy and its dissipation rate for improvements in overall accuracy. In the present work, the turbulence model constant values are the same as reported in Abe et al.

The impingement of the gas jet causes the liquid surface to deform. A body-fitted nonorthogonal curvilinear coordinate system was used to accommodate the curved interface in the solution domain (Karki and Patankar, 1989). The physical regions of interest for the gas and the liquid phases are transformed into

rectangular regions in (ξ, η) coordinates. The transformation equations are introduced as

$$r = \xi$$

$$z = \eta[b(\xi) - f(\xi)] + f(\xi)$$

or

$$\xi = r$$

$$\eta = \frac{z - f(r)}{b(r) - f(r)} \quad (2)$$

where $b(r)$ is the top boundary function describing the geometry of the top boundary and $f(r)$ is the bottom boundary function for a given computational domain. The bottom boundary function for the gas-phase domain is the top boundary function for the liquid-phase domain. In the (ξ, η) coordinates, the governing equation (for the generalized dependent variable ϕ) may be rewritten as

$$\begin{aligned} & \frac{1}{J\xi} \frac{\partial}{\partial \xi} (\xi \rho U \phi) + \frac{1}{J} \frac{\partial}{\partial \eta} (\rho V \phi) \\ & = \frac{1}{J\xi} \frac{\partial}{\partial \xi} \left[\xi \frac{\Gamma}{J} \left(c_1 \frac{\partial \phi}{\partial \xi} - c_2 \frac{\partial \phi}{\partial \eta} \right) \right] \\ & \quad + \frac{1}{J} \frac{\partial}{\partial \eta} \left[\frac{\Gamma}{J} \left(c_3 \frac{\partial \phi}{\partial \eta} - c_2 \frac{\partial \phi}{\partial \xi} \right) \right] + S \quad (3) \end{aligned}$$

where $U = u(\partial z / \partial \eta)$ (contravariant velocity in the ξ -direction)

$$\text{and } V = v - u \frac{\partial z}{\partial \xi}$$

(contravariant velocity in the η -direction).

The coefficients c_1-c_3 appearing in Eq. (3) are given as

$$c_1 = \left(\frac{\partial z}{\partial \eta} \right)^2, \quad c_2 = \frac{\partial z}{\partial \xi} \frac{\partial z}{\partial \eta}, \quad c_3 = 1 + \left(\frac{\partial z}{\partial \xi} \right)^2$$

and

$$J = \frac{\partial z}{\partial \eta} \quad (\text{Jacobian of the inverse coordinate transformation}).$$

The projections of the velocity vector along the grid lines are chosen as the dependent variables U and V . The discretized equations for these velocity components are obtained by an algebraic manipulation of the corresponding equations for cylindrical coordinate velocity components. Details of this method can be found in Karki and Patankar (1989) and Qian (1996).

The gas and liquid-phase domains (as shown in Fig. 2) are coupled via continuity of pressure, velocity, shear stress, temperature, and heat transfer along the gas/liquid interface (assuming no evaporation of the liquid phase due to gas-jet impingement). The conditions for the dependent variables in the above governing equations must be defined along the boundaries of the computational domain shown in Fig. 2 for both the gas and the liquid phases. The gas-phase domain is given by "h-e-d-c-b-a-h." The jet velocity profile is given as the 1/7th power-law distribution along the boundary "ab." A constant temperature (T_j) boundary condition is applied along "ab." Along the far-field boundary "cd," zero radial gradients for all variables are specified. No-slip boundary conditions are specified along the boundary "de" as it is part of the liquid vessel. Zero heat flux boundary condition is used along "de." Along the open boundary "bc," the gradient of the radial velocity is given as zero and zero axial velocity is specified. Constant temperature (T_w) boundary condition is applied along "bc." Symmetry boundary conditions are used along "ha" for the gas-phase domain. The liquid-phase domain is given by "h-e-f-g-h." Zero velocities and specified temperature (T_w) are specified along the wall of the vessel "efg" and zero heat and mass flux at

the axis of symmetry “*ag*.” The interface boundary “*he*” is common to both the gas and the liquid phases. Specifying boundary conditions along the gas-liquid interface (along with the prediction of its shape) is challenging. A novel solution method was developed for specifying the boundary conditions at the interface along with the prediction of the deformed interface. The method allows the gas-phase and liquid-phase flow domains to be solved simultaneously. The iterative solution method developed can be summarized as follows:

- (i) The gas-phase flow-field computation is initiated with a flat and motionless interface (line “*mn*”).
- (ii) The flat interface is assumed to be rigid and insulated. The pressure, temperature, and shear stress at the surface can then be calculated.
- (iii) The interface shape is then calculated by considering that the pressure at the (gas side) interface causes the indentation on the interface.
- (iv) A new grid is generated for the gas-phase and liquid-phase flow domains.
- (v) The liquid-region flow field is then calculated with the new interface shape, the interfacial shear stress and temperature distribution at the interface. This allows the determination of the velocity and heat flux at the interface.
- (vi) The flow field of the gas jet region is then recalculated with updated interfacial heat flux, interface velocity, and shape. The pressure, temperature, and shear stress distributions at the interface are now recalculated. Wall boundary conditions (Abe et al., 1994) are used for k and ϵ along the gas-liquid interface.
- (vii) This sequence of computational steps (i)–(vi) is continued until converged solutions are reached for both the gas and the liquid phases.

The above governing equations along with the boundary conditions were solved by a control-volume-based finite difference approach in the curvilinear coordinates. The procedure is based on the SIMPLE algorithm with the hybrid scheme. Nonuniform meshes were used for effectively capturing the steep gradients in the interface region. When the relative change in variables between consecutive iterations was less than 10^{-3} , the convergence was assumed to have been reached. The predictions reported here are nearly grid-independent based upon a grid-size variation (± 50 percent) study. Typical mesh size used was 80×50 ($r \times z$) for both the gas-phase and the liquid-phase regions. The parameters of interest (maximum depression of the free surface, average temperature of the liquid bath, etc.) predicted with the mesh used are within three percent of the grid-independent solutions. All computations were performed on an IBM-RISC-6000 (Model 360) workstation. Typical computation time ranged from 600 to 200 minutes for the combined gas and liquid-phase computations.

The accuracy of the code was assessed by first obtaining predictions for a gas jet impinging upon a rigid surface. Huang and El-Genk (1994) measured heat transfer characteristics for a constant wall heat-flux rigid plate subjected to an impinging gas jet. Predictions of the local Nusselt number as a function of the radial location (for $Re = 6000$ and $H/d_j = 6$) agreed well with the measurements (Qian et al., 1995). Further validation of the computational scheme for the prediction of the deformed free surface was obtained via the measurement of the deformed surface (Qian et al., 1996). Both photographic and probe (electroresistive) measurements of the deformed gas-liquid interface were compared with the numerical predictions. The predicted profiles of the deformed interface were also compared with the relation suggested by Cheslak et al. (1966).

Results and Discussion

Both numerical computations and experimental measurements were done for the air jet/liquid bath interaction studies where silicone oil and a molten metal alloy were used as the bath liquid. The jet nozzle diameter and the distance between the jet nozzle and

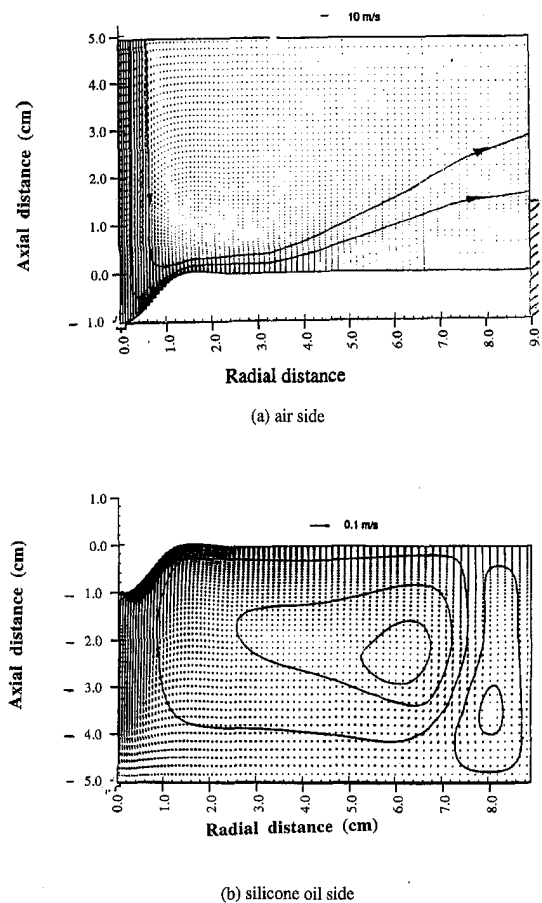


Fig. 3 Computed velocity fields in the air jet and the silicone oil bath, jet $Re = 10,800$, bath wall temperature = $127^\circ C$

the undisturbed liquid layer (see Table 1(a)) were held fixed for all computations and measurements reported in this paper. The jet Reynolds number was varied between 0 and 10,800 for both bath fluids at different heat inputs (correspondingly at different bath wall temperatures).

Computational Studies. For the computational studies, the jet-exit and the gas-phase ambient temperatures were both considered to be $25^\circ C$. The heated bath wall was considered to be isothermal. The dimensions of the liquid bath, jet nozzle diameter, etc., were identical to those in the experimental set-up described earlier. The interface shape and the temperature distribution along the interface were predicted along with flow and temperature fields in the gas-phase and the liquid-phase regions. Solutions were obtained for an air jet impinging on a bath partially filled with either silicone oil or a molten metal alloy. This aspect of the geometry was explicitly considered in the computational model.

Figures 3 show the velocity fields in the silicone oil bath where the jet Reynolds number was 10,800 and the bath wall temperatures was held at $127^\circ C$. Only one-half of the flow domain is shown in the figure due to symmetry. The flow field is driven by both shear and buoyancy forces. The gas jet impinges on the liquid surface, forms a depression and the shear stress along the interface generates the liquid circulation. Since the wall of the vessel has a higher temperature, buoyancy forces also drive the liquid up from the bottom and along the side wall. Thus two vortices are generated in the flow field. Figure 4 shows the jet-induced flow field in the molten metal bath for the same jet Reynolds number. The bath wall (both bottom and side) temperatures were held constant at $123^\circ C$. The wall temperatures were based on a total heat input of 100 W into the bath. For the silicone oil, the jet momentum causes a much more pronounced depression than for the molten metal

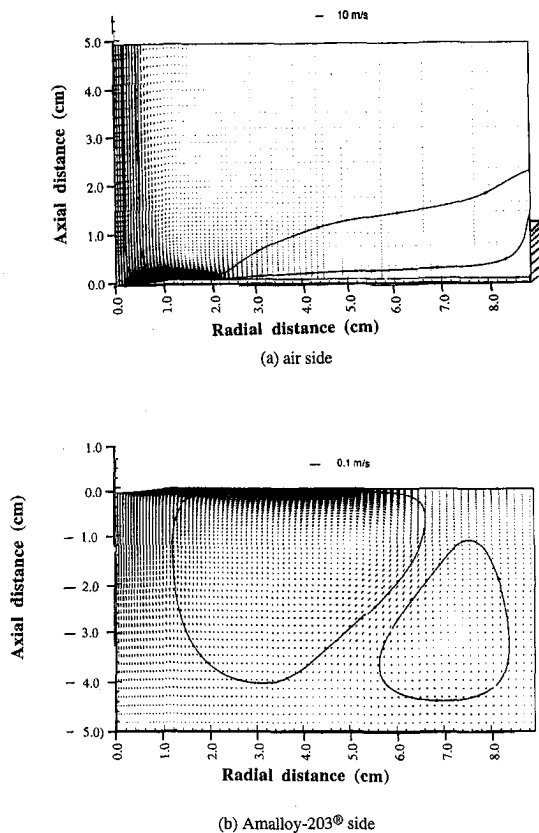


Fig. 4 Computed velocity fields in the air jet and the Amalloy-203[®] bath, jet $Re = 10,800$, bath wall temperature = $123^{\circ}C$

alloy. This is due to the large density difference between the two fluids. The shear driven vortex in the silicone oil case is larger than the corresponding vortex in the alloy case, suggesting that the displacement of the fluid perhaps contributes to the fluid motion. The density of the oil is about ten times lower and its viscosity approximately nine times greater in comparison to the alloy. The buoyancy-induced vortex (the one near the wide wall) is thinner and stronger for the silicone oil case than the molten metal alloy case due to the differences in thermal conductivities of the two liquids. The temperature gradients in the fluid and associated flow due to buoyancy contribute to the size of this vortex.

Figures 5 and 6 show the temperature fields for the liquid bath for the flows illustrated earlier. Temperature gradients are caused

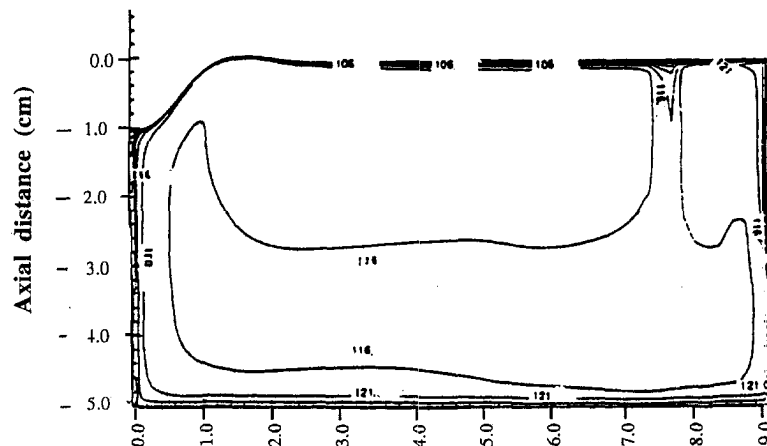


Fig. 5 Computed temperature contours in the silicone oil bath, jet $Re = 10,800$, bath wall temperature = $127^{\circ}C$

by forced convection at the gas/liquid interface and the buoyant convection in the liquid due to the heated bottom and vertical walls. In our calculations, (see domain "h-e-f-g-h" in Fig. 2), isothermal boundary conditions have been applied for the walls "e-f-g." For computational ease, the adiabatic strip "ed" was assumed to be just above the liquid surface. Jet cooling is much more effective in the alloy as compared to the oil. This is due to the fact that the alloy thermal conductivity is approximately 100 times larger than that of the oil. Figures 3–6 also illustrate the effect of Prandtl number. The oil has a high Prandtl number, with higher viscosity while the alloy has a low Prandtl number with higher thermal diffusivity.

Figure 7 shows the computed local heat transfer coefficients for both gas side and liquid side for the case described earlier in Figs. 3 and 5. Here we define a local heat transfer coefficient at the gas side based on the difference between the jet and liquid surface temperature as follows:

$$h_g(r) = \frac{q(r)}{[T_j - T_s(r)]} \quad (4)$$

The local heat transfer coefficient at the liquid side is defined as

$$h_l(r) = \frac{q(r)}{[T_s(r) - T_b]} \quad (5)$$

The local heat flux $q(r)$ along the interface was calculated from the local temperature gradients normal to the interface for the air and liquid sides. The maximum local heat transfer coefficients are at the stagnation point at the center ($r = 0$). The heat transfer coefficients decreased rapidly with distance from the center. The minimum heat transfer occurs where the two vortices (driven by the buoyancy force and the jet shear stress force) meet. The heat transfer coefficient on the liquid side is four to five times larger than that on the gas side. The increase in $h_g(r)$ beyond $r = 0.07$ m is due to the combined effect of the buoyancy-induced vortex and the insulated wall which extends above the liquid level (see Fig. 1). The extension was considered in the gas-phase computational domain (see Fig. 2).

Figure 8 shows the local heat transfer coefficients in both air and Amalloy-203[®] for the case described in Figs. 4 and 6. The maximum local heat transfer coefficients occur, as expected, at the stagnation point. The lowest heat transfer on the liquid side occurred where the two vortices (driven by the buoyancy force and the jet shear stress force) meet. The heat transfer coefficient on the liquid side was four to six times larger than on the gas side. The variation of the heat transfer coefficients along the radial direction is similar to that shown in Fig. 7.

The overall heat transfer coefficient U_{avg} at the interface can be

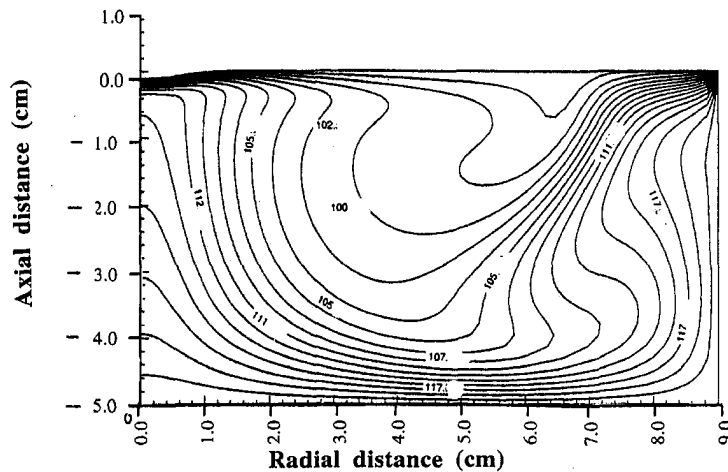


Fig. 6 Computed temperature contours in the Amalloy-203[®] bath, jet Re = 10,800

calculated by using both local heat transfer coefficients of the liquid side and gas side:

$$U_{avg} = \frac{2}{R^2} \int_0^R \frac{r}{\frac{1}{h_g(r)} + \frac{1}{h_l(r)}} dr \quad (6)$$

The detailed derivation of Eq. (6) can be found in Qian (1996). The overall heat transfer coefficient (for the computed results shown on Fig. 6) is $U_{avg} = 47 \text{ W/m}^2\text{°C}$ for the silicone oil case. For the molten alloy case (Fig. 7), $U_{avg} = 54.0 \text{ W/m}^2\text{°C}$. The overall interfacial heat transfer can be expressed as

$$U_{avg} = \frac{Q}{A(T_b - T_j)} \quad (7)$$

where A is the exposed liquid surface area. It is noted that for the silicone case (Fig. 3), the free surface deformation is much larger—resulting in larger surface area. Previous studies (Cheslak et al., 1969) have shown that the deformed surface results in increased total heat transfer.

Experimental Studies. As indicated in Table 1, geometric parameters, including bath diameter and depth as well as jet distance were held constant. The jet Reynolds number varied from 0 (free convection only) to 10,800 and the adjustable heat input to the bath provided a range in bath wall temperatures. The thick-walled aluminum bath provided isothermal wall temperatures for given heat inputs.

Figures 9 and 10 compare measured and predicted values of liquid bath temperatures at a fixed radial distance in the silicone oil and metal alloy baths respectively. Note that the bulk temperature of the alloy is approximately 10 deg lower than the silicone oil for nearly identical experimental conditions. The thermocouple diameter was about 0.8 mm and hence the local temperature in the boundary layer near the bottom surface could not be accurately measured. For the measurements at the free surface, the thermocouple was positioned just below the surface. The agreement between the numerical results and the experimental data shown in the figures is very good, particularly in the bulk of the fluid. The thermocouple system was calibrated and the uncertainty in temperature was estimated as $\pm 0.5^\circ\text{C}$ at 100°C . The precision in depth measurement was $\pm 0.5 \text{ mm}$. Experimental uncertainties were calculated using the procedure outlined by Kline and McClintock (1953).

Figure 11 illustrates the variation of the measured overall heat transfer coefficient, U_{avg} , with jet flow at different heat inputs. The maximum flow rate of 5.1 SCMh corresponds to the jet Reynolds number of 10,800. The experimental uncertainty in heat transfer coefficient varied from four to eight percent and the uncertainty in flow was 6–14 percent. At no jet flow, the circulation in the bath is entirely buoyancy induced and the heat transfer at the interface is due to free convection only. The heat transfer across the interface (supplied heat along the bath wall) is dependent on the heat transfer coefficient, the temperature difference between the liquid surface and the jet (fixed at 25°C), and the area of the interface.

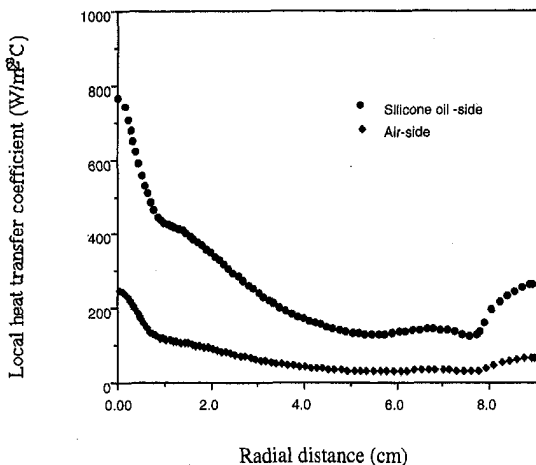


Fig. 7 Computed heat transfer coefficients for the air jet side and the silicone oil side; jet Re = 10,800, bath wall temperature = 127°C

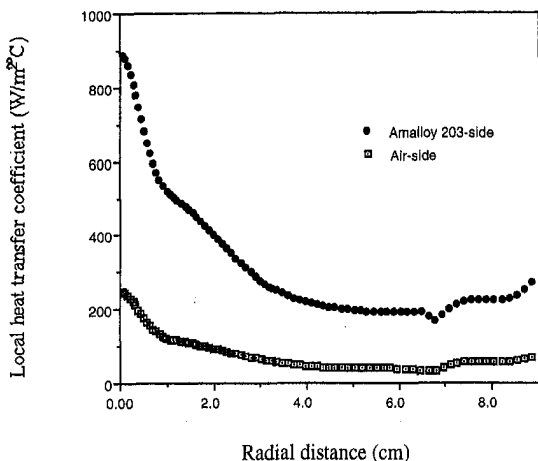


Fig. 8 Computed heat transfer coefficients for the air-jet side and the Amalloy-203[®] side; jet Re = 10,800, bath wall temperature = 123°C

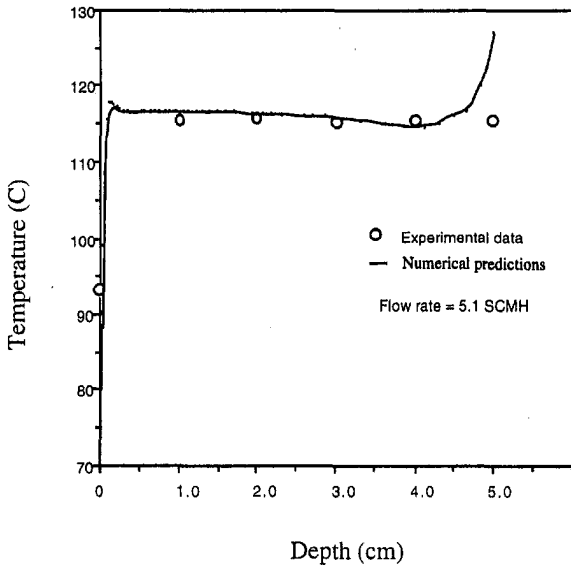


Fig. 9 Comparison of measured and computed temperature distribution in the silicone oil bath at a radial distance = 2.7 cm, $Re = 10,800$, bath wall temperature = $127^{\circ}C$ (heat input = 100 W)

The variation of the area of the interface and the temperature difference between the liquid surface and the jet ambient is highly nonlinear with jet velocity. This explains the crossover of the 100 W curve and the 50 W curve for jet flow higher than 3.5 SCMH in Fig. 11.

The mixed free and forced convection at lower Reynolds numbers combine to increase the heat transfer coefficient significantly. At higher jet flows (for a given heat input), the heat transfer coefficient approached a relatively constant maximum value. The higher values of U_{avg} at 50 W input in the high flow region is perhaps due to the reduced relative significance of free convection at low wattage. It is also shown in Fig. 11 that $U_{avg} = 44 \text{ W/m}^2\text{C}$ at jet flow value of 5.1 SCMH ($Re = 10,800$) for the case where the total heat input is 100 W. This is very close to the calculated value of $47 \text{ W/m}^2\text{C}$ reported earlier. Figure 12 illustrates the variation of the measured overall heat transfer coefficient U_{avg} with jet flow for different heat inputs for the air jet/molten alloy cases. The heat transfer coefficient increased as the jet flow was in-

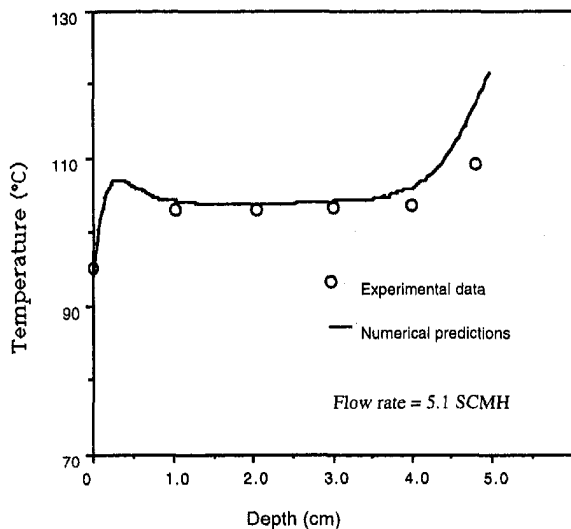


Fig. 10 Comparison of measured and computed temperature distribution in the Amalloy-203[®] bath at a radial distance = 2.7 m, $Re = 10,800$, bath wall temperature = $123^{\circ}C$ (heat input = 100 W)

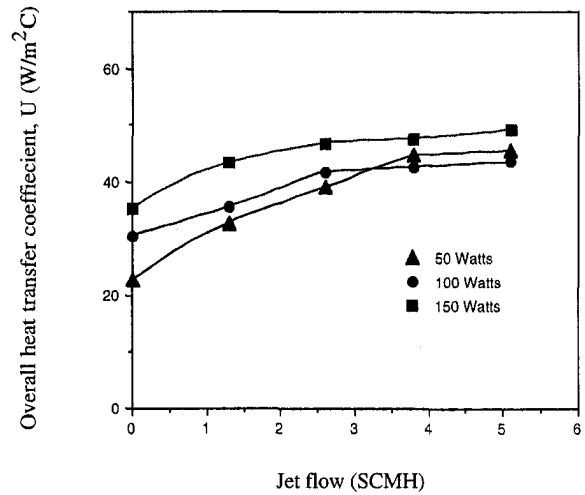


Fig. 11 Measured overall heat transfer coefficient (U_{avg}) as functions of gas flow rate and input heat for air-jet/silicone oil bath

creased. The rate of increase, however, was greater at the low flow range than at the higher flow range. The figure also shows that $U_{avg} = 51 \text{ W/m}^2\text{C}$ at flow rate of 5.1 SCMH ($Re = 10,800$) for a total heat input of 100 W. This is again very close to the calculated value of $54 \text{ W/m}^2\text{C}$ reported earlier.

Correlation for Overall Interfacial Heat Transfer Coefficient. The experimental data were used to develop a correlation predicting the heat transfer between an impinging gas jet and a liquid bath for the range of parameters considered in this investigation. The parameters considered for the correlation are the jet Reynolds number, the liquid Prandtl number, a "bath Grashof number," and the interfacial Nusselt number where the bath Grashof number and the interfacial Nusselt number are defined as follows:

$$Gr' = \frac{g\beta(T_b - T_{\infty})H_l^3}{\nu^2}$$

$$Nu = \frac{U_{avg}d_j}{k_l}$$

For the present interfacial (gas/liquid) heat transfer problem, $Nu = f(Re, Gr', Pr)$. The parameters effectively capture the coupled nature of the heat transfer process at the interface due to a gas jet impingement at the liquid bath at moderately high Re . It is also

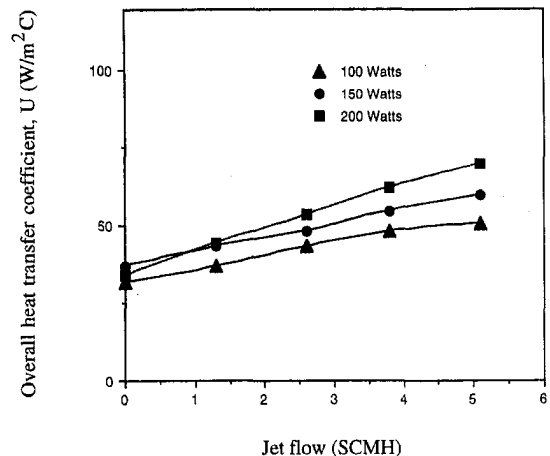


Fig. 12 Measured overall heat transfer coefficient (U_{avg}) as functions of gas flow rate and input heat for air jet/molten alloy bath

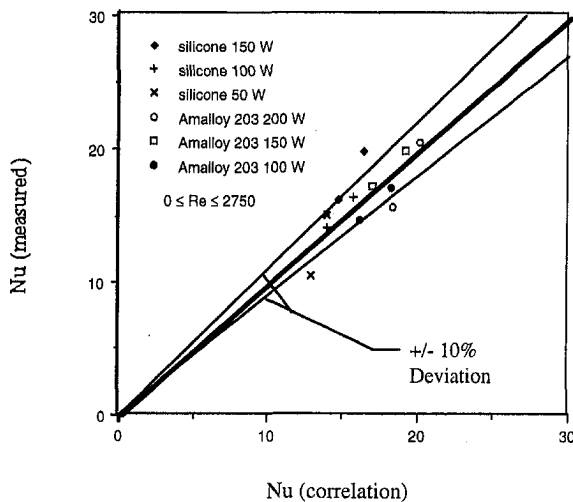


Fig. 13 Parity plot showing degree of correlation of experimental data; $0 < Re < 2700$

noted that for the present studies, the ambient and jet exit temperatures were the same for all cases studied.

Using standard curve fitting techniques, an empirical correlation was found as follows:

$$Nu = \begin{cases} 0.178 (4.85 + Re^{0.01}) Gr'^{0.2} Pr^{0.16} & 0 \leq Re \leq 2750 \\ 0.025 (16.7 + Re^{0.4}) Gr'^{0.2} Pr^{0.16} & 2750 < Re < 10,800. \end{cases}$$

The above correlation uses three independent parameters (Re , Gr' , Pr) to correlate 12 data points distributed by two Re , two Pr , and several heating levels (Gr'). Despite the paucity of the data points, the correlation clearly indicate the roles of the jet Re , the Gr' , and the liquid Pr in determining heat transfer from the liquid bath due to gas jet impingement. Figures 13 and 14 are parity plots showing the degree of correlation of data. Figure 13 is for Re between 0 and

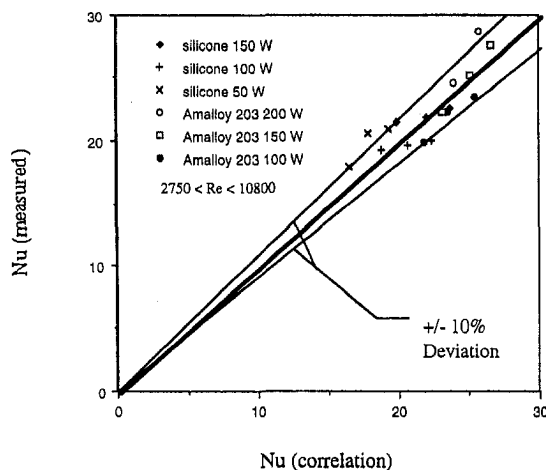


Fig. 14 Parity plot showing degree of correlation of experimental data; $2750 < Re < 10,800$

2750 and Fig. 13 is for Re between 2750 and 10,800. Experimental uncertainty in the measured and correlated Nusselt numbers were six to nine percent. The figures show that the correlation represents 90 percent of the experimental data within ± 10 percent of the measured values. Thus the empirical correlation is a reasonably good fit of the data.

Conclusions

The heat transfer results for cooling two different kinds of liquid baths (silicone oil and liquid Amalloy-203[®]) using air jets have been reported. The bath geometry and jet distance have been held constant with the jet flow and bath wall temperature varying over given ranges. The computational model indicated that bath heat transfer was a result of both forced convection from the jet and natural convection caused by the buoyancy force. For air/silicone oil or air/liquid Amalloy-203[®] system, it is seen that the heat transfer coefficient on the liquid side was several times larger than on the air-jet side. Therefore the air side heat transfer is the rate controlling parameter in this system. Fluid properties have a substantial effect on the velocity and temperature distributions in the bath. There was good agreement between the numerical model and the experiments. An empirical correlation was developed for predicting heat transfer due to an gas jet impinging on a liquid bath. It represents the interaction between forced and free convection for the current range of experiments and can perhaps be extended to describe heat transfer in other jet cooling problems.

References

- Abe, K., Kondoh, T., and Nagano, Y., 1994, "A New Turbulence Model for Predicting Fluid Flow and Heat Transfer in Separating and Reattaching Flows—I. Flow Field Calculations," *Int. J. Heat Mass Transfer*, Vol. 37, No. 1, p. 139.
- Banks, R. B., and Chandrasekhara, D. V., 1963, "Experimental Investigation of the Penetration of a High-Velocity Gas Jet through a Liquid Surface," *J. Fluid Mech.*, Vol. 15, p. 13.
- Banks, R. B., and Bhavamani, A., 1965, "Experimental Study of the Impingement of a Liquid Jet on the Surface of a Heavier Liquid," *J. Fluid Mech.*, Vol. 25, Part 2, p. 229.
- Cheslak, F. R., Nicholls, J. A., and Sichel, M., 1969, "Cavities Formed on Liquid Surfaces by Impinging Gaseous Jets," *J. Fluid Mech.*, Vol. 36, Part 1, p. 55.
- Dai, X., and Warner, N. A., 1992, "Gas Phase Mass Transfer on Top-Blown Liquid Surfaces," *Trans. IChemE*, Vol. 70, Part A, p. 585.
- Hrycak, P., 1982, "Heat Transfer and Flow Characteristics of Jets Impinging on a Concave Hemispherical Plate," *Proceedings of the Seventh International Heat Transfer Conference*, Vol. 3, p. 357.
- Huang, L., and El-Genk, M. S., 1994, "Heat Transfer of Impinging Jet on a Flat Surface," *Int. J. Heat Transfer*, Vol. 37, No. 13, p. 1915.
- Karki, K. C., and Patankar, S. V., 1989, "Pressure Based Calculation Procedure for Viscous Flows at All Speeds in Arbitrary Configurations," *AIAA Journal*, Vol. 27, No. 9, p. 1167.
- Kline, S. J., and McClintock, F. A., 1953, "Describing Uncertainties in Single-Sample Experiments," *Mechanical Engineering*, Vol. 75, pp. 3–8.
- Martin, H., 1997, "Heat and Mass Transfer between Impinging Gas Jets and Solid Surfaces," *Advances in Heat Transfer*, Vol. 13, Academic Press, New York, p. 112.
- Maatsch, J., 1962, "Über das Eindringen eines freien Gasstrahles in eine Flüssigkeitsoberfläche," *Tech. Mitt. Krupp Forsch.*, Vol. 20, p. 1.
- Olmstead, W. E., and Raynor, S., 1963, "Depression of an Infinite Liquid Surface by an Incompressible Gas Jet," *J. Fluid Mech.*, Vol. 19, p. 561.
- Patankar, S. V., 1980, *Numerical Heat Transfer and Fluid Flow*, Hemisphere, Washington, DC.
- Qian, F., Mutharasan, R., and Farouk, B., 1996, "Studies of Deformations in a Liquid Bath due to Direct Impinging Gas Jet," *Metallurgical and Materials Transactions B*, Vol. 27B, p. 911.
- Qian, F., Farouk, B., and Mutharasan, R., 1995, "Numerical Study of Heat Transfer From a Liquid Pool due to an Impinging Gas Jet," *National Heat Transfer Conference*, Portland, OR, ASME HTD-Vol. 306, pp. 51–62.
- Qian, F., 1996, "Transport Processes in Liquid Baths and Gas/Liquid Interfaces due to Impinging Gas and Plasma Jets," Ph.D. thesis, Drexel University, Philadelphia, PA.
- Wakelin, D. H., 1966, "Impinging Gas Jets on Liquid Baths," Ph.D. thesis, Imperial College, University of London.

Local and Instantaneous Heat Transfer Characteristics of Arrays of Pulsating Jets

H. S. Sheriff
Graduate Assistant.

D. A. Zumbrunnen¹
Professor,
Mem. ASME.

Department of Mechanical Engineering,
Clemson University,
Clemson, SC 29634-0921

Recent investigations have revealed that pulsations in an incident jet flow can be an effective technique for modifying convective heat transfer characteristics. While these studies focused on single impinging jets, industrial applications of impinging jets usually involve arrays of jets. To explore the effects of flow pulsations on the heat transfer performance of jet arrays, an experimental investigation has been performed of instantaneous and time-averaged convective heat transfer to a square, in-line array of circular air jets within a unit cell of the array. Hot-film anemometry was used to document the jet flow field. Instantaneous and time-averaged convective heat transfer rates were measured using a heat flux microsensors. An ensemble averaging technique was used to separate the pulsating component of flow velocity and heat transfer from the turbulent components and thereby assess the effect of flow pulsation on turbulence intensity and heat transfer. For the ranges of parameters considered, results indicate convective heat transfer distributions become more uniform in response to pulsations but heat transfer is not enhanced. Improved uniformity can be a useful aspect in many jet applications.

Introduction

Impinging jets are often formed into arrays in efforts to duplicate the effect of a single jet over large surface areas. A concern in these applications is the uniformity of heat or mass transfer rates on the impingement surface in order to avoid hot or cold spots or regions where moisture is not effectively removed. Because convective heat and mass transfer distributions of impinging jets are inherently nonuniform, designers must add additional jet rows or increase fluid expenditures to ensure that cooling, heating, or drying is adequate. Research with *single* air or unsubmerged water jets has demonstrated that convective heat transfer distributions can be enhanced and also be made markedly more uniform by pulsating the incident jet flow (Sheriff and Zumbrunnen, 1994; Mladin and Zumbrunnen, 1997). Improved uniformity resulted from reductions in time-averaged heat transfer coefficients within the stagnation region due to thickening thermal boundary layers on average in response to time-varying incident flow velocities. Enhancements occurred downstream due to early transition and the influence of coherent flow structures formed as a result of pulsations. These results provided motivation for the present work where the effect of flow pulsations on heat transfer to an array of air jets is assessed experimentally.

Insights into mechanisms that can alter heat or mass transfer within the stagnation region of impinging jets can be gained from other flows where stagnation regions are formed. Enhancement of stagnation region convective heat transfer due to free stream turbulence was studied by Hargrave et al. (1985) for a hemispherical end of a cylindrical body of revolution. Visualization revealed a repeated sequence of vortex formation, growth, and disintegration in the vicinity of the stagnation point. A phenomenological model ascribing enhanced convective heat transfer to the random penetration of free stream vortices into the laminar boundary layer was found to represent well experimental results for free-stream turbulence intensities less than 15 percent and Reynolds numbers based on the diameter of

the hemisphere between about 5900 and 10,500. Van Fossen and Simoneau (1987) studied heat transfer from the stagnation region of a cylinder in a cross flow to determine the effect of free-stream turbulence. Simultaneous smoke-wire flow visualization and heat transfer measurements using liquid crystals were performed for turbulence generated using an array of parallel wires oriented perpendicular to the cylinder axis. Pairs of counterrotating vortices formed near the stagnation region on the cylinder but were well outside the theoretical laminar boundary layer. Heat transfer was found to be maximum where the induced velocity due to the vortex pairs was directed toward the cylinder.

Vortical structures in single air jets impinging on a flat plate and developed in a contoured circular nozzle have been observed beyond the hydrodynamic boundary layer using smoke-wire flow visualization (Popiel and Trass, 1991). Reynolds numbers, based on the diameter of the nozzle opening, were 5000, 10,000 and 20,000. The impingement of the vortical structures induced small, secondary vortices near the surface. Similar secondary vortical structures were also observed by Fox et al. (1993). They pointed out that the secondary vortices were formed due to boundary layer separation resulting from unsteady adverse pressure gradients induced by the impinging primary vortices. Secondary vortices were not formed for nozzle-to-impingement surface spacings greater than six nozzle diameters. Because of their direct association with the boundary layer, convective heat or mass transfer rates to jets likely depend appreciably on the characteristics of incident vortices developed due to shear layer instabilities within the jet itself. It is noteworthy here that flow pulsations may promote and influence the formation of these flow structures (Glezer, 1988; Hura et al., 1994). In film cooling of gas turbine blades, blade motion relative to fixed nozzles leads to static pressure fluctuations and unsteadiness in flows through injection holes (Ligrani et al., 1997). The unsteadiness has been found in low-pulsation frequency experiments to spread injected fluid over larger regions and redistribute Reynolds stresses.

While fine-scale turbulence generated using wire grids is known to enhance stagnation region heat transfer in jet flows (Hoogenboom, 1977), Kataoka et al. (1987) concluded that large-scale coherent flow structures may also result in an enhancement of the stagnation region heat transfer due to surface renewal effects. Surface renewal occurs due to the intrusion of the flow structures into the thermal boundary layer. It was pointed out that heat transfer enhancement due to surface renewal effects does not

¹To whom correspondence should be addressed. e-mail: zdavid@ces.clemson.edu

Contributed by the Heat Transfer Division for publication in the JOURNAL OF HEAT TRANSFER and presented at '96 IMECE. Manuscript received by the Heat Transfer Division, Nov. 5, 1997; revision received, Dec. 22, 1998. Keywords: Forced Convection, Heat Transfer, Jets, Pulsating, Unsteady. Associate Technical Editor: J.-C. Han.

require that the boundary layer be turbulent. Kataoka et al. (1988) investigated impingement heat transfer to a circular air jet ($d = 40$ mm) with and without controlled acoustic excitation. A modified form of the conditional sampling technique used by Kataoka et al. (1987) was used to show that impinging large-scale flow structures were responsible for the heat transfer enhancements in both cases.

Several studies of nonimpinging jets have investigated the influence of flow pulsations on the formation of large-scale vortical structures. Curtet and Girard (1973) introduced flow pulsations in the mean jet velocity of an axisymmetric air jet exiting into a stagnant surrounding fluid. Most photographs pertained to a Reynolds number of 8050 and a Strouhal number of 0.107, both based on the nozzle diameter and the mean exit velocity. The pulsation amplitude, defined as the ratio of the root mean square of the fluctuating component of the flow velocity to the mean flow velocity, was 54 percent. It was observed that flow pulsations resulted in the cyclic generation of vortex rings at the nozzle exit, thus producing a sharp expansion of the jet very near the nozzle exit in comparison to its steady counterpart. Farrington and Clauch (1994) investigated a pulsating planar jet of air exiting into a stagnant environment. Smoke-wire visualization of the flow indicated large, symmetrical pairs of vortices formed near the nozzle exit for pulsating conditions but not for steady conditions. Hussain and Zaman (1981) investigated steady and pulsating circular air jets. It was suggested that flow pulsations organized the formation of the vortical structures which in a natural jet were temporally and spatially dispersed.

Although no prior information about the flow fields in arrays of pulsating jets is available, studies with single, nonimpinging pulsating jets have concluded that pulsation increases entrainment and turbulence intensity. Binder and Favre-Marinet (1973) observed that the steady jet potential core length of about five to six nozzle diameters in a single nonimpinging jet was reduced to about one nozzle diameter by large-amplitude pulsations. They also observed that the rate of decrease in the centerline axial velocity increased with increasing Strouhal number up to a certain value, beyond which it remained independent of Strouhal number. The rate of decrease was also found to be larger at higher pulsation magnitudes. Higher turbulence intensities in pulsating, nonimpinging single jets have been reported by Seno et al. (1987) and Kataoka et al. (1988). Bremhorst (1979) observed for single jets that the highest entrainments were reported for jets with the largest pulsa-

tion magnitudes and at frequencies of pulsation significantly below the natural frequencies of jets ($S_d \cong 0.3$), as in the present investigation. If the increased turbulence intensities that have been measured in single, nonimpinging jets are found to also pertain to arrays of pulsating jet flows, transport rates might be enhanced.

In addition to promoting the formation of flow structures which upon impingement can affect the boundary layer, flow pulsations also can directly influence the boundary layer due to nonlinear dynamical effects related to momentum and energy transport. Because the transient equations governing the boundary layer thicknesses are highly nonlinear (Mladin and Zumbrennen, 1994, 1995; Sheriff and Zumbrennen, 1994), sinusoidal pulsations lead to nonsinusoidal responses in boundary layer thicknesses such that the average boundary layer thicknesses increase and Nusselt numbers decrease. On/off jet flows have also been shown to instill periodic boundary layer renewal. In this case, boundary layer thicknesses repetitively approach a value corresponding to the recently established steady jet flow. Prior to attaining the steady values, resistance to heat transfer is reduced. Above a threshold frequency, the time-averaged boundary layer thicknesses on the impingement surface can be maintained thinner than those for steady jets, resulting in enhanced heat transfer when averaged over time (Zumbrennen and Aziz, 1993).

The studies above have demonstrated the importance of flow structures, boundary layer dynamics, and pulsations to heat transfer to single jets. There appears to have been no prior investigation of the effect of flow pulsations in the context of jet arrays. As described earlier, jets are often configured as arrays and the results for single jets may not be directly applicable. When the flow is pulsating, for example, the situation is more complex on account of the potential dynamic interaction of the effluents from neighboring jets. In order to assess the influence of pulsations, convective heat transfer to an array of pulsating, circular jets was studied over a range of jet Reynolds numbers, pulsation frequencies, pulsation amplitudes, and array-to-impingement surface distances. Orifices were used to generate the jets since these are most commonly used in industrial applications.

Experimental Apparatus and Procedures

Overview. A schematic diagram of the experimental apparatus is shown in Fig. 1. Dehumidified air from a compressor was

Nomenclature

A = local flow pulsation magnitude (Eq. (4))	PSD = power spectral density, m^2/s^2 Hz or 1/Hz	u_p = pulsating component of centerline axial velocity, m/s
A_N = flow pulsation magnitude at the orifice exit	Re_d = Reynolds number evaluated at film temperature = $u_N d / \nu$	u' = turbulent component of flow velocity in axial direction, m/s
C = steady-state free-stream velocity gradient, 1/s	S = center-to-center orifice spacing (Fig. 2), m	U_{Nu} = relative uncertainty in Nusselt number
d = diameter of a circular orifice or nozzle opening, m	S_d = Strouhal number = fd/u_N	U_v = relative uncertainty in jet velocity
f = pulsation frequency, Hz	t = time, s	$x_{1,2,3}$ = distances along coordinate axes within the unit cell (Fig. 2), m
f_* = dimensionless frequency = f/C	t_p = time period for flow pulsation, s	z = axial distance from the jet discharge point on the orifice plate, m
h = convective heat transfer coefficient, W/m^2K	T_f = film temperature = $(T_s + T_w)/2$, K	ϵ = mean-to-peak pulsation amplitude (Eq. (5))
H = spacing between the orifice plate and the impingement plate, m	T_s = impingement surface temperature, K	ϵ_N = mean-to-peak pulsation amplitude at the orifice exit
k_f = thermal conductivity of fluid, W/mK	T_w = adiabatic wall temperature, K	ν = kinematic viscosity, m^2/s
$l_{1,2,3}$ = distances between the center and the edge of a unit cell along axes 1, 2, and 3 (Fig. 2), m	Tu = longitudinal turbulence intensity (Eq. (1))	
n = number of data points in each flow pulsation cycle	u = longitudinal component of flow velocity, m/s	Subscripts
N = number of pulsation cycles used in ensemble-averaging of data	u_{fl} = longitudinal component of fluctuating flow velocity, m/s	N = pertaining to one orifice diameter downstream of orifice exit
Nu_d = Nusselt number = hd/k_f	u_N = mean centerline axial velocity at one orifice diameter downstream of orifice exit, m/s	avg = component obtained from time-averaging a time series

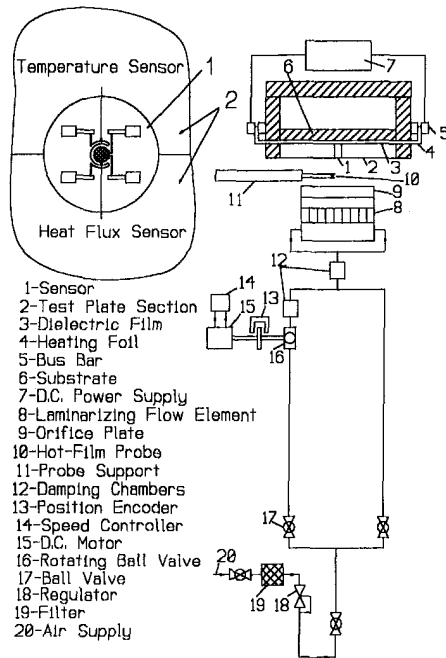


Fig. 1 Schematic diagram of the experimental apparatus

filtered, regulated, and divided into two parts. While one part of the flow proceeded without any modification providing a constant mean flow, the other part passed through a rotating ball valve arrangement to produce a nearly sinusoidal variation in the flow velocity. Farther downstream, the mean flow component and the sinusoidal flow component were combined. The resulting pulsating flow was fed into a plenum chamber. The flow left the plenum chamber through a multiple hole orifice plate and impinged onto an instrumented test plate containing a heat flux microsensor for good spatial and temporal resolution. Experiments were performed for $2500 < Re_d < 10000$, $2 < H/d < 6$, $0 \text{ Hz} < f < 65 \text{ Hz}$, $0 < S_d < 0.028$, and 0 percent $< A_N < 60$ percent.

Flow System and Measurements. Flow entered the plenum chamber through two hose fittings. In the plenum chamber, the flow proceeded through a laminarizing flow element to the orifice plate. The flow element was comprised of a block of stainless steel honeycomb with 0.79 mm hexagonal cells and was 31 mm in length. The plenum chamber and the orifice plate were constructed from 12.7-mm thick lexan plastic plates and were held together with screws. The orifice plate, which is shown in Fig. 2, contained a square array of nine sharp-edged orifices. In addition, four spent-air holes were located at the corners of the unit cell for the central orifice and were equidistant from the adjacent orifice holes. The orifice-to-orifice spacing S was six orifice diameters and the orifice diameter d was 6 mm. The sharp-edged orifices were formed within longer concentric cylinders of twice the diameter of each orifice hole. Since the jets were produced with sharp-edged orifices, no appreciable vorticity due to boundary layer development occurred along an internal orifice wall. The temperature of the air at the orifice inlet was measured using an ANSI Type T thermocouple. This temperature was found by measurement to be within 0.1°C of the temperature of the discharged air.

The shaft of the rotating ball valve (Fig. 1) was connected using a flexible coupling to the shaft of a variable speed direct current motor, which provided the rotating torque. To generate a pulsating jet, the throttle valves were partially opened and the ball valve was rotated by setting the frequency of rotation on the speed controller of the motor. The speed controller maintained the motor speed to within two percent of the set speed which was calibrated with a digital strobe light. The maximum speed of the motor was 2500 revolutions per minute. This corresponded to a maximum pulsation

frequency of 83.3 Hz where each rotation resulted in two pulsations. To separate the pulsating component of velocity from the turbulent component, a shaft position encoder was designed and built to provide phase information (Fig. 1). The position encoder consisted of a disk with two radial slots, mounted on the shaft of the rotating ball valve. When the ball valve was rotated, the slots passed at regular intervals between a light emitting diode and a photoelectric sensor located opposite it. In this manner, an electric signal was generated such that heat transfer and flow measurements could be associated during the pulsation cycle.

The flow field of the jet array was characterized using a TSI (St. Paul, Minnesota) IFA-100 anemometer and a single-axis hot-film probe (TSI Model 1240-20). The related probe support was attached to a traversing mechanism with three degrees-of-freedom which allowed positioning of the probe in a plane parallel to the plane of the orifice plate and at specified vertical separation distances. The horizontal traverses had a positioning accuracy of 0.03 mm. The vertical positioning accuracy was 0.15 mm.

Data were acquired using a multichannel high-speed data acquisition board which will be discussed in further detail below. All flow measurements were performed with the test plate in place. For steady flow, the mean flow information was extracted by time-averaging the data and the turbulence intensity Tu was obtained from Eq. (1), where m is the number of data points in the data set.

$$Tu = \frac{1}{u_N} \sqrt{\frac{1}{m} \sum_{j=1}^m u'^2_j} \quad (1)$$

For the pulsating jet flow, the instantaneous flow velocity $u(t)$ was comprised of a mean flow velocity u_{avg} , a time-varying component u_p due to pulsation, and a time-varying component u' due to turbulent fluctuations.

$$u(t) = u_{avg} + u_p + u' \quad (2)$$

As in the steady jet, the mean component of flow velocity was obtained by time-averaging the flow data. To obtain u_p , the method of ensemble averaging was employed (Evans, 1975). In this method, the anemometer signal was divided into cycles using information from the shaft position encoder. For N pulsation cycles, the ensemble average at an instant of time t_i from the beginning of a cycle was calculated with Eq. (3), where $u_k(t_i)$ was the velocity reading in the k th cycle at time t_i .

$$\bar{u}(t_i) = \lim_{N \rightarrow \infty} \frac{1}{N} \sum_{k=1}^N u_k(t_i) \quad (3)$$

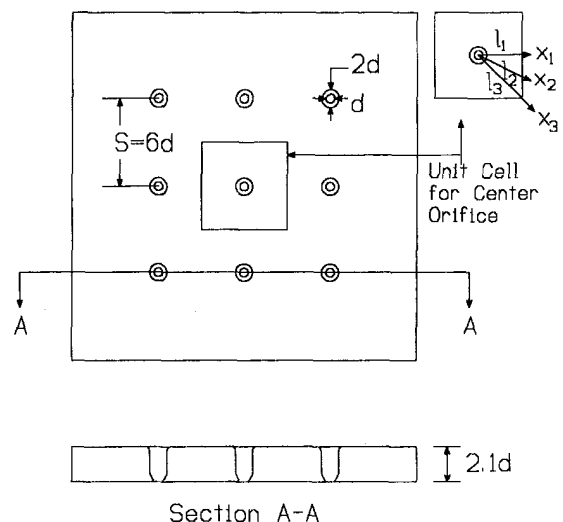


Fig. 2 Details of orifice plate and unit cell within jet array

Ensemble averages were performed for a minimum of 200 flow cycles and 160 readings per cycle. Under these sampling conditions, calculated turbulence intensities and pulsation magnitudes changed by less than one percent in comparison to their values when larger numbers of cycles or readings were used. Because pulsations were mechanically generated (Fig. 1), cycle-to-cycle variations were not discernible and ensemble averaging provided an effective basis for flow characterization.

The pulsation magnitude was defined as the square root of the mean of the squares of the ensemble-averaged pulsating component of flow velocity,

$$A = \frac{1}{u_N} \sqrt{\frac{1}{n} \sum_{j=1}^n (\tilde{u}_j - u_{avg})^2} \quad (4)$$

The local root-mean-square value of the pulsating component of flow velocity was normalized by the mean velocity at a distance of one diameter downstream of the nozzle exit which was well within the jet potential core. The local mean velocity u_{avg} was obtained by time-averaging the jet velocity data. For a sinusoidal waveform, the root-mean-square pulsation amplitude is related to the mean-to-peak pulsation amplitude by Eq. (5).

$$\epsilon = \sqrt{2}A \quad (5)$$

With the mean and the pulsation velocity components known, the turbulence component of velocity was determined using Eq. (2) and the turbulence intensity was calculated from Eq. (1).

Heat Transfer Measurements and Uncertainty. The test cell was composed essentially of a heated rectangular test plate with instrumentation to measure convective heat transfer at its surface. The test plate consisted of two separate aluminum sections (see inset to Fig. 1) with 25.4-mm diameter semicircular slots designed to accommodate the 25.4-mm diameter substrate of the heat flux microsensor. The two sections were tightly pressed against the substrate using screws. The test plate had overall dimensions of 216 mm by 127 mm. Both the aluminum sections and the aluminum nitride substrate plate were 6.35 mm thick. The test plate was firmly mounted on a thin (0.084-mm) metallic electrical foil heater which rested on an electrically insulative substrate plate made of phenolic, a composite material which has low thermal conductivity (0.54 W/m-K). A thin dielectric coating of kapton was applied to the test plate to electrically insulate it from the foil. The heating foil was attached to bus bars that were connected using welding cables to a 10-volt d.c. power supply. The test cell was mounted on a linear traversing mechanism with a lead screw pitch of 0.635 mm to obtain the vertical separation between the test plate and the orifice plate. To provide accurate and automated positioning, the lead screw was coupled to a digitally controlled stepper motor (200 steps per revolution) that was controlled via the personal computer used for data acquisition purposes.

The local heat transfer rate from the test plate was measured using a heat flux microsensor (Model HFM-1A-AIN-B, Vatel Corporation, Christiansburg, VA) located at the center of the test plate. The sensing element, which was less than two microns thick, was deposited on a 25.4-mm diameter electrically insulative substrate of aluminum nitride inserted at the center of the aluminum test plate. The test plate material was selected to closely match the thermal properties of the substrate. The sensing element consisted of a layer of thermal resistance and multiple thermocouple layers which were vapor deposited on either side to form a differential thermopile. The thermocouples were made from nickel and nichrome and the thermal resistance was a 1- μ m thick layer of silicon monoxide. A platinum resistance sensor was vapor deposited adjacent to the thermopile to measure the surface temperature. The combined sensing elements had overall dimensions of 2.29 mm by 1.78 mm. This was smaller than the orifice diameter of 6

mm and orifice spacing of 36 mm (Fig. 2), thus allowing local heat transfer measurements within the jet array.

The heat flux microsensor provided a voltage proportional to the heat flux (Terrell et al., 1992). The calibration constant over the temperature range 20°C–180°C was provided by the sensor manufacturer to specified accuracies for heat flux of ± 7.3 percent and for temperature of ± 5.0 percent. The heat flux calibration range was from 0.187 W/cm² to 9 W/cm². Holmberg and Diller (1994) calculated the dynamic sensitivity of a similar heat flux sensor when it was subjected to a step change in heat flux. A one-dimensional semi-infinite conduction model of the heat transfer in the sensor substrate was developed based on the substrate properties to convert measured surface heat flux to surface temperature. The sensitivity was evaluated numerically by minimizing the sum of the errors between the measured surface temperature and the temperature calculated from the measured heat flux. Excellent agreement was obtained between the calculated sensitivities and the manufacturer specified static sensitivities from exposing the sensor to a known heat source. In the present investigation, the sensor temperature was maintained between 45°C and 70°C and the heat flux ranged from about 0.2 W/cm² to about 1.0 W/cm². Pulsation frequencies (10–65 Hz) were well below the rated frequency response of the sensor (100 kHz). The surface temperatures along the test plate exhibited less than four percent temporal and spatial variations due to the high thermal conductivity of the aluminum nitride substrate and the aluminum test plate. The thermal boundary condition of the experiment was therefore nearly that of a uniform and constant surface temperature.

A multichannel data acquisition board with a maximum sampling rate of 100 kHz was interfaced with a personal computer and was used in a multiplexing arrangement to record jet velocity, heat flux, incident jet temperature, surface temperature, and the shaft encoder signal. Selected sampling rates of 6.4 kHz to 14 kHz per channel were based upon the desired physical mechanisms to be captured. For example, the sampling rates were sufficiently high to capture the voltage spike from the shaft encoder and provide detailed flow measurements which could be associated with heat transfer. The minimum sampling rate provided 160 readings per channel for each pulsation cycle and a Nyquist frequency of at least 3.2 kHz.

To perform heat transfer measurements, the microsensor was located at a position of interest relative to the central orifice along axes x_1 , x_2 , or x_3 in Fig. 2. The axis x_2 formed an angle of 22.5 deg with the axes x_1 and x_3 . The Reynolds number Re_d was referenced to the orifice diameter and the centerline axial velocity at one orifice diameter downstream of the orifice exit within the potential core of the jet. Flow-field measurements were first recorded and the hot-film sensor was withdrawn to avoid flow distortions downstream that might affect heat transfer on the test plate. All properties were evaluated at the local film temperature.

The convective heat transfer coefficient was calculated based on Newton's law of cooling where the adiabatic wall temperature was used as the reference temperature. The adiabatic wall temperature was measured using the surface temperature sensor after a required flow had been established, but with the heater off. This procedure has been shown to effectively account for entrainment effects where the surrounding fluid and incident jet temperatures in general may differ (Bouchez and Goldstein, 1975). The heat transfer coefficient was corrected for any contribution from radiative heat transfer by considering the test surface as a gray, diffuse body emitting to black surroundings at ambient temperature. The steady-state time-averaged Nusselt numbers at the stagnation point were about 13 percent higher than the results for a single impinging jet given by Gardon and Akfirat (1965) for a nozzle-to-impingement plate distance of two orifice diameters. In their study, the orifice diameter was 6.35 mm in comparison to six mm in the present study. For $2500 < Re_d < 5000$, the steady jet Nusselt numbers at the stagnation point for $H/d = 2$ such that the potential jet core was incident on the test plate were less than 15 percent higher than those given by a theoretical expression for a single, laminar cir-

cular jet (Hoogendoorn, 1977). These differences are representative of previously reported variations in heat transfer measurements by different investigators for similar flow conditions.

The precision limit for the evaluation of local Nusselt number was found to be two percent based on the differences in results for measurements repeated under flow, thermal, and geometric conditions that were identical to within measurement readings. Experimental uncertainties in reported values at a 95 percent confidence level were determined by combining individual uncertainties in physical dimensions, thermophysical properties, and measurements by the method presented by Kline and McClintock (1953). These included, for example, an uncertainty in orifice diameter of 0.0127 mm, an uncertainty of 7.3 percent for heat flux, and an uncertainty of five percent in surface temperature readings. Bias limits of 10.3 percent and 4.4 percent in Reynolds number were found for $Re_d = 2500$ and $Re_d = 10000$, respectively. A bias limit of 8.7 percent was found for Nusselt number. The uncertainties in the Reynolds number ranged from 10.5 percent for $Re_d = 2500$ to 4.8 percent for $Re_d = 10000$. The uncertainty at a 95 percent confidence level in Nusselt numbers was 8.9 percent. The ability to discern differences between the steady and pulsating flow cases is reflected by the two-percent precision limit.

Results and Discussion

Unlike for a steady jet issuing from an orifice where little flow organization occurs, flow pulsations may cause shear layers downstream of orifices within an array to roll up and form a train of vortices. This situation is suggested by the starting vortices formed when a jet flow is first generated beginning from zero velocity (Glezer, 1988; Hura et al., 1994). Changes to the flow field due to pulsations within the jet array are therefore discussed before presenting the heat transfer results. Given the large number of parameters inherent in unsteady convection studies, representative or unique cases will be presented in figures and the general effects will be described.

The variation of axial velocity and turbulence intensity along the jet centerline for various pulsation magnitudes is documented in Fig. 3 for a spacing between the test plate and orifice plate of six

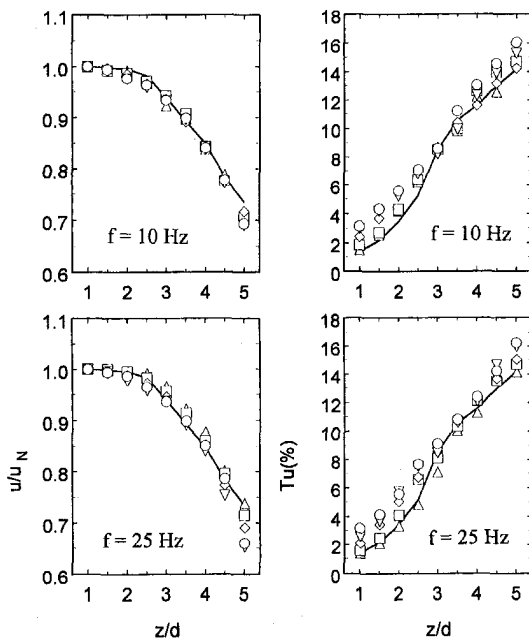


Fig. 3 Axial velocity and turbulence intensity along the jet centerline for various pulsation magnitudes with $U_v = 3.5$ percent, $Re_d = 5000$, $H/d = 6$ (top, $f = 10$ Hz, $S_d = 0.0044$; bottom, $f = 25$ Hz, $S_d = 0.0109$; — steady jet, Δ $A_N = 10$ percent, \square $A_N = 25$ percent, \diamond $A_N = 40$ percent, ∇ $A_N = 50$ percent, \circ $A_N = 60$ percent)

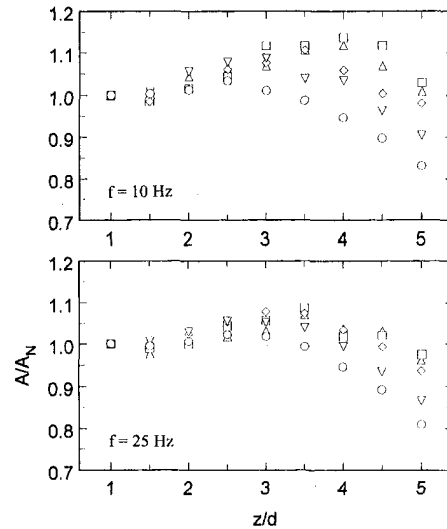


Fig. 4 Pulsation magnitude variation along the jet centerline with $Re_d = 5000$ and $H/d = 6$ (top, $f = 10$ Hz, $S_d = 0.0044$; bottom, $f = 25$ Hz, $S_d = 0.0109$; Δ $A_N = 10$ percent, \square $A_N = 25$ percent, \diamond $A_N = 40$ percent, ∇ $A_N = 50$ percent, \circ $A_N = 60$ percent)

orifice diameters. The results for $f = 10$ Hz ($S_d = 0.0044$) are presented in the upper panels and those for $f = 25$ Hz ($S_d = 0.0109$) are presented in the lower panels. The velocity reductions for $f = 10$ Hz were found to be similar to the steady jet case for pulsation amplitudes up to 40 percent. With the potential core length defined as the distance from the nozzle where the centerline axial velocity reduces to 97 percent of the maximum value (Martin, 1977), the potential core lengths were about 2.5 orifice diameters. With further increases in the pulsation magnitude, the core length reduced to about two orifice diameters due to greater jet interaction as evidenced by increased turbulence intensities above steady jet values. For example, the turbulence intensity at a pulsation magnitude of 60 percent was 3.1 percent at $z/d = 1$ and 16.0 percent at $z/d = 5$. The corresponding values for the steady jet case were 1.4 percent and 14.2 percent. Such greater jet interaction may stem from the promotion of coherent flow structures in pulsating jet flows in comparison to steady jet flows (Mladin and Zumbrennen, 1997). Vortices that develop near each orifice may eventually interfere as they grow radially and lead to higher turbulence levels at the expense of more rapid degradation of the jet flow. For the higher pulsation frequency of 25 Hz, core length was reduced from about 2.5 to about two orifice diameters at a pulsation magnitude of 60 percent while decreases in centerline axial velocity remained nearly unchanged. The exception was the position closest to the plate ($z/d = 5$) where the velocities decreased from 74 percent of the maximum velocity for the steady jets, to 66 percent for the pulsating jets with a pulsation magnitude of 60 percent. This more pronounced decrease was reflected in slightly higher turbulence intensities.

The variations of the pulsation magnitudes with distance from the central orifice along the jet centerline are given in Fig. 4. The flow pulsations were initially amplified and then decayed rapidly. It should be recalled here that the pulsation magnitude was calculated as the root mean squared value of the ensemble-averaged velocity and thus indicates only changes in the periodic, organized components of the jet flow. Pulsation amplifications occur when coherent flow structures form as a result of pulsation. For $f = 10$ Hz (upper panel), a maximum pulsation amplification of 14 percent occurred at a pulsation magnitude of 25 percent and $z/d = 4$. Pulsation amplifications for $f = 25$ Hz (lower panel) were smaller in comparison. With further increase in the pulsation magnitude, the amplification decreased and the location of the peak amplification moved upstream. The increase in turbulence intensity above steady jet levels in Fig. 3 are consistent with a breakdown of

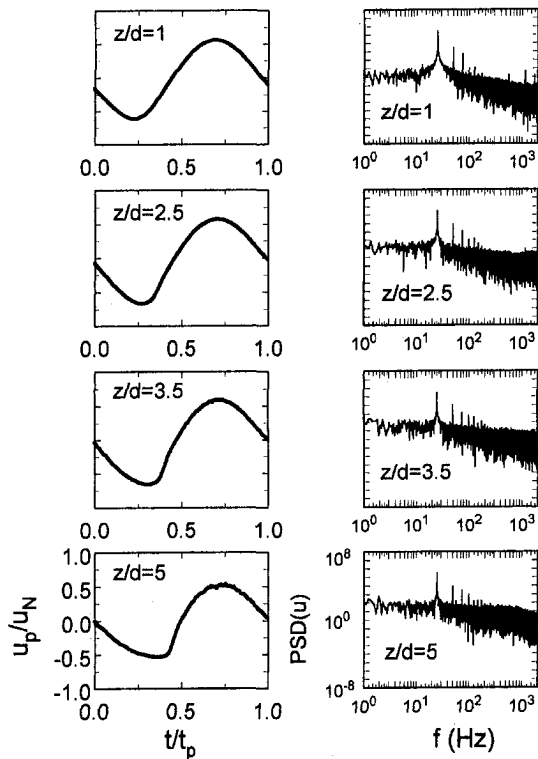


Fig. 5 Ensemble averages and power spectra of centerline axial velocity for $Re_d = 5000$, $f = 25$ Hz, $S_d = 0.0109$, $A_N = 40$ percent, and $H/d = 6$

vortices generated during pulsation. Similar amplifications were also observed by Binder and Favre-Marinet (1973). They found for a nonimpinging single jet that the pulsation magnitude reached a maximum at about four nozzle diameters downstream, and then decayed very rapidly to zero by about ten diameters downstream. As was mentioned earlier, Farrington and Clauch (1994) observed that flow pulsations increased flow organization and resulted in the cyclic generation of vortex rings. It was further observed that large amplitude pulsations entrained surrounding fluid more rapidly and produced greater mixing as compared to steady jets. In contrast, smaller amplitude pulsations were initially amplified but decayed less rapidly. Upon forming, organized flow structures persisted and were more effectively advected downstream. Similar results are reflected for $A_N < 40$ percent in Fig. 4 and also in Fig. 3, where axial velocities and turbulence intensities were nearly unchanged in comparison to steady jet values for $z/d < 5$.

Representative pulsation waveforms over a pulsation period t_p and power spectra at different distances from the orifice opening are shown in Fig. 5. The power spectra were calculated using the instantaneous flow data without ensemble averaging so that both periodic and random variations can be compared. The power spectra indicated that most of the flow energy resided at the pulsation frequency and that higher harmonic frequencies became increasingly important downstream as coherent flow structures degraded. The power spectra reflect that vortex formation is expected to occur at the pulsation frequency, since the pulsation frequency becomes the dominant frequency in the shear layer (Michalke, 1972). While the orifice hole locations of Fig. 2 were chosen to be optimal for the steady flow case, it is noteworthy that other locations may lead to optimal heat transfer conditions when the flow is pulsating due to the presence of coherent flow structures that are largely absent in steady jet flows discharging from orifices. The actual optimal locations would depend on the flow structures and interactions between them.

Ensemble averages and power spectra of instantaneous Nusselt numbers at various distances along the x_1 -axis are presented in

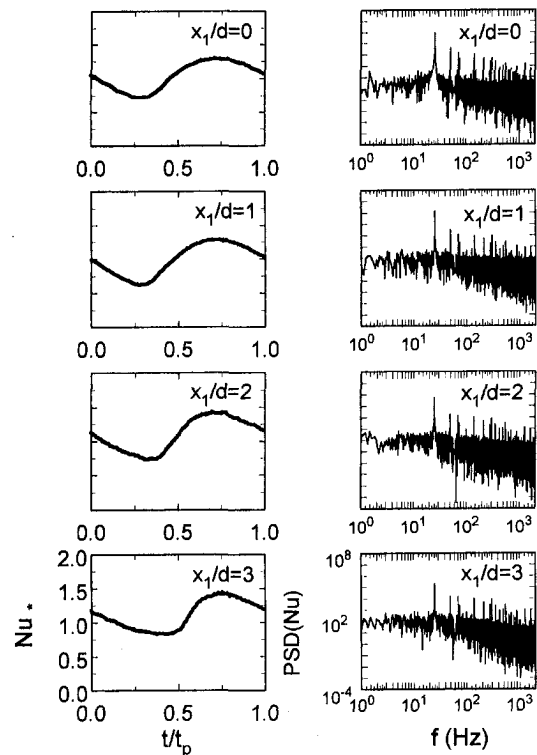


Fig. 6 Ensemble averages and power spectra of Nusselt number along the plate for $Re_d = 5000$, $f = 25$ Hz, $S_d = 0.0109$, $A_N = 40$ percent, and $H/d = 2$

Figs. 6 and 7 for dimensionless separation distances H/d between the test plate and orifice plate of two and six orifice diameters. As in Fig. 5, the power spectra pertain to the instantaneous heat

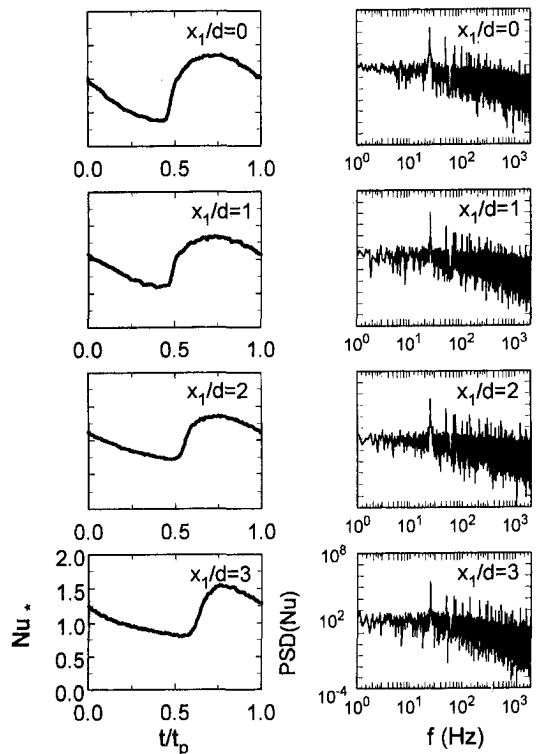


Fig. 7 Ensemble averages and power spectra of Nusselt number along the plate for $Re_d = 5000$, $f = 25$ Hz, $S_d = 0.0109$, $A_N = 40$ percent, and $H/d = 6$

transfer measurements without ensemble averaging. Nusselt numbers were normalized by the corresponding Nusselt number for the steady jet array so that changes due to pulsations can be readily seen. Variations of Nusselt number were less sinusoidal for $H/d = 6$ in Fig. 7, reflecting the more complex incident flow stemming from vortex amplification and jet interactions. Heat transfer responses were primarily at the pulsation frequency and its harmonics. These frequencies were also dominant in the flow (Fig. 5). The dominance of the pulsation frequency decreased with distance along the test plate from the stagnation point and reached a minimum at $x_1/d = 3$, which was the midpoint between two adjacent orifices (Fig. 2). Similar results were obtained along axes x_2 and x_3 .

The influence of pulsation amplitude on time-averaged Nusselt number at the stagnation point ($x_1/d = 0$) is shown in Fig. 8. In all cases, Nusselt numbers generally remained unchanged to within the precision limit or decreased with increasing pulsation amplitude. It has been demonstrated theoretically with a semianalytical model of boundary layer dynamics that sinusoidal flow variations in a stagnation flow can induce nonsinusoidal variations in boundary layer thicknesses (Mladin and Zumbrennen, 1994). The thermal boundary layer can thereby become thicker on average and heat transfer can be reduced in comparison to the steady flow case. The results for $S_d = 0.0109$ were compared to the model predictions summarized by Eq. (6) (Mladin and Zumbrennen, 1995), where the stagnation point velocity gradient was evaluated with Eq. (7) applicable to submerged axisymmetric jets (Martin, 1977). (Comparisons are not presented for the lower Strouhal number case since it was outside the applicable frequency range of Eq. (6).)

$$Nu_* = 1 - 0.2854 \epsilon_N^{2.2874} e^{-11.822f_*} \quad 0.01 < f_* < 0.1 \quad (6)$$

$$C = \frac{u_N}{d} \left(1.04 - 0.034 \frac{H}{d} \right) \quad 1 \leq H/d \leq 10 \quad (7)$$

For $H/d = 6$, the measured Nusselt numbers were within five percent of the theoretical predictions. However, the more complex variation for $H/d = 2$ was not well represented. In arrays of

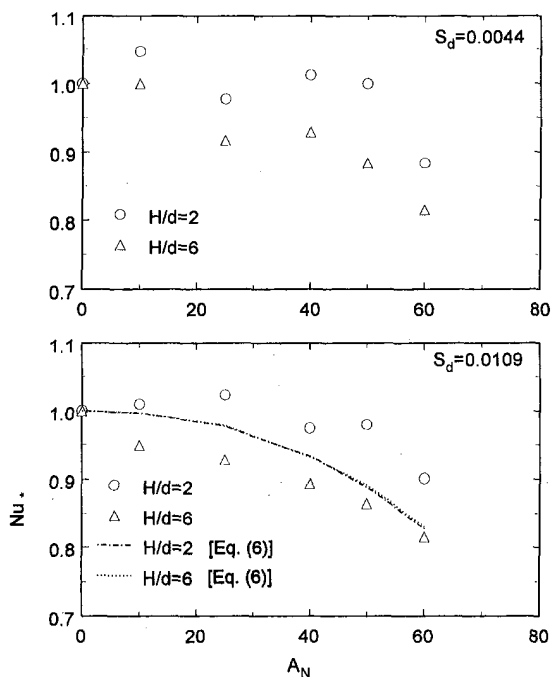


Fig. 8 Effect of pulsation magnitude on time-averaged Nusselt number for $x_1/d = 0$ and $Re_d = 5000$ (top, $f = 10$ Hz, $S_d = 0.0044$; bottom, $f = 25$ Hz, $S_d = 0.0109$)

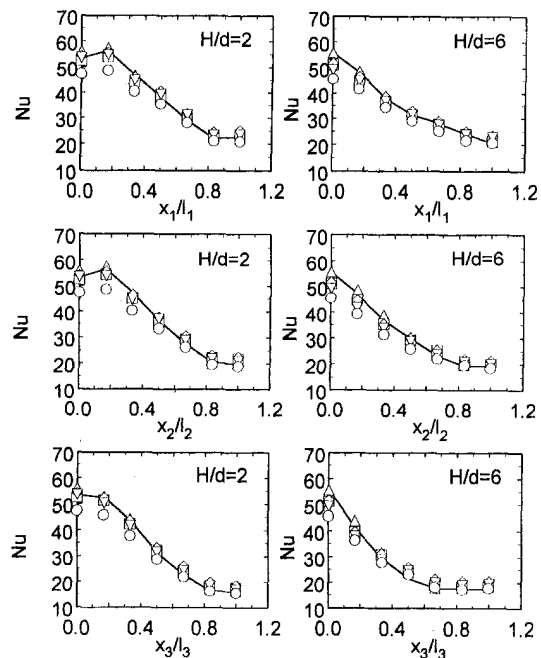


Fig. 9 Effect of pulsation magnitude on time-averaged Nusselt number distribution for $Re_d = 5000$, $f = 10$ Hz, $S_d = 0.0044$ and $U_{Nu} = 8.9$ percent (—steady jet, $\Delta A_N = 10$ percent, $\square A_N = 25$ percent, $\diamond A_N = 40$ percent, $\nabla A_N = 50$ percent, $\circ A_N = 60$ percent)

pulsating jets, the well-known effects on heat transfer for steady jets of decreasing jet velocity and increasing turbulence level (e.g., see Gardon and Akfirat (1965)) due to entrainment are retained, although trends are altered from the steady flow case, as discussed above in relation to Fig. 3. However, to these effects must be added those due to nonlinear boundary layer dynamics and the influence of coherent flow structures evolved by the flow pulsations. For example, heat transfer enhancements due to small scale turbulence and surface renewal due to incident vortices can be offset by reductions due to nonlinear dynamical effects. Reductions in Fig. 8 for $H/d = 6$ likely reflect the decreased incident jet velocity shown in Fig. 3 in tandem with nonlinear dynamical responses to the flow pulsation clearly incident on the test plate in Fig. 5. Similar reductions in Nusselt numbers have also been reported for a single, pulsating submerged air jet (Azevedo et al., 1994). It can be concluded from these results that flow pulsations can similarly decrease heat transfer in the stagnation regions of jets within arrays even if larger turbulence levels are generated.

The local time-averaged Nusselt number distributions within an unit cell at various pulsation magnitudes are presented in Fig. 9 for a pulsation frequency of 10 Hz. These results are representative of distributions for other frequencies within the parametric range $0 < f < 65$ Hz. The distributions for the steady jet case are plotted as solid lines for comparison. The abscissa denotes distance along the axes x_1 , x_2 , and x_3 (Fig. 2), normalized by the distances l_1 , l_2 and l_3 . Results for the pulsating jets followed trends similar to those for the steady jets except for the reductions in Nusselt numbers documented in Fig. 8 near the stagnation point. For $H/d = 2$, small off-center peaks in Nusselt number were observed on either side of the stagnation point. The occurrence and location of the off-center peaks agreed with the experimental results of Huber and Viskanta (1994) for steady jet arrays and numerical predictions for laminar jet arrays by Chen et al. (1994). Interestingly, the peaks were less pronounced at higher pulsation magnitudes since decreases due to pulsations in Nusselt numbers at the stagnation point extended radially outward by short distances.

Convective heat transfer distributions for pulsation frequencies in the range $0 \text{ Hz} < f < 65 \text{ Hz}$ and $2500 < Re_d < 10,000$ were also found to agree closely with the steady jet case except for the

reductions near the stagnation point. Although enhancements were not obtained, the reductions in the stagnation region heat transfer resulted in improved uniformity in the overall heat transfer rates since the heat transfer away from the stagnation region was largely unchanged. Such improvements in uniformity are desirable in many applications where jet arrays are used and can make possible decreases in fluid expenditures when increased flow to jet arrays is provided to compensate for lower transport rates at specific locations.

Conclusions and Practical Significance

The flow-field characteristics and convective heat transfer distributions for a square, in-line array of axisymmetric pulsating air jets were investigated. The rationale for this work was the observation that flow pulsations can induce more uniform heat transfer and the formation of coherent vortex structures in jet flows discharging from orifices, whereas little organization of the flow normally arises under steady flow conditions. When incident on a surface, convective heat and mass transfer rates might be enhanced due to surface renewal effects or increased turbulence levels. Increased jet interaction at large magnitude flow pulsations was found to reduce the jet potential core length by up to 20 percent. Turbulence intensities in the pulsating jets were 7 percent to 15 percent higher than the steady jet array values close to the impingement plate. Initial flow pulsation amplitudes were amplified in manners consistent with the formation of coherent flow structures. Despite evidence of coherent flow structures and increased turbulence levels, Nusselt numbers at the stagnation point were reduced by as much as 18 percent for a pulsation magnitude of 60 percent, with smaller reductions occurring at lower pulsation magnitudes. For pulsating jet arrays, heat transfer enhancements due to turbulence and surface renewal caused by incident vortices can be offset by reductions due to nonlinear dynamical boundary layer responses. Although enhancements were not obtained, the reductions in the stagnation region heat transfer resulted in improved uniformity in the overall heat transfer rates since the heat transfer away from the stagnation region was largely unchanged. Such improvements in uniformity are desirable in many applications where overall flow must be increased to compensate for lower cooling rates at specific locations due to nonuniformities that are characteristic of convective heat and mass transfer distributions for jet arrays.

Acknowledgments

Support for this work has been provided by the National Science Foundation of the United States of America under grant number CMS-9253640 in conjunction with a Presidential Faculty Fellow Award to D. A. Zumbrunnen.

References

- Azevedo, L. F. A., Webb, B. W., and Queiroz, M., 1994, "Pulsating Air Jet Impingement Heat Transfer," *Experimental Thermal and Fluid Science*, Vol. 8, pp. 206–213.
- Binder, G., and Favre-Marinet, M., 1973, "Mixing Improvement in Pulsating Turbulent Jets," *Proceedings, The Joint Meeting of the Fluids Engineering Division—Fluid Mechanics of Mixing*, edited by E. M. Uram, and V. W. Goldschmidt, eds., June 20–22, Atlanta, GA, pp. 167–172.
- Bouchez, J.-P., and Goldstein, R. J., 1975, "Impingement Cooling from a Circular Jet in a Cross Flow," *International Journal of Heat and Mass Transfer*, Vol. 18, pp. 719–730.
- Bremhorst, K., 1979, "Unsteady Subsonic Turbulent Jets," *Recent Developments in Theoretical and Experimental Fluid Mechanics*, U. Müller, K. G. Roesner, and B. Schmidt, eds., Springer-Verlag, Berlin, pp. 480–500.
- Chen, J., Wang, T., and Zumbrunnen, D. A., 1994, "Numerical Analysis of Convective Heat Transfer from a Moving Plate Cooled by an Array of Submerged Planar Jets," *Numerical Heat Transfer*, Vol. 26, pp. 141–160.

- Curtet, R. M., and Girard, J. P., 1973, "Visualization of a Pulsating Jet," *Proceedings, The Joint Meeting of the Fluids Engineering Division—Fluid Mechanics of Mixing*, edited by E. M. Uram, and V. W. Goldschmidt, eds., June 20–22, Atlanta, GA, pp. 173–180.
- Evans, R. L., 1975, "Turbulence and Unsteadiness Measurements Downstream of a Moving Blade Row," *ASME Journal of Engineering for Power*, Vol. 97, pp. 131–139.
- Farrington, R. B., and Claunch, S. D., 1994, "Infrared Imaging of Large-Amplitude, Low-Frequency Disturbances on a Planar Jet," *AIAA Journal*, Vol. 32, pp. 317–323.
- Fox, M. D., Kurosaka, M., Hedges, L., and Hirano, K., 1993, "The Influence of Vortical Structures on the Thermal Fields of Jets," *Journal of Fluid Mechanics*, Vol. 255, pp. 447–472.
- Gardon, R., and Akfirat, J. C., 1965, "The Role of Turbulence in Determining the Heat-Transfer Characteristics of Impinging Jets," *International Journal of Heat and Mass Transfer*, Vol. 8, pp. 1261–1272.
- Glezer, A., 1988, "The Formation of Vortex Rings," *Physics of Fluids*, Vol. 31, pp. 3532–3542.
- Hargrave, G. K., Fairweather, M., and Kilham, J. K., 1985, "Turbulence Enhancement of Stagnation Point Heat Transfer on a Body of Revolution," *International Journal of Heat and Fluid Flow*, Vol. 6, pp. 91–98.
- Holmberg, D. G., and Diller, T. E., 1994, "High-Frequency Heat Flux Sensor Calibration and Modeling," *Journal of Fluids Engineering*, Vol. 117, pp. 659–664.
- Hoogendoorn, C. J., 1977, "The Effect of Turbulence on Heat Transfer at a Stagnation Point," *International Journal of Heat and Mass Transfer*, Vol. 20, pp. 1333–1338.
- Huber, A. M., and Viskanta, R., 1994, "Convective Heat Transfer to a Confined Impinging Array of Air Jets With Spent Air Exits," *ASME JOURNAL OF HEAT TRANSFER*, Vol. 116, pp. 570–576.
- Hura, H. S., Breen, B. P., Hung, L. S., and Yao, S.-C., 1994, "An Experimental Study of Vortex Ring Formation and Penetration in Opposed Flow," *ASME FED-Vol. 92, Unsteady Flows*, ASME FED-Vol. 92, ASME, New York, pp. 57–66.
- Hussain, A. K. M. F., and Zaman, K. B. M. Q., 1981, "The Preferred-Mode Coherent Structure in the Near Field of an Axisymmetric Jet With and Without Excitation," *Unsteady Turbulent Shear Flows*, Springer-Verlag, New York, pp. 390–401.
- Kataoka, K., Suguro, M., Degawa, H., Maruo, K., and Mihata, I., 1987, "The Effect of Surface Renewal Due to Large-Scale Eddies on Jet Impingement Heat Transfer," *International Journal of Heat and Mass Transfer*, Vol. 30, pp. 559–567.
- Kataoka, K., Ase, H., and Sako, N., 1988, "Unsteady Aspects of Large-Scale Coherent Structures and Impingement Heat Transfer in Round Air Jets With and Without Controlled Excitation," *International Journal of Engineering Fluid Mechanics*, Vol. 1, pp. 365–382.
- Kline, S. J., and McClintock, F. A., 1953, "Describing Uncertainties in Single-Sample Experiments," *Mechanical Engineering*, Vol. 75, pp. 3–8.
- Ligrani, P. M., Cuthrell, J. M., and Gong, R., 1997, "Bulk Flow Pulsations and Film Cooling: Flow Structure Just Downstream of the Holes," *ASME Journal of Turbomachinery*, Vol. 119, pp. 568–573.
- Martin, H., 1977, "Heat and Mass Transfer Between Impinging Gas Jets and Solid Surfaces," *Advances in Heat Transfer*, Vol. 13, pp. 1–60.
- Michalke, A., 1972, "The Instability of Free Shear Layers," *Progress in Aerospace Sciences*, Vol. 12, pp. 213–239.
- Mladin, E. C., and Zumbrunnen, D. A., 1994, "Nonlinear Dynamics of Laminar Boundary Layers in Pulsatile Stagnation Flows," *Journal of Thermophysics and Heat Transfer*, Vol. 8, pp. 514–523.
- Mladin, E. C., and Zumbrunnen, D. A., 1995, "Dependence of Heat Transfer to a Pulsating Stagnation Flow on Pulsation Characteristics," *Journal of Thermophysics and Heat Transfer*, Vol. 9, pp. 181–192.
- Mladin, E. C., and Zumbrunnen, D. A., 1997, "Local Convective Heat Transfer to Submerged Pulsating Jets," *International Journal of Heat and Mass Transfer*, Vol. 40, No. 14, pp. 3305–3321.
- Popiel, C. O., and Trass, O., 1991, "Visualization of a Free and Impinging Round Jet," *Experimental Thermal and Fluid Science*, Vol. 4, pp. 253–264.
- Seno, T., Kageyama, S., and Ito, R., 1987, "Effect of Controlled Pulsation on Axisymmetric Jet Behavior," *Journal of Chemical Engineering of Japan*, Vol. 20, pp. 128–133.
- Sheriff, H. S., and Zumbrunnen, D. A., 1994, "Effect of Flow Pulsations on the Cooling Effectiveness of an Impinging Jet," *ASME JOURNAL OF HEAT TRANSFER*, Vol. 116, pp. 886–895.
- Terrell, J. P., Hager, J. M., Onishi, S., and Diller, T. E., 1992, "Heat Flux Microsensor Measurements and Calibrations," NASA CP3161, pp. 69–80.
- Van Fossen, G. J., and Simoneau, R. J., 1987, "A Study of the Relationship Between Free-Stream Turbulence and Stagnation Region Heat Transfer," *ASME JOURNAL OF HEAT TRANSFER*, Vol. 109, pp. 10–15.
- Zumbrunnen, D. A., and Aziz, M., 1993, "Convective Heat Transfer Enhancement Due to Interference in an Impinging Jet," *ASME JOURNAL OF HEAT TRANSFER*, Vol. 115, pp. 91–98.

Analysis of Combined Forced and Free Flow in a Vertical Channel With Viscous Dissipation and Isothermal-Isoflux Boundary Conditions

A. Barletta

Associate Professor,
Dipartimento di Ingegneria Energetica,
Nucleare e del Controllo Ambientale (DIENCA),
Università di Bologna,
Viale Risorgimento 2,
I-40136 Bologna, Italy
e-mail: antonio.barletta@mail.ing.unibo.it
Mem. ASME

Fully developed and laminar mixed convection in a parallel-plate vertical channel is investigated in the case of non-negligible viscous heating. The channel walls are subjected to asymmetric boundary conditions: One wall experiences a constant and uniform heat flux, while the other is kept at a uniform and constant temperature. The velocity field and the temperature field are evaluated analytically by means of perturbation expansions with respect to a buoyancy parameter, i.e., the ratio between the Grashof number and the Reynolds number. The Nusselt numbers and the friction factors are obtained as functions of the buoyancy parameter.

Introduction

In the last years, several analyses of combined forced and free convection in vertical channels have appeared in the literature. Most of the interest in this subject is due to its applications, for instance, in the design of cooling systems for electronic devices and in the field of solar energy collection. Some of these papers, such as Aung and Worku (1986), Cheng et al. (1990), and Hamadah and Wirtz (1991), deal with the evaluation of the temperature profiles and the velocity profiles for the parallel-flow fully developed regime. Others examine the stability of these flows either in the case of uniform and asymmetric wall temperatures (Chen and Chung, 1998) or in the case of linearly varying wall temperatures (Chen and Chung, 1996). Lavine (1988, 1993) analysed the laminar mixed convection in inclined parallel plate channels, thus including the solution for vertical channels as a special case. In particular, the flow reversal regimes (Lavine, 1988) and the linear stability of the parallel flow solution (Lavine, 1993) are investigated.

All the above quoted analyses of mixed convection in vertical channels are based on the hypothesis that the viscous dissipation effect within the fluid is negligible. The reliability of this hypothesis depends on the flow regime and on the fluid properties. Indeed, both for flows with small wall heat fluxes and for fluids with a high viscosity and a small thermal conductivity, viscous heating may become relevant. Some investigations on the interplay between buoyancy forces and viscous dissipation have been presented by Gebhart (1962), Turcotte et al. (1974), Iqbal et al. (1970), Rokerya and Iqbal (1971), and Soundalgekar et al. (1997). In particular, the papers by Iqbal et al. (1970) and by Rokerya and Iqbal (1971) refer to mixed convection in vertical circular or annular tubes.

Recently, Barletta (1998) and Zanchini (1998) have analysed the effect of viscous dissipation for combined forced and free convection in a vertical channel. In particular, both the case of symmetric or asymmetric temperatures prescribed at the channel walls (Barletta, 1998) and the case of convective boundary conditions (Zanchini, 1998) have been studied. In these papers, mixed con-

vection without viscous dissipation is considered as the base flow, while viscous dissipation is taken into account through a perturbation expansion with respect to a dimensionless parameter proportional to the Brinkman number. By this method, both the velocity and the temperature field are expressed as perturbation series. These series ensure a satisfactory convergence only for sufficiently small values of the Brinkman number. As a consequence, the method is specially suitable for flows such that the buoyancy forces have a strong influence and viscous heating is relatively small.

The aim of the present paper is the analysis of fully developed and laminar mixed convection with viscous dissipation in a vertical channel such that one wall is subjected to a prescribed and uniform heat flux while the other wall is kept at a uniform temperature. The solution of the governing equations is obtained by a perturbation method which differs from that employed by Barletta (1998) and by Zanchini (1998). More precisely, forced convection with viscous dissipation is considered as the base heat transfer process. Then, the effect of buoyancy is evaluated through perturbation expansions with respect to a buoyancy parameter given by the ratio between the Grashof number and the Reynolds number. Indeed, this approach allows the estimation of buoyancy-induced corrections to the laminar forced-convection regime with viscous heating.

Mathematical Model

In this section, the momentum balance and energy balance equations are written in a dimensionless form.

Let us consider a Newtonian fluid which steadily flows between two vertical and parallel plane walls. The distance between the walls, i.e., the channel width, is $2L$. A coordinate system is chosen such that the X -axis is parallel to the gravitational acceleration vector \mathbf{g} , but with the opposite direction. The Y -axis is orthogonal to the channel walls, and the origin of the axes is such that the positions of the channel walls are $Y = -L$ and $Y = L$. A sketch of the system and of the coordinate axes is reported in Fig. 1. The wall at $Y = -L$ is isothermal with a given temperature T_w , while the wall at $Y = L$ is subjected to a uniform heat flux q_w . The fluid velocity \mathbf{U} is assumed to be parallel to the X -axis, so that only the X -component U of the velocity vector does not vanish.

The Boussinesq approximation is employed. Then, according to this approximation, the mass balance equation implies that \mathbf{U} is

Contributed by the Heat Transfer Division for publication in the JOURNAL OF HEAT TRANSFER. Manuscript received by the Heat Transfer Division, Aug. 4, 1998; revision received, Dec. 14, 1998. Keywords: Analytical, Channel Flow, Heat Transfer, Mixed Convection, Viscous. Associate Technical Editor: R. Dougllass.

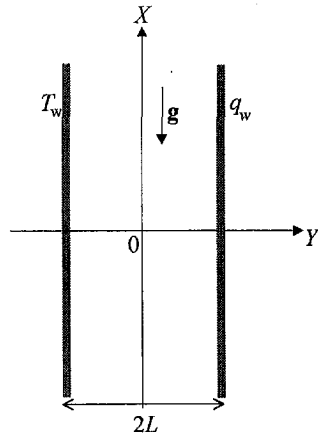


Fig. 1 Drawing of the system and of the coordinate axes

solenoidal. As a consequence, $\partial U/\partial X$ is zero, i.e., U depends only on the transverse coordinate Y . Moreover, the following equation of state for the mass density is supposed to hold:

$$\rho = \rho_0[1 - \beta(T - T_0)], \quad (1)$$

where the reference temperature T_0 is chosen as the mean temperature in a channel cross section, i.e.,

$$T_0 = \frac{1}{2L} \int_{-L}^L T dY. \quad (2)$$

Indeed, this choice of T_0 yields, at each section of the channel, the smallest average difference between the local temperature and the reference temperature. Therefore, the evaluation of T_0 through Eq. (2) provides the best conditions for the validity of the approximate linear equation of state given by Eq. (1). It is easily verified that T_0 evaluated through Eq. (2) is, in general, a function of X . Then, also ρ_0 should be considered as a function of X and not as a constant. However, a further approximation stated by Morton (1960) in a study on mixed convection in vertical circular ducts can be adopted. Morton's approximation is as follows. If the reference

temperature depends on the streamwise coordinate, the value of the reference mass density ρ_0 as well as those of the other thermo-physical properties such as β , k , and μ should be referred to a fixed value of the reference temperature T_0 . For instance, the fixed value of T_0 can be chosen as that at $X = 0$. Therefore, according to Morton's approximation, the thermophysical properties of the fluid are treated as constants.

The streamwise momentum balance equation is given by

$$\rho_0 \beta g (T - T_0) - \frac{\partial P}{\partial X} + \mu \frac{d^2 U}{dY^2} = 0, \quad (3)$$

while the transverse momentum balance equation yields

$$\frac{\partial P}{\partial Y} = 0. \quad (4)$$

Equation (4) implies that P depends only on X . Then, by evaluating the derivative with respect to X of both sides of Eq. (3), one obtains

$$\frac{\partial T}{\partial X} = \frac{dT_0}{dX} + \frac{1}{\rho_0 \beta g} \frac{d^2 P}{dX^2}. \quad (5)$$

By integrating both sides of Eq. (5) with respect to Y in the interval $[-L, L]$ and by employing Eq. (2), one can conclude that

$$\frac{d^2 P}{dX^2} = 0, \quad (6)$$

i.e., that dP/dX is a constant. It should be pointed out that this conclusion holds for any choice of the boundary conditions. Equations (5) and (6) yield

$$\frac{\partial T}{\partial X} = \frac{dT_0}{dX}. \quad (7)$$

Equation (7) implies that $\partial T/\partial X$ is independent of Y , so that its value can be determined at the channel walls. In particular, at the wall $Y = -L$, where the temperature is uniform, the value of $\partial T/\partial X$ is zero. Therefore, both T and T_0 do not depend on X . In this case, the energy balance equation can be written as

Nomenclature

$Br_q = \mu U_0^2 / (L q_w)$, heat-flux Brinkman number
 $Br_T =$ temperature Brinkman number defined by Eq. (18)
 $f_-, f_+ =$ Fanning friction factors defined by Eqs. (19) and (20)
 $g =$ gravitational acceleration, m/s^2
 $Gr = 64g\beta\Delta T L^3 / \nu^2$, Grashof number
 $j =$ non-negative integer
 $k =$ thermal conductivity, $W/(mK)$
 $L =$ channel half-width, m
 $n =$ non-negative integer
 $Nu_-, Nu_+ =$ Nusselt numbers defined by Eqs. (21) and (22)
 $p =$ pressure, Pa
 $P = p + \rho_0 g X$, difference between the pressure and the hydrostatic pressure, Pa
 $q_w =$ prescribed heat flux at $Y = L$, W/m^2

$R =$ radius of convergence of the perturbation series
 $Re = 4LU_0/\nu$, Reynolds number
 $T =$ temperature, K
 $T_b =$ bulk temperature defined by Eq. (23), K
 $T_0 =$ mean temperature defined by Eq. (2), K
 $T_w =$ prescribed temperature at $Y = -L$, K
 $u = U/U_0$, dimensionless velocity component in the X -direction
 $U =$ velocity component in the X -direction, m/s
 $U =$ velocity, m/s
 $U_0 =$ mean velocity defined by Eq. (15), m/s
 $X =$ axial coordinate, m
 $Y =$ transverse coordinate, m
 $y = Y/L$, dimensionless transverse coordinate

$\beta =$ coefficient of thermal expansion, K^{-1}
 $\Delta T = \mu U_0^2 / k$, reference temperature difference, K
 $\epsilon = Gr/Re$, dimensionless buoyancy parameter
 $\eta = k(T_0 - T_w) / (\mu U_0^2)$, dimensionless parameter
 $\theta = k(T - T_0) / (\mu U_0^2)$, dimensionless temperature
 $\lambda = -[L^2 / (\mu U_0)] dP/dX$, dimensionless pressure-drop parameter
 $\mu =$ dynamic viscosity, $Pa \cdot s$
 $\nu = \mu/\rho_0$, kinematic viscosity, m^2/s
 $\rho =$ mass density, kg/m^3
 $\rho_0 =$ mass density evaluated at $T = T_0$, kg/m^3

$$k \frac{d^2 T}{dY^2} + \mu \left(\frac{dU}{dY} \right)^2 = 0. \quad (8)$$

The velocity profile $U(Y)$ and the temperature profile $T(Y)$ can be determined by solving Eqs. (3) and (8) provided that the boundary conditions are specified. In particular, the velocity field is subjected to no-slip boundary conditions

$$U(\pm L) = 0. \quad (9)$$

On the other hand, the boundary conditions for the temperature field are

$$T(-L) = T_w, \quad k \frac{dT}{dY} \Big|_{Y=L} = q_w. \quad (10)$$

Equations (3) and (8)–(10) can be rewritten in a dimensionless form as follows:

$$\frac{d^2 u}{dy^2} = -\frac{\text{Gr}}{16 \text{Re}} \theta - \lambda, \quad (11)$$

$$\frac{d^2 \theta}{dy^2} = -\left(\frac{du}{dy} \right)^2, \quad (12)$$

$$u(\pm 1) = 0, \quad (13)$$

$$\theta(-1) = -\eta, \quad \frac{d\theta}{dy} \Big|_{y=1} = \frac{1}{\text{Br}_q}. \quad (14)$$

Since the dimensionless quantities have been defined by employing the mean velocity

$$U_0 = \frac{1}{2L} \int_{-L}^L U(Y) dY, \quad (15)$$

an additional constraint on the dimensionless velocity is present, i.e.,

$$\int_{-1}^1 u(y) dy = 2. \quad (16)$$

Moreover, since the reference temperature T_0 is given by Eq. (2), the dimensionless temperature $\theta(y)$ must fulfill the relation

$$\int_{-1}^1 \theta(y) dy = 0. \quad (17)$$

For prescribed values of Br_q and of the ratio Gr/Re , Eqs. (11)–(14), (16), and (17) determine uniquely the dimensionless velocity $u(y)$, the dimensionless temperature $\theta(y)$ and the dimensionless parameters λ and η .

In order to express the temperature difference between the channel walls, a temperature Brinkman number,

$$\text{Br}_T = \frac{\mu U_0^2}{k[T(L) - T_w]} = \frac{1}{\theta(1) - \theta(-1)}, \quad (18)$$

is defined. The Fanning friction factors are given by

$$f_- \text{Re} = \frac{8L}{U_0} \frac{dU}{dY} \Big|_{Y=-L} = 8 \frac{du}{dy} \Big|_{y=-1}, \quad (19)$$

$$f_+ \text{Re} = -\frac{8L}{U_0} \frac{dU}{dY} \Big|_{Y=L} = -8 \frac{du}{dy} \Big|_{y=1}, \quad (20)$$

while the Nusselt numbers are defined as

$$\text{Nu}_- = -\frac{4L}{T_w - T_0} \frac{dT}{dY} \Big|_{Y=-L} = \frac{4}{\eta} \frac{d\theta}{dy} \Big|_{y=-1}, \quad (21)$$

$$\begin{aligned} \text{Nu}_+ &= \frac{4L}{T(L) - T_0} \frac{dT}{dY} \Big|_{Y=L} = \frac{4}{\theta(1)} \frac{d\theta}{dy} \Big|_{y=1} \\ &= \frac{4 \text{Br}_T}{\text{Br}_q(1 - \eta \text{Br}_T)}. \end{aligned} \quad (22)$$

In the definition of the Nusselt numbers, the hydraulic diameter $4L$ is considered as the reference length, exactly as in the definitions of Re and Gr . Moreover, the reference fluid temperature employed in the definition of the Nusselt numbers is the mean temperature T_0 instead of the more conventional bulk temperature

$$T_b = \frac{1}{2LU_0} \int_{-L}^L TU dY. \quad (23)$$

The bulk temperature is usually preferred because in most cases it coincides with the mixing-cup temperature, which can be easily measured. In fact, the mixing-cup temperature “is the temperature one would measure if the duct were cut off at a section, and escaping fluid were collected and thoroughly mixed in an adiabatic container” (Shah and London, 1978). However, it is easily verified that, when viscous heating is not negligible, the bulk temperature T_b loses its physical meaning of mixing-cup temperature. Indeed, the effect of viscous dissipation causes the mixing-cup temperature to be greater than the bulk temperature. As a consequence, the bulk temperature can be obtained only by processing a sufficiently high number of temperature and velocity data in a channel section in order to get a satisfactory approximation of the integral on the right-hand side of Eq. (23). Therefore, it seems more convenient to utilize the mean temperature T_0 , whose value can be approximated merely by means of temperature data in a channel section.

A simple relation between the Fanning friction factors and the pressure drop parameter can be easily determined. In fact, by integrating Eq. (11) with respect to y in the interval $[-1, 1]$ and by employing Eq. (17), one obtains

$$\frac{du}{dy} \Big|_{y=1} - \frac{du}{dy} \Big|_{y=-1} = -2\lambda. \quad (24)$$

Then, on account of Eqs. (19) and (20), Eq. (24) can be rewritten as

$$f_+ + f_- = \frac{16\lambda}{\text{Re}}. \quad (25)$$

Equation (25) shows that the Grashof number does not appear explicitly in the relation between f_- , f_+ and λ . Indeed, the relation between f_- , f_+ and λ in the case of mixed convection is the same which holds in the case of forced convection. Obviously, in the latter case, the Fanning friction factors f_- and f_+ are equal.

Perturbation Method

In this section, Eqs. (11)–(14) and (16), (17) are solved by a perturbation method. Moreover, the special case of forced convection is outlined.

As it has been pointed out in the preceding section, if Br_q and $\epsilon = \text{Gr}/\text{Re}$ are prescribed, Eqs. (11)–(14), (16), and (17) allow the evaluation of $u(y)$, $\theta(y)$ as well as of the dimensionless parameters λ and η . Then, for any fixed value of Br_q , these quantities can be expressed as power series with respect to ϵ , namely

$$u(y) = u_0(y) + u_1(y)\epsilon + u_2(y)\epsilon^2 + \dots = \sum_{n=0}^{\infty} u_n(y)\epsilon^n, \quad (26)$$

$$\theta(y) = \theta_0(y) + \theta_1(y)\epsilon + \theta_2(y)\epsilon^2 + \dots = \sum_{n=0}^{\infty} \theta_n(y)\epsilon^n, \quad (27)$$

$$\lambda = \lambda_0 + \lambda_1\epsilon + \lambda_2\epsilon^2 + \dots = \sum_{n=0}^{\infty} \lambda_n\epsilon^n, \quad (28)$$

$$\eta = \eta_0 + \eta_1\epsilon + \eta_2\epsilon^2 + \dots = \sum_{n=0}^{\infty} \eta_n\epsilon^n. \quad (29)$$

The perturbation method can be described as follows (Aziz and Na, 1984). First, one substitutes the perturbation series expressed by Eqs. (26)–(29) into Eqs. (11)–(14), (16), and (17). Then, one collects terms having like powers of ϵ and equates to zero the coefficient of each power of ϵ . Finally, one obtains a sequence of boundary value problems which allow the evaluation of each term of the perturbation series.

For $n = 0$, one obtains

$$\frac{d^2 u_0}{dy^2} = -\lambda_0, \quad u_0(-1) = u_0(1) = 0, \quad \int_{-1}^1 u_0(y) dy = 2, \quad (30)$$

$$\frac{d^2 \theta_0}{dy^2} = -\left(\frac{du_0}{dy}\right)^2, \quad \theta_0(-1) = -\eta_0,$$

$$\left.\frac{d\theta_0}{dy}\right|_{y=1} = \frac{1}{Br_q}, \quad \int_{-1}^1 \theta_0(y) dy = 0. \quad (31)$$

The solution of Eq. (30) is easily obtained and is given by

$$u_0(y) = \frac{3}{2}(1 - y^2), \quad \lambda_0 = 3. \quad (32)$$

On the other hand, the solution of Eq. (31) can be expressed as

$$\theta_0(y) = 3y\left(1 - \frac{y^3}{4}\right) + \frac{y}{Br_q} + \frac{3}{20}, \quad \eta_0 = \frac{18}{5} + \frac{1}{Br_q}. \quad (33)$$

Indeed, $u_0(y)$, λ_0 , $\theta_0(y)$, and η_0 coincide, respectively, with $u(y)$, λ , $\theta(y)$ and η , in the case $\epsilon = 0$, i.e., in the case of forced convection. In particular, $u_0(y)$ is the well-known Hagen-Poiseuille velocity profile. When $\epsilon = 0$, the parameters Br_r, f_-, f_+, Nu_- and Nu_+ can be evaluated by employing Eqs. (18)–(22), (32), and (33), namely

$$Br_r = \frac{Br_q}{2(3Br_q + 1)}, \quad f_- Re = 24 = f_+ Re,$$

$$Nu_- = 20 \frac{6 Br_q + 1}{18 Br_q + 5}, \quad Nu_+ = \frac{20}{12 Br_q + 5}. \quad (34)$$

Obviously, the dimensionless parameter Br_q is positive if the wall $Y = L$ is heated, while it is negative if the wall $Y = L$ is cooled. Equation (34) reveals that, if $Br_q = -\frac{1}{3} \cong -0.3333$, the temperature Brinkman number Br_r becomes singular, i.e., the temperature at $Y = L$ is equal to T_w . Moreover, Nu_- is singular if $Br_q = -\frac{5}{18} \cong -0.2778$, while, Nu_+ is singular if $Br_q = -\frac{5}{12} \cong -0.4167$. On account of Eqs. (21) and (22), the former case corresponds to $T_w = T_0$ and the latter case to $T(L) = T_0$. On account of Eq. (34), another interesting condition is $Br_q = -\frac{1}{6} \cong -0.1667$, which yields $Nu_- = 0$, i.e., a vanishing heat flux at $Y = -L$.

The values of the Nusselt numbers Nu_- and Nu_+ expressed by Eq. (34) are in agreement with those reported by Shah and London (1978) in the special case of forced convection without viscous dissipation. In this case, i.e., in the limit $Br_q \rightarrow 0$, Eq. (34) yields $Nu_- = Nu_+ = 4$. The same values are reported by Shah and London (1978). It is easily proved that, if $Br_q \rightarrow 0$ and $\epsilon \rightarrow 0$, the

bulk temperature T_b coincides with the mean temperature T_0 , so that the Nusselt numbers defined in Shah and London (1978) and those defined in the present paper can be compared.

The terms of order $n > 0$ in the perturbation expansions given by Eqs. (26)–(29) can be evaluated by a recursive solution of the following boundary value problem:

$$\frac{d^2 u_n}{dy^2} = -\frac{\theta_{n-1}}{16} - \lambda_n, \quad u_n(-1) = u_n(1) = 0,$$

$$\int_{-1}^1 u_n(y) dy = 0, \quad (35)$$

$$\frac{d^2 \theta_n}{dy^2} = -\sum_{j=0}^n \frac{du_j}{dy} \frac{du_{n-j}}{dy}, \quad \theta_n(-1) = -\eta_n,$$

$$\left.\frac{d\theta_n}{dy}\right|_{y=1} = 0, \quad \int_{-1}^1 \theta_n(y) dy = 0. \quad (36)$$

Indeed, for an arbitrary $n > 0$, if $\theta_{n-1}(y)$ is known, Eq. (35) uniquely determines $u_n(y)$ and λ_n , namely

$$u_n(y) = -\frac{1}{16} \int_{-1}^y dy'' \int_{-1}^{y''} dy' \theta_{n-1}(y')$$

$$+ \frac{y+1}{32} \int_{-1}^1 dy'' \int_{-1}^{y''} dy' \theta_{n-1}(y') + \frac{\lambda_n}{2} (1 - y^2), \quad (37)$$

$$\lambda_n = \frac{3}{32} \left[\int_{-1}^1 dy \int_{-1}^y dy'' \int_{-1}^{y''} dy' \theta_{n-1}(y') \right.$$

$$\left. - \int_{-1}^1 dy'' \int_{-1}^{y''} dy' \theta_{n-1}(y') \right]. \quad (38)$$

Moreover, if $u_j(y)$ is known for every j such that $0 \leq j \leq n$, Eq. (36) uniquely determines $\theta_n(y)$ and η_n , namely

$$\theta_n(y) = -\eta_n + \int_{-1}^y dy'' \int_{y''}^1 dy' \left[\sum_{j=0}^n \frac{du_j(y')}{dy'} \frac{du_{n-j}(y')}{dy'} \right], \quad (39)$$

$$\eta_n = \frac{1}{2} \int_{-1}^1 dy \int_{-1}^y dy'' \int_{y''}^1 dy' \left[\sum_{j=0}^n \frac{du_j(y')}{dy'} \frac{du_{n-j}(y')}{dy'} \right]. \quad (40)$$

By employing perturbation series truncated to the second term, one obtains

$$\lambda \cong 3 - \frac{3}{560} \epsilon, \quad \eta \cong \frac{18}{5} + \frac{1}{Br_q} + \left(\frac{71}{1400} + \frac{1}{60 Br_q} \right) \epsilon,$$

$$Br_r \cong \frac{30 Br_q}{(1 + 3Br_q)(60 + \epsilon)}, \quad (41)$$

$$f_- Re \cong 24 - \left(\frac{19}{35} + \frac{1}{6 Br_q} \right) \epsilon,$$

$$f_+ Re \cong 24 + \left(\frac{16}{35} + \frac{1}{6 Br_q} \right) \epsilon, \quad (42)$$

Table 1 Values of Nu_- , Nu_+ , $f_- Re$, $f_+ Re$, for $|Br_q| = 0.5$

ϵ	$Br_q = -0.5$				$Br_q = 0.5$			
	Nu_-	Nu_+	$f_- Re$	$f_+ Re$	Nu_-	Nu_+	$f_- Re$	$f_+ Re$
-13	11.29	-33.66	26.32	22.78	6.849	2.175	33.86	15.39
-11	11.11	-31.01	26.01	22.92	6.673	2.130	32.46	16.56
-9	10.92	-28.60	25.68	23.08	6.497	2.082	31.04	17.78
-7	10.72	-26.40	25.34	23.26	6.322	2.030	29.58	19.04
-5	10.52	-24.39	24.98	23.45	6.147	1.975	28.08	20.36
-3	10.32	-22.53	24.60	23.65	5.973	1.915	26.51	21.75
-1	10.11	-20.81	24.21	23.88	5.800	1.852	24.86	23.22
0	10.00	-20.00	24.00	24.00	5.714	1.818	24.00	24.00
1	9.891	-19.22	23.79	24.13	5.629	1.783	23.11	24.81
3	9.666	-17.73	23.34	24.40	5.459	1.710	21.22	26.52
5	9.434	-16.34	22.87	24.70	5.292	1.630	19.14	28.41
7	9.194	-15.03	22.36	25.04	5.129	1.542	16.82	30.53
9	8.944	-13.79	21.80	25.41	4.971	1.445	14.13	32.96
11	8.684	-12.62	21.20	25.83	4.822	1.336	10.92	35.86
13	8.411	-11.50	20.54	26.31	4.687	1.207	6.791	39.53

$$Nu_- \cong \frac{4(6 Br_q + 1)}{\frac{18}{5} Br_q + 1 + \left(\frac{71}{1400} Br_q + \frac{1}{60}\right) \epsilon}$$

$$Nu_+ \cong \frac{4}{\frac{12}{5} Br_q + 1 + \left(\frac{69}{1400} Br_q + \frac{1}{60}\right) \epsilon} \quad (43)$$

Discussion of the Results

In this section, 26-terms perturbation series are employed to evaluate the dimensionless temperature profile and the dimensionless velocity profile for some values of Br_q .

The radius of convergence of the power series expressed by Eqs. (26)–(29), i.e., the domain of the dimensionless parameter ϵ where the perturbation expansions converge, represents an important feature of the perturbation method. If the radius of convergence is finite, the method is considered *singular*, otherwise it is considered *regular* (Aziz and Na, 1984). The perturbation method employed in the present paper is singular. In fact, a finite radius of convergence R for the perturbation expansions given by Eqs. (26)–(29) exists for any prescribed value of Br_q , as it can be verified by evaluating D’Alembert’s ratio limit, i.e.,

$$R = \lim_{n \rightarrow \infty} \left| \frac{\lambda_{n-1}}{\lambda_n} \right| \quad (44)$$

In Eq. (44), reference has been made to the power series expressed by Eq. (28). However, the same value of R is obtained if one evaluates D’Alembert’s ratio limit for any other perturbation expansion expressed by Eqs. (26)–(29). Since, in practice, one deals with truncated power series, the value of R can be only estimated. In this section, the power series expressed by Eqs. (26)–(29) are approximated by the finite sums of the first 26 terms. In the following, the estimation of the radius of convergence is described with reference to the perturbation expansion given by Eq. (28). First, one considers the coefficients λ_n for $10 \leq n \leq 25$ and recognizes that $\log_{10} |\lambda_{n-1}/\lambda_n|$ is approximately a linear function of $1/n$. Then, one expresses this function by a least-squares fit. Finally, one extends the domain of the linear function to $n > 25$ and evaluates the limit for $1/n \rightarrow 0$: This limit is the estimated value of $\log_{10} R$. The above procedure has been repeated for some values of the dimensionless parameter Br_q . By employing this method, one deduces that R depends on the modulus of Br_q and also on its sign, although the dependence on the sign becomes negligible as the modulus increases. This behavior can be illustrated by the following examples. For $Br_q = -0.5$, R is equal to 28.3, while, for $Br_q = 0.5$, R is equal to 17.3. For $Br_q = -1$, R is equal to 23.3, while for $Br_q = 1$, R is equal to 18.7. Finally, if $Br_q \rightarrow \pm \infty$, i.e., if the wall $Y = L$ is adiabatic, R is equal to 20.6.

In Tables 1–4, values of Nu_- , Nu_+ , $f_- Re$, $f_+ Re$ are reported for some values of ϵ , with reference to $|Br_q| = 0.5$, $|Br_q| = 1$, $|Br_q| = 10$ and $|Br_q| \rightarrow \infty$. Indeed, for the cases examined in these

Table 2 Values of Nu_- , Nu_+ , $f_- Re$, $f_+ Re$, for $|Br_q| = 1$

ϵ	$Br_q = -1$				$Br_q = 1$			
	Nu_-	Nu_+	$f_- Re$	$f_+ Re$	Nu_-	Nu_+	$f_- Re$	$f_+ Re$
-15	9.095	-3.841	28.68	20.61	7.405	1.463	32.99	16.42
-13	8.919	-3.710	28.14	20.98	7.232	1.430	31.91	17.28
-11	8.740	-3.580	27.58	21.36	7.058	1.396	30.80	18.19
-9	8.558	-3.449	26.99	21.77	6.883	1.360	29.67	19.12
-7	8.372	-3.318	26.39	22.21	6.707	1.323	28.51	20.10
-5	8.183	-3.187	25.75	22.68	6.531	1.283	27.30	21.13
-3	7.990	-3.056	25.08	23.18	6.354	1.242	26.03	22.23
-1	7.792	-2.924	24.37	23.72	6.176	1.199	24.70	23.39
0	7.692	-2.857	24.00	24.00	6.087	1.176	24.00	24.00
1	7.591	-2.790	23.62	24.30	5.998	1.153	23.28	24.64
3	7.385	-2.656	22.81	24.93	5.819	1.105	21.75	25.99
5	7.174	-2.520	21.94	25.62	5.641	1.053	20.08	27.48
7	6.957	-2.381	21.00	26.39	5.463	0.9983	18.23	29.13
9	6.734	-2.239	19.96	27.24	5.286	0.9384	16.13	31.02
11	6.504	-2.094	18.79	28.21	5.112	0.8726	13.66	33.22
13	6.267	-1.943	17.46	29.33	4.943	0.7985	10.64	35.90
15	6.021	-1.784	15.91	30.64	4.784	0.7114	6.650	39.41

Table 3 Values of Nu_- , Nu_+ , $f_- Re$, $f_+ Re$, for $|Br_q| = 10$

ϵ	$Br_q = -10$				$Br_q = 10$			
	Nu_-	Nu_+	$f_- Re$	$f_+ Re$	Nu_-	Nu_+	$f_- Re$	$f_+ Re$
-17	8.263	-0.2288	31.33	18.19	8.107	0.2088	31.82	17.72
-15	8.092	-0.2228	30.58	18.75	7.936	0.2036	31.01	18.33
-13	7.920	-0.2168	29.81	19.33	7.763	0.1983	30.19	18.96
-11	7.745	-0.2106	29.01	19.94	7.589	0.1929	29.34	19.63
-9	7.568	-0.2043	28.19	20.59	7.413	0.1873	28.46	20.32
-7	7.389	-0.1979	27.34	21.27	7.235	0.1815	27.55	21.06
-5	7.207	-0.1912	26.44	21.98	7.055	0.1756	26.60	21.83
-3	7.023	-0.1845	25.51	22.75	6.872	0.1695	25.60	22.65
-1	6.837	-0.1775	24.52	23.57	6.688	0.1632	24.55	23.54
0	6.743	-0.1739	24.00	24.00	6.595	0.1600	24.00	24.00
1	6.648	-0.1703	23.46	24.45	6.501	0.1567	23.43	24.48
3	6.456	-0.1628	22.33	25.41	6.312	0.1499	22.23	25.51
5	6.262	-0.1551	21.11	26.45	6.121	0.1428	20.92	26.64
7	6.065	-0.1470	19.76	27.62	5.927	0.1354	19.48	27.89
9	5.864	-0.1384	18.26	28.92	5.732	0.1275	17.87	29.30
11	5.661	-0.1294	16.54	30.42	5.534	0.1191	16.03	30.92
13	5.456	-0.1196	14.52	32.18	5.335	0.1099	13.84	32.84
15	5.247	-0.1087	12.04	34.35	5.135	0.09964	11.12	35.22
17	5.038	-0.09633	8.766	37.20	4.937	0.08768	7.450	38.42

tables, the first 26 terms of the perturbation expansions are sufficient to obtain four decimal places accuracy. Tables 1-4 show that Nu_- , $|Nu_+|$ and $f_- Re$ are decreasing functions of ϵ , while $f_+ Re$ is an increasing function of ϵ . This means that, for downward flow ($\epsilon < 0$), the absolute values of the Nusselt numbers on both walls and the friction factor on the boundary $Y = -L$ are increased by buoyancy. On the other hand, for upward flow ($\epsilon > 0$), the values of these parameters are lowered when buoyancy forces are taken into account. Tables 1-4 also show that, for $Br_q < 0$, the values of Nu_+ are negative. This result can be explained as follows. Figure 2, which refers to $Br_q = -0.5$, shows that $T(L) > T_0$ and that the derivative of T at $Y = L$ is negative, i.e., that the heat flux density at $Y = L$ is directed outside the channel. Therefore, one infers that, for $Br_q < -0.5$, viscous dissipation is so intense that the heat subtraction at $Y = L$ is not sufficient to induce a condition $T(L) < T_0$. Indeed, if one considers an engine oil at 300 K with $\mu = 0.486$ Pa s (Incropera and DeWitt, 1985) and a channel flow with $L = 0.5$ cm, $U_0 = 0.5$ m/s, one obtains that the condition $Br_q < -0.5$ corresponds to a heat flux density at $Y = L$ whose modulus is smaller than 48.6 W/m². Figures 2-5 show that the effect of buoyancy is more important in the case of upward flow than in the case of downward flow. In particular, these figures

reveal that, for upward flow, buoyancy causes both an increase of the temperature difference between the channel walls and an increase of the velocity at any given position in the region $0 < Y < L$. An analysis of Tables 1-4 and of Figs. 2-5 leads to the following conclusion. As the modulus of Br_q increases, the sign of Br_q becomes less and less important in the evaluation of both the velocity distribution and the temperature distribution. This conclusion is reasonable since an increase of $|Br_q|$ corresponds to a decrease of the heat flux at $Y = L$. Therefore, when the modulus of q_w is small, a change of direction of the heat flux density yields small changes of both the velocity distribution and the temperature distribution. In particular, the flow and heat transfer regimes which correspond to $Br_q \rightarrow +\infty$ and $Br_q \rightarrow -\infty$ are coincident. In fact, both these limits refer to the same physical circumstance, i.e., a

Table 4 Values of Nu_- , Nu_+ , $f_- Re$, $f_+ Re$, for $|Br_q| \rightarrow \infty$

ϵ	$ Br_q \rightarrow \infty$		
	Nu_-	$f_- Re$	$f_+ Re$
-17	8.183	31.58	17.95
-15	8.012	30.80	18.54
-13	7.839	30.00	19.15
-11	7.665	29.18	19.79
-9	7.488	28.33	20.45
-7	7.310	27.44	21.16
-5	7.129	26.52	21.91
-3	6.946	25.55	22.70
-1	6.760	24.53	23.55
0	6.667	24.00	24.00
1	6.572	23.45	24.47
3	6.382	22.28	25.46
5	6.189	21.02	26.55
7	5.994	19.62	27.75
9	5.796	18.06	29.11
11	5.596	16.28	30.67
13	5.393	14.18	32.51
15	5.189	11.58	34.78
17	4.986	8.116	37.80

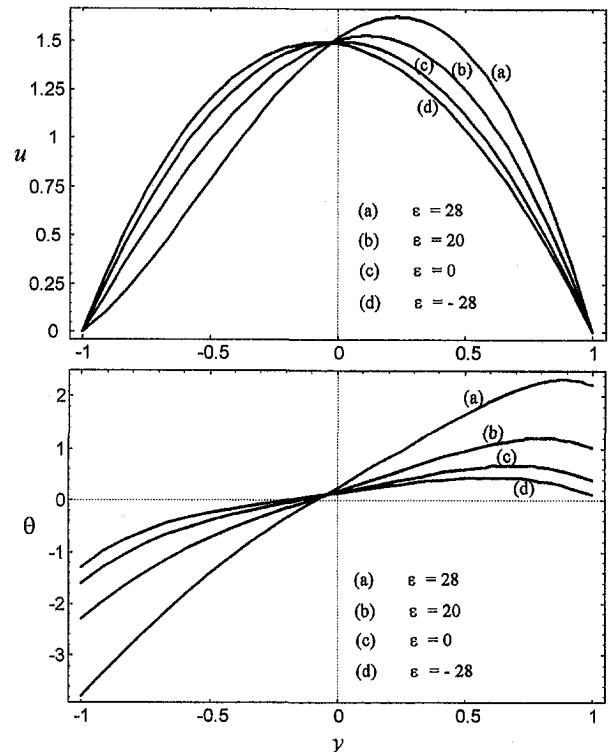


Fig. 2 Plots of u and θ versus y for $Br_q = -0.5$

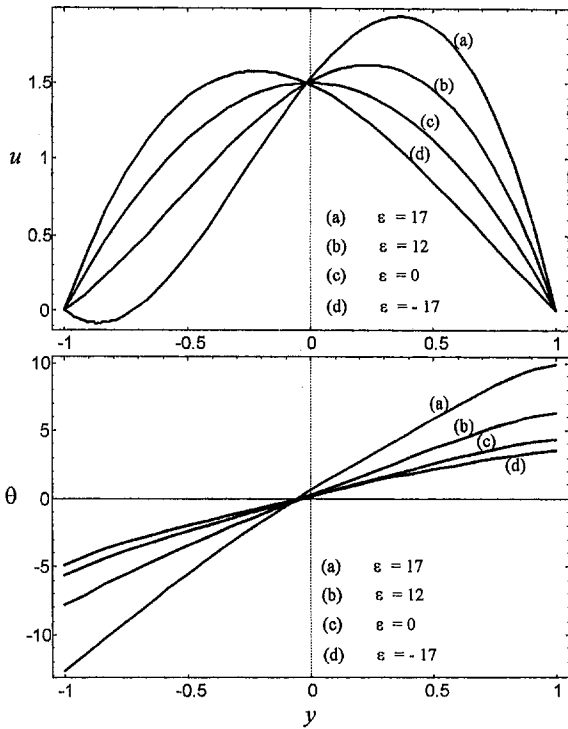


Fig. 3 Plots of u and θ versus y for $Br_q = 0.5$

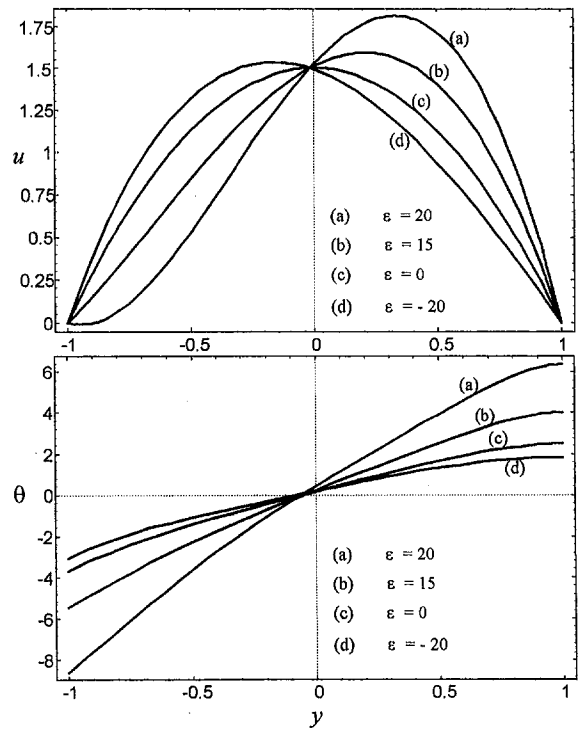


Fig. 5 Plots of u and θ versus y for $Br_q = 10$

channel with the wall $Y = L$ insulated. Tables 3 and 4 show that the values of Nu_- , Nu_+ , $f_- Re$, $f_+ Re$ for $Br_q = -10$ and for $Br_q = 10$ do not differ substantially from those obtained in the limit $|Br_q| \rightarrow \infty$. More precisely, for any given ϵ and in the limit $|Br_q| \rightarrow \infty$, the value of each of the parameters Nu_- , Nu_+ , $f_- Re$, $f_+ Re$ lies in the interval between the value for $Br_q = -10$ and that for $Br_q = 10$. In Table 4, the values of Nu_+ do not appear because, in the limit $|Br_q| \rightarrow \infty$, $Nu_+ = 0$ for every ϵ .

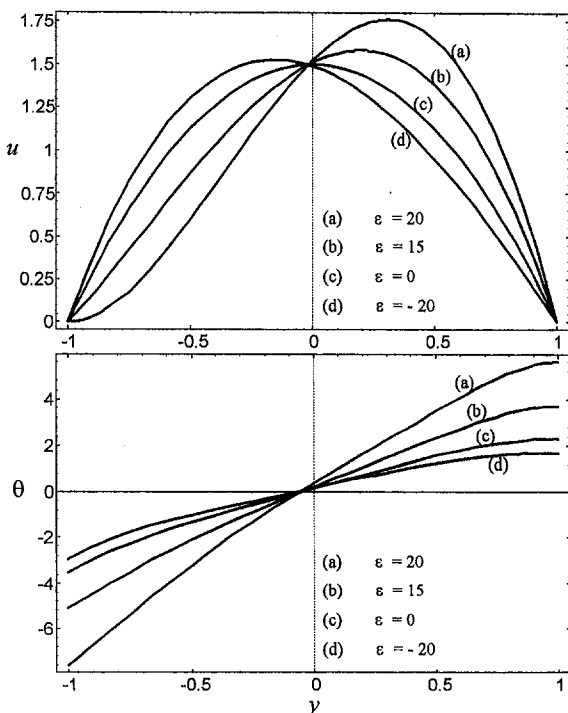


Fig. 4 Plots of u and θ versus y for $Br_q = -10$

Figure 3 refers to the case $Br_q = 0.5$ and shows that, for $\epsilon = 17$, a flow reversal occurs in the neighborhood of $Y = -L$, where u is negative. Also Fig. 5, which refers to $Br_q = 10$, displays a less apparent flow reversal in the neighborhood of $Y = -L$ for the case $\epsilon = 20$. Indeed, the occurrence of flow reversal phenomena is a well-known feature of mixed convection in inclined and vertical channels. Aung and Worku (1986), Lavine (1988), Cheng et al. (1990), Hamadah and Wirtz (1991) have presented wide analyses of flow reversal in fully developed channel flow, based on the assumption that viscous dissipation can be considered as negligible.

In Figs. 6–8, plots of Br_T , λ , and η versus ϵ are reported for different values of Br_q . Figure 6 shows that, for every Br_q , the temperature Brinkman number Br_T is a decreasing function of ϵ . On the other hand, for every ϵ , Br_T is a decreasing function of $|Br_q|$ if $Br_q < 0$, while Br_T is an increasing function of Br_q if $Br_q > 0$. Indeed, in Fig. 6, the narrow region bounded by the curves for $Br_q = -10$ and for $Br_q = 10$ would contain all the curves for every Br_q such that $|Br_q| > 10$. On account of Fig. 6 and of Eq. (18) one can conclude that, for upward flow, buoyancy enhances the temperature difference between the channel walls, while, for down-

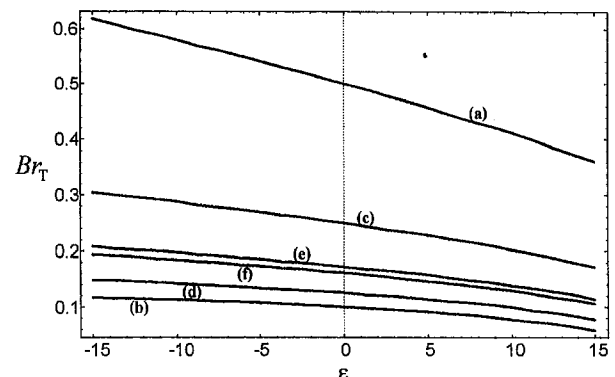


Fig. 6 Plots of Br_T versus ϵ for (a) $Br_q = -0.5$, (b) $Br_q = 0.5$, (c) $Br_q = -1$, (d) $Br_q = 1$, (e) $Br_q = -10$, (f) $Br_q = 10$

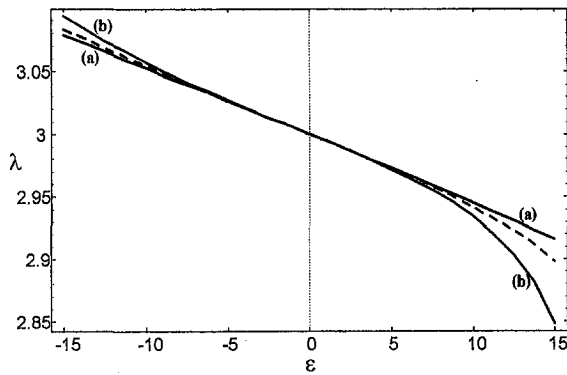


Fig. 7 Plots of λ versus ϵ for (a) $Br_q = -0.5$, (b) $Br_q = 0.5$. The dashed line refers to $Br_q \rightarrow \pm\infty$.

ward flow, buoyancy reduces the difference between the wall temperatures. Figure 7 shows that, for a fixed value of Br_q , the dimensionless pressure drop λ is a decreasing function of ϵ . In the interval $-0.5 \leq \epsilon \leq 0.5$, the curves for every Br_q such that $|Br_q| > 0.5$ are almost coincident. Indeed, in Fig. 7 only the curves for $Br_q = -0.5$, $Br_q \rightarrow \pm\infty$ and for $Br_q = 0.5$ are reported. However, the plots for every Br_q such that $|Br_q| > 0.5$ would lie in the region between the curve for $Br_q = -0.5$ and that for $Br_q = 0.5$. Moreover, Fig. 7 reveals that the effect of the dimensionless parameter Br_q is more apparent for upward flow than for downward flow. Figure 8 shows that η is an increasing function of ϵ . On the other hand, for every ϵ , η is an increasing function of $|Br_q|$ if $Br_q < 0$, while η is a decreasing function of Br_q if $Br_q > 0$. The narrow region bounded by the curves for $Br_q = -10$ and for $Br_q = 10$ would contain all the curves for every Br_q such that $|Br_q| > 10$. Figures 6 and 8 as well as Figs. 2–5 reveal that, in the case of downward flow, buoyancy causes the temperature distribution to become more uniform, while the opposite occurs in the case of upward flow.

Conclusions

The effect of buoyancy in the laminar mixed convection with viscous dissipation has been analysed with reference to a channel flow such that one of the boundaries is isothermal and the other is subjected to a uniform heat flux. The velocity field has been assumed to be parallel. The governing equations have been written in a dimensionless form such that the dimensionless velocity profile and the dimensionless temperature profile are uniquely determined by the heat-flux Brinkman number Br_q and by the ratio between the Grashof number and the Reynolds number, $\epsilon =$

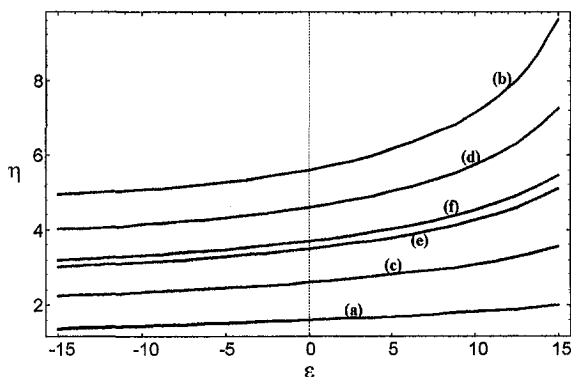


Fig. 8 Plots of η versus ϵ for (a) $Br_q = -0.5$, (b) $Br_q = 0.5$, (c) $Br_q = -1$, (d) $Br_q = 1$, (e) $Br_q = -10$, (f) $Br_q = 10$

Gr/Re . The parameter Br_q accounts for the effect of viscous dissipation, while the parameter ϵ accounts for the effect of buoyancy. The laminar forced convection with viscous heating has been considered as the base flow. The changes of the base flow induced by the effect of buoyancy have been taken into account by means of a perturbation series method. More precisely, the dimensionless velocity and the dimensionless temperature have been expressed as power series with respect to ϵ . Obviously, the zero-order term of the perturbation series corresponds to the base flow, i.e., to forced convection. The finite radius of convergence of the perturbation series has been evaluated for some values of Br_q by estimates of D'Alembert's ratio limit. Tables of the Nusselt numbers and of the Fanning friction factors have been presented. An analysis of the results has led to the following outcomes.

- The effect of buoyancy is more apparent for upward flow than for downward flow.
- Flow reversal next to the boundary with a prescribed temperature has been shown to occur for upward flow with a sufficiently high value of ϵ and for positive values of Br_q .
- In the case of downward flow, the absolute values of the Nusselt numbers on both walls and the friction factor on the boundary with a prescribed temperature are increased by buoyancy. The opposite occurs in the case of upward flow.
- For a given value of Br_q , the effect of buoyancy yields, for upward flow, an increase of the temperature difference between the channel walls, while, for downward flow, buoyancy causes a decrease of this difference.

References

- Aung, W., and Worku, G., 1986, "Theory of Fully Developed, Combined Convection Including Flow Reversal," *ASME JOURNAL OF HEAT TRANSFER*, Vol. 108, pp. 485–488.
- Aziz, A., and Na, T. Y., 1984, *Perturbation Methods in Heat Transfer*, Hemisphere, Washington, DC.
- Barletta, A., 1998, "Laminar mixed convection with viscous dissipation in a vertical channel," *International Journal of Heat and Mass Transfer*, Vol. 41, pp. 3501–3513.
- Chen, Y.-C., and Chung, J. N., 1996, "The linear stability of mixed convection in a vertical channel flow," *Journal of Fluid Mechanics*, Vol. 325, pp. 29–51.
- Chen, Y.-C., and Chung, J. N., 1998, "Stability of Mixed Convection in a Differentially Heated Vertical Channel," *ASME JOURNAL OF HEAT TRANSFER*, Vol. 120, pp. 127–132.
- Cheng, C.-H., Kou, H.-S., and Huang, W.-H., 1990, "Flow reversal and heat transfer of fully developed mixed convection in vertical channels," *Journal of Thermophysics*, Vol. 4, pp. 375–383.
- Gebhart, B., 1962, "Effects of viscous dissipation in natural convection," *Journal of Fluid Mechanics*, Vol. 14, pp. 225–232.
- Hamadah, T. T., and Wirtz, R. A., 1991, "Analysis of Laminar Fully Developed Mixed Convection in a Vertical Channel With Opposing Buoyancy," *ASME JOURNAL OF HEAT TRANSFER*, Vol. 113, pp. 507–510.
- Incropera, F. P., and DeWitt, D. P., 1985, *Fundamentals of Heat and Mass Transfer*, John Wiley and Sons, New York, p. 772.
- Iqbal, M., Aggarwala, B. D., and Rokerya, M. S., 1970, "Viscous Dissipation Effects on Combined Free and Forced Convection Through Vertical Circular Tubes," *ASME Journal of Applied Mechanics*, Vol. 37, pp. 931–935.
- Morton, B. R., 1960, "Laminar convection in uniformly heated vertical pipes," *Journal of Fluid Mechanics*, Vol. 8, pp. 227–240.
- Lavine, A. S., 1988, "Analysis of fully developed opposing mixed convection between inclined parallel plates," *Wärme- und Stoffübertragung*, Vol. 23, pp. 249–257.
- Lavine, A. S., 1993, "On the linear stability of mixed and free convection between inclined parallel plates with fixed heat flux boundary conditions," *International Journal of Heat and Mass Transfer*, Vol. 36, pp. 1373–1387.
- Rokerya, M. S., and Iqbal, M., 1971, "Effects of viscous dissipation on combined free and forced convection through vertical concentric annuli," *International Journal of Heat and Mass Transfer*, Vol. 14, pp. 491–495.
- Shah, R. K., and London, A. L., 1978, *Laminar Flow Forced Convection in Ducts*, Academic Press, New York, p. 45.
- Soundalgekar, V. M., Lahurikar, R. M., and Pohanerkar, S. G., 1997, "Transient free convection flow of an incompressible viscous dissipative fluid," *Heat and Mass Transfer*, Vol. 32, pp. 301–305.
- Turcotte, D. L., Hsui, A. T., Torrance, K. E., and Schubert, G., 1974, "Influence of viscous dissipation on Bénard convection," *Journal of Fluid Mechanics*, Vol. 64(Part 2), pp. 369–374.
- Zanchini, E., 1998, "Effect of viscous dissipation on mixed convection in a vertical channel with boundary conditions of the third kind," *International Journal of Heat and Mass Transfer*, Vol. 41, pp. 3949–3959.

Radiative Heat Transfer in Periodic Geometries Using a Finite Volume Scheme

S. R. Mathur

J. Y. Murthy

Mem. ASME

Fluent, Inc.,
10 Cavendish Court,
Lebanon, NH 03766

A procedure for computing radiative heat transfer in translationally and rotationally periodic geometries is presented. The finite volume scheme is applied to meshes composed of arbitrary polyhedral control volumes. The angular domain is discretized into a finite number of control angles over which radiant energy is conserved. At periodic boundaries, control angle overhang occurs because of the misalignment of the arbitrary periodic face with the global angular discretization and due to the arbitrary rotation of adjacent modules with respect to each other. A discretization scheme using control angle pixelation is developed to conservatively transfer radiant energy between adjacent modules. The method is tested for a variety of radiation problems and shown to perform satisfactorily.

Introduction

Periodic flow and heat transfer occurs in a number of engineering applications. Heat exchangers employ repeating units of fins, dimples, or indentations to increase heat transfer area and improve heat exchanger performance. In many applications, rotational periodicity may be invoked. Burners and combustors, for example, employ swirler vanes and secondary air inlets which destroy axisymmetry. However, it is frequently possible to restrict computations to a single rotationally periodic module and thus to reduce computational time. It would be useful to devise general-purpose calculation procedures for radiative heat transfer in arbitrary geometries with arbitrary rotational and translational periodicity.

Our objective is to devise a method for computing radiative heat transfer in periodically repeating domains, either of the translational or the rotational type, using the finite volume method (Raithby and Chui, 1990; Chai et al., 1994; Chui and Raithby, 1993; Murthy and Mathur, 1998a). In the discrete ordinates and finite volume schemes, the angular space is divided into finite solid angles, each associated with an ordinate direction. These directions are fixed in the global coordinate system. At translationally periodic boundaries, there is, in general, no guarantee that the boundary will align with the global angular discretization, resulting in control angle overhang. For rotational periodicity, radiant energy leaving the periodic boundary in a given direction reenters the domain at the opposing periodic boundary in a direction rotated by the periodic angle. For an arbitrary periodic angle in an arbitrary domain, there is no guarantee that either the original ray direction or the rotated direction coincides with the global angular discretization, and again, control angle overhang results. It is necessary to account for this overhang in a manner which conserves radiant energy, so as to maintain the fundamental conservative property of finite volume schemes. Furthermore, unless the correct rotation angle is imposed on the ray, incorrect results are obtained.

A few examples of rotational and translational periodicity have been published in the literature. Kaviany and Singh (1993) used translationally periodic boundary conditions in conjunction with a Monte Carlo technique for computing radiation heat transfer in a bed packed with randomly placed spheres. Maruy-

ama and Higano (1997) applied the REM² technique to radiation in a toroid for a fusion reactor application. Here, a rotationally periodic domain of 36 deg was chosen, and "mirror" conditions were applied at the periodic boundaries. In axisymmetric geometries, rotational periodicity is invoked in the tangential direction to deduce a reduced set of governing equations (Modest, 1993). Chui and Raithby (1992) and Murthy and Mathur (1998b) exploited rotational periodicity in deriving conservative numerical schemes for axisymmetric geometries in the context of the finite volume method. However, in both these cases, the azimuthal angular discretization is adjusted to match the spatial discretization in the tangential spatial direction, avoiding control angle overhang.

In this paper, we formulate a treatment of translationally and rotationally periodic domains based on the unstructured finite volume scheme of Murthy and Mathur (1998a). Energy conservation is imposed on meshes of arbitrary polyhedra for each discrete angular direction. A pixelation algorithm is used to conservatively transfer energy between periodic modules. The scheme is applied to a number of periodic problems and shown to match ray tracing results and published numerical solutions.

Governing Equations

Radiative Transport Equation. The radiative transfer equation for a gray absorbing, emitting, and scattering medium in the direction \mathbf{s} may be written as

$$\frac{\partial I_{s_i}}{\partial x_i} = -(\kappa(\mathbf{r}) + \sigma_s(\mathbf{r}))I(\mathbf{r}, \mathbf{s}) + B(\mathbf{r}, \mathbf{s}) \quad (1)$$

where s_i are the components of \mathbf{s} and

$$B = \kappa(\mathbf{r})I_b(\mathbf{r}) + \frac{\sigma_s(\mathbf{r})}{4\pi} \int_{4\pi} I(\mathbf{r}, \mathbf{s}')\Phi(\mathbf{s}', \mathbf{s})d\Omega'. \quad (2)$$

Boundary Conditions

The treatment of gray-diffuse boundaries has been described in Murthy and Mathur (1998a). We consider here radiative boundary conditions at periodic boundaries.

Definition of Periodicity. A translationally periodic domain is shown in Fig. 1(a). Here, each periodic boundary in the domain is associated with a corresponding periodic shadow. The periodic boundary is translated by a vector \mathbf{L} to obtain the shadow boundary. A rotationally periodic do-

Contributed by the Heat Transfer Division for publication in the JOURNAL OF HEAT TRANSFER and presented at the '98 IMECE, Anaheim, CA. Manuscript received by the Heat Transfer Division, Mar. 30, 1998; revision received Oct. 1, 1998. Keywords: Computational, Heat Transfer, Periodic, Radiation. Associate Technical Editor: P. Menguc.

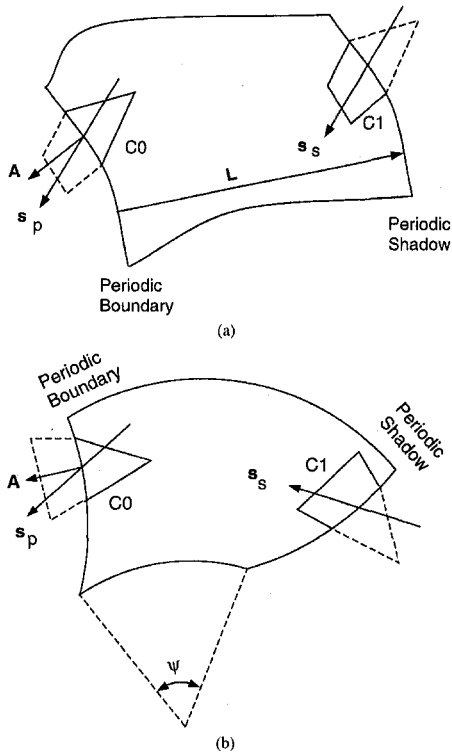


Fig. 1 Periodic domains; (a) translationally periodic, (b) rotationally periodic

main is shown in Fig. 1(b). Here, the shadow boundary is obtained by rotating the periodic boundary by an angle Ψ about a unit axis vector \mathbf{e}_a .

Thermal Periodicity. Consider the geometry in Fig. 1(a). For translationally periodic radiative transfer, the temperature exhibits a periodicity of the type

$$T(\mathbf{r}) = T(\mathbf{r} + \mathbf{L}) \quad (3)$$

where \mathbf{L} is the translation vector.

For rotationally periodic domains, such as that in Fig. 1(b),

$$T(\mathbf{r}) = T(\hat{\mathbf{r}}) \quad (4)$$

where

$$\hat{\mathbf{r}} = \mathbf{M}^T \mathbf{C} \mathbf{M} \mathbf{r} \quad (5)$$

\mathbf{M} and \mathbf{C} are orthogonal transformation matrices given by

$$\mathbf{M} = \begin{bmatrix} -e_{ay}/\sqrt{1-e_{az}^2} & e_{ax}/\sqrt{1-e_{az}^2} & 0 \\ -e_{ax}e_{az}/\sqrt{1-e_{az}^2} & -e_{ay}e_{az}/\sqrt{1-e_{az}^2} & \sqrt{1-e_{az}^2} \\ e_{ax} & e_{ay} & e_{az} \end{bmatrix} \quad (6)$$

Nomenclature

\mathbf{A} = area vector
 \mathbf{e}_a = rotation axis for rotational periodicity
 I = intensity
 I_b = black-body intensity $\sigma T^4/\pi$
 κ = absorption coefficient
 \mathbf{L} = translation vector for translational periodicity
 \mathbf{n} = unit normal vector
 N_θ, N_ϕ = polar and azimuthal control angles per octant

q = radiative heat flux
 \mathbf{r} = position vector
 \mathbf{r}_p = position vector on periodic boundary
 \mathbf{r}_s = position vector on periodic shadow
 s = coordinate along ray
 \mathbf{s} = ray direction vector
 \mathbf{s}_p = ray direction vector at periodic boundary
 \mathbf{s}_s = ray direction vector at periodic shadow
 T = temperature

$$\mathbf{C} = \begin{bmatrix} \cos \Psi & -\sin \Psi & 0 \\ \sin \Psi & \cos \Psi & 0 \\ 0 & 0 & 1 \end{bmatrix} \quad (7)$$

Here, $\mathbf{e}_a = [e_{ax}, e_{ay}, e_{az}]^T$.

Translational and rotational periodicity of the type described here is realizable without any restriction on thermal boundary conditions and fluid properties, save that they exhibit the same spatial periodicity imposed by the geometry.

Radiative Boundary Conditions at Translationally Periodic Boundaries. Consider Fig. 1(a). A ray in the direction \mathbf{s}_p , which leaves the periodic boundary reenters the domain at the periodic shadow boundary in the direction \mathbf{s}_s , parallel to \mathbf{s}_p . The intensities on the periodic and shadow boundaries are thus related by

$$I(\mathbf{r}_p, \mathbf{s}_p) = I(\mathbf{r}_p + \mathbf{L}, \mathbf{s}_s) \quad (8)$$

Radiative Boundary Conditions at Rotationally Periodic Boundaries. Consider Fig. 1(b). A ray leaving the periodic boundary in the direction \mathbf{s}_p reenters the domain at the periodic shadow boundary in the direction \mathbf{s}_s , where

$$\mathbf{s}_s = \mathbf{M}^T \mathbf{C} \mathbf{M} \mathbf{s}_p \quad (9)$$

The intensities at the periodic and shadow boundaries are given by

$$I(\mathbf{r}_p, \mathbf{s}_p) = I(\mathbf{r}_s, \mathbf{s}_s) \quad (10)$$

where \mathbf{r}_s is given by

$$\mathbf{r}_s = \mathbf{M}^T \mathbf{C} \mathbf{M} \mathbf{r}_p \quad (11)$$

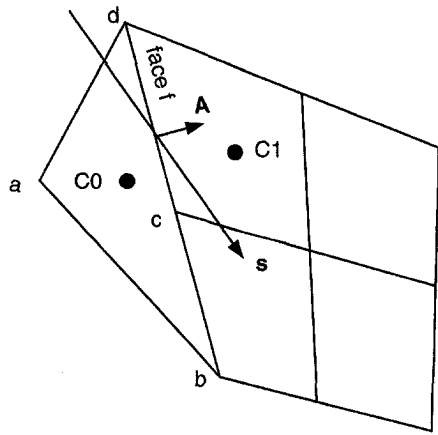
Numerical Method

A detailed description of the basic method is available in Murthy and Mathur (1998a). We briefly summarize the main ideas and then consider the treatment of periodic boundaries.

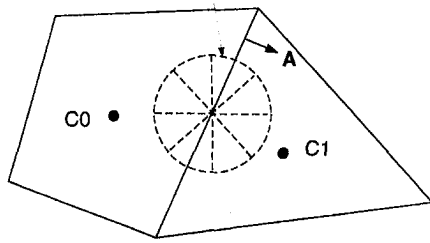
Spatial and Angular Discretization. The domain is discretized into arbitrary unstructured convex polyhedral cells, as shown in Fig. 2(a). All unknowns are stored at cell centers. The angular space 4π at any spatial location is discretized into discrete nonoverlapping solid angles ω_i , the centroids of which are denoted by the direction vector \mathbf{s}_i . The associated polar and azimuthal angles are (θ_i, ϕ_i) . Here θ is measured from the z-axis and ϕ is measured from the y-axis. The (θ, ϕ) extents of the solid angle are given by $\Delta\theta$ and $\Delta\phi$, and are assumed constant. Each octant is discretized into $N_\theta \times N_\phi$ solid angles.

Control Volume Balance. For each discrete direction i , Eq. (1) is integrated over the control volume $C0$ and the control angle ω_i to yield

x_j = coordinate direction
 ΔV = volume of control volume
 Φ = scattering phase function
 Ψ = periodic rotation angle
 Ω = solid angle
 ω_i = discrete solid angle associated with direction i
 θ = polar angle
 ϕ = azimuthal angle
 σ_s = scattering coefficient
 σ = Stefan-Boltzmann constant



(a)
Overhanging
Control Angle



Face f
(b)

Fig. 2 (a) Control volume; (b) control angle overhang

$$\sum_f J_f I_{if} = -(\kappa + \sigma_s) I_{i0} + B_i \omega_i \Delta V_0. \quad (12)$$

Here I_{if} is the intensity associated with the direction i at the face f of the control volume, and I_{i0} is the intensity at the cell $C0$. J_f is a geometric factor defined below.

The source term B_i is given by

$$B_i = \kappa I_{b0} + \frac{\sigma_s}{4\pi} \sum_j I_{j0} \gamma_{ij} \quad (13)$$

where

$$\gamma_{ij} = \frac{1}{\omega_i} \int_{\omega_j} \int_{\omega_j} \Phi(\mathbf{s}_i \cdot \mathbf{s}_j) d\omega_j d\omega_j'. \quad (14)$$

The black-body intensity I_{b0} is based on the temperature of the cell $C0$. I_{j0} are the cell intensities in the directions j .

Face Intensity Treatment. Since the directions \mathbf{s}_i are defined with respect to a global coordinate system (x, y, z) , the boundaries of the discrete solid angles ω_i do not necessarily align with arbitrary control volume faces and control-angle overhang results (Murthy and Mathur, 1998a). An example of control angle overhang is shown in Fig. 2(b). For unstructured and body-fitted meshes, control-angle overhang can occur at all interior and boundary faces, as well as at periodic boundaries.

We define the vector S_i as

$$S_i = \int_{\Delta\phi_i} \int_{\Delta\theta_i} \mathbf{s} \sin \theta d\theta d\phi. \quad (15)$$

The integration in Eq. (15) is done analytically. For directions i with no control angle overhang at the face f , the left-hand side of Eq. (12) is written as

$$J_f I_{if} = \mathbf{A} \cdot S_i I_{if}. \quad (16)$$

Here, \mathbf{A} is the area vector at face f pointing out of the $C0$ cell, as shown in Fig. 2. Using a first-order (step) scheme, we may write I_{if} using the value in the “upwind” cell

$$I_{if} = I_{i,\text{upwind}}. \quad (17)$$

A second-order approximation to I_{if} may also be written (Mathur and Murthy, 1997) but is not pursued in this paper.

Treatment of Control Angle Overhang. Two different approaches have been taken in the literature, and are described in Murthy and Mathur (1998a). Because these approaches are relevant for the treatment of periodic boundaries, we discuss them in detail below.

Approach A. Consider the direction i at an interior face f . The solid angle ω_i is considered wholly outgoing when $\mathbf{s}_i \cdot \mathbf{A} \geq 0$, where \mathbf{s}_i is the mean direction associated with ω_i . Once a solid angle is determined to be either incoming or outgoing to f , the radiative transfer at the face in the solid angle ω_i is written using Eq. (16), with Eq. (17) providing I_{if} . This approach has been taken by Chai et al. (1994).

Approach B. Here, the incoming and outgoing portions of the overhanging control angle i are treated differently. The face intensity I_{if} on the face f is written as

$$I_{if} = I_{i,\text{out}} \alpha_{i,\text{out}} + I_{i,\text{in}} \alpha_{i,\text{in}} \quad (18)$$

where

$$\alpha_{i,\text{out}} = \mathbf{A} \cdot \int_{\Delta\theta_i} \int_{\Delta\phi_i} \mathbf{s} \sin \theta d\theta d\phi, \quad \mathbf{s} \cdot \mathbf{A} > 0 \quad (19)$$

and

$$\alpha_{i,\text{in}} = \mathbf{A} \cdot \int_{\Delta\theta_i} \int_{\Delta\phi_i} \mathbf{s} \sin \theta d\theta d\phi, \quad \mathbf{s} \cdot \mathbf{A} \leq 0. \quad (20)$$

In Eq. (19) the integration is over the outgoing portion of the control angle while in Eq. (20) it is over the incoming portion. $I_{i,\text{out}}$ is the face intensity associated with the outgoing portion of the control angle and $I_{i,\text{in}}$ is that associated with the incoming portion. Under a first-order approximation

$$I_{i,\text{out}} = I_{i0} \quad (21)$$

and

$$I_{i,\text{in}} = I_{i1}. \quad (22)$$

Here, I_{i0} is the intensity in direction i in cell $C0$, and I_{i1} is that in cell $C1$ (see Fig. 2).

Pixelation. The integrals in Eqs. (19) and (20) are computed using pixelation (Murthy and Mathur, 1998a). Briefly, each control angle ω_i is subdivided into $N_{\theta_i} \times N_{\phi_i}$ pixels. Each pixel l in solid angle ω_i is identified by a pixel direction \mathbf{s}_{li} , written in terms of the pixel centroid angles (θ_{li}, ϕ_{li}) . The subtended solid angle is ω_{li} and the angular extents are $\Delta\theta_{li}$ and $\Delta\phi_{li}$. For the purposes of this paper, an equal angular distribution $(\Delta\theta_i, \Delta\phi_i)$ is used. For every pixel we define the vector S_{li} as

$$S_{li} = \int_{\Delta\theta_{li}} \int_{\Delta\phi_{li}} \mathbf{s} \sin \theta d\theta d\phi \quad (23)$$

and the integration is done analytically. The pixel \mathbf{s}_{li} is considered outgoing to f if $\mathbf{s}_{li} \cdot \mathbf{A} \geq 0$ and incoming otherwise. The quantities $\alpha_{i,\text{out}}$ and $\alpha_{i,\text{in}}$ are computed as

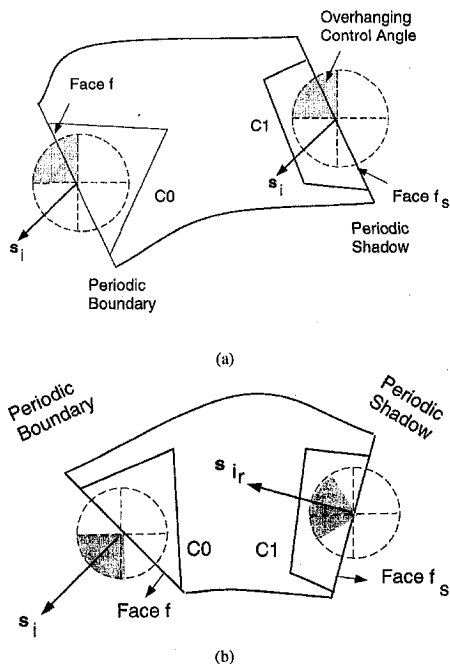


Fig. 3 Control angle overhang at (a) translationally periodic boundaries and (b) rotationally periodic boundaries

$$\alpha_{i,\text{out}} = \mathbf{A} \cdot \sum_i S_{ii}, \quad \text{pixels with } \mathbf{s}_{ii} \cdot \mathbf{A} \geq 0 \quad (24)$$

$$\alpha_{i,\text{in}} = \mathbf{A} \cdot \sum_i S_{ii}, \quad \text{pixels with } \mathbf{s}_{ii} \cdot \mathbf{A} < 0. \quad (25)$$

This procedure resolves control angle overhang up to the pixel resolution. Approach A is equivalent to approach B using 1 × 1 pixelation.

We emphasize that pixelation is not merely a refined angular discretization. Rather, it is a discrete method for computing the integrals in Eq. (19) and (20). Other methods, such as analytical integration, could be used as well. The same number of differential equations, $N_\theta \times N_\phi$ per octant, is solved regardless of whether approach A or approach B is used.

It was found in Murthy and Mathur (1998a) that approaches A and B yielded results of similar accuracy when used at interior faces. At gray-diffuse boundaries, approach B resulted in more accurate solutions when the angular discretization was coarse, but was not necessary for fine angular discretizations. For the calculations in this paper, interior faces are treated using approach A, and all gray-diffuse boundaries are treated using approach B.

Translationally Periodic Boundaries. Consider face f of cell $C0$ on the periodic face in Fig. 3(a). All energy leaving $C0$ through f in the direction \mathbf{s}_i in the solid angle ω_i enters cell $C1$. The entry face is f_s at the periodic shadow boundary, and the energy remains in the same solid angle in the same direction. Correspondingly, all energy leaving cell $C1$ in a given direction within a given solid angle enters cell $C0$. In this sense, $C0$ and $C1$ are neighbors, just like any other set of neighbor cells sharing an interior face. The treatment of translationally periodic boundaries is thus identical to that described above.

Rotationally Periodic Boundaries. Here, all control angles exhibit overhang for arbitrary rotational periodicity. We consider the two approaches in turn.

Approach A. Consider Fig. 3(b). The direction i is considered outgoing to the periodic face f if $\mathbf{s}_i \cdot \mathbf{A} \geq 0$, where \mathbf{s}_i is the mean ray direction associated with the solid angle. The

outgoing radiative transfer from cell $C0$ at the periodic boundary face f is given by

$$J_f I_{if} = \mathbf{A} \cdot S_i I_{i0} \quad (26)$$

for a first-order approximation.

This energy enters cell $C1$ at the periodic face f_s in the direction \mathbf{s}_i , where

$$\mathbf{s}_i = \mathbf{M}^T \mathbf{C} \mathbf{M} \mathbf{s}_i. \quad (27)$$

However, \mathbf{s}_i is not guaranteed to be coincident with any of the discrete directions \mathbf{s}_k of the underlying angular discretization. The energy transfer from the periodic face is assigned to the control angle \mathbf{s}_j at f_s within which \mathbf{s}_i falls. That is, \mathbf{s}_j satisfies

$$\left(\theta_j - \frac{\Delta\theta}{2} \right) < \theta_i \leq \left(\theta_j + \frac{\Delta\theta}{2} \right) \quad (28)$$

and

$$\left(\phi_j - \frac{\Delta\phi}{2} \right) < \phi_i \leq \left(\phi_j + \frac{\Delta\phi}{2} \right). \quad (29)$$

Thus rotationally periodic boundaries result in a transfer of energy from the solid angle ω_i to the solid angle ω_j . Once outgoing directions at both the periodic and shadow face are visited, the energy transfer from ω_i to all other solid angles, as well as the energy transfer from all other solid angles to ω_i , is complete. This transfer is completely conservative.

Approach B. Consider radiation in the solid angle ω_i at the face f on the periodic boundary as in Fig. 3(b). As before, the solid angle is divided into $N_{\theta_i} \times N_{\phi_i}$ pixels. An outgoing pixel ($S_{ii} \cdot \mathbf{A} \geq 0$) at f contributes

$$S_{ii} \cdot \mathbf{A} I_{if} \quad (30)$$

to the radiative transfer leaving cell $C0$. Using a first-order approximation, we may write the contribution as

$$S_{ii} \cdot \mathbf{A} I_{i0}. \quad (31)$$

The energy leaving cell $C0$ in the pixel centered about \mathbf{s}_{ii} enters cell $C1$ in the direction \mathbf{s}_{ir} , where

$$\mathbf{s}_{ir} = \mathbf{M}^T \mathbf{C} \mathbf{M} \mathbf{s}_{ii}. \quad (32)$$

If the pixel mean direction \mathbf{s}_{ir} falls within the boundaries of the solid angle ω_j at the periodic shadow, the radiative transfer to the direction j for cell $C1$ is augmented by the pixel energy (Eq. (30)). Here, \mathbf{s}_j satisfies Eqs. (28) and (29), with (θ_{ir}, ϕ_{ir}) substituted for (θ_i, ϕ_i) . With a first-order scheme, the energy transfer is given by Eq. (31).

Thus energy leaving in a pixel at the periodic boundary is transferred to a rotated direction at the periodic shadow boundary. By visiting all the outgoing pixels associated at both the periodic and shadow faces, the radiative transfer from solid angle ω_i to other solid angles as well as the transfer from other solid angles to ω_i may be computed. Approach B is thus a pixel-by-pixel implementation of approach A, and is completely conservative. The computation is accurate up to the pixel resolution.

For rotationally periodic geometries, accounting for control angle overhang is critical in correctly rotating the intensity field to capture periodic behavior. Pixelation allows this rotational property to be captured up to the pixel resolution. Though pixelation cannot eliminate the fundamentally discrete representation of the angular space that results in ray effects, it can mitigate these effects to a degree by improving the angular integration of radiant energy.

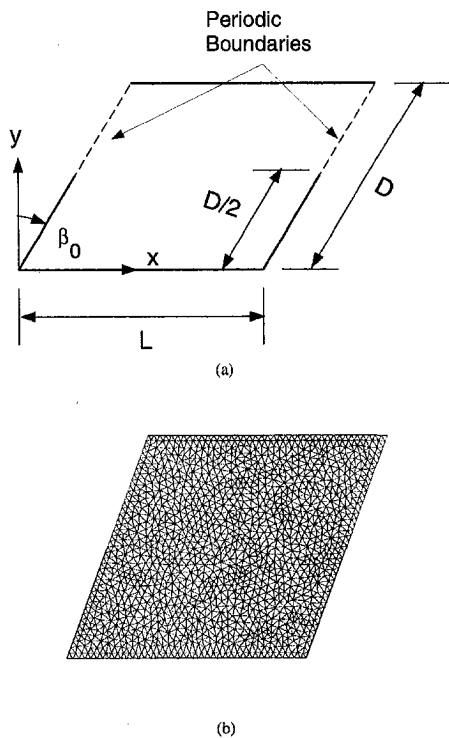


Fig. 4 Translationally periodic rhomboid: (a) schematic and (b) triangular mesh

Linear Solver. The discretization procedure leads to a set of linear equations relating the value of I_i at the cell center to its cell neighbors:

$$a_p I_{i,p} = \sum_{nb} a_{nb} I_{i,nb} + b. \quad (33)$$

Here, nb is the number of cell neighbors of cell P .

The cells $C0$ and $C1$ are coupled implicitly across translationally periodic boundaries because the energy transfer remains in the same direction. At rotationally periodic boundaries, however, there is a transfer of energy from one direction to another. The outgoing energy in the direction i again appears implicitly in the a_p term for cell $C0$ for direction i . However, the energy transferred to other directions from i appears explicitly in the b terms for those directions. Similarly, the energy transferred from other directions to the i direction appears in the b term for the i equation.

The algebraic set for each direction is solved iteratively, looping through all the discrete directions in turn until convergence. The contributions of other directions are computed from prevailing values. The system is solved using an algebraic multigrid procedure (Hutchinson and Raithby, 1986). For the examples in this paper, the Brandt cycle is used for intensity calculations. A Gauss-Seidel relaxation procedure is used at each multigrid level.

Results

Here we present results for a variety of radiation problems involving periodic boundaries. In the sections below, the angular discretization refers to that for an octant. The pixelation refers to that used for each control angle. Only boundary pixelation is used in all examples below. For two-dimensional cases, there is no need for pixelation in the θ direction; only ϕ pixelation is necessary. For purposes of timing, a solution is judged to have achieved convergence when the solution residual falls by four orders of magnitude. All timing results have been obtained using a Sun Ultra 1 work station. For the first two prob-

lems the present results are compared with the results of ray-tracing solutions. The solutions are obtained with a large number of rays (typically 800 per control surface); quadrupling the number of rays changes the solution by less than 0.3 percent.

Radiation in Translationally Periodic Rhomboid. Radiation with translationally periodic boundaries is considered in this problem. The domain is shown in Fig. 4(a). The aspect ratio L/D is chosen as unity. The lateral walls extend half way up the cavity, as shown. All the walls of the domain are black, and at $T = 0$. The cavity contains an absorbing and emitting medium at T_h . The angle β_0 is 20 deg. The periodic boundaries exhibit control angle overhang in the ϕ direction for all the angular discretizations used in the problem. The objective is to compute the net radiative heat flux on the bottom cavity wall for a variety of absorption coefficients and angular discretizations. The results are compared to a ray tracing solution obtained by dividing the boundaries into control surfaces of length $L/40$, with 800 rays per control surface.

Baseline calculations are done using structured quadrilateral meshes of 10×10 , 20×20 and 40×40 cells for $\kappa L = 1.0$. An angular discretization of 4×4 is used, with 1×1 pixelation (approach A). The maximum errors in the dimensionless incoming heat flux $q^* (=q/\sigma T_h^4)$ with respect to the ray tracing

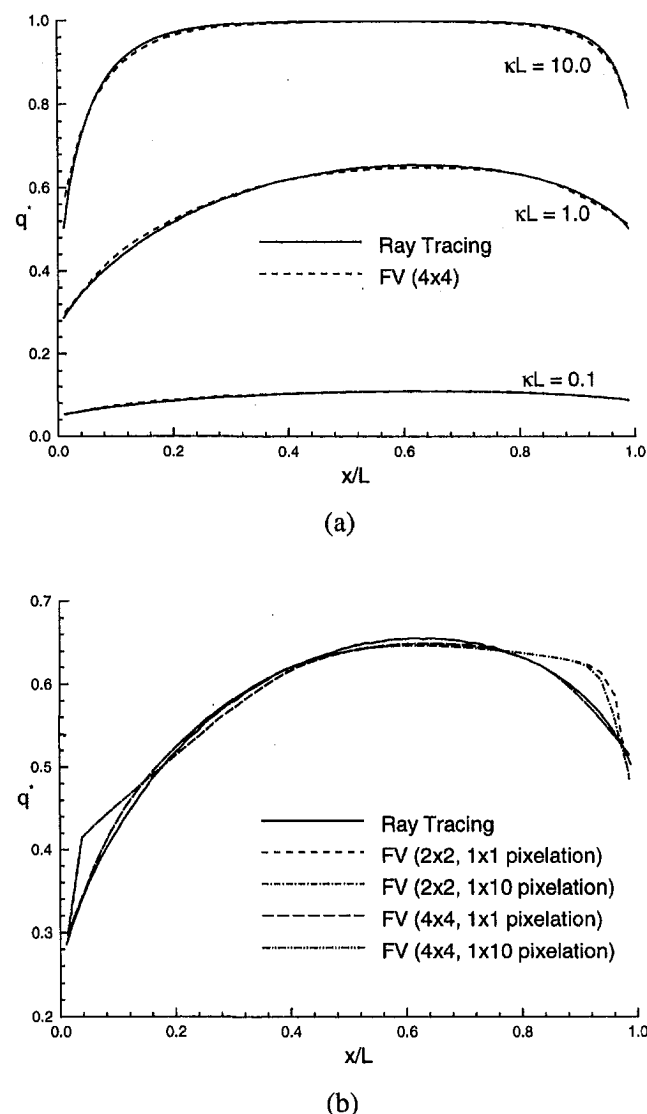


Fig. 5 Translationally periodic rhomboid: heat flux on bottom wall for (a) different optical thicknesses and (b) different angular discretizations

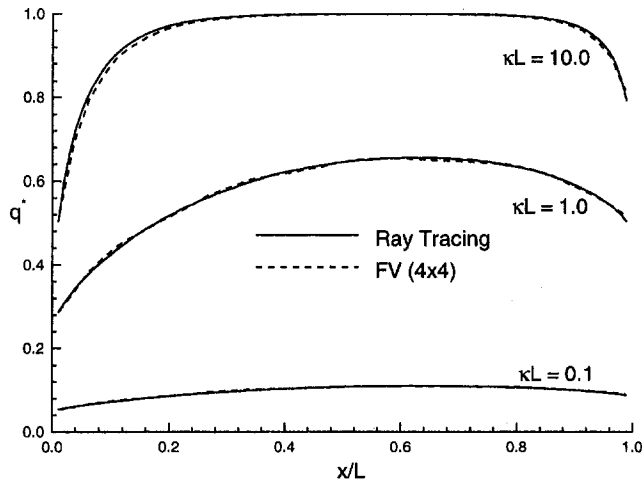


Fig. 6 Translationally periodic rhomboid: heat flux on bottom wall for different optical thicknesses using triangular mesh

solution for the 10×10 , 20×20 and 40×40 mesh are 3.4 percent, 1.5 percent, and 1 percent, respectively. The 40×40 mesh is used for all further calculations.

Figure 5(a) shows the prediction of q^* for $\kappa L = 0.1, 1.0$, and 10.0 . An angular discretization of 4×4 with 1×1 pixelation (approach A) is used. The maximum errors for the three cases are under two percent.

Figure 5(b) shows a comparison of computed q^* for various angular discretizations and pixelations for $\kappa L = 1.0$. The 2×2 angular discretization is not fine enough to capture the details at the corners of the domain. The 4×4 discretizations produces good results, with maximum errors of under two percent. Pixelation appears to offer no significant gain in accuracy. This result is in keeping with those obtained in Murthy and Mathur (1998a) where interior pixelation was shown not to change results substantially.

For the 40×40 mesh, a 2×2 angular discretizations with 1×1 pixelation requires approximately 3.1 seconds to converge. The corresponding time for 4×4 angular discretization is 11.2 seconds. For a 1×10 pixelation, the corresponding times for the 2×2 and 4×4 discretizations are 3.2 seconds and 11.3 seconds, respectively. Because the number of boundary faces is so small, there is no appreciable performance difference between approaches A and B.

Calculations are also done using an unstructured triangular mesh of 2542 cells, shown in Fig. 4(b). Figure 6 shows the variation of q^* on the bottom wall for different optical thicknesses for a 4×4 angular discretization for 1×1 pixelation. The errors with respect to the ray-tracing solution are found to be under two percent for all three optical thicknesses, and are of approximately the same magnitude as those using the quadrilateral mesh.

Radiation in Rotationally Periodic Domain. Here we consider participating radiation in the domain shown in Fig. 7(a). We consider the cylindrical annulus formed by two cylinders of radius r_i and r_o , respectively. The inner cylinder has vanes attached to it, spaced at an angle $\Delta\beta_d$, and angled at β_0 with respect to the radial direction. The vanes extend half way across the annulus. The calculation domain consists of one rotationally periodic module of extent $\Delta\beta_d$ and is positioned as shown in Fig. 7 with respect to the global coordinate system. The annulus is filled with an absorbing and emitting medium at T_h , with an optical thickness κr_i . As before, all walls are black and at $T = 0$. The objective is to compute the dimensionless incoming radiative heat flux q^* to the bottom wall and to compare it with that obtained by a ray tracing solution using 800 rays per control surface, with 40 control surfaces on the

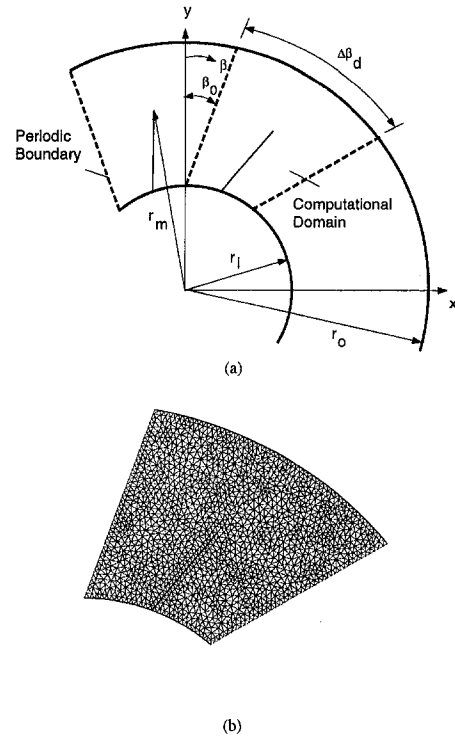


Fig. 7 Rotationally periodic domain: (a) schematic and (b) triangular mesh

cylindrical and periodic boundaries and 20 control surfaces on the vanes. For the calculations performed here, β_0 is 20 deg, $\Delta\beta_d$ is 40 deg, $r_o/r_i = 2$ and $r_m/r_i = 1.5$.

Baseline computations are done with two quadrilateral structured meshes of 20×20 and 40×40 cells, respectively, for $\kappa r_i = 1.0$. An angular discretization of 4×4 with 1×10 pixelation is used. The maximum error with respect to the ray tracing solution for the coarse and fine meshes are 2.9 percent and 1.8 percent, respectively. The 40×40 mesh is used for all further comparisons.

Figure 8 shows q^* on the bottom wall for different optical thicknesses using a 4×4 angular discretization with 1×10 pixelation. The data on the bottom wall has been rearranged so that the angular range covered by the plot is $-20 \text{ deg} \leq \beta \leq 20 \text{ deg}$, with β being measured from the y-axis, as shown in

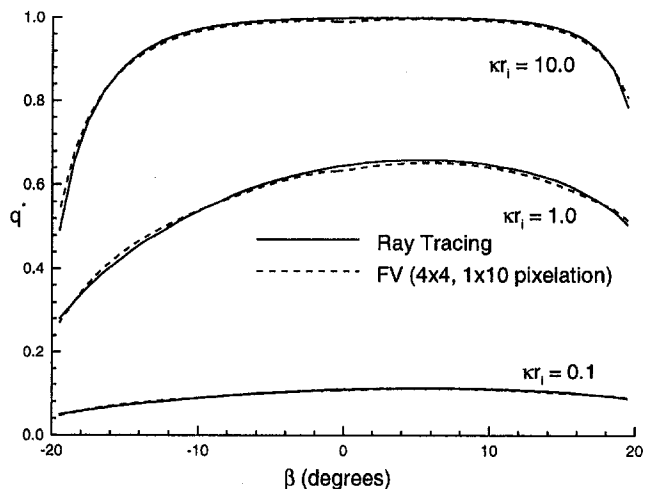
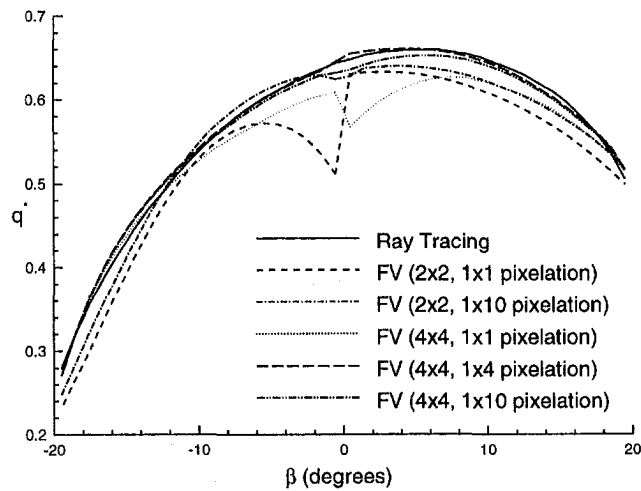
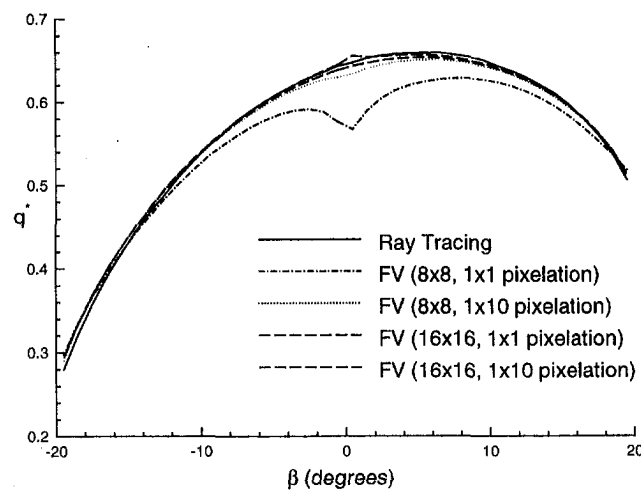


Fig. 8 Rotationally periodic domain: heat flux on bottom wall for different κr_i



(a)



(b)

Fig. 9 Rotationally periodic domain: heat flux on bottom wall for different angular discretizations

Fig. 7. The errors with respect to the ray-tracing solution are 1.6 percent, 1.8 percent, and 0.7 percent for $\kappa r_i = 0.1$, 1.0, and 10.0, respectively. Figures 9(a) and (b) show a comparison of different angular discretizations and pixelations for $\kappa r_i = 1.0$. A measure of solution correctness is the continuity of q^* across the periodic boundary, which occurs at $\beta = 0$. For coarse angular discretizations using approach A (1×1 pixelation) a jump in q^* is seen at $\beta = 0$, signaling errors in ray rotation at the periodic boundary. These errors persist even with an 8×8 angular discretization (Fig. 9(b)), but are substantially reduced for a 16×16 angular discretization. When 1×10 pixelation is used, the predicted q^* improves dramatically, with the maximum error under three percent for all the angular discretizations considered; for the 16×16 angular discretization, the maximum error is 0.76 percent. Calculations with a coarser 1×4 pixelation and a 4×4 angular discretization yielded results similar to the 1×10 pixelation.

For the 40×40 mesh, a 2×2 angular discretization with 1×1 pixelation requires approximately 3.9 seconds to converge. The corresponding time for 4×4 angular discretization is 14 seconds. For a 1×10 pixelation, the corresponding times for the 2×2 and 4×4 discretizations are 4.7 seconds and 14.25 seconds, respectively. Typically, about eight iterations are required to obtain convergence.

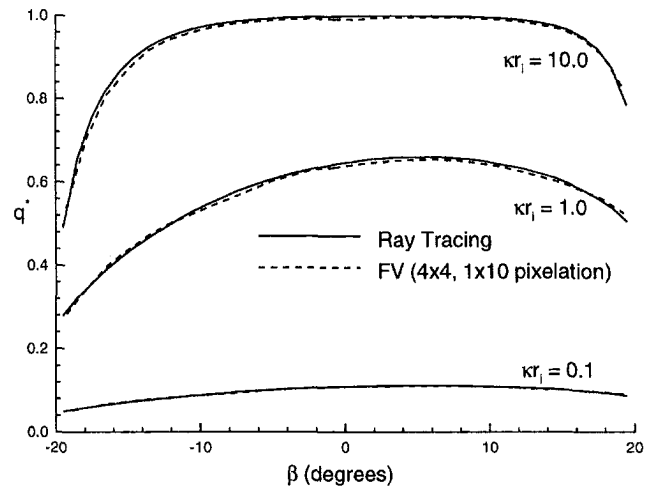


Fig. 10 Rotationally periodic domain: heat flux on bottom wall for different κr_i for triangular mesh

Calculations are also done using a triangular mesh of 2888 cells, shown in Fig. 7(b). Figure 10 shows the variation of q^* on the bottom wall for $\kappa r_i = 1.0$ for an angular discretization of 4×4 for 1×10 pixelation. The maximum errors for $\kappa r_i = 0.1$, 1.0 and 10.0 are 1.2 percent, 1.5 percent, and 0.7 percent, respectively. These errors are approximately of the same order as those obtained on the quadrilateral mesh.

Scattering in Cylindrical Enclosure. In this final problem, we consider isotropic scattering in an axisymmetric cylindrical domain shown in Fig. 11. The top and bottom walls of the cylinder are cold at $T = 0$, as is the medium contained in the cylinder. The lateral curved walls are black and hot, at T_h . The medium does not absorb or emit, but scatters isotropically with $\sigma_{r_o} = 1$. The ratio r_o/L is 0.5. Kim and Baek (1997) have presented the dimensionless net radiative flux on the lateral curved wall assuming axisymmetry. Here we use a three-dimensional rotationally periodic domain as shown in Fig. 11, with $\Delta\beta_d = 40$ deg centered symmetrically about the x -axis. This ensures that both rotationally periodic boundaries exhibit control angle overhang for all the angular discretizations considered here. Our objective is to match the axisymmetric results for radiative heat flux on the lateral wall.

A uniform mesh of $20 \times 21 \times 20$ cells is used in the r , β , and z directions, respectively. Figure 12(a) shows the variation of the dimensionless net radiative heat flux q_{net} ($=q/\sigma T_h^4$) leaving the lateral curved wall for 2×2 angular discretization. Two β locations are considered; the first is located at $\beta = 70.95$ deg

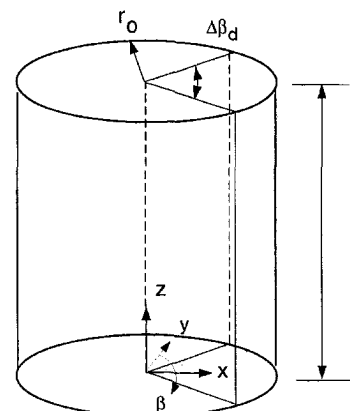


Fig. 11 Scattering in cylindrical domain: schematic

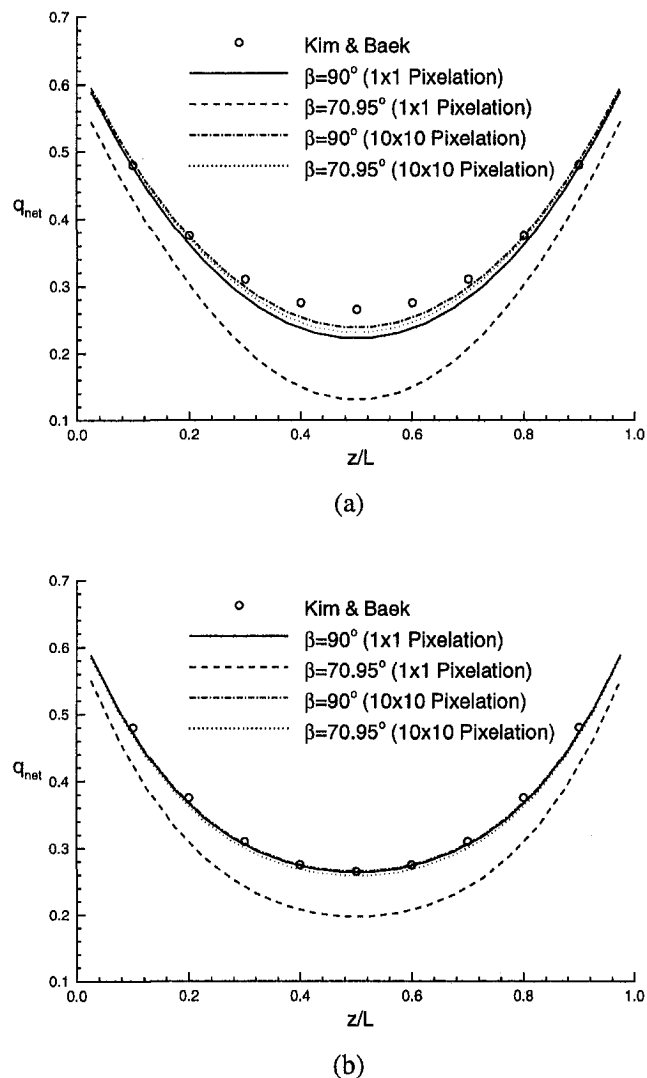


Fig. 12 Scattering in cylindrical domain: heat flux on lateral wall for (a) 2×2 angular discretization, and (b) 4×4 angular discretization

and the other is at $\beta = 90$ deg i.e., along the vertical centerline on the wall; β is measured from the y -axis. Figure 12(b) shows the corresponding plots for a 4×4 angular discretization. For 1×1 pixelation, the results on the two locations differ significantly from each other. The maximum errors for the 2×2 angular discretization are 16 percent and 50.5 percent at the 90 deg and the 70.95 deg locations, respectively. The corresponding errors for the 4×4 case are 0.32 percent and 25.59 percent, respectively. With pixelation, the answers improve dramatically, and the solutions at the two β locations become much closer. For 10×10 pixelation, the errors for the 2×2 case are 9.8 percent and 12.7 percent at the 90 deg and 70.95 deg locations, respectively. The corresponding values for the 4×4 discretization are 0.2 percent and 2.4 percent, respectively. A calculation is also done with the 4×4 angular discretization, but with 4×4 pixelation (not shown). The maximum error with respect to the solution of Kim and Baek is under 0.2 percent. When very fine angular discretization is used (16×16), the computations become insensitive to pixelation and

nearly identical solutions are obtained with approaches A and B (not shown); the departure from the solution of Kim and Baek is under 0.2 percent.

The 2×2 and 4×4 angular discretizations with 1×1 pixelation require 3.8 minutes and 14.22 minutes to achieve convergence on this 8400-cell mesh. A 4×4 pixelation requires 11 percent more computational time than the 1×1 pixelation. A 10×10 pixelation requires approximately 40 percent more computer time than the 1×1 pixelation in this three-dimensional problem. For many practical problems, a coarse pixelation offers a good compromise between accuracy and cost.

Closure

The finite volume method for computing radiative heat transfer has been extended to domains with periodic boundaries. Pixelation is used to account for control angle overhang, and to correctly redistribute radiant energy at rotationally periodic boundaries. In the examples considered here, pixelation has been shown to be very important in controlling solution error in rotationally periodic geometries.

In the present treatment, the intensity equations are solved sequentially, visiting each direction in turn. At rotationally periodic boundaries, this leads to an explicit coupling between the different intensity equations. The calculation procedure may benefit from implicit coupling, whereby all intensity equations at a cell are solved simultaneously. This approach will also benefit other situations where this type of explicit coupling is encountered: domains with symmetry and specular boundaries, interfaces between semi-transparent media, and strong scattering. This and other extensions are currently being pursued.

Acknowledgments

We wish to acknowledge the use of Fluent, Inc.'s solver FLUENT/UNS, and its mesh generators PreBFC and TGrid, in this work.

References

- Chai, J. C., Parthasarathy, G., Patankar, S. V., and Lee, H. S., 1994, "A Finite-Volume Radiation Heat Transfer Procedure for Irregular Geometries," AIAA 94-2095, June.
- Chui, E. H., and Raithby, G. D., 1992, "Prediction of Radiative Transfer in Cylindrical Enclosures With the Finite Volume Method," *J. Thermophysics and Heat Transfer*, Vol. 6, No. 4, pp. 605-611.
- Chui, E. H., and Raithby, G. D., 1993, "Computation of Radiant Heat Transfer on a Non-orthogonal Mesh Using the Finite-Volume Method," *Numer. Heat Transfer*, Vol. 23, pp. 269-288.
- Hutchinson, B. R., and Raithby, G. D., 1986, "A Multigrid Method Based on the Additive Correction Strategy," *Numer. Heat Transfer*, Vol. 9, pp. 511-537.
- Kaviany, M., and Singh, B. P., 1993, "Radiative Heat Transfer in Porous Media," *Advances in Heat Transfer*, Vol. 23, J. P. Hartnett and T. Irvine, eds., Academic Press, San Diego, CA, pp. 133-186.
- Kim, M. Y., and Baek, S. W., 1997, "Analysis of Radiative Transfer in Cylindrical Enclosures Using the Finite Volume Method," *J. Thermophysics and Heat Transfer*, Vol. 11, No. 2, pp. 246-252.
- Maruyama, S., and Higano, M., 1997, "Radiative Heat Transfer of Torus Plasma in Large Helical Device by Generalized Numerical Method REM²," *Energy Convers. Mgmt.*, Vol. 38, Nos. 10-13, pp. 1197-1195.
- Mathur, S. R., and Murthy, J. Y., 1997, "A Pressure Based Method for Unstructured Meshes," *Numerical Heat Transfer*, Vol. 31, No. 2, pp. 195-216.
- Modest, M. F., 1993, *Radiative Heat Transfer* (Series in Mechanical Engineering), McGraw-Hill, New York.
- Murthy, J. Y., and Mathur, S. R., 1998a, "Finite Volume Method for Radiative Heat Transfer Using Unstructured Meshes," *J. Thermophysics and Heat Transfer*, Vol. 12, No. 3, July-Sept., pp. 313-321.
- Murthy, J. Y., and Mathur, S. R., 1998b, "Radiative Heat Transfer in Axisymmetric Geometries Using an Unstructured Finite Volume Method," *Numer. Heat Transfer*, Vol. 33, No. 4, pp. 397-416.
- Raithby, G. D., and Chui, E. H., 1990, "A Finite-Volume Method for Predicting Radiant Heat Transfer in Enclosures With Participating Media," *ASME JOURNAL OF HEAT TRANSFER*, Vol. 112, Vol. 415-423.

Nucleate Boiling Heat Transfer of Binary Mixtures at Low to Moderate Heat Fluxes

R. J. Benjamin¹
Research Scholar

A. R. Balakrishnan²
Professor,
Mem. ASME

Department of Chemical Engineering,
Indian Institute of Technology Madras,
Chennai 600 036, India

A model for nucleate pool boiling heat transfer of binary mixtures has been proposed based on an additive mechanism. The contributing modes of heat transfer are (i) the heat transferred by microlayer evaporation, (ii) the heat transferred by transient conduction during the reformation of the thermal boundary layer, and (iii) the heat transferred by turbulent natural convection. The model takes into account the micro-roughness of the heating surface which has been defined quantitatively. The model compares satisfactorily with data obtained in the present study and in the literature. These data were obtained on a variety of heating surfaces such as a vertical platinum wire, a horizontal stainless steel tube and flat horizontal aluminium, and stainless steel surfaces (with various surface finishes) thereby demonstrating the validity of the model.

Introduction

Nucleate boiling is characterized by the formation of vapor at preferred sites ("nucleation" sites) on a heating surface that is submerged in the liquid and maintained at a temperature above the saturation temperature of the liquid. In the present study, a model has been developed for pool boiling of binary mixtures based on an additive mechanism. Nucleate pool boiling of binary mixtures finds many applications in the refrigeration and air conditioning industry, the chemical process industries such as the liquid natural gas industry, and in the reboilers of distillation columns among others.

A number of empirical correlations and models are available to estimate the heat flux and to explain the mechanism in saturated nucleate pool boiling of pure liquids. These have been summarized by Hsu and Graham (1976), Hahne and Grigull (1977), Van Stralen and Cole (1979), and Stephan (1992) among others. On the other hand, for boiling of binary mixtures a number of correlations are available to estimate the heat transfer coefficients (summarized by Van Stralen and Cole, 1979; Thome and Shock, 1984; Kadhum et al., 1994; Celata et al., 1994; among others) though only a few models. In most of the earlier investigations available in the literature, the heat transfer coefficient in the boiling of a binary mixture was correlated in terms of an "ideal" heat transfer coefficient and a "reduction factor." The ideal heat transfer coefficient was generally the heat transfer coefficient obtained from correlations for pure liquids using average mixture properties. The reduction factor is a function of the thermophysical and transport properties of the binary mixtures, the vapor-liquid equilibrium relationship and the slope of the vapor pressure curve. It apparently takes into account slower bubble growth rates, smaller departure diameters, and nonlinear variation of the mixture properties with composition.

One of the earliest correlations for binary mixtures was developed by Palen and Small (1964) for reboilers of distillation columns. The ideal heat transfer coefficient was calculated from McNelly's (1953) correlation proposed for pure liquids using

average physical properties and the temperature difference used was the difference between the dew point and the bubble point. Tolubinskiy and Ostrovskiy (1969) obtained experimental data for ethanol-water mixtures and proposed a correlation in terms of the Nusselt number based on their data. They assumed that the Lewis-Lykov number (ratio of conduction heat transfer and diffusion mass transfer, commonly known as the Lewis number) is unity for binary mixtures.

Stephan and Körner (1969) suggested that the wall superheat in the boiling of binary mixtures consisted of two terms, an ideal superheat and an "excess" superheat. The ideal superheat for the mixture is obtained using the linear molar mixing law at a given heat flux. They observed that the maximum wall superheat corresponded to a maximum in $|Y-X|$, the absolute value of the difference in the mole fractions of the more volatile component in the vapor and in the liquid. Their correlation took into account the influence of pressure (the pressure ranged from one to ten atmospheres) and contained a constant which varied with the binary system used. Happel and Stephan (1970) proposed an empirical correlation for the heat transfer coefficient in the boiling of binary mixtures in terms of an ideal heat transfer coefficient and the concentration difference $|y-x|$. The correlation contained two constants which had to be determined experimentally for each system, heat flux, and pressure. Calus and Rice (1972) obtained a semi-empirical correlation by relating the reduction in the bubble growth rate in the boiling of binary mixtures to the reduction in the heat transfer coefficient. They obtained boiling data of different aqueous mixtures on wires and tubes. Calus and Rice (1972) used Scriven's (1959) bubble growth expression for spherical bubble growth remote from a wall and related the heat transfer coefficient to the concentration difference $|y-x|$ and the ratio of the mass and thermal diffusivities. The ideal heat transfer coefficient was estimated using the correlation due to Borishanskii et al. (1969). Calus and Leonidopoulous (1974) studied the variation of wall superheat with composition. They obtained an expression for the empirical constant in Stephan and Körner's (1969) correlation by using a modified Jakob number in Scrivan's (1959) bubble growth expression. They compared their correlation with their own experimental data obtained with 11 mixtures of *n*-propanol—water boiling on a thin, horizontal nickel-aluminium alloy wire.

Thome (1981) followed an approach similar to that of Calus and Leonidopoulous (1974). He used the ideal superheat definition of Stephan and Körner (1969), that is assuming the

¹ Present address: Assistant Research Scientist, Hindustan Lever Research Center, Mumbai 400 099, India.

² Author to whom correspondence should be addressed.

Contributed by the Heat Transfer Division for publication in the JOURNAL OF HEAT TRANSFER. Manuscript received by the Heat Transfer Division July 7, 1997; revision received Oct. 21, 1998. Keywords: Boiling, Evaporation, Phase-Change Phenomena. Associate Technical Editor: M. Sohal.

linear molar mixing law. He further assumed that the thermal boundary layer is replaced in a cyclic manner due to recurring bubble growth and departure. Using literature correlations for the bubble departure diameter, the frequency, and the thermal boundary layer thickness, Thome (1981) obtained an expression for the heat transfer coefficient in terms of an ideal heat transfer coefficient and a correction factor (due to the presence of a second liquid) as proposed by Calus and Leonidopolous (1974). On the other hand, Schlünder (1983) assumed that the latent heat accounts for all the heat transferred from the surface during bubble growth and that the concentration difference of the more volatile component between the liquid and the vapor at the interphase is the same as that in the bulk. Using these assumptions, he developed a correlation for the nucleate boiling of binary mixtures which contained only one adjustable parameter and the mass transfer coefficient of the more volatile component.

Thome (1983) assumed that the rise in local boiling point due to preferential evaporation of the more volatile component is controlled by the rate of evaporation. This boiling point rise was determined by Thome (1983) using only phase equilibrium data. The correlation obtained matched available boiling data of six binary mixtures and was valid up to 28 atmospheres pressure. Ünal (1986) proposed an empirical correlation relating the heat transfer coefficient to an ideal heat transfer coefficient and four constants using dimensional analysis. The correlation requires only knowledge of the phase equilibrium data and does not include an empirical constant or the properties of the binary mixture. Thome and Shakir (1987) analysed the expression for the slope of the bubble point curve used by Schlünder (1983) and concluded that the actual slope is predicted by the expression due to Schlünder (1983) only at one composition. The authors then used the boiling range (the difference between the dew point and the bubble point) to approximate the slope of the bubble point curve. They compared their heat transfer correlation with four sets of boiling data on aqueous binary systems.

Yang and Chou (1988) proposed an expression to estimate the peak heat flux for binary mixtures. Only phase equilibrium data are required and there are no empirical constants. The authors assumed that the rate of depletion of the more volatile

component is controlled by the rate of evaporation and used an approach similar to Palen and Small (1964) and Thome (1983). However, while Palen and Small (1964) and Thome (1983) proposed correlations for estimating the boiling heat transfer coefficients, Yang and Chou's (1988) correlation is only for the peak heat flux.

Kadhun et al. (1994) analyzed the available correlations for prediction of nucleate pool boiling heat transfer coefficients of binary mixtures. They concluded that the correlations due to Schlünder (1983) and Thome and Shakir (1987) give the best fit, when the ideal heat transfer coefficient was estimated from the correlations for pure liquids due to Stephan and Abdelsalam (1980).

Fujita and Tsutsui (1997) measured heat transfer coefficients in nucleate pool boiling of five binary mixtures at atmospheric pressure over a wide range of heat flux. Fujita and Tsutsui (1997) also found that the heat transfer coefficients of mixtures were less compared to the values interpolated between those of the constituent pure liquids. They found the reduction to be a function of the mixture composition and was more pronounced at higher heat fluxes. Fujita and Tsutsui (1997) proposed a correlation which is a modification of Thome's (1983) correlation and this fit their data within ± 20 percent. Chiou et al. (1997) generated pool boiling heat transfer data for the system R22-R124 on plain tubes at reduced pressures. Significant reductions in heat transfer coefficients were found for the mixtures, the reduction being greater in the vicinity of the pure components and a strong function of the nonlinear variation of liquid mixture viscosity and mixture latent heat. Based on their data, Chiou et al. (1997) proposed a correlation which satisfactorily predicted the reduction in heat transfer coefficients for their data as well as those in the literature.

There are a few heat transfer models available which can be used to estimate and explain the dominant modes of heat transfer in nucleate pool boiling of binary mixtures. Thome (1982) extended the analysis of Mikic and Rohsenow (1969) for the nucleate pool boiling of pure liquids to binary mixtures by assuming the volume of the liquid carried away by a departing bubble to be twice the diameter of the bubble at departure. The departure or growth time is estimated from a conduction view point. The model showed good agreement with published data.

Nomenclature

a = area of influence, m^2
 A = surface area, m^2
 A_i = instantaneous area of the microlayer, m^2
 Ar = Archimedes number $(= (g/\nu^2) (\sigma/(\rho_l g))^{1.5})$
 B = constant defined by Eq. (9)
 C_p = specific heat, $J/(kg \cdot K)$
 D = bubble diameter, m
 D_{AB} = mass diffusivity, m^2/s
 D_b = departure diameter of the bubble, m
 D_d = diameter of dry area under the bubble, m
 Gr = Grashof number $((g\beta L^3(T_w - T_s))/\nu^2)$
 h = heat transfer coefficient, $W/(m^2 \cdot K)$
 Ja = Jakob number $(= (\rho_l C_p (T_w - T_s))/(\rho_l \lambda))$
 k = thermal conductivity, $W/(m \cdot K)$
 L = characteristic length of heating surface in Eq. (24), m
 N = number of active nucleation sites
 P = pressure, N/m^2

Pr = Prandtl number $(= C_p \mu/k)$
 q = heat flux, W/m^2
 R_a = centerline average, μm
 t = time, s
 T = temperature, K
 ΔT = temperature driving force, K
 V = volume, m^3
 x = mass fraction of the more volatile component in the liquid phase
 X = mole fraction of the more volatile component in the liquid phase
 y = mass fraction of the more volatile component in the vapor phase
 Y = mole fraction of the more volatile component in the vapor phase

Greek Letters

α = thermal diffusivity, m^2/s
 β = volumetric coefficient of thermal expansion, K^{-1}
 γ = parameter defined by Eq. (3)
 δ = instantaneous microlayer thickness, m
 θ = surface roughness defined by Eq. (27)

λ = latent heat of vaporisation, J/kg
 μ = dynamic viscosity, $Pa \cdot s$
 ν = kinematic viscosity, m^2/s
 ξ_{mix} = properties-profile parameter
 ρ = density, kg/m^3
 σ = surface tension, N/m
 ϕ = constant defined by Eq. (4)

Subscripts

av = average
 B = bubble
eff = effective
 g = growth (time)
 l = liquid
ME = microlayer evaporation
mix = binary mixture
NC = natural convection
pure = pure liquid
 R = reformation
 s = saturation
tot = total
 v = vapor
 w = heating surface; waiting (time)

However, the effect of the microroughness of the heating surface on the boiling phenomena of binary mixtures has not been examined in detail. The present study is concerned with the development of a mechanistic model for nucleate pool boiling of binary mixtures incorporating the effect of the surface microroughness, and an experimental investigation of the boiling phenomena of binary mixtures on heating surfaces with different surface microroughness.

In an earlier study, Benjamin and Balakrishnan (1996) examined the nucleate pool boiling phenomena of pure liquids at low to moderate heat fluxes. Different pure liquids were boiled on two surfaces, namely aluminium and stainless steel, polished with different grades of emery paper. A mechanistic model incorporating the effect of the microroughness of the heating surface on the boiling heat flux was also developed. They assumed that the liquid layer trapped under a growing bubble (the microlayer) contributes almost the entire liquid for bubble growth and phase change and that the heat transferred by microlayer evaporation accounts for more than 45 percent of the total heat flux. In the boiling of a pure liquid, the liquid and vapour compositions are the same and hence the entire boiling process is heat transfer controlled. In contrast, when a binary mixture is boiled, the vapor-liquid equilibrium of the mixture allows the vapor and liquid phases to be at different compositions. Hence, as a binary mixture evaporates on a heating surface, the bubble contains more of the lighter component. This implies that the microlayer is depleted of the more volatile component. This results in mass diffusion of the more volatile component from the bulk to the microlayer. Therefore, in the boiling of binary mixtures, a portion of the driving force ($T_w - T_s = \Delta T_s$) is utilized in overcoming this mass transfer resistance. This effective driving force in the case of binary mixtures has been correlated in terms of the apparent wall superheat and the thermal and mass diffusivities of the liquid by many investigators (summarized by Thome and Shock (1984) and Celata et al. (1994)). In the present study also the wall superheat is corrected for mass transfer effects and incorporated in the model.

The Model

The total boiling heat flux consists of

- (i) the heat flux associated with the evaporation of the microlayer (q_{ME}),
- (ii) the heat flux associated with the reformation of the thermal boundary layer by transient conduction after the bubble departs (q_R), and
- (iii) the heat flux associated with turbulent natural convection (q_{NC}).

The heat transfer area is subdivided into (i) active area, over which phase change occurs and (ii) nonactive area over which turbulent natural convection alone occurs. The first two modes occur over the active area, temporally divided, while the last occurs over the nonactive area at all times.

The total boiling heat flux is given by

$$q_{tot} = \frac{q_{ME} t_g + q_R t_w}{t_g + t_w} + q_{NC}. \quad (1)$$

Microlayer Evaporation. As a bubble forms over a hot surface a thin liquid layer (the microlayer) is left under the bubble owing to the high viscous stresses close to the heating surface and the bubble grows by the evaporation of this microlayer. The inherent assumption made in this study is that the bubble grows only by the evaporation of the microlayer and therefore mass transfer of the more volatile component is only to the microlayer. Benjamin and Balakrishnan (1996) derived an analytical expression for the volume of microlayer evaporated in the boiling of a pure liquid (Appendix) as

$$V_{ME} = \frac{\gamma \phi \sqrt{\pi}}{10} B^2 Ar^{0.27} Ja(\alpha t_g)^{1.5} \quad (2)$$

where γ is the surface-liquid interaction parameter and is defined as

$$\gamma = \sqrt{\frac{k_w \rho_w C_{pw}}{k_l \rho_l C_{pl}}}. \quad (3)$$

ϕ is a constant given by

$$\phi = 1 - \left(\frac{D_d}{D}\right)^2. \quad (4)$$

B is the bubble growth constant, Ar the Archimedes number, and Ja the Jakob number.

Using dimensional analysis, Cooper et al. (1978) developed an expression for the bubble volume of a pure liquid as

$$V_{pure} = 1.1 \int A_{pure} Ja_{pure} \sqrt{\alpha_{pure}} \frac{dt}{\sqrt{t}} \quad (5)$$

where A is the surface area of the growing bubble. Extending this to a binary mixture by including the mass fraction of the more volatile component and using mixture physical properties, the above equation can be written as

$$V_{mix} = 1.1 \int A_{mix} Ja_{mix} x \sqrt{\alpha_{mix}} \frac{dt}{\sqrt{t}} \quad (6)$$

The Jakob number, Ja_{mix} , is estimated using the effective wall superheat.

In the present study, the effective and actual temperature driving forces are related by

$$\Delta T_{eff} = T_w - T_{g,mix} \left[1 - \left(|y - x| \sqrt{\frac{D_{AB}}{\alpha_{mix}}} \right)^{0.5} \right]. \quad (7)$$

The form of the correction term is similar to the proportionality of the mass transfer coefficient to the mass diffusivity in the penetration theory of Higbie (1935). The above equation is also similar to that used by Calus and Rice (1972). The concentration difference $|y - x|$ is the driving force for mass diffusion of the more volatile component to occur. Since mass diffusion is obviously the slower (and rate controlling) process ($D_{AB} \ll \alpha_{mix}$), $(D_{AB}/\alpha_{mix})^{0.5}$ is a measure of the resistance to heat transfer. Equation (7) therefore quantifies the effective driving force in the boiling of binary mixtures.

Using the bubble growth data of Zmola (1950) and Siegel and Keshock (1964), Benjamin and Balakrishnan (1996) correlated the instantaneous bubble diameter of a growing bubble as

$$D(t) = B Ar^{0.135} (Ja \alpha t)^{0.5}. \quad (8)$$

In the present study, the above equation is assumed to describe the bubble growth of a binary mixture also, with the physical properties used being the binary mixture physical properties and the effective wall superheat (while estimating Jakob number) as given by Eq. (7). Further, in the present study, the bubble growth constant was estimated (by curve fitting experimental data from the literature with the final model equations) as

$$B = 1.65 \times 10^{-3} \left(\frac{C_{p,mix} T_{g,mix}}{\lambda_{mix}} \right) \sqrt{Ar_{mix}}. \quad (9)$$

The performance of the bubble growth correlation after de-

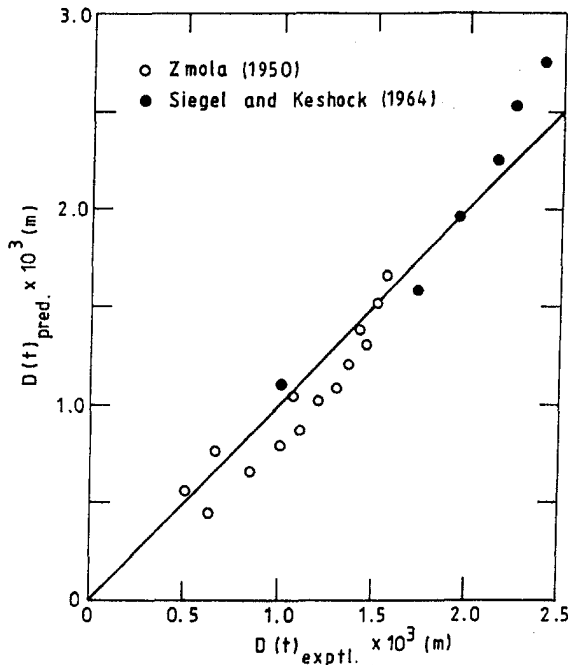


Fig. 1 Performance of the bubble growth correlation

fining B (as in Eq. (9)) is shown in Fig. 1. Using Eqs. (5) to (9), the ratio of the bubble volume of a binary mixture to that of a pure liquid is

$$\frac{V_{\text{mix}}}{V_{\text{pure}}} = \left(\frac{\rho_{\text{mix}} C_{p_{\text{mix}}}}{\rho_{\text{pure}} C_{p_{\text{pure}}}} \right)^2 \left(\frac{\rho_{\nu_{\text{pure}}} \lambda_{\text{pure}}}{\rho_{\nu_{\text{mix}}} \lambda_{\text{mix}}} \right)^2 \left(\frac{C_{p_{\text{mix}}} T_{g_{\text{mix}}}}{C_{p_{\text{pure}}} T_{g_{\text{pure}}}} \right)^2 \left(\frac{\lambda_{\text{pure}}}{\lambda_{\text{mix}}} \right)^2 \times \left(\frac{\alpha_{\text{mix}}}{\alpha_{\text{pure}}} \right)^{1.5} \left(\frac{Ar_{\text{mix}}}{Ar_{\text{pure}}} \right)^{1.27} x \left[1 - \left(|y - x| \sqrt{\frac{D_{AB}}{\alpha_{\text{mix}}}} \right)^{0.5} \right]^2 \quad (10)$$

The volume of microlayer evaporated in the boiling of a binary mixture is obtained by assuming that the ratio of the volumes of microlayer evaporated is equal to the ratio of the bubble volumes. That is

$$V_{\text{ME}_{\text{mix}}} = V_{\text{ME}_{\text{pure}}} \left(\frac{V_{\text{mix}}}{V_{\text{pure}}} \right) \quad (11)$$

Using Eq. (2) and Eq. (10) in Eq. (11), the volume of microlayer evaporated in the boiling of a binary mixture is obtained. The heat flux associated with the microlayer evaporation of a binary mixture is

$$q_{\text{ME}} = \frac{(1.65 \times 10^{-3})^2}{20} \left(\frac{C_{p_{\text{pure}}} T_{g_{\text{pure}}}}{\lambda_{\text{pure}}} \right)^2 \gamma \phi \sqrt{\pi} Ar_{\text{pure}}^{1.27} Ja_{\text{pure}} (\alpha_{\text{pure}})^{1.5} \times \rho_{\text{pure}} \lambda_{\text{pure}} \frac{1}{\sqrt{f}} \left(\frac{\rho_{\text{mix}} C_{p_{\text{mix}}}}{\rho_{\text{pure}} C_{p_{\text{pure}}}} \right)^2 \left(\frac{\rho_{\nu_{\text{pure}}} \lambda_{\text{pure}}}{\rho_{\nu_{\text{mix}}} \lambda_{\text{mix}}} \right)^2 \times \left(\frac{C_{p_{\text{mix}}} T_{g_{\text{mix}}}}{C_{p_{\text{pure}}} T_{g_{\text{pure}}}} \right)^2 \left(\frac{\lambda_{\text{pure}}}{\lambda_{\text{mix}}} \right)^2 \left(\frac{\alpha_{\text{mix}}}{\alpha_{\text{pure}}} \right)^{1.5} \left(\frac{Ar_{\text{mix}}}{Ar_{\text{pure}}} \right)^{1.27} \times x \left[1 - \left(|y - x| \sqrt{\frac{D_{AB}}{\alpha_{\text{mix}}}} \right)^{0.5} \right]^2 (N/A) \quad (12)$$

where N/A is the nucleation site density.

Thermal Boundary Layer Reformation. After a bubble departs, fresh liquid comes into contact with the heating surface. This liquid is assumed to be heated by transient conduction, with a step change in temperature at the surface. The instantaneous heat flux for this situation is given by Carslaw and Jaeger (1959) as

$$q_{\text{cond}} = \frac{k_{\text{mix}} (T_w - T_{g_{\text{mix}}})}{(\pi \alpha_{\text{mix}} t)^{0.5}} \quad (13)$$

Therefore, the average heat flux during the waiting time (t_w) is

$$q_{\text{av}} = \frac{1}{t_w} \int_0^{t_w} q_{\text{cond}} dt = \frac{2k_{\text{mix}} (T_w - T_{g_{\text{mix}}})}{(\pi \alpha_{\text{mix}} t_w)^{0.5}} \quad (14), (15)$$

As each bubble departs, it carries along with it a portion of the thermal boundary layer in its wake (the area of influence, a). Han and Griffith (1965) have postulated that this area is four times the projected area of the bubble for pure liquids. That is, the area of influence is

$$a = \frac{4\pi D_b^2}{4} = \pi D_b^2 \quad (16)$$

Equation (16) is assumed to be valid for binary mixtures also.

The correlation for bubble departure diameter given by Stephan (1992) for a pure liquid is assumed for a binary mixture using mixture properties and compared with the experimental data of Tolubinskiy and Ostrovskiy (1966, 1969) and Isshiki and Nikai (1973). While the equation appears to fit reasonably well (± 60 percent) the data on ethanol-water and ethanol-butanol mixtures of Tolubinskiy and Ostrovskiy (1969) if the constant in Stephan's (1992) correlation is changed from 0.25 to 0.48, it does not fit the data of Isshiki and Nakai (1973) at all. The modified correlation of Stephan (1992) is

$$D_b = 0.48 \sqrt{\left[\frac{\sigma_{\text{mix}}}{g(\rho_{\text{mix}} - \rho_{\nu_{\text{mix}}})} \right] \left[1 + \left(\frac{Ja_{\text{mix}}}{Pr_{\text{mix}}} \right)^2 \frac{1}{Ar_{\text{mix}}} \right]^{1/2}} \quad (17)$$

Therefore the heat flux associated with thermal boundary layer reformation is given by

$$q_R = 2 \left(\frac{k_{\text{mix}} \rho_{\text{mix}} C_{p_{\text{mix}}}}{\pi t_w} \right)^{0.5} (N/A) a (T_w - T_{g_{\text{mix}}}) \quad (18)$$

$T_w - T_{g_{\text{mix}}}$ is used here (and not Eq. (7)) because during the reformation of the thermal boundary layer, there is no evaporation and consequently no mass transfer effects which reduce the available driving force. Therefore, the average heat flux for one bubble cycle is

$$q_{\text{cycle}} = \frac{q_{\text{ME}} t_g + q_R t_w}{t_g + t_w} \quad (19)$$

q_{ME} and q_R are time weighted because they occur alternately over the active area. The heat flux q_{ME} represents the latent heat absorbed by the bubble as it grows, while q_R is the heat flux associated with the thermal layer reformation—that is the heat required to superheat the fresh liquid that fills the nucleation site from the bulk when a bubble departs. The waiting and the growth times are related to the bubble frequency by

$$f = \frac{1}{t_g + t_w} \quad (20)$$

The bubble frequency can be estimated by a correlation due to Malenkov (reported by Stephan, 1992), assuming the correlation to be valid for binary mixtures when the mixture properties are used.

$$f = \frac{1}{\pi} \sqrt{\frac{g}{2D_b}} \left[1 + \frac{4\sigma_{\text{mix}}}{D_b^2 \rho_{\text{mix}} g} \right]^{0.5} \quad (21)$$

When compared to the data of Tolubinskiy and Ostrovskiy (1966) for ethanol-water and ethanol-butanol mixtures, there is wide scatter but there does not seem to be any trend in any direction. The waiting and the growth times are related for pure liquids as (Van Stralen et al., 1975)

$$t_w = 3t_g \quad (22)$$

Equation (22) is assumed to be valid for binary mixtures also. From the above, q_{cycle} can be estimated.

Turbulent Natural Convection. The heat transfer coefficient according to McAdams (1954) for turbulent natural convection is

$$h_{\text{NC}} = 0.14 \frac{k_l}{L} (\text{Gr}_{\text{mix}} \text{Pr}_{\text{mix}})^{0.33} \quad (23)$$

where Gr is the Grashof number. The nonactive area is $1 - (N/A).a$. Hence the heat flux associated with turbulent natural convection is

$$q_{\text{NC}} = h_{\text{NC}} [1 - (N/A).a] (T_w - T_{g_{\text{mix}}}) \quad (24)$$

The total boiling heat flux can now be estimated from Eq. (1).

The nucleation site density (N/A) is estimated by a correlation proposed by Benjamin and Balakrishnan (1997). Different compositions of binary mixtures were boiled on aluminium and stainless steel surfaces polished with different grades of emery paper. The nucleation site densities obtained were correlated as

$$N/A = 5 \times 10^{-5} (\xi_{\text{mix}})^{-0.25} (\text{Pr}_{\text{mix}})^{1.63} \gamma_{\text{mix}} \theta_{\text{mix}}^{0.4} (\Delta T_{\text{mix}})^3 \quad (25)$$

ξ_{mix} is the properties-profile parameter defined as

$$\xi_{\text{mix}} = \frac{\rho_{\text{mix}} R_a^2 g}{\sigma_{\text{mix}}} \quad (26)$$

The properties-profile parameter as defined above is similar in form to the Bond number but does not have the same physical meaning. The properties-profile parameter takes into account the variation of the physical properties of the mixture with composition. The characteristic length in the case of the Bond number is the bubble departure diameter while in the properties-profile parameter used in this study, the characteristic length is the centerline average R_a .

The center line average (R_a) is measured using a profilometer after polishing the heating surface using a particular grade of emery paper. The R_a value is defined as the average absolute value of the peaks and the valleys on the heating surface. Pr_{mix} is the Prandtl number of the binary mixture. The surface-liquid interaction parameter γ is defined by Eq. (3). The dimensionless surface roughness θ is defined as

$$\theta_{\text{mix}} = 14.5 - 4.5 \left(\frac{R_a P}{\sigma_{\text{mix}}} \right) + 0.4 \left(\frac{R_a P}{\sigma_{\text{mix}}} \right)^2 \quad (27)$$

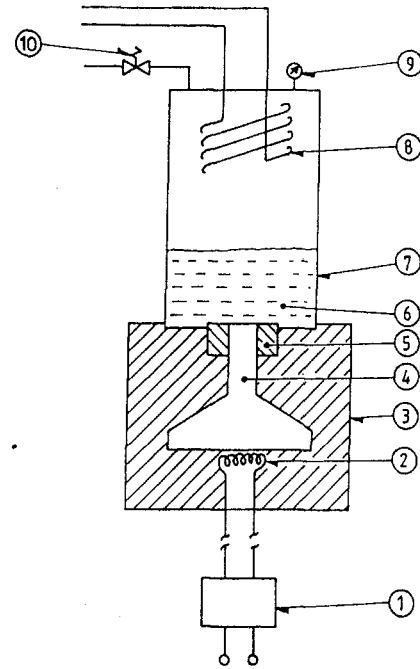
The range of parameters over which the correlation is valid are

$$5.3 < \text{Pr} < 6.1 \quad 21.5 < \gamma_{\text{mix}} < 61.6$$

$$0.19 \mu\text{m} < R_a < 1.2 \mu\text{m}$$

$$14.6 \times 10^{-3} \text{ N/m} < \sigma_{\text{mix}} < 21.8 \times 10^{-3}$$

$$1.8 < \theta_{\text{mix}} < 10.6 \quad 5 < \Delta T_{\text{eff}} < 25.$$



1. Dimmerstat, 2. Plate heater, 3. Insulation, 4. Heating block, 5. Teflon hollow cylinder, 6. Liquid, 7. Double-walled glass vessel, 8. Cooling coil, 9. Pressure gauge, 10. Relief valve.

Fig. 2 Schematic of the experimental setup

Experimental

A schematic of the experimental setup used in the present study is shown in Fig. 2. The heating blocks used were aluminium and stainless steel. The dimensions of the heating blocks are shown in Fig. 3. The blocks were shaped as shown, and insulated sufficiently at the sides using glass wool so that one-dimensional axial conduction along the axis of the block can be assumed. This shape of the block and sufficient insulation at the sides facilitates accurate estimation of the heating surface temperature. The test section consisted of a double-walled glass cylinder with the annular space under vacuum. The glass vessel is held tightly between two stainless steel slabs. The bottom slab holds the heating block through a teflon annular cylinder. The block is heated electrically using a 3 kW plate heater and the current and the voltage are measured. Using these, the heat flux was estimated. Temperatures are measured at three points along the axis of the block using platinum resistance thermometers and using these, the surface temperature was evaluated. The liquid temperature was also measured using a platinum resistance thermometer.

About 150 ml of the test liquid was boiled in each run. The boiled liquid was condensed back into the test section using cooling water. Therefore, the bulk composition of the binary mixture does not change during the course of a boiling experiment. Hence, average mixture physical properties were used to evaluate the dimensionless numbers, the bubble departure diameter and the frequency. Before the start of each boiling experiment, the heating surface was polished with the grade of emery paper required. The microroughness was increased by starting with the smoothest grade and progressively proceeding to coarser grades of emery paper. It was observed that polishing the heating surface was sufficient to clean it and therefore further cleaning was not required.

After polishing the heating surface, the centerline average R_a was measured using a profilometer. The profilometer consists of a conical diamond bit with tip radius $0.1 \mu\text{m}$. The tip traverses

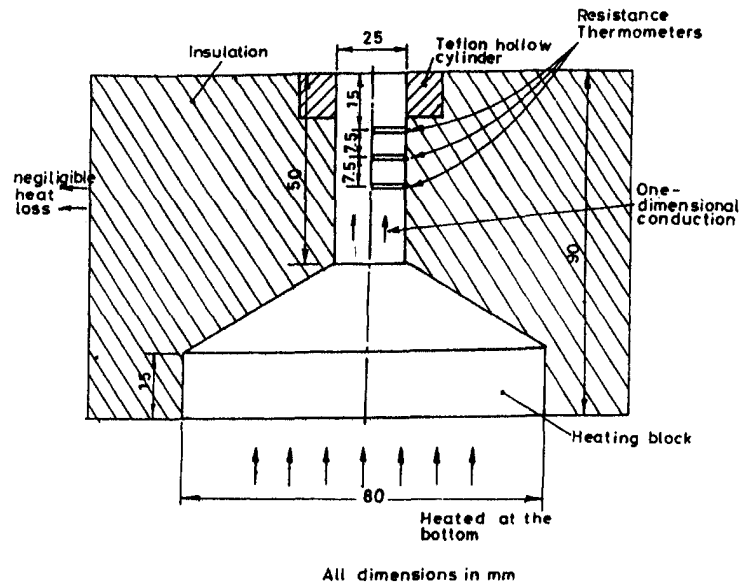
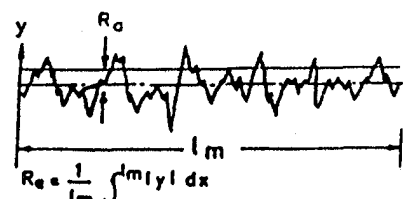


Fig. 3 Dimensions of the heating blocks used in the present study

over the heating surface for a distance of 5.6 mm and the surface profile and the R_a is obtained. Four sweeps were taken in different directions for each surface finish. The centerline average R_a was used in the present study to quantitatively define the surface microroughness. The R_a value has been used extensively in the literature to quantify the surface microroughness by a number of investigators and these have been summarized by Benjamin (1996). Further R_a is recognized by the International Standards Organisation (ISO, 1984) as a parameter to quantify the surface microroughness. Figure 4 gives the definition of R_a and the instantaneous output of the profilometer.



CENTRE LINE AVERAGE R_a
IS THE ARITHMETICAL AVERAGE VALUE OF ALL ABSOLUTE DISTANCES OF THE ROUGHNESS PROFILE R FROM THE CENTRE LINE WITHIN THE MEASURING LENGTH l_m

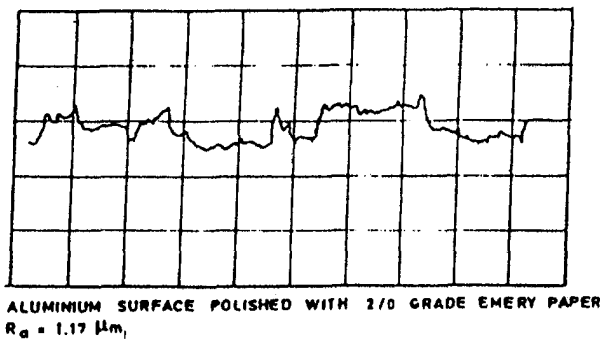


Fig. 4 The definition of R_a and the instantaneous output of the profilometer

Three different compositions of two binary mixtures, acetone-carbon tetrachloride and *n*-hexane-carbon tetrachloride were used. All the experiments were conducted at atmospheric pressure and standard gravity conditions. The test liquid was boiled and cooled before each run in order to degas it. The surfaces, the compositions of the binary mixtures used, the R_a values, and the thermophysical and transport properties of the liquid mixtures (the systems used in the present study and that from the literature used for comparison) are summarized in Tables 1 and 2.

Experimental Uncertainty. The resolution of the voltmeter used in the present study was 1 volt. The resolution of the ammeter was 0.01 ampere. The resolution of the temperature indicator (calibrated and connected to the platinum resistance thermometers in the axis of the heating block) was 0.1°C. In the temperature range encountered in this study, the uncertainty in temperature measurement is ± 1 percent. Therefore, the uncertainty in estimating the wall superheat (ΔT) is ± 2 percent (four percent). The uncertainty in estimating the heat flux (from the voltage—current measurements) is ± 3 percent.

Results

Figure 5 shows the comparison of the model predictions and the experimental data of three compositions of acetone-carbon tetrachloride obtained in the present study, for the three surface finishes of the aluminium heating surface (i.e., three R_a values). Figure 6 shows the model predictions with three compositions of *n*-hexane-carbon tetrachloride for three R_a values. Figure 7 shows the experimental data obtained when stainless steel polished with 1/0 emery paper ($R_a = 0.2 \mu\text{m}$) was used as the heating surface and the predictions of the model developed for each composition of the two binary systems. Figure 8 shows the comparison of the model with the experimental data of Tzan and Yang (1990). Tzan and Yang (1990) obtained experimental data of different compositions of *n*-propanol-water on a horizontal stainless steel tube. The tube was polished with no. 1200 sandpaper. Since the R_a value was not explicitly stated by them, in the present study a stainless steel block was polished using a no. 1200 sand paper and the R_a value was measured using the profilometer. The measured R_a value of 0.12 μm was used to evaluate the nucleation site density and the estimated nucleation site density was used in the present model to predict the heat flux. Figure 9 shows the prediction of the model devel-

Table 1 Surface materials, R_a values and binary systems used in validating the model

Source of data	Heating surface	Polished with	Binary system
Present study	Aluminium	4/0 grade of emery paper ($R_a = 0.52 \mu\text{m}$)	acetone-carbon tetrachloride (53.5, 22.9, and 8.3 mass % acetone)
Present study	Aluminium	3/0 grade of emery paper ($R_a = 0.89 \mu\text{m}$)	acetone-carbon tetrachloride (53.5, 22.9, and 8.3 mass % acetone)
Present study	Aluminium	2/0 grade of emery paper ($R_a = 1.17 \mu\text{m}$)	acetone-carbon tetrachloride (53.5, 22.9, and 8.3 mass % acetone)
Present study	Aluminium	4/0 grade of emery paper ($R_a = 0.52 \mu\text{m}$)	<i>n</i> -hexane-carbon tetra chloride (67.5, 29.35, and 7.67 mass % <i>n</i> -hexane)
Present study	Aluminium	3/0 grade of emery paper ($R_a = 0.89 \mu\text{m}$)	<i>n</i> -hexane-carbon tetra chloride (67.5, 29.35, and 7.67 mass % <i>n</i> -hexane)
Present study	Aluminium	2/0 grade of emery paper ($R_a = 1.17 \mu\text{m}$)	<i>n</i> -hexane-carbon tetra chloride (67.5, 29.35, and 7.67 mass % <i>n</i> -hexane)
Present study	Stainless steel	1/0 grade of emery paper ($R_a = 0.2 \mu\text{m}$)	acetone-carbon tetra chloride (53.5, 22.9, and 8.3 mass % acetone)
Present study	Stainless steel	1/0 grade of emery paper ($R_a = 0.2 \mu\text{m}$)	<i>n</i> -hexane-carbon tetra chloride (67.5, 29.35, and 7.67 mass % <i>n</i> -hexane)
Tzan and Yang (1990)	Stainless steel	No. 1200 sand paper ($R_a = 0.12 \mu\text{m}$)	<i>n</i> -propanol-water (20 and 10 mass % <i>n</i> -propanol)
Van Stralen (1959)	Platinum	1/0 grade of emery paper ($R_a = 0.04 \mu\text{m}$)	4.1 mass % methyl ethyl ketone-water
Van Stralen (1959)	Platinum	1/0 grade of emery paper ($R_a = 0.04 \mu\text{m}$)	1.3 mass % <i>n</i> -butanol-water

oped in comparison with the data of Van Stralen (1959) obtained using a vertical platinum wire as the heating surface. The systems used were methyl ethyl ketone-water and *n*-butanol-water. For such a thin wire, surface finishing was not possible and hence for comparison purposes the R_a value was assumed to be $0.04 \mu\text{m}$ (which was obtained by polishing a flat platinum surface using a 1/0 grade of emery paper). Figure 10 shows the comparison of predicted and experimental heat fluxes of all the data used in the present study (including literature data). The comparison is satisfactory validating the postulated mechanisms of heat transfer. Figure 11 shows the model prediction with the boiling data of acetone-carbon tetrachloride used (all compositions) for two R_a values obtained in this study.

Discussion

From Figs. 5-9, it can be seen that for a given wall superheat, the heat flux obtained on a wire is greater than that obtained over a tube or a flat surface. This is probably due to the fact that the ratio of area over which phase change occurs (the "active" area) to the total area is highest for a thin wire. Also, the departure diameter of the bubbles are comparable to the wire diameter itself. This leads to lower departure diameters in the case of wires (and higher frequencies). Further, the heat transfer retardation due to the mass transfer of the more volatile component towards the bubbles is probably less in boiling over a wire.

Table 2 Thermophysical and transport properties of the binary systems

x	y	ρ_l	$\lambda \times 10^{-3}$	C_p	$\mu \times 10^3$	k	$\sigma \times 10^3$	$\alpha \times 10^8$	$D_{AB} \times 10^9$
acetone-carbon tetrachloride system									
0.5345	0.6	980	293	1632	0.4034	0.12	20.33	7.5	3.2
0.229	0.373	1225.85	226.7	1225.3	0.5115	0.107	21.17	7.12	2.37
0.083	0.2213	1392.85	203	1035.5	0.5466	0.1	21.7	6.93	1.68
<i>n</i> -hexane-carbon tetrachloride system									
0.675	0.72	761.1	291.5	1950	0.302	0.1	14.67	6.74	3.16
0.2935	0.35375	1046.7	234.4	1373.37	0.4224	0.0969	16.6	6.94	2.37
0.0767	0.1145	1327.3	199.33	1041.25	0.491	0.09537	18.79	6.9	1.75
<i>n</i> -propanol-water system									
0.2	0.6422	911.1	1943.7	3971.3	0.358	0.56767	46.05	15.7	3.575
0.1	0.5584	936.6	2100	4091.93	0.3338	0.62	52.245	16.177	3.62
methyl ethyl ketone-water system									
0.041	0.7217	955.23	2219.374	4121.7	0.351	0.6458	58.32	16.4	3.26
<i>n</i> -butanol-water system									
0.013	0.3139	956.92	2235.55	4200	0.3535	0.6723	57.87	16.73	4.075

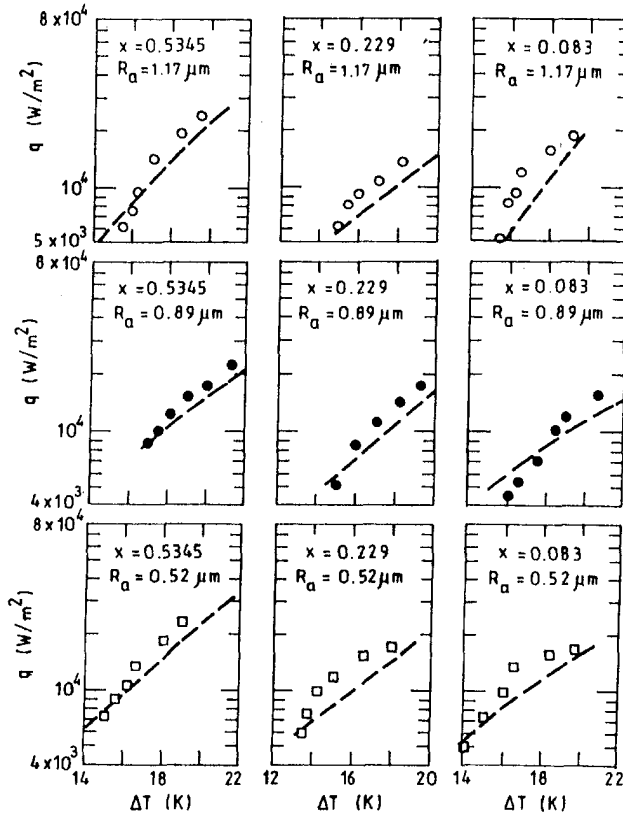


Fig. 5 Comparison of the model with present experimental data; surface: aluminium; system: acetone-carbon tetrachloride

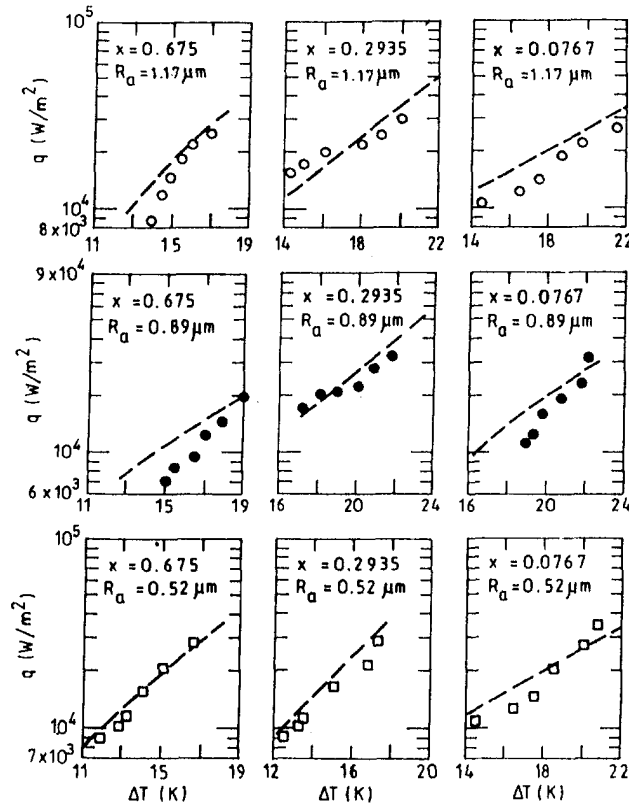


Fig. 6 Comparison of the model with present experimental data; surface: aluminium; system: *n*-hexane-carbon tetrachloride

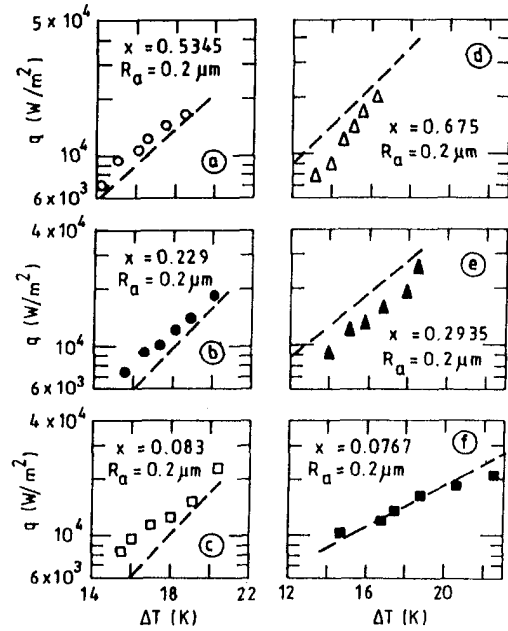


Fig. 7 Comparison of the model with present experimental data; surface: stainless steel; systems: acetone-carbon tetrachloride and *n*-hexane-carbon tetrachloride

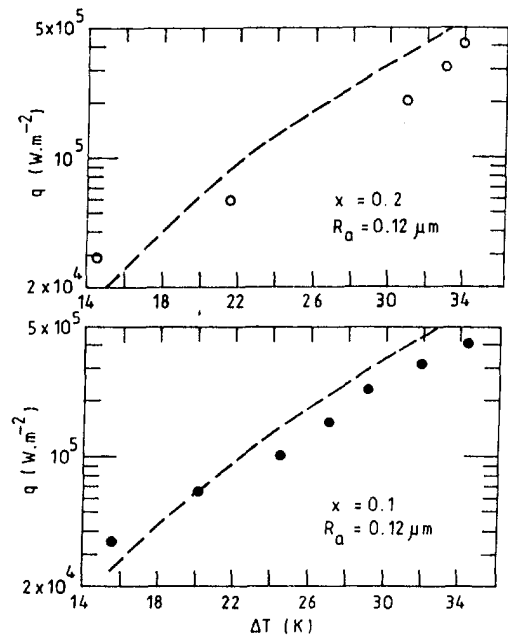


Fig. 8 Comparison of the model with data of Tzan and Yang (1990); surface: stainless steel; system: *n*-propanol-water

In the boiling of a pure liquid, the heat flux due to microlayer evaporation amounts to more than 45 percent of the total heat flux (Benjamin and Balakrishnan, 1996). On the other hand, in the present study, it is seen that microlayer evaporation contributes only 40 percent or less to the total heat flux in the boiling of binary mixtures. During the microlayer evaporation of a binary mixture, there is diffusion of the more volatile component to the microlayer and this diffusion leads to a reduction in the net driving force. The effective driving force, ΔT_{mix} is always less than the wall superheat of pure liquids, ΔT_{pure} (except for an azeotropic mixture at the azeotropic composition), which leads to lower nucleation site densities and lower q_{ME} . Further,

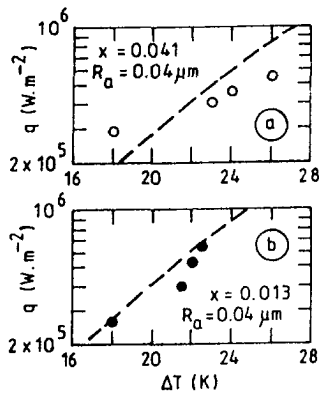


Fig. 9 Comparison of the model with the data of Van Stralen (1959); surface: platinum; systems: methyl ethyl ketone–water and *n*-butanol–water

the microlayer in the boiling of a binary mixture does not completely evaporate, according to the experimental results of Zeugin et al. (1975) which again reduces the contribution of the microlayer evaporation to the total boiling heat flux. Moreover, the constant ϕ (defined by Eq. (4)), is about 25 percent less for a binary mixture in comparison to a pure liquid, leading to lower departure diameters in the boiling of a binary mixture.

Figure 11 depicts the boiling data obtained in the present study and the model predictions for $R_a = 0.52 \mu\text{m}$ and for $R_a = 1.17 \mu\text{m}$. It can be that at the lower R_a value, the experimental data and the model predictions are clustered together, irrespective of the liquid composition. This indicates that at low R_a values the boiling phenomena is not controlled by the thermophysical and transport properties of the liquid boiled, or the surface properties, or the vapor–liquid equilibrium. That is, a binary mixture behaves like a pure liquid at low R_a values. This is because at low R_a values the cavity sizes are small. Therefore, unevaporated microlayer (which is depleted of the more volatile component) in the cavity is also less. After bubble departure, fresh liquid mixes with the liquid left behind and fills the cavity. Since the liquid left behind is small in quantity, the composition difference between the liquid in the cavity and the bulk liquid is negligible and mass transfer of the more volatile component is also negligible. At higher R_a values, the amount of such liquid left behind following bubble departure is significant in quantity

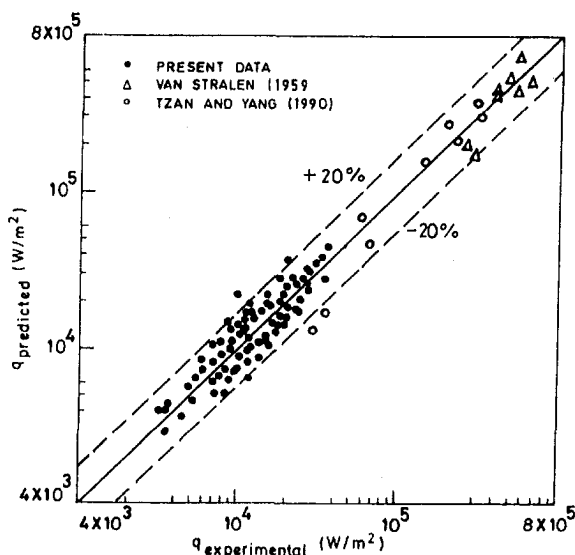


Fig. 10 Comparison of predicted and experimental heat fluxes (both present and literature data)

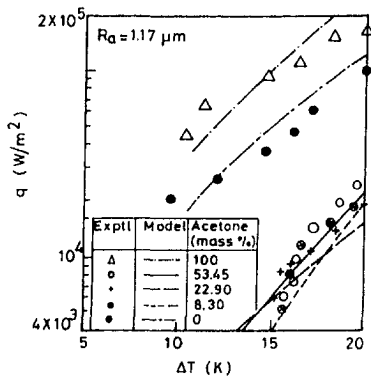
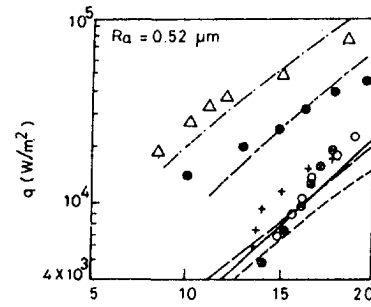


Fig. 11 Model prediction with experimental data at two R_a values

and when nucleation occurs (during the transient heat conduction mode of heat transfer), there is already a significant difference in concentration between the liquid in the cavity and the bulk liquid, leading to an increased mass diffusion of the more volatile component to the cavities. This reasoning is in accordance with the analysis of Sternling and Tichacek (1961). They suggested that the clogging of the nucleation sites by the less volatile component, caused by the preferential evaporation of the more volatile component decreases nucleation. This clogging is significant for large-size cavities. Therefore, the properties and the vapor–liquid equilibrium relationship exert an influence at higher R_a values, leading to widely differing wall superheats for different compositions for the same heat flux.

The present model differs slightly from the analysis of Thome (1982). According to Thome's (1982) analysis, the presence of the second liquid decreases the contribution of the thermal boundary layer reformation also. On the other hand, in the present study it is suggested that during the thermal boundary layer reformation there is no phase change and mass transfer retards heat transfer only when there is phase change. Therefore, the reduction in the boiling heat flux according to the present study is only due to a reduction in the contribution of the microlayer evaporation to the total heat flux. The present model takes into account the heating surface microroughness and its effect on the boiling heat flux, unlike Thome's (1982) model. Further, the dimensionless roughness parameter θ used to define the surface character makes use of both R_a , the centerline average of the surface profile and the surface tension thereby implicitly taking into account the effect of the contact angle.

Conclusions

A model based on an additive mechanism of heat transfer has been proposed for the boiling of binary mixtures. The model takes into account the surface finish of the heating surface, the composition of the liquid and the thermophysical and transport properties of the boiled liquid and the heating surface. The study

shows that at lower R_n values the properties of the liquid boiled and the heating surface and the vapor-liquid relationship are not important because mass transfer effects are negligible. Furthermore, the contribution of the microlayer evaporation mechanism to the total boiling flux is less in the boiling of a binary mixture, in contrast to a pure liquid. Boiling data from the literature obtained on a wire indicate higher heat fluxes probably because mass transfer effects are less significant in boiling over a wire. The model proposed satisfactorily matches the data obtained in the present study using two flat circular surfaces (aluminium and stainless steel with different surface finishes) and the data from the literature (data obtained on a platinum wire and on a stainless steel tube) validating the postulated mechanisms of heat transfer.

Acknowledgments

This study was funded by a research grant from the Department of Atomic Energy, Government of India through the Board of Research in Nuclear Sciences, Bhabha Atomic Research Centre, Mumbai, India.

References

- Benjamin, R. J., and Balakrishnan, A. R., 1996, "Nucleate pool boiling heat transfer of pure liquids at low to moderate heat fluxes," *International Journal of Heat and Mass Transfer*, Vol. 39, pp. 2495–2504.
- Benjamin, R. J., and Balakrishnan, A. R., 1997, "Nucleation site density in pool boiling of binary mixtures: Effect of surface micro-roughness and surface and liquid physical properties," *Canadian Journal of Chemical Engineering*, Vol. 75, pp. 1080–1089.
- Borishanskii, V. M., Bobrovich, G. I., and Minchenko, F. P., 1969, "Heat transfer from a tube to water and to ethanol in nucleate boiling," *Problems of Heat Transfer and Hydraulics*, S. S. Kutadlatze, ed., Pergamon Press, Oxford, UK, pp. 85–106.
- Calus, W. F., and Leonidopolous, D. J., 1974, "Pool boiling—binary liquid mixtures," *International Journal of Heat and Mass Transfer*, Vol. 17, pp. 249–256.
- Calus, W. F., and Rice, P., 1972, "Pool boiling—binary liquid mixtures," *Chemical Engineering Science*, Vol. 27, pp. 1687–1697.
- Carslaw, H. S., and Jaeger, J. C., 1959, *Conduction of Heat in Solids*, 2nd Ed., Oxford University Press, London, UK.
- Celata, G. P., Cumo, M., and Setaro, T., 1994, "A review of pool and forced convective boiling of binary mixtures," *Experimental Thermal and Fluid Science*, Vol. 9, pp. 367–381.
- Chiou, C. B., Lu, D. C., and Wang, C. C., 1997, "Investigations of pool boiling of refrigerant mixtures," *Heat Transfer Engineering*, Vol. 18, pp. 61–72.
- Cooper, M. G., Judd, A. M., and Pike, R. A., 1978, "Shape and departure of single bubbles growing at a wall," Paper PBI, *Proceedings, 6th International Heat Transfer Conference*, Toronto.
- Fujita, Y., and Tsutsui, M., 1997, "Heat transfer in nucleate boiling of binary mixtures," *JSME International Journal*, Vol. 40, pp. 134–141.
- Hahne, E., and Grigull, U., 1977, *Heat Transfer in Boiling*, Hemisphere, Washington, DC.
- Han, C. Y., and Griffith, P., 1965, "The mechanism of heat transfer in nucleate pool boiling—Parts I and II," *International Journal of Heat and Mass Transfer*, Vol. 8, pp. 887–914.
- Happel, O., and Stephan, K., 1970, "Heat transfer from nucleate to beginning of film boiling in binary mixtures," *Proceedings 4th International Heat Transfer Conference*, Paris—Versailles, Vol. 6, Paper B-7-6.
- Higbie, R., 1935, "The rate of absorption of a pure gas into a still liquid during short periods of exposure," *Trans. AIChE*, Vol. 31, pp. 365–389.
- Hsu, Y. Y., and Graham, R. W., 1976, *Transport Processes in Boiling and Two-phase Systems* Hemisphere, Washington, DC.
- International Standard, 1984, ISO 4287/1: 1984.
- Isshiki, N., and Nikai, I., 1973, "Boiling of Binary Mixtures," *Heat Transfer—Japanese Research*, Vol. 1, pp. 56–61.
- Kadhun, A. S., Varshney, B. S., and Mohanty, B., 1994, "Correlations for nucleate pool boiling of binary mixtures," *Journal of Energy, Heat and Mass Transfer*, Vol. 16, pp. 157–163.
- McAdams, W. H., 1954, *Heat Transmission*, 3rd Ed., McGraw-Hill, New York, p. 180.
- McNelly, M. J., 1953, "A correlation for nucleate pool boiling," *Journal of Imperial College Chemical Engineering Society*, Vol. 7, pp. 18–34.
- Mikic, B. B., and Rohsenow, W. M., 1969, "A New Correlation of Pool Boiling Data Including the Effect of Surface Characteristics," *ASME JOURNAL OF HEAT TRANSFER*, Vol. 81, pp. 245–250.
- Palen, J. W., and Small, W., 1964, "A new way to design kettle and internal reboilers," *Hydrocarbon Processing*, Vol. 43, pp. 199–208.
- Schlünder, E. U., 1983, "Heat transfer in nucleate boiling of mixtures," *International Chemical Engineering*, Vol. 23, pp. 585–599.

Scriven, L. E., 1959, "On the dynamics of phase growth," *Chemical Engineering Science*, Vol. 10, pp. 1–13.

Sernas, V., and Hooper, F. C., 1969, "The initial vapour bubble growth on a heated wall during nucleate boiling," *International Journal of Heat and Mass Transfer*, Vol. 12, pp. 1627–1639.

Siegel, R., and Keshock, E. G., 1964, "Effects of reduced gravity on nucleate boiling bubble dynamics in water," *AIChE Journal*, Vol. 20, pp. 509–517.

Stephan, K., 1992, *Heat Transfer in Condensation and Boiling* Springer-Verlag, New York.

Stephan, K., and Abdelsalam, M., 1980, "Heat transfer correlations for natural convection boiling," *International Journal of Heat and Mass Transfer*, Vol. 23, pp. 73–87.

Stephan, K., and Körner, M., 1969, "Berechnung des wärmeübergangs Verdampfer binärer flüssigkeitgemische," *Chemie Ingenieur Technik*, Vol. 41, pp. 409–417.

Sternling, C. V., and Tichacek, L. J., 1961, "Heat transfer coefficients for boiling mixtures," *Chemical Engineering Science*, Vol. 16, pp. 297–337.

Thome, J. R., 1981, "Nucleate pool boiling of binary mixtures—An analytical equation," *Chemical Engineering Progress Symposium Series*, Vol. 77, pp. 238–250.

Thome, J. R., 1982, "Latent and Sensible Heat-Transfer Rates in the Boiling of Binary Mixtures," *ASME JOURNAL OF HEAT TRANSFER*, Vol. 104, pp. 474–478.

Thome, J. R., 1983, "Prediction of binary mixture boiling heat transfer coefficients using only phase equilibrium data," *International Journal of Heat and Mass Transfer*, Vol. 26, pp. 965–973.

Thome, J. R., and Shakir, S., 1987, "A new correlation for nucleate pool boiling of aqueous mixtures," *Chemical Engineering Progress Symposium Series*, Vol. 83, pp. 46–51.

Thome, J. R., and Shock, R. A. W., 1984, "Boiling of multicomponent liquid mixtures," *Advances in Heat Transfer*, Vol. 16, J. P. Hartnett and T. F. Irvine, Jr., eds., Academic Press, London, pp. 159–156.

Tolubinskiy, V. I., and Ostrovskiy, Y. N., 1966, "Mechanism of heat transfer in boiling of binary mixtures," *International Journal of Heat and Mass Transfer*, Vol. 23, pp. 73–78.

Tolubinskiy, V. I., and Ostrovskiy, Y. N., 1969, "Mechanism of heat transfer in boiling of binary mixtures," *Heat Transfer—Soviet Research*, Vol. 1, pp. 6–11.

Torikai, K., Hori, M., Akiyama, M., Kobori, T., and Adachi, H., 1964, "Boiling heat transfer and burnout mechanism in boiling water cooled reactor," *Proceedings, Third International Conference on the peaceful uses of atomic energy*, Paper No. 28/P/50.

Tzan, Y. L., and Yang, Y. M., 1990, "Experimental Study of Surfactant Effects on Pool Boiling Heat Transfer," *ASME JOURNAL OF HEAT TRANSFER*, Vol. 112, pp. 207–212.

Ünal, H. C., 1976, "Maximum bubble diameter, maximum bubble growth time and bubble growth rate during subcooled nucleate flow boiling of water upto 17.7 MN/m²," *International Journal of Heat and Mass Transfer*, Vol. 19, pp. 643–649.

Ünal, H. C., 1986, "Prediction of nucleate boiling heat transfer coefficients for binary mixtures," *International Journal of Heat and Mass Transfer*, Vol. 29, pp. 637–640.

Van Stralen, S. J. D., 1959, "Heat transfer to boiling binary mixtures Part I," *British Chemical Engineering*, Vol. 4, pp. 8–17.

Van Stralen, S. J. D., and Cole, R., 1979, *Boiling Phenomena*, Vol. 1 and 2, Hemisphere Washington, DC.

Van Stralen, S. J. D., Sohal, M. S., Cole, R., and Sluyter, W. M., 1975, "Bubble growth rates in pure and binary systems: Combined effect of relaxation and evaporation microlayers," *International Journal of Heat and Mass Transfer*, Vol. 18, pp. 453–467.

Yang, Y. M., and Chou, C. C., 1988, "Prediction of pool boiling critical heat flux using phase equilibrium data," *International Communications in Heat and Mass Transfer*, Vol. 15, pp. 645–655.

Zmola, P., 1950, "Investigation of the mechanism of boiling in liquids," Ph.D. thesis, Purdue University, West Lafayette, IN.

Zeugin, L., Donovan, J., and Mesler, R., 1975, "A study of microlayer evaporation for three binary mixtures during nucleate boiling," *Chemical Engineering Science*, Vol. 30, pp. 679–683.

APPENDIX

Volume of Microlayer Evaporated in the Boiling of a Pure Liquid

Benjamin and Balakrishnan (1996) developed an analytical expression for the volume of microlayer evaporated in the nucleate pool boiling of a pure liquid based on the bubble growth description of Ünal (1976). The instantaneous area of the microlayer according to Ünal (1976) is

$$A_i = \frac{\pi D^2}{4} \left[1 - \left(\frac{D_d}{D} \right)^2 \right] = \frac{\pi D^2}{4} \phi. \quad (A1)$$

$1 - (D_d/D)^2$ is denoted as ϕ , a constant since D_d/D can be assumed to be a constant at a given pressure in accordance with the data of Torikai et al. (1964). Sernas and Hooper (1969) derived an expression for the heat flux to the bubble from the microlayer as

$$q_b = \frac{(T_w - T_g)\gamma k_l}{(\pi\alpha_l t)^{0.5}} \quad (\text{A2})$$

An energy balance on the evaporating microlayer for saturated boiling gives

$$-\frac{d}{dt} [A_l \delta \rho_l C_p (T_w - T_g)] = \frac{(T_w - T_g)\gamma k_l \pi D^2}{(\pi\alpha_l t)^{0.5}} \phi \quad (\text{A3})$$

where δ is the instantaneous microlayer thickness. The resulting differential equation is

$$\frac{d\delta}{dt} + \frac{2\delta}{D} \frac{dD}{dt} = \frac{-\gamma\alpha_l}{(\pi\alpha_l t)^{0.5}} \quad (\text{A4})$$

Using the bubble growth data of Zmola (1950) and Siegel and Keshock (1964) the bubble diameter was correlated as a function of time as

$$D(t) = B \text{Ar}^{0.135} (\text{Ja} \alpha_l t)^{0.5} \quad (\text{A5})$$

Differentiation of Eq. (A5) gives

$$\frac{dD}{dt} = \frac{D}{2t} \quad (\text{A6})$$

Substituting Eq. (A6) in Eq. (A4) gives

$$\frac{d\delta}{dt} + \frac{\delta}{t} = -\frac{\gamma\alpha_l}{(\pi\alpha_l t)^{0.5}} \quad (\text{A7})$$

The above ordinary differential equation is solved using the integrating factor t and the solution is

$$\delta(t) = \frac{2\gamma}{3} \left(\frac{\alpha_l t}{\pi} \right)^{0.5} - \frac{C}{\sqrt{t}} \quad (\text{A8})$$

The microlayer is assumed to completely evaporate when the bubble is fully grown. Therefore, the boundary condition to evaluate C is

$$\text{when } t = t_g, \delta = 0 \quad (\text{A9})$$

Therefore,

$$C = \frac{2\gamma\alpha_l}{3(\pi\alpha_l)^{0.5}} t_g^{1.5} \quad (\text{A10})$$

Using Eq. (A10) in Eq. (A8) gives the instantaneous thickness of the microlayer as

$$\delta(t) = \frac{2\gamma}{3t} \left(\frac{\alpha_l}{\pi} \right)^{0.5} (t_g \sqrt{t_g} - t\sqrt{t}) \quad (\text{A11})$$

The volume of microlayer evaporated (V_{ME}) is obtained from

$$V_{ME} = \frac{\int_0^{t_g} A_l(t) \delta(t) dt}{\int_0^{t_g} dt} \quad (\text{A12})$$

Using Eq. (A1), Eq. (A5), and Eq. (A11) in Eq. (A12), the volume of microlayer evaporated for a pure liquid is

$$V_{ME} = \frac{\gamma\phi\sqrt{\pi}}{10} B^2 \text{Ar}^{0.27} (\alpha_l t_g)^{1.5} \text{Ja} \quad (2)$$

Nucleate Pool Boiling on Ribbed Surfaces With Micro-Roughness at Low and Moderate Heat Flux

S.-S. Hsieh

Sun Yat-Sen Professor of Mechanical Engineering,
Dean of Engineering,
Fellow ASME

C.-J. Weng

Graduate Student

J.-J. Chiou

Graduate Student

Department of Mechanical Engineering,
National Sun Yat-Sen University,
Kaosiung, Taiwan 80424
Republic of China

Nucleate pool boiling correlation was developed for five different rib-type roughened tube geometries (including plain tube) with different rib angles of 30 deg, 45 deg, 60 deg, and 90 deg for both distilled water and R-134a as the working media. A scanning electron micrograph (SEM) examination was made for these horizontal roughened tubes. Bubble departure diameter, frequency of bubble emission, and the active nucleation site density with the influence of the rib angle for this type of roughened surface were obtained. Boiling heat flux incorporating natural convection, nucleate boiling, and microlayer evaporation mechanisms following Benjamin and Balakrishnan (1996) was predicted. Heat transfer correlation was also developed in terms of the degree superheat and active nucleation site density. The dependence for these two parameters was found in favorable agreement with that of previous study for smooth surfaces.

1 Introduction

Behavior in boiling of pure liquid from a horizontal tube surface during evaporation has been extensively studied and many generalized correlations applicable to the design of evaporators for various liquids have been developed. On the contrary, the published literature shows that a complete understanding is still lacking about the mechanism of boiling on enhanced surface and the theoretical modeling seems very scarce, especially for the particular enhanced surfaces such as rib-roughened surface (see Fig. 1 for details).

Modeling on a GEWA-TW surface was first reported by Ayub and Bergles (1987). They assumed that the energy transport is thin liquid film evaporation from the internal channels and agitation natural convection from the copper surface, which is the same as in the Nakayama et al. (1980) model for boiling on a planar GEWA-T surface. The model assumes steady-state evaporation of a thin film spreading over the inside surface of the tunnel.

Of the models previously discussed, only the Nakayama et al. (1980) model appears to have a sound and solid rational basis, of which the bubble dynamics is included. In spite of this, it appears that a greater physical understanding is required to model the boiling process of the rib-roughened surfaces than is used by the models of Nakayama et al. (1980) and Xin and Chao (1985). The modeling efforts to date invariably require knowledge of how the bubble frequency, departure diameter, and density of active sites vary with wall superheat. But, nevertheless, the modeling efforts support different dependencies of q on n and $T_w - T_{sat}$ where n is the active nucleation site density and they (q , n , and $T_w - T_{sat}$) can be correlated using the following expression:

$$q = C(T_w - T_{sat})^a n^b \quad (1)$$

General experimental studies, such as those of Tien (1962) and Zuber (1963), support that “ a ” lies somewhere between 1.0, and 1.8 and “ b ” is between 0.3 and 0.5. The exact values of the exponents in the power-law relation of Eq. (1) continue to be a subject of investigation and debate especially for the roughened surfaces.

To analyze the present boiling process from rib-roughened surfaces, the heat transfer model used features the following: (1) the heat transferred on latent heat to the evaporating microlayer, (2) the heat transferred by transient conduction during reformation of the thermal boundary layer, and (3) the heat transferred by turbulent natural convection from the heating surface not influenced by the bubble.

The objective of the present study is to broaden our fundamental understanding of pool nucleate boiling heat transfer from rib-roughened tubes and the results can be used to examine the extension of applicability of the model suggested by Benjamin and Balakrishnan (1996) to simulate the mechanism of pool boiling heat transfer for rib-roughened surfaces.

2 Analysis

2.1 General Description. The objective of the present study is mainly to model the heat transfer of the boiling process for the present rib-roughened geometry. Before this can be done, a data base of nucleate pool boiling data (e.g. n , ΔT , r_c . . . etc.) is needed. The paper presents the necessary information and salient feature regarding the modeling.

The present analysis relies entirely on a heat balance and is generally much simpler in concept and formulation compared to those of previous studies (see, for example, Bier et al., 1976). The heat transfer model proposed for this study involves the thermal layer forming at the nucleation sites between periods of bubble nucleation and thin film evaporation, a turbulent natural convection mechanism taking place in the regions uninvolved in bubble nucleation. Model verification was performed through nucleate pool boiling experimental data for five different tube geometries for two different working fluids of distilled water and R-134a.

In addition, as mentioned earlier, the nucleate pool boiling heat flux (q) depends upon both the superheat and the bubble population. The value of exponents was also found through the present experiments.

To meet these aforementioned needs, the following work was conducted: (1) modeling for heat transfer mechanism was developed using the model reported by Benjamin and Balakrishnan (1996) in which there are natural convection (q_{nc}), transient conduction (q_{tc}), and microlayer evaporation (q_{ME}) on boiling heat transfer; (2) active nucleation site density (n) was found from (q)

Contributed by the Heat Transfer Division for publication in the JOURNAL OF HEAT TRANSFER and presented at '96 IMECE. Manuscript received by the Heat Transfer Division, May 23, 1997; revision received Dec. 21, 1998. Keywords: Boiling, Enhancement, Heat Transfer. Associate Technical Editor: J.-C. Han.

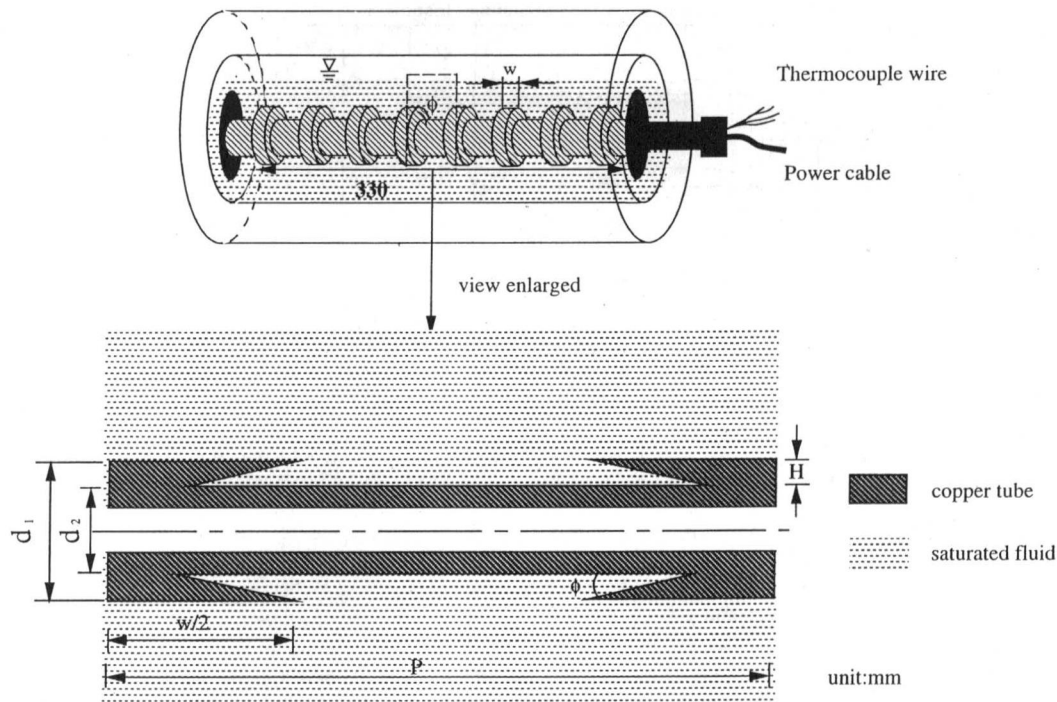


Fig. 1 Test section details of the present study

for both distilled water and R-134a; (3) verification of boiling heat transfer model using both distilled water and R-134a was conducted; (4) correlations of q on n and $(T_w - T_{sat})$ was explored and compared with existing correlations; and (5) correlations of n in relation with the present roughened surface rib angle ϕ and Jacob number Ja .

2.2 The Model. The total boiling heat transfer rate is obtained from the above three items through the following weighted equation:

$$q_p = \frac{q_{ME} t_g + q_{tc} t_w}{t_g + t_w} + q_{NC} \quad (2)$$

where t_g is the time of bubble growth and t_w is the waiting time for reformation of the thermal boundary layer. Both are related to the bubble frequency f by

$$f = \frac{1}{t_g + t_w} \quad (3)$$

and f can be estimated by a correlation from Stephan (1992). Van Stralen et al. (1975) assumed in pure liquids and highly polished surface, like the present study, that the waiting time is three times the growth time

$$t_w = 3t_g \quad (4)$$

Nomenclature

a = constant
 A = total heat transfer surface area
 A_b = area of influence of the bubble on the heating surface = πND_b^2
 Ar = Archimedes number
 b = constant
 B = constant in Eqs. (5) and (15)
 c_p = specific heat
 D_b = bubble departure diameter
 D_d = diameter of dry area under the bubble
 $d_{1/or2}$ = tube inner/or outer diameter shown in Fig. 1
 f = frequency of bubble emission
 g = gravitational constant
 H = rib height
 h = heat transfer coefficient
 h_{fg} = latent heat
 Ja = Jacob number
 K = constant
 k = thermal conductivity
 L = length of the test tube
 N = number of active nucleation site

n = active nucleation site density = N/A
 Pr = Prandtl number
 p = pitch of rib
 q = heat flux
 R_b = bubble departure radius
 Ra = Rayleigh number
 r_c = cavity radius
 t_g = bubble growth time
 t_w = waiting period = $3t_g$
 T = temperature
 ΔT = wall and bulk fluid temperature difference unless otherwise stated
 ΔT_{sat} = wall superheat = $T_w - T_{sat}$
 \bar{V}_{ME} = volume of microlayer evaporated within time t_g
 W = width of rib
 x = midpoint of the range x_j
 x_j = range of cavity radius

Greek Symbols

α = thermal diffusivity
 δ = thickness of microlayer

δ_{nc} = extrapolated thermal layer thickness used in Fig. 4
 θ = contact angle
 μ = dynamic viscosity
 ν = kinematic viscosity
 ρ_l = liquid density
 ρ_v = vapor density
 σ = surface tension coefficient
 ϕ = rib angle

Subscripts

b = bubble
 d = dry
 l = liquid
 M = measured
 ME = microlayer evaporation
 NC = natural convection
 ONB = onset of nucleating boiling
 p = predict
 sat = saturation
 tc = transient conduction
 v = vapor
 w = wall

Table 1 The dimensions of test tubes

Test tube	Tube (No.)	d ₁ (mm)	d ₂ (mm)	Number of rib elements	p (mm)	W (mm)	H (mm)	φ	A (mm ²)
Smooth	1	27	-	-	-	-	-	-	27992
Rib	2	27	19	8	39.4	15	4	90°	27502
Rib	3	27	19	8	39.4	15	4	60°	29973
Rib	4	27	19	8	39.4	15	4	45°	32787
Rib	5	27	19	8	39.4	15	4	30°	38292

Note: "-" means data not applicable

Prior to proceeding with the modeling, several major assumptions should be made as follows: (1) the area available for heat transfer is subdivided into an active area and in-active area; (2) assuming only pure conduction to the liquid in the action area during the waiting period, this mechanism may be considered as transient conduction to a semi-infinite medium; (3) the present bubble growth is in isolated bubble regime; and (4) the present boiling occurs in the low and moderate heat flux regime. In addition, the proposed model is a direct follow-up the work by Benjamin and Balakrishnan (1996) and, hence, all the limitations as well as constraints made by them are assumed here also.

A bubble grows by the vaporization of the thin liquid film left under the bubble. Development of an expression for the instantaneous microlayer thickness is based on the bubble growth description of Unal (1976). Similarly, all the assumptions made by Unal (1976) are also applied to the present study.

For microlayer evaporation during time t_g , the heat flux associated is given by (Benjamin and Balakrishnan, 1996)

$$q_{ME} = \frac{\sqrt{\pi}}{10} \left[1 - \left(\frac{D_d}{D} \right)^2 \right] \times \left[\frac{k_w \rho_w c_{pw}}{k_l \rho_l c_{pl}} \right]^{0.5} B^2 Ar^{0.27} Ja (\alpha_l)^{1.5} \sqrt{t_g} \rho_l h_{fg} n \quad (5)$$

where $B = \text{constant} = 1.55$ for water and $\frac{1}{1.35}$ for R-134a (Benjamin and Balakrishnan, 1996)

$$Ar = \text{Archimedes number} = (g/v_f^2)(\sigma/\rho_l g)^{0.5}$$

$$Ja = \text{Jacob number} = (\rho_l c_{pl} \Delta T_{sat}) / \rho_w h_{fg}$$

For thermal boundary layer reformation, the average heat flux of total nucleation sites on the surface during the waiting period t_w will be (Benjamin and Balakrishnan, 1996)

$$q_{nc} = 2 \left(\frac{k_w \rho_w c_{pw}}{k_l \rho_l c_{pl}} \right)^{0.5} n A_b \Delta T_{sat} \quad (6)$$

where $A_b = \pi N D_b^2$.

For turbulent natural convection, using McAdams (1933), the heat flux due to natural convection can be estimated from

$$q_{NC} = \frac{0.14 k_l}{L} (Ra)^{1/3} [1 - n A_b] \Delta T_{sat} \quad (7)$$

Incorporating Eqs. (2) through (6), one may find q_p .

The n used in Eqs. (5), (6), and (7) can be found in the following form (Jamialahmadi et al., 1991):

$$n = \frac{1}{\pi D_b^2} \left(\frac{h - h_{NC}}{h_b - h_{NC}} \right), \quad (8)$$

since the pool boiling heat transfer

$$q = h \Delta T \quad (9)$$

can be also divided into two mechanisms, namely, bulk convection, and natural convection as follows:

$$q_b = h_b \Delta T \quad (10)$$

$$q_{NC} = h_{NC} \Delta T \quad (11)$$

where ΔT stands for the temperature difference between the wall and liquid bulk temperature and $A = A_b + A_{NC}$ and $qA = q_b A_b + q_{NC} A_{NC}$. h , h_b , and h_{NC} can be found through Eqs. (7)–(9).

Finally, the minimum cavity radius (Griffith and Wallis, 1960) at a particular condition is calculated from

$$r_c = \frac{2\sigma T_{sat}}{\rho_w h_{fg} (\Delta T_{sat})} \quad (12)$$

In summary, since the problem is that the model uses experimental data q to predict (correlate) q itself through an intermediate parameter " n ," nucleation site density, the analysis is by no means a prediction but a correlation.

3 Experimental Setup and Procedure

Table 1 depicts the dimensions of these test tubes. This rib-roughened geometry and the tube were made using an innovative manufacturing method (Hsieh and Weng, 1997). This involves a machining process using a lathe. The definition of each term can be directly seen in Fig. 1 (e.g. p , H , ... etc.). It was fabricated from a copper tube. The copper tubes were 27 mm in diameter over the ribs with an inner diameter of 11 mm. Unless otherwise stated, the surface of the test tube was prepared with No. 400 emery paper which results in about 0.03- μm surface roughness. The cavities on the surfaces of these test tubes were observed by a scanning electron micrograph (SEM) to get the cavity radius for all the test tubes and the cavity probability density function in terms of the cavity radius for the plain surfaces of the rib-roughened tubes (i.e., between two consecutive ribs) according to Yang and Kim (1988) and their assumption. Due to the limit of the SEM operation range, only the central area (about $20 \times 14 \text{ mm}^2$) is examined. Before SEM examination, the surface condition of the test tube was prepared as follows: the tube was washed by an ultrasonic vibrating cleaner (model Bandelin Sonorex RK-100) with an acetone solution applied three times and each time lasted five minutes.

The working fluid used in the present experiments was distilled water (H_2O) and R-134a. The properties of R-134a and H_2O are listed in Table 2. The experimental apparatus and measurement positions for the study is similar to that of Hsieh and Hsu (1994). Saturated nucleate pool boiling data were taken on a plain tube and rib-roughened surfaces which were machined knife sharp with 30 deg, 45 deg, 60 deg, and 90 deg wedge angles. This minimized any possible effect due to contact between the two walls. The surface roughness of the rib wall was found influential in the present study. Distilled water and R-134a is the working medium. More than 50 runs for each tube were conducted. Some (e.g., 30 deg and 60 deg rib-roughened tubes) of these tests were repeated after several

Table 2 Properties of R-134a at $T_{sat} = 4.4^\circ\text{C}$, 303.4 kPa (data from ICI) and H_2O at $T_{sat} = 99.9^\circ\text{C}$, 101.3 kPa

properties	distilled water	R-134a
composition(formula)	H_2O	$\text{CH}_2\text{F}-\text{CF}_3$
substitute for	-	R-12
ODP[R-11=1.0]	-	0
GWP[R-11=1.0]	-	0.26
flammability	no	no
toxicity [AEL(TLV)][ppm]	-	1000
boiling temperature at 1 atm [$^\circ\text{C}$]	100	-26
critical temperature [$^\circ\text{C}$]	374.2	101
lubricant (compressor)	-	(Polyol-)Easter
ρ_l [kg/m^3]	958.300	1280.230
ρ_v [kg/m^3]	0.597	16.781
C_{p_l} [kJ/KgK]	4.22	1.358
C_{p_v} [kJ/KgK]	2.03	0.795
h_{fg} [kJ/Kg]	2256.7	193.707
k_f [W/mK]	0.679	0.093
μ_l [cP]	0.277	0.259
σ [N/m]	0.059	0.011
molecular weight	18.016	102.030
boiling point [bar]	1.013	3.421
dew point pressure [bar]	-	-
bubble point pressure [bar]	-	-

Note: ODP: Ozone Depletion Potential
AEL: Allowable Exposure Limit

GWP: Global Warming Potential
TLV: Threshold Limit Value

months to verify the reproducibility. Both increasing and decreasing q of boiling data were obtained. However, only the data in decreasing heat flux order was shown.

Four thermocouples were equally circumferentially at the middle of the test-roughened surfaces which have been proved to give a good accuracy of average wall temperature. Calibrated Chromel-Alumel thermocouples (within $\pm 0.3^\circ\text{C}$) of diameter 0.12 mm were employed to measure the wall temperature. To minimize longitudinal heat conduction silicon rubber and Devon five-minute epoxy glue, mixed with polystyrene foam, was applied to the ends of the thermocouples for use with water and R-134a, respectively. The variation in hydrostatic pressure due to change of pool level was taken into account in determining the saturation temperature. The pool temperature monitored by two thermocouples placed close to the free surface of the liquid. The temperature difference between these two points was between $\pm 0.1^\circ\text{C}$ at the maximum power input. The saturation temperature at measured pressure agreed within 0.1°C . Another thermocouple used to measure the vapor temperature was positioned midway along the test tube about 15 mm about the liquid surface. The uncertainty in the experimental data was estimated using a propagation of error analysis. The uncertainty in the wall superheat was dominated by the uncertainty in the wall temperature measurements. The values of the four wall circumferentially positioned temperatures (see Hsieh and Weng (1997) for details) were recorded and compared to examine variations caused either by nonuniformities in the cartridge heater or by the test tube soldering and assembly procedure. The maximum variation of the four measured wall temperatures was $\pm 0.5^\circ\text{C}$ at the maximum heat flux ($\approx 50 \text{ kW}/\text{m}^2$) and $\pm 0.1^\circ\text{C}$ at the minimum heat flux ($\approx 0.8 \text{ kW}/\text{m}^2$). The uncertainty in the saturation temperature was estimated to be less than $\pm 0.1^\circ\text{C}$. These caused the uncertainty of the corresponding wall superheat ($T_w - T_{sat}$) to be within ± 14 percent at low heat flux and within ± 2 percent at high

heat flux. The heat flux accuracy was $\pm 0.01 \text{ kW}/\text{m}^2$ at the minimum heat flux of $0.8 \text{ kW}/\text{m}^2$.

4 Data Reduction

The present experiments include the pool boiling data base and a scanning electron microscope examination of test tubes. The raw data to be obtained were the distributions of q (measured) versus ΔT and the cavity radius. Once these values are found n can be obtained.

The values of microlayer evaporation was calculated based on \bar{V}_{ME} found from the following form (Benjamin and Balakrishnan, 1996):

$$\bar{V}_{ME} = \frac{\int_0^{t_g} A_m(t) \delta(t) dt}{t_g} \quad (13)$$

where $A_m(t) = \pi D_d/4 [1 - (D_d/D)^2]$. The instantaneous area of the microlayer at the base of the bubble and the instantaneous thickness from Jamialahmadi, et al. (1991) of the microlayer is the following:

$$\delta(t) = \frac{2h_{fg}}{3t} \sqrt{\left(\frac{\alpha}{\pi}\right)} (t_g^{3/2} - t^{3/2}). \quad (14)$$

Based on Benjamin and Balakrishnan (1996), it gives

$$\bar{V}_{ME} = \frac{\sqrt{\pi}}{10} \left[1 - \left(\frac{D_d}{D}\right)^2 \right] \left[\frac{k_w \rho_w c_{pl}}{k_l \rho_l c_{pl}} \right]^{0.5} \times B^2 \text{Ar}^{0.27} \text{Ja} (\alpha t_g)^{1.5}. \quad (15)$$

This volume of liquid evaporates during time t_g . Hence, this gives Eq. (5) for q_{ME} .

Following Fritz (1935) and assuming the present condition is in an isolated bubble region (at low to moderate heat fluxes),

$$D_b = 0.0146\theta[2\sigma/g(\rho_l - \rho_v)]^{0.5} \quad (16)$$

with $\theta = 45$ deg (distilled water) and 35 deg (R-134a) for the cases under study (Jamialahmadi, et al., 1991). f can be calculated from Zuber (1959).

$$D_b f = 0.59[\sigma g(\rho_l - \rho_v)/\rho_l^2]^{0.25} \quad (17)$$

For SEM examination, it is long recognized that the statistical approach is a better technique to analyze the cavities on the surface. Random locations on the surface area were determined with PC software based on the identification of a specified area. The present work uses an SEM examination to get the cavity probability density function in terms of the cavity mouth radius.

5 Results and Discussion

The rib angle was observed to significantly affect the local nucleate boiling near the contact line of the heated wall and the roughened wall, where bubbling was remarkably more vigorous than elsewhere on the heated wall. The influence of the present roughened surfaces on the incipient boiling, nucleation site density, and local heat transfer performance can be observed in the following subsections.

5.1 Scanning Electron Micrograph Examination for Boiling Incipience. A typical result of JSM-6400 SEM examination for rib angles of $\phi = 30$ deg, 45 deg, and 60 deg of the tube central part between two consecutive ribs is shown in Fig. 2. Roughly speaking, the black spots and scars are all cavities. It happened to be the way that the micrographs of the surface show dependence on the rib angle. This does not indicate that micro-roughness depends on ϕ . Surface orientation is random, some lying vertically and some horizontally, which results in a microstructure with an average surface roughness of $0.03 \mu\text{m}$. Table 3 summarizes the observed data for the radius of the cavity. The cavity distribution is plotted in terms of the radius of the cavity in Fig. 3. The cavity distribution was assumed to be fitting the Poisson distribution. By applying the Chi-square test on the measurements with a 99 percent confidence level, it is found that the acceptance region $\chi_0^2 \leq \chi_{0.01}^2(5) = 15.09$ and has the following form:

$$f(x) = 1.3641e^{-\lambda x} \quad \text{where } \lambda = 1.3641 \mu\text{m}^{-1}. \quad (18)$$

Obviously, the experiments showed that the roughened tubes have a lesser degree of superheats for both distilled water and R-134a as shown in Fig. 4. The variation of the active nucleation sites between the distilled water and R-134a seems large. By plotting the cavity radius r_c predicted by the well-known Han and Griffith's formula (1965) for five surfaces tested against the degree of superheat ΔT , Fig. 4 was obtained. Table 4 lists the corresponding ΔT_{sat} at this moment for the five tubes tested. It is found that ΔT_{sat} is the smallest for a 60-deg rib angle of roughened surface (tube 3). No cavities having radii in the vicinity of the upper branch of the curve were observed to be active which coincided with the fact that such cavities did not exist on the tubes tested with the present SEM examination. With the aid of the present SEM examination and the r_c obtained, the present active nucleation site was determined in a shaded area as shown in Fig. 4 for distilled water and R-134a. This indicates that the experimental results tend to fall along the lower branch of the curve ("—" sign shows). It is seen that cavities of larger radii were not active on the surfaces tested. This is perhaps because the smaller cavities exist in greater numbers than the larger cavities. Based on the calculated bubble departure diameter and frequency for all the cases studied herein, it is found that the distilled water bubble size ($D_b \cong 2.33 \times 10^{-3}$ m) seems always bigger than that of R-134a ($D_b \cong 6.81 \times 10^{-4}$

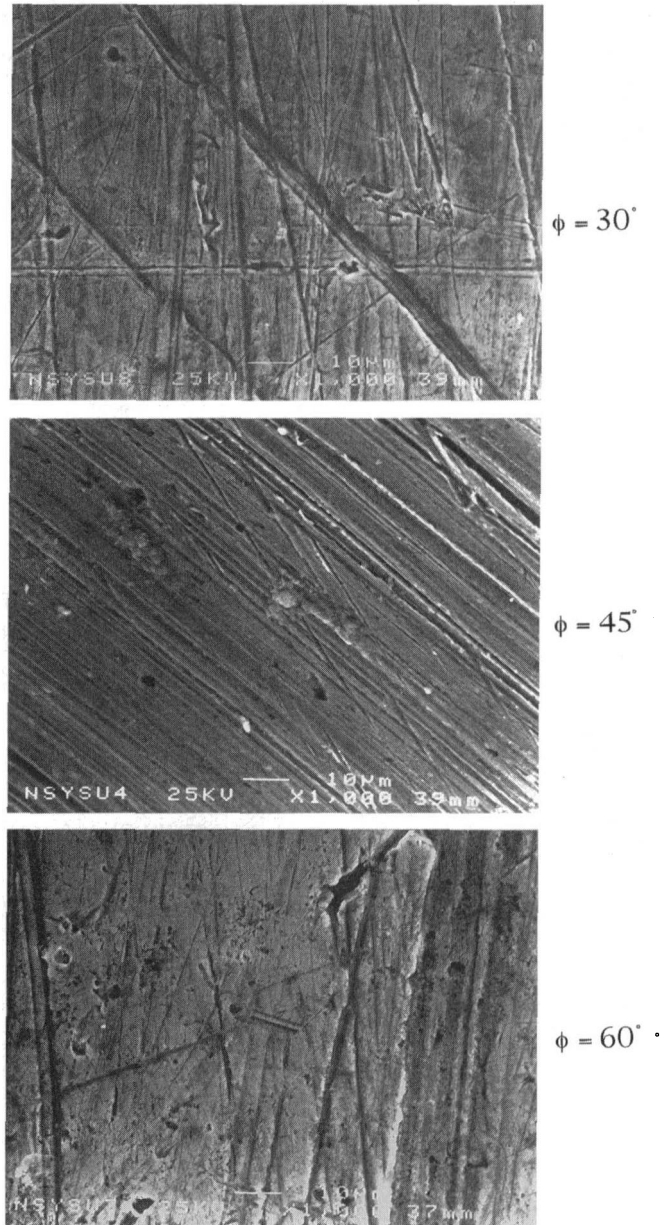


Fig. 2 Typical SEM (scanning electron micrographs) for different rib angles

m) due to a higher surface tension of the water. The variation of bubble emission frequency f has a tendency similar to that of the bubble departure diameter. However, the f exhibits a reverse, namely, 39.72 s^{-1} for H_2O and 82.74 s^{-1} for R-134a.

5.2 Boiling Modeling and Heat Transfer Correlation/Prediction.

5.2.1 Nucleation Site Density. To use the above model for the calculation of the heat transfer flux, the nucleation site density n is required to solve Eq. (8). Bier et al. (1976) proposed an expression of active site density in the following form:

$$\ln(n) = \ln(n_{\text{max}}) \left[1 - \left(\frac{r_{\text{min}}}{r_{\text{max}}} \right)^{m_a} \right] \quad (19)$$

where r_{min} is the radius of the first active nucleation site, n_{max} is the total number of nucleation sites available on the heat transfer surface, and m_a is characterized from the heating surface. Values for $(n)_{\text{max}}$, r_{max} , and m_a vary for different surface preparations (see

Table 3 Number of cavity in cavity radius ranges

Item no.	Range of cavity mouth radius (μm)	Middle point value of radius (μm)	Number of cavity within the range
1	0.34-0.52	0.43	14
2	0.52-0.69	0.60	9
3	0.69-0.86	0.78	6
4	0.86-1.03	0.95	7
5	1.03-1.21	1.12	4
6	1.21-1.38	1.29	3
7	1.38-1.55	1.47	4
8	1.55-1.72	1.64	2
9	1.72-1.90	1.81	0
10	1.90-2.07	1.98	1
11	2.07-2.24	2.16	0
12	2.24-2.41	2.33	0

$$\chi^2 = 13.4901 < \chi_{\text{min}}^2(5) = 15.09$$

Blöchl (1986) for details). The minimum cavity radius r_c ($=r_{\text{min}}$) is determined from Eq. (12).

Based on Eq. (19), a correlation of an active nucleation site density for distilled water and R-134a on the enhanced tube was developed and plotted in Fig. 5 and compared with the results from previous statistical analysis based on SEM measurements (i.e., from Eq. (18)). The differences were probably due to different approaches. In spite of this, all results indicate that as the minimum cavity radius increased, the activated nucleation site density decreased. This again verifies that there are more smaller cavities than larger cavities. Moreover, the small cavity is apparently more

capable of holding a residual of vapor and is also able to be activated by its neighbors when boiling is initiated on the heating surface. Consequently, the performance of a heat transfer device in which vaporization occurs may strongly depend on the heated wall. Based on the properties of the working liquid, R-134a is more likely to form nucleate sites than distilled water, and this phenomenon can be explained by the fact of the surface tension difference between two liquids. The data obtained from the model proposed for distilled water and R-134a have the following form:

$$n = 0.00042r_{\text{min}}^{-1.41} \quad \text{for H}_2\text{O}$$

$$n = 0.00002r_{\text{min}}^{-1.45} \quad \text{for R-134a} \quad (20)$$

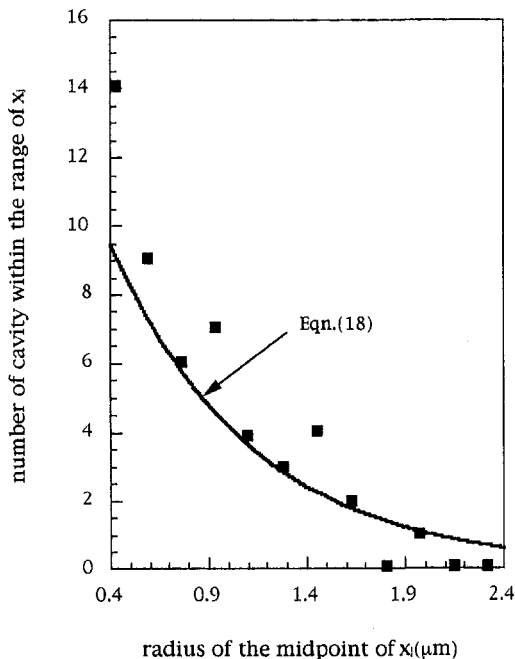


Fig. 3 Probability density function of cavity radius

which are more convenient to work with than Eq. (19). They are essentially different in nature from the one used in SEM measurements. But the trend of the curve is similar, especially for the power of r_{min} . The exponent of each correlation stated before appears to vary slightly, having a tendency to increase with R-134a and the values for statistical analysis shown were a little bit lower than those calculated from proposed model as one would expect because the proposed model does take the rib effect into account. This is because n was found from Eqs. (8) through (11) which were all obtained from experiments. Further examination of Fig. 5 shows the degree to which entrapped gas in a surface rib angle can act as initial vaporization may be affected by the rate at which the gas in a cavity dissolves into the liquid and diffuses away from the gas-liquid interface. Figure 6 depicts the variation of an active nucleation site density as a function of the ΔT (measured). The significant increase in an active nucleation site density with increasing heat flux in Fig. 6 can be attributed to the fact that superheat increases slightly with increasing heat flux (see Hsieh and Hsu, 1994). The values of n are always higher with R-134a than those with distilled water. The influence of the rib angle on the nucleation site density in Figs. 5 and 6 could also be noted. It appears that there is a higher value of nucleation site density with rib angles of 30 deg and 45 deg. This clearly indicates that an enhanced incipient boiling would occur at a small rib angle in which a possible favorable local thermal environment within the

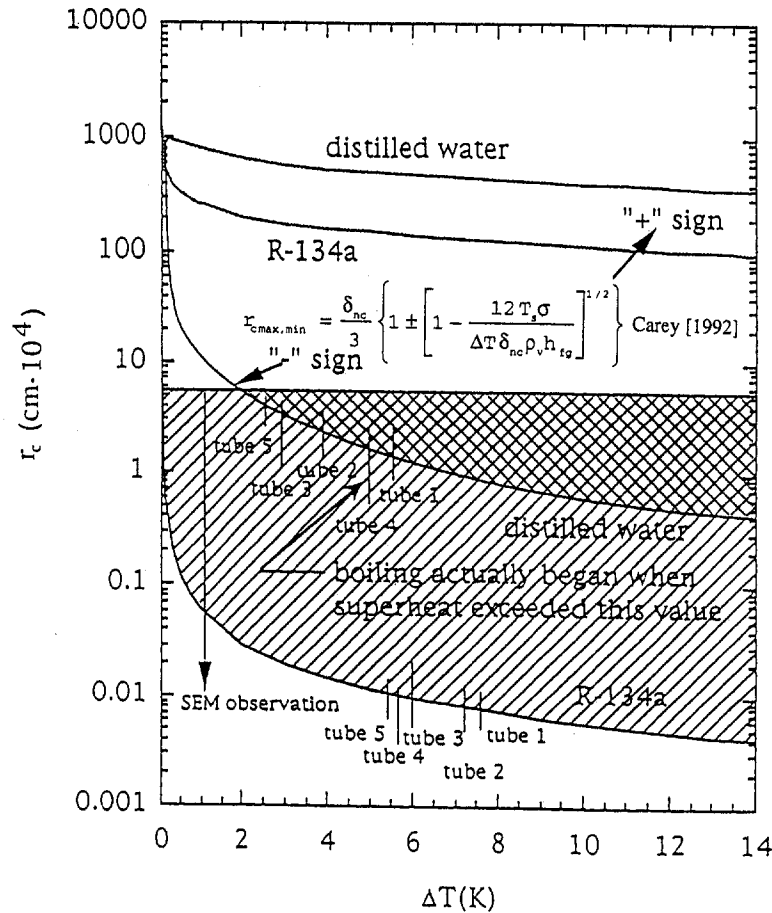


Fig. 4 The range of the present active cavity sizes

angular geometry exists. This is because at a small angle, vapor phase always formed at a low superheat near the contact line of the two walls while there was no significant sign of nucleate boiling elsewhere on the heated wall. Based on data of 30 deg and 45 deg compared to that of 60 deg and 90 deg, the nucleate boiling heat transfer rates are also higher. These findings coincided with those of Chyu and Fei (1991). Following Fig. 6, Fig. 7 shows the variation in bubble flux density obtained by multiplying the active site density and the frequency of bubble emission is a function of measured heat flux. Again, nf values are also having a higher value in R-134a than those in distilled water. However, in both figures (Figs. 6 and 7), the rib-roughened surface effect is not clearly noted and the experiments were carried out in increasing order of heat flux.

Finally, the active nucleation site density was plotted as a function of ΔT for distilled water and R-134a, respectively, with five tubes tested, which was shown in the upper and lower parts of Fig. 8, respectively. It is seen that the nucleation site density increases qualitatively as the temperature increases, and it can be concluded that n is not only effected by working fluids but by the rib angles and fluid properties. It is also found that the strong influence on the active nucleation site density occurs for tubes with 30 deg- and 45 deg-rib angles for the distilled water and R-134a, respectively. Moreover, the present active nucleation density function can be correlated into the following form in terms of the Jacob number Ja and the rib angle ϕ (in radians) within ± 15 percent to the original data.

$$n = 283.162[Ja]^{1.642}[\pi - \phi]^{-0.913} \quad \text{for H}_2\text{O}$$

Table 4 ΔT_{sat} for distilled water and R-134a

ΔT_{sat} (K)	working medium	
	distilled water	R-134a
tube no.		
tube 1	8.7	7.7
tube 2	6.0	7.3
tube 3	5.2	5.6
tube 4	7.0	7.5
tube 5	5.5	7.0

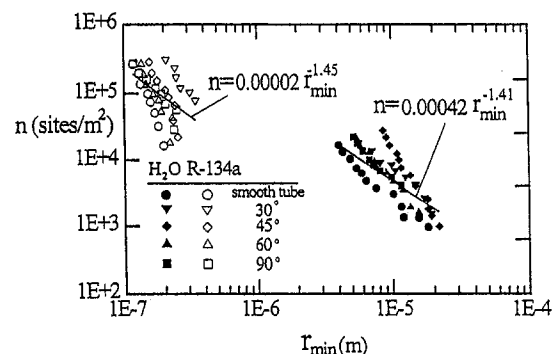


Fig. 5 Nucleation site density as a function of r_{min} for H₂O and R-134a ($\Delta T_{\text{sat}} = 5-9$ K)

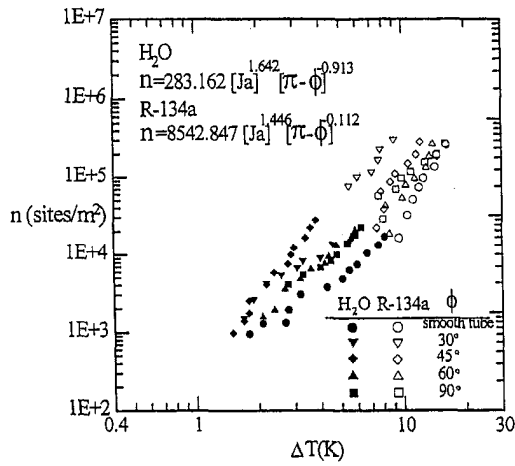


Fig. 6 Nucleation site density as a function of Ja and ϕ

$$n = 8542.847[\text{Ja}]^{1.446}[\pi - \phi]^{-0.112} \quad \text{for R-134a} \quad (21)$$

where Ja is the Jacob number ($(\rho_l c_{pl} \Delta T_{\text{sat}}) / \rho_v h_{fg}$) and ϕ is the rib angle (in radians).

5.2.2 Heat Transfer Correlation/Prediction. As mentioned earlier, following Benjamin et al. (1996), a predicted heat flux for the present rib-roughened tube can also be divided into the microlayer evaporation component, nucleate boiling component, and natural convection component. Figure 9 depicts the total predicted heat flux q_p and each component of q with measured heat flux (q_m) on different rib angles for distilled water. Also shown in Fig. 9(a), for comparison, is the smooth tube data from Gottzmann et al. (1973). It is obvious that the predicted heat flux almost exactly coincides with the measured heat flux as stated previously. It can be seen that $q_{\text{CYCLE}} = (q_{ME} \cdot t_g + q_{NB} \cdot t_w) / (t_g + t_w)$; that is, latent heat dominates the heat transfer contribution among the predicted heat flux. The contribution of latent heat transfer increases sharply with the increase of wall superheat. Moreover, initially, the natural convection component takes the largest part of the heat flux contribution as one would expect, because the term of q_{CYCLE} was completely suppressed. As time goes by, the heat transfer area affected by the natural convection was gradually replaced by latent heat transfer exchange due to both microlayer evaporation and nucleate boiling. Consequently, the slope of q_{NC} for each tube becomes smaller as ΔT increases, and this phenomena can be explained due to the change of the bubble influenced area.

Similarly, Fig. 10 shows the comparison of the present model

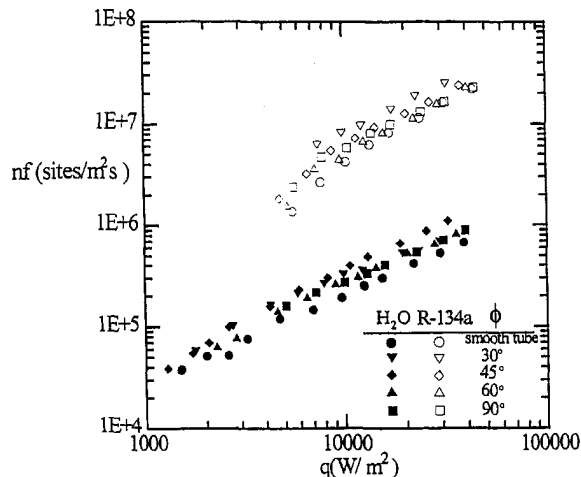


Fig. 7 Nucleate site density and frequency as a function of heat flux

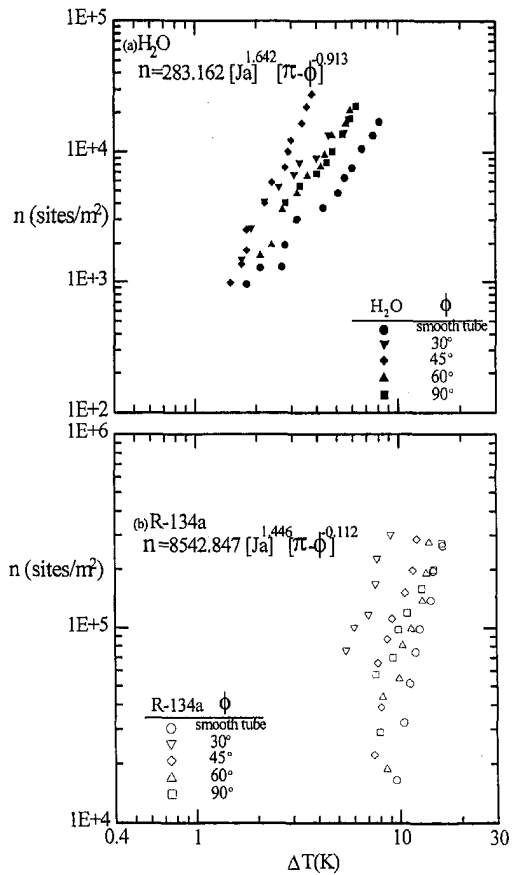


Fig. 8 Nucleation site density as a function of ΔT

with experimental data for R-134a. Again, the similar behavior was found as that for distilled water and, again, it clearly shows the good agreement between the prediction and the experimental data. The tendency and magnitude seem similar compared to Fig. 9. However, the transient latent heat portion, q_{CYCLE} , takes most part of heat transfer contribution this time compared to the q cycle in Fig. 9. Consequently, natural convection component plays a minor role in this heat transfer process. This is perhaps because distilled water has a lower wetting ability than that of R-134a and, in turn, the active nucleation site density in distilled water is lower than that in R-134a. On the contrary, the heat transfer due to latent heat and transient conduction during reformation of the thermal boundary layer is large compared to R-134a. Comparing Figs. 9 and 10, it can also be seen that the boiling curve is much more steep for distilled water than that in R-134a. Again, this is because the latent heat of water is much higher than that of R-134a and the thermal properties of water and R-134a also contribute to the difference in boiling curve slopes as well. Moreover, the quantitative contribution of each component could be calculated. Benjamin and Balakrishnan (1996) proposed that the heat flux due to microlayer evaporation alone can be up to about 50 percent for water and 45 percent for the organic liquids. The present study also found that the contribution of the heat flux to microlayer evaporation is as high as 45–50 percent for distilled water and R-134a. In fact, the present model is similar to that of Benjamin and Balakrishnan (1996) with slight modifications due to the effects of rib angle of enhanced tubes.

5.3 Correlation of Heat Flux With Parameters (ΔT , n). As previously stated, Eq. (1) continues to be an interesting subject because this nearly identical power-law dependence on heat flux and superheat for many wall material-and-liquid combinations makes it possible to develop relatively simple nucleate boiling heat transfer correlations that can be used with fair accuracy for a wide

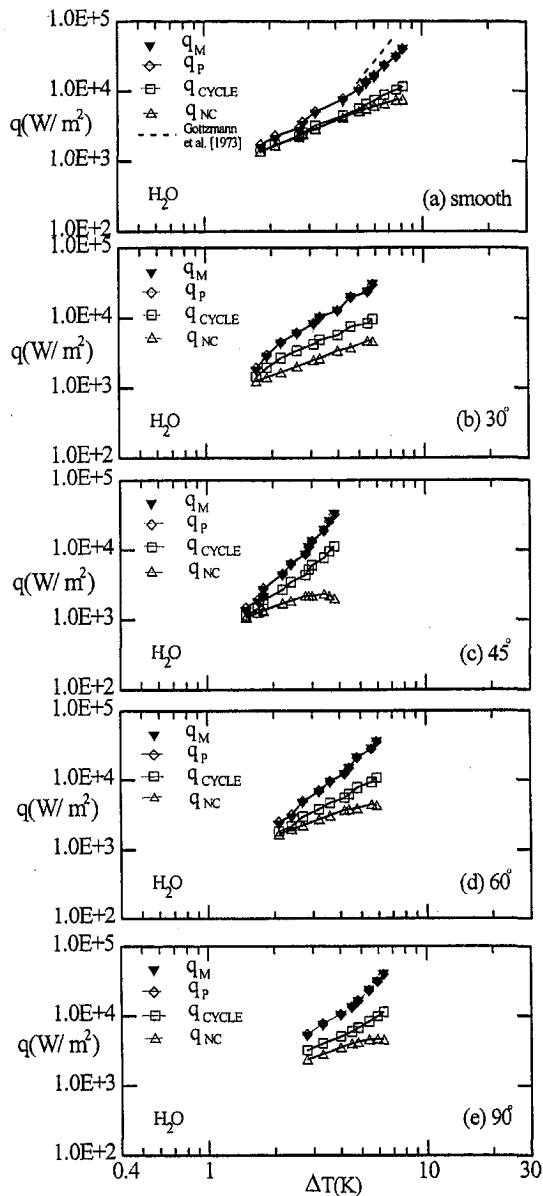


Fig. 9 Comparison of the model with the experimental data for H₂O

variety of conditions. It is therefore necessary to extend its applicability to roughened surfaces. The correlation of Eq. (1) was thus reexamined using the present experimental data for five tubes tested in distilled water and R-134a and q (measured) were plotted against n as shown in Fig. 11. The agreement between the correlation and the data measured shown in Fig. 12 is quite good, within ± 15 percent. It can be found that the curve exhibits a definite distribution and the slope seems near 1. This gives the value of a in Eq. (1) 0.98 and the dependence on n was found to be 0.41. Furthermore, the agreement between the present results and those of the previous study for smooth surfaces (also shown in Fig. 11) reported by Tien (1962) in the values of a and b was good. The value of a is almost the same as that of Tien (1962). With present roughened surface and its larger gap size between two consecutive ribs compared with the conventional GEWA-T and Thermoexcel surfaces, it is believed the entrapment of gas, which serves as a seed for nucleation, depends on the contact angle and the present rib angle. A strong interdependence of this type of roughened surface makes the complexity and difficulty to interpret the present results. Moreover, the problem with Eq. (1) is that it introduces what engineers call a "nuisance variable" (Lienhard, 1981) which results in the site of a particular surface having a typical distribu-

tion of sizes, n (and hence q) can increase very strong with ΔT . Therefore, n was also plotted as a function of ΔT for distilled water and R-134a, respectively, with five tubes tested as also shown in Fig. 8. The contribution of n on ΔT is different from n versus q_M for which the present result is not only affected by working fluids but by rib angles, indicating the strong effect of fluid properties and rib geometry. As a result, unlike the paper reported by Ayub and Bergles (1987) for GEWA-T surfaces, the present n cannot be solely correlated as a function of ΔT . Nevertheless, n still increases as ΔT increases.

6 Conclusion

The present analysis of nucleate pool boiling on rib-roughened surfaces with micro-roughness at low and moderate heat flux has made it possible to examine for the first time the heat transfer mechanism and its modeling for four rib-roughened surfaces and a smooth surface tested in pools of saturated distilled water and R-134a for an isolated bubble regime. Based on the present results, significant features can be drawn in the following:

- 1 The SEM examination again indicates that the experimental results for boiling incipience tend to fall along the lower branch of

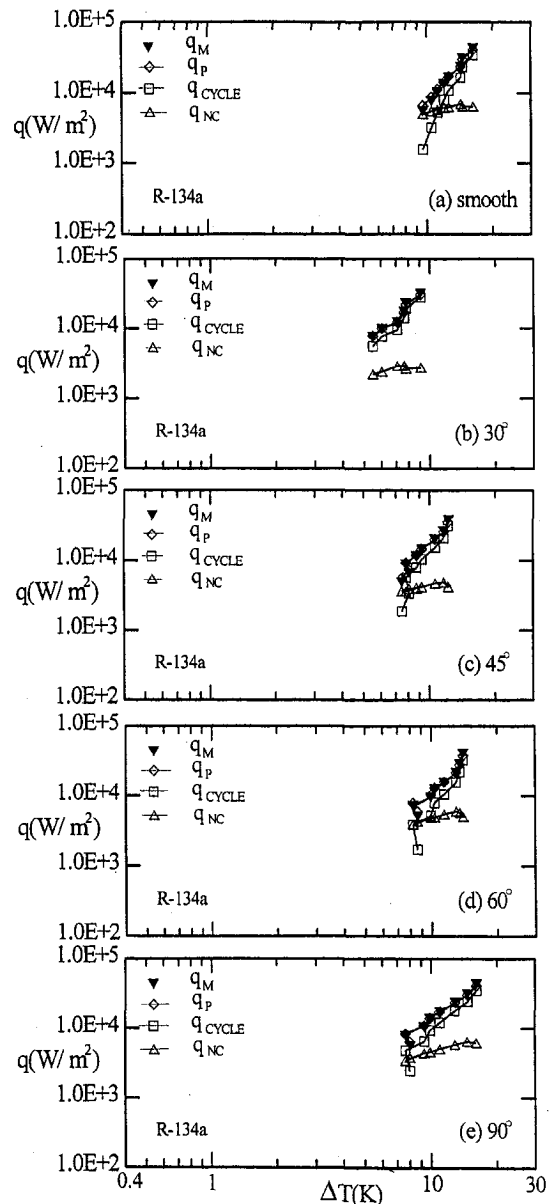


Fig. 10 Comparison of the model with the experimental data for R-134a

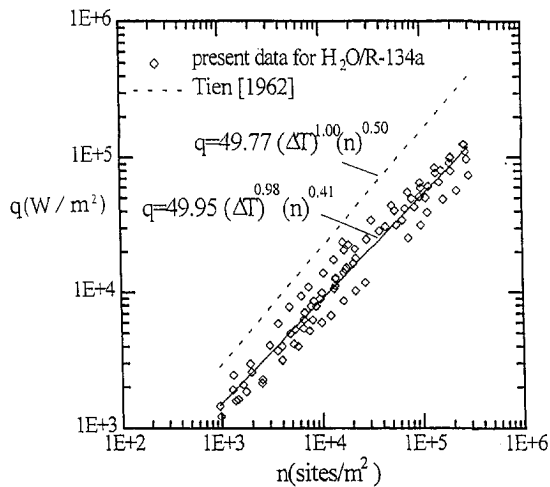


Fig. 11 Correlation of heat flux with nucleation site density and degree of superheat

the curves generated by Han and Griffith (1965). A Chi-square test was made for the cavity distribution.

2 Following the model developed by Benjamin and Balakrishnan (1996) with slight modifications, it is found that the model can be applied to the present rib geometry as well.

3 Due to the surface tension difference between distilled water and R-134a, each contribution of q_{NC} , q_{NB} , and q_{ME} on total q is different. Again, the contribution due to microlayer evaporation is dominant among the rest of two (q_{NC} and q_{NB}).

4 It is found that n is not a sole function of ΔT for the present rib-roughened surfaces as those of previously reported for GEWA-T surfaces. In addition, the rib angle was also found to be one of the important parameters.

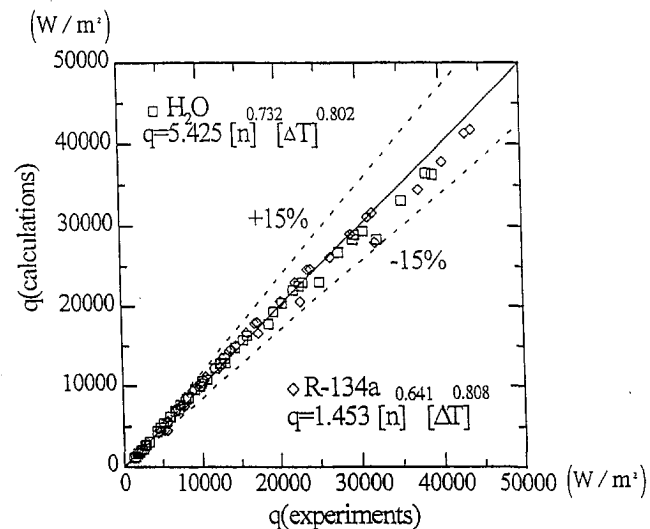


Fig. 12 q calculated versus q from experiment for H₂O and R-134a

Acknowledgment

This work was supported by a research grant (NSC 85-2212-E-110-006) from the National Science Council, Taiwan, R.O.C.

References

- Ayub, Z. H., and Bergles, A. E., 1987, "Pool boiling from GEWA surfaces in water and R-113," *Wärme- und Stoffübertragung*, Vol. 21, pp. 209–219.
- Benjamin, R. J., and Balakrishnan, A. R., 1996, "Nucleate pool boiling heat transfer of pure liquids at low to moderate heat fluxes," *Int. J. Heat Mass Transfer*, Vol. 39, pp. 2495–2504.
- Bier, K., Engelhorn, H.-R., and Gorenflo, D., 1976, "Heat Transfer with Low-Boiling Halogene Refrigerants, Measurements Taken with Single Tubes and Transmission in Tube Nets," *Klima Kaelte Ing.*, Vol. 11, pp. 399–406 (in German).
- Blöchl, R., 1986, "Zum Einfluß der Oberflächenstruktur unterschiedlich bearbeiteter Heizflächen auf die Wärmeübertragung beim Blasensieden," Doctoral dissertation, University of Karlsruhe.
- Chyu, M.-C., and Fei, J., 1991, "Enhanced Nucleate Boiling in an Angular Geometry Found in Structured Surfaces," *Int. J. Heat Mass Transfer*, Vol. 34, pp. 437–448.
- Carey, V. P., 1992, *Liquid-Vapor Phase-Phenomena*, Hemisphere, Washington, DC.
- Fritz, W., 1935, "Berechnung des maximalvolumens von dampfbblasen," *Phys. Z.*, Vol. 36, p. 379.
- Gottzmann, C. F., O'Neil, P. S., and Minton, P. E., 1973, "High Efficiency Heat Exchangers," *Chemical Engineering Progress*, Vol. 69, No. 98, pp. 69–75.
- Griffith, P., and Wallis, J. D., 1960, "The Role of Surface Conditions in Nucleate Boiling," *Chemical Engineering Progress Symposium Series*, Vol. 56, No. 30, pp. 49–63.
- Han, C. Y., and Griffith, P., 1965a, "The mechanism of heat transfer in nucleate pool boiling. Part 1: Bubble initiation, growth and departure," *Int. J. Heat Mass Transfer*, Vol. 8, pp. 887–904.
- Han, C. Y., and Griffith, P., 1965b, "The mechanism of heat transfer in nucleate pool boiling. Part 2: The heat flux-temperature difference relation," *Int. J. Heat Mass Transfer*, Vol. 8, pp. 905–914.
- Hsieh, S.-S., and Hsu, P. T., 1994, "Nucleate boiling characteristics of R-114a, distilled water (H₂O) and R-134a on plain and rib-roughened tube geometries," *Int. J. Heat Mass Transfer*, Vol. 37, pp. 1423–1432.
- Hsieh, S.-S., and Weng, C. J., 1997, "Nucleate Pool Boiling Heat Transfer Coefficients of Distilled Water (H₂O) and R-134a/Oil Mixtures From Rib-Roughened Surfaces," *ASME JOURNAL OF HEAT TRANSFER*, Vol. 119, pp. 142–151.
- Hsieh, S.-S., and Weng, C. J., 1997, "A New High Performance Rib Tube," ROC (Taiwan) Patents (Innovation No. 118759).
- Jamialahmadi, M., Blöchl, R., and Müller-Steinhagen, H., 1991, "Pool boiling heat transfer to saturated water and refrigerant 113," *The Canadian J. of Chem. Engr.*, Vol. 69, pp. 764–754.
- Lienhard, J. H., 1981, *A Heat Transfer Text Book*, 2nd Ed., Prentice-Hall, Englewood Cliffs, NJ, p. 421.
- McAdams, W. H., 1933, *Heat Transfer*, McGraw-Hill, New York.
- Nakayama, W., Daikoku, T., Kuwahara, H., and Nakajima, T., 1980a, "Dynamic Model of Enhanced Boiling Heat Transfer of Porous Surface. Part 1: Experimental Investigation," *ASME JOURNAL OF HEAT TRANSFER*, Vol. 102, pp. 445–450.
- Nakayama, W., Daikoku, T., Kuwahara, H., and Nakajima, T., 1980b, "Dynamic Model of Enhanced Boiling Heat Transfer of Porous Surface. Part 2: Analytical Modeling," *ASME JOURNAL OF HEAT TRANSFER*, Vol. 102, pp. 451–456.
- Stephan, K., 1992, *Heat Transfer in Condensation and Boiling*, Springer Verlag, New York, pp. 135–136; 145–149.
- Tien, C. L., 1962, "Hydrodynamic model for nucleate pool boiling," *Int. J. Heat Mass Transfer*, Vol. 5, pp. 533–540.
- Unal, H. C., 1976, "Maximum Bubble Diameter, Maximum Bubble Growth Time and Bubble Growth Rate During Sub-Cooled Nucleate Flow Boiling of Water up to 17.7 MN m⁻²," *Int'l J. Heat Mass Transfer*, Vol. 19, pp. 643–649.
- Van Stralen, S. J. D., Sohal, M. S., Cole, R., and Sluyter, W. M., 1975, "Bubble growth rates in pure and binary systems combined effect of relaxation and evaporation microlayers," *Int. J. Heat Mass Transfer*, Vol. 18, pp. 453–467.
- Xin, M. D., and Chao, Y. D., 1985, "Analysis and experiment of boiling heat transfer on T-shaped finned surfaces," presented at the 23rd Nat. Heat Transfer Confer. Aug. 4–7, Denver, CO.
- Yang, S. R., and Kim, R. H., 1988, "A mathematical model of the pool boiling nucleation site density in terms of the surface characteristics," *Int. J. Heat Mass Transfer*, Vol. 31, pp. 1127–1135.
- Zuber, N., 1959, "Hydrodynamic aspects of boiling heat transfer," AECU-4439, Doctoral dissertation, University of California at Los Angeles, Los Angeles, CA.
- Zuber, N., 1963, "Nucleate Boiling, the region of isolated bubbles and the similarity with natural convection," *Int. J. Heat Mass Transfer*, Vol. 6, pp. 53–78.

Heat Transfer Behavior on Small Horizontal Heaters During Pool Boiling of FC-72¹

T. D. Rule

School of Mechanical and
Materials Engineering,
Washington State University,
Pullman, WA 99163-3920

J. Kim

Department of Mechanical Engineering,
University of Maryland,
College Park, MD 20742

Detailed local measurements of wall heat flux during saturated pool boiling of FC-72 on a small heated area without sidewalls were made using an array of 96 temperature-controlled heaters. Data were obtained in the nucleate boiling, critical heat flux, and transition boiling regimes. The space and time resolved data were used to conditionally sample the heat flux according to whether or not boiling occurred on the surface, enabling the separation of the heat flux due to boiling from that due to natural convection or vapor contact. The heat transfer from the edge heaters was observed to be much higher than that for the inner heaters above the critical temperature. The heat transfer during liquid contact in transition boiling was constant for a given wall superheat for the inner heaters, and was observed to decrease with increasing wall superheat.

Introduction

The vast majority of experimental work performed to date regarding boiling utilized single heaters that were large compared to individual bubble sizes, making it difficult to look at details of the boiling process. These studies also used surfaces that supplied neither a constant wall heat flux nor a constant wall temperature boundary condition. Typically, constant power was supplied to a thick thermally conducting substrate such as copper—the bubbles generated on the surface cause the surface to cool locally, causing heat to flow within the substrate and making it difficult to determine the *local* heat flux from the wall to the liquid. Studies in the transition boiling and critical heat flux regimes were also difficult because the wall heat flux was the independent variable. Other experiments have utilized surfaces held at constant temperature averaged across the surface, but the *local* heat flux and temperature were not measurable and can vary significantly across the heater. Even when local measurements were obtained (e.g., Cooper and Lloyd, 1969; Lee et al., 1985; Marquardt and Auracher, 1990; Hohl et al., 1997; Ohta et al., 1998), these were done at only a few locations on the heater surface.

Kenning (1992) and Watwe and Hollingsworth (1994) used liquid crystals on thin, electrically heated stainless steel plates to study boiling on surfaces that were very nearly constant wall heat flux. Their use of thin stainless steel sheets minimized the lateral conduction of heat in the substrate, enabling local heat transfer coefficients to be determined. Their work did much to elucidate the heat transfer mechanisms associated with large-scale phenomenon (e.g., the role of bubble driven convective flows, the spread of boiling on large scale heaters, and nucleation site interactions) because information regarding temperature fluctuations were available with high resolution across the heater surface.

This paper examines local wall heat flux variations during boiling of FC-72 on a small heated area using an array of microscale heaters each maintained at constant surface temperature—it is the first study known to the authors that documents boiling heat transfer behavior in such detail on surfaces with this boundary condition. This work complements the liquid crystal work in that boiling on a comparatively small surface is investigated with high spatial and temporal resolution, simulating boiling

on thick surfaces with high thermal conductivity. An array of microscale heaters, each maintained at constant temperature using electronic feedback loops, were used to provide the boundary condition. The scale of the individual heaters is approximately the same as that of the departing bubbles in nucleate boiling, and much smaller than the large bubble that departs the surface near critical heat flux and in transition boiling. Since the heat flux is measured directly instead of being inferred from average heat flux data and void fraction measurements, the local heat transfer data obtained are much more reliable than those obtained to date. These measurements provide to the modeling community a data set in which it is not needed to take into account substrate conduction since the surface is at constant temperature everywhere. The objective of this work was to obtain a detailed picture of the boiling process on a small square heater without sidewalls by (1) obtaining boiling curves for a small, square heated area including CHF and the transition boiling regime, and (2) measuring spatial and temporal variations in the wall heat flux over the heater array at various wall superheats. Discussion of the validity of various models of boiling based on the results is presented.

It should be noted that the behavior of boiling on small heated areas can differ from that on large heated areas. First, the total number of nucleation sites is much smaller, and can result in heaters smaller than the corresponding average distance between nucleation sites on large heaters. Boiling can be delayed to higher wall superheats as a result, or the number of nucleation sites may not be statistically representative. Second, the Taylor wavelength, which is significant in transition and film boiling, can be larger than the heater size, resulting in boiling behavior that is not representative of that on large heaters. Third, edge-effects due to entrainment of the bulk fluid surrounding the heater can significantly affect the boiling behavior. The absence of sidewalls does affect the results, especially near critical heat flux and in the transition regimes since the heat transfer behavior in these regimes are greatly influenced by the vapor dynamics above the heater. It does not have as much influence in the isolated bubble regime because the bubbles are influenced only by the behavior of the fluid immediately surrounding the bubble.

Experimental Procedure

Experimental Apparatus. Local surface heat flux and temperature measurements are provided by an array of 96 platinum resistance heater elements deposited on a quartz wafer as shown in Fig. 1 (the inoperative heaters are indicated by the dark squares). Each of these elements was 0.26 mm × 0.26 mm in size, had a

¹ This work was performed while Jungho Kim was an assistant professor at the University of Denver and T. D. Rule was a visiting graduate student.

Contributed by the Heat Transfer Division for publication in the JOURNAL OF HEAT TRANSFER. Manuscript received by the Heat Transfer Division, Sept. 8, 1997; revision received, Feb. 1, 1999. Keywords: Boiling, Heat Transfer, Measurement Techniques, Microscale, Temperature. Associate Technical Editor: M. Kaviany.

	96		94	93	92	91	90	89	
65	37		63	62	61	60	59	58	88
66	38	17	36	35	34	33	32	57	87
67	39	18	5	16	15	14	31	56	86
68	40	19	6	1	4	13	30	55	85
69	41	20	7	2	3	12	29	54	84
70	42	21	8	9	10	11	28	53	83
71	43	22	23	24	25	26	27	52	82
72	44	45	46	47	48	49	50	51	81
	73	74	75	76	77	78	79	80	

Fig. 1 Arrangement of 96 heaters in the array, with nonfunctional heaters represented by the black squares

nominal resistance of 1000Ω and a nominal temperature coefficient of resistance of 0.002°C^{-1} . Up to 17 heater arrays were fabricated simultaneously on a single quartz wafer using VLSI circuit fabrication techniques. Platinum was sputtered onto the entire surface of a $500\text{-}\mu\text{m}$ thick wafer to a thickness of $0.2 \mu\text{m}$, a layer of photoresist was deposited and patterned to define the heater geometry, then the platinum from the unmasked areas was removed using an ion mill resulting in a resistance heater of nominally 1000Ω . The platinum lines within each individual heater were $5 \mu\text{m}$ wide and spaced $5 \mu\text{m}$ apart. The spacing between each heater in the array varied from $7 \mu\text{m}$ near the center of the array to typically $40 \mu\text{m}$ between heaters on the outer edge of the array. Aluminum was then vapor-deposited onto the surface to a thickness of $1 \mu\text{m}$, the aluminum power leads were masked off, and the remaining aluminum was removed using a wet chemical etch. A layer of SiO_2 was finally deposited over the heater array to provide the surface with a uniform surface energy. The boiling surface was viewed under an electron microscope, and the surface roughness was found to be on the order of the thickness of the aluminum power leads to the heaters ($\sim 1 \mu\text{m}$). This dimension is not really significant, however, since the critical size of the cavities required to nucleate bubbles is well below $0.1 \mu\text{m}$ for highly wetting fluids such as FC-72 (Bar-Cohen and Simon, 1988). Because the critical cavity size is so small, and because the electron microscope used could not resolve such small sizes, it could not be predicted in advance where nucleation occurred or the size distribution of the cavities. Nucleation could have occurred anywhere on the heated surface.

The completed quartz wafer was diced into chips, each containing a single heater array. The chips were mounted on a pin-grid-array (PGA) package using epoxy adhesive, and the pads on the PGA were connected to the power leads of the heater array chip using a conventional wire-bonding technique. The completed package was then mounted in a PGA socket that was connected to the control and data-acquisition apparatus.

The temperature of each heater in the array was kept constant by feedback circuits similar to those used in constant temperature hot-wire anemometry as shown in Fig. 2. The op-amp measures the imbalance in the bridge and outputs whatever voltage is needed to keep the ratio R_H/R_1 equal to R_C/R_2 . The temperature of the heater can be changed by changing R_C . The instantaneous voltage required to keep each heater at a constant temperature was measured (V_{out}) and used to determine the heat flux from each heater element. The large $200 \text{K}\Omega$ resistor at the top of the bridge was used to provide a small trickle current through the heater, and resulted in a voltage across the heater of about 100mV even when the op-amp was not regulating. Because all the heaters in the array were at the same temperature, heat conduction between adjacent

heaters was negligible. There was conduction from each heater element to the surrounding quartz substrate (and ultimately to the walls of the chamber where it was dissipated by natural convection), but this could be measured and subtracted from the total power supplied to the heater element enabling the heat transfer from the wall to the fluid to be determined. Additional details regarding the measurement of the substrate conduction are provided in the section on data reduction.

The frequency response of the heaters along with the control circuit was found to be 15kHz by measuring the time it took for the voltage across a heater to stabilize after a step change in V_C . Because this is much faster than the time scales typically associated with pool boiling, the heater temperatures were essentially constant throughout the bubble departure cycle.

Shown on Fig. 3 is a schematic of the experimental apparatus. The bellows and the surrounding housing allowed the test section pressure to be controlled. A stirrer was used to break up stratification within the test chamber, and a temperature controller and a series of Kapton heaters attached to the boiling chamber were used to control the bulk fluid temperature. A detailed description of the experimental apparatus and the heater array is given in Rule et al. (1999) and Rule (1997).

Degassing of Fluid. In order to minimize dissolved gas effects, the FC-72 liquid was degassed using the following procedure. After the test chamber was filled with gas saturated FC-72 and heated to the saturation temperature corresponding to atmospheric pressure in Denver, CO ($T_{\text{sat}} = 52.6^\circ\text{C}$, 0.85atm), the chamber was sealed and the test rig was turned upside down. A vacuum pump was used to decrease the pressure around the bellows causing it to expand and creating a low pressure above the liquid. This caused gas to come out of solution. Once the pressure above the liquid reached steady state (about 12 hours), the vapor above the liquid was drawn out using a vacuum pump. This procedure was repeated until the vapor pressure within the test chamber reached the saturation pressure of FC-72 at the corresponding bulk temperature. The final dissolved gas concentration in the liquid, determined using the vapor temperature and pressure, the properties of FC-72 (3M Fluorinert Manual, 1995), and Henry's Law, was less than 1.5×10^{-3} moles/mole.

Heater Calibration. In order to set each of the 96 heaters to a single temperature, a relationship between the control voltage (V_C) and heater temperature was needed. It would have been a complicated problem to measure the relationship between temperature and heater resistance (R_H) for each heater in the array, to

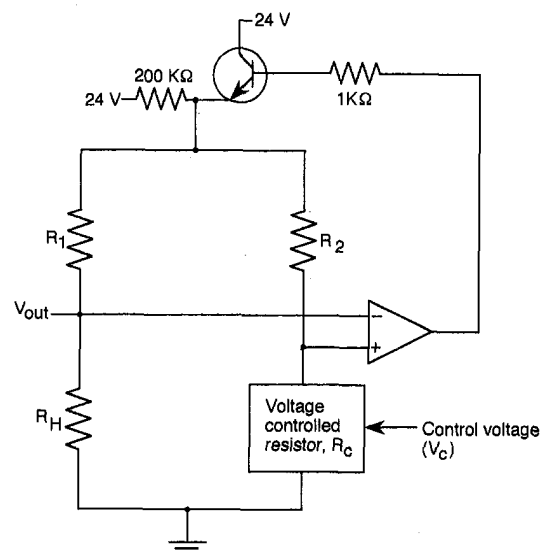


Fig. 2 Schematic of feedback loop circuit

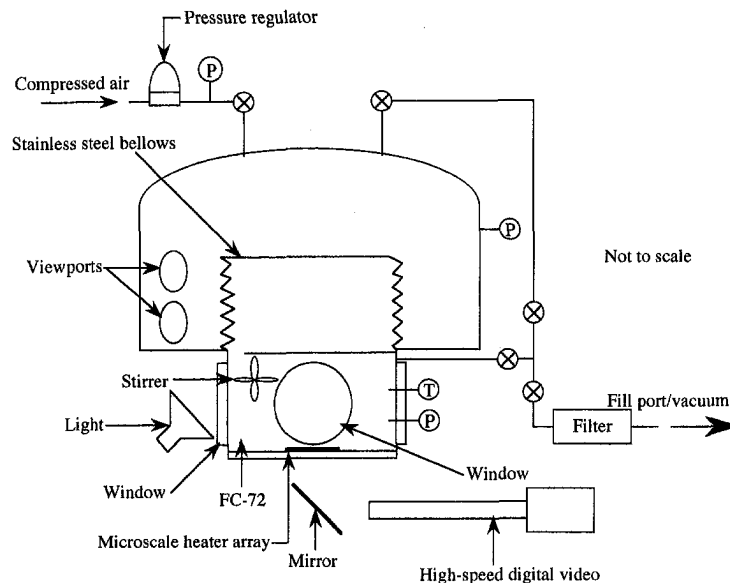


Fig. 3 Schematic of experimental apparatus

measure the relationship between V_C and R_C in each control circuit, then to calculate the relationship between V_C and R_H . A more reliable method was to calibrate the command voltage, V_C , directly with the heater temperature. This was performed according to the following procedure. An insulated, circulating constant temperature oil bath was heated to the desired calibration temperature within 0.2°C , and the heater array was placed in the bath. The control resistance (R_C) was initially set at a low value, so the voltage across the heater V_{out} was at its minimum value of 100 mV. The control voltage was then incremented until the voltage across the bridge approached zero and the amplifier began to regulate the heater resistance by applying power to the top of the bridge circuit. When the voltage across the heater reached a threshold voltage of 300 mV, the value of the control voltage was noted, and was used in future experiments to set the heater to that calibration temperature. This procedure was then repeated for the rest of the heaters in the array. The result of a calibration routine was a set of 96 voltage values which, when applied by the computer control system to the voltage-controlled resistance, caused the feedback control circuit to maintain the heater at the calibration temperature. The value of the threshold voltage was important. For the threshold voltage used (300 mV), a heat flux of approximately 0.14 W/cm^2 was dissipated in the heater. This was shown experimentally to cause a negligible change in heater temperature. It was also high enough that it ensured that the heater control circuit was operating in its linear range.

Data Acquisition. Two data acquisition systems were used. The first was a commercial system (Daqbook 216 from I/O Tech) that was used to digitize the voltage across each heater at up to 1000 samples per second. Data were acquired using this unit at a sampling rate of 20 Hz over 50 s, after allowing the heater array to remain at a set temperature for ten minutes. The data were found to be quite repeatable under these conditions. The long time between data points was chosen because boiling on the surface was observed to change with time. Figure 4 shows how the array averaged heat flux changed after the wall superheat was suddenly decreased from 47.5°C to 17.5°C . Visual observations showed that the steps in heat flux seen in Fig. 4 were associated with nucleation sites being reactivated as evidenced by new streams of bubbles appearing on the surface. Initially, nucleation occurred from only a single point on the surface. Between 30s and 60s, two streams of bubbles were observed. For times greater than 60s, bubbles nucleated from three sites on the surface.

The second data acquisition system is a custom designed unit

that is capable of sampling 16,000 data points from each heater at up to 10 kHz. This system was used to obtain time-resolved data at 2500 samples/sec from each heater for 0.5 seconds.

Data Reduction. The heat flux calculated from the voltage across the heater and the heater resistance (q_{raw}) must be corrected to account for substrate conduction. The procedure used to determine the magnitude of this correction is explained below.

Wall heat flux versus wall temperature were measured for each heater over the range $T_w = 50$ to 100°C with the test chamber pressurized to 2.72 atm and with the bulk fluid at the saturation temperature corresponding to atmospheric pressure. The increased pressure effectively suppressed boiling on the heater array over this temperature range. The measured heat flux from a heater under these conditions represents the sum of natural convection and substrate conduction from that heater (q_{nc+sc}). The magnitude of q_{nc+sc} compared to q_{raw} over the temperature range of interest is seen in Fig. 5. Although q_{nc+sc} is relatively small compared to q_{raw} in the high nucleate boiling and CHF regimes, it becomes a substantial fraction of q_{raw} in the low nucleate boiling and transition boiling regimes. The average natural convection component over the entire heater (q_{nc}) was calculated using the correlation of Lloyd and Moran (1974) (flat, upward facing, isothermal heaters),

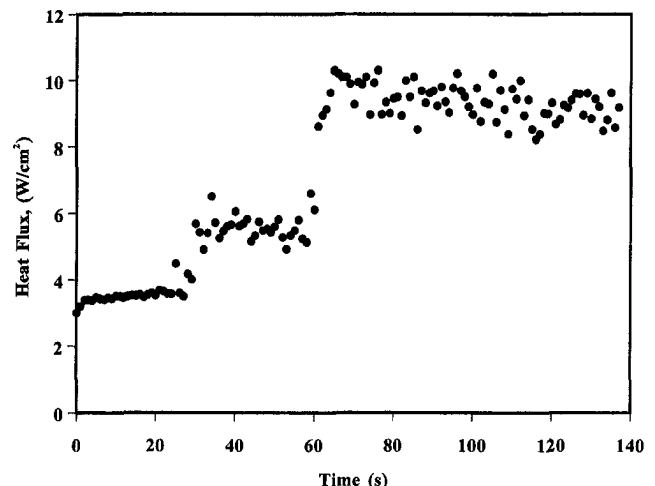


Fig. 4 Changes in array averaged heat flux with time at $\Delta T = 17.5^\circ\text{C}$

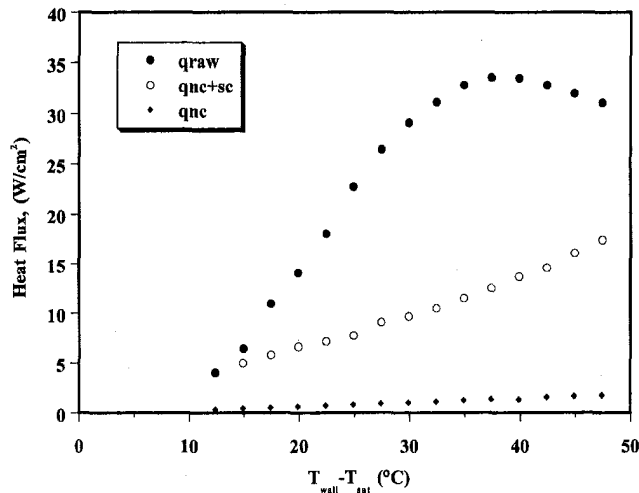


Fig. 5 Uncorrected boiling curve, substrate conduction, and natural convection data

then subtracted from q_{nc+sc} to obtain the heat flux due to substrate conduction (q_{sc}). q_{sc} for each individual heater was then subtracted from q_{raw} to obtain the heat flux due to boiling (q_b). Because the heater array is held at constant temperature, the value of q_{sc} for each individual heater does not depend much on the state of the fluid above the surface. q_{nc} was not subtracted from q_{raw} since natural convection does not exist once boiling occurs. Heat fluxes in the natural convection portion of the boiling curve are not presented because the above procedure simply results in the calculated value of q_{nc} .

Uncertainty Analysis. The circuit that allows the wall temperature to be adjusted exhibits offset voltages and nonlinearities which needed to be carefully compensated for. These compensations could still result in a certain amount of uncertainty in heater temperature since the offset voltages could drift with time. The temperature uncertainty due to this drift was estimated to be 0.4 to 0.6°C. The calibration bath temperature uncertainty was small compared to the above uncertainties, and could be neglected. However, the value of the heater calibration could be as much as 0.7°C too high because of self heating, since it was necessary to calibrate the heaters at a current level of close to 1 mA in order to reduce the uncertainty in the electrical measurements. An additional uncertainty resulted from the inability to precisely control the bulk fluid temperature in the test chamber, which was seen to vary during a ten hour run by about 0.5°C. The final uncertainty in wall superheat was calculated to be 1.1°C.

The uncertainty in q_b results from uncertainties in q_{raw} , q_{nc+sc} , q_{nc} , and q_{sc} . Uncertainties in q_{raw} and q_{nc+sc} resulted from uncertainties in measured voltage across the heaters, the resistance of the heaters, and the heater array area. All three of these uncertainties were very small compared to the uncertainties that follow, and could be neglected. The uncertainty in q_{nc} was assigned the value of 100 percent since significant variations in q_{nc} could occur across the heater array. However, since q_{nc} represented only about 12 percent of q_{nc+sc} , this resulted in a relatively small uncertainty in q_{sc} . An additional uncertainty in q_{sc} resulted when boiling occurred on the surface since the heat transfer coefficient in the fluid surrounding the heater increased above that associated with natural convection, and this could change the value of q_{sc} calculated from the above procedure. To quantify this effect, a FLUENT simulation was performed in which the heat transfer coefficient on the substrate surrounding the heater was increased from 300 to 1000 W/m²-K (typical values of the natural convection heat transfer coefficient obtained from the above correlation varied between 280–380 W/m²-K). Variations in q_{sc} of approximately 11 percent were calculated. The uncertainties in q_{raw} , q_{nc+sc} , q_{nc} , and q_{sc} were

combined according the methodology of Kline and McClintock (1953) to find the final uncertainty at each data point.

Results

Spatially Averaged Time-Averaged Boiling Curve. Data were taken over a ten-hour period (20 Hz, 50 s for each data point) in which the wall temperature was increased and decreased twice between 65°C and 100°C in 2.5°C increments. The bulk fluid was slightly subcooled by about 1.5°C. The boiling curves for all four runs are shown on Fig. 6. The boiling curves are seen to be remarkably repeatable with time, although a small hysteresis is observed between the increasing and decreasing temperature runs. Similar behavior has been observed by other investigators (Ungar and Eichhorn, 1996; Rajab and Winterton, 1990). The CHF for all cases is similar, however, and is seen to be somewhat higher than that obtained from a correlation for small vertical heaters of short width (Park and Bergles, 1988). This is not surprising since they operated their heaters in a constant heat flux mode, in contrast to the constant temperature boundary condition of the current array. Park and Bergles (1988) did observe that CHF increased for heaters with higher thermal conductivity, which is consistent with the observed trends. No hysteresis associated with boiling incipience was observed due to a flaw in the software—whenever the temperature of the heaters was changed, the heater temperatures were set to random temperatures for about one second, causing some heaters to shut down while others were set to very high temperatures. Boiling therefore occurred somewhere on the heater every time the array temperature was changed. The heater temperatures were decreased to the set temperature after this time, however. The resulting boiling curve is similar to what one would obtain by decreasing the wall temperature without the software problem.

Also shown in Fig. 6 is data taken a few days earlier at a sampling rate of 2.5k Hz (labeled “High speed”). This data is quite different from the data taken earlier, and is thought to be due to incomplete degassing of the fluid. Unfortunately, high-speed data was not obtained after this data run. The data shown in Figs. 7–13 correspond to this high-speed data.

Spatially Averaged Time-Resolved Results. Spatially averaged time-resolved heat flux is shown on Fig. 7. Not surprisingly, the signal during nucleate boiling ($\Delta T_{sat} = 25^\circ\text{C}$) is seen to be quite random since the average heat flux over the surface is the result of boiling from many individual sites on the surface that do not necessarily occur in phase. A FFT of this signal showed no strong peaks.

At CHF ($\Delta T_{sat} = 35^\circ\text{C}$) and transition boiling, the heat flux begins to become dominated by the large vapor mass that occasionally departs the surface, and a quasi-periodic signal is observed

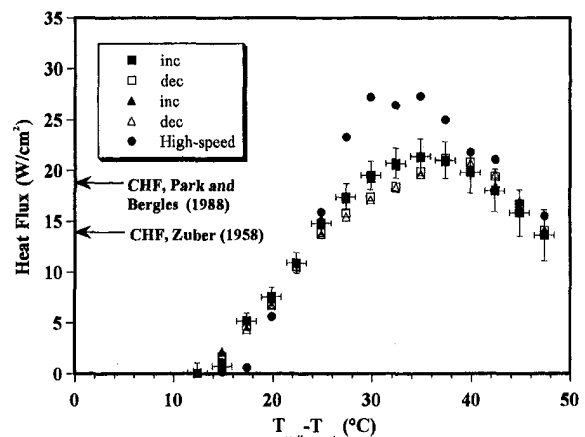


Fig. 6 Boiling curve for the heater array

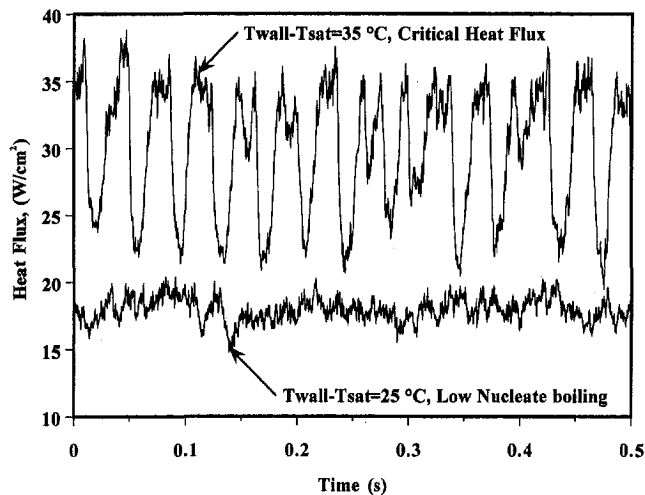


Fig. 7(a) Array averaged time-resolved heat flux versus time at $\Delta T_{\text{sat}} = 25^\circ\text{C}$ and $\Delta T_{\text{sat}} = 35^\circ\text{C}$

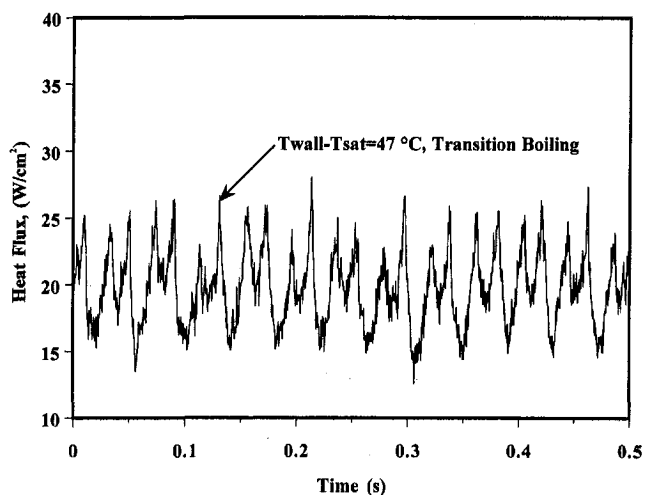


Fig. 7(b) Array averaged time-resolved heat flux versus time at $\Delta T_{\text{sat}} = 47^\circ\text{C}$

to appear. A FFT indicated the emergence of several distinct peaks at approximately 26 and 52 Hz at CHF. In transition boiling, the secondary peaks become more pronounced and the overall heat flux level decreases. The emergence of the two peaks is thought to occur due to the formation of “mushroom” bubbles on the surface, an example of which is shown on Fig. 8. These “mushroom” bubbles were observed in the test facility during a demonstration of a high-speed video camera. Although many investigators have observed the existence of “mushroom” bubbles, these measurement are believed to be the first to document the wall heat flux signature due to these bubbles.

Time-Resolved Data From Individual Heaters. Seen on Fig. 9 are time-resolved heat flux traces for heater 18 in the array at various wall superheats. It must be remembered when interpreting this data that bubble behavior on scales smaller than the individual heater sized cannot be resolved. Consider first the heat flux trace for low nucleate boiling ($\Delta T_{\text{sat}} = 22^\circ\text{C}$, Fig. 9(a)). Examples of regions where natural convection, enhanced convection, and boiling are thought to occur on the surface are indicated. Nucleate boiling is assumed to occur when large variations in heat flux are seen. Natural convection is assumed to be characterized by low heat flux levels along with small variations in heat transfer. Enhanced convection is assumed to occur when the heat flux level is higher than occurs for natural convection, but without the large variations in heat flux characteristic of nucleate boiling, and could

be heat transfer due to bubble-induced liquid motion. The categorization of nucleate boiling and natural convection are based on observations of the heat flux variation on the surface and correlating them to the visual observations of boiling on the surface. For example, when large variations in heat flux at relatively high levels were observed on a particular heater, a stream of bubbles was seen from that heater location. The categorization of enhanced convection, however, is somewhat murky, since there is no method of distinguishing it from natural convection other than by the heat flux level.

The heat flux trace at a slightly higher wall temperature ($\Delta T_{\text{sat}} = 25^\circ\text{C}$) consisted almost entirely of nucleate boiling (Fig. 9(b)). The average heat flux level at this temperature was significantly higher than at lower temperatures, indicating that the increase in heat transfer from the surface is partly due to increased heat transfer from *individual heaters* and not just due to the activation of additional nucleation sites on the surface or a higher bubble departure frequency as commonly assumed when modeling nucleate boiling. If the view that the increase in average wall heat flux is due to an increase in bubble departure frequency is correct, an increase in the time-averaged heat flux from an individual heater would be observed, but not an increase in the peak heat fluxes associated with individual bubbles. The heat flux trace in Fig. 9(b), however, is clearly higher than that for the lower temperature, indicating that the peak heat flux from a given heater does increase. Bubbles nucleating from other sites on the heater should not affect the heat flux from an individual heater in the array since the bubble departure size is on the order of the individual heaters. The bubbles nucleating on a given heater must be transferring more energy from that heater. This data suggests that the models of nucleate boiling commonly used may need to be reexamined. There might be other phenomenon such as bubble merging or chaotic bubble behavior that might be responsible for the increased heat flux. Observations of the bubble using a high-speed camera would have

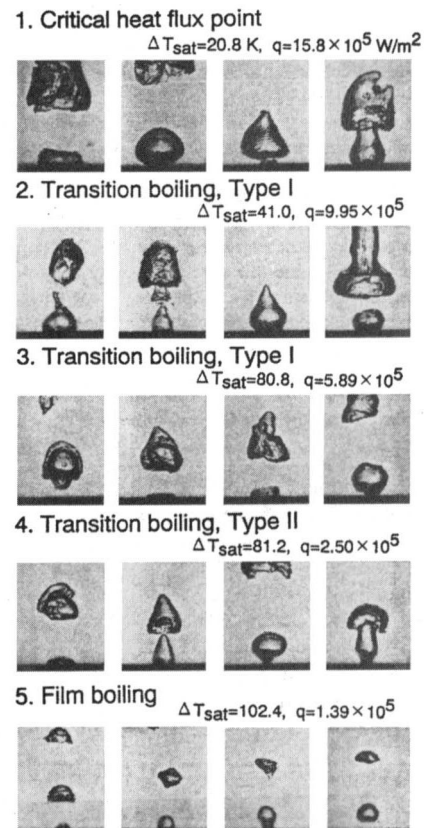


Fig. 8 Photograph of mushroom bubbles (Huang, Yokoya, and Shoji, *JSME International Journal, Series B*, 1994, Vol. 37, No. 4, p. 899)

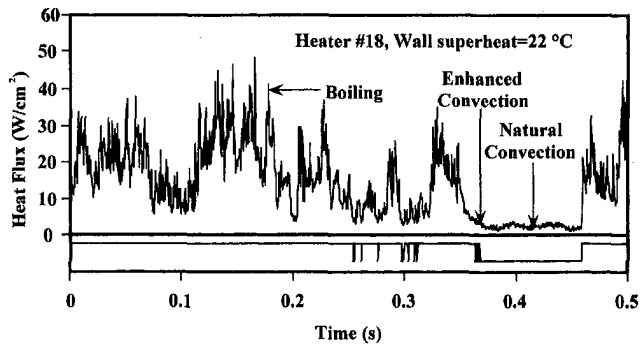


Fig. 9(a) Heat flux versus time for heater #18 along with the boiling function for $\Delta T_{\text{sat}} = 22^\circ\text{C}$

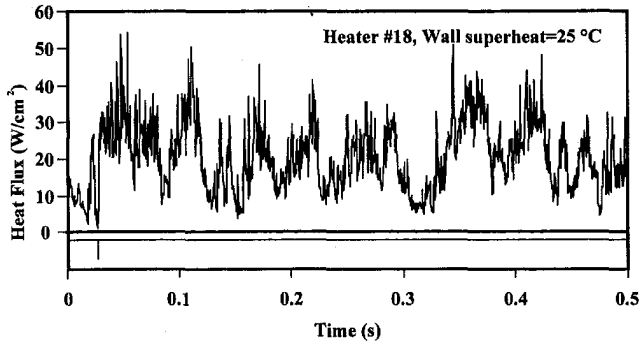


Fig. 9(b) Heat flux versus time for heater #18 along with the boiling function for $\Delta T_{\text{sat}} = 25^\circ\text{C}$

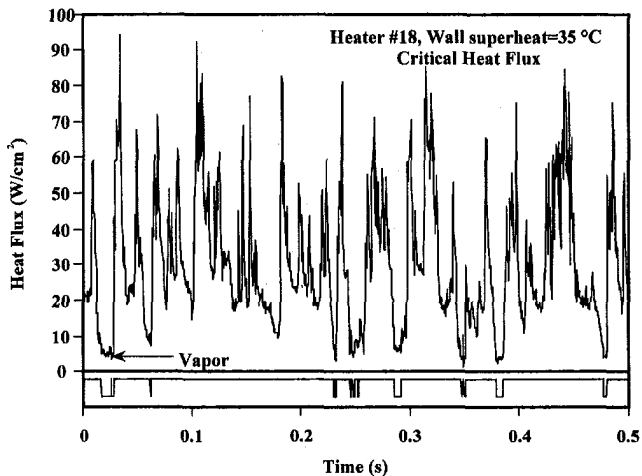


Fig. 9(c) Heat flux versus time for heater #18 along with the boiling function for $\Delta T_{\text{sat}} = 35^\circ\text{C}$

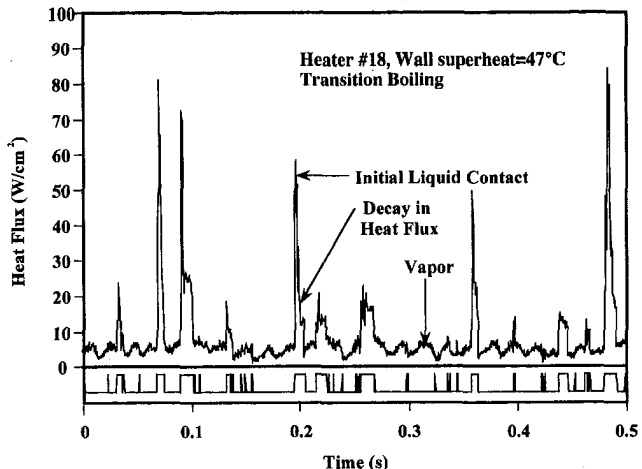


Fig. 9(d) Heat flux versus time for heater #18 along with the boiling function for $\Delta T_{\text{sat}} = 47^\circ\text{C}$

been helpful in determining the bubble heat transfer mechanism, but such a camera was not available.

At CHF ($\Delta T_{\text{sat}} = 35^\circ\text{C}$, Fig. 9(c)), regions of low heat transfer are observed in the heat flux traces. It is felt that these represent the heat transfer when vapor covers the surface. Visual confirmation of this is not available at this time, but it is implausible that these low heat flux regions would represent natural convection due to the high level of bubble activity on the surface. The existence of vapor on the surface during CHF has also been observed by other researchers (Lee et al., 1985; Kalinin et al., 1987; Alem Rajabi and Winterton, 1988a, b).

Within the transition boiling region (Fig. 9(d)), the heat flux traces indicate that vapor covers the heaters for an increasingly larger fraction of time. The shape of the peaks is interesting. Typically, a sharp increase in heat flux is initially seen followed by a rapid decay and a sharp drop to the vapor state. Similar behavior was observed by Chen and Hsu (1995) who obtained transient wall temperature and heat flux measurements during droplet contact on a superheated surface. They observed that the wall heat flux jumped to a high level immediately upon contact, but then decayed with time until the droplet evaporated or left the surface.

Spatially Resolved Time-Averaged Data. Boiling curves generated for “rings” of heaters are shown on Fig. 10. In the nucleate boiling region, all the heater rings have similar boiling curves. The scatter in the data for a given wall superheat is due to boiling being initiated at random sites on the surface. Note that CHF for the inner heaters (Rings 1–4) occurs at a lower wall superheat ($30\text{--}32^\circ\text{C}$) than CHF for the entire array (about 35°C). At a wall superheat of 35°C , transition boiling occurs on the inner heaters. The boiling curves for Rings 1 and 2 are very similar, and the minimum heat flux point is almost reached at the highest wall temperature. The boiling curves for Rings 3 and 4 are somewhat higher than those for the inner rings, while the curve for Ring 5 shows no decrease in heat flux over the wall superheats tested. In fact, the heat flux from the edge heaters (Ring 5) is seen to increase with wall superheat to a level about 150 percent above the CHF for the inner heaters at the maximum superheat. The explanation for this, of course, is that the edge heaters can be supplied with liquid from the side, while the liquid supply to heaters in Rings 1–4 is cut off by bubbles generated on the surface.

Conditional Sampling. In order to conditionally sample the heat flux only when boiling occurs on the surface, a *boiling function* was generated. This function is a bimodal signal that is set to HIGH when boiling or enhanced convection occurs on the surface, and LOW otherwise. Enhanced convection was counted as

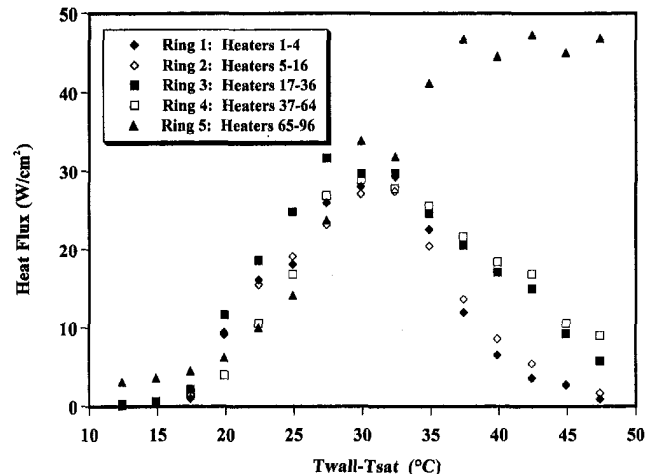


Fig. 10 Boiling curve for “rings” of heaters

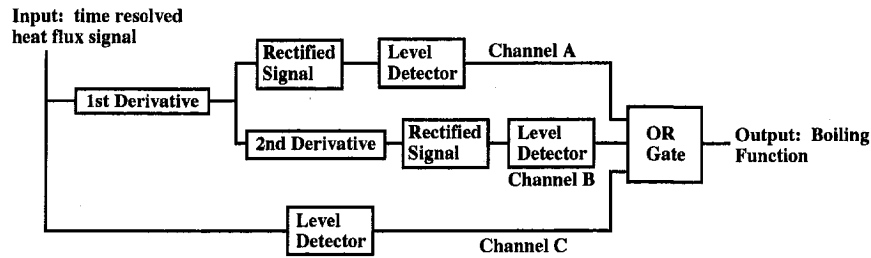


Fig. 11 Schematic of boiling function generation method

HIGH when computing the boiling function since it represents additional heat transfer due to bubble motion on the surface. The *boiling fraction* is defined as the time average of the boiling function, and represents the time fraction that boiling or enhanced convection occurs on the surface. Within transition boiling, where the surface is alternately wetted by liquid and vapor, the boiling fraction is related to void fraction according to

$$\text{Boiling Fraction} = 1 - (\text{Void Fraction}).$$

A schematic of the process by which the boiling function is generated is shown in Fig. 11. The time resolved signal is processed according to three criteria. Channel C is a simple level detector—if the heat flux is higher than what would be expected during natural or forced convection or when vapor covers the surface, then Channel C is set to HIGH. Simply relying on this one channel, however, does not enable a clear discrimination of the boiling signal. Channel A assumes that the time derivative of the heat flux signal is large when boiling occurs on the surface, and is set to HIGH when the rectified first derivative exceeded a certain threshold value. Channel B computes the rectified second derivative of the heat flux signal and compares it to a threshold value—the output is set to HIGH if the threshold value is exceeded. Channels A and B are used to solve the problem of zero crossing—the first derivative unavoidable falls below the threshold value as it changes sign, resulting in Channel B occasionally being falsely declared LOW. The zero crossing problem can be eliminated by monitoring Channels A and B simultaneously—both channels have crossing dropouts, but the zero crossings of the two channels do not coincide in time since the second derivative is zero when the first derivative is maximum and vice versa. The OR gate sets the boiling function to HIGH if the output from any of the three channels is HIGH. The three threshold values used produced acceptable boiling functions across the heater array at a given superheat, as well as for a given heater at various superheats. Examples of the performance of the above criteria in generating the boiling function for a given heater at various temperatures is shown on Figures 9(a–d).

Boiling Fraction. The time average of the boiling function for each heater in the array was calculated, and these values were averaged over heaters within a particular ring. This yields the *boiling fraction* for a particular ring, i.e., the fraction of time the heaters in the ring see boiling on the surface. A plot of the boiling fraction versus wall superheat is shown on Fig. 12. The boiling fraction is seen to reach a value close to unity at a wall superheat of about 25°C, well before the temperature corresponding to CHF for all rings. The boiling fraction at CHF ($\Delta T_{\text{sat}} = 35^\circ\text{C}$) is observed to be lower than unity for the inner heaters, indicating the occurrence of vapor patches on the surface. This is consistent with the data shown on Fig. 10, which shows that the transition boiling region has been entered at this wall superheat for the inner rings of heaters. The boiling fraction for Rings 1–4 decreases quite rapidly after CHF. At the highest wall superheat, the innermost heaters see boiling only six percent of the time, while boiling is nearly continuous on the outer ring of heaters.

A monotonic increase in the boiling fraction with ring number is

seen at any given superheat in transition boiling. This agrees with the observed bubble dynamics and wall heat transfer pattern. Within transition boiling, the heaters were rewetted as the large vapor bubbles left the surface. The liquid front was observed to move from the outside of the heater array towards the inside heaters, then move outward again as the vapor bubble formed once again above the heater array. The heaters towards the outside of the array thus experience boiling a larger fraction of the time than the heaters toward the center of the array. This monotonic increase with boiling fraction is not seen during nucleate boiling since boiling can initiate anywhere on the surface.

Conditionally Sampled Heat Flux. The time-resolved heat flux data for each heater was conditionally sampled according to the boiling function to obtain the heat flux *only when boiling or enhanced convection occurred on the surface*, and averaged over the heaters within a particular ring. This results in the average heat transfer for a particular ring that is uninfluenced by heat flux during vapor contact or natural convection. This quantity is referred to as the *boiling heat flux*. The results are shown in Fig. 13. It is seen that if one excludes the edge heaters (Ring 5), the boiling heat flux more or less collapses onto a single curve for all wall superheats, implying that the heat flux at a given wall superheat during boiling is constant over the heater surface. For example, the heat flux during boiling at $\Delta T_{\text{sat}} = 47^\circ\text{C}$ for Ring 1 is similar to that for Ring 4, even though Ring 1 sees boiling only six percent of the time while Ring 4 sees boiling 55 percent of the time. It is possible that even the data for Ring 5 would collapse onto the other data if there were sidewalls around the edge of the heater array.

During transition boiling, the boiling heat flux for the inner heaters is observed to decrease with increasing temperature. The reason for this is currently not known, but it may be a result of the shorter liquid contact time and/or the establishment of a vapor layer underneath the liquid. Similar trends have been seen by other

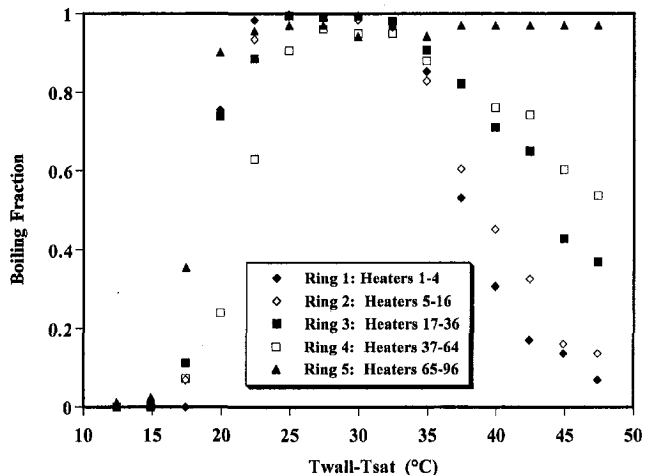


Fig. 12 Boiling fraction versus wall superheat for "rings" of heaters

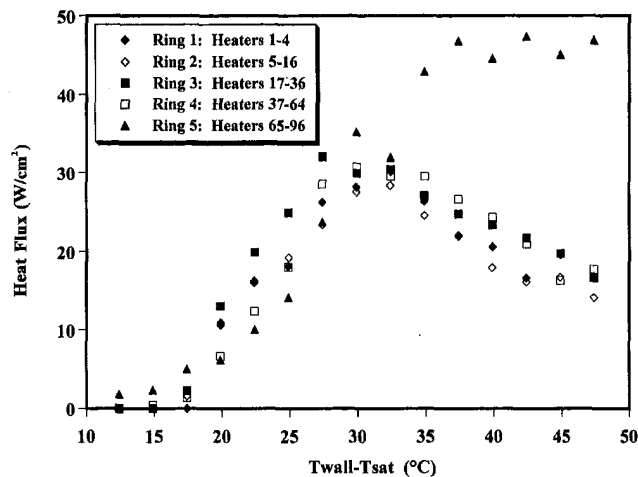


Fig. 13 Boiling heat flux for "rings" of heaters

researchers (Marquardt and Auracher, 1990; Alem Rajabi and Winterton, 1988a, b; Chen and Hsu, 1995).

The current data indicates that some of the models used to predict transition boiling heat flux may be in error. Often, the heat flux during transition boiling is modeled as

$$q_{tr} = q_{CHF}(F) + q_{MHF}(1 - F)$$

where F is the fraction of time the surface is covered with liquid and q_{MHF} is the heat flux at the Leidenfrost point. A variation on this model is to extend the nucleate boiling and film boiling curves, and weight these values at a given wall temperature on F to find the transition boiling heat flux. It is seen from the current data that heat transfer during liquid contact does not remain constant at the CHF level nor does it increase in the transition boiling region as the above two models would suggest.

Summary and Conclusions

Time and space resolved heat transfer behavior on a small heater without sidewalls was documented in detail using a microscale heater array held at constant temperature. Data were obtained in the nucleate boiling, critical heat flux, and transition boiling regimes. The measurements indicate that some of the commonly accepted views of boiling heat transfer may need to be reexamined. Some of the more important observations and conclusions are summarized as follows.

1 The array averaged heat flux was seen to vary quasi-periodically above CHF due to the formation of "mushroom" bubbles over the surface. The wall heat transfer signature due to these bubbles was measured.

2 The inner heaters reach CHF at lower wall superheats than that for the array averaged heat flux, as would be expected. The heat flux for the edge heaters was observed to increase continuously with wall superheat, reaching heat flux levels much higher than the maximum heat flux for the inner heaters. It is possible that similar CHF levels would be observed across the array if sidewalls were present to limit the flow of liquid to the edge heaters. Vapor was observed on the surface at CHF.

3 Increases in heat transfer with temperature from individual heaters in the nucleate boiling regime were observed, suggesting

that the increase in space averaged heat transfer is not just due to an increase in the bubble departure frequency or an increase in the number of nucleation sites, as commonly assumed.

4 Heat transfer during liquid contact in transition boiling was constant for a given wall superheat for the inner heaters and was observed to decrease with increasing wall superheat, contrary to the behavior during liquid contact assumed in many models.

Acknowledgments

The work presented here was sponsored by NASA Headquarters under Grant #NCC3-470. The contract monitor is Mr. John McQuillen. The assistance of Mr. R. W. Quine, Mr. C. P. Ch'ng, and Mr. J. Mullen is gratefully acknowledged.

References

- 3M Corporation, 1995, *3M Fluorinert Liquids Product and Contact Guide*.
- Alem Rajabi, A. A., and Winterton, R. H. S., 1988a, "Low Thermal Capacity Heaters for Steady State Transition Boiling Measurements," *Experimental Thermal and Fluid Science*, Vol. 1, pp. 405-407.
- Alem Rajabi, A. A., and Winterton, R. H. S., 1988b, "Liquid-Solid Contact in Steady-State Transition Boiling," *International Journal of Heat and Fluid Flow*, Vol. 9, pp. 215-219.
- Bar-Cohen, A., and Simon, T. W., 1988, "Wall superheat excursions in the boiling incipience of dielectric fluids," *Heat Transfer Engineering*, Vol. 9, No. 3.
- Chen, J. C., and Hsu, K. K., 1995, "Heat Transfer During Liquid Contact on Superheated Surfaces," *ASME JOURNAL OF HEAT TRANSFER*, Vol. 117, pp. 693-697.
- Cooper, M. G., and Lloyd, A. J. P., 1969, "The microlayer in nucleate boiling," *International Journal of Heat and Mass Transfer*, Vol. 12, pp. 895-913.
- Hohl, R., Auracher, H., Blum, J., and Marquardt, W., 1997, "Identification of Liquid-Vapor Fluctuations Between Nucleate and Film Boiling in Natural Convection," *Proceedings of the 1997 Engineering Foundation Conference on Convective Flow and Pool Boiling*, Irsee, Germany.
- Kalinin, E. K., Berlin, I. I., and Kostyuk, V. V., 1987, "Transition Boiling Heat Transfer," *Advances in Heat Transfer*, Vol. 18, pp. 241-323.
- Kenning, D. B. R., 1992, "Wall Temperature Patterns in Nucleate Boiling," *International Journal of Heat and Mass Transfer*, Vol. 35, pp. 73-86.
- Kline, S. J., and McClintock, F. A., 1953, "Describing Uncertainties in Single Sample Experiments," *Mechanical Engineering*, Vol. 75, pp. 3-8.
- Lee, L. Y. W., Chen, J. C., and Nelson, R. A., 1985, "Liquid-Solid Contact Measurements Using a Surface Thermocouple Temperature Probe in Atmospheric Pool Boiling Water," *International Journal of Heat and Mass Transfer*, Vol. 28, pp. 1415-1423.
- Lloyd, J. R., and Moran, W. R., 1974, "Natural Convection Adjacent to Horizontal Surfaces of Various Platforms," ASME Paper 74-WA/HT-66.
- Marquardt, W., and Auracher, H., 1990, "An Observer-Based Solution of Inverse Heat Conduction Problems," *International Journal of Heat and Mass Transfer*, Vol. 33, pp. 1545-1562.
- Ohta, H., Kawaji, M., Azuma, H., Inoue, K., Kawasaki, K., Okada, S., Yoda, S., and Nakamura, T., 1998, "Heat transfer in nucleate pool boiling under microgravity conditions," *Proceedings of the 11th International Heat Transfer Conference*, Kyungju, Korea, Vol. 2, pp. 401-406.
- Park, K. A., and Bergles, A. E., 1988, "Effects of Size of Simulated Microelectronic Chips on Boiling and Critical Heat Flux," *ASME JOURNAL OF HEAT TRANSFER*, Vol. 110, pp. 728-734.
- Rajab, I., and Winterton, R. H. S., 1990, "The two transition boiling curves and solid-liquid contact on a horizontal surface," *International Journal of Heat and Fluid Flow*, Vol. 11, No. 2, pp. 149-153.
- Rule, T. D., 1997, "Design, Construction, and Qualification of a Microscale Heater Array for use in Boiling Heat Transfer," Master's thesis, School of Mechanical and Materials Engineering, Washington State University, Pullman, WA.
- Rule, T. D., Kim, J., Quine, R. W., Kalkur, T. S., and Chung, J. N., 1999, "Measurements of Spatially and Temporally Resolved Heat Transfer Coefficients in Subcooled Pool Boiling," *Convective Flow and Pool Boiling*, M. Lehner and F. Mayinger, eds., Taylor & Francis, London, pp. 135-142.
- Ungar, E. K., and Eichhorn, R., 1996, "Transition Boiling Curves in Saturated Pool Boiling From Horizontal Cylinders," *ASME JOURNAL OF HEAT TRANSFER*, Vol. 118, pp. 654-661.
- Watwe, A. A., and Hollingsworth, D. K., 1994, "Liquid Crystal Images of Surface Temperature During Incipient Pool Boiling," *Experimental Thermal and Fluid Science*, Vol. 9, pp. 22-33.
- Zuber, N., 1958, "On the Stability of Boiling Heat Transfer," *Transactions of the ASME*, Vol. 80, pp. 711-720.

Assessment of CHF Enhancement Mechanisms in a Curved, Rectangular Channel Subjected to Concave Heating

J. C. Sturgis

Graduate Student

I. Mudawar¹

Professor and Director,
Fellow ASME

Boiling and Two-Phase Flow Laboratory,
School of Mechanical Engineering,
Purdue University,
West Lafayette, IN 47907

An experimental study was undertaken to examine the enhancement in critical heat flux (CHF) provided by streamwise curvature. Curved and straight rectangular flow channels were fabricated with identical 5.0×2.5 mm cross sections and heated lengths of 101.6 mm in which the heat was applied to only one wall—the concave wall (32.3 mm radius) in the curved channel and a side wall in the straight. Tests were conducted using FC-72 liquid with mean inlet velocity and outlet subcooling of 0.25 to 10 m s⁻¹ and 3 to 29°C , respectively. Centripetal acceleration for curved flow reached 315 times earth's gravitational acceleration. Critical heat flux was enhanced due to flow curvature at all conditions but the enhancement decreased with increasing subcooling. For near-saturated conditions, the enhancement was approximately 60 percent while for highly subcooled flow it was only 20 percent. The causes for the enhancement were identified as (1) increased pressure on the liquid-vapor interface at wetting fronts, (2) buoyancy forces and (3) increased subcooling at the concave wall. Flow visualization tests were conducted in transparent channels to explore the role of buoyancy forces in enhancing the critical heat flux. These forces were observed to remove vapor from the concave wall and distribute it throughout the cross section. Vapor removal was only effective at near-saturated conditions, yielding the observed substantial enhancement in CHF relative to the straight channel.

Introduction

Critical heat flux represents a thermal limit that if surpassed can result in destructive failure of a device. Since many modern devices operate at high heat fluxes, it is desirable to increase this limit permitting both a broader heat transfer operating range and a larger margin of safety. Applications which may benefit from such an increase are direct-immersion cooling of electronic components, nuclear reactor cooling, transfer of solar energy to a working fluid, and rocket engine combustion chamber cooling. One means for enhancing CHF in flow boiling is streamwise curvature. Of particular interest to the present study are curved, rectangular passages subjected only to concave heating since this configuration isolates the enhancement effect. Realizing the drastic consequences of surpassing the CHF limit and the implications of raising it, the present authors sought to examine this enhancement effect through both heat transfer measurements and flow visualization.

Streamwise curvature has been shown to enhance both single and two-phase heat transfer. Hughes and Olson (1975) performed flow boiling tests in one-side-heated rectangular channels using thin, ribbon heaters. For heating along the entire 180-deg turn of the concave wall, they measured an enhancement in CHF compared to a straight wall for highly subcooled flow (28 – 61°C). Wu and Simon (1995) conducted tests with a thin, low thermal-capacitance platinum surface located at 90 deg along the concave wall. With this localized heater, they recorded CHF enhancements that decreased with increasing subcooling. Wu and Simon (1994)

performed similar tests with a thick copper-bar heater which provided a boiling surface extending over only a portion of the channel width. Galloway and Mudawar (1995) used a thick but short copper heater which provided heat to the entire width of the concave wall over a short length centered at 135 deg into the turn. Their tests at near-saturated conditions and low velocities yielded an average CHF enhancement of 23 percent.

The results of these investigators are closely related to the conditions under which the experiments were conducted. For example, heated length is known to affect CHF. Vapor generated on upstream regions of long heaters coalesces downstream impeding the movement of cooler bulk liquid toward the surface. The vapor layer is not as thick on short localized heaters operating at the same heat flux. Gersey and Mudawar (1995a) showed that CHF decreases with increasing heated length for the same inlet conditions.

Secondly, the thermal mass of the heater influences surface boiling. Ribbon heaters (0.08 – 0.13 -mm thick nichrome (Hughes and Olson (1975)) and sputtered boiling surfaces (800 -Å thick platinum (Wu and Simon (1995)) are more susceptible to imperfections which could lead to local hot spots and the coexistence of different heat transfer regimes on the surface. A thick heater would not support this behavior since heat would be conducted to locations of least resistance.

Thirdly, the cross-sectional geometry of the heated section affects coalescence. Vapor generated from a localized heater that does not extend the full width of the channel is not as confined by the side walls as vapor from a full-width heater. Coalescence also depends on whether the shorter or longer dimension of a high aspect ratio channel is heated.

Additionally, there is disagreement regarding the effects of subcooling and centripetal acceleration on CHF enhancement. The generally reported trend is one of decreasing enhancement with increasing subcooling. Leland and Chow (1992) even measured a detrimental curvature effect for highly subcooled flow though many other researchers did not. Gambill and Green (1958) and Gu

¹To whom correspondence should be addressed. e-mail: mudawar@ecn.purdue.edu.

Contributed by the Heat Transfer Division for publication in the JOURNAL OF HEAT TRANSFER. Manuscript received by the Heat Transfer Division, Feb. 13, 1998; revision received, Jan. 15, 1999. Keywords: Boiling, Enhancement, Experimental, Forced Convection, Heat Transfer, Visualization. Associate Technical Editor: P. Ayyaswamy.

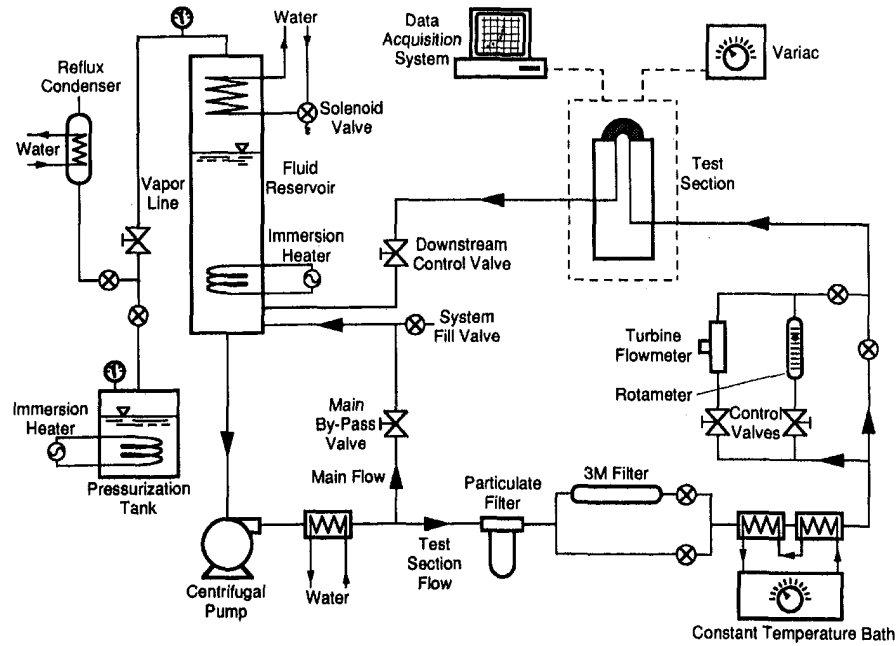


Fig. 1 Closed two-phase flow loop and auxiliary components

et al. (1989) correlated their respective enhancement factors with centripetal acceleration to the one-fourth power, drawing on the pool boiling correlation proposed by Zuber et al. (1961) which contained earth's gravity to the $\frac{1}{4}$ -power. This dependence of CHF on centripetal acceleration remains inconclusive requiring further rigorous evaluation.

The limitations of these prior studies point to a need to more systematically explore the enhancement mechanisms using both CHF data and flow visualization. The present experimental study was set up to obtain CHF data for near-saturated and subcooled flow in a curved, rectangular channel subjected only to concave heating using a long thick heater. The same test matrix, which included a broad range of velocity, was repeated for a straight channel in order to assess the enhancement for which curvature is responsible. In this manner, the curvature enhancement effect

could be isolated and quantified. Additionally, flow visualization tests were conducted to gain insight into the mechanisms responsible for the enhancement indicated in the data.

Experimental Methods

Flow Loop. Heat transfer experiments were conducted using a closed two-phase flow loop, a schematic of which is shown in Fig. 1. It consisted of a large cylindrical reservoir, centrifugal pump, flat-plate heat exchangers, flow control valves, flowmeters, test section, and CPVC piping. The fluid selected for this investigation was FC-72, a dielectric Fluorinert manufactured by 3M Company. Its main-attributes are a low boiling point (57°C at 1 atm) and a relatively low heat of vaporization, allowing for only a modest heat input to achieve boiling.

Nomenclature

C_1, C_2 = constants in Eq. (1)
 C_3, C_4 = constants in Eq. (2)
 d_{up} = measured distance from heater inlet to upstream edge of vapor patch
 D_h = hydraulic diameter of channel
 g^* = centripetal acceleration nondimensionalized with respect to g_e
 g_c = centripetal acceleration
 g_e = earth's gravitational acceleration
 h = change in position along an acceleration vector
 l_{meas} = measured liquid length between vapor patches
 P_o = fluid pressure at outlet of heated section
 P_{2c} = pressure at concave wall of curved channel
 P_{2s} = pressure throughout cross section of straight channel

ΔP = radial pressure rise in curved channel
 q'' = heat flux
 q''_m = maximum nucleate boiling heat flux, CHF
 r = radial coordinate in curved heater
 R_1 = radius of inner wall of curved channel
 R_2 = radius of outer wall of curved channel
 Re_D = Reynolds number, UD_h/ν_f
 T = temperature
 T_b = fluid bulk temperature
 T_o = fluid temperature at outlet of heated section
 $T_{sat,o}$ = fluid saturation temperature (at P_o) at outlet of heated section
 T_w = wall temperature
 $\Delta T_{sub,o}$ = fluid subcooling at outlet of heated section at CHF
 U = mean inlet velocity

x = transverse coordinate in straight heater, $x = 0$ at fluid-surface interface
 z = streamwise coordinate, $z = 0$ at heater inlet

Greek

δ_{meas} = measured vapor patch height
 λ_{meas} = measured vapor patch length
 ρ = density
 ν = kinematic viscosity

Subscripts

cur = curved channel/heater
 f = liquid
 o = outlet of heated section
 sat = saturated
 str = straight channel/heater

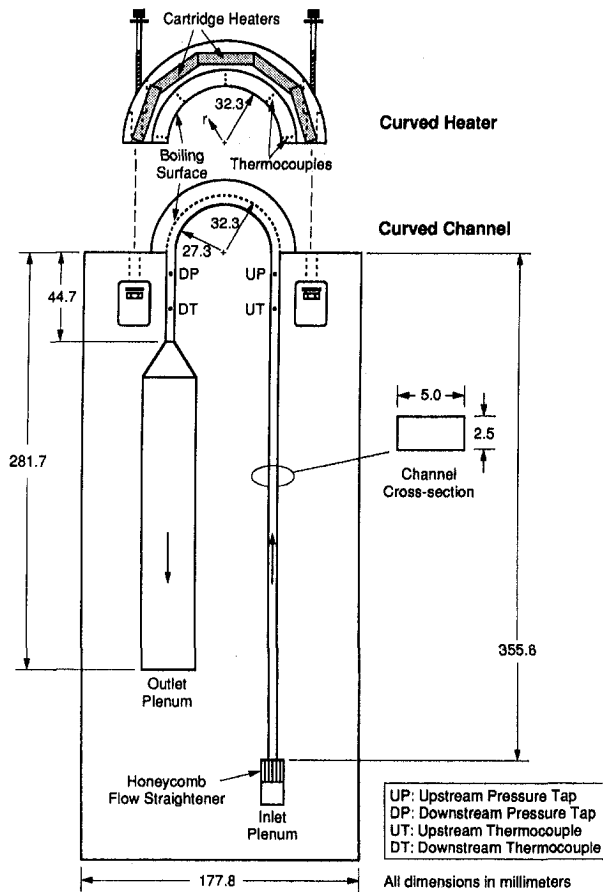


Fig. 2 Curved heater and bottom plate of curved channel

Fluid temperature was controlled by an immersion heater submerged in the reservoir and by a series of flat-plate heat exchangers. System pressure could be adjusted by the addition of FC vapor into the reservoir which was generated in a pressurization tank.

Test Channels. Two channel designs were tested in this investigation—a curved and a straight channel, shown in Figs. 2 and 3, respectively. Nearly identical except for the curvature of the heated section, they had the same cross section (5.0×2.5 mm), hydrodynamic entry length (106 hydraulic diameters), heated length (101.6 mm), flow instrumentation, and material.

Each channel was fabricated from two plates of opaque high-temperature G-10 fiberglass plastic. In the bottom plate of each channel (shown in Figs. 2 and 3) was machined a groove that had the width and depth of the channel. This groove had three surfaces except at the heater location where one of the walls had been removed. The heater was installed in this location and aligned with the aid of a microscope flush with the interrupted wall. In this manner, the flow channel remained rectangular with smooth, continuous walls—one of which contained a 101.6-mm long heated segment. In the curved channel, this heated segment was the concave wall whereas in the straight channel it was a side wall. When the second plate of G-10 fiberglass plastic was placed on top, it closed out the channel, forming the fourth wall. A flexible Teflon cord placed in a shallow O-ring groove on the underside of the top piece sealed the channel when the two G-10 plates and copper heater were bolted together. Flow channel instrumentation consisted of upstream and downstream thermocouples and pressure transducers as indicated in Figs. 2 and 3.

Copper Heaters. Two heaters were fabricated for testing, one curved, Fig. 4(a), and the other straight, Fig. 4(b). They were made from 99.99 percent pure oxygen-free copper and were identical in

most respects except for the curvature. For each, the heated surface exposed to the flow measured 2.5 mm in width and 101.6 mm along the flow direction.

Three Type-K thermocouples were placed at each of five locations along the heaters to determine the local heat flux and wall temperature, with corresponding locations the same distance from the inlet in both the curved and straight heaters. These thermocouples are indicated in Fig. 4, with Locations 1 and 5 referring to the inlet and outlet sets, respectively. The three small holes at each location were precisely drilled with respect to each other and the heated wall. Thermocouple beads (0.33-mm diameter) were inserted into these holes then secured in place with high conductivity epoxy.

Power was supplied by cylindrical cartridge heaters connected to a 240-volt variac and embedded in the thick portions of the curved and straight heaters as shown in Figs. 2 and 3, respectively. Distributing cartridge heaters as shown and using a high conductivity material for both heaters ensured power was evenly applied along the beginning of the thin portion. Heat then flowed through this thin portion toward the fluid resulting in a temperature gradient measured by the thermocouples.

Data Reduction. The component of flux perpendicular to the channel wall was approximated from the temperature gradient in the same direction. The three thermocouple readings were used in a one-dimensional analysis to determine this average flux for the corresponding instrumented location. This was accomplished using a linear-squares best-fit solution to first calculate the logarithmic profile in the curved heater or linear profile in the straight heater, which are given, respectively, by

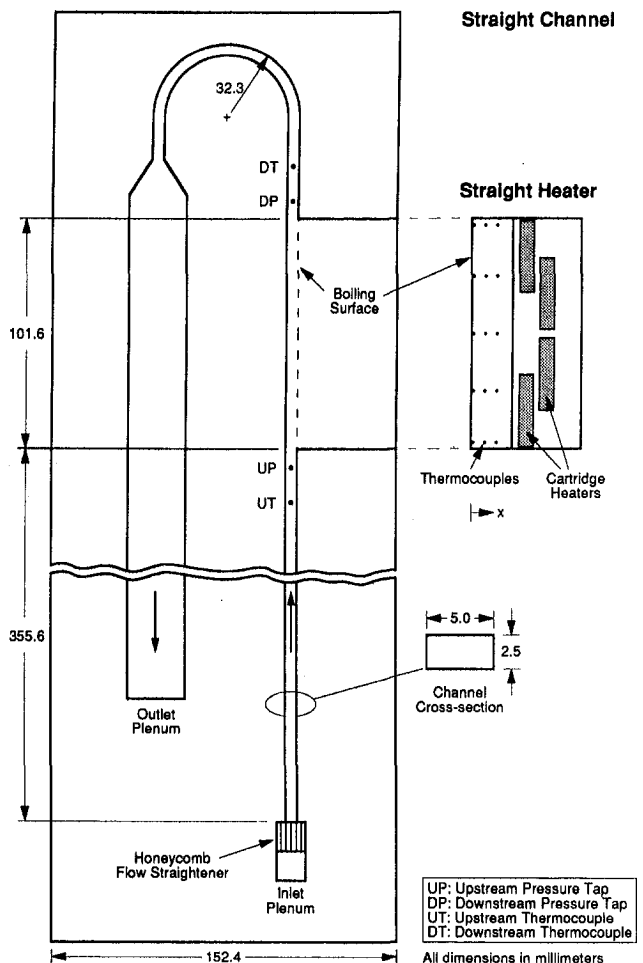


Fig. 3 Straight heater and bottom plate of straight channel

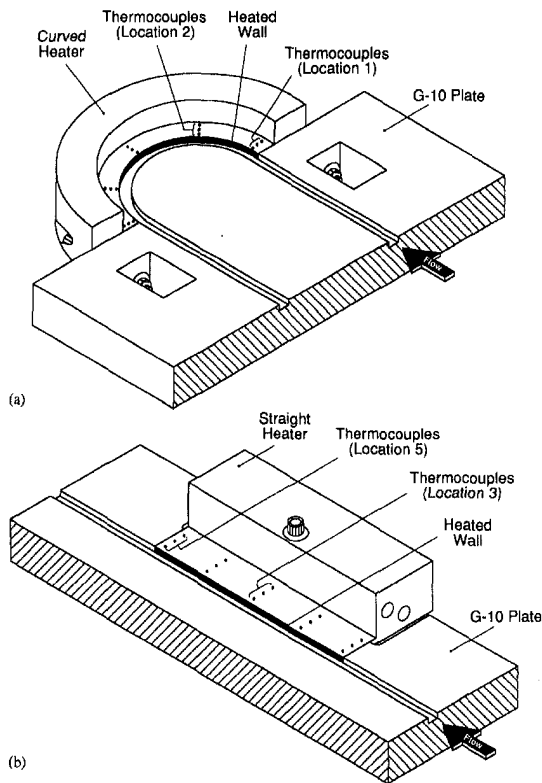


Fig. 4 (a) Curved and (b) straight heaters inserted into their respective channels with the five thermocouple locations in each heater shown

$$T(r) = C_1 \ln\left(\frac{r}{R_2}\right) + C_2 \quad (1)$$

and

$$T(x) = C_3 x + C_4, \quad (2)$$

where $r = R_2$ indicates the concave surface and $x = 0$ the straight surface. With the profile established, calculations of wall heat flux, q'' , and wall temperature, T_w , at a given location were straightforward, with a constant copper conductivity of $391 \text{ W m}^{-1} \text{ K}^{-1}$ assumed. The consequences of calculating a slope and extrapolating a value from a profile that was based on discrete data points were minimized by using a best-fit solution and by averaging temperature readings over 14 seconds while at steady-state conditions.

The calculations of bulk fluid temperature, T_b , at each location and outlet temperature, T_o , were based on heat input up to the respective locations and the assumption of a well-mixed flow. Since it is difficult to measure temperature when vapor exists in a subcooled liquid, the bulk average temperature (i.e., thermodynamic equilibrium temperature) is calculated in order to be able to plot a boiling curve and compare data.

The critical heat flux, q''_m , was defined as the largest flux attained under steady conditions. Since at CHF a vapor blanket essentially insulates the surface, heat supplied by the cartridge heaters could no longer be removed by the liquid and remained in the copper to cause a temperature rise and gradient decrease. Hence, CHF was detected by observing the data for an unsteady increase in calculated wall temperature accompanied by a sudden decrease in calculated wall flux. Since power increments were small, the flux prior to this unsteady behavior was recorded as the critical heat flux.

Test Conditions. Fluid in the loop was deaerated prior to each series of tests. Once inlet temperature, outlet pressure and flow rate were adjusted to desired values, power to the heater was incre-

mented. A data point was recorded at each power setting after thermal conditions were deemed steady. Each test proceeded through single and two-phase heat transfer regimes generating a boiling curve which terminated immediately after critical heat flux.

These heat transfer tests were conducted at three outlet subcoolings ($\Delta T_{\text{sub},o} = T_{\text{sat},o} - T_o = 3, 16, \text{ and } 29^\circ\text{C}$) with 13 flow velocities ($U = 0.25 \text{ to } 10 \text{ m s}^{-1}$) examined at each subcooling. $\Delta T_{\text{sub},o}$ refers to the prevailing subcooling value at the outlet of the heated section at the time of critical heat flux. Since the outlet pressure was held constant at $P_o = 1.38 \text{ bar}$ for all tests, the prevailing FC-72 saturation temperature at the outlet remained constant ($T_{\text{sat},o} = 66.3^\circ\text{C}$) as well. Therefore, at the time of critical heat flux, the outlet fluid bulk temperature achieved a prescribed value ($T_o = 63.3, 50.3 \text{ or } 37.3^\circ\text{C}$) depending on the subcooling value desired for that test. The inlet temperature remained constant during a particular test and was chosen such that the outlet temperature would equal its desired value at CHF. Maintaining a constant outlet pressure for all tests as well as a constant outlet temperature (at CHF) for tests with the same subcooling allowed for a meaningful comparison of CHF data.

For the velocity range tested, the Reynolds number based on hydraulic diameter and inlet conditions, $Re_D = UD_h/\nu_f$, ranged from 2,000 to 130,000. Considering also that the hydrodynamic entry length measured over 100 hydraulic diameters, fully developed turbulent flow was assumed to exist at the heater inlet. Correspondingly, centripetal acceleration, defined as

$$g^* = \frac{U^2}{R_2 g_e}, \quad (3)$$

ranged from 0 to 315. Though T_m remained constant for a given test, it had to be increased as test velocity increased, such that it varied over the ranges of 48 to 62, 32 to 49 and 17 to 35°C corresponding to outlet subcooling values of 3, 16 and 29°C, respectively.

Earth's gravity had a negligible effect on the flow even at low velocities due to the small channel width and the orientation of the gravity vector parallel to the heated surface and perpendicular to the bulk motion.

Repeatability and Uncertainty Analysis. The procedures for assembling the channel and acquiring data were consistent throughout the test program. Boiling curves for duplicated tests were nearly identical indicating repeatable results, negligible aging of the channel and consistent assembly procedures. For multiple tests at the same test condition, CHF values differed from their average by less than 3.4 percent. This is within the uncertainty in heat flux, which is approximately 8.5 percent at low fluxes ($q'' \approx 300 \text{ kW m}^{-2}$) decreasing to less than five percent at high fluxes ($q'' \approx 1500 \text{ kW m}^{-2}$). Uncertainty in calculated flux arose from uncertainties in temperature differences among the three thermocouples, thermocouple spacing and copper conductivity. The latter two uncertainties were assumed constant while the former decreased in significance as magnitude of temperature difference (i.e. flux) increased. Wall temperature calculations were accurate to within 0.3°C and flow rate uncertainty was less than 2.3 percent.

Numerical modeling revealed that heat losses from the thin, instrumented portion of the heater represented only about five percent of the heat flowing into this segment for low fluxes ($q'' \approx 150 \text{ kW m}^{-2}$) and decreased for higher fluxes. Using low conductivity ($0.26 \text{ W m}^{-1} \text{ K}^{-1}$) G-10 channel plates, high conductivity copper for the heater, and a short span for the thin instrumented portion helped minimize the heat losses, which were neglected in calculations.

Experimental Results

The CHF values measured in the present study are given in Tables 1 and 2 for the straight and curved channels, respectively. In both cases, CHF increased with increasing velocity and increas-

Table 1 Critical heat flux data for the straight channel

	U (m s ⁻¹)	0.25	0.5	1.0	1.5	2	3	4	5	6	7	8	9	10
$\Delta T_{sub,o}$ (°C)														
3		240 ^a 250	251 249	282	305	313 329	343 348 347	368	365 365	378	423	469	529 ^b	628 ^c
16		318 ^a 319	352 355	388 383	418 420	443 440 428	470	524 518	631	717 693	766 764	858	937	1025 1036
29		389 ^a 394	427 431	488 484	540 515 512	594	707 736	869	971	1087	1182	1293	1416	1526

CHF values in kW m⁻²; a: $\Delta T_{sub,o}$ is more than 1 °C below nominal value; b: $\Delta T_{sub,o} = 4$ °C; c: $\Delta T_{sub,o} = 5$ °C.

ing subcooling. The increase associated with subcooling is due to the cooler bulk temperature more readily condensing the bubbles before they coalesce into a vapor blanket. This relationship was linear in the straight channel as shown in Fig. 5, a result supported by the work of Wu and Simon (1994) and Collier and Thome (1994). However, CHF in the curved channel did not display a consistently linear relationship with subcooling over the same range of velocity. One reason for this inconsistency, which will become more apparent later, concerns the different influence buoyancy forces have on vapor removal from the concave wall for highly subcooled conditions as compared to near-saturated conditions.

The comparison of straight and curved-channel boiling curves in Fig. 6 reveals the enhancement of both single and two-phase heat transfer that streamwise curvature provides. Shown are increases in the single-phase convection coefficient, the incipient boiling heat flux and the critical heat flux. For $\Delta T_{sub,o} = 29$ °C, Fig. 6 shows the enhancement in CHF decreases with increasing velocity—from 48 percent at $U = 2$ m s⁻¹ to 20 percent at $U = 10$ m s⁻¹.

Figure 7 shows CHF data for the curved channel normalized relative to those for the straight channel in the form of enhancement ratios. The x-axis shows flow velocity on a linear scale along with the nondimensional centripetal acceleration, g^* . In most cases, the lowest subcooling, $\Delta T_{sub,o} = 3$ °C, offered the largest enhancement ratio and for $U > 2$ m s⁻¹ this was between 60 and 70 percent. At the low end of the velocity range, the middle and high subcooling values alternated in offering the better enhancement due in part to the fact that at some of these velocities CHF was detected at different locations along the heater. At higher velocities, where CHF was detected solely at the outlet, the CHF enhancement ratios tended toward constant values, approximately

60 percent for $\Delta T_{sub,o} = 3$ °C, 40 percent for $\Delta T_{sub,o} = 16$ °C and 20 percent for $\Delta T_{sub,o} = 29$ °C.

The CHF enhancement ratio, but not CHF, decreased with increasing subcooling. Hughes and Olson (1975) recorded similar trends for the curvature enhancement effect. They performed tests with Freon-113 for velocities of 1 to 4 m s⁻¹ for highly subcooled flow (28–61°C) in rectangular channels in which heat was applied to the straight, convex, or concave wall. Their data also showed the concave-to-straight-channel CHF ratio decreased with increasing subcooling. Gu et al. (1989) reported CHF enhancement of greater than 40 percent for FC-72 at $U = 4$ m s⁻¹ at both low (0.5°C) and moderate (20°C) subcooling. However, at $U = 1$ m s⁻¹, the curvature enhancement dropped as subcooling increased. Wu and Simon (1994) also noted the tendency for the curved-to-straight CHF ratio to diminish with increasing subcooling, as did Leland and Chow (1992) who actually reported a detrimental curvature effect for 35°C subcooling in their smaller radius ($R_2 = 28.6$ mm) channel.

The solid curve in Fig. 7 represents the curvature enhancement ratio if it were a function of centripetal acceleration to the one-fourth power. Several researchers (Gambill and Green, 1958; Gu et al., 1989), following the work of Zuber et al. (1961), have proposed this relationship for CHF in curved channels. Zuber et al. offered a correlation for *pool boiling* in which CHF is proportional to earth's gravitational acceleration, g_e , to the $\frac{1}{4}$ -power. Researchers have sought to extend this dependence to curved flow by replacing g_e with the local centripetal acceleration resulting in a CHF ratio dependent on g^* to the one-fourth power. This relation is not reflected by the CHF data obtained for the wide ranges of velocity and subcooling in the present investigation. The radial pressure gradient in curved flow must therefore be responsible for

Table 2 Critical heat flux data for the curved channel

	U (m s ⁻¹)	0.25	0.5	1.0	1.5	2	3	4	5	6	7	8	9	10
g^*		0	1	3	7	13	28	50	79	114	154	202	255	315
$\Delta T_{sub,o}$ (°C)														
3		370 374	411 413	436 443	473 472	435 481 482	559	586 582	598 620	651	695	757 759	863 ^b	1006 ^c
16		444 445	509 507	570 560	660 671 657	570	634	701 739	791	883	998	1156	1267	1438 1436
29		470 ^a 467	578 580	683 673	804 787	880 874	1021	1158	1309 1277	1376	1446	1562	1673	1825

CHF values in kW m⁻²; a: $\Delta T_{sub,o}$ is more than 1 °C below nominal value; b: $\Delta T_{sub,o} = 4$ °C; c: $\Delta T_{sub,o} = 5$ °C.

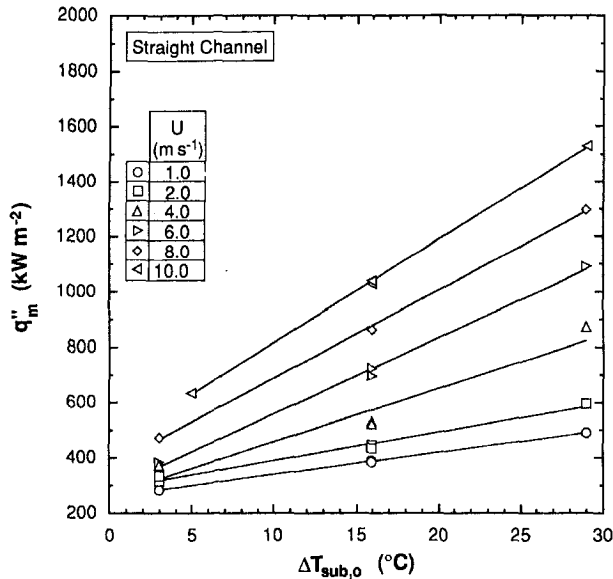


Fig. 5 Linear relationship between critical heat flux and outlet subcooling in straight channel

several complex enhancement effects which are not reflected in the Zuber et al. model.

Enhancement Mechanisms

Figure 8 illustrates three key mechanisms for CHF enhancement in a curved channel: *buoyancy forces, additional pressure on liquid-vapor interface, and increase in wall subcooling*, all resulting from the radial pressure gradient.

The first mechanism is a buoyancy force which arises when matter that is less dense than its surroundings is in the presence of a pressure gradient. In this case, the force on a vapor bubble surrounded by the denser liquid pulls the bubble toward the inner wall. This results in a more efficient removal of vapor from the concave surface, making it less likely bubbles will coalesce on the heated surface and form a vapor blanket, as shown in Fig. 8(a). CHF is therefore delayed to higher fluxes where vapor production becomes so intense that coalescence outpaces vapor removal. Insight into the manner in which the buoyancy forces enhance

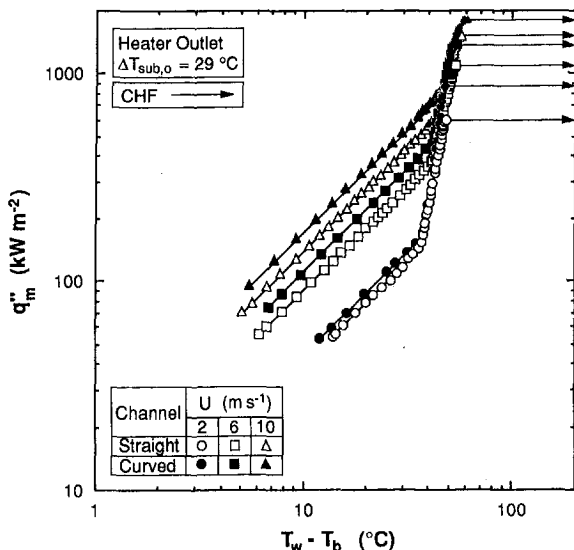


Fig. 6 Comparison of boiling curves at outlet of straight and curved heated sections for $\Delta T_{sub,o} = 29^\circ\text{C}$

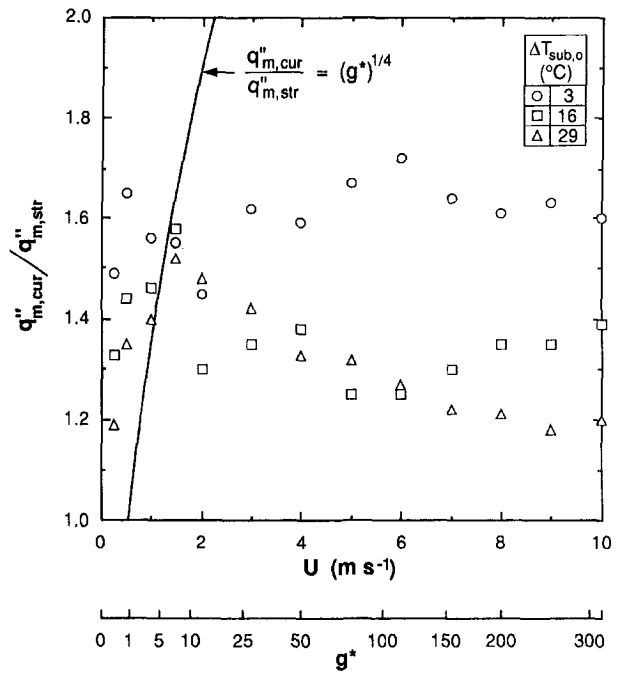


Fig. 7 Ratio of curved-to-straight-channel critical heat flux data versus velocity and centripetal acceleration at three subcoolings

CHF was obtained through flow visualization tests and will be discussed in the next section.

Secondly, the pressure gradient enables the liquid contact with the wall, which occurs at wetting fronts (troughs) in the wavy liquid-vapor interface, to be maintained until higher fluxes, as illustrated in Fig. 8(b). Galloway and Mudawar (1993a, b) and Gersey and Mudawar (1995a, b) showed that CHF is triggered by lift-off of the liquid-vapor interface from the heated surface which occurs when the vapor momentum flux in the wetting front overcomes the pressure force exerted upon the wavy interface. The increase in pressure at the concave wall enables the liquid-vapor interface to withstand a greater vapor momentum which postpones lift-off to higher fluxes, thereby increasing CHF.

Thirdly, the radial pressure gradient increases the pressure and, consequently, the saturation temperature of the fluid at the concave wall, as indicated in Fig. 8(c). Compared to a straight channel, this leads to a local increase in subcooling which helps enhance CHF. This increase in subcooling may be estimated by making a few approximations. Pressure rise in a gravitational field is expressed by

$$\Delta P = \rho g h, \quad (4)$$

where ρ is the medium density, g the local acceleration, and h the change in position along the acceleration vector. The local acceleration in the curved channel may be approximated as the centripetal acceleration experienced by a fluid particle moving along the channel centerline (earth's gravity is neglected),

$$g \approx g_c = \frac{U^2}{\frac{1}{2}(R_1 + R_2)}. \quad (5)$$

For the sake of calculations, consider a straight and curved channel that have similar centerline pressures and bulk-averaged velocities. Fluid throughout the cross-section of the straight channel has the same pressure. But for curved flow, pressure increases at the concave wall, above that for straight flow, due to the gradient acting over half the channel height, i.e., $h = (R_2 - R_1)/2$. With these approximations, the pressure increase between the centerline and concave wall is given by

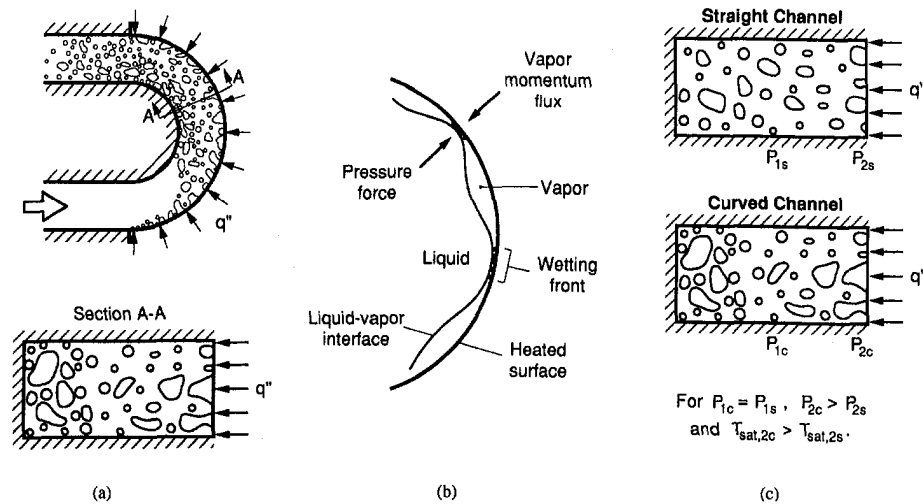


Fig. 8 Two-phase heat transfer enhancement mechanisms for flow boiling in a curved channel: (a) inward bubble motion due to buoyancy force, (b) increased pressure on liquid-vapor interface at wetting fronts, and (c) increased subcooling at wall

$$\Delta P = P_{2c} - P_{2s} = \rho_f U^2 \frac{R_2 - R_1}{R_1 + R_2} \quad (6)$$

This represents the estimated increase in wall pressure between the curved and straight channels as a result of the radial pressure gradient, indicated in Fig. 8(c) as $P_{2c} - P_{2s}$. Using channel outlet pressure ($P_o = 1.38$ bar) as a reference point for saturation temperature, the increase in saturation temperature corresponding to this pressure increase can be determined using FC-72 property data. Assuming similar bulk temperatures between the two channels, this saturation temperature increase represents the increase in wall subcooling as well. Performing these calculations for $U = 10$ m s⁻¹ reveals that the radial pressure gradient is responsible for a 3.2°C rise in subcooling. The associated rise in CHF may then be ascertained by referring to Fig. 5 which shows the linear relation between critical heat flux and subcooling in the straight channel. Extracting the slope for $U = 10$ m s⁻¹ and multiplying by 3.2°C yields a CHF enhancement of 120 kW m⁻² attributed to this radial increase in wall subcooling. This increment in critical heat flux represents only 32 percent of the enhancement measured for the near-saturated ($\Delta T_{sub,o} = 3^\circ\text{C}$) case and 40 percent for the highly subcooled ($\Delta T_{sub,o} = 29^\circ\text{C}$) case, at this velocity. This indicates that the other two mechanisms illustrated in Fig. 8 contribute significantly to the curvature enhancement. These issues are explored in the next section.

Flow Visualization Results

Equipment and Procedure. In order to gain insight into the relation between vapor dynamics and CHF, a visual investigation of the flow boiling process was undertaken. Two additional channels were fabricated from optical-grade polycarbonate (trade name Lexan MP750) with designs identical to those used in obtaining CHF data. Tests with these clear channels used the same heaters, instrumentation, fluid and flow loop, the only difference being optical access to the heated length.

A Canon L1 8-mm video camera was configured with its lens located a few millimeters above the channel. The camera was mounted on a tripod which enabled it to be translated in any coordinate direction and to traverse the entire heated length. Video sequences were recorded with a 30X lens at a rate of 30 frames per second and a shutter speed of 1/10,000 of a second. The view through the camera was parallel to the heated surface and perpendicular to the flow direction. Approximately 30 mm of the channel length were captured in a frame, so the 101.6-mm heated length was videotaped in four segments by traversing the camera.

For each flow visualization test, the heated length was videotaped for every heat flux increment (data point) of the boiling curve though only the vapor characteristics at CHF were measured and categorized. Video allowed for the collection of significantly more frames of vapor activity than could be acquired with still photography. This proved to be a tremendous asset in conducting the statistical analysis of vapor size, shape and percentage of occurrence.

Video sequences were obtained in both channels for only the near-saturated ($\Delta T_{sub,o} = 3^\circ\text{C}$) and highly subcooled ($\Delta T_{sub,o} = 29^\circ\text{C}$) cases for velocities of $U = 0.25, 1, 2$ and 4 m s⁻¹. Higher velocities were not attempted since vapor dimensions were approaching sizes too small to be measured reliably and since the integrity of the polycarbonate channels would be compromised at the higher heater temperatures associated with higher velocities. Small holes precisely spaced near the edge of the channel and captured in the video images provided a scale by which to make measurements of vapor dimensions. These measurements were obtained manually using a video monitor and a scale constructed for each test based on the known spacing of the small holes.

Flow Boiling Images. Composite video images of the straight and curved heated lengths, shown in Figs. 9 through 11, represent typical observations of vapor development along each channel. Channel height is 5.0 mm and width (depth of view into page) is 2.5 mm. The dark region along the channel edge is the heater (which is much thicker than actually shown) with upstream and downstream adiabatic sections of the channel revealed by the lighter shade. Thin dark lines that may be seen in some images are microcracks in the polycarbonate material which did not affect the boiling process. The small holes used as a measurement scale are visible along the edge of the channel.

Figure 9 shows flow boiling in the straight channel at CHF for near-saturated ($\Delta T_{sub,o} = 3^\circ\text{C}$) and subcooled ($\Delta T_{sub,o} = 29^\circ\text{C}$) conditions at a bulk velocity of $U = 1$ m s⁻¹. Flow is from left to right and the channel is flush with the heater at the inlet though the edge is not visible. These images clearly show vapor patches growing in both length and height. The larger patches restrict the access of liquid at high heat fluxes. Increasing subcooling reduces this restriction by decreasing vapor length and height as illustrated in Fig. 9(b). The series of vapor patches display an undulating, periodic nature which is the basis of the idealized wavy interface for CHF modeling first proposed by Galloway and Mudawar (1993a, b).

Vapor development at CHF in the curved channel is shown in Figs. 10 and 11 for near-saturated and subcooled conditions,

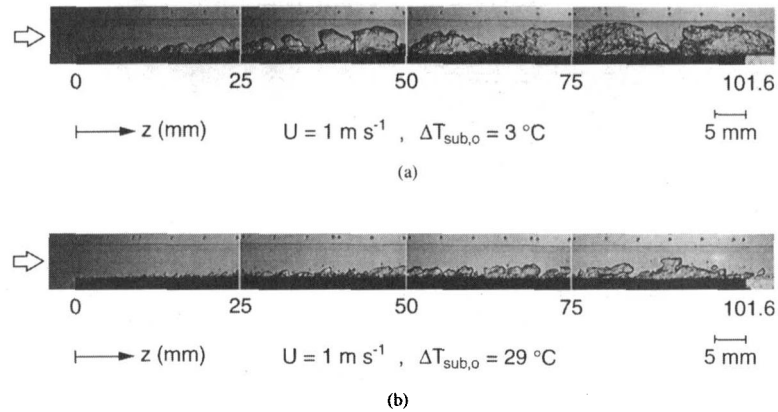


Fig. 9 Video images of flow boiling at CHF in straight channel at $U = 1 \text{ m s}^{-1}$ for (a) near-saturated ($\Delta T_{\text{sub},o} = 3^\circ\text{C}$) and (b) subcooled ($\Delta T_{\text{sub},o} = 29^\circ\text{C}$) conditions

respectively. Figure 10 shows a clear tendency of the buoyancy force to pull vapor inward removing it from the concave wall, especially near $z = 25 \text{ mm}$ where the vapor is being elongated and pinched. Farther downstream vapor exists throughout the cross section. It appears as though the buoyancy force pinches off a portion of the vapor mass that had formed along the concave wall and pulls this portion into the bulk. The result is numerous vapor fragments distributed throughout the cross section. Another consequence is that the vapor which does remain on the surface is not organized in large patches; this provides less resistance to the rewetting liquid. For subcooled flow, shown in Fig. 11, vapor production is significantly reduced but buoyancy can still be seen to act on small patches that are elongated toward the inner wall.

Comparing the near-saturated case of both the straight [Fig. 9(a)] and curved (Fig. 10) channels highlights the important effect of buoyancy forces. Vapor is removed from the concave wall, fragmented and distributed in the bulk flow where it is better able to condense, while in the straight channel it remains near the

heated surface providing an impediment to the rewetting liquid. Also, the greater height of vapor patches near the inlet region in the curved channel are associated with a greater interfacial curvature at the wetting fronts, which results in a larger pressure difference across the interface. This pressure force acts to maintain liquid contact with the surface by more effectively resisting the vapor momentum flux, leading to an increased CHF. These phenomena are also present in the subcooled case where there is less vapor on the curved heated surface (Fig. 11) than on the straight [Fig. 9(b)] despite the fact that at the condition shown CHF is 40 percent greater in the curved channel.

Vapor Measurements. In an effort to quantify these observations, numerous near-wall vapor patches were measured in each channel at similar velocity and subcooling conditions. Particular characteristics of interest were vapor length, λ_{meas} , maximum height, δ_{meas} , and location of upstream edge, d_{up} , as illustrated in Fig. 12. Additionally, the length of liquid contact with the surface

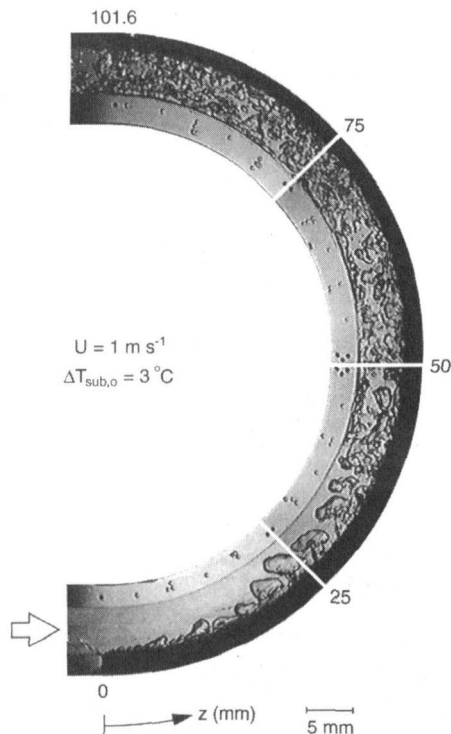


Fig. 10 Video images of flow boiling at CHF in curved channel at $U = 1 \text{ m s}^{-1}$ for near-saturated ($\Delta T_{\text{sub},o} = 3^\circ\text{C}$) conditions

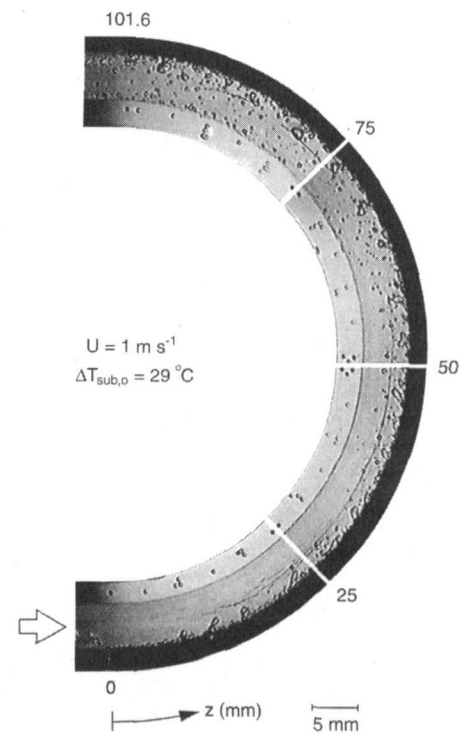


Fig. 11 Video images of flow boiling at CHF in curved channel at $U = 1 \text{ m s}^{-1}$ for subcooled ($\Delta T_{\text{sub},o} = 29^\circ\text{C}$) conditions

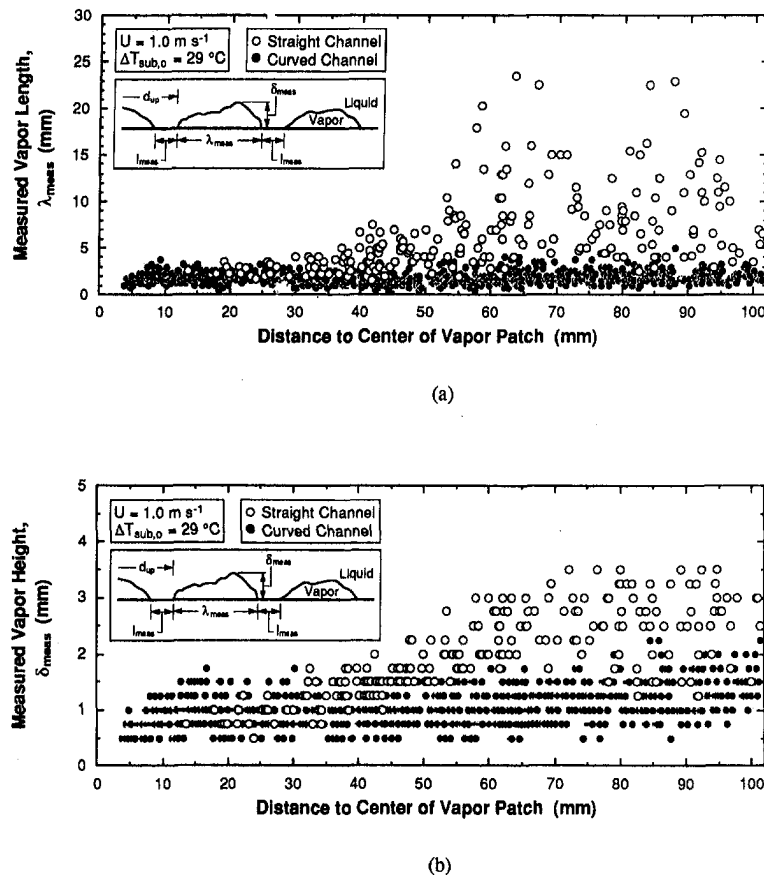


Fig. 12 Measured (a) lengths and (b) heights of vapor patches at CHF in straight and curved channels for $U = 1 \text{ m s}^{-1}$ and $\Delta T_{\text{sub},o} = 29^\circ\text{C}$

between adjacent patches, l_{meas} , was measured. In some cases, the identification of a vapor patch itself was difficult since boundaries were not always distinct. Considering the seemingly random nature of the boiling process, measurements were made on 50 video frames for each segment of the heater. In this manner, the bubble dynamics could be analyzed statistically to identify characteristics that might not be apparent in a few frames.

The measurements were analyzed individually by plotting them versus streamwise location and collectively by averaging values for each of the four heater segments. In general, the data show that for straight channel flow the vapor length, vapor height, and liquid length all increase along the flow direction, decrease with increasing subcooling, and decrease with increasing velocity. The liquid and vapor lengths vary such that their ratio is relatively constant for a given subcooling. For curved flow, vapor length and height do not grow downstream, instead they assume relatively constant values.

The effect of curvature on vapor length is ascertained by plotting the measured length of a vapor patch against the distance to the center of that vapor patch as measured from the heater inlet. Measurements made for the straight and curved channels are shown in Fig. 12(a) for conditions of $U = 1 \text{ m s}^{-1}$ and $\Delta T_{\text{sub},o} = 29^\circ\text{C}$. The vapor length grew downstream in the straight channel (albeit with scatter) whereas it remained at a lower, constant value in the curved channel. This is a direct consequence of the buoyancy forces present in the curved flow. These forces pull the vapor inward, eventually breaking off a portion of the patch such that the vapor remaining on the surface is reduced in length and height. Buoyancy continues to act along the entire curved trajectory preventing the vapor mass from growing significantly.

An illustration of attenuated vapor height in curved flow is given in Fig. 12(b) for $U = 1 \text{ m s}^{-1}$ and $\Delta T_{\text{sub},o} = 29^\circ\text{C}$. The vapor height increased downstream in the straight channel but remained

fairly constant in the curved. Of particular interest is the upstream region (0–25 mm) of both heaters where CHF is believed to be triggered due to wetting front lift-off. The plot shows that vapor height in this region is greater in the curved channel. Buoyancy forces pull vapor patches inward, elongating them in the radial direction, such that their heights measured normal to the heated surface are greater than at corresponding locations in the straight channel. Shortly downstream though, buoyancy forces pinch off portions and the heights of the vapor patches remaining on the curved surface are less than on the straight surface. This is particularly evident by comparing the video images for the near-saturated case in Figs. 9(a) and 10. With respect to Fig. 12(b), the “row-effect” displayed by the data is merely a consequence of making vapor measurements to the nearest 0.25 mm.

Vapor Shape Analysis. In addition to obtaining measurements, the vapor patches were categorized based on shape to identify characteristics pertinent to CHF. These categories are depicted in Fig. 13. By far the most common form observed was the generic wave-like shape with no special features. It was typically a vapor mass with maximum thickness near its center and tapered on the ends. This wave-like formation, depicted in Fig. 13(a), grows by the addition of newly generated vapor and by coalescence with other vapor masses.

Two other shapes that warrant discussion highlight the forces acting on the vapor. The overhanging vapor type, shown in Fig. 13(b), was observed almost exclusively in the straight channel though far less frequently than the wave-like type. This formation is initiated with vapor generated at the heated surface. The momentum of the newly created vapor is directed away from the wall toward the center of the channel where the local velocity is greater. The liquid momentum in the middle of the channel moves the vapor in the streamwise direction while its base maintains contact

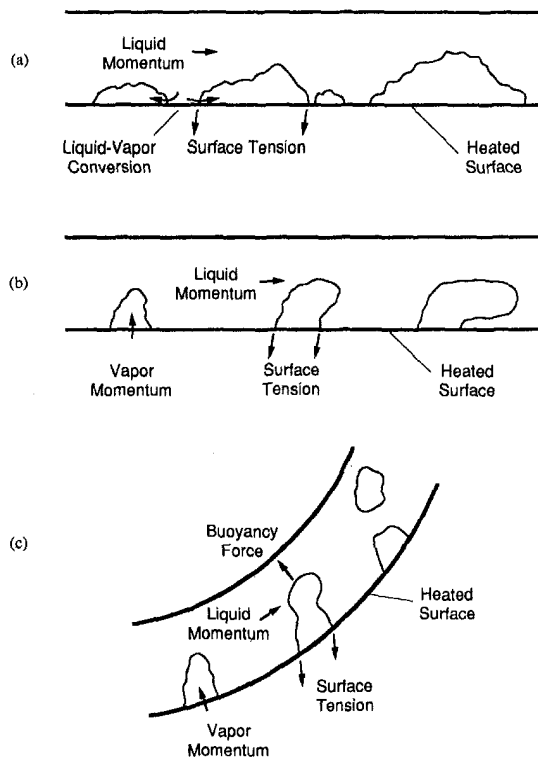


Fig. 13 Vapor formations observed in straight and curved channels: (a) wave-like, (b) overhanging, and (c) pinching

with the wall through surface tension forces, creating the overhanging formation. Once the trapped liquid is evaporated, rewetting of the surface by the cooler bulk is hindered by the interference of the overhanging vapor.

The pinching type formation illustrated in Fig. 13(c) was observed chiefly in the curved channel. Similar to the overhanging formation, it too is initiated by vapor generated at the surface and thrust outward due to its momentum. Streamwise inertia acts to push it along the flow while a buoyancy force provides the distinguishing effect. This buoyancy force pulls the vapor toward the inner wall elongating it in the radial direction. Eventually, portions of the vapor are pinched off with the fragmented portions being pulled toward the inner wall. Unlike in the straight channel where the large, overhanging vapor remains near the surface hindering the liquid rewetting, in the curved channel this vapor is moved away from the surface toward the opposite wall. This pinching behavior is evident in Fig. 10 near $z = 25$ mm.

These two vapor formations illustrate an important distinction between straight and curved channel flow boiling that is a major contributor to the CHF enhancement. In both cases, vapor is generated at the wall while surface tension and streamwise inertia act to maintain it there. However, the radial pressure gradient present in curved flow leads to buoyancy forces which move vapor away from the concave wall.

Statistical results reveal that the dominant vapor shape is that of the wave-like formation. The overhanging vapor formation occurred mostly in the straight channel typically less than ten percent of the time. However, for subcooled flow at $U = 1 \text{ m s}^{-1}$, it represented nearly one quarter of the observed patches over the downstream half of the heater. The pinching formation appeared only in the curved channel due the buoyancy forces pulling on the vapor. It also was observed less than ten percent of the time except at $U = 1 \text{ m s}^{-1}$ for $\Delta T_{\text{sub},o} = 29^\circ\text{C}$ where it was noted up to 20.4 percent of the time.

Effects of Buoyancy Mechanism. The flow visualization results, both the qualitative observations and the quantitative mea-

surements, along with the CHF data permit several conclusions to now be drawn regarding the effects of buoyancy on CHF.

First, near-saturated flow realizes a greater benefit from flow curvature. The experimental data plotted in Fig. 7 show that the critical heat flux enhancement ratio is greatest for the lowest subcooling. The vapor generated in near-saturated flow does not readily condense and hence must be removed from the surface. The buoyancy forces arising from the radial pressure gradient aid in removing this vapor thereby delaying coalescence and CHF. On the other hand, highly subcooled flow is already very efficient at removing vapor from the heated wall by condensing it in the cooler bulk. Hence, the effect of an additional mechanism such as that provided by a buoyancy force is less significant in highly subcooled flow. Therefore, curvature has a more pronounced enhancement effect for near-saturated flow.

Secondly, curved flow better utilizes the available subcooling of the bulk flow. As clearly shown in Fig. 10, buoyancy forces break off portions of surface vapor patches and move these smaller portions into the cooler bulk flow where they condense. In this manner, the subcooling throughout the cross-section is available for condensing the vapor. Additionally, condensation is aided by the fact that there are numerous small, jagged patches in the bulk. This greatly increases the surface area available for the transfer of heat from saturated vapor to subcooled liquid as compared to the vapor remaining in large patches, typical of straight channel flow.

Thirdly, the buoyancy mechanism aids in providing the bulk liquid greater access to the concave wall. Buoyancy forces pull vapor away from the wall attenuating the length and height of vapor remaining on the surface. This counters the continual coalescence and restriction that occur as vapor is advected downstream, as in the straight channel. The flow boiling images in Fig. 10 and the vapor measurements in Fig. 12 illustrate that the buoyancy forces continually pinch off portions of the vapor. Consequently, the smaller surface vapor patches result in greater access for the rewetting liquid and a corresponding increase in heat transfer; hence, a higher CHF limit in the curved channel.

Finally, curvature of the liquid-vapor interface is greater for curved flow. The buoyancy forces pull on the surface vapor patches elongating them in the radial direction. This elongation takes place over the upstream region before the forces become strong enough to break off portions and pull them into the bulk. Figure 12(b) shows that the individually measured vapor heights are larger in the curved channel over approximately the first 25 mm. Consequently, the amplitude of the vapor wave is larger resulting in greater interfacial curvature. This leads to a larger interfacial pressure difference which is able to withstand a greater vapor momentum flux, thereby maintaining liquid contact with the surface at higher fluxes, increasing CHF. This interfacial pressure difference plays a significant role in the lift-off criterion of the critical heat flux model first proposed by Galloway and Mudawar (1993b).

Conclusions

This paper details an investigation into critical heat flux enhancement resulting from streamwise curvature in a rectangular concave-heated channel. Test were conducted in curved and straight channels to obtain CHF data and to visualize the corresponding vapor characteristics. Key conclusions from this study are as follows:

- 1 Critical heat flux increases with increasing velocity and subcooling for both straight and curved flow. CHF increases linearly with outlet subcooling in straight flow but does not show a consistently linear relationship in curved flow.

- 2 For all flow conditions tested, curvature augments the critical heat flux limit. At high velocities, this augmentation is approximately 60 percent for $\Delta T_{\text{sub},o} = 3^\circ\text{C}$, 40 percent for $\Delta T_{\text{sub},o} = 16^\circ\text{C}$, and 20 percent for $\Delta T_{\text{sub},o} = 29^\circ\text{C}$. Clearly, the enhancement in CHF is better realized at low subcooling where the flow is more dependent upon the buoyancy force for vapor removal.

3 Prior to CHF, vapor bubbles in both channels coalesce into a wavy vapor layer consisting of vapor patches which propagate downstream along the heated wall. Vapor patch length and height grow along the flow direction and decrease with increasing velocity and subcooling in the straight channel. An additional overhanging vapor formation was observed in the straight channel while a pinching formation occurred in the curved channel. The distinguishing factor between these latter two is attributed to buoyancy forces pulling the vapor toward the inner wall in the curved channel. The buoyancy forces elongate, then pinch off portions of the vapor patches in the curved channel; these fragmented portions are pulled into the bulk flow. As a consequence, vapor length and height are smaller at most locations in the curved channel and do not increase in the flow direction.

4 The key mechanisms for CHF enhancement in curved flow can be summarized as follows:

(a) Radial increase in pressure leads to a higher local subcooling at the concave wall.

(b) Buoyancy forces pull vapor away from the concave wall thereby delaying coalescence and providing the rewetting liquid greater access to the heated surface.

(c) Buoyancy forces pinch off and transport portions of the vapor into the cooler bulk. In this way, curved flow is better able to utilize the available subcooling throughout the cross section.

(d) Buoyancy forces pull on the surface vapor patches elongating them in the radial direction. This results in a larger pressure difference across the liquid-vapor interface which acts to maintain liquid contact with the surface by more effectively resisting the vapor momentum flux, leading to an increased CHF.

Acknowledgments

The authors are grateful for the support of the Office of Basic Energy Sciences of the U.S. Department of Energy (Grant No. DE-FG02-93ER14394.A003). Financial support for the first author was provided through the Air Force Palace Knight Program.

References

- Collier, J. G., and Thome, J. R., 1994, *Convective Boiling and Condensation*, 3rd Ed., Clarendon Press, Oxford.
- Gambill, W. R., and Green, N. D., 1958, "Boiling Burnout with Water in Vortex Flow," *Chemical Engineering Progress*, Vol. 54, pp. 68–76.
- Galloway, J. E., and Mudawar, I., 1993a, "CHF Mechanism in Flow Boiling From a Short Heated Wall—Part I. Examination of Near-Wall Conditions with the Aid of Photomicrography and High-Speed Video Imaging," *International Journal of Heat and Mass Transfer*, Vol. 36, pp. 2511–2526.
- Galloway, J. E., and Mudawar, I., 1993b, "CHF Mechanism in Flow Boiling From a Short Heated Wall—Part II. Theoretical CHF Model," *International Journal of Heat and Mass Transfer*, Vol. 36, pp. 2527–2540.
- Galloway, J. E., and Mudawar, I., 1995, "A Theoretical Model for Flow Boiling CHF From Short Concave Heaters," *ASME JOURNAL OF HEAT TRANSFER*, Vol. 117, pp. 698–707.
- Gersey, C. O., and Mudawar, I., 1995a, "Effects of Heater Length and Orientation on the Trigger Mechanism for Near-Saturated Flow Boiling Critical Heat Flux—I. Photographic Study and Statistical Characterization of the Near-Wall Interfacial Features," *International Journal of Heat and Mass Transfer*, Vol. 38, pp. 629–641.
- Gersey, C. O., and Mudawar, I., 1995b, "Effects of Heater Length and Orientation on the Trigger Mechanism for Near-Saturated Flow Boiling Critical Heat Flux—II. CHF Model," *International Journal of Heat and Mass Transfer*, Vol. 38, pp. 643–654.
- Gu, C. B., Chow, L. C., and Beam, J. E., 1989, "Flow Boiling in a Curved Channel," *Heat Transfer in High Energy/High Heat Flux Applications*, R. J. Goldstein, L. C. Chow, and E. E. Anderson, eds., ASME, New York, ASME HTD-Vol. 119, pp. 25–32.
- Hughes, T. G., and Olson, D. R., 1975, "Critical Heat Fluxes for Curved Surfaces During Subcooled Flow Boiling," *U.S. National Heat Transfer Conference*, Vol. 3, San Francisco, CA, ASME, New York, pp. 122–130.
- Leland, J. E., and Chow, L. C., 1992, "Effect of Channel Height and Radius of Curvature on Forced Convective Boiling in a Rectangular Channel," *30th Aerospace Sciences Meeting & Exhibit*, Reno, NV.
- Wu, P. S., and Simon, T. W., 1994, "Critical Heat Flux and Subcooled Flow Boiling with Small Heated Regions on Straight and Concave-Curved Walls," *10th International Heat Transfer Conference*, Institute of Chemical Engineers, Rugby, UK, Vol. 7, pp. 569–574.
- Wu, P. S., and Simon, T. W., 1995, "Subcooled Flow Boiling Over a Thin, Low-Capacitance Surface on a Concave Wall," *ASME National Heat Transfer Conference*, Portland, OR, Vol. 12, pp. 177–184.
- Zuber, N., Tribus, M., and Westwater, J. M., 1961, "The Hydrodynamic Crisis in Pool Boiling of Saturated and Subcooled Liquids," *International Developments in Heat Transfer: Proceedings of the 1961–62 International Heat Transfer Conference*, Boulder, CO, ASME, New York, pp. 230–236.

Condensation of Downward-Flowing Zeotropic Mixture HCFC-123/HFC-134a on a Staggered Bundle of Horizontal Low-Finned Tubes

H. Honda

e-mail: hhonda@cm.kyushu-u.ac.jp

H. Takamatsu

N. Takata

Institute of Advanced Material Study,
Kyushu University,
Kasuga,
Fukuoka 816-8580, Japan

Experiments were conducted to obtain row-by-row heat transfer data during condensation of downward-flowing zeotropic refrigerant mixture HCFC-123/HFC-134a on a 3×15 (columns \times rows) staggered bundle of horizontal low-finned tubes. The vapor temperature and the HFC-134a mass fraction at the tube bundle inlet were maintained at about 50°C and nine percent, respectively. The refrigerant mass velocity ranged from 9 to $34 \text{ kg/m}^2 \text{ s}$, and the condensation temperature difference from 3 to 12 K. The measured distribution of the vapor mass fraction in the tube bundle agreed fairly well with that of the equilibrium vapor mass fraction. The vapor phase mass transfer coefficient was obtained from the heat transfer data by subtracting the thermal resistance of the condensate film. The heat transfer coefficient and the mass transfer coefficient decreased significantly with decreasing mass velocity. These values first increased with the row number up to the third (or second) row, then decreased monotonically with further increasing row number, and then increased again at the last row. The mass transfer coefficient increased with condensation temperature difference, which was due to the effect of suction associated with condensation. On the basis of the analogy between heat and mass transfer, a dimensionless correlation of the mass transfer coefficient for the 4th to 14th rows was developed.

Introduction

Zeotropic refrigerant mixtures have been investigated as working fluids of refrigeration and heat pump systems because of their potential of improving the coefficient of performance over pure refrigerants. The equilibrium temperature of the zeotropic mixture changes as evaporation or condensation proceeds. This characteristic can be used to minimize the energy loss of the system by matching the temperature glides of the working fluid in the evaporator and condenser with those of the heat source and the heat sink, respectively. Several zeotropic mixtures have been tested successfully (Küver and Kruse, 1986; Murloy et al., 1988; NEDO, 1993). Recent researches are focused on several kinds of two component and three component HFC mixtures that are to be used as replacements for HCFC-22 and R-502.

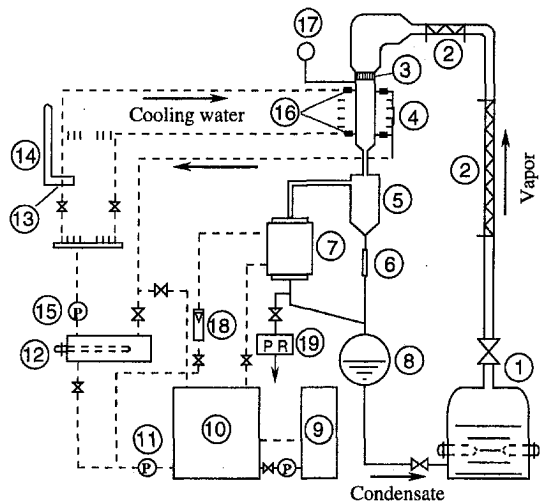
One of the adverse effects associated with the use of zeotropic refrigerant mixture is that the condensation heat transfer coefficient is considerably lower than that for pure refrigerants. This is due to the existence of diffusion layer in the vapor phase. Uchida et al. (1994a, b) and Ebisu et al. (1995) tested several kinds of enhanced tubes for in-tube condensation of R-407C, a replacement for HCFC-22. The heat transfer performance of the best performing tube was still lower than that obtained for condensation of HCFC-22 in commercially available microfin tubes.

Relatively little work has been reported on the condensation of zeotropic refrigerant mixtures on horizontal tubes and bundles of horizontal tubes. Hijikata et al. (1989) studied forced convective condensation of CFC-113/CFC-114 (10 wt % CFC-

114) mixture with vertical and horizontal vapor flows on a smooth tube and two kinds of finned tubes with high fins and low fins, respectively. The vapor Reynolds number Re_v ranged from 1.3×10^3 to 9.3×10^3 . The highest performance was obtained with the combination of the high-fin tube and the horizontal vapor flow. They calculated the heat transfer coefficient of the diffusion layer by subtracting the resistance of liquid film from the overall heat transfer resistance. For the finned tubes with vertical vapor flow, the calculated value was 1.0 to 1.9 times as large as that obtained from the analogy between heat and mass transfer. Singe et al. (1995) reported the average heat transfer data for condensation of nearly stagnant HFC-134a/HFC-23 (8-12 wt % HFC-23) on 4×13 (columns \times rows) staggered bundles of smooth tubes and finned tubes with Y-shape fins. Two columns at the center were active tubes and the other columns consisted of dummy tubes. For the finned tube, the average heat transfer coefficient was considerably lower than the previous results for HFC-134a (about a factor of 7) and the difference increased with decreasing condensation temperature difference. Comparison of the smooth and finned tubes revealed that the heat transfer coefficient was about the same at a small condensation temperature difference (around 6 K). For the finned tube, the heat transfer coefficient increased significantly with increasing condensation temperature difference. For the smooth tube, on the other hand, it decreased slightly with increasing condensation temperature difference.

The objective of the present study is to obtain a better understanding of the heat transfer characteristics during condensation of a downward-flowing zeotropic mixture on a staggered bundle of horizontal low finned tubes. Row-by-row experimental data were obtained for a standard low-finned tube with HCFC-123/HFC-134a (about 9 wt % HFC-134a) as a test fluid. This mixture is suited to study the effect of vapor-phase mass transfer resistance on the condensation heat transfer, because it shows

Contributed by the Heat Transfer Division for publication in the JOURNAL OF HEAT TRANSFER. Manuscript received by the Heat Transfer Division, Aug. 1, 1997; revision received Oct. 2, 1998. Keywords: Condensation, Finned Surfaces, Mass Transfer. Associate Technical Editor: M. Sohal.



- | | | |
|------------------------------|------------------------|--------------------|
| 1. Boiler | 7. Dump condenser | 14. Inverse U-tube |
| 2. Superheater | 8. Condensate receiver | manometer |
| 3. Calming section | 9. Chilling unit | 15. Feed pump |
| 4. Test section | 10. Cooling water tank | 16. Mixing chamber |
| 5. Drain separator | 11. Feed pump | 17. Pressure gauge |
| 6. Condensate measuring tube | 12. Circulation tank | 18. Rotameter |
| | 13. Orifice | 19. Vacuum pump |

Fig. 1 Schematic diagram of experimental apparatus

a large temperature difference (11 to 20 K) between the dew point and the boiling point for the experimental conditions described in the next section. The results were compared with those for HCFC-123 and previous results for HFC-134a (Honda et al., 1995b).

Experimental Apparatus and Procedure

The experimental apparatus, which consisted of a natural circulation loop of HCFC-123/HFC-134a and a forced circulation loop of cooling water, is schematically shown in Fig. 1. It was basically the same as those used in the previous studies for CFC-113 (Honda et al., 1991 and 1992), HCFC-123 (Honda et al., 1995a), and HFC-134a (Honda et al., 1995b). The experimental apparatus was thermally insulated using insulating materials made of glass fiber and urethane foam. The test section was a 3×15 (columns \times rows) staggered bundle of horizontal tubes. The test tube was a standard low-finned tube made of

Table 1 Dimensions of test tube

Tube diameter at fin tip d	15.6 mm
Tube inside diameter	11.2 mm
Effective tube length l	100 mm
Fin pitch	0.96 mm
Fin spacing at fin tip	0.72 mm
Fin height	1.43 mm
Fin half-tip angle	0.082 rad

copper. The dimensions of the test tube are listed in Table 1. A 9-mm-i.d. rod made of PVC was inserted concentrically in the test tube to enhance the coolant side heat transfer. The tube bundle was assembled in a vertical duct with inner dimensions of $66 \times 100 \text{ mm}^2$, as shown in Fig. 2. Both the horizontal and vertical tube pitches were 22 mm. The odd rows consisted of three active tubes, while the even rows consisted of two active tubes and dummy half tubes on the duct walls.

The vapor pressure at the tube bundle inlet was measured by a precision Bourdon tube gage. The local vapor and condensate temperatures just upstream and/or downstream of each row were measured by T-type thermocouples inserted in the test section. A shield and a gutter were attached just above and below the thermocouples that were used for the measurements

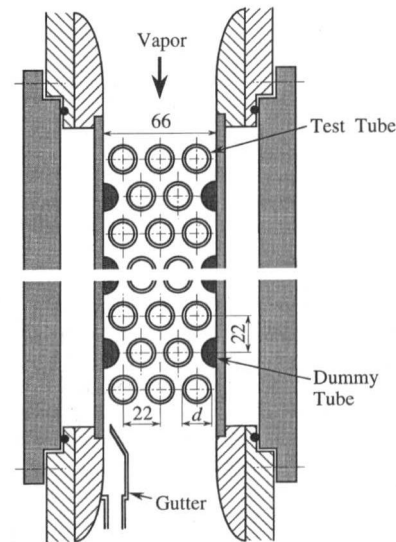


Fig. 2 Cross-sectional view of test section

Nomenclature

A = cross-sectional area of duct
 c_D = drag coefficient
 D = diffusion coefficient
 d = tube diameter at fin tip
 G = mass velocity of refrigerant based on maximum flow cross section
 h = specific enthalpy
 k = number of condensing tubes in a horizontal row
 l = effective tube length
 \dot{m} = condensation mass flux
 n = vertical row number counted from top row
 p = vapor pressure
 Q = heat transfer rate for a horizontal row
 Q_i = heat loss for a horizontal row

q = average heat flux for a horizontal row
 Re_v = vapor Reynolds number based on minimum flow cross-section = $\zeta G x d / \mu_v$
 Sc_v = Schmidt number of vapor
 Sh = Sherwood number = $\beta d / D$
 T = temperature
 T_w = average wall temperature at fin root for a horizontal row
 ΔT = condensation temperature difference = $T_v - T_w$
 x = quality
 y = mass fraction of more volatile component
 α = average heat transfer coefficient for a horizontal row

α_s = average heat transfer coefficient for a condensate film
 β = average mass transfer coefficient for a horizontal row
 ζ = ratio of maximum and minimum flow cross sections
 μ = dynamic viscosity
 ρ = specific density
 ω = dimensionless parameter = $(y_v - y_{ii}) / (y_{vi} - y_{ii})$

Subscripts

c = cooling water
 i = interface
 l = condensate
 n = n th row
 v = vapor

of the vapor and condensate temperatures, respectively. The cooling water temperatures at the inlet and outlet of each tube row were measured by two-junction thermopiles inserted in mixing chambers. All thermocouples and thermopiles were carefully calibrated by using a precision constant water bath and a standard resistance thermometer. The readings were repeated ten times consecutively and they were recorded by a programmable data logger to $1 \mu\text{V}$ for the thermocouples and to $0.1 \mu\text{V}$ for the thermopiles. Then the average values of the ten measurements were adopted as the experimental data.

The tube wall temperature was measured by the resistance thermometry. The test tubes were electrically insulated from the duct wall and voltage taps were soldered at both ends of 100-mm long condensing sections. Thirty-eight test tubes and a standard resistor of $1 \text{ m}\Omega$ were connected in series to a 40 A DC current supply to measure the voltage drops. Preliminary experiments were conducted to obtain the calibration curves for the temperature-resistance relation of each test tube and the heat loss to the environment from the tubing between the inlet and outlet mixing chambers of each tube row Q_l . The test section was evacuated using a vacuum pump to minimize heat loss from the tube surface. Then water at a prescribed temperature was passed through the test tubes. The thermopile outputs and the voltage drops of the test tubes and the standard resistor were read five times consecutively and recorded by a programmable data logger to $0.1 \mu\text{V}$. In order to avoid the effect of parasitic voltage on the measured voltage drops, the readings were repeated another five times after reversing the DC current. Then the average values of the ten measurements were adopted as the experimental data. The cooling water flow rate for each tube row was measured by an orifice and an inverse U-tube manometer. For the measurement of the temperature-resistance relation, the water flow rate was kept at a high value so as to minimize the temperature drop of water between the inlet and outlet mixing chambers ($<0.05 \text{ K}$) and the wall temperature was assumed to be equal to the average value of the measured water temperatures. For the measurement of Q_l , the water flow rate was kept at a low value so as to obtain a relatively large water temperature variation between the inlet and outlet mixing chambers ($\approx 0.2 \text{ K}$). The value of Q_l , which was obtained from the flow rate and temperature variation of water, was plotted as a function of the temperature difference between the water and the ambient air. The calibration curve for the heat loss to the environment from the boiler, the vapor supply duct and the test section was also obtained by a preliminary experiment. The refrigerant loop was shut at the outlet of the test section by using a brass plate. The valve at the inlet of the boiler was also closed. Then a low electric power was supplied to the boiler. After a steady-state was reached, the temperatures of vapor in the test section and ambient air were measured. The temperature difference between the vapor and the ambient air increased linearly with the electric power input. It was found that the heat loss was less than 350 W for the experimental conditions described below.

The local composition of refrigerant vapor in the tube bundle was measured by a gas chromatograph. Sampling probes made of a 1.5-mm-o.d. stainless steel tube were inserted just upstream of the odd rows. A shield was attached just above the tip of the probe to avoid sampling of condensate. The probes were connected to buffer tanks of the gas chromatograph via small containers for storing vapor samples. Stop valves were attached to the tubing at the inlet and outlet of each container. The tubing was heated to prevent condensation of vapor. Before sampling the vapor, the valve at the inlet of each container was closed and the tubing was evacuated using a vacuum pump. Then the valve at the outlet of the container was closed and the gas sample was introduced into each container by opening the valve at the inlet. Then the valve at the inlet was closed. The gas samples were introduced to the buffer tanks just before the measurement started. Measurements were repeated twice start-

ing from the first row. The calibration curve for the relation between the mass fraction and the peak area ratio of the chromatogram was obtained by preliminary experiments using gas samples with known mass fractions.

The wall temperature measured by the resistance thermometry is considered to be a kind of average temperature of the test tube. The contribution of fins to the electrical resistance of the tube was estimated by using the thermal conductance data for infinite plates with repeated rectangular grooves normal to the heat flow on one side of the plate (Schneider, 1985). The results indicated that the difference in the electrical resistance between the finned tube and a superficial smooth tube obtained by cutting off the fins was about five percent. It was also revealed that the fin efficiency was about 99 percent. Thus the measured wall temperature was assumed to be equal to the average temperature of the superficial smooth tube and the wall temperature at fin root was obtained from the measured value making a small correction ($\leq 0.1 \text{ K}$) for the wall conduction for one half of the tube thickness.

Experiments were performed at the inlet vapor temperature $T_{v,\text{in}}$ of about 50°C , and the inlet vapor mass fractions of HFC-134a, $y_{v,\text{in}}$, of zero and about nine percent. The vapor pressure at the tube bundle inlet was about 209 and 246 kPa for $y_{v,\text{in}} =$ zero and nine percent, respectively. In order to attain a dry saturated condition at the tube bundle inlet, the superheater was switched off. The refrigerant mass velocity G (based on the duct cross section) was changed in three steps (10, 20, and 34 $\text{kg/m}^2\text{s}$) by changing the power input to the boiler from 10 to 35 kW. This corresponded to the range of Re_v at the tube bundle inlet of 4.1×10^4 to 1.4×10^5 . The condensation temperature difference $\Delta T = T_v - T_w$ was changed in four steps from 3 to 12 K, where T_v is the local vapor temperature and T_w is the arithmetic average of wall temperatures at the fin root for two or three active tubes in a horizontal row. It is relevant to note here that for the mixture, the value of T_v decreased as condensation proceeded. The variation of T_v in the tube bundle ranged from 1.2 to 12 K depending on the operating condition. Hence it was impossible to maintain a constant ΔT for all tube rows. The value of ΔT described in this paper is the nominal value that applies to the upper rows. The maximum variation among the ten temperature measurements ranged to 0.2 K for T_v , 0.5 K for the condensate temperature T_l and the tube wall temperature, and 0.04 K for the cooling water temperature. These results indicate an unsteady nature of condensation phenomena in the tube bundle. Considering the measurement procedure and the temperature variation described above, the uncertainties in the time average values of T_v and T_w are estimated to be within 0.05 and 0.1 K, respectively. The measured wall temperatures of the two or three tubes in the same horizontal row increased in the direction of coolant flow. The tube-by-tube variation in the wall temperature ΔT_w was less than 18 percent of the condensation temperature difference for the first to the 14th rows. However, the $\Delta T_w/\Delta T$ ratio ranged from 27 to 76 percent for the 15th row. Thus the experimental data for the last row were affected considerably by the tube-by-tube variation of the wall temperature.

The average heat flux q and the average heat transfer coefficient α for a horizontal row are, respectively, defined on the projected area basis as

$$q = (Q + Q_l)/k\pi dl, \quad (1)$$

$$\alpha = q/\Delta T \quad (2)$$

where Q is the heat transfer rate calculated from the temperature rise and flow rate of the cooling water, Q_l is the heat loss to the environment, k is the number of condensing tubes in a horizontal row ($=2$ or 3). The temperature rise of the cooling water was kept within the range of 1 to 3.3 K by adjusting the flow rate. The value of Q ranged from 76 to 906 W, and that of Q_l from 1 to 7 W. The Q_l/Q ratio was less than four percent.

The heat generation at each tube as a result of the thermometry current was about 0.1 W. The uncertainty in the measured value of q was estimated to be within five percent, and that of ΔT within five percent for $\Delta T \geq 3$ K. Thus the uncertainty in α is estimated to be within seven percent for $\Delta T \geq 3$ K.

The heat balance and the mass balance for the n th row are, respectively, written as

$$GA[h_v x + h_l(1-x)]_n = (Q + Q_l)_n + GA[h_v x + h_l(1-x)]_{n+1} \quad (3)$$

$$y_{\text{vin}} = [y_v x + y_l(1-x)]_{n+1} \quad (4)$$

where A is the duct cross-sectional area, x is the quality, h_l and h_v are the specific enthalpies of falling condensate and bulk vapor, respectively, y_l and y_v are the mass fractions of falling condensate and bulk vapor, respectively, and subscript n for the refrigerant denotes the condition just upstream of the n th row. It is assumed that the mass fraction of condensate generated on each tube row is equal to the equilibrium liquid mass fraction y_{li} that corresponds to the liquid-vapor interface temperature T_i and pressure p . If no mixing is assumed between the condensate generated on each row and the falling condensate from the upper row, $y_{l,n+1}$ is given by

$$y_{l,n+1}(1-x_{n+1}) = \sum_{j=1}^n y_{li,j}(x_j - x_{j+1}) \quad (5a)$$

On the other hand, if a complete mixing of condensate is assumed at each tube row, $y_{l,n+1}$ is given by

$$y_{l,n+1} = y_{li,n} \quad (5b)$$

The actual value of $y_{l,n+1}$ is supposed to lie in between those given by Eqs. (5a) and (5b). The interfacial temperature T_i was obtained from the following equation:

$$q = \alpha_s(T_i - T_w) \quad (6)$$

where α_s is the heat transfer coefficient for the condensate film. The value of α_s was estimated by using a dimensionless correlation of experimental data for HCFC-123 and HFC-134a (Honda et al., 1995b) that were obtained by using the same experimental apparatus. The dimensionless correlation had the form $\alpha_s/\alpha_{Nu} = f(\text{Re}_v, n)$, where α_{Nu} denotes the prediction of the Nusselt (1916) equation for a horizontal smooth tube. The pressure drop in the tube bundle was obtained from the following equation (Fujii, 1983):

$$p_{n+1} = p_n + [(Gx)^2/\rho_v]_n - [(Gx)^2/\rho_v]_{n+1} - 2c_D \zeta^2 [(Gx)^2/\rho_v]_m \quad (7)$$

where ζ ($=3.44 - 3.55$) is the ratio of the maximum and minimum flow cross sections, c_D is the drag coefficient and subscript m denotes the mean value between the n th and $(n+1)$ th rows. The value of c_D was estimated from the experimental results for HCFC-123. The calculated value of pressure drop was less than 2.3 percent of the inlet pressure (about 2.45×10^5 Pa for the mixture). In the data reduction, the thermodynamic properties of the mixture were obtained from the SRK equation of state and an estimation program based on this equation (Takamatsu and Ikegami, 1990). The values of 0.275 and 0.319 recommended by Kubota et al. (1990) were used for the acentric factors for HCFC-123 and HFC-134a, respectively. The binary interaction parameter was determined to be 0.034 based on the phase-equilibrium data obtained by Kubota et al. (1991). The transport properties of the mixture were estimated from those of HCFC-123 and HFC-134a given in the JAR Data Book (1990) by using representative mixing rules recommended by Reid et al. (1987).

If it is assumed that the vapor is saturated and $x = 1$ at the tube bundle inlet, the values of x , y_l , y_v , T_i and p for a horizontal

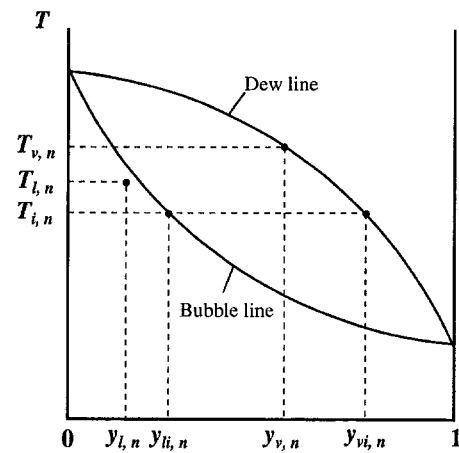


Fig. 3 Conditions of bulk liquid and vapor and equilibrium condition at condensate surface plotted on the phase diagram

row are obtained iteratively from Eqs. (3)–(7) with the known values of $(Q + Q_l)$, T_i , T_v and T_w , and the calculated values of x , y_l , y_v , y_{li} and p for the upper row. However, it was revealed that the calculated value of y_v was smaller than the equilibrium vapor mass fraction corresponding to T_v and p , with the difference increasing with the row number. This was probably due to the inaccuracy of the equation of state and the fact that the value of h_v was relatively insensitive to the variation of y_v . Hence a small error in the estimated value of h_v resulted in a large error in y_v . Thus, the vapor was assumed to be saturated at each tube row and the equilibrium vapor mass fraction corresponding to T_v and p was assumed for y_v instead of the value obtained from the foregoing procedure. This means that Eq. (4) was not used in the data reduction. The maximum difference in the calculated value of x between the two procedures was about five percent at the tube bundle exit.

The condensation mass flux \dot{m} and the vapor phase mass transfer coefficient β for each tube row are, respectively, defined on the projected area basis as

$$\dot{m} = \frac{GA\Delta x}{k\pi dl} \quad (8)$$

$$\beta = \frac{\dot{m}}{\rho_v(1-\omega)} \quad (9)$$

where $\omega = (y_v - y_l)/(y_{vi} - y_{li})$, y_{vi} is the equilibrium vapor mass fraction corresponding to the interfacial condition. It is relevant to note here that two values of β are obtained from Eq. (9) depending on the definition of y_l given by Eqs. (5a) and (5b). Experimental results showed that the difference between the two was small (less than nine percent). For the finned tube, in which active condensation occurs mainly at the thin film region near the fin tip, the actual value of y_l is considered to be close to that given by Eq. (5a).

Thus, in the following consideration is given to the value of β based on Eq. (5a). Figure 3 shows schematically the conditions of bulk liquid and vapor and the equilibrium condition at the surface of condensate film on the tube plotted on the phase diagram.

Experimental Results

Figure 4 shows an example of the distributions of measured and calculated quantities in the tube bundle. In Fig. 4(a), the distributions of T_v , T_l , T_i , T_w , and T_c are presented, where T_{v1} and T_{v2} denote the vapor temperatures measured at different positions in a tube row, and T_c the average cooling water temperature for a tube row. It is seen from Fig. 4(a) that T_v and

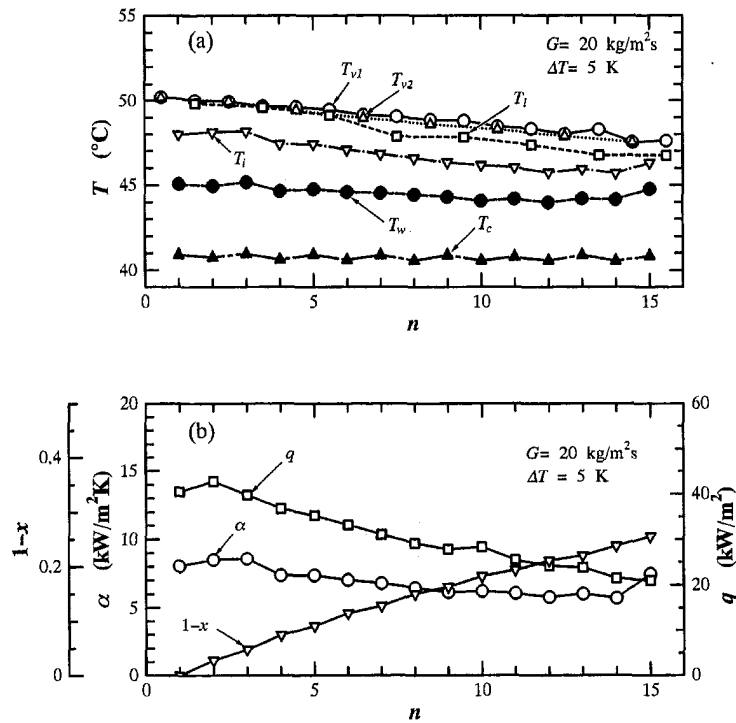


Fig. 4 Distribution of measured and calculated quantities in tube bundle

T_i decreases gradually with increasing n . This is due to the temperature glide associated with the progress of condensation. It is also seen that T_i is generally higher than T_v and is close to T_w for the upper rows. This indicates that the falling condensate is heated by the surrounding vapor. In Fig. 4(b), the distributions of q , α and $(1-x)$ are presented. It is seen from Fig. 4(b) that q and α takes the maximum values at $n = 2$ and $n = 3$, respectively. These values decrease with further increasing n and the value of α increases again at the last row. This is due to the increase in T_w at the last row observed in Fig. 4(a). It is not clear at present why α increased at the last row. In this connection it is relevant to note here that the experimental data for the last row was affected by a large row-by-row variation of the wall temperature.

Figure 5 compares the measured and calculated distributions of y_v in the tube bundle. In Fig. 5, three cases with the same G ($=20 \text{ kg/m}^2\text{s}$) and different ΔT are presented. Except for the first three data points for $\Delta T = 12 \text{ K}$, the measured y_v increases with the vertical row number n , with the increase being more

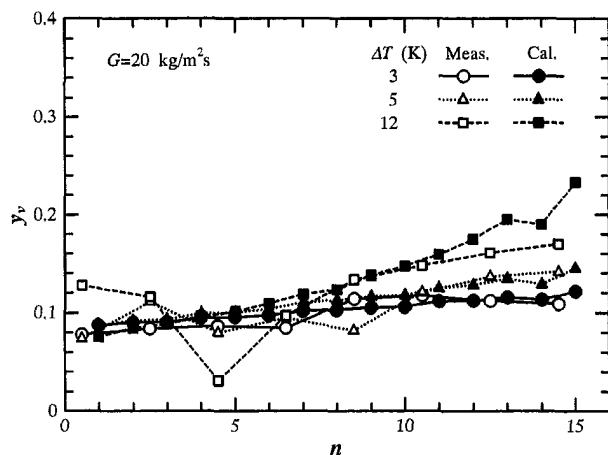


Fig. 5 Distribution of vapor mass fraction in tube bundle

significant for larger ΔT . It is also seen that the measured values agree fairly well with the calculated values. An irregular variation of the measured y_v observed for $\Delta T = 12 \text{ K}$ at the upper part of the tube bundle is probably due to the difficulty associated with the sampling of vapor.

Figure 6 shows α for the first row plotted as a function of ΔT with G as a parameter. The open and closed symbols show the cases of HCFC-123/HFC-134a and HCFC-123, respectively. In Fig. 6, experimental data for HFC-134a reported by Honda et al. (1995b) are also shown for comparison. The α value for the mixture is considerably lower than those for HCFC-123 and HFC-134a, and the difference between the mixture and pure refrigerants is more significant for smaller G . This is due to the increase in the vapor-phase mass transfer resistance for smaller G . For both cases of the mixture and pure refrigerants, α decreases as ΔT increases. However, the mixture shows a smaller dependence on ΔT than the pure refrigerants, and even shows an upturn at $\Delta T > 8 \text{ K}$ for $G = 10 \text{ kg/m}^2\text{s}$.

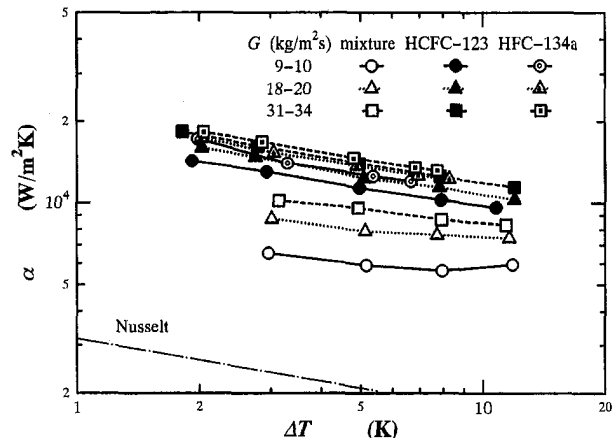


Fig. 6 Effect of condensation temperature difference on heat transfer coefficient; comparison of mixture and components

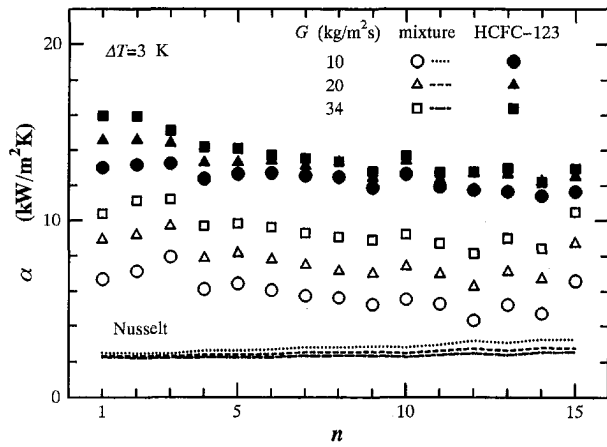


Fig. 7 Variation of heat transfer coefficient with vertical row number; comparison of mixture and HCFC-123 for different mass velocities

This may be due to the decrease in the mass transfer resistance as a result of the suction effect, which acts to thin the boundary layer thickness. Similar results are reported by Hijikata et al. (1989) for single tubes and by Signe et al. (1996) for the first row of finned tubes.

Figure 7 shows α plotted as a function of n with G as a parameter. The open and closed symbols show the cases of mixture and HCFC-123, respectively. Generally the effect of vertical row number is more significant for the mixture. For the mixture, the α value first increases with n up to the third row. Then it decreases gradually with further increasing n and then increases again at the last row. It is also seen that the α value for the mixture is smaller than that for HCFC-123, and the difference between the two is more significant for smaller G and larger n (except the last row). Four lines in Fig. 7 show the predictions of the Nusselt (1916) equation for a horizontal smooth tube. For the case of $G = 10 \text{ kg/m}^2\text{s}$, the α value for the mixture is only a little higher than the prediction of the Nusselt equation at the lower rows.

Figure 8 shows α plotted as a function of n with ΔT as a parameter. For both cases of the mixture and HCFC-123, α decreases as ΔT increases. However, the decrease is less significant for the mixture than for HCFC-123. It is also seen that for the mixture, the highest value of α is obtained at $n = 3$ for $\Delta T \leq 5 \text{ K}$ and at $n = 2$ for $\Delta T \geq 8 \text{ K}$.

Figure 9 shows the mass transfer coefficient β plotted as a function of n with G as a parameter. It is seen that the depen-

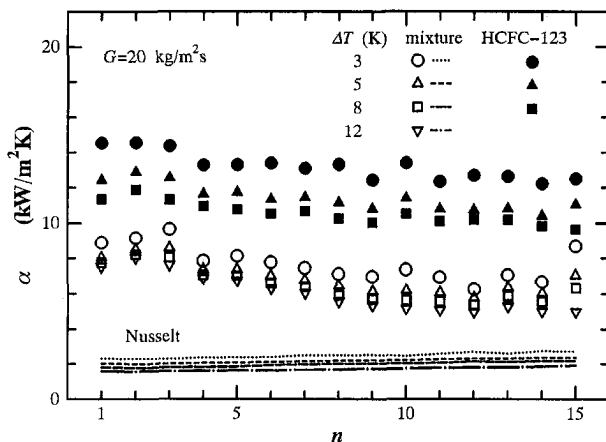


Fig. 8 Variation of heat transfer coefficient with vertical row number; comparison of mixture and HCFC-123 for different condensation temperature differences

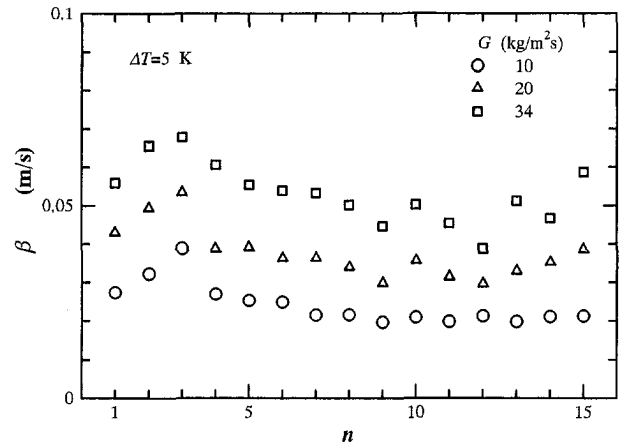


Fig. 9 Variation of mass transfer coefficient with vertical row number; effect of mass velocity

dence of β on n and G is basically the same as the case of α shown in Fig. 7. However, the effect of G is more significant for β than for α .

Figure 10 shows β plotted as a function of n with ΔT as a parameter. The data points are the same as those presented in Fig. 8. It is seen from Fig. 10 that β increases as ΔT increases. This is due to the effect of suction associated with condensation, which acts to thin the diffusion layer. This result is in contrast to the case of α shown in Fig. 8, where it decreases as ΔT increases.

The decrease in the heat transfer coefficient for the mixture compared to that for HCFC-123 as shown in Figs. 6–8 is due to the presence of diffusion layer in the vapor phase. Here we try to develop a dimensionless correlation for the mass transfer coefficient. Zukauskas (1972) proposed a correlation for forced convection heat transfer in a staggered bundle of smooth tubes. By use of the analogy between heat and mass transfer, this correlation may be transformed to the mass transfer correlation for the limiting case of $m \rightarrow 0$ as follows:

$$\text{Sh}_0 = a \text{Re}_v^{0.6} \text{Sc}_v^{0.36} \quad (10)$$

where $\text{Sh}_0 = \beta_0 d/D$, $\text{Re}_v = \zeta G x d / \mu_v$, β_0 is the mass transfer coefficient for $m \rightarrow 0$, and a is the proportionality constant. The value of a increases with n and is equal to 0.35 for $n \geq 10$. In the actual condensation process, the vapor phase mass transfer is subject to the effect of suction and β is greater than β_0 . According to the stagnant film model, β is related to β_0 by the following equation:

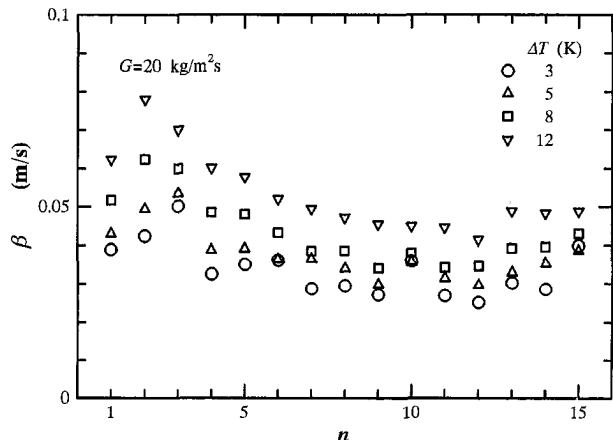


Fig. 10 Variation of mass transfer coefficient with vertical row number; effect of condensation temperature difference

$$\frac{Sh}{Sh_0} = \frac{1}{(1-\omega)} \ln\left(\frac{1}{\omega}\right) \quad (11)$$

where $Sh = \beta d/D$. For forced convection condensation of vapor-gas mixture on a cylinder, Rose (1980) proposed a theoretically based approximate expression for β . This expression may be extended to the present case as follows:

$$\frac{Sh}{Re_v^{0.6}} = \frac{b\{[1 + 2(1/\omega - 1) Sc_v^{0.36}]^{0.5} - 1\}}{(1-\omega)} \quad (12)$$

Also, Hijikata et al. (1989) proposed the following equation:

$$Sh = c(\rho_v/\rho_{vi})^{1/3}(1/\omega)^{1/3} Re_v^{0.6} Sc_v^{1/3} \quad (13)$$

Figure 11 shows Sh for the 4th to 14th rows plotted as a function of Re_v with ΔT as a parameter. The experimental data for the other rows are omitted because these data are supposed to include the entrance effect or the exit effect. In Fig. 11, three groups of experimental data are plotted for each ΔT , which correspond to the cases of $G = 10, 20,$ and $34 \text{ kg/m}^2 \text{ s}$, respectively. The solid line shows the relation $Sh \propto Re_v^{0.6}$. It is seen that Sh increases as ΔT increases and the data for each ΔT are roughly in accord with the above relation. At a small value of ΔT , however, the group of experimental data for each G shows a sharper increase in Sh than the solid line. This is due to the fact that the decrease in the condensation temperature difference relative to the nominal value of ΔT with increasing row number (i.e., decreasing Re_v) was more significant for smaller ΔT . At $\Delta T = 12 \text{ K}$, on the other hand, the experimental data for the lower rows show a smaller dependence on Re_v than the solid line. This may be ascribed to the fact that the measured values of y_v at the lower rows were smaller than the calculated value assuming the saturated condition (see Fig. 5).

Figure 12 shows β for the first to 14th rows plotted on the coordinates of $Sh/Re_v^{0.6}$ versus $1/\omega$. The experimental data for the 15th row were omitted because they were affected by a large wall temperature variation. It is relevant to note here that $1/\omega \rightarrow 1$ and $1/\omega \rightarrow \infty$ correspond to the limiting cases of $m \rightarrow 0$ and $m \rightarrow \infty$, respectively. In Fig. 12, closed triangles show the data for the first row, open triangles those for the second and third rows, and open circles those for the 4th to 14th rows. It is seen from Fig. 12 that the data for the second and third rows are considerably higher than those for the other rows. Except for several data points for the lower rows, the experimental data for the 4th to 14th rows may be correlated by the following equation:

$$Sh = 0.38(1/\omega) Re_v^{0.6} Sc_v^{0.36} \quad (14)$$

In Fig. 12, Eq. (14) is shown by the solid line. For the limiting

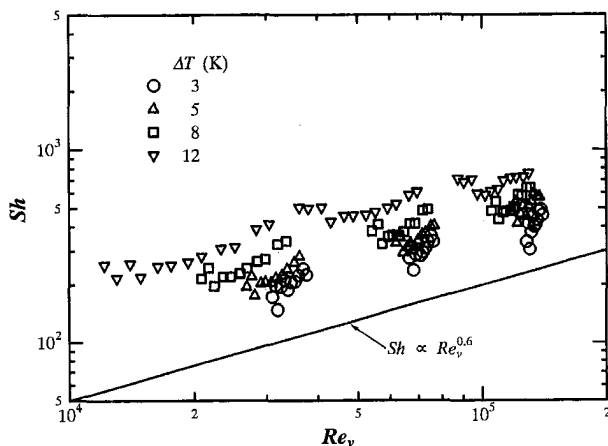


Fig. 11 Variation of Sherwood number with vapor Reynolds number; effect of condensation temperature difference

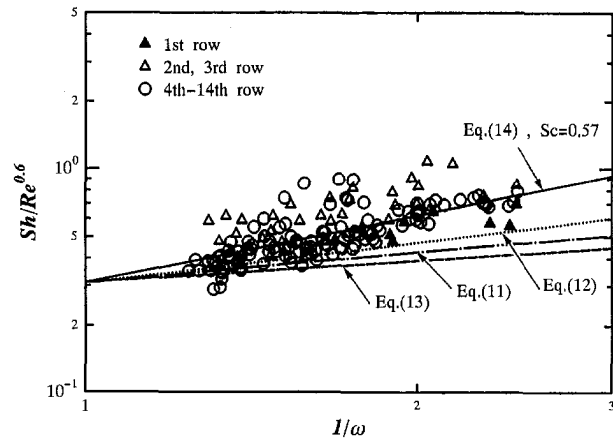


Fig. 12 Mass transfer data plotted on the coordinates of $Sh/Re_v^{0.6}$ versus $1/\omega$

case of $m \rightarrow 0$, Eq. (14) reduces to Eq. (10) with $a = 0.38$. This value of a is 1.09 times as large as that obtained from the analogy between heat and mass transfer for a staggered bundle of smooth tubes for $n \geq 10$. However, when β is evaluated on the actual surface area basis, a is reduced to 0.11 (about 32 percent of the latter). This indicates that for a finned tube, only a small part of the tube surface is effective for vapor phase mass transfer. This is probably due to the fact that condensate flow on the finned tube is affected by the surface tension forces and a very thin condensate film is formed only at a limited part of the tube surface. The chain, dotted and broken lines in Fig. 12 show Eqs. (11) to (13) in which a to c were adjusted to take the same $Sh_v/Re_v^{0.6}$ as the solid line at $1/\omega = 1$. Comparison of the four lines reveals that the present data are subject to a stronger effect of suction than Eqs. (11) to (13).

Concluding Remarks

Row-by-row experimental data were obtained for condensation of downward-flowing zeotropic refrigerant mixture HCFC-123/HFC-134a on a 3×15 (columns \times rows) staggered bundle of standard low-finned tubes. The measured distribution of the bulk vapor mass fraction in the tube bundle agreed fairly well with the equilibrium vapor mass fraction. As expected, the heat transfer coefficient for the mixture was lower than those for HCFC-123 and HFC-134a. The difference between the two cases was more significant for a lower mass velocity. The effect of condensation temperature difference on the heat transfer coefficient was less significant for the mixture than for the pure refrigerants. The heat transfer coefficient increased with the vertical row number up to the third (or second) row. Then it decreased gradually with further increasing row number and then increased again at the last row. The vapor phase mass transfer coefficient showed similar dependencies on the mass velocity and the vertical row number. However, contrary to the case of the heat transfer coefficient, the mass transfer coefficient increased with increasing condensation temperature difference. This was due to the effect of suction associated with condensation, which acted to thin the diffusion layer. The measured mass transfer coefficient (based on the projected surface area) was a little higher than that obtained from the analogy between heat and mass transfer for a staggered bundle of smooth tubes. The mass transfer coefficient was subject to a stronger effect of suction than the predictions of the previously proposed equations. Most of the experimental data for the 4th to 14th rows were correlated fairly well by Eq. (14).

Acknowledgments

The authors wish to thank Mr. Y. Sakamoto and Mr. Y. Takemae at the Interdisciplinary Graduate School of Engi-

neering Sciences, Kyushu University for their help in the experimental work. We would also like to thank Daikin Industries Ltd. for providing the test fluids.

References

- Ebisu, T., Toda, K., Okuyama, K., and Torikoshi, K., 1995, "Enhancement of Heat Transfer of Zeotropic Mixture HFC-32/125/134a," *Proc. 29th Air Conditioning and Refrigeration Joint Conference*, pp. 69–72.
- Fujii, T., 1983, "Condensation in Tube Banks," *Condensers—Theory and Practice*, Institution of Chemical Engineers Symposium Series No. 75, pp. 3–22.
- Hijikata, K., Himeno, N., and Goto, S., 1989, "Forced Convection Condensation of a Binary Mixture of Vapors," *Trans. JSME*, Vol. 55, pp. 3190–3198.
- Honda, H., Uchima, B., Nozu, S., Nakata, H., and Torigoe, E., 1991, "Film Condensation of R-113 on In-Line Bundles of Horizontal Finned Tubes," *ASME JOURNAL OF HEAT TRANSFER*, Vol. 113, pp. 479–486.
- Honda, H., Uchima, B., Nozu, S., Torigoe, E., and S. Imai, 1992, "Film Condensation of R-113 on Staggered Bundles of Horizontal Finned Tubes," *ASME JOURNAL OF HEAT TRANSFER*, Vol. 114, pp. 442–449.
- Honda, H., Takamatsu, H., Takada, N., and Makishi, O., 1995a, "Condensation of HCFC-123 in Bundles of Horizontal Finned Tubes: Effects of Fin Geometry and Tube Arrangement," *Int. J. Refrigeration*, Vol. 19, pp. 1–9.
- Honda, H., Takamatsu, H., Takada, N., and Yamasaki, Y., 1995b, "Condensation of HFC-134a and HCFC-123 in a Staggered Bundle of Horizontal Finned Tubes," *Proc. Eurotherm Seminar 47*, Elsevier, New York, pp. 110–115.
- JAR and JFGA, 1990, "Thermophysical Properties of Environmentally Acceptable Fluorocarbons—HFC-134a and HCFC-123," Japanese Association of Refrigeration.
- Kubota, H., Zheng, Q., Tanaka, Y., and Matsuo, S., 1990, "Vapor-Liquid Equilibria of the HCFC123 + HFC134a System under High Pressure," *Proc. 11th Japan Symposium on Thermophysical Properties*, Japan Society of Thermophysical Properties, pp. 465–468.
- Kubota, H., Zheng, Q., Zheng, X.-Y., and Makita, T., 1991, "High Pressure Vapor-Liquid Equilibria of the HFC134a + HCFC123 System," *J. Chemical Engineering Japan*, Vol. 24, pp. 659–661.
- Küster, M., and Kruse, H., 1986, "The Application of Non-Azeotropic Refrigerant Mixtures in Two Temperature Refrigerators," *Proc. IIR Commission B2 Meeting at Purdue*, pp. 47–53.
- Murloy, W., Kauffeld, M., McLinden, M., and Didion, D., 1988, "An Evaluation of Two Refrigerant Mixtures in a Breadboard Air Conditioner," *Proc. IIR Commissions B1, B2, E1, E2 Meetings at Purdue*.
- NEDO, 1993, "Research and Development on Super Heat Pump Energy Accumulation System, Final Report," New Energy and Industrial Technology Development Organization, Japan.
- Nusselt, W., 1916, "Die Oberflächenkondensation des Wasserdampfes," *Zeit. Ver. Deut. Ing.*, Vol. 60, pp. 541–546; 569–575.
- Reid, R. C., Prausnitz, J. M., and Poling, B. E., 1987, *The Properties of Gases and Liquids*, 4th Ed., McGraw-Hill, New York.
- Rose, J. W., 1980, "Approximate Equation for Forced-Convection Condensation in the Presence of a Non-Condensing Gas on a Flat Plate and Horizontal Tube," *Int. J. Heat Mass Transfer*, Vol. 23, pp. 539–546.
- Schneider, P. J., 1985, "Conduction," *Handbook of Heat Transfer Fundamentals*, W. M. Rohsenow et al., eds., McGraw-Hill, New York, pp. 4.1–4.187.
- Signe, J., Bontemps, A., and Marvillet, C., 1995, "Condensation of R134a/R23 Outside a Bundle of Smooth and Enhanced Surface Tubes," *Proc. Eurotherm Seminar 47*, Elsevier, New York, pp. 146–153.
- Takamatsu, H., and Ikegami, Y., 1990, "Program Package for Thermophysical Properties of Binary Mixtures by the SRK Equation of State," *Reports of Institute of Advanced Material Study*, Kyushu Univ., Vol. 4, pp. 39–46.
- Uchida, M., Itoh, M., and Kudoh, M., 1994a, "Enhanced Heat Transfer in Horizontal Tubes for a Zeotropic Refrigerant Mixture by Improved Inner Surface Configuration (1)," *Proc. JSME Thermal Engineering Conference '94*, JSME, pp. 227–229.
- Uchida, M., Itoh, M., and Kudoh, M., 1994b, "Enhanced Heat Transfer in Horizontal Tubes for a Zeotropic Refrigerant Mixture by Improved Inner Surface Configuration (2)," *Proc. JSME Thermal Engineering Conference '94*, JSME, pp. 230–232.
- Zukauskas, A., 1972, "Heat Transfer from Tubes in Crossflow," *Advances in Heat Transfer*, Vol. 8, Academic Press, San Diego, CA, pp. 93–160.

A. Ito

Department of Production System Engineering,
Oita University,
Oita 870-11, Japan

A. Narumi

Department of Mechanical Engineering,
Kanagawa Institute of Technology,
1030 Shimo-Ogino, Atsugi,
Kanagawa 243-02, Japan

T. Konishi

Department of Mechanical Engineering,
Oita National College of Technology,
1666 Maiki Oita 870-01, Japan

G. Tashtoush

K. Saito¹

Mem. ASME

C. J. Cremers

Fellow ASME

Department of Mechanical Engineering,
University of Kentucky,
521 CRMS Building,
Lexington, KY 40506

The Measurement of Transient Two-Dimensional Profiles of Velocity and Fuel Concentration Over Liquids

We recently developed two different optical techniques in order to simultaneously measure transient two-dimensional profiles of velocity, temperature, and fuel concentration that were generated by a spreading flame over liquid fuels. One technique employs a particle-track system combined with a laser-sheet system (LSPT) and a high-speed camera, while the other technique employs dual wavelength holographic interferometry (DWHI). The LSPT system revealed transient two dimensional profiles of flame-induced flow, while DWHI revealed two-dimensional profiles of fuel concentration over liquids. In this paper we present a series of velocity profiles for a pulsating flame spread over 1-propanol and concentration profiles for gaseous 1-propanol determined with LSPT and DWHI, respectively.

Introduction

The phenomenon of flame spread over liquids is of current interest because of its importance to fire safety and the curiosity of combustion researchers about the fundamental mechanism of the flame spread. Ross (1994) and Hirano and Suzuki (1993) published an excellent review of the literature on this problem. Williams (1985) provided the theoretical background of the problem. All those studies discussed many of the problems that need to be investigated.

The present paper is a continuation of our previous studies on flame spread over liquids (Ito, Masuda, Saito, 1991; Ito, Saito, and Cremers, 1995; and Tashtoush, Narumi, Ito, Saito, and Cremers, 1996). In these studies we applied holographic interferometry (HI) to obtain a detailed and instantaneous temperature distribution in the liquid phase near the fuel surface. In each of methanol, ethanol, and 1-propanol we found subsurface-liquid convection in both the uniform spread and pulsating spread regions. To understand the mechanisms of flame spread in both regions, researchers tried to identify the heat transfer process occurring between the flame's leading edge and the liquid, whether it occurs through the gas phase, liquid phase, or both. When the liquid convection is produced and it travels ahead of the flame's leading edge, the flame spread is likely to be controlled by it because the convection carries the high-temperature liquid ahead of the flame's leading edge. This enhances evaporation of liquid vapor resulting in the

formation of a flammable mixture of fuel and air through which the flame can spread. If there is no liquid convection ahead of the flame's leading edge, the major heat transfer can occur between the flame's leading edge and the liquid by conduction and by radiation in the gas phase because conduction through the liquid is negligible (Glassman and Dryer, 1981).

However, the proposed mechanism for the uniform spread is questionable, because the gas-phase conduction may not transfer sufficient heat for the flame to spread at a rate of nearly 10 cm/s. Liquid convection is unique to flame spread over liquids and it complicates the spreading process in comparison to flame spread over solids, which have no condensed phase convection (Williams, 1985). Thus, it is important to accurately measure temperature and velocity profiles in the liquid phase. Akita (1972) was the first researcher to apply a shadowgraph technique to visualize the liquid convection. He reported the formation of liquid convection in the pulsating region, but no liquid convection in the uniform spread region. Based on Akita's data, Glassman and Dryer (1981) proposed that the uniform spread is controlled by heat conduction through the gas phase, while in the pulsating region the liquid convection plays an important role.

To solve this problem, we developed an HI system to measure the transient temperature of the liquid (Ito, Masuda, and Saito, 1991). The response time of our HI system was less than 1 microsecond. We estimate the uncertainty of the spatial resolution to be 0.1 mm, and the temperature resolution to be $\pm 0.1^\circ\text{C}$ (Ito, Masuda, and Saito, 1991). Using the HI system, we observed a large liquid convection both in the uniform and pulsating spread regions. The liquid convection in the uniform spread region was a surprise because the head of the liquid convection preceded the flame's leading edge by approximately 1 cm (Ito, Masuda, and Saito, 1991), which was entirely different from Akita's result

¹ To whom correspondence should be addressed. e-mail: saito@engr.uky.edu.

Contributed by the Heat Transfer Division for publication in the JOURNAL OF HEAT TRANSFER and presented at '97 IMECE. Manuscript received by the Heat Transfer Division, Feb. 25, 1998; revision received, Oct. 15, 1998. Keywords: Fire, Flame, Heat Transfer, Laser, Measurement Techniques. Associate Technical Editor: M. Kaviany.

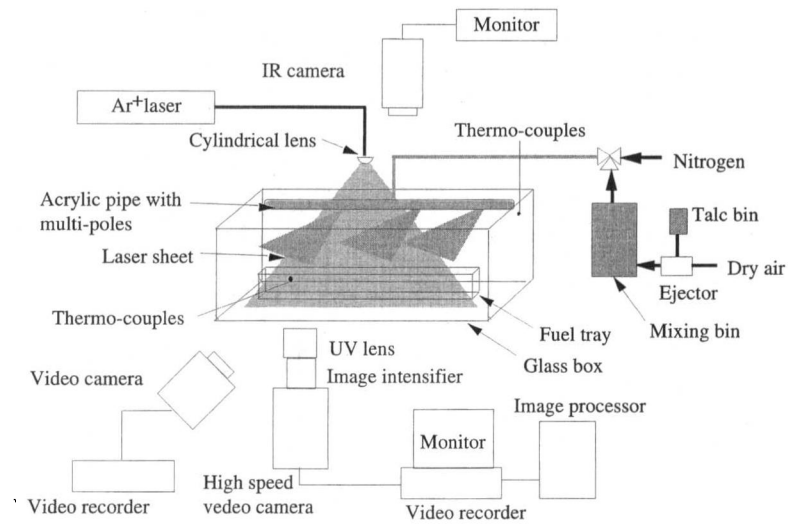


Fig. 1 Experimental apparatus of the particle-track laser-sheet (LSPT) system

(1972). To make sure of the accuracy of the data, we repeated the experiments several times and found the reproducibility to be within 90 percent. Based on our experiments, we propose a new mechanism: that the flame spread in the uniform spread region is governed by the liquid convection (Ito, Masuda, and Saito, 1991). However, at that time we did not fully understand why Akita's shadowgraph results were so different from our HI results.

Later, Howard Ross' group at NASA Lewis Research Center applied Rainbow Schlieren Deflectometry (RSD) to measure liquid convection generated by the spreading flame (Miller and Ross, 1992). They found little liquid convection ahead of the flame's leading edge in the uniform spread region. Their RSD data were similar to Akita's shadowgraph data and they disagreed with our HI results. Over the past three years, both NASA and our group tried to understand the reasons for the disagreement, but were unsuccessful until a series of parametric experiments were undertaken. In those experiments, the effects of six different parameters were investigated: sensitivity of both RSD and HI systems, purity of the 1-propanol, relative humidity of the air, ambient air temperature, type of ignition method, and finally different tray widths. We found that the first five parameters had little influence on the disagreement. However, when we checked the effect of tray width (0.5, 1, and 2 cm) on the liquid convection, the least suspected parameter, a surprising result emerged: The 0.5 cm wide tray had a large liquid convection in the uniform spread region, while the 1 cm and 2 cm wide trays had a thin layer of liquid convection. It was so thin and small that only a very sensitive measurement technique could detect it. The result for the 2-cm tray was very similar to NASA's result for the 2-cm tray. A closer look at their RSD result also revealed a small and thin layer of liquid convection that was always ahead of the flame's leading edge. Comparison of these findings led us to agree that in the uniform spread region there is always a small liquid convection indicating that the major heat transfer is by that mode. It also became clear that the shadowgraph (Akita, 1972) did not detect the liquid convection because the size of the liquid convection was too small and beyond the limitation of the spatial resolution of the shadowgraph. Later we applied the shadowgraph technique and proved this explanation.

The validity of this new mechanism has already been proven for the tray that is 0.5 cm wide (Ito, Masuda, and Saito, 1991) and extended to one that is 4 cm wide. Beyond that width there are no experimental data. We are continuing a series of flame-spread experiments using 0.5, 1, 2, 4, and 10-cm wide trays under normal gravity.

The Current Problem. NASA's microgravity test results showed that pulsating spread did not occur in either shallow or

deep pool experiments (Ross, 1994); instead the flame was extinguished, indicating the importance of the buoyancy effect in the gas phase on the mechanism of pulsation. Schiller and Sirignano, using numerical calculations (1992), predicted the existence of a very small circulation in the gas phase ahead of the flame's leading edge. They suggested that the gas-phase circulation, which is unique in the pulsating spread and appears with the liquid-phase circulation, may play an important role in flame pulsation (Schiller and Sirignano, 1992, 1996). There are flow measurement data obtained with Laser-Doppler Velocimetry (LDV) by Santoro et al. (1978) showing a gas-phase circulation of approximately 1-cm diameter in the pulsating spread region. However, their LDV result is rather a qualitative indication of the formation of circulation.

To confirm the prediction (Schiller and Sirignano, 1992, 1996) and understand the role of the small gas-phase circulation in the flame pulsation, transient velocity profiles in the gas phase just above the liquid surface and just ahead of the flame's leading edge must be measured. These measurements are not easy, because the rate of flame spread varies from a few centimeters to a few tens of centimeters per second at the target region, while the region where detailed velocity profiles are needed is approximately a few mm in diameter.

Previously we learned that LDV was not sufficiently accurate for our measurements (Venkatesh, Ito, Saito, and Wichman, 1996). Instead we used Laser Sheet Particle Tracking (LSPT) technique to measure flow profiles in two-dimensional with a spatial resolution on the order of a millimeter in the primary anchoring region of a

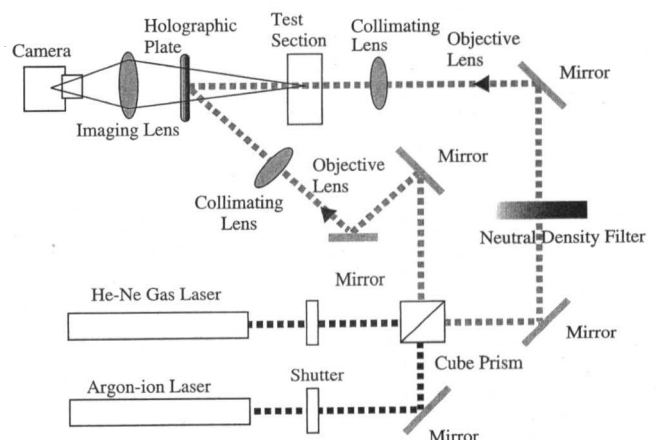


Fig. 2 A schematic of the DWHI system

small pool fire. Based on that experience, we applied the LSPT technique to measure a time series of detailed velocity profiles in the pulsating spread region and successfully confirmed the formation of a small circulation in approximately the same location as predicted by the UCI numerical model (Schiller and Sirignano, 1992). We also confirmed, in agreement with the model prediction, that the formation of a small circulation appears only in the pulsating spread region.

Experimental Apparatus and Procedures

Flame-Spread Apparatus. The Flame-spread apparatus (Fig. 1) used for this study is essentially the same as that used in a previous flame-spread studies (Ito, Masuda, and Saito, 1991; Ito, Saito, and Cremers, 1995; and Tashtoush, Narumi, Ito, Saito, and Cremers, 1996). A Pyrex tray of 2-cm wide \times 2.5-cm deep \times 25-cm long was used. The two long sides of the fuel tray were made of Pyrex of 0.2-cm thickness. The entire liquid tray was enclosed in a glass cell, 14-cm high \times 15-cm wide \times 35-cm long, to minimize laboratory draft and provide a repeatable flame-spread condition. The temperature of fuel was measured by placing a chromel-alumel thermocouple with 75- μ m wire diameter that was placed at the center of the tray 2 mm below the fuel surface. The temperature of ambient air was measured near the glass sidewall by the same type of the thermocouple used in the above. An ejector-nozzle was added to the previously developed particle feeder (Venkatesh, Ito, Saito, and Wichman, 1996) so that talc particles could uniformly disperse over the liquid surface. The uniformity of particle distribution was checked visually. An infrared (IR) camera and thermal imaging system that were developed during our previous upward flame-spread experiments (Qian, Ishida, and Saito, 1994) were applied to measure the two-dimensional temporal map of the liquid-surface temperature. A Sony video camera was used to record the entire flame-spread process.

To compare our data with NASA's microgravity data (Ross, 1994; and Miller and Ross, 1992) and our previous experiments (Ito, Masuda, and Saito, 1991; Ito, Saito, and Cremers, 1995; and Tashtoush, Narumi, Ito, Saito, and Cremers, 1996), 1-propanol was used as fuel. The fuel was uniformly ignited at one end by a small pilot flame. High-pressure nitrogen was supplied from a nitrogen cylinder to extinguish the flame.

Velocity Measurement With LSPT and Visualization of Flame-Induced Air Flow With a Smoke-Trace Technique (STT). From our previous studies (Qian, Ishida, and Saito, 1994; and Hirano and Saito, 1995), we learned that a LSPT technique with a high-speed video camera (500 frames/s with a shutter speed of 0.2 ms) best served our purpose. With significantly fewer particles, the LSPT can measure two-dimensional profiles of both streamlines and velocity simultaneously. A high-speed camera with an ultraviolet lens and an image intensifier was used to obtain the velocity of particles with 500 frames/s speed. Using an Ar-Ion (4 W) laser with a beam stabilizer and a cylindrical lens, a 0.8-mm thick sheet of laser light with an approximately 45-deg opening

Table 1 Uncertainty estimates for LSPT

precision	Laser sheet thickness	negligible
	Image processing discreteness	6%
	Time	negligible
	Total	6%
bias	Laser sheet thickness	negligible
	Image processing discreteness	6%
	Time	negligible
	Total	6%
Uncertainty	Total	8.5%

Table 2 Uncertainty estimates for DWHI

precision	Wavelength	negligible
	Fringe shift number	5%
	Pathlength	negligible
	fuel vapor density	negligible
	Gladstone-Dale constant	negligible
	Molecular weight	negligible
	Total	5%
bias	Wavelength	negligible
	Fringe shift number	negligible
	Pathlength	15%
	fuel vapor density	2%
	Gladstone-Dale constant	negligible
	Molecular weight	negligible
	Total	15.1%
Uncertainty	Total	15.8%

angle was established (Fig. 1) and guided by an optical fiber to the place where the measurement was to be done.

Velocity profiles of the liquid and gas convection were measured independently using LSPT. For the measurement of gas-phase convection, talc particles were dispersed uniformly above the fuel surface. For the measurement of liquid convection, aluminum particles of 15 (± 5) μ m diameter were sprinkled onto the liquid surface. Some aluminum particles floated on the liquid surface and others entered into the liquid. The aluminum particles used each weighed less than 0.01 grams so that the particles had little effect on the fuel properties.

The trajectories of these particles were recorded by a high-speed video camera that was connected to a video system and a TV monitor for the real-time observation of both flow field and spreading flame. In order to construct a single two-dimensional flow-vector diagram by combining the independently obtained gas-phase LSPT and liquid-phase LSPT, a smoke-trace technique (STT) was applied to visualize the overall structure of flame-induced air flow in the gas phase and liquid convection in the liquid phase simultaneously. The glass container enclosing the flame-spread tray was filled with incense smoke. The tray was filled with 1-propanol and the fuel was seeded with the small aluminum particles as used for the earlier LSPT measurements. After a uniform smoke layer was formed above the liquid surface the fuel was ignited.

Dual Wavelength Holographic Interferometry (DWHI).

The basic principles behind DWHI are the same as those for the single HI (Ito, Masuda, and Saito, 1991; Ito, Saito, and Cremers, 1995; and Tashtoush, Narumi, Ito, Saito, and Cremers, 1996). A schematic of DWHI is shown in Fig. 2. DWHI is an indirect measurement technique with a response time of less than a microsecond and a spatial resolution of less than ± 0.1 mm in identifying concentration difference. The DWHI has significant advantages over the micro-sampling technique (Saito, Williams, and Gordon, 1986), which has a spatial resolution of several millimeters and a response time that is at best on the order of a second. In addition, the micro-sampling is a direct gas sampling technique that will cause a large physical disturbance in the flow field.

We start using a two-dimensional model of DWHI in the present study and experimentally determined the best possible two-dimensional condition for the measurement. The basic principles of DWHI are detailed in Spatz and Poulidakos (1992) and Ito, Narumi, Saito, and Cremers (1995). In general, the equations for the temperature and fuel concentration in DWHI are as follows:

$$T = \frac{3P(R_{\alpha\lambda 1}D_{\lambda 2} - R_{\alpha\lambda 2}D_{\lambda 1})}{2R(\delta_{\lambda 1}D_{\lambda 2} - \delta_{\lambda 2}D_{\lambda 1})} \quad (1)$$

$$C = \frac{\delta_{\lambda 2}R_{\alpha\lambda 1} - \delta_{\lambda 1}R_{\alpha\lambda 2}}{\delta_{\lambda 1}D_{\lambda 2} - \delta_{\lambda 2}D_{\lambda 1}} \quad (2)$$

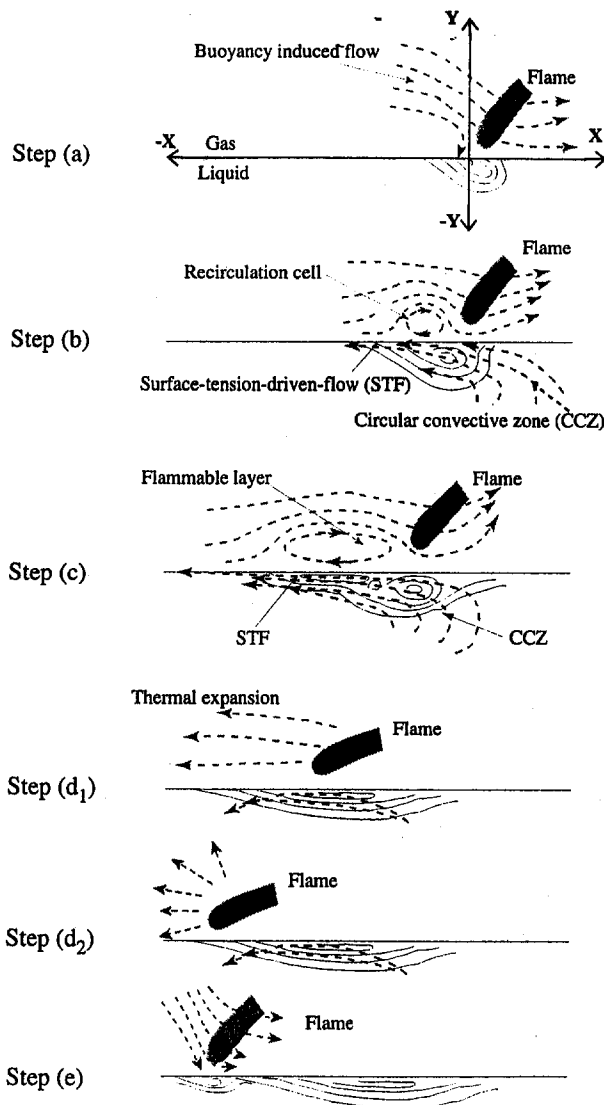


Fig. 3 Schematics of the pulsating flame spread

$$\delta = n - 1 \quad (3)$$

$$D = R_\beta - R_\alpha \quad (4)$$

where T = temperature, C = mole fraction of fuel vapor, P = pressure, R_o = universal gas constant; n = refractive index, R = molar refractivity of species, subscripts; λ_1 = wavelength of laser beam (1) (632.8-nm-He-Ne-laser beam), and λ_2 = wavelength of laser beam (2) (488-nm-Ar-Ion-laser beam), α = air, β = fuel. The DWHI method is susceptible to small errors because the Gladstone-Dale constants are only weak functions of wavelength. Applying DWHI to the flame-spread process, the path length (or tray width) must be determined to preserve the flame in two dimensions. Therefore, as the fringe difference between the two beams is very small, it is very difficult to perform a quantitative measure using the Eqs. (1) through (4). Consequently, we propose the single-wavelength method, which is shown in Eq. (5), to process the DWHI data:

$$C_i = \frac{\lambda_i N_i}{L \rho_\beta \left(\kappa_{\beta i} - \frac{M_\alpha}{M_\beta} \kappa_{\alpha i} \right)} \quad (5)$$

where λ = wavelength of laser beam, N = fringe-shift number, L = pathlength, ρ = density, κ = Gladstone-Dale constant, M =

molecular weight, subscripts $i = 1$ stands for the He-Ne laser beam, and $i = 2$ stands for Ar-ion laser beam.

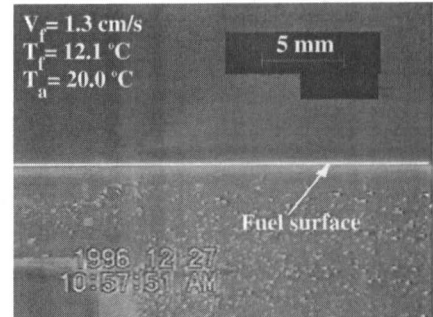
DW holograms contain holograms of two different wavelengths that need to be separated. We first recorded the DW holograms on a holographic plate. Then, during the printing process, two different filters were used to separate the two holograms. These filters have narrow band-pass widths, each passing the wavelength match to that of its respective laser beam.

Uncertainty Analysis

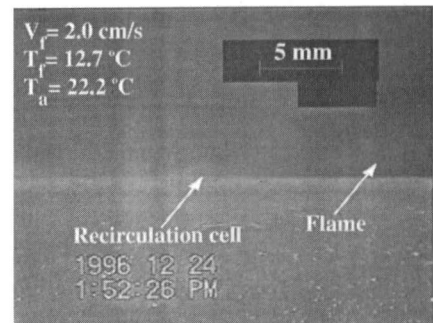
Uncertainty estimates were made for LSPT and DWHI using the method of Kline and McClintock (1953).

LSPT: Uncertainties account for geometric uncertainty caused by the finite thickness of the laser sheet, measurement

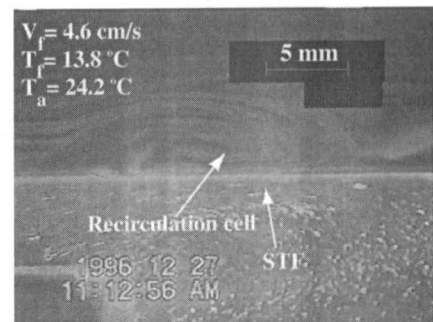
Step (a)



Step (b)



Step (c)



Step (d₁)

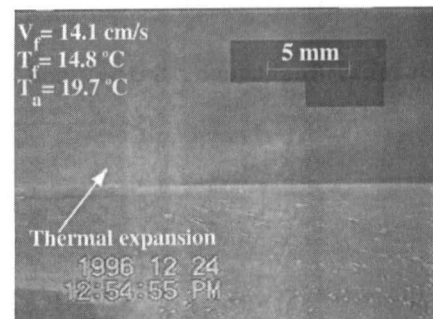


Fig. 4 Four different flow-visualization photographs obtained for steps (a, b, c, and d₁)

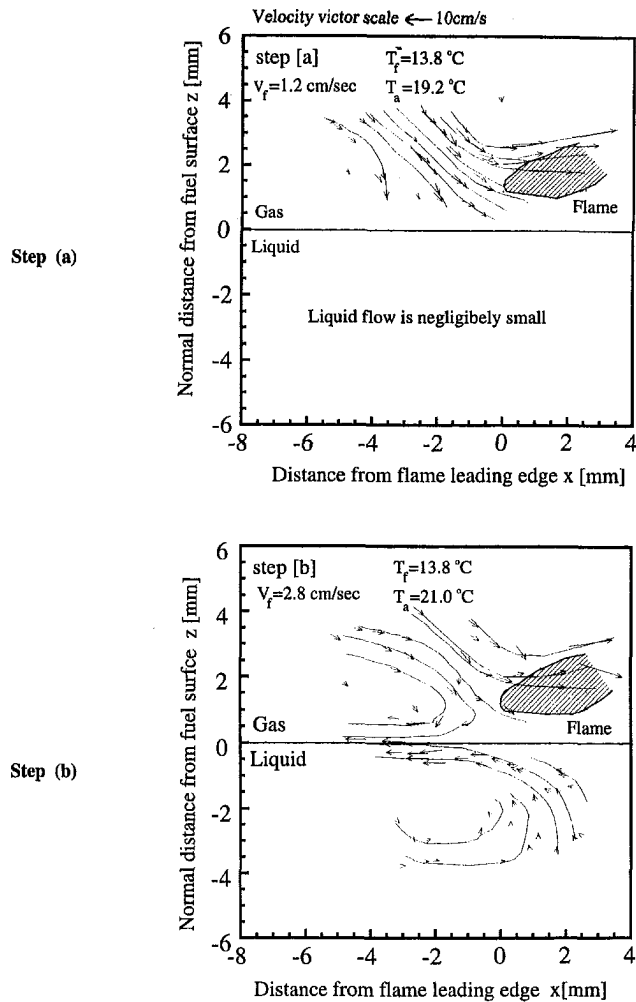


Fig. 5 Four different LSPT-flow diagrams obtained for the pulsating flame steps (a, b, c, and d₁)

resolution caused by image processing discreteness, calibration error of distance, and the time variation of the high-speed camera. The precision and bias limits are listed in Table 1. The total uncertainty of LSPT is estimated to be ± 8.6 percent.

DWHI: The contributions to the measured concentration error come from the wavelength of the laser, path length, fringe-shift number, Gladstone-Dale constants, and molecular weight as shown in Eq. (5). The bias limit associated with path length may be attributed to three types of errors. (a) spatial error in the position of fringes that is due to deflection of coordinates, (b) concentration error that is due to the variation in concentration along the ray path caused by deflection, and (c) concentration error that is due to the change in path length. A more detailed discussion is provided in Konishi et al. (1997). The precision and bias limits are listed in Table 2. The total uncertainty of DWHI is estimated to be ± 15.9 percent.

Results and Discussion

LSPT Results. Figure 3 shows a schematic of the pulsating flame spread consisting of six different steps. Figure 4 shows (representative) photographs of gas-phase STT and liquid-phase LSPT for four different steps (a, b, c, and d₁). Figure 5 shows two-dimensional flow vector diagrams for steps (a, b, c, and d₁). Step (a) is the beginning of the cycle of pulsation and the process moves on to steps (b), (c), (d₁), (d₂), (e), and returns to step (a) to complete the cycle. The schematic of step (d₁), not shown in the

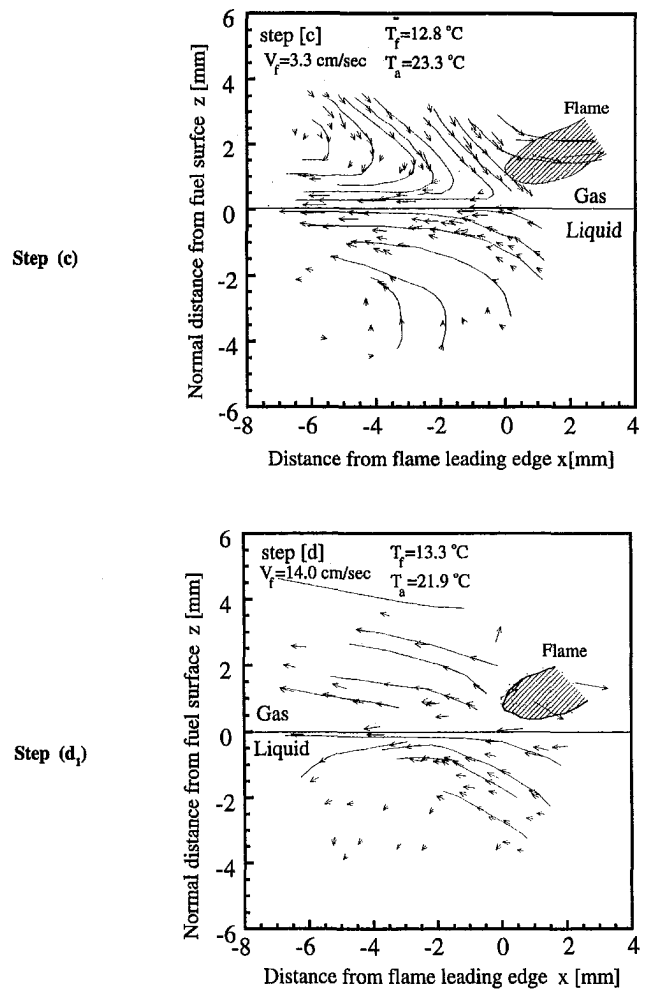


Fig. 5 (con't)

original diagram published in 1991 (Ito, Masada, and Saito, 1991), was added because it helps us better understand the process of flame pulsation.

At step (a) the flame spreads slowly to the left and there may be a buoyancy-induced air flow over the fuel surface ahead of the flame. There is a hot zone formed in the liquid phase near the flame's leading edge, but no surface-tension flow is formed in the liquid phase. At step (b) the flame propagated faster than in step (a) generating a surface-tension (Marangoni effect) flow that flows in the same direction as the flame. In the gas phase, there is a buoyancy-induced air flow that moves opposite to the flame-spread direction. The buoyancy-induced air flow and the liquid surface-tension flow act against each other creating a small circulation in the gas phase just ahead of the flame leading edge creating a flammable gas-air mixture over the extended upstream direction. Thus, the diameter of air circulation also increased in the upstream direction preparing for a fast "jump" flame spread (step d₁) to occur. Because of a sudden increase of the flame-spread rate at step (d₁), the flame front push the air in the circulation zone destroying the circulation and creating a new air flow concurrent to the flame spread. This concurrent air flow accelerates the liquid-surface-tension flow, the flame spreads along with the flow, and eventually the flame almost stops after its leading edge reaches the head of the liquid flow (step d₂). A few seconds later, step (e) took place. Then the process returned to step (a) completing the cycle. (Ito, Masada, and Saito, 1991) provide five interferograms corresponding to steps a, b, c, d₂, and e).

STT Results. Figures 4(a), (b), (c), and (d₁) shows four different smoke-streak photographs for steps (a, b, c, and d₁) are

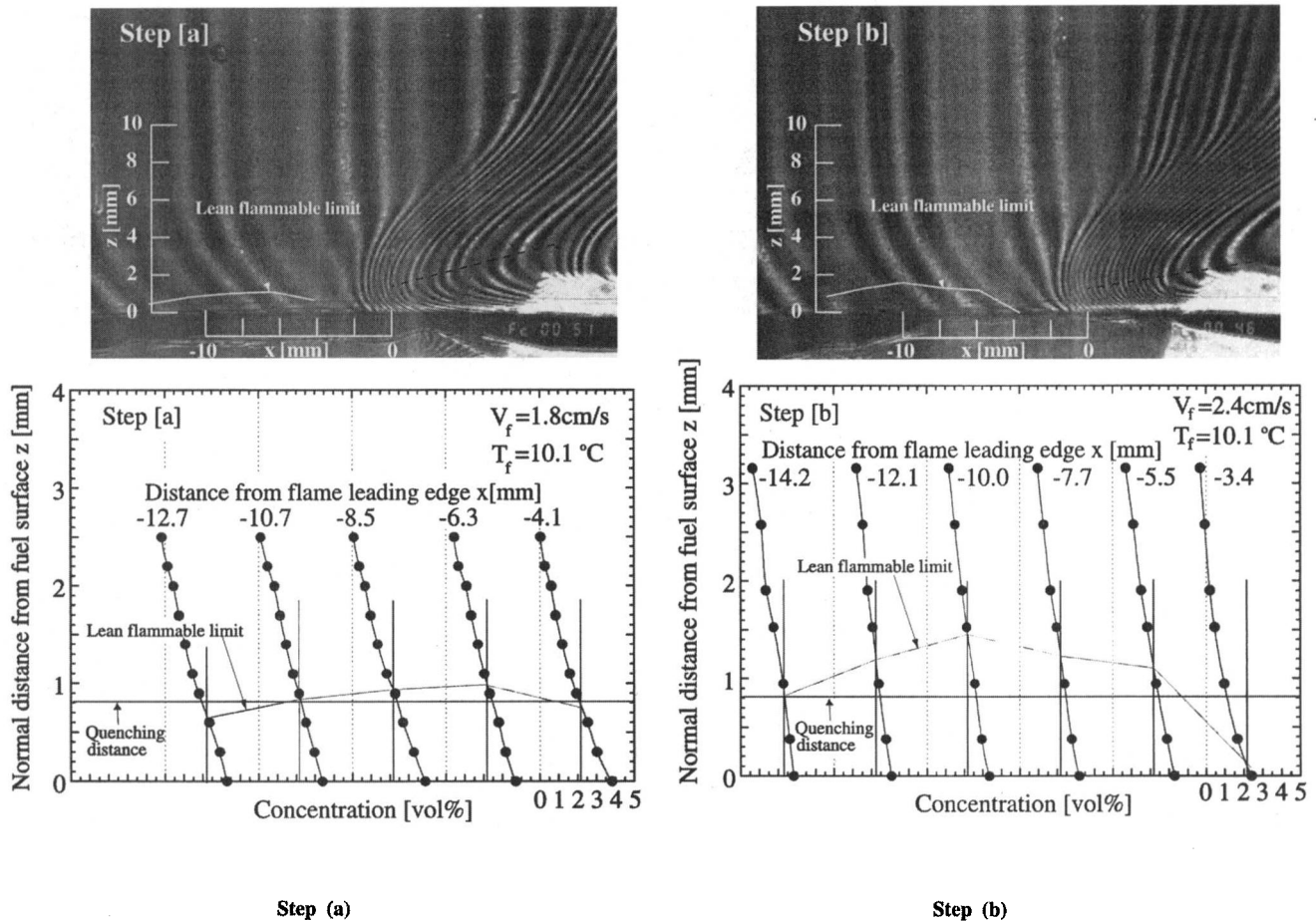


Fig. 6 DW-holograms (top) and vertical concentration profiles (bottom) in the pulsating steps (a, b, and d₁)

Fig. 6 (con't)

shown in. Figure 4(a), where the flame spread rate is 1.2 cm/s, shows no liquid convective and surface tension flow and there are small flames induced airflow that was clear visually, but not clear in the STT photograph. Figure 4(b), where the flame spread rate is 2.0 cm/s, shows both a small circulation 5 mm in length and 2 mm in height and its circulation center is located approximately 5 mm from the flame leading edge) and surface-tension flow. Figure 4(c), where the flame spread rate is 4.6 cm/s, shows a fully developed circulation in the gas and liquid phases. The center of the gas-phase circulation (15.7 mm in length (4.1 mm in height) is located 8.5 mm upstream from the flame leading edge. Figure 4(d₁) shows the flame-spread rate to be 14.1 cm/s. Note that both the liquid and gas-phase circulation decrease their diameter.

DWHI Results. High-speed video and IR photographs taken from above the tray revealed that for the 0.5-cm wide tray, both the surface-temperature distribution and the shape of the flame front are parabolic in nature, while for the 1, 2 and 4-cm wide trays, small twin vortices are generated on the fuel surface (Ross and Miller, 1996) suggesting that the character of the flow profile of the gas-phase flow profile is changed from two dimensions to three dimensions by increasing the width of the tray. A recent study by Garcia-Ybarra (Garcia-Ybarra et al., 1996) also suggested the three-dimensional nature of the gas-phase flow induced by a spreading flame over alcohol. To increase the accuracy of the DWHI, the three-dimensional effect needs to be minimized. We took a series of video pictures and DW holograms simultaneously and identified the best two-dimensional flame shape with 80 percent accuracy.

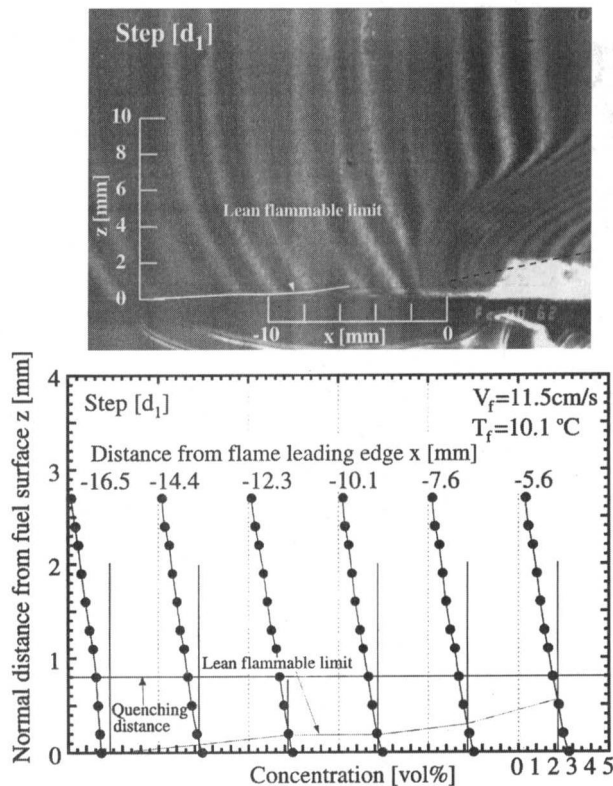
We used a 40-mm wide tray and conducted flame spread tests

over n-propanol at its initial temperature 10°C since the spatial resolution of our DWHI is better for the wider tray width (Narumi, et al.). However, we confirmed that the flame-spread rate over the 20-mm wide and 40-mm wide trays is approximately the same and the flame structure over both trays is very similar in nature. Figure 6 shows DW holograms and vertical profiles of propanol fuel concentration for steps (a, b, and d₁). The lean flammability limit for n-propanol air (2.2 mole percent) is shown as a solid line in Fig. 6 (top). Figure 6 (bottom) shows that the propanol concentration in the area below the solid line satisfies the lean flammability limit; thus, the flame is able to spread through a premixed propanol-air mixture (Glassman and Dryer, 1981).

Summary and Conclusions

1 We developed a unique LSPT system for measuring velocity profiles for transient flow in a very limited space and confirmed the existence of a gas-phase circulation in the pulsating spread region together with a liquid-phase convection, both of which were predicted by other researchers.

2 We obtained a series of two-dimensional DW holograms and confirmed that the flame spread occurs only when the propanol-fuel concentration over the fuel surface is higher than the lean flammability limit. Thus the accuracy of the DWHI needs to be improved if it is to be applied to three-dimensional problems. To overcome this limitation, we are in progress in the development of an advanced three-dimensional DWHI system, which is beyond the scope of this paper.



Step (d₁)

Fig. 6 (con't)

Acknowledgments

This study was supported in part by the National Institute of Standards and Technology under Grant #60NANB4D1674, in part by the NASA-Kentucky-EPSCoR Program, in part by the Japanese Ministry of Education under US-Japan-Collaborative-Agreement Travel Grant, and in part by the Center for Robotics and Manufacturing Systems at the University of Kentucky under a matching grant. We would like to thank H. Ross and F. Miller of NASA Lewis Research Center for providing us with their experimental data and many stimulating discussions.

References

- Akita, K., 1972, "Some Problems of Flame Spreading along a Liquid Surface," *Fourth International Symposium on Combustion*, The Combustion Institute, pp. 1075-1083.
- Garcia-Ybarra, P. L., et al. 1996, "Study of Thermocapillary Layer Preceding Slow Steadily-Spreading Flames over Liquid Fuels," *Twenty-sixth International Symposium on Combustion*, The Combustion Institute, pp. 1469-1475.
- Glassman, I., and Dryer, F. L., 1981, "Flame Spreading Across Liquid Fuels," *Fire Safety Journal*, Vol. 3, pp. 123-138.
- Hirano, T., and Saito, K., 1995, "Fire Spread Phenomenon: The Role of Observation in Experiment," *Prog. Energ. Combust. Sci.*, Vol. 20, pp. 461-485.
- Hirano, T., and Suzuki, T., 1993, "Flame Propagation Across Liquid-Gas Phase Phenomenon," *Fire Safety Journal*, Vol. 21, pp. 207-229.
- Ito, A., Masuda, D., and Saito, K., 1991, "A Study of Flame Spread over Alcohols Using Holographic Interferometry," *Combustion and Flame*, Vol. 83, pp. 375-389.
- Ito, A., Narumi, A., Saito, K., and Cremers, C. J., 1995, "Temperature Measurement by Holographic Interferometry in Liquids," *Eighth International Symposium on Transport Phenomena in Combustion*, S. H. Chen, ed., Taylor and Francis, Washington, DC, No. 9-A-3, pp. 1657-1669.
- Ito, A., Saito, K., and Cremers, C. J., 1995, "Pulsating Flame Spread over Liquids," *Fire Safety Science-Proceedings Fourth International Symposium*, T. Kashiwagi, ed., International Association for Fire Safety Science, pp. 445-456.
- Kline, S. J., and McClintock, F. A., 1953, "Describing Uncertainties in Single-Sample Experiments," *Mechanical Engineering*, Vol. 75, Jan., pp. 3-8.
- Konishi, T., Naka, S., Ito, A., and Saito, K., 1997, "Transient Two-Dimensional Fuel-Concentration Measurement Technique," *Applied Optics*, Vol. 36, No. 33, pp. 8815-8819.
- Miller, F. J., and Ross, H. D., 1992, "Further Observation of Flame Spread over Laboratory-Scale Alcohol Pools," *Twenty-fourth International Symposium on Combustion*, The Combustion Institute, pp. 1075-1083.
- Narumi, et al., "Dual Wave-Length Holographic Interferometry," to be published.
- Qian, C., Ishida, H., and Saito, K., 1994, "Upward Flame Spread Along PMMA Vertical Corner Wall, Part II," *Combustion and Flame*, Vol. 99, pp. 331-338.
- Ross, H., and Miller, F. J., 1996, "Detailed Experiments of Flame Spread Across Deep Butanol Pools," *Twenty-sixth International Symposium on Combustion*, The Combustion Institute, pp. 1327-1334.
- Ross, H. D., 1994, *Prog. Energ. Combust. Sci.*, Vol. 20, pp. 17-63.
- Saito, K., Williams, F. A., and Gordon, A. S., 1986, "Structure of Laminar Coflow Methane-Air Diffusion Flames," *ASME JOURNAL OF HEAT TRANSFER*, Vol. 108, pp. 640-648.
- Santoro, R. J., Fernandez-Pello, A. C., Dryer, F. L., and Glassman, I., 1978, *Applied Optics*, Vol. 17, No. 23, pp. 3843-3850.
- Schiller, D. N., and Sirignano, W. A., 1992, *Journal of Thermophys. Heat Transfer*, Vol. 6, pp. 105-130.
- Sirignano, W. A., and Schiller, D. N., 1996, *Twenty-sixth International Symposium on Combustion*, The Combustion Institute, pp. 1319-1325.
- Spatz, T. L., and Poulikakos, D., 1992, *ASME JOURNAL OF HEAT TRANSFER*, Vol. 114, pp. 998-1010.
- Tashtoush, G., Narumi, A., Ito, A., Saito, K., and Cremers, C. J., 1996, "Combined Techniques of Holographic Interferometry and Particle Track Laser Sheet to Study Flame Spread over Liquids," *Eighth International Symposium of Application of Fluid Mechanics*, Lisbon, Portugal.
- Venkatesh, S., Ito, A., Saito, K., and Wichman, I. S., 1996, "Anchoring Mechanism of Liquid Pool Fires," *Twenty-sixth International Symposium on Combustion*, The Combustion Institute, pp. 1437-1443.
- Williams, F. A., 1985, *Combustion Theory*, 2nd ed; Benjamin/Cummings, Menlo Park, CA, Chapter 12.

Effect of Combined Particle-Phase Diffusivity and Viscosity on the Compressible Boundary Layer of a Particulate Suspension Over a Flat Plate

A. J. Chamkha

Department of Mechanical and
Industrial Engineering,
Kuwait University,
Safat 13060, Kuwait

A mathematical dilute fluid-particle suspension model governing steady, laminar, compressible, boundary layer flow and heat transfer over a semi-infinite flat plate based on the Eulerian or continuum approach is developed. The model accounts for both particulate viscous and diffusive effects. Both the fluid and the particle phases are assumed to have general power-law viscosity-temperature relations. For the case of finite particle-phase viscosity, a general boundary condition borrowed from rarefied gas dynamics is used for the particle phase at the surface. Uniform and nonuniform particle-phase slip coefficients are investigated. Numerical solution of the governing equations is obtained by an implicit, iterative, tridiagonal finite difference method. Graphical results for the displacement thicknesses and skin-friction coefficients of both phases as well as the wall heat transfer are presented for various parametric conditions.

Introduction

Boundary layer flow and heat transfer of pure and contaminated fluids have been an attractive research area for many investigators for many years due to its direct application in the aerospace, automotive, petroleum, geothermal, and many other industries. There has been considerable work carried out on incompressible and compressible boundary layer flow of a fluid through and over many different geometries (see, for instance, Young, 1949; Kuerti, 1951; Stewartson, 1974). The presence of solid particles in fluid processes, such as gas purification, has led to the consideration and investigation of two-phase fluid-particle flow systems.

It has been shown by many previous investigators that the presence of a second phase (like solid particles) in the fluid with a relatively high level of concentration significantly alters the flow and heat transfer characteristics as well as adds complexity in obtaining a solution to the problem from both numerical and experimental points of view. The present paper considers a fundamental problem in two-phase flow. This problem is that of steady, laminar, compressible, boundary layer flow and heat transfer of a gas-particle suspension over a semi-infinite flat plate. The particle phase is assumed to consist of very tiny particles and exhibits a motion of Brownian type and has relatively high concentration to account for the particulate viscous effects. In addition, interparticle forces are neglected so that the system is dilute. This has possible applications in such processes as fluidized beds, gas purification, conveying of powdered materials and transport process, and environmental related problems such as dust storms. Special cases of the present problem have been considered earlier by Singleton (1965) and Wang and Glass (1988). Both of these references obtained asymptotic solutions using the series expansion method. In addition, Wang and Glass (1988) reported numerical solutions based on the finite-difference methodology. Recently, Chamkha (1996a) generalized the problem considered by Singleton (1965) and Wang and Glass (1988) for a relatively dense

suspension for which particle-phase viscous effects are important. In another contribution, Chamkha (1996b) has also considered the case of finite particulate volume fraction where, a uniform particle-phase density distribution is predicted. Recently, Chamkha (1998) has investigated the influence of particle-phase diffusive effects which produced significant changes in the wall particle-phase density distribution and heat transfer.

A literature survey shows that extensive research investigations have been carried out on the incompressible version of the problem under consideration. Reviews of this work can be seen in the works of Soo (1968), Osipov (1980), Prabha and Jain (1982), Datta and Mishra (1982), Chamkha and Peddieson (1989, 1992), and Chamkha (1994). A major conclusion of the work on the incompressible problem is that when the original dusty-gas model (a model meant for the description of particulate suspension having small particulate volume fraction and excludes particulate viscous and diffusive effects) discussed by Marble (1970), a singular behavior in which the particle-phase density at the plate surface becomes infinite is predicted. In contrast with this conclusion, the work of Chamkha (1996a) has shown that for a compressible boundary layer flow of a dense particulate suspension, a particle-free zone is predicted somewhere downstream of the leading edge of the plate.

The presence of particle-phase diffusivity in the original dusty-gas model have shown to be capable of removing the singularity predicted in the incompressible problem (see Chamkha and Peddieson, 1989; Chamkha 1994). It is of interest in the present work to investigate whether the inclusion of particle-phase diffusive effects in the dusty-gas model will have the same influence on the compressible problem for both inviscid and viscous particle-phase conditions. Also, of interest is the study of the effects of both uniform and nonuniform particle-phase wall-slip conditions. The dynamic viscosities of both phases, the fluid-phase thermal conductivity and the particle-phase diffusivity are represented by general power-law functions of the fluid-phase temperature and the particle-phase temperature, respectively. The interaction between the phases is limited to drag and heat transfer. The particles are assumed to be very small and of spherical shape, and their volume fraction is assumed small.

Contributed by the Heat Transfer Division for publication in the JOURNAL OF HEAT TRANSFER. Manuscript received by the Heat Transfer Division, Oct. 7, 1998; revision received, Dec. 1, 1998. Keywords: Computational, Forced Convection, Heat Transfer, Laminar, Two-Phase. Associate Technical Editor: R. Douglass.

Governing Equations

Consider steady, compressible, laminar, boundary layer two-phase flow in a half-space bounded by a semi-infinite flat surface. The surface or plate is coincident with the plane $y = 0$ and the flow is a uniform stream in the plane $y > 0$ parallel to the surface. Far from the surface, both phases are in both hydrodynamic and thermal equilibrium. The particles are all assumed to be of one size and spherical in shape and moving with the same velocity. Radiative heat transfer from one particle to another, chemical reaction, coagulation, phase change, and deposition are all neglected. The fluid phase is assumed to behave as a perfect gas. The fluid and particles motions are coupled only through drag and heat transfer between them. The drag force is modeled using Stokes linear drag theory and the small particle volume fraction assumption inherent in the dusty-gas model (see Marble, 1970) is retained in this problem.

The governing equations for this investigation are based on the balance laws of mass, linear momentum, and energy for both phases. These can be written

$$\nabla \cdot (\rho \mathbf{V}) = S_f \quad (1a)$$

$$\nabla \cdot (\rho_p \mathbf{V}_p) = S_p \quad (1b)$$

$$\rho \mathbf{V} \cdot \nabla \mathbf{V} = \nabla \cdot \underline{\underline{\sigma}} - \mathbf{f} \quad (1c)$$

$$\rho_p \mathbf{V}_p \cdot \nabla \cdot \mathbf{V}_p = \nabla \cdot \underline{\underline{\sigma}}_p + \mathbf{f} \quad (1d)$$

$$\rho c \mathbf{V} \cdot \nabla T = \nabla \cdot (k \nabla T) + \underline{\underline{\sigma}} : \nabla \mathbf{V} + (\mathbf{V} - \mathbf{V}_p) \cdot \mathbf{f} + Q_T \quad (1e)$$

$$\rho_p c_p \mathbf{V}_p \cdot \nabla T_p = \underline{\underline{\sigma}}_p : \nabla \mathbf{V}_p - Q_T \quad (1f)$$

The previous equations are supplemented by the following constitutive equations:

$$S_f = 0, S_p = D_p \nabla^2 \rho_p \quad (2a,b)$$

$$\underline{\underline{\sigma}} = -PI + \mu(T)(\nabla \mathbf{V} + \nabla \mathbf{V}^T) \quad (2c)$$

$$\underline{\underline{\sigma}}_p = \mu_p(T_p)(\nabla \mathbf{V}_p + \nabla \mathbf{V}_p^T) \quad (2d)$$

$$\mathbf{f} = \rho_p(\mathbf{V} - \mathbf{V}_p)/\tau_v \quad (2e)$$

$$Q_T = \rho_p c_p (T_p - T)/\tau_T \quad (2f)$$

$$P = \rho RT. \quad (2g)$$

It is seen from Eqs. (2) that the particle phase is assumed to have diffusive and viscous effects which are not present in the models reported by Singleton (1965) and Wang and Glass (1988). It should be mentioned that Eq. (1b) for the particle phase is familiar from dynamics of chemically reacting flows. Also, the particle-phase diffusivity can be incorporated into the mathematical model through the particle-phase momentum equation. Since the present formulation has worked well for the incompressible version (see Chamkha and Peddieson, 1989) and for the sake of comparison, it is adopted herein. Particle-phase diffusivity is needed to model Brownian motion and is often employed to facilitate numerical solutions (see Chamkha and Peddieson, 1989; Chamkha, 1994). Particle-phase viscosity is often employed to model particle-particle interaction and particle-wall interaction. Theoretically, it can result from the averaging processes involved in representing a discrete system of particle as a continuum (see, for instance, Drew, 1983; Drew and Segal, 1971). The particle-phase viscous effects have been investigated by many previous investigators (see Gidaspow, 1986; Tsuo and Gidaspow, 1990; Gadiraju et al., 1991; Chamkha and Peddieson, 1994). Also, the particles are assumed to be dragged along by the fluid and, therefore, have no analog of pressure.

Equation (2g) assumes that the fluid phase is treated as an ideal gas. This equation is needed to render the problem determinate. The hydrodynamic and thermal coupling between the phases is accounted for by the interphase drag force and the interphase heat transfer. Other interphase mechanisms such as the virtual mass force (Zuber, 1964), the shear lift force (Saffman, 1965), and the spin-lift force (Rubinow and Keller, 1961) are neglected compared to the drag force. This is feasible when the particle Reynolds number is assumed to be small (see, for instance, Apazidis, 1985) as is the case in the present work.

Nomenclature

C = fluid-phase skin-friction coefficient	Q_T = interphase heat transfer rate per unit volume to the particle phase	η = transformed normal (vertical) coordinate
c = fluid-phase specific heat at constant pressure	r, S_R = constants defined in Eq. (16)	Γ = fluid-phase viscosity coefficient
D_p = particle-phase diffusion coefficient	q_w = wall heat transfer	κ = particle mass loading ratio
Ec = fluid-phase Eckert number	R = ideal gas constant	μ = fluid-phase viscosity coefficient
e_x, e_y = unit vectors in x and y directions, respectively	Re = Reynolds number	ρ = fluid-phase density
F = nondimensionalized fluid-phase tangential (horizontal) velocity	S_f = fluid-phase source term	σ = fluid-phase stress tensor
f = interphase force per unit volume acting on the particle phase	S_p = particle-phase source term	τ^* = wall shear stress
G = nondimensionalized fluid-phase transformed normal (vertical) velocity	S = particle-phase slip parameter	τ_T = temperature relaxation time
H = nondimensionalized fluid-phase temperature	t_o = nondimensionalized fluid-phase wall temperature	τ_v = momentum relaxation time
I = unit tensor	T = fluid-phase temperature	ω = power index for viscosity relation
k = fluid-phase thermal conductivity	u = x -component of velocity	ξ = transformed tangential (horizontal) coordinate
P = fluid-phase pressure	U_∞ = free-stream velocity	∇ = gradient operator
Pr = fluid-phase Prandtl number	v = y -component of velocity	∇^2 = Laplacian operator
Q = nondimensional fluid-phase density	V = fluid-phase velocity vector	
	x, y = Cartesian coordinate variables	Subscripts
	β = viscosity ratio	∞ = free stream
	δ = particle-phase inverse Schmidt's number	p = particle phase
	γ = specific heat ratio	Superscripts
	Δ = fluid-phase displacement thickness	T = transpose of a second-order tensor

The viscosity-temperature relation for the gas phase is assumed to be

$$\frac{\mu}{\mu_\infty} = \left(\frac{T}{T_\infty}\right)^\omega \quad (0.5 \leq \omega \leq 1.0). \quad (3)$$

This equation is similar to that employed by Wang and Glass (1988). Singleton (1965) employed $\omega = 0.5$ in his work on this problem.

In the absence of a fundamental knowledge on how the particle-phase diffusivity and dynamic viscosity vary with temperature and because the particle phase is treated as a continuum, it will be assumed that

$$\frac{D_p}{D_{p\infty}} = \left(\frac{T_p}{T_\infty}\right)^{\omega_p}, \quad \frac{\mu_p}{\mu_{p\infty}} = \left(\frac{T_p}{T_\infty}\right)^{\omega_p} \quad (0.5 \leq \omega_p \leq 1.0) \quad (4a,b)$$

where ω_p is a particle-phase power index coefficient.

An appropriate set of boundary conditions suggested by the physics of the problem can be written as

$$u(x, 0) = 0, \quad v(x, 0) = 0, \quad T(x, 0) = T_w,$$

$$u_p(x, 0) = S \frac{\partial u_p}{\partial y}(x, 0),$$

$$v_p(x, 0) = 0, \quad \frac{\partial \rho_p}{\partial y}(x, 0) = 0 \quad (5a-f)$$

$$u(x, \infty) = U_\infty, \quad u_p(x, \infty) = U_\infty,$$

$$v_p(x, \infty) = v(x, \infty), \quad T(x, \infty) = T_\infty$$

$$T_p(x, \infty) = T_\infty, \quad \rho(x, \infty) = \rho_\infty, \quad \rho_p(x, \infty) = \kappa \rho_\infty. \quad (5g-l)$$

Equations (5a-c) indicate that the fluid phase exhibits a no-slip condition at the plate surface, has no normal velocity at the wall, and is maintained at a uniform temperature, T_w , at the wall, respectively. The exact form of boundary conditions to be satisfied by a particle phase at the wall is unknown at present. There is, however, certain evidence that the particle phase experiences some slip near a boundary. Because of this and since the particle phase may resemble a rarefied gas, a boundary condition similar to that usually employed in rarefied gas dynamics is used in Eq. (5d). It is clear that this boundary condition allows for no slip when $S = 0$ and perfect slip when $S = \infty$. A similar form has been employed by Soo (1989). Equation (5e) indicates that there is normal velocity for the particle phase at the wall. Equation (5f) causes the particle-phase diffusivity effects to vanish at the plate. The rest of Eqs. (5) are matching conditions for both phases far above the plate and they indicate that both phases are in equilibrium with the free-stream conditions.

In the present work, a convenient set of modified Blasius transformations (similar to those employed previously by Chamkha and Peddieson, 1994) converts the tangential distance from being semi-infinite in $x(0 \leq x < \infty)$ to finite in $\xi(0 \leq \xi \leq 1)$. The transformed equations eliminate the singularities associated with the leading edge of the plate and allows an exact solution at the leading edge of the plate ($\xi = 0$) (instead of assuming initial profiles of the dependent variables to start off the solution procedure as used by Wang and Glass, 1988). The set of transformations is as follows:

$$x = U_\infty \xi \tau_v / (1 - \xi), \quad y = U_\infty \tau_v / \text{Re}_\infty^{1/2} (2\xi / (1 - \xi))^{1/2} \eta$$

$$u = U_\infty F, \quad v = U_\infty ((1 - \xi) / (2\xi))^{1/2} (G + \eta F) / \text{Re}_\infty^{1/2}$$

$$u_p = U_\infty F_p, \quad v_p = U_\infty ((1 - \xi) / (2\xi))^{1/2} (G_p + \eta F_p) / \text{Re}_\infty^{1/2}$$

$$T = T_\infty H, \quad T_p = T_\infty H_p, \quad \rho = \rho_\infty Q, \quad \rho_p = \kappa \rho_\infty Q_p, \quad \mu_p = \mu_{p\infty} \Gamma$$

$$\mu = \mu_\infty \Gamma, \quad \beta = \mu_{p\infty} / \mu_\infty, \quad \delta = D_{p\infty} \rho_\infty / \mu_\infty,$$

$$\text{Pr} = \mu c / k, \quad \text{Ec} = U_\infty^2 / (c T_\infty)$$

$$\gamma = c / c_p, \quad \text{Re}_\infty = \rho_\infty U_\infty \tau_v / \mu_\infty. \quad (6)$$

Substituting Eqs. (6) (with $\kappa = 1$ following Wang and Glass, 1988) along with Eqs. (3) and (4) into Eqs. (1) and (2) transforms the problem to

$$\frac{\partial(QG)}{\partial \eta} + QF + 2\xi(1 - \xi) \frac{\partial(QF)}{\partial \xi} = 0 \quad (7)$$

$$\Gamma \frac{\partial^2 F}{\partial \eta^2} + \left(\frac{d\Gamma}{dH} \frac{\partial H}{\partial \eta} - QG\right) \frac{\partial F}{\partial \eta} - \frac{2\xi}{1 - \xi} \left((1 - \xi)^2 QF \frac{\partial F}{\partial \xi} - Q_p \Gamma (F_p - F) \right) = 0 \quad (8)$$

$$\Gamma \frac{\partial^2 H}{\partial \eta^2} + \left(\frac{d\Gamma}{dH} \frac{\partial H}{\partial \eta} - \text{Pr}QG\right) \frac{\partial H}{\partial \eta} - 2\xi(1 - \xi) \text{Pr}QF \frac{\partial H}{\partial \xi} + \text{Pr} \text{Ec} \Gamma \left(\frac{\partial F}{\partial \eta}\right)^2 + \left(\frac{2\xi}{1 - \xi}\right) \left(\text{Pr} \text{Ec} \Gamma Q_p (F_p - F)^2 + \frac{2\Gamma Q_p}{3} (H_p - H) \right) = 0 \quad (9)$$

$$QH = 1 \quad (10)$$

$$\delta D_p \frac{\partial^2 Q_p}{\partial \eta^2} + \left(\delta \frac{dD_p}{dH_p} \frac{\partial H_p}{\partial \eta} - G_p\right) \frac{\partial Q_p}{\partial \eta} - \left(F_p + \frac{\partial G_p}{\partial \eta}\right) Q_p - 2\xi(1 - \xi) \frac{\partial(Q_p F_p)}{\partial \xi} = 0 \quad (11)$$

$$\beta \Gamma_p \frac{\partial^2 F_p}{\partial \eta^2} + \left(\beta \frac{d\Gamma_p}{dH_p} \frac{\partial H_p}{\partial \eta} - Q_p G_p\right) \frac{\partial F_p}{\partial \eta} - \left(\frac{2\xi}{1 - \xi}\right) (\Gamma Q_p (F_p - F) + (1 - \xi)^2 Q_p F_p \frac{\partial F_p}{\partial \xi}) = 0 \quad (12)$$

$$\beta \left(\Gamma_p \frac{\partial^2}{\partial \eta^2} (G_p + \eta F_p) + \frac{d\Gamma_p}{dH_p} \frac{\partial H_p}{\partial \eta} \frac{\partial}{\partial \eta} (G_p + \eta F_p) \right) - Q_p G_p \frac{\partial G_p}{\partial \eta} - \eta Q_p G_p \frac{\partial F_p}{\partial \eta} + \eta Q_p F_p^2 - \left(\frac{2\xi}{1 - \xi}\right) \left((1 - \xi)^2 Q_p F_p \frac{\partial}{\partial \xi} (G_p + \eta F_p) + \Gamma Q_p (G_p - G + \eta(F_p - F)) \right) = 0 \quad (13)$$

$$Q_p G_p \frac{\partial H_p}{\partial \eta} + \left(\frac{2\xi}{1 - \xi}\right) \left((1 - \xi)^2 Q_p F_p \frac{\partial H_p}{\partial \xi} + \frac{2\Gamma \gamma}{3 \text{Pr}} Q_p (H_p - H) \right) - \beta \text{Ec} \gamma \Gamma_p \left(\frac{\partial F_p}{\partial \eta}\right)^2 = 0. \quad (14)$$

Equations (7) through (14) represent the transformed boundary layer equations for a more generalized two-phase gas-solid model than that discussed by Marble (1970).

The dimensionless boundary conditions become

$$F(\xi, 0) = 0, \quad G(\xi, 0) = 0,$$

$$F_p(\xi, 0) = S((1 - \xi) / (2\xi))^{1/2} \frac{\partial F_p}{\partial \eta}(\xi, 0)$$

$$H(\xi, 0) = t_0, \quad G_p(\xi, 0) = 0, \quad \frac{\partial Q_p}{\partial \eta}(\xi, 0) = 0, \quad F(\xi, \infty) = 1$$

$$F_p(\xi, \infty) = 1, G_p(\xi, \infty) = G(\xi, \infty), H(\xi, \infty) = 1$$

$$H_p(\xi, \infty) = 1, Q(\xi, \infty) = 1, Q_p(\xi, \infty) = 1 \quad (15)$$

where $t_0 = T_w/T_\infty$ is a dimensionless fluid-phase surface temperature.

In reality the particle-phase tangential velocity at the wall is controlled by many physical effects such as sliding friction, the nature of particle/surface collision, etc. It is not possible to model such effects with precision at present. Physically, a wall-slip condition should depend on the slip velocity between the fluid and the particle phases. It is known for this relaxation-type problem that the slip velocity is a function of the tangential distance ξ (see Soo, 1989). Therefore, to allow for a variety of particle-phase wall tangential velocity profiles, two wall-particle slip conditions will be investigated. The first condition is based on the assumption that the particle phase experiences a uniform slip action along the plate ($S = 1$) while in the second it is assumed that the wall-slip parameter S has the general form

$$S = S_R((1 - \xi)/\xi)^r \quad (16)$$

(where S_R and r are constants). It can be seen that the form of Eq. (16) allows for perfect particulate slip taking $\xi = 0$, approaching a no-slip condition as determined by the values of S_R and r .

Of special practical significance for this problem are the fluid-phase displacement thickness δ^* , the particle-phase displacement thickness δ_p^* , the fluid-phase wall shear stress τ^* , the particle-phase wall shear stress τ_p^* , and the wall heat transfer coefficient q^* . These physical parameters are defined in dimensional form as

$$\delta^* = \int_0^\infty \left(1 - \frac{\rho u}{\rho_\infty u_\infty}\right) dy, \quad \delta_p^* = \int_0^\infty \left(1 - \frac{\rho_p u_p}{\rho_{p\infty} u_{p\infty}}\right) dy$$

$$\tau^* = \mu \frac{\partial u}{\partial y}(x, 0), \quad \tau_p^* = \mu_p \frac{\partial u_p}{\partial y}(x, 0)$$

$$q^* = k \frac{\partial T}{\partial y}(x, 0). \quad (17)$$

Substituting the dimensionless parameters in Eqs. (6) into Eqs. (17) produces the following dimensionless displacement thicknesses for the fluid and particle phases Δ and Δ_p , the skin-friction coefficients for the fluid and particle phases C and C_p , and the dimensionless wall heat transfer coefficient q_w .

$$\Delta(\xi) = \int_0^\infty (1 - QF)d\eta, \quad \Delta_p(\xi) = \int_0^\infty (1 - Q_p F_p)d\eta,$$

$$C(\xi) = \Gamma(\xi, 0) \frac{\partial F}{\partial \eta}(\xi, 0)$$

$$C_p(\xi) = \beta \Gamma_p(\xi, 0) \frac{\partial F_p}{\partial \eta}(\xi, 0),$$

$$q_w(\xi) = \frac{\Gamma(\xi, 0)}{\text{Ec Pr}} \frac{\partial H}{\partial \eta}(\xi, 0) \quad (18)$$

Results and Discussion

Equations (7) through (14) are obviously nonlinear and, unfortunately, exhibit no closed-form or similar solution subject to Eqs. (15). They, therefore, must be solved numerically. The tridiagonal, implicit, iterative, finite difference method discussed by Blottner (1970) and Patankar (1980), which is similar to that used by Wang and Glass (1988), has proven to be successful in the solution of boundary layer problems. For this reason, it is adopted in the present work.

All first-order derivatives with respect to ξ are represented by

three-point backward difference formulas. All second-order differential equations in η are discretized using a three-point central difference quotient while all first-order differential equations in η are discretized using the trapezoidal rule. The computational domain was divided into 1001 nodes in the ξ -direction and 195 nodes in the η -direction. Since it is expected that most changes in the boundary layer occur in the vicinity of the wall, variable step-sizes in η are utilized with $\Delta\eta_1 = 0.001$ and a growth factor of 1.03. Also, constant small step-sizes in ξ with $\Delta\xi = 0.001$ are used. The governing equations are then converted into sets of linear tridiagonal algebraic equations which are solved by the Thomas algorithm (see Blottner, 1970) at each iteration. The convergence criterion required that the difference between the current and the previous iterations be 10^{-5} . It should be mentioned that many numerical experimentations were performed by altering the step-sizes in both directions to ensure accuracy of the results and to assess grid independence. For example, when $\Delta\eta_1$ was set to 0.01 instead 0.001, an average error of about eight percent was observed in the results with the maximum error being close to $\xi = 1$. Also, when $\Delta\eta_1$ was equated to 0.0001 no significant changes of results were observed. For this reason $\Delta\eta_1 = 0.001$ was chosen and employed in producing the numerical results. The flow and heat transfer parameter are not as sensitive to $\Delta\xi$ as they are sensitive to $\Delta\eta_1$. For this reason, a constant step-size was used in the ξ -direction. The sensitivity analysis of the results to changes in $\Delta\xi$ was also performed. For instance, when $\Delta\xi$ was set to 0.01, an average deviation of five percent from the results with $\Delta\xi = 0.001$. Smaller values of $\Delta\xi$ than 0.001 produced no changes in the results and, therefore, $\Delta\xi$ was set to 0.001 in all the produced results. As far as the convergence criterion is concerned, two types were tried. One was based on the percentage error between the previous and the current iterations and the other was based on their difference. Since we are not dealing with very small numbers, the convergence criterion based on the difference between the previous and current iterations was employed in the present study. No convergence problems were encountered even with the small value of 10^{-5} used in this work. Equations (7) through (14) were solved for $G, F, H, Q, Q_p, F_p, G_p,$ and H_p , respectively. Many results were obtained throughout the course of this work. A representative set is presented in Figs. 1 through 23 to show the effects of the physical parameters on the solutions. In all of the results to be reported subsequently, ω_p was equated to ω . This was done in order to minimize the number of figures after it was found that altering ω_p produced the same effects as that obtained by changing ω .

Nondiffusive Viscous Particle Phase. The governing equations and conditions for this special case are obtained by formally setting $\delta = 0$ in Eq. (11) and ignoring the boundary condition on Q_p at the wall. This special case has been solved previously by Chamkha (1996a). The major conclusion of his work was that a particle-free zone is predicted in which the particle-phase density

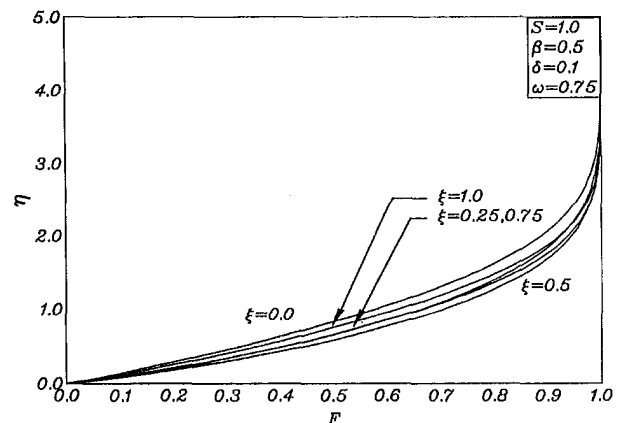


Fig. 1 Fluid-phase tangential velocity profiles

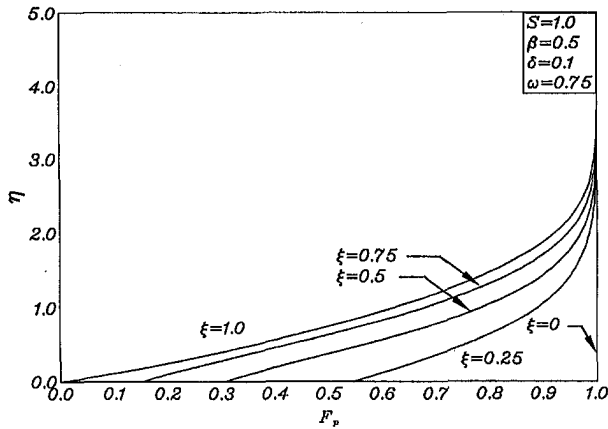


Fig. 2 Particle-phase tangential velocity profiles

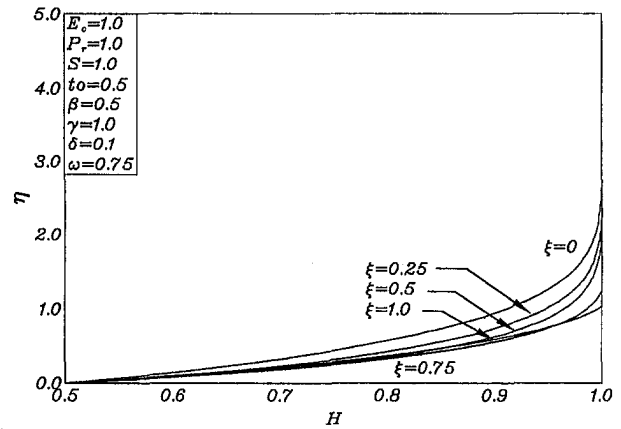


Fig. 5 Fluid-phase temperature profiles

at the wall vanished somewhere downstream of leading edge of the plate. In the present work, the particle-free zone phenomenon discussed by Chamkha (1996a) is reproduced as a limiting case as will be shown in Fig. 22.

If the vanishing of the particle-phase density at the wall represents a physical phenomenon, then the modified dusty-gas model employed by Chamkha (1996a) may be inadequate because the equations of this model are derived under the assumption that the entire space is occupied by both phases. Enhancements to the model which eliminates the existence of the particle-free zone is discussed later in this work.

Diffusive Inviscid Particle Phase. The mathematical model governing the present flow and heat transfer problem are obtained

by setting $\beta = 0$ in Eqs. (12) through (14) and ignoring the third boundary condition given in Eq. (15). This case has also been considered by Chamkha (1998). It was found that qualitatively different results from those reported by Chamkha (1996a) were predicted. In fact, no particle-free zone was predicted. The influence of the particle-phase diffusivity was found to smooth off the sharp peaks in the wall particle-phase density distribution obtained for the case of $\beta = 0$ and $\delta = 0$. Therefore, it can be concluded from this and the previous case that a small change in the mathematical model can produce great changes in the predictions. Validation of this case with the present work is shown in Figs. 16 and 17.

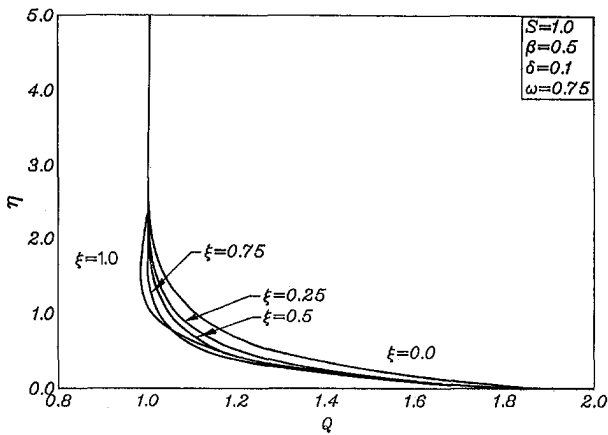


Fig. 3 Fluid-phase density profiles

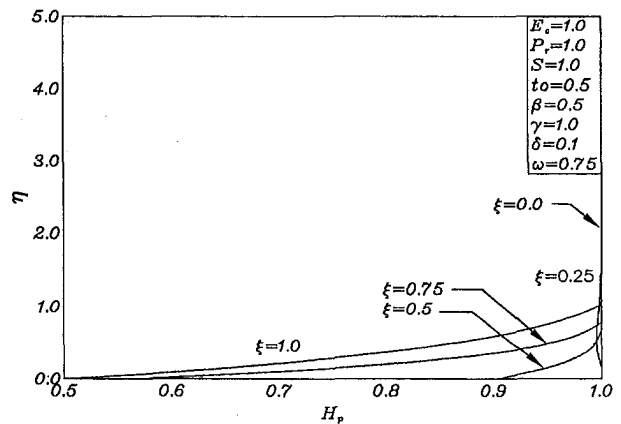


Fig. 6 Particle-phase temperature profiles

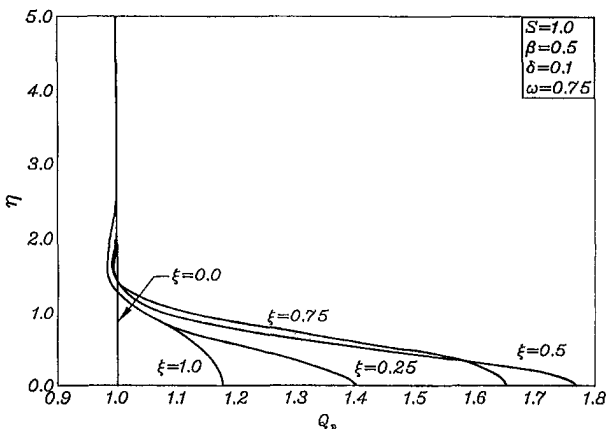


Fig. 4 Particle-phase density profiles

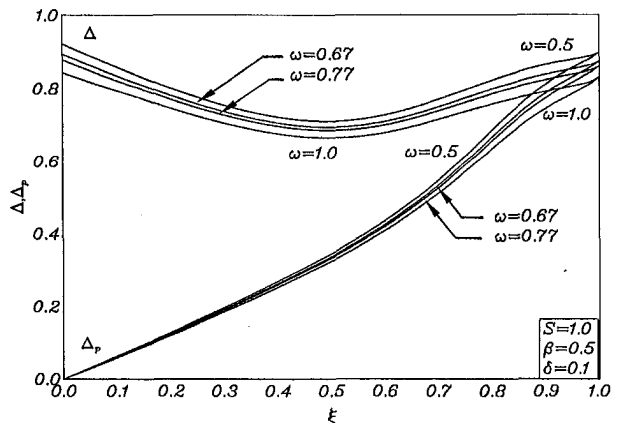


Fig. 7 Fluid and particle-phase displacement thicknesses profiles

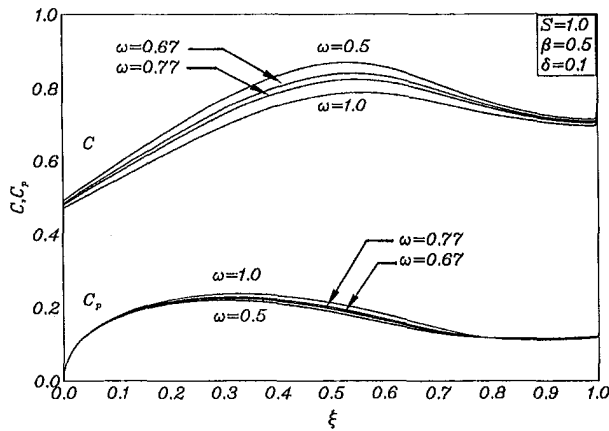


Fig. 8 Fluid and particle-phase skin friction coefficients profiles

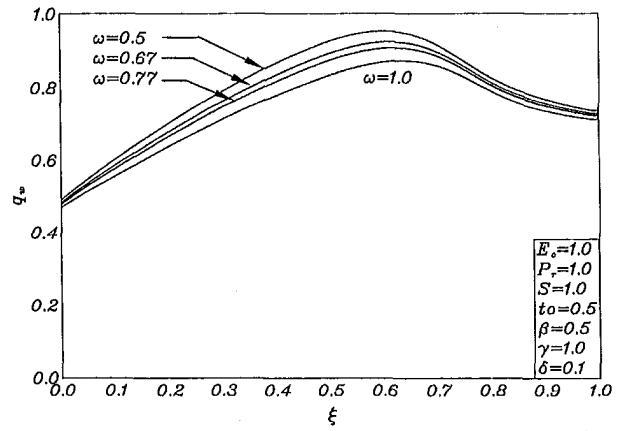


Fig. 11 Wall heat transfer coefficient profiles

Diffusive and Viscous Particle Phase. In this section the combined effects of particulate diffusivity and viscosity on the flow and heat transfer aspects of the problem under consideration are investigated. For this general case, the full equations given by Eqs. (7) through (14) subject to Eqs. (15) are solved numerically by the finite difference method previously discussed. Representative numerical results for this case are illustrated for both uniform and variable wall particle-phase slip conditions in Figs. 1 through 23. Figures 1 through 11 are for the uniform particle-phase wall slip ($S = 1$) while Figs. 12 through 23 are for the case of variable particle-phase wall slip according to Eq. (16) with $S_R = 50$ and $r = 1$.

Figures 1 through 6 present representative profiles for the fluid-phase tangential velocity F , particle-phase tangential velocity F_p , fluid-phase density Q , particle-phase density Q_p , fluid-phase temperature H , and the particle-phase temperature H_p at various locations along the plate, respectively. Equations (7) through (14) show that at $\xi = 0$, the motion of the fluid phase is uncoupled from the motion of the particle phase. This is called the frozen flow condition. In addition, it is observed that at $\xi = 1$ both phases move together with the same velocity and thermal conditions every where. This condition is called the equilibrium flow and thermal conditions. Figures 1 through 6 show the proper transition from

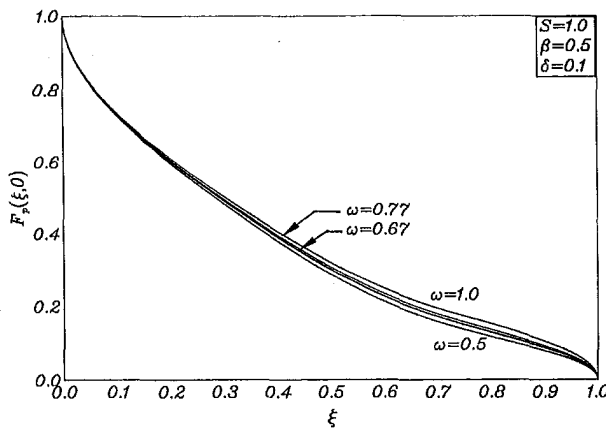


Fig. 9 Wall particle-phase tangential velocity profiles

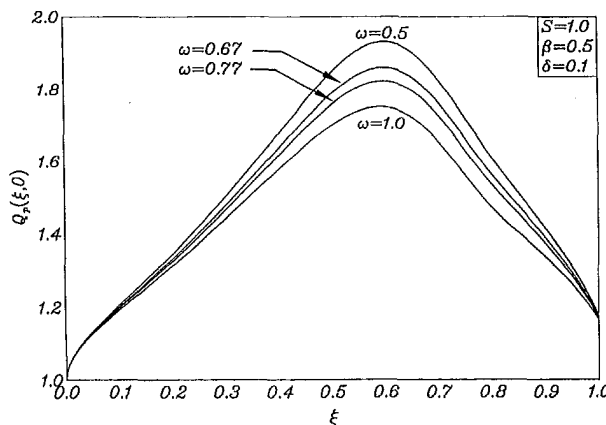


Fig. 10 Wall particle-phase density profiles

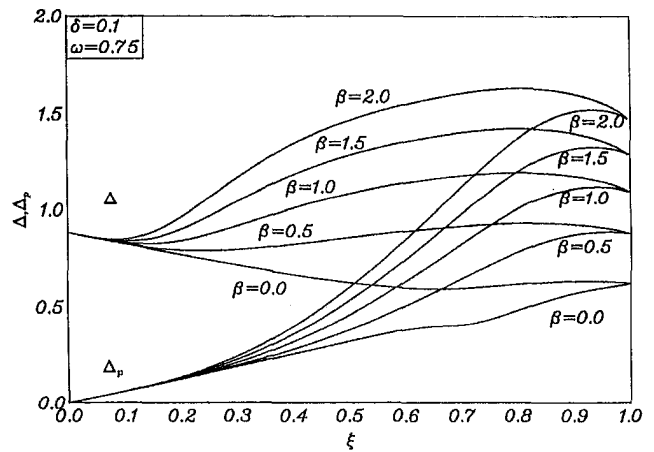


Fig. 12 Fluid and particle-phase displacement thicknesses profiles

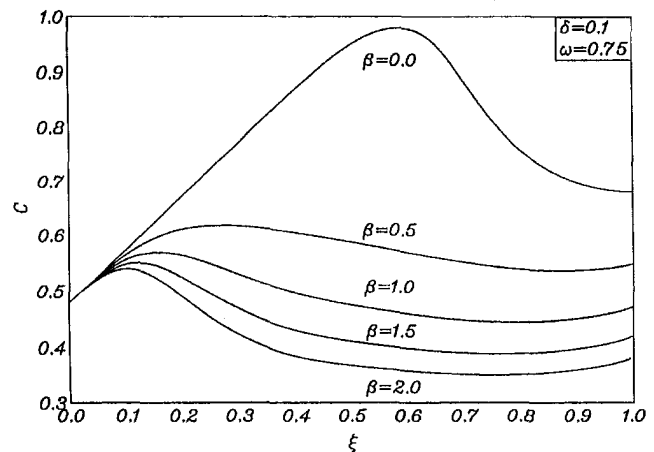


Fig. 13 Fluid-phase skin friction coefficient profiles

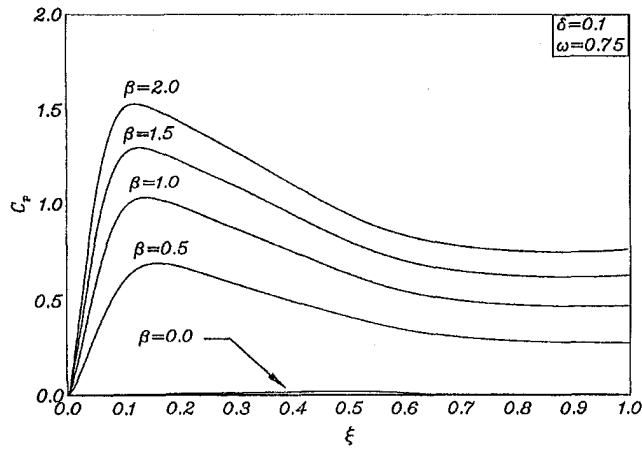


Fig. 14 Particle-phase skin friction coefficient profiles

frozen to equilibrium flow conditions. For large values of η both F and F_p approach unity while both the transformed normal velocities G and G_p (not shown here for brevity) approach $-\eta$. This is consistent with the definitions of the actual normal velocities v and v_p in Eqs. (6) since they must vanish at the edge of the boundary layer. The effect of the particle-phase wall slip on the profiles of F_p is apparent in Fig. 2 as it causes $F_p(\xi, 0)$ to decrease from unity (perfect slip) to zero (no slip). Figures 3 and 4 show that all deviations of Q and Q_p from uniformity are confined to a small region close to the plate surface where significant deviations from

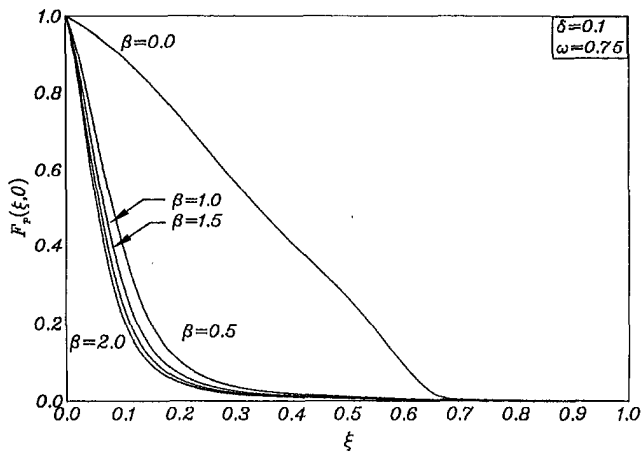


Fig. 15 Wall particle-phase tangential velocity profiles

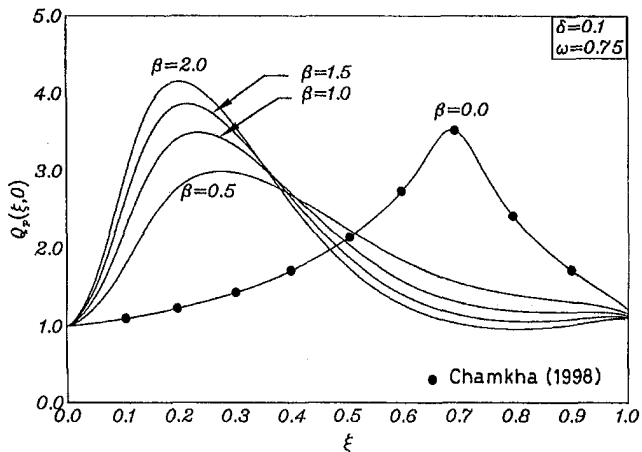


Fig. 16 Wall particle-phase density profiles

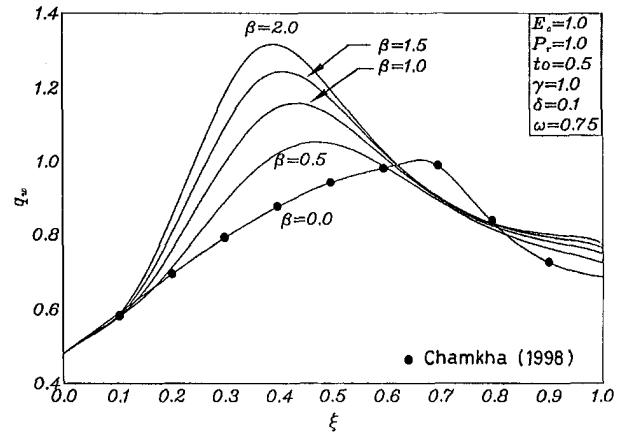


Fig. 17 Wall heat transfer coefficient profiles

equilibrium exist. The development of the particle-phase wall temperature $H_p(\xi, 0)$ as the suspension moves from $\xi = 0$ to $\xi = 1$ and the thermal equilibrium condition where the profile of H_p is the same as that of H at $\xi = 1$ are apparent from Figs. 5 and 6.

Figures 7 and 8 illustrate the development of the displacement thicknesses (Δ and Δ_p) and the skin-friction coefficients (C and C_p) for both the fluid and particle phases along the plate tangential distance ξ for various fluid-phase power index coefficients ω . Physically speaking, at the leading edge of the plate, a frozen flow condition exists where both phases move independently. As a result, the drag force between the phases is maximum. As the flow

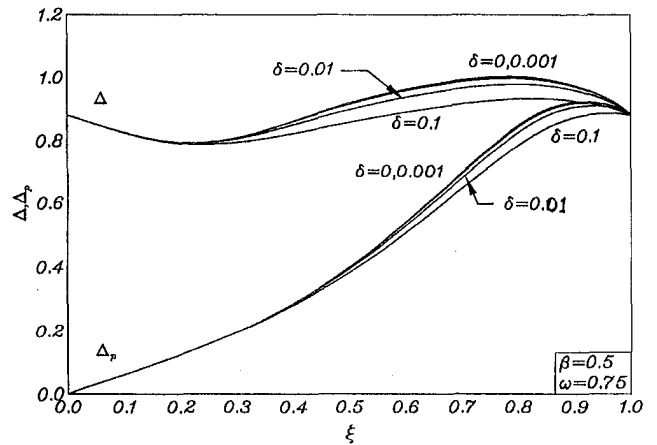


Fig. 18 Fluid and particle-phase displacement thicknesses profiles

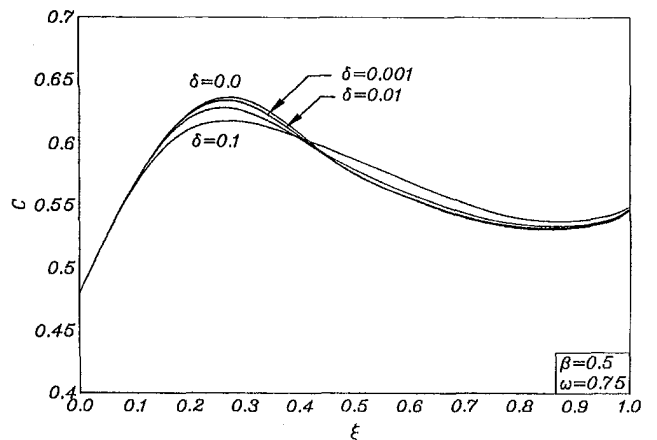


Fig. 19 Fluid-phase skin friction coefficient profiles

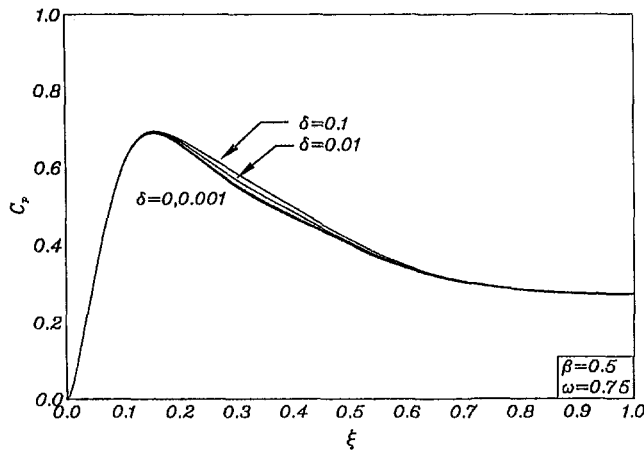


Fig. 20 Particle-phase skin friction coefficient profiles

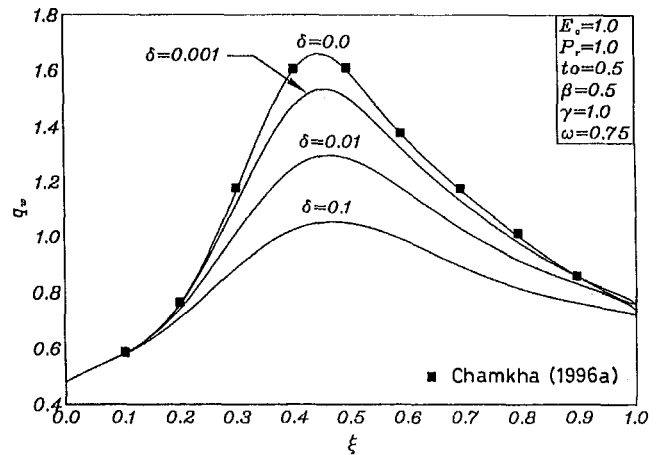


Fig. 23 Wall heat transfer coefficient profiles

moves downstream of the plate's leading edge, the momentum exchange mechanism through the drag force increases causing Δ to decrease and Δ_p to increase until an equilibrium condition where both the fluid and the particle phases move together is reached at $\xi = 1$. However, the values of C and C_p tend to increase to a peak and then decrease to their corresponding equilibrium values. The nonzero or finite values of Δ at the leading edge of the plate ($\xi = 0$) seems contrary to conventional single-phase flow over a semi-infinite flat plate (the Blasius problem). However, with the use of the modified Blasius transformations (Eqs. (6)) for the two-phase

flow situation, the obtained solutions of F and Q at $\xi = 0$ are not uniform as seen from Figs. 1 and 3 as required for a vanishing value of Δ (see Eq. (18)). Therefore, it is expected that Δ takes on a nonzero or finite value at $\xi = 0$. These behaviors for Δ , Δ_p , C , and C_p are clearly depicted in Figs. 7 and 8. Furthermore, as the fluid-phase power index coefficient ω increases, moderate reductions in Δ , Δ_p , and C and slight increases in C_p are predicted as seen in Figs. 7 and 8.

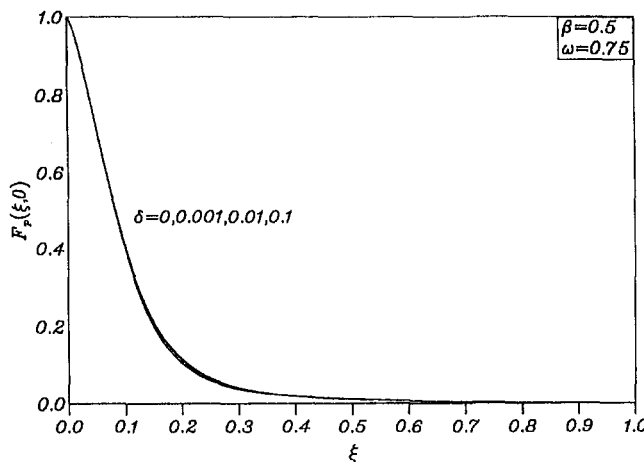


Fig. 21 Wall particle-phase tangential velocity profiles

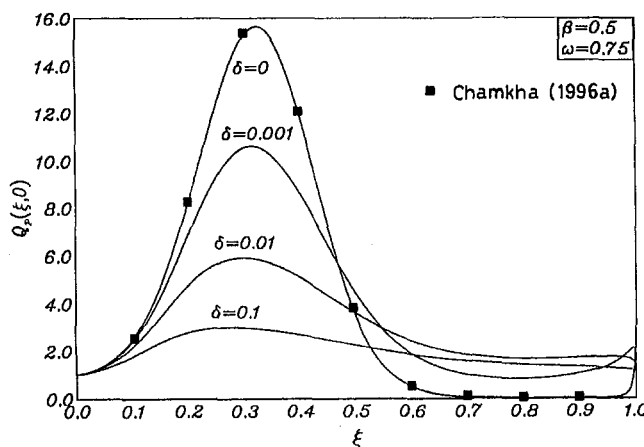


Fig. 22 Wall particle-phase density profiles

Figures 9 and 10 present representative profiles for the particle-phase tangential velocity and density at the wall for various values of the fluid-phase power index coefficient ω . At $\xi = 0$, the particle phase experiences a perfect slip condition at the wall with a uniform density distribution. As ξ increases and the interaction between the phases takes place, the drag force begins to decrease. As a result, the particle-phase wall tangential velocity $F_p(\xi, 0)$ starts to decrease and the particle-phase wall density $Q_p(\xi, 0)$ starts to increase until it reaches a maximum value in the vicinity of $\xi = 0.6$ after which it decreases until it reaches a quasi-equilibrium condition at $\xi = 0.1$. This type of behavior for $Q_p(\xi, 0)$ was predicted in analysis of the incompressible version of the present problem but there it became infinite (suggesting the presence of a singularity) when $F_p(\xi, 0)$ vanished (see, for instance, Osipov, 1980; Datta and Mishra, 1982; Chamkha and Peddieson, 1989). However, in the present analysis a continuous nonsingular solution exists throughout the computational domain. These behaviors in $F_p(\xi, 0)$ and $Q_p(\xi, 0)$ are clearly illustrated in Figs. 9 and 10, respectively. The effect of increasing ω is seen to increase $F_p(\xi, 0)$ slightly and to spread the particles away from the wall causing a significant reduction in the peak values of $Q_p(\xi, 0)$ as shown in Figs. 9 and 10.

In Fig. 11, the wall heat transfer coefficient q_w is presented along the plate for various values of ω . It is seen from this figure that q_w increases to a peak in the vicinity of $\xi = 0.6$ where $Q_p(\xi, 0)$ is maximum and then decreases to a limiting value at $\xi = 1$. It is also seen that as ω is increased q_w is decreased due to the corresponding decreases in $Q_p(\xi, 0)$. This suggests that the energy transfer between the phases increases as the density of the particles increases which, in turn, augments the wall heat transfer as depicted in Fig. 11.

Figures 12 through 14 depict the influence of β on Δ , Δ_p , C , C_p in the presence of a finite value of diffusivity ($\delta = 0.1$) respectively. At $\xi = 0$, the drag force between the phases is maximum and decreases as ξ increases until it vanishes at $\xi = 1$ where equilibrium exists. This momentum exchange causes Δ to decrease (which causes an increase in C) and Δ_p to increase until equilibrium at $\xi = 1$ is reached. However, as β increases, the effective viscosity of the mixture increases and causes a rapid increase in the values of Δ as the flow moves downstream towards equilibrium. Also, increasing β increases the domain of particle-phase viscous

effects causing Δ , Δ_p , and C_p to increase and C to decrease. These facts are clearly shown in Figs. 12 through 14. In addition, the distinctive peak in the values of C for $\beta = 0$ and $\delta = 0$ (inviscid nondiffusive particle phase discussed by Chamkha (1996a)) is still seen for the case where δ is included in the model. However, the effect of including δ in the model is seen to reduce the value of C as clearly shown in Fig. 13.

Figures 15 through 17 illustrate the distributions of the particle-phase tangential velocity and density at the wall and the wall heat transfer coefficient in the presence of particulate diffusivity ($\delta = 0.1$) along the plate for various values of the viscosity ratio β , respectively. It is seen from Fig. 15 that the region of large particulate wall slip is confined to the range $0 \leq \xi \leq 0.25$ for $\beta \neq 0$. As mentioned before, this range is controlled by the choice of the parameters S_R and r . Also, as discussed earlier, the presence of particulate diffusion in the mathematical model (with $\beta = 0$) introduces a smoothing effect which, in turn, causes significant reductions in the values of $Q_p(\xi, 0)$ and q_w . The presence of a particulate viscosity in the dusty-gas model (with $\delta = 0$) results in reductions in the peak values observed for $Q_p(\xi, 0)$ and q_w and causes the peaks to move upstream towards the plate's leading edge as β increases. However, a comparison of Figs. 16 and 17 with the results reported by Chamkha (1996a, 1998) shows that when both β and δ are finite, a particle-free zone does not exist in the entire region $0 \leq \xi \leq 1$. Also, there exists no catastrophic growth in the particle-phase density at the wall. This appears to be ensured by the presence of the particulate diffusivity. However, what appears to be different when the combined effects of δ and β are present in the model is that as β increases the values of $Q_p(\xi, 0)$ and q_w increase above what is predicted for $\beta = 0$. This is in sharp contrast with what is observed earlier (see Chamkha, 1996a). This behavior in q_w appears to be physically reasonable since as the particle viscous effects increase, the heat dissipation from the particle-particle interaction or particle-surface interaction is transferred to the carrier fluid through the interphase heat transfer mechanism. This, in turn, tends to increase the fluid-phase heat transfer to the wall. Therefore, it can be concluded that a dusty-gas model allowing for both inertial transport and diffusion of particles is capable of predicting results that are singularity-free and physically acceptable.

Figures 18 through 23 present the influence of δ on Δ , Δ_p , C , C_p , $F_p(\xi, 0)$, $Q_p(\xi, 0)$ in the presence of particulate viscous effects, respectively. These results compare qualitatively with those reported by Chamkha (1998) for $\beta = 0$. However, it is worth noticing the smoother transition of the values of $F_p(\xi, 0)$ shown in Fig. 21 from perfect slip at $\xi = 0$ to no-slip conditions downstream than those shown earlier by Chamkha (1998). Also, it can easily be seen from Fig. 22 that $Q_p(\xi, 0)$ vanishes in the vicinity of $\xi = 0.7$ for the case of $\delta = 0$ and $\beta \neq 0$ which is consistent with what is discussed before. Figures 22 and 23 illustrate clearly that, in the presence of particulate viscous effects, the particle-phase diffusivity effect is amplified since it causes more variations in the quantitative values of $Q_p(\xi, 0)$ and q_w than observed before for $\beta = 0$. Furthermore, Fig. 22 suggests that the presence of a particulate diffusivity in the dusty-gas model no matter how small is capable of removing the particle-free zone observed for cases where $\beta \neq 0$ and $\delta = 0$.

It should be mentioned that the results associated with $\beta = 0$ and $\delta = 0$ were put in terms of their primitive untransformed variables and compared with those reported by Wang and Glass (1988) and were found to be in good agreement. Furthermore, additional favorable comparisons were performed with the incompressible results reported by Chamkha and Peddieson (1989) and Chamkha (1994) for $\beta = 0$ and $\delta \neq 0$.

In the absence of reported experimental results on the problem considered in this paper, and in spite of the favorable comparisons made (which lend confidence in the numerical procedure), it is difficult to be certain that the phenomena predicted in this work and the work reported previously by Chamkha (1996a, 1998) are physically possible. This is difficult to evaluate because of the

contrast that these results offer when a small change in the mathematical model occurs. Therefore, it is highly recommended that experimental investigation of this problem be undertaken. The present and the previously reported results (Chamkha 1996a, 1998) can serve as a stimulus for this investigation by identifying a particular phenomenon to be investigated.

Conclusion

A continuum dusty-gas model modified to include combined particle-phase diffusive viscous effects was employed in analyzing steady, compressible, laminar, boundary layer flow of a particulate suspension over a flat surface. The mathematical model included balance equations for mass, momentum, and energy for each phase where diffusive transport of thermal energy in the particle phase was neglected and where thermal and momentum exchange between the phases was specified in terms of relaxation time constants. Following the carrier fluid viscosity, the particle phase was assumed to have a general power-law viscosity-temperature and diffusivity-temperature relation. The governing equations were solved numerically using an implicit, iterative, finite difference method. A parametric study was performed to show the effects of the particle-phase viscosity and diffusivity. In contrast with the incompressible version of the flat-plate problem, it was found that a continuous solution existed throughout the computational domain. Other major predictions of the present work are summarized as follows: for a viscous nondiffusive particle phase a particle-free zone is formed at the plate surface; for a diffusive nonviscous particle phase a significant reduction in wall heat transfer and particle concentration at the plate surface is predicted. When both particle-phase diffusive and viscous effects were included in the dusty-gas model, singularity-free solutions were predicted and significant differences in wall particle-phase density concentrations and wall heat transfer with those of previous cases were observed. These various predictions could not be verified by experimental data due to the absence of such data at present. However, favorable comparisons with previously published results on special cases of this problem were made which gave confidence in the accuracy of the numerical method. It is hoped that the present results will be of use to environmental agencies in Kuwait and the Gulf countries in understanding the dynamics of dust storms, in validating computer routines and serve as a stimulus for experimental work on the present problem.

References

- Apazidis, N., 1985, "On Two-Dimensional Laminar Flows of a Particulate Suspension in the Presence of Gravity Field," *Int. J. Multiphase Flow*, Vol. 11, pp. 657–698.
- Blotner, F. G., 1970, "Finite-Difference Methods of Solution of the Boundary-Layer Equations," *AIAA Journal*, Vol. 8, pp. 193–205.
- Chamkha, A. J., 1994, "Effects of Particulate Diffusion on the Thermal Flat Plate Boundary Layer of a Two-Phase Suspension," *ASME JOURNAL OF HEAT TRANSFER*, Vol. 116, pp. 236–239.
- Chamkha, A. J., 1996a, "Compressible Dusty-Gas Boundary-Layer Flow Over a Flat Surface," *ASME Journal of Fluids Engineering*, Vol. 118, pp. 179–185.
- Chamkha, A. J., 1996b, "Compressible Two-Phase Boundary-Layer Flow with Finite Particulate Volume Fraction," *International Journal of Engineering Science*, Vol. 34, pp. 1409–1422.
- Chamkha, A. J., 1998, "Effects of Particulate Diffusion on the Compressible Boundary-Layer Flow of a Two-Phase Suspension Over a Horizontal Surface," *ASME Journal of Fluids Engineering*, Vol. 120, pp. 146–151.
- Chamkha, A. J., and Peddieson, J., 1989, "Boundary-Layer Flow of a Particle-Fluid Suspension Past a Flat Plate," *Developments in Mechanics*, Vol. 15, pp. 315–316.
- Chamkha, A. J., and Peddieson, J., 1992, "Singular Behavior in Boundary-Layer Flow of a Dusty Gas," *AIAA Journal*, Vol. 30, pp. 2966–2968.
- Chamkha, A. J., and Peddieson, J., 1994, "Boundary-Layer Theory of a Particulate Suspension with Finite Volume Fraction," *ASME Journal of Fluids Engineering*, Vol. 116, pp. 147–153.
- Datta, N., and Mishra, S. K., 1982, "Boundary Layer Flow of a Dusty Fluid Over a Semi-Infinite Flat Plate," *Acta Mechanica*, Vol. 42, pp. 71–83.
- Drew, D. A., 1983, "Mathematical Modeling of Two-phase Flow," *Annual Review of Fluid Mechanics*, Vol. 15, pp. 261–291.
- Drew, D. A., and Segal, L. A., 1971, "Analysis of Fluidized Beds and Foams Using Averaged Equations," *Studies in Applied Mathematics*, Vol. 50, pp. 233–252.
- Gadiraju, M., et al., 1992, "Exact Solutions for Two-Phase Vertical Pipe Flow," *Mechanics Research Communications*, Vol. 19, pp. 7–13.

- Gidaspow, D., 1986, "Hydrodynamics of Fluidization and Heat Transfer: Super Computer Modeling," *ASME Applied Mechanics Reviews*, Vol. 39, pp. 1-23.
- Kuerti, G., 1951, "The Laminar Boundary Layer in Compressible Flow," *Advances in Appl. Mech.*, II, pp. 21-92.
- Marble, F. E., 1970, "Dynamics of Dusty Gases," *Annual Review of Fluid Mechanics*, Vol. 2, pp. 297-446.
- Osipov, A. N., 1980, "Structure of the Laminar Boundary Layer of a Disperse Medium on a Flat Plate," *Fluid Dynamics*, Vol. 15, pp. 512-517.
- Patankar, S. V., 1980, *Numerical Heat Transfer and Fluid Flow*, McGraw-Hill, New York.
- Prabha, S., and Jain, A. C., 1980, "On the Use of Compatibility Conditions in the Solution of Gas Particulate Boundary Layer Equations," *Applied Scientific Research*, Vol. 36, pp. 81-91.
- Rubinow, S. I., and Keller, J. B., 1961, "The Transverse Force on a Spinning Sphere Moving in a Viscous Fluid," *Journal of Fluid Mechanics*, Vol. 11, pp. 447-459.
- Saffman, P. G., 1965, "The Lift on a Small Sphere in a Slow Shear Flow," *Journal of Fluid Mechanics*, Vol. 22, pp. 385-400.
- Singleton, R. E., 1965, "The Compressible Gas-Solid Particle Flow Over a Semi-Infinite Flat Plate," *ZAMP*, Vol. 16, pp. 421-449.
- Soo, S. L., 1968, "Non-equilibrium Fluid Dynamics-Laminar Flow Over a Flat Plate," *ZAMP*, Vol. 19, pp. 545-563.
- Soo, S. L., 1989, *Particulates and Continuum Multiphase Fluid Dynamics*, Hemisphere, New York, pp. 282, 292.
- Stewartson, K., 1974, "Multistructured Boundary Layers on Flat Plates and Related Bodies," *Adv. Appl. Mech.*, 14, Academic Press, New York, pp. 146-239.
- Tsuo, Y. P., and Gidaspow, D., 1990, "Computation of Flow Patterns in Circulating Fluidized Beds," *AIChE Journal*, Vol. 36, pp. 888-896.
- Wang, B. Y., and Glass, I. I., 1988, "Compressible Laminar Boundary-Layer Flows of a Dusty Gas Over a Semi-Infinite Flat Plate," *Journal of Fluid Mechanics*, Vol. 186, pp. 223-241.
- Young, A. D., 1949, "Skin Friction in the Laminar Boundary Layer of a Compressible Flow," *Aero. Quart.*, I, pp. 137-164.
- Zuber, N., 1964, "On the Dispersed Two-Phase Flow in a Laminar Flow Region," *Chem. Engng Sci.*, Vol. 19, pp. 897-917.
-

An Experimental Investigation Into the Effects of Grain Transport on Columnar to Equiaxed Transition During Dendritic Alloy Solidification

J. W. Gao

C. Y. Wang

Department of Mechanical Engineering,
The Pennsylvania State University,
University Park, PA 16802
e-mail: cxw31@psu.edu

An experimental study has been conducted to investigate the effects of grain transport on the columnar to equiaxed transition (CET) in dendritic alloy solidification. Using the aqueous ammonium chloride solution as a transparent model alloy, experiments were performed in a vertical test cell with cooling from the top, resulting in unidirectional columnar crystals growing downwards. Ahead of the columnar front, equiaxed nuclei were observed to originate mostly by fragmentation of the columnar dendrites in the presence of a thermally driven flow in the melt beneath the columnar mushy zone. Being heavier than the liquid, these fragments fall into the bulk melt where they may grow or remelt. The survived equiaxed crystals finally settle towards the floor and pile up to form an equiaxed bed. The CET occurs when the bottom equiaxed packed bed rises and eventually obstructs the columnar mushy zone growing from the upper surface. Therefore, the CET in the present configuration was predominantly controlled by the sedimentation of equiaxed crystals. A parametric study by varying initial concentration, cooling rate, and superheat was performed.

Introduction

Dendritic alloy solidification is characterized by the presence of two basic microstructures, namely columnar and equiaxed structures. Transport phenomena during these solidification processes are complex, involving thermosolutal convection in the liquid melt and movement of free solid crystals. These transport phenomena further interact with the microstructural development to dictate the structural as well as compositional features in the final solidified part. Therefore, obtaining a basic understanding of the physical mechanisms for the evolution of the two grain structures has been the focus of extensive research recently.

Research on columnar dendritic solidification has used flow visualization in salt systems such as aqueous ammonium chloride during both horizontal and vertical solidification. Beckermann and Viskanta (1988) chilled an aqueous NH_4Cl solution from a side wall in a rectangular cell and observed the interaction between double-diffusive convection and the mushy region growth using the shadowgraph method. It is revealed that there are a variety of double-diffusive convection patterns developing in the liquid, which considerably influences the local solidification rates and causes partial remelting of the mushy zone. McCay et al. (1989) used Schlieren photography and particle tracking to study Rayleigh-Benard type instabilities and subsequent plume development in solidification from below. Chen and Chen (1991) performed experiments to reveal the nature of salt fingering and plume-like convection in upward solidification of an $\text{NH}_4\text{Cl}-\text{H}_2\text{O}$ solution over a wide range of cold-plate temperatures. The critical Rayleigh number for the onset of plume convection was correlated. Both shadowgraph and dye injection techniques were employed by Magirl and Incropera (1993) to observe the flow and morpholog-

ical conditions associated with the solidification from side walls and from the bottom of a rectangular cavity. Finger-type double-diffusive convection, plume, and channel formation in the columnar mushy zone were observed and identified. Garimella et al. (1995) investigated the characteristics of the mushy zone during upward unidirectional solidification in the presence of vibration. It was found that the application of low-amplitude vibration to the test cell suppressed the channel formation, but the frequency of vibration appeared to have no influence.

In comparison to columnar solidification, equiaxed solidification is less understood and more complicated due to the movement of free solid crystals. The formation of equiaxed crystals in ingots was first studied by Jackson and Hunt (1966), in which various $\text{NH}_4\text{Cl}-\text{H}_2\text{O}$ solutions were cooled from the bottom as well as left and right side walls. Columnar growth was observed in the early stages of solidification, while in the later stages the equiaxed crystals filled the central region. The origin of these crystals was attributed to fragmentation resulting from remelting and detachment of columnar dendrite arms. Hellawell et al. (1993) speculated that the formation of plumes rising through the bulk liquid is a mechanism for sweeping the dendrite fragments out of the columnar mushy zone. Paradies et al. (1997) conducted experiments in a model alloy (succinonitrile and acetone) to investigate the effects of convection on dendrite fragmentation. Using a 30 percent aqueous ammonium chloride solution, Beckermann et al. (1994) visualized the convective transport and sedimentation of free crystals as well as thermosolutal convection in the melt in a square test cell evenly cooled from all the walls. Melt convection in the form of two circulatory cells was found to have a profound influence on the movement of the solid phase and consequently the formation and shape of the sediment bed.

The most complicated solidification mode occurs when columnar and equiaxed grains coexist in a single ingot, leading to a mixed columnar/equiaxed grain structure. This mixed mode of solidification occurs if equiaxed grains can nucleate and grow in the bulk liquid ahead of an advancing columnar front, resulting in a transition from the columnar to equiaxed zone (Flood and Hunt,

Contributed by the Heat Transfer Division for publication in the JOURNAL OF HEAT TRANSFER. Manuscript received by the Heat Transfer Division, Dec. 10, 1997; revision received, Dec. 10, 1998. Keywords: Heat Transfer, Microstructures, Solidification, Two-Phase, Visualization. Associate Technical Editor: D. Zumbrennen.

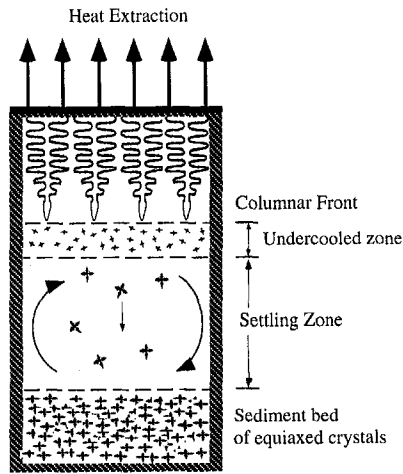


Fig. 1 Illustration of columnar to equiaxed transition (CET) in an ingot solidifying from the top

1988). This columnar-to-equiaxed transition (CET) represents an important topic in solidification science and technology.

There have been several experimental studies on CET. Mahapatra and Weinberg (1987) experimentally measured the CET locations in Sn-Pb alloys, while Ziv and Weinberg (1989) obtained CET data for an Al 3pct Cu alloy solidified directionally upwards. Both studies dealt with the diffusion-dominated solidification, in which case a predictive model for CET was recently developed and validated by the experimental data available in the literature (Wang and Beckermann, 1994).

The CET in the presence of melt convection and grain transport, however, remains largely unexplored (Flood and Hunt, 1988). To develop a basic physical understanding in this case, Jang and Hellawell (1991) recently performed a visualization experiment on CET in a continuous casting configuration using the $\text{NH}_4\text{Cl-H}_2\text{O}$ model alloy. Their study clearly indicated the important roles played by crystal sedimentation in the development of an equiaxed zone and subsequently blocking of the columnar front. The CET data in metal systems featuring the influences of both melt convection and grain transport were measured by McCartney and co-workers (Griffith and McCartney, 1993; McCartney and Ahmady, 1994) from the micrographs of Al-Cu and Al-Si alloys solidified from above. In some experiments grain refiners were added in the alloy melt to promote equiaxed solidification and, as a result, equiaxed grains were observed in the bottom half of an ingot whereas columnar grains were present in the upper half.

Although the detailed dynamics of CET could not be revealed in these metal experiments due to their opacity, a series of sequences can be hypothesized to explain the final CET observed in solidified micrographs. These sequences are schematically described in Fig. 1 for a one-dimensional coupled columnar and equiaxed solidification occurring in an ingot cooling from the top. First, columnar crystals nucleate at the top chill surface and grow unidirectionally downwards into the liquid melt. Ahead of the columnar zone, there exists an undercooled zone as the columnar front growth requires a certain degree of undercooling. Secondly, equiaxed grain growth occurs inside the undercooled melt provided that tiny nuclei (e.g., impurities, dendrite fragments, etc.) are present. Thirdly, the growing equiaxed crystals settle and finally deposit at the bottom, forming an equiaxed sediment bed. The final CET results when the bottom equiaxed zone meets the advancing columnar front from above.

If the sequences depicted in Fig. 1 are physically correct, it would be readily possible to predict the CET in the presence of melt convection and grain transport using the recently developed multiscale/multiphase model of Wang and Beckermann (1996). This modeling framework is capable of integrating the microstructure growth features into the macroscopic calculations of heat flow

and solute redistribution with melt convection and solid phase transport.

The present work is therefore to investigate the grain structural development and CET during directional dendritic solidification from the top, a configuration corresponding to the metal system studied recently by Griffith and McCartney (1993) and McCartney and Ahmady (1994), but now using the $\text{NH}_4\text{Cl-H}_2\text{O}$ model alloy. The transparency of this model system permits us to accomplish two main objectives: (1) to visualize and develop a physical understanding of the processes leading to the final CET so as to assist forthcoming model development, and (2) to provide a quantitative set of experimental data on the dynamic processes of solidification in action for model validation (i.e., the temporal evolution of various structural zones). The present work is the first part of an ongoing effort to ultimately model and simulate the CET in the presence of crystal sedimentation and melt convection using the multiphase model of Wang and Beckermann (1996).

Experimental Methods

Solidification experiments were carried out in a rectangular test cell consisting of a stainless steel heat exchanger cold plate as the top wall, a Plexiglas bottom wall, and a transparent center section to allow visual access from the front and back sides. The test cell has inner dimensions of 4.20 cm height \times 2.8 cm width \times 1.27 cm depth, as shown in Fig. 2. The system was insulated on all sides with 2.54 cm thick black urethane closed-cell foam insulation materials. Two removable covers fabricated from the insulation material were placed over the front and back walls as brief but periodic optical access to the test cell during imaging tests, which typically were of only 1–2 minutes duration.

The heat exchanger was made of a Lexan block of dimensions 2.54 cm high by 2.54 cm wide by 5.54 cm long. Small coolant passages were machined into the block. The lower surface of the block was bonded to a 0.04-cm thick stainless steel sheet which served as heat transfer surface contacting with the test solution. Cooling was accomplished by passing a mixture of ethanol glycol and water (1:1) through the heat exchanger. A low-temperature thermal bath circulator (RM20 LAUDA) maintained the cold plate at preset temperatures. The coolant with the desired temperature was then pumped into the heat exchanger by a Dayton Silicon Oil pump.

Temperature measurements were performed using copper-constantan (type-T) thermocouples that were mounted through the side panel of the test cell. Modular plug-in thermocouples (Omega Model number TMQSS-020-6) were used, calibrated to an accuracy of $\pm 0.3^\circ\text{C}$. Figure 2 also details the positioning of the thermocouple probes within the test cell. All the probe tips were positioned in the midplane of the cell. A scale attached to the test

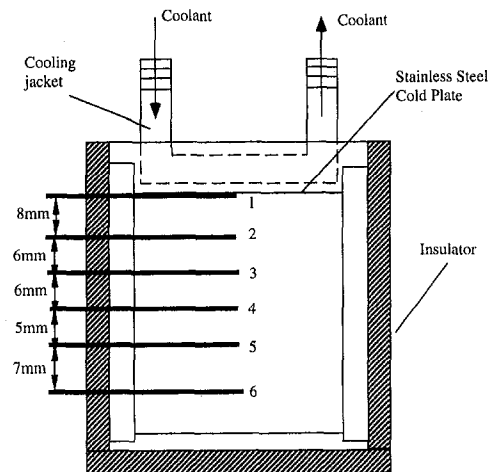


Fig. 2 Schematic of test cell

Table 1 Experimental conditions

Experiment run no.	Initial concentration of NH ₄ Cl (wt.%)	Superheat (°C)	Cooling plate temperature (°C)
1	32	1	-19
2	34	1	-19
3	32	5	-19
4	32	13	-19
5	32	5	-14

cell was used to position the thermocouple tips. The scale has a resolution of 1 mm and thus the error in thermocouple positioning was estimated to be ± 1 mm. Each of the thermocouples was wired into a data acquisition system which consisted of a Macintosh II computer equipped with a Fluke HELIOS I data logger. A visual instrument program based on Labview was written to control the data acquisition. The temperature readings were scanned and saved at three-second intervals during each experiment.

Qualitative observations of the solidification phenomena and flow structures within the test cell were recorded by two methods: a shadowgraph visualization system and normal photography. The optical system included a light source, optics, translucent glass, and camera. The light source consisted of a beam from an ORIEL mercury arc lamp which was collimated by reflecting it off a parabolic mirror and then the resulting parallel light passed through the test cell. In the shadowgraph setup, the light through the test cell was then imaged onto a movable translucent glass served as a screen. The translucent glass was placed in front of the test cell in the light pass for normal photography. Both kinds of images were photographed by Nikon N70 camera using Kodak TMAX 100 Black and White films. During the time at which the photographs were taken, the front and back insulations were removed from the cell momentarily.

The binary phase-change material chosen for this study was aqueous ammonium chloride (NH₄Cl-H₂O). This system has an eutectic temperature of -15.4°C and the eutectic concentration of 19.7 wt%. Before pouring the test material into the inner cavity, the test cell walls were preheated to the test temperature of the melt. The pouring temperature was about 5°C higher than the test temperature. The NH₄Cl-H₂O solution was injected into the cell with a syringe and all bubbles were removed from the melt. Before commencing each experiment, the cell was left idle for about half an hour to reach equilibrium with the test cell walls, and then stirred to eliminate any solutal gradients within the liquid solution. After the melt was allowed to become quiescent again, the coolant was started to pump into the heat exchanger to induce cooling and the experiment was commenced.

The heights of the columnar and equiaxed zones were recorded by a scale attached to the test cell vertically along the center of the front wall. The scale has a resolution of 1 mm and therefore the uncertainty associated with the height measurements was estimated to be ± 1 mm. Since the surfaces of both the columnar region and sediment bed were not smooth, the uncertainties associated with an irregular interface were estimated by taking readings of the maximum and minimum heights of the interface and are denoted by the error bars for each point in the figures (Figs. 8(b) and 10). The qualitative experiments (i.e., photography and shadowgraphy) and quantitative experiments (i.e., temperature, columnar, and equiaxed zone measurements) were conducted separately so as not to interfere with each other.

Results and Discussion

A total of five experiments were conducted with variations in the initial concentration of ammonium chloride, superheat and cooling plate temperature. The experimental conditions are summarized in Table 1.

General Observations. Observations are first presented for a representative case (i.e., experiment #1) with an initial ammonium

chloride concentration of 32 wt% (corresponding to a liquidus temperature of 42°C), a cold plate temperature of -19°C , and melt superheat of 1°C . The time evolutions of the solidification process are displayed in the selected images shown in Figs. 3 through 7.

Immediately after the experiment was commenced, crystals were nucleated over the cold plate and grew rapidly. As soon as they were formed, these crystals were separated from the top wall and swept into the melt, as can be seen from Fig. 3. This is due to the strong thermal convection developing in the melt upon initiation of cooling. The convection exerted a shear force on the crystals and shook them to break from the root and separate from the wall. Notice the movement of the crystals in the shadowgraph image; they did not fall straightly towards the bottom, instead, they were swirling and swept into the melt, revealing that there must be a cellular, counterclockwise flow. This flow pattern can be explained by the fact that the left side was close to the inlet of the coolant, and hence the melt in this region was colder and heavier leading to the downwards flow on this side.

At about 15 seconds a layer of columnar dendrites began to penetrate from the top wall and grow unidirectionally downwards into the melt (see Fig. 4). As a result, the temperature difference prevailing in the liquid melt decreases from 62°C to approximately 1°C , which substantially weakens the thermal convection. Therefore, vertical sedimentation of the crystals became predominant, as evidenced by the uniform distribution and settling of separated crystals (see Fig. 4). At this moment, it is seen that a lot of free crystals were growing in the undercooled melt during settling, resulting in the "showering" of small equiaxed crystals. The settled crystals deposited on the floor of the test cell and formed a sediment bed of equiaxed crystals.

As the solidification process continued, the melt became more undercooled. The free equiaxed grains settling through the melt grew into larger crystals and fell faster, as shown in Fig. 5 (120 seconds into the experiment). Since the shadowgraph was not time

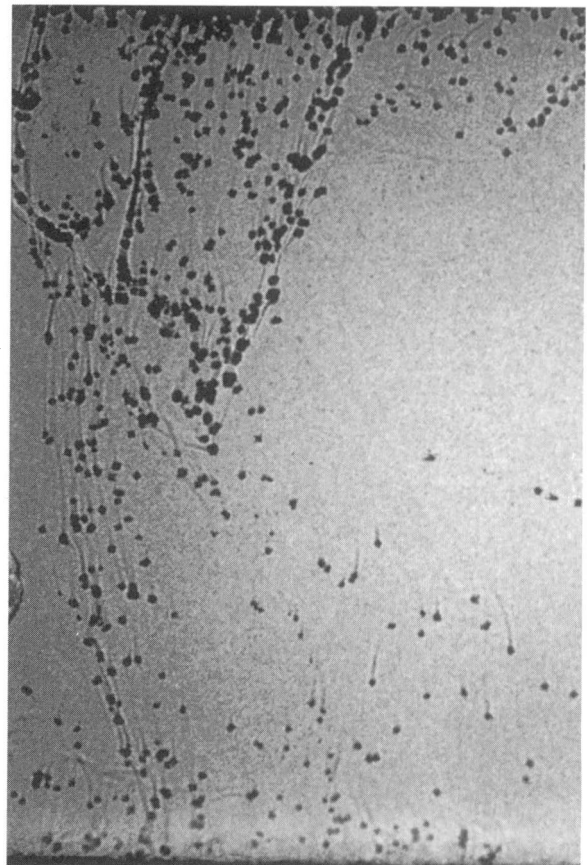


Fig. 3 Shadowgraph image (exp. #1, $t = 1$ second)

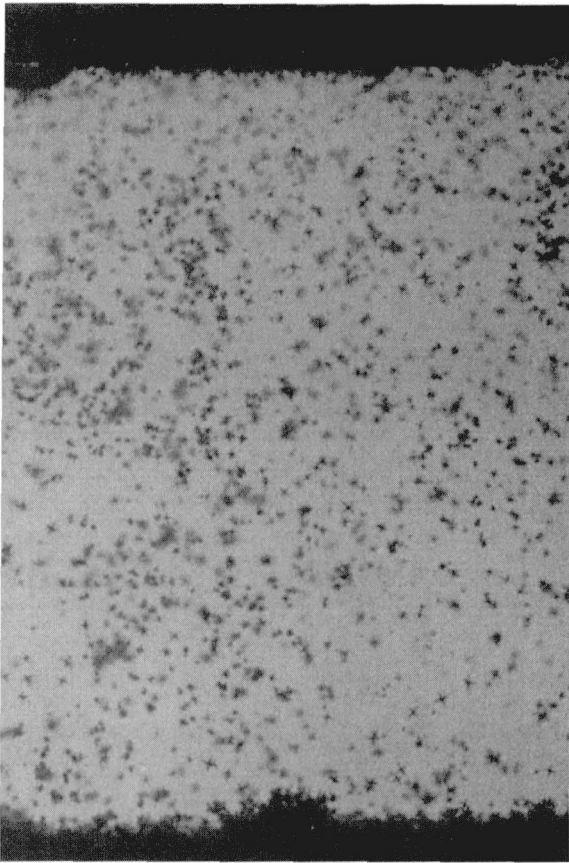


Fig. 4 Normal photograph (exp. #1, $t = 15$ seconds)

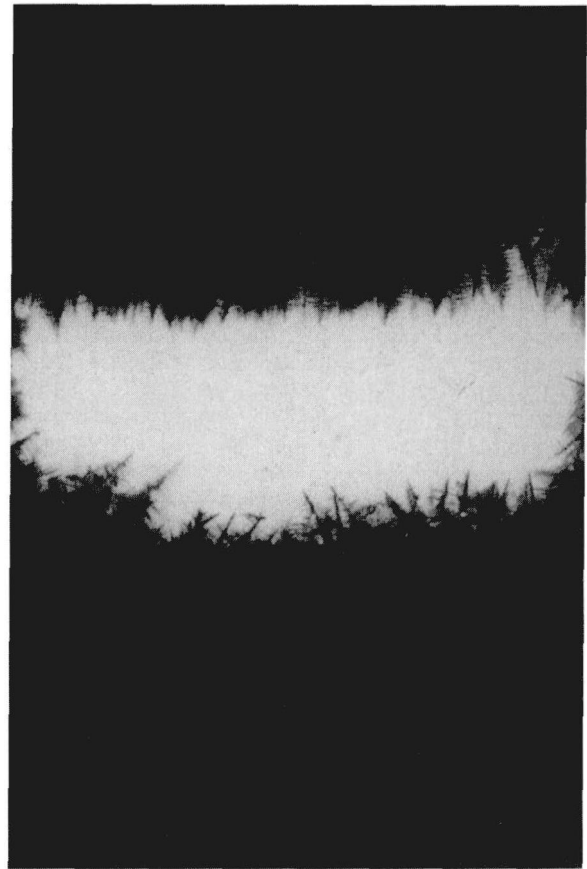


Fig. 6 Normal photograph (exp. #1, $t = 1800$ seconds)

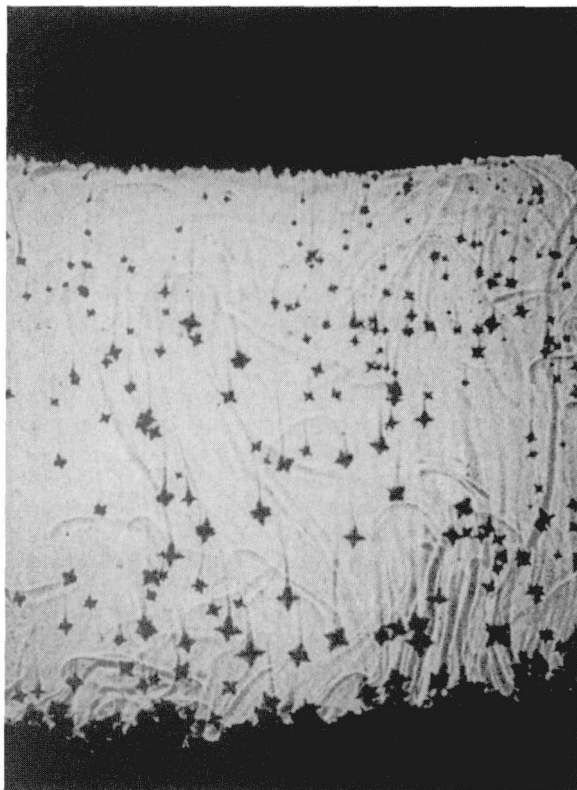


Fig. 5 Shadowgraph image (exp. #1, $t = 120$ seconds)

exposed (exposure time was $1/125$ seconds), the tails behind the crystals did not represent the motion of the crystals through a time exposure but rather solutal wakes left by the crystals as they traveled through the melt. According to the phase diagram of $\text{NH}_4\text{Cl-H}_2\text{O}$, the forming solid is almost pure ammonium chloride and thus, the solute (here is water), which is less dense, is rejected from the crystals to the immediately surrounding liquid. The water-rich liquid formed the wakes behind each crystal. Due to a low liquid mass diffusivity ($4.9 \times 10^{-9} \text{ m}^2/\text{s}$), these wakes retained their composition identity and were clearly visible in the shadowgraph image as a result of the density difference between the wakes and the surrounding melt. Therefore, the wakes were an indication of the crystal growth during settling and they also clearly showed the direction of the crystal movement, which was essentially downwards for almost all the crystals. It is worth noticing that the tails in Figs. 3 and 5, although similar in appearance, are of different compositions. In the case of Fig. 3 the crystals undergo remelting during settling since their sizes decrease towards the cell bottom, and the wake left behind each crystal is composed of remelted NH_4Cl liquid. However, density gradients in the wakes of remelting crystals look similar to those of growing crystals in a shadowgraph.

At this point in time ($t = 120$ seconds), the thermal convection in the melt becomes weaker mainly because the spatial dimension of the liquid melt was reduced to about two-thirds of the total height of the cell due to the growth of the columnar and equiaxed zones. The small temperature difference ($\Delta T \sim 7^\circ\text{C}$) and the smaller size of the liquid region resulted in a weak thermal convection. The solutal convection can also be seen at this stage in the form of plume convection (see Fig. 5). It may appear from Fig. 5 that the plume convection is strong, but this is somewhat misleading. The photograph shows that there are about ~ 30 plumes rising with diameter of ~ 1 mm. The bulk liquid region in the cross section was 28 mm wide and 12.7 mm deep. Therefore, the actual

fraction of the plume liquid was small and estimated to be $\sim [(\pi/4)(1 \text{ mm})^2(30)/(28 \text{ mm})(12.7 \text{ mm})] \sim 6$ percent of a horizontal cross section. The present result is in good agreement with the observations and estimate of Jang and Hellawell (1991). Thus, at this moment, the solutal convection was fairly weak.

Upon further cooling, the upper columnar region and lower equiaxed sediment bed continued to grow, keeping essentially flat in appearance and at a reduced rate. Due to the weak convective flow in the melt, there were no more flow-generated fragments. There was also no sign of nuclei generated by other mechanisms (e.g., heterogeneous nucleation of foreign nuclei or impurities). The melt was continually becoming more water-rich due to the precipitation of solid crystals. At this time, both growth rates of columnar zone and equiaxed sediment bed were decreasing because the melt continued to be water enriched and its liquidus temperature dropped. At about 1800 seconds into the experiment, the equiaxed zone growth almost ceased, while the columnar front kept advancing at a rather low velocity, as shown in Fig. 8(b). The equiaxed crystals on the top edge of the sediment bed began to slowly grow in a preferential direction towards the upper melt, whereas the growth of its lower branches was suppressed by dendrite packing. This can be visualized in Fig. 6 where the crystals in the vicinity of the edge of the sediment layer evolved into a columnar-like morphology. This grain evolution was found in all experiments in this study and may represent a feature of the late stage of the CET.

At about 4200 seconds into the experiment, the upper crystal layer and lower crystal layer met together, blocking each other as shown in Fig. 7. The final CET occurred at this time (see Fig. 8(b)).

Cooling Curves. The cooling curves shown in Figure 8(a) can be further scrutinized by dividing into two groups of different

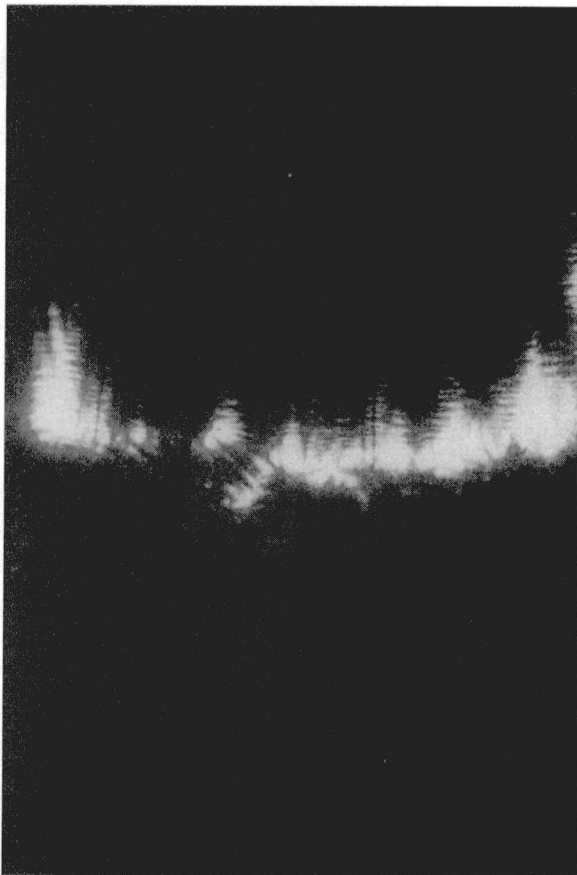
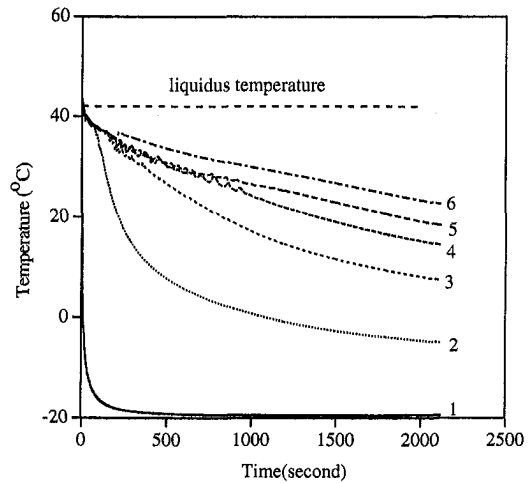
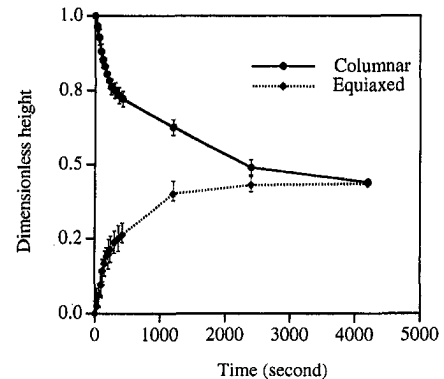


Fig. 7 Normal photograph (exp. #1, $t = 4200$ seconds)



(a)



(b)

Fig. 8 (a) Cooling curves and (b) growth of columnar and equiaxed zones for exp. #1

features. The first group consisting of the thermocouple plots at locations 2 and 6 is displayed in Fig. 9(a) with a magnified scale. Note that minimums existed in both temperature curves. This phenomenon, which is commonly observed in equiaxed solidification, is known as *recalescence*. This occurs when the latent heat released upon solidification exceeds the rate of heat removed externally, resulting in a local temperature rise. However, the mechanisms behind the temperature rises of the two locations appear different. The *recalescence* at location 2 occurred at $t = 15$ seconds when the equiaxed crystals “showering” began and location 2 coincided with the point where a large amount of free crystals nucleated and grew at the instant of time. Therefore this *recalescence* is believed to be associated closely with nucleation. The temperature rise at location 2 was about 1°C and short in duration (about ten seconds) due to a high local cooling rate, which is in agreement with the theoretical predictions available in the literature (Rappaz and Thevoz, 1987). According to Hollands et al. (1975), natural convection in an analogous system with heating from below becomes turbulent at the Rayleigh number of 10^6 . Thus, the melt flow in the present system could be turbulent due to a Rayleigh number of approximately 2×10^6 . However, notice that the duration of the temperature rise at location 2 is about two seconds, while the fluctuation of turbulent thermals is usually less than one second (Sparrow et al. 1970; Kirkpatrick and Bohn, 1986). Hence, we believe that the temperature rise in location 2 is more attributed to *recalescence* than turbulent fluctuation. In fact, due to the low sampling rate of thermocouples (i.e., three seconds) used in the present study, the turbulent fluctuations are unlikely to be picked up.

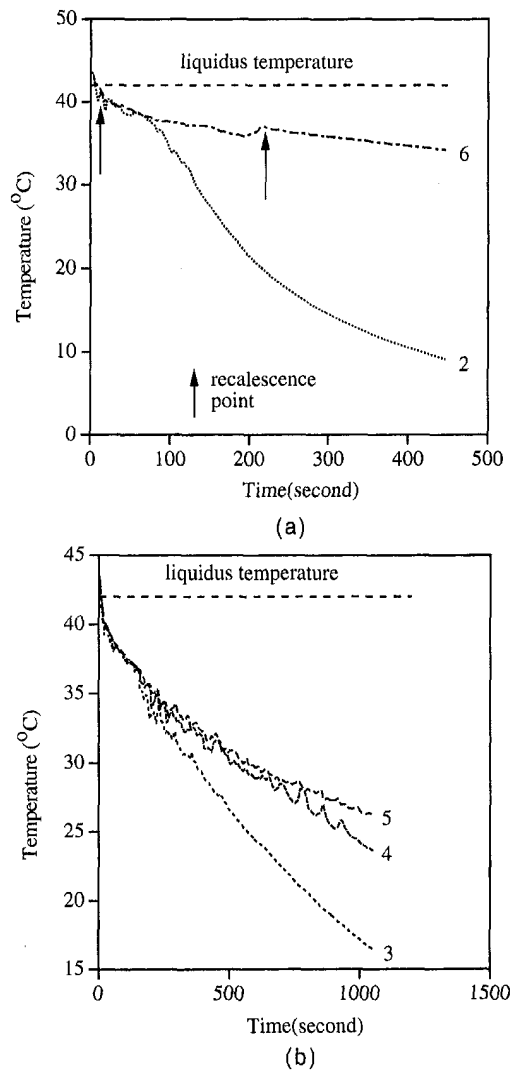


Fig. 9 Cooling curves for exp. #1 at (a) locations 2 and 6, and (b) locations 3, 4, and 5

Location 6, where recalescence occurred much later ($t = 200$ seconds), was located near to the bottom of the sediment layer. At the moment recalescence began, the equiaxed deposit layer was just passing this point. This recalescence is therefore a result of crystal sedimentation, as also observed in other experiments (Beckermann and Wang, 1996). This can be explained as follows. The melt right above the sediment layer was in an undercooled state, while the melt inside the sediment bed can be expected to be solutally well mixed and at a temperature corresponding to the local equilibrium liquidus concentration. Therefore, as the crystals settled on the edge of the sediment bed, the system locally adjusted from an undercooled to an equilibrium state by raising its temperature instead of adjusting the concentration due to the lower mass diffusivity than the thermal diffusivity.

Other cooling curves show relatively strong temperature fluctuations (see Fig. 9(b)), especially in the melt at early stages of solidification and at locations and instants when columnar front passed by. At the thermocouple locations 3 to 5, the fluctuation began almost upon "showering" of equiaxed crystals, primarily due to the highly transient equiaxed crystal growth and movement. At location 3, the temperature curve became smooth at about 480 seconds into the experiments, when the columnar front had passed this point (Fig. 8(b)). The temperature fluctuations at location 4 and 5 lasted much longer. These two points were inside the liquid melt during most of the solidification process, thereby experienc-

ing transient equiaxed crystal growth and motion as well as highly transient and complicated thermosolutal convection. The temperature fluctuation diminished when the melt no longer contained equiaxed crystals.

Parametric Study. Experiments were performed to investigate the effects of solidification conditions, such as the superheat, cooling rate, and initial concentration on the columnar-to-equiaxed transition described in the preceding section.

An aqueous solution of 34 percent ammonium chloride (liquidus temperature of 51°C) was solidified at the same superheat ($\Delta T = 1^{\circ}\text{C}$) and cold plate temperature (-19°C) as for the previous 32 percent solution. The columnar versus equiaxed growth is shown in Fig. 10(a). It can be seen that at higher concentration, the equiaxed zone is larger and the CET occurred earlier (about 1800 seconds for the 34 percent $\text{NH}_4\text{Cl-H}_2\text{O}$ solution versus 4200 seconds for the 32 percent solution). Our observation indicated that, upon initial cooling, a larger amount of crystals were detached and advected into the melt of higher concentration of NH_4Cl . Due to the higher pouring temperature (52°C) of the melt, the thermal convection was also stronger, leading to more separation of the crystals from the top cooling wall. These crystals grew and settled towards the bottom of the test cell, resulting in an earlier block of the columnar front and thus the earlier CET.

Figures 10(b) and 10(c) show the columnar versus equiaxed growth in solidification with superheats of 5°C and 13°C , respectively. Compared to Fig. 8(b), it can be seen that the higher superheat results in a longer columnar zone and a shallower equiaxed sediment layer. At higher superheat, the undercooled zone for equiaxed crystals to survive was narrowed. Note the equiaxed zone evolution in Fig. 10(c). At the early stage of solidification, the crystals originated from fragmentation rarely survived due to the remelting in the superheated melt when traveling towards the bottom, leading to almost no sediment layer on the floor of the cell. The growth of the equiaxed zone started to increase at about 300 seconds into the solidification but decreased again at about 600 seconds. This can be explained as follows. At the early stage of solidification, high superheat causes more vigorous thermal convection in the melt, which promotes the separation of crystals from the wall. On the other hand, the high superheat melt kills the free crystals entering it by remelting. A combination of the two effects results in an overall thin equiaxed sediment layer observed in this experiment. At about 300 seconds, the melt started to become undercooled, which promotes equiaxed crystals to grow and equiaxed sediment layer to increase markedly. At about 600 seconds, thermal convection was weakened, leading to a decreased number of flow-induced fragments and thereby a drop in the growth of the equiaxed zone.

A comparison between the cases presented in Figs. 10(b) and 10(d) shows the effect of the cold plate temperature. For the cases studied here, a higher cold plate temperature, which means a lower cooling rate, favors the development of the equiaxed region. A low cooling rate would slow down the columnar dendrite formation from the top wall, and the crystals formed on the cooling wall have more chances to be detached by melt flow.

Discussion. From the above experimental study, five steps can be identified to be involved in the columnar-to-equiaxed transition: (1) origin of free fragments; (2) survival of the free crystals; (3) growth of survived equiaxed crystals in an undercooled liquid; (4) sediment of the growing crystals to form an equiaxed bed on the bottom; and finally (5) the columnar-to-equiaxed transition when the equiaxed sediment bed obstructs the columnar growth from the upper cooling surface.

Origin of Free Equiaxed Crystals. In the present study, the origin of the equiaxed nuclei appears to be due to the fragmentation of the columnar front. There are two stages of fragmentation associated with the melt flow developing in the solidification process. Upon initiation of the cooling from the top, a counter-clockwise thermally driven flow developed within the melt. In the

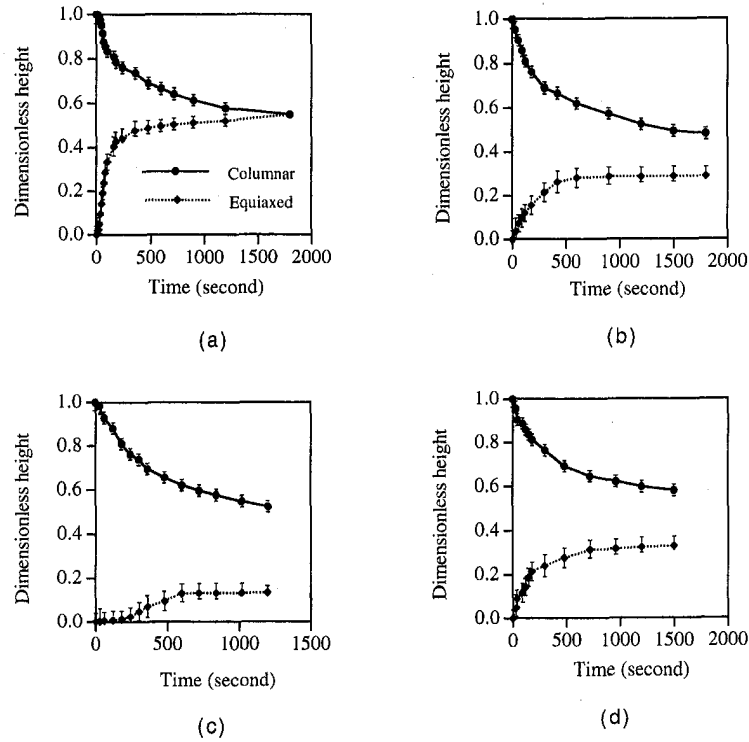


Fig. 10 Growth of columnar and equiaxed zones for (a) exp. #2, (b) exp. #3, (c) exp. #4, and (d) exp. #5

presence of this strong convective flow prevailing in the entire melt, the nucleating dendrites were stripped away from the cold surface. The bonding energy between nucleating dendrites and the cold surface was not strong enough to overcome the drag imposed from the liquid currents. Consequently, these crystals were separated from the cooling wall. The fragments generated at this stage are typically of 1 mm in size (see Fig. 4).

With the progression into the solidification and formation of a mushy layer on the cold surface, convection diminishes. At this stage, the drag imposed on the columnar dendrites may only be sufficient to break small arms (such as secondary arms), generating fragments that are small in size. A close up of the vicinity of the columnar front shown in Fig. 5 was recorded and processed, showing that the fragments ejected from the upper columnar layer have the size of about 20 μm .

Once produced, the fragments may be transported into the melt by convective flow and by gravity, with gravity settling usually being dominant.

Survival of Fragments. When free particles enter a superheated melt, they may be remelted and have a limited life span. In order to ascertain the effects of an initial superheat in the melt, it is instructive to estimate the life span of particles falling through a superheated environment. According to Han and Hellawell (1997), under the present experimental conditions, where the superheat is low, the melting of particles is solutal dissolving controlled. The melting rate, v_s , can thus be given by

$$v_s = \frac{D_l \Delta T}{-m_l(1 - C_0)\delta_s} \quad (1)$$

where D_l is the liquid diffusion coefficient, C_0 is the melt concentration, δ_s is the thickness of the diffusion boundary layer, ΔT is the melt superheat and m_l is the slope of the liquidus line. Equation (1) is valid also in the convection case provided δ_s is properly estimated. For the diffusion-controlled remelting, δ_s is equal to the radius of a spherical dendrite, r . Accounting for the internal porosity of an equiaxed dendrite, the melting rate can be defined as

$$v_s = f_s \frac{dr}{dt} \quad (2)$$

where f_s is the internal solid fraction of the dendrite. Combining Eq. (1) with $\delta_s = r$ (in the diffusion case) and Eq. (2), the remelting time of a dendrite can be estimated by

$$t_{\text{remelting}} = \frac{-m_l(1 - C_0)f_s}{2D_l\Delta T} r_0^2 \quad (3)$$

where r_0 is the initial radius of the sphere. In the $\text{NH}_4\text{Cl-H}_2\text{O}$ system, take $D_l = 4.8 \times 10^{-9} \text{ m}^2/\text{s}$, $C_0 = 68 \text{ wt\%}$ (water here), $m_l = -4.67 \text{ K/wt pct}$. Furthermore, it has been reported that $\text{NH}_4\text{Cl-H}_2\text{O}$ crystals is highly porous ($f_s < 5$ percent) (Jang and Hellawell, 1994). If we use $f_s = 0.02$, the results of the remelting time are given in Table 2. Keep in mind that these remelting times correspond to the diffusion-controlled condition and thus are the most conservative estimates. With convection, the thickness of the diffusion boundary layer δ_s would be thinner and therefore the remelting time would be shorter. Also, the above analysis is intended only for the fate of dendrite fragments at the initial stages of solidification where the superheat remains in the melt.

Sedimentation. Due to the high dendriticity of NH_4Cl crystals, its settling velocity reaches the terminal value very quickly, although the particles accelerate as they grow (Jang and Hellawell, 1994). The modified Stokes' equation can thus be used to estimate the terminal velocity of particles.

Table 2 Comparison between remelting time and settling time of equiaxed crystals

	$t_{\text{remelting}}$ (seconds)		t_{settling} (seconds)
	Superheat = 1°C	Superheat = 10°C	
$d = 20 \mu\text{m}$	0.03	0.003	42000
$d = 1 \text{ mm}$	75	7.5	16

$$v_T = \frac{\alpha [f_s \Delta \rho_{sl} + (1 - f_s) \rho_{ll}] r^2}{\mu} \quad (4)$$

where $\alpha < \frac{2}{3}$, g is the gravitational acceleration, f_s is the solid fraction within each grain, $\Delta \rho_{sl}$ is the solid-liquid density difference, $\Delta \rho_{ll}$ is the density difference between the liquids inside and outside the envelope (i.e., interdendritic and extradendritic liquids), and μ is the liquid viscosity. Analysis of sedimentation rates in the $\text{NH}_4\text{Cl-H}_2\text{O}$ system using Eq. (4) gives good agreement with experimental observations with $\alpha = 0.1$ and $f_s = 0.02$ (Jang and Hellawell, 1994). Therefore, the following estimate can be obtained for the sedimentation rates (taking $\mu = 1.03 \times 10^{-3}$ kg/ms, $\Delta \rho_{sl} = 572$ kg/m³, and noting that $\Delta \rho_{ll} \ll \Delta \rho_{sl}$ and thus is neglected):

$$v_T = 2.7 \text{ mm/s for } d = 1.0 \text{ mm and}$$

$$v_T = 1 \text{ } \mu\text{m/s for } d = 20 \text{ } \mu\text{m.}$$

Knowing the height of this test cell (i.e., 42 mm), the settling times for various fragments can be estimated, as listed in Table 2 along with the respective remelting times. Once again, these estimates of the settling time do not take account of a convective melt and the variable size of dendrites during settling.

Columnar-to-Equiaxed Transition. The results in Table 2 indicate that the small fragments of 20 μm in diameter will hardly survive in both environments with the superheats of 1°C and 10°C. For large fragments of 1 mm in diameter, at the superheat of 1°C, they most likely survive and settle to the bottom of the test cell, although subject to partial remelting during settling. However, they are likely to be remelted and disappear with the superheat of 10°C. This simple analysis further supports the formation of a thin equiaxed zone shown in Fig. 10(c) at the early stages of solidification. It should be cautioned that the results of crystal settling and remelting listed in Table 2 are only accurate to their orders of magnitude due to the various assumptions made above.

As survived equiaxed crystals reach the bottom, they tend to pile up and form a packed bed. In the literature, the columnar-to-equiaxed transition has been investigated in a situation where equiaxed crystals move towards the columnar front and grow sufficiently in size and number to block the advancing columnar front. In the present study, the equiaxed crystals move away from the columnar mushy zone and settle to form an equiaxed region, which determines the final CET. Thus, the CET in the present study is controlled by the equiaxed zone formation as a result of crystal sedimentation. As long as the solidification environment promotes the formation of an equiaxed sediment zone, the CET will occur and the location of the CET is determined primarily by the extent of the equiaxed zone.

Conclusions

The following major conclusions can be drawn from the present experimental study:

1 With cooling from the top, CET was observed with a columnar structure in the upper portion of the test cell and an equiaxed sediment bed in the lower portion.

2 The origin of equiaxed nuclei was found to be due to crystal fragmentation in the presence of thermal convection during solidification. The fragments were then transported into the melt, where they may grow or be remelted. The survived crystals settled under gravity towards the floor of the test cell and piled up to form an equiaxed sediment layer, thereby leading to the CET.

3 The effects of the initial concentration, superheat and cooling rate on CET were investigated. Higher initial concentrations of NH_4Cl resulted in longer equiaxed zones and hence earlier CET.

Higher superheats and higher cooling rates favored the columnar growth over that of equiaxed crystals.

4 Columnar-to-equiaxed transition in this study was found to be controlled by the formation and extent of the equiaxed sediment bed, which is a direct result of generation, transport, survival, and eventual growth of dendrite fragments.

Parallel efforts to develop a physical model and provide computer simulations for the same problem in question are presently underway. Simulation results as well as comparison to the experimental data obtained herewith will be reported in a forthcoming publication.

Acknowledgment

This work was partially supported by the National Science Foundation under Grant No. CTS-9733662.

References

- Beckermann, C., and Viskanta, R., 1988, "Double-diffusive Convection during Dendritic Solidification of a Binary Mixture," *PhysicoChemical Hydrodynamics*, Vol. 10, No. 2, pp. 195–213.
- Beckermann, C., Feller, R. J., Irwin, T. R., Muller-Spath, H., and Wang, C. Y., 1994, "Visualization of Sedimentation and Thermo-Solutal Convection During Equiaxed Alloy Solidification," AIAA Paper No. 94-0570, AIAA, Washington DC.
- Beckermann, C., and Wang, C. Y., 1996, "Equiaxed Dendritic Solidification with Convection, Part III: Comparisons with $\text{NH}_4\text{Cl-H}_2\text{O}$ Experiments," *Metall. Trans. A*, Vol. 27A, pp. 2784–2795.
- Chen, C. F., and Chen, F., 1991, "Experimental Study of Directional Solidification of Aqueous Ammonium Chloride Solution," *J. Fluid Mech.*, Vol. 227, pp. 567–586.
- Flood, S. C., and Hunt, J. D., 1988, "Columnar to Equiaxed Transition," *Metals Handbook*, 9th Ed., Vol. 15, Casting, Metals Park, OH, pp. 130–141.
- Garimella, S. V., McNulty, J. P., and Schlitz, L. Z., 1995, "Formation and Suppression of Channels during Upward Solidification of a Binary Mixture," *Metall. Trans. A*, Vol. 26A, pp. 971–981.
- Griffith, W. D., and McCartney, D. G., 1993, "Macrostructural Development in Aluminum Alloys Solidified Vertically Downwards," *Mater. Sci. and Eng. A*, Vol. A173, pp. 123–127.
- Han, Q., and Hellawell, A., 1997, "Primary Particle Melting Rates and Equiaxed Grain Nucleation," *Metall. Trans. B*, Vol. 28B, pp. 169–173.
- Hellawell, A., Saragin, J. R., and Steube, R. S., 1993, "Channel Convection in Partly Solidified Systems," *Phil. Trans. R. Soc., Lond.*, Vol. A345, pp. 507–544.
- Hollands, K. G. T., Raithby, G. D., and Konicek, L., 1975, "Correlation Equations for Free Convection Heat Transfer in Horizontal Layers of Air and Water," *Int. J. Heat Mass Transfer*, Vol. 18, pp. 879–884.
- Jackson, K. A., Hunt, J. D., Uhlemann, D. R., and Seward, III, T. P., 1966, "On the Origin of the Equiaxed Zone in Castings," *Trans. AIME*, Vol. 236, pp. 149–158.
- Jang, J., and Hellawell, A., 1991, "Use of $\text{NH}_4\text{Cl-H}_2\text{O}$ Analogue Castings to Model Aspects of Continuous Casting," *Ironmaking and Steelmaking*, Vol. 18, No. 4, pp. 275–283.
- Kirkpatrick, A. T., and Bohn, M., 1986, "An Experimental Investigation of Mixed Cavity Natural Convection in the High Rayleigh Number Regime," *Int. J. Heat Mass Transfer*, Vol. 29, pp. 69–82.
- Magirl, C. S., and Incropera, F. P., 1993, "Flow and Morphological Conditions Associated with Unidirectional Solidification of Aqueous Ammonium Chloride," *ASME JOURNAL OF HEAT TRANSFER*, Vol. 115, pp. 1036–1043.
- Mahapatra, R. B., and Weinberg, F., 1987, "The Columnar to Equiaxed Transition in Tin-Lead Alloys," *Metall. Trans. B*, Vol. 18B, pp. 425–432.
- McCartney, D. G., and Ahmady, S. M., 1994, "Solidification Macrostructures and Macrosegregation in Aluminum Alloys Cooled from Above," *Metall. Trans. A*, Vol. 25A, pp. 1097–1102.
- McCay, T. D., McCay, M. H., Lowry, S. A., and Smith, L. M., 1989, "Convective Instabilities During Directional Solidification," *J. Thermophysics*, Vol. 3, No. 3, pp. 345–350.
- Paradies, C. J., Smith, R. N., and Glicksman, M. E., 1997, "The Influence of Convection during Solidification on Fragmentation of the Mushy Zone of a Model Alloy," *Metall. Mater. Trans. A*, Vol. 28A, pp. 875–883.
- Rappaz, M., and Thevoz, P. H., 1987, "Solute Diffusion Model for Equiaxed Dendritic Growth," *Acta Metall.*, Vol. 35, No. 7, pp. 1487–1497.
- Sparrow, E. M., Husar, R. B., and Goldstein, R. J., 1970, "Observations and Other Characteristics of Thermals," *J. Fluid Mech.*, Vol. 41, pp. 793–800.
- Wang, C. Y., and Beckermann, C., 1994, "Prediction of Columnar to Equiaxed Transition during Diffusion-Controlled Dendritic Alloy Solidification," *Metall. Mater. Trans. A*, Vol. 25A, pp. 1081–1093.
- Wang, C. Y., and Beckermann, C., 1996, "Equiaxed Dendritic Solidification with Convection: Part I. Multi-Phase/Multi-Scale Modeling," *Metall. Mater. Trans. A*, Vol. 27A, pp. 2754–2764.
- Ziv, I., and Weinberg, F., 1989, "The Columnar-to-Equiaxed Transition in Al 3 Pct Cu," *Metall. Trans. B*, Vol. 20B, pp. 731–734.

Temperature Response of Heat Transport in a Micro Heat Pipe

G. P. Peterson¹

Tenneco Professor and
Executive Associate Dean,
Fellow ASME

H. B. Ma

Assistant Research Professor,
Mem. ASME

Department of Mechanical Engineering,
Texas A&M University,
College Station, TX 77843-3123

A detailed mathematical model for predicting the heat transport capability and temperature gradients that contribute to the overall axial temperature drop as a function of heat transfer in a micro heat pipe has been developed. The model utilizes a third-order ordinary differential equation, which governs the fluid flow and heat transfer in the evaporating thin film region; an analytical solution for the two-dimension heat conduction equation, which governs the macro evaporating film region in the triangular corners; the effects of the vapor flow on the liquid flow in the micro heat pipe; the flow and condensation of the thin film caused by the surface tension in the condenser; and the capillary flow along the axial direction of the micro heat pipe. With this model, the temperature distribution along the axial direction of the heat pipe and the effect on the heat transfer can be predicted. In order to verify the model presented here, an experimental investigation was also conducted and a comparison with experimental data made. This comparison indicated excellent correlation between the analytical model and experimental results, and as a result, the analysis provides a better understanding of the heat transfer capability and temperature variations occurring in micro heat pipes.

Introduction

Effective cooling of electronic components is crucial to the successful operation and high reliability of modern electronic devices. The amount of heat generated in these electronic devices must be dissipated in order to maintain the operating temperature limit and peak performance. Along with the limitation on the heat flux level and maximum temperature, there may be further requirements on the temperature drop and the level of temperature uniformity. Heat pipes as a cooling strategy for electronic equipment present a promising alternative to traditional cooling schemes and offer the possibility of high local heat removal rates and high levels of temperature uniformity across individual electronic components.

Since the initial conceptualization of micro heat pipes in 1984 (Cotter, 1984), a number of analytical and experimental investigations have been conducted. Because the fundamental phenomena that governs the operation of micro heat pipes arises from the difference in the capillary pressure across the liquid-vapor interfaces in the evaporator and condenser regions, most of these investigations have concentrated on the capillary heat transport capability. Several analytical models (Cotter, 1984; Babin et al., 1990; Longtin et al., 1994; Khurstalev and Faghri, 1994; Peterson and Ma, 1996a) have been developed and verified experimentally, which are capable of predicting the capillary limits and performance characteristics of these devices. Recently, Longtin et al. (1994), Khurstalev and Faghri (1994), and Peterson and Ma (1996a) recognized the importance of vapor-liquid frictional interaction to the heat transport capability of micro heat pipes, and Ma and Peterson (1998) derived an expression for the minimum meniscus radius, which is important in the accurate determination of the capillary heat transport limit. For some applications, the maximum temperature and the temperature distribution are of interest, and while many of these previously developed models can be used to predict the heat transport limit, none of them can be used to accurately predict the axial temperature distribution and its effect on the heat transport limitation.

In order to predict the temperature variation and the heat transport capacity, a mathematical model was established with the following comparatively new features. First, the temperature distribution along the axial direction of the heat pipe can be predicted. The technique utilized incorporates the temperature distribution effect on the heat transfer through the micro region of the thin liquid film. Second, the model includes the effects of the disjoining pressure, the viscous shear stress, and thermal resistance on both the vapor temperature and the wall temperature distributions. Third, a two-dimensional model for the vapor flow effect on the liquid flow and a corresponding two-dimensional analytical solution for the temperature distribution in the liquid film is developed and included. In this way, the heat transfer through the macro region of liquid film can be determined. Finally, a simplified capillary analytical model was employed to calculate the meniscus radius occurring in the evaporator and condenser.

Analysis

The current model is developed for the trapezoidal micro heat pipe with triangular grooves shown in Fig. 1. The present analysis is performed with the following assumptions:

- 1 steady-state laminar flow for both the vapor flow and liquid flow in the micro heat pipes;
- 2 no slip conditions for both liquid and vapor flows;
- 3 the vapor is at saturation conditions;
- 4 liquid flow in the thin film region in the evaporating section results from gradients in the disjoining pressure and surface curvature;
- 5 liquid flow in the thin film region in the condensing section results from gradients in the capillary pressure;
- 6 liquid flow in the macro region and the axial direction results from the capillary flow, i.e., the disjoining pressure effect on the axial flow is neglected;
- 7 the meniscus radius of curvature of liquid flow is constant in the meniscus region at a given z -location;
- 8 convective terms are neglected when solving the energy equations governing the liquid film temperature; and
- 9 since the wall conductivity is large compared with that in the liquid film, the temperature in the wall at a given cross section is assumed to be uniform.

Heat Transfer Through the Evaporating Film. Stephan and Busse (1992) established a mathematical model to calculate the

¹To whom all correspondence should be addressed. Office of the Vice Chancellor-301 WERC, Texas A&M University, College Station, TX 77843-3123.

Contributed by the Heat Transfer Division for publication in the JOURNAL OF HEAT TRANSFER. Manuscript received by the Heat Transfer Division, Jan. 29, 1998; revision received, Dec. 21, 1998. Keywords: Condensation, Evaporation, Film Cooling, Heat Transfer, Microscale. Associate Technical Editor: D. A. Kaminski.

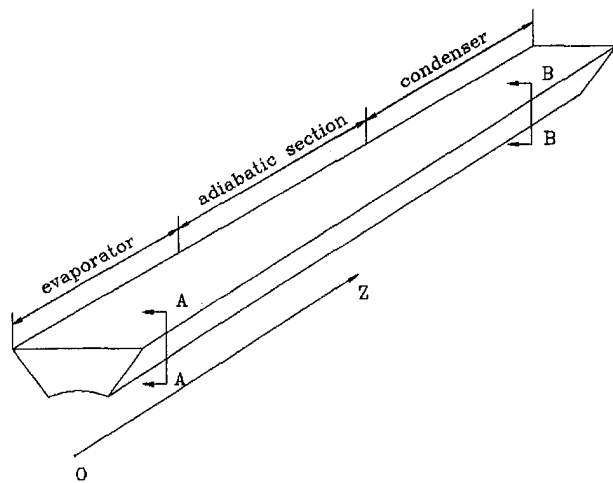


Fig. 1 Schematic of a micro heat pipe

heat transfer coefficient, and found that the interfacial temperature variation is very important. More recently, Khrustalev and Faghri (1995) established a model based on a constant meniscus radius assumption including the evaporating thin film region to try to overcome the mathematical difficulty occurring in solving the governing equation presented by Stephan and Busse (1992). However, with this assumption, the heat flux effects on the film profile cannot be determined as shown in the paper presented by Wayner (1994). Most recently, Ma and Peterson (1997b) established a model which considered the disjoining pressure, the surface curvature, the viscous shear stress, and the apparent contact angle variation to predict the heat flux and temperature variation along the axial direction of a triangular groove. Based on conservation of momentum, Ma and Peterson (1997b) derived an expression

$$\sigma \frac{dK}{ds_e} - \frac{dp_d}{ds_e} = - \frac{f_{l,e}^+ \cdot \text{Re}_{\delta_e} \mu_l \int_0^{s_e} \frac{q(s_e)}{h_{fg}} ds_e}{2\delta_e^3(s_e) \rho_l} \quad (1)$$

for the steady-state evaporating process of a thin film in a triangular groove, where the meniscus curvature, K , and the disjoining pressure (Holm and Goplen, 1979) can be found by

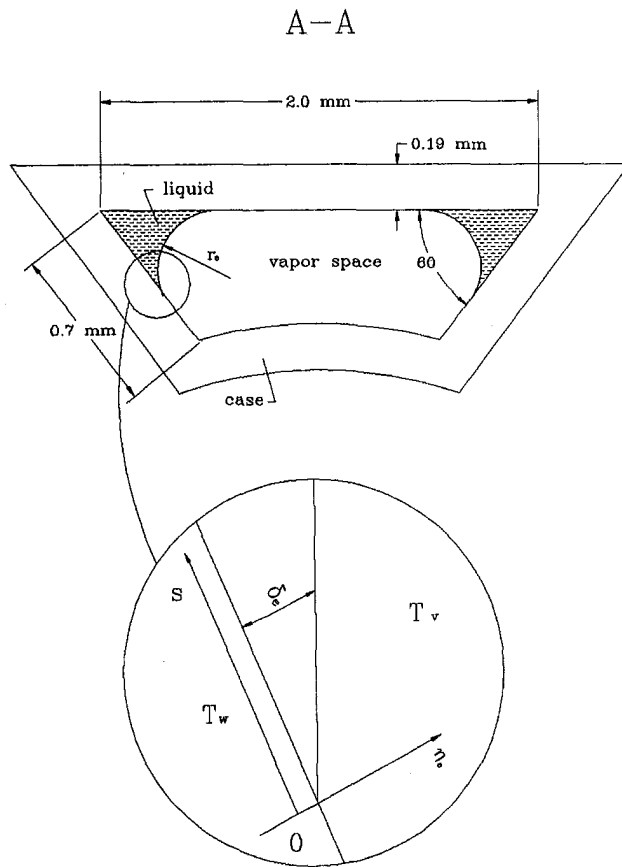


Fig. 1 (con't)

$$K = \frac{d^2 \delta_e}{ds_e^2} \left[1 + \left(\frac{d\delta_e}{ds_e} \right)^2 \right]^{3/2} \quad (2)$$

$$p_d = \rho_l R T_{lv} \ln [a \delta_e^b] \quad (3)$$

Nomenclature

a = constant
 A = cross-sectional area, m^2
 b = constant
 C_1 = coefficient defined by Eq. (27)
 C_2 = coefficient defined by Eq. (28)
 C^* = coefficient defined by Eq. (31)
 D = diameter, m
 f = friction factor
 g = gravitational acceleration, m/s^2
 h_{fg} = latent heat of vaporization, kJ/kg
 K = curvature, m^{-1}
 L = length, m
 L_{eff} = effective length defined by Eq. (29)
 \dot{m} = mass flow rate, $kg/m \cdot s$
 p = pressure, N/m^2
 P = perimeter, m
 q = heat flux, W/m^2
 r = radius, m
 r_1 = radius defined by Eq. (17)

r_2 = radius defined by Eq. (18)
 r_w = groove dimension, m
 R = gas constant, $J/kg \cdot K$
 Re = Reynolds number
 s = coordinate, m
 T = temperature, K
 u = velocity, m/s
 \bar{u} = average velocity, m/s
 x = coordinate, m
 y = coordinate, m
 z = coordinate, m

Greek

α = contact angle, degree
 δ = film thickness, m
 δ_0 = no evaporating film thickness, m
 η = coordinate, m
 θ = coordinate, degree
 Λ = coordinate defined by Eq. (14)
 μ = viscosity, Ns/m^2

ρ = density, kg/m^3
 σ = surface tension, N/m
 ϕ = half-channel angle, degree
 ψ = tilt angle, degree

Subscripts

a = adiabatic
 c = condensing, condenser
 cap = capillary
 d = disjoining
 e = evaporating, evaporator
 h = hydraulic
 l = liquid
 lv = liquid-vapor interface
 mic = micro
 mac = macro
 tot = total
 v = vapor
 w = wall
 $+$ = along the s -direction

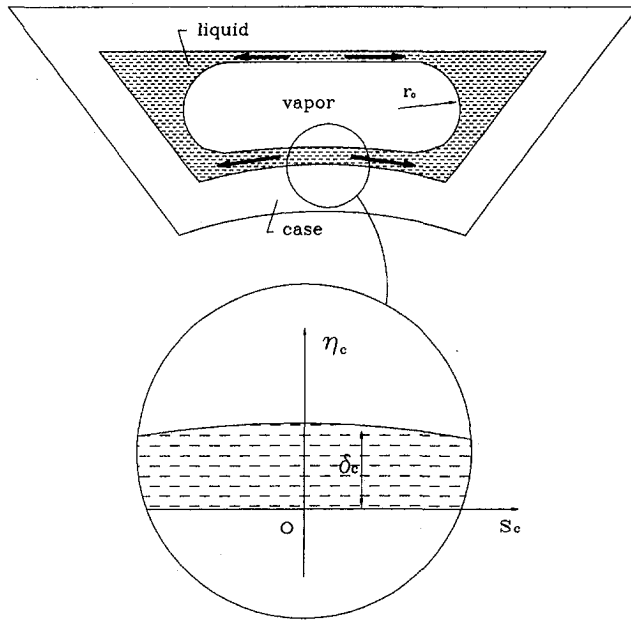


Fig. 1 (cont'd)

respectively. The friction factor and Reynolds number product, $f_{l,e}^+ \cdot Re_{\delta_e}$, for the liquid flow in the thin film shown in Fig. 1, can be determined by

$$f_{l,e}^+ \cdot Re_{\delta_e} = \frac{\mu_l \left. \frac{\partial u_l^+}{\partial \eta_e} \right|_{\eta_e=0}}{\frac{1}{2} \rho_l (\bar{u}_l^+)^2} \cdot \frac{\bar{u}_l^+ \delta_e \rho_l}{\mu_l} \quad (4)$$

where

$$\bar{u}_l^+ = \frac{\dot{m}^+}{\delta_e \rho_l} \quad (5)$$

$$\dot{m}^+ = \int_0^{s_e} \frac{q(s_e)}{h_{fg}} ds_e \quad (6)$$

When the temperature increases in the direction of flow, and the surface tension decreases with an increase in temperature, temperature-induced surface shear stress will hinder the fluid flow towards the contact line. Since the contribution to the pressure drops is very small compared with the other terms in Eq. (1) (Ma and Peterson, 1997b), the surface tension effect due to the temperature variation was not considered. The boundary conditions corresponding to Eq. (1) can be found as

$$\delta_e = \delta_0; \quad K = 0; \quad \frac{d\delta_e}{ds_e} = 0; \quad \text{at } s_e = 0 \quad (7)$$

and the nonevaporating film thickness as (Ma and Peterson, 1997c)

$$\delta_0 = e^{[(T_w/T_v)-1]((h_{fg}/RT_w) - \ln a)/b} \quad (8)$$

where $a = 1.5787$ and $b = 0.0243$, and the interface temperature, T_{lv} , can be obtained from

$$T_{lv} = T_v \left(1 + \frac{\Delta p_{l,e}^+}{\rho_l h_{fg}} \right) \quad (9)$$

Since the disjoining pressure is a very important factor in the micro thin film region, the curvature effect on the film thickness variation and evaporating heat transfer in the micro thin film region due to the groove shape was not considered. As the film thickness increases, the disjoining pressure effect decreases, and at some point, the disjoining pressure will have no effect on the liquid flow and evaporating heat transfer in the liquid film. Obviously, the model developed for the micro thin film region is not appropriate for this film region. However, a two-dimensional heat conduction equation can be used to describe the temperature distribution of the liquid film in the corner region shown in Fig. 1 and the heat transfer through the liquid film can be determined. When the film thickness is only slightly thicker than those at which the disjoining pressure has no effect, it is difficult to solve the two-dimensional heat conduction equation and find accurate solutions for the region between the micro film region and the real macro region. Fortunately, the heat transfer through this film region can be approximated as one-dimensional, and based on the constant curvature assumption in the meniscus region, the film thickness variation can be expressed as

$$\delta_e = \frac{r_{w2} \sin \theta}{\cos(\alpha + \phi)} \{ \cos \alpha \cos(\phi - \theta) - [\sin^2 \phi - \cos^2 \alpha \sin^2(\phi - \theta)]^{0.5} \} \quad (s_{mic} < s < s_{mac}) \quad (10)$$

where s_{mic} is the point where the disjoining pressure can be neglected, and s_{mac} is the point where the two-dimensional heat conduction equation can be readily solved and accurate solutions obtained. In this investigation, s_{mac} was chosen to be 10^{-5} m from the origin along the s -coordinate. The angle, θ , in Eq. (10) can be found from the following relationship:

$$\{ \cos \alpha \cos(\phi - \theta) - [\sin^2 \phi - \cos^2 \alpha \sin^2(\phi - \theta)]^{0.5} \} \cos \theta = \frac{(r_{w2} - s) \cos(\alpha + \phi)}{r_{w2}} \quad (11)$$

For a given value of s , the angle θ can be found from Eq. (11), the film thickness can be determined by Eq. (10), and the resulting heat transfer through this film region can be found, while the interface temperature can be determined using Eq. (9).

For the macro film region, the heat transfer through the liquid film in the groove, as shown in Fig. 2, can be approximated by the two-dimensional heat conduction equation

$$\frac{\partial^2 T}{\partial r^2} + \frac{1}{r} \frac{\partial T}{\partial r} + \frac{1}{r^2} \frac{\partial^2 T}{\partial \theta^2} = 0 \quad (12)$$

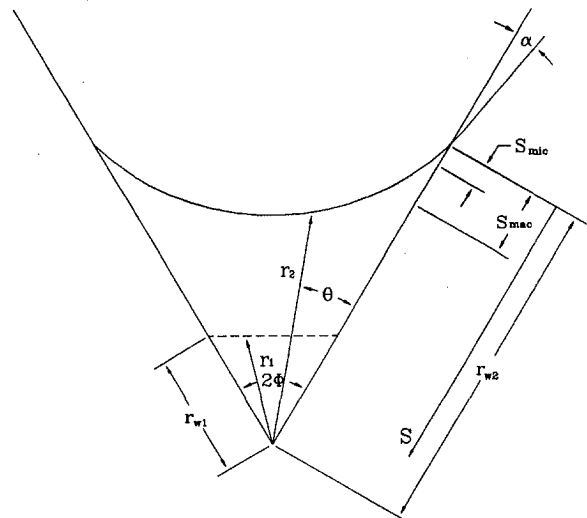


Fig. 2 Schematic of a triangular groove

Because the conductivity of the wall is large compared with that of the liquid film, the temperature in the wall at one cross section can be assumed to be uniform. The corresponding boundary conditions for Eq. (12) can be obtained as

$$T = T_w \quad \text{at} \quad \theta = 0; \quad \text{and} \quad \theta = 2\phi$$

$$T = T_{lv} \quad \text{at} \quad r = r_2. \quad (13)$$

Applying a coordinate transformation

$$\Lambda = \ln \frac{r}{r_1}, \quad (14)$$

Eq. (12) becomes

$$\frac{\partial^2 T}{\partial \Lambda^2} + \frac{\partial^2 T}{\partial \theta^2} = 0. \quad (15)$$

Applying the method of separation of variables, the solution of Eq. (15) can be obtained as

$$T = T_w + (T_{lv} - T_w) \sum_{n=1}^{\infty} \frac{1 - (-1)^n}{n\pi}$$

$$\times \frac{\cosh \frac{n\pi}{2\phi} \left(\Lambda - \ln \frac{r_2}{r_1} \right) - \cosh - \frac{n\pi}{2\phi} \left(\Lambda + \ln \frac{r_2}{r_1} \right)}{\sinh \left(\frac{n\pi}{2\phi} \ln \frac{r_2}{r_1} \right)}$$

$$\times \sin \frac{n\pi}{2\phi} \theta \quad (16)$$

where r_1 and r_2 can be determined by

$$r_1 = r_w \frac{\cos \phi}{\cos(\phi - \theta)} \quad (17)$$

and

$$r_2 = r_w \frac{\cos \alpha \cos(\phi - \theta) - [\sin^2 \phi - \cos^2 \alpha \sin(\phi - \theta)]^{0.5}}{\cos(\alpha + \phi)}, \quad (18)$$

respectively. The radius r_1 is assumed as shown in Fig. 2. Because most of the heat passes through the thin film region, the value of r_1 has little or no effect when it is smaller than 10^{-6} m. In the current investigation, r_1 was assumed to have a value of 10^{-10} m.

Vapor Flow in the Heat Pipe. For the vapor space shown in Fig. 1, a three-dimensional model should be established to find the velocity distribution and vapor pressure drop, but since the vapor space shape is not regular and evaporation occurs near the interline region, it is difficult to obtain the boundary conditions and find the solutions. For this reason, a simplified "three"-dimensional model was used, i.e., at a given z -location the pressure drop is determined by a two-dimensional (x and y -directions) model (Ma and Peterson, 1997a) as

$$\frac{\partial^2 u_v}{\partial x^2} + \frac{\partial^2 u_v}{\partial y^2} = \frac{1}{\mu_v} \frac{dp_v}{dz}. \quad (19)$$

After the friction factor was obtained by Eq. (19) based on the cross-sectional shape of the flow path, the one-dimensional momentum equation for vapor flow along the z -direction was expressed as

$$\frac{dp_v}{dz} + \rho_v g \sin \psi + \rho_v \bar{u}_v \frac{d\bar{u}_v}{dz} = -f_v \frac{2\rho_v \bar{u}_v^2}{D_{h,v}}. \quad (20)$$

Due to the frictional vapor flow, the vapor pressure will vary from the evaporator to the condenser and will result in the temperature

variation due to the saturated vapor flow. Based on the Clapeyron equation, the vapor temperature variation can be found as

$$T_v = \frac{T_{v,0}}{1 - \frac{RT_{v,0}}{h_{fg}} \ln \frac{p_v}{p_{v,0}}} \quad (21)$$

where $t_{v,0}$ and $p_{v,0}$ are the reference temperature and the reference pressure, respectively.

Heat Transfer Through the Condensing Film. The vapor generated in the evaporator will be condensed in the condenser region due to the phase-change driving force, and the condensate in the thin film region will flow into the corners due to the surface tension. Because the film thickness in the condensing film region is very thin compared with the meniscus thickness in the corners, most of the condensing heat transfer will occur in the thin film region as shown in Fig. 1. In this region, the Reynolds number of the condensate is very small, hence the inertial terms can be neglected and based on conservation of momentum in the thin film, the pressure drop due to the viscous flow can be found as

$$\frac{dp_{l,c}^+}{ds_c} = - \frac{f_{l,c}^+ \cdot \text{Re}_{\delta_c} \mu_l \int_0^{s_c} \frac{q_c(s_c)^+}{h_{fg}} ds_c}{2\delta_c^3 \rho_l}. \quad (22)$$

For the steady-state condensation process of the thin film, the pumping pressure head should be equal to the pressure drop, i.e.,

$$\sigma \frac{dK}{ds_c} = - \frac{f_{l,c}^+ \cdot \text{Re}_{\delta_c} \mu_l \int_0^{\bar{s}_c} \frac{q_c(s_c)^+}{h_{fg}} ds_c}{2\delta_c^3 \rho_l}, \quad (23)$$

where \bar{s}_c is the average length of the condensing film region. Since the corners with the 120-deg angles play only a small part in pumping the working fluid along the axial direction of the micro heat pipe, it is assumed that these regions have no effect on the capillary flow along the axial direction from the condenser to the evaporator. Therefore, the flow regions of interest in this micro heat pipe are those with an angle of 60 degrees, and the average condensing length can be found by

$$\bar{s}_c = \frac{s_{\text{tot}}}{2N} \quad (24)$$

where s_{tot} is the total length of the thin condensing region and N is the number of the corners which are used to pump the working fluid from the condenser to the evaporator. The boundary conditions required for solving Eq. (23) can be given as

$$K = 0; \quad \frac{d\delta_c}{ds_c} = 0; \quad \text{at} \quad s_c = 0$$

$$K = K_c \quad \text{at} \quad s_c = \bar{s}_c \quad (25)$$

where K_c is the curvature of the condensing film in the corner regions.

The Capillary Flow Along the Corner Regions. In order to calculate the heat transfer through the evaporating and condensing film, the meniscus radii at the evaporator and the condenser, which are directly related to the heat transport capability in a micro heat pipe, must be determined. Since the heat transport capability in the micro heat pipe has been shown to be limited by the capillary pumping force, the successful operation of micro heat pipes requires that the capillary pumping pressure be greater than the sum of all the pressure drops occurring in the flow path, i.e., vapor pressure drops, liquid pressure drops including the vapor-liquid frictional interaction, and gravitational pressure drop. Based on

this principle, Ma and Peterson (1998) developed an analytical model to determine the heat transport in a micro heat pipe as

$$q = \left(\frac{\sigma}{r_{\text{cap},e}} - \frac{\sigma}{r_{\text{cap},c}} - \Delta p_v - \rho_l g L \sin \psi \right) \times \left(\frac{2C_1(C^*C_2r_{\text{cap},e})^4 \rho_l h_{fg}}{f_l \cdot \text{Re}_{h,l} \mu_l L_{\text{eff}}} \right) \quad (26)$$

where the $r_{\text{cap},e}$ and $r_{\text{cap},c}$ are the average capillary meniscus radii of curvature occurring in the evaporator and condenser, respectively. If the heat transfer is given, the meniscus radius at the evaporator can be found from Eq. (26), while the meniscus radius in the condenser can be approximated based upon the groove geometry.

Based on the corner region shape shown in Fig. 1, the coefficients, C_1 and C_2 can be determined by

$$C_1 = \left\{ 2 \int_0^{2\phi} \left[\frac{\cos \alpha \cos(\phi - \theta) - [\sin^2 \phi - \cos^2 \alpha \sin^2(\phi - \theta)]^{0.5}}{\cos(\alpha + \phi)} \right]^2 d\theta \right\}^{-1} \quad (27)$$

$$C_2 = \frac{1}{\cos(\alpha + \phi) \sin \phi} \int_0^{2\phi} [\cos \alpha \cos(\phi - \theta) - [\sin^2 \phi - \cos^2 \alpha \sin^2(\phi - \theta)]^{0.5}]^2 d\theta \quad (28)$$

The effective length, L_{eff} , can be found as

$$L_{\text{eff}} = \frac{\int_0^{L_e} \dot{m} dz}{\dot{m}_a} + L_a + \frac{\int_{L_e+L_a}^L \dot{m} dz}{\dot{m}_a} \quad (29)$$

Since the length of the evaporator and the condenser were both equal to 12.7 mm, which is much shorter than the length of the adiabatic section, a uniform heat flux distribution, similar to that used previously by Babin et al. (1990) and Wu and Peterson (1991) was assumed. The effective length L_{eff} yields

$$L_{\text{eff}} = \frac{L_e}{2} + L_a + \frac{L_c}{2} \quad (30)$$

From Eqs. (27) and (28), it can be found that C_1 and C_2 depend not only on the channel angle, but also on the apparent contact angle. The contact angle at the evaporator can be calculated from the film thickness variation obtained by solving Eq. (1). The contact angle at the condenser was assumed to be zero due to condensation. The contact angle in the adiabatic region will vary with the length from the value obtained in Eq. (1) in the evaporator to zero in the condenser. In order to simplify the model and calculate the values of C_1 and C_2 , an average value for the contact angle was used.

Because the vapor flow has an important effect on the capillary heat transport in a micro heat pipe, the term, $f_l \cdot \text{Re}_{h,l}$, must be considered in analyzing the vapor flow effect. Using the analytical method presented by Peterson and Ma (1996b), the value of $f_l \cdot \text{Re}_{h,l}$ with the vapor flow effect can be found.

The coefficient C^* can be found to be

$$C^* = \frac{1}{2} \left(1 + \frac{r_{h,c}}{r_{h,e}} \right) = \frac{1}{2} \left(1 + \frac{r_{\text{cap},c}}{r_{\text{cap},e}} \right) \quad (31)$$

From Eq. (31) it can be shown that when the heat transfer is different, the cross-sectional area of liquid flow will vary resulting in a variation of C^* . Obviously, when there is no heat load in the evaporator, the coefficient, C^* , will be equal to unity for $\psi = 0$ or $g = 0$. With increased heat transfer, the value of C^* will increase, and when the heat transfer in the micro heat pipe reaches a maximum, the value of C^* will be maximized, where the minimum meniscus radius in the micro heat pipe can be determined as

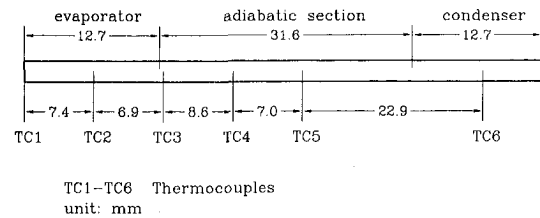


Fig. 3 Micro heat pipe dimensions and thermocouple positions

$$r_{\text{cap},e} = \frac{3\sigma}{4 \left(\frac{\sigma}{r_{\text{cap},c}} + \Delta p_v + \rho_l g L \sin \psi \right)} \quad (32)$$

(Ma and Peterson, 1998) and the maximum meniscus radius in the condenser can be found from the geometric shape of the micro heat pipe. After the maximum value of C^* was found, other values of C^* can be approximated by a linear assumption corresponding to the heat transported by the micro heat pipe.

Experimental Apparatus and Procedure

In order to find the temperature variation along the micro heat pipe and the heat transport capability in a micro heat pipe experimental investigations have been conducted. The experimental system (Szeto, 1992) consisted of a test section including a micro heat pipe, two constant temperature cooling baths, a power supply, and a data collection system. The micro heat pipe was made of silver, and was 57 mm long with a trapezoidal cross section as shown in Fig. 1. The micro heat pipe was charged with 0.0032 grams of ultrapure deionized water. This micro heat pipe was identical to the micro heat pipes tested by Wu and Peterson (1991). The aluminum cooling block provided a 12.7-mm long constant temperature condenser. The nichrome heater, constructed from 0.8 mm \times 0.0254 mm nichrome ribbon, covered a 12.7-mm length of the evaporator. Six Omega TT-K-36 SLE 36 AWG teflon insulated chromel-alumel thermocouples were used to monitor the temperature profiles along the heat pipe. As shown in Fig. 3, one thermocouple was attached to the condenser, two thermocouples were located in the adiabatic section between the evaporator and condenser, and three thermocouples were placed in the evaporator section. Detailed dimensions are shown in Fig. 3.

Prior to the start of the experiment, the system was allowed to equilibrate and reach steady-state such that the desired condenser temperature was achieved and a uniform temperature distribution with no heater power input was observed throughout the heat pipe. At this point, the data acquisition program was initiated and the system recorded the steady-state temperatures with no power to the heater. After five seconds, power was supplied to the heater at a preset interval for three minutes, at which time the power was turned off and the test section was allowed to cool down for 17 minutes prior to the next test cycle. Three minutes was selected as the time required for steady-state operation based upon previous results obtained by Wu and Peterson (1991), which showed that steady-state operation occurred within 90 seconds of the onset of heater operation. Throughout the test program, the power supplied to the heater was increased in 0.025 W increments between 0.025 and 0.5 W. The temperature variations measured by the six thermocouples were sent directly to a personal computer along with the voltage and current to the heater. The steady-state temperature of each thermocouple as a function of input power for a given condenser temperature could then be obtained.

Results and Discussion

The completed mathematical model used to predict the temperature distribution along the micro heat pipe and the overall heat transfer consisted of a third-order ordinary differential equation

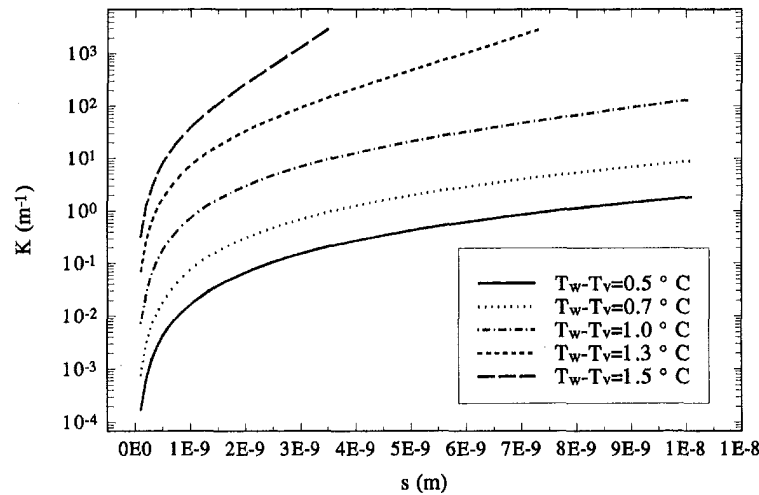


Fig. 4 Curvature variation in the thin film region

shown in Eq. (1) for the micro thin film region, Eqs. (10) and (16) which govern the macro film region, Eq. (26) for the capillary flow along the axial direction, and Eq. (23) for the condensing heat transfer in the condenser. For a given temperature difference, $T_w - T_v$, the film thickness variation and heat flux distribution in the evaporating thin film region can be found from Eq. (1), along with the curvature of the meniscus in the thin film region, which can be determined as shown Fig. 4. From Fig. 4 it is apparent that with the increased film thickness, the curvature of the meniscus increases sharply. Since the curvature of the meniscus in the macro region of the triangular cornered groove in the micro heat pipe was constant if the heat transfer rate and operating conditions were constant, the variation of the meniscus curvature in the film would be limited to $1/r_e$, where r_e is the meniscus radius in the evaporator. Therefore, in the current investigation, it was assumed that when the meniscus curvature calculated from Eq. (1) was larger than the meniscus curvature in the evaporator, the meniscus curvature was assumed to be constant and equal to the meniscus curvature in the evaporator.

As discussed previously, when the film thickness is very thin the disjoining pressure plays an important role, and the film thickness variation will be governed by Eq. (1) as the dot-dash line shown in Fig. 5. With increases in the film thickness the disjoining pressure effect decreases and becomes so small that it can be neglected. Equation (1) cannot continue to function for the film thickness variation in the macro film region, or it may result in an overprediction of the evaporating heat transfer and will not predict the true film thickness variation in the macro film region due to the groove shape and surface tension. The film thickness variation will be

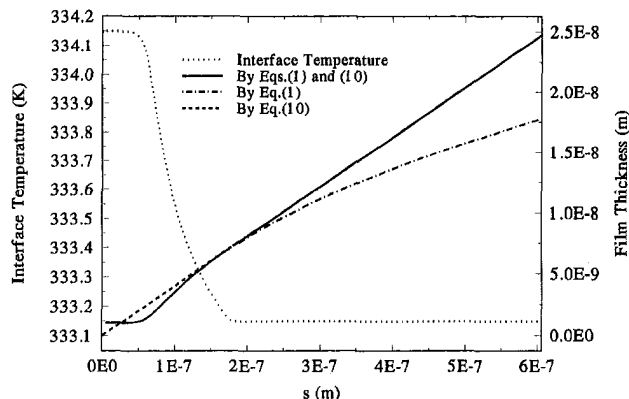


Fig. 5 Thin film thickness variations and interface temperature profile

governed by Eq. (10) where the constant meniscus curvature was assumed and the actual contact angle approaches the apparent contact angle. Obviously, if the film thickness variation including the evaporating thin film region was governed by Eq. (10) described by Khrustalev and Faghri (1995), the film thickness will vary as the short-dash line shown in Fig. 5. It is not possible here to completely predict the film thickness variation and the effect on the heat flux distribution and interface temperature profile near the interline region. Therefore, in this analysis the film thickness variation will be assumed to be governed by the combination of Eqs. (1) and (10) as the solid line shown in Fig. 5. From Fig. 5, it can be found that with the increase of the thin film thickness, the interface temperature decreases and approaches a constant value where the film thickness is governed by Eq. (10).

The temperature distribution along the micro heat pipe is dependent on the heat transfer which will determine the film thickness distributions and temperature profiles in the evaporator and condenser; however, the film thickness profiles and temperature distribution are related to the heat flux rate and heat transfer. For this reason, an iterative approach was used to determine the heat transfer and temperature distribution along the micro heat pipe. The detailed procedure for the temperature distribution along the micro heat pipe was based on the following steps:

- 1 Solve Eq. (26) based on a given heat transfer and assumed contact angle, and the average meniscus radius in the evaporator can be found.
- 2 Using this meniscus radius and a given heat transfer, Eq. (1) can be solved by a Runge-Kutta method in order to find the evaporating thin film thickness variation, the temperature drop occurring in this thin film, the heat flux distribution, and the contact angle (Ma and Peterson, 1997c).
- 3 With the contact angle calculated from step 2, Eqs. (10) and (16) can be solved and the heat flux distribution and temperature profiles in the macro film region can be found.
- 4 Using the film thickness variations obtained from steps 1 and 2, the contact angle can be calculated. If this contact angle is different from the contact angle assumed in Eq. (26), go back to step 1 with the new contact angle. Repeat the calculation until the converged results are obtained.
- 5 Solve Eq. (21), and the temperature drop occurring in the vapor flow path can be determined. Based on the calculation, this term is very small and can be neglected.
- 6 Solve Eq. (23) and the condensing film thickness and the temperature drop occurring in the condenser can be found.

Using the procedures outlined here, the heat transfer through the liquid film regions and temperature profiles as a function of heat

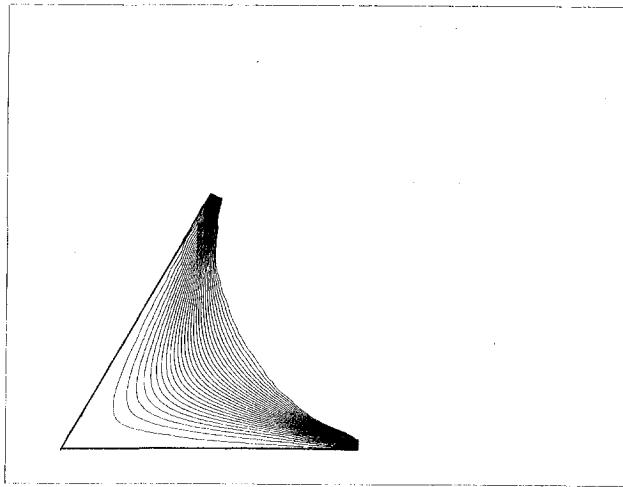


Fig. 6 Isotherms in the macro liquid film region (temperature difference between two isotherms: $\Delta T = 0.05$ K)

transfer can be obtained. Figure 6 shows the temperature distribution in the macro liquid film region, and it can be shown that most of the heat will pass through the thin film region. Figure 7 illustrates quantitatively the heat transfer ratio passing through the thin film region. It can be concluded, therefore, that the key to increasing the evaporating heat transfer is to increase the evaporating thin film regions.

Since the temperature drop from the evaporator to the condenser is strongly affected by the actual application and the maximum heat transfer transported by a micro heat pipe, the temperature drops as a function of the heat transfer have been investigated experimentally and theoretically. The experimental results presented in Figs. 8(a) through 8(c) were obtained from the experimental system and procedure discussed previously. The various points shown in Figs. 8(a) through 8(c) illustrate the steady-state temperature distribution at condenser temperatures equal to 40°C, 50°C, and 60°C. Examining Figs. 8(a) through 8(c), it can be seen that the temperatures of the thermocouples TC1, TC2, and TC3 shown in Fig. 3 increase slowly at low power levels. With increased input power the area around thermocouple TC1 first began to dry out and the temperature of thermocouple TC1 rose sharply. Small increases in input power resulted in dramatic temperature increases. When the input power was continuously increased, the temperature of TC2 started to increase sharply as did the temperature of TC3. After the dryout front had reached thermocouple TC3, and the entire evaporator section had dried out, some regions of the adiabatic section acted as the evaporator, and the overall effective length of the heat pipe was reduced. Consequently, the overall heat transport capacity of the heat pipe was reduced.

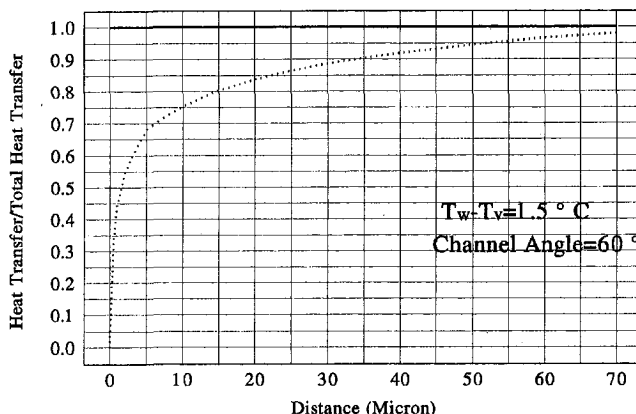


Fig. 7 Heat transfer distribution through the thin film region

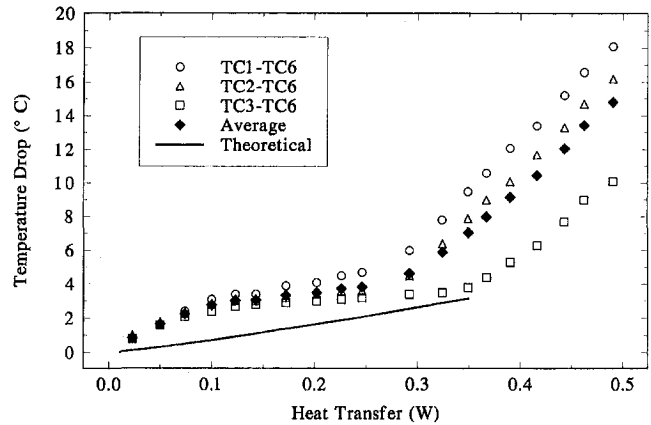


Fig. 8(a)

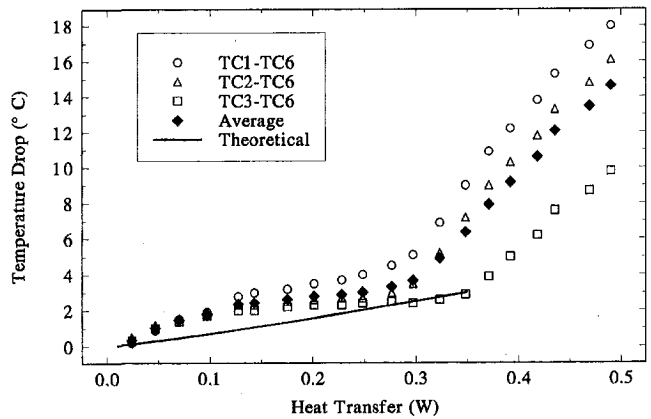


Fig. 8(b)

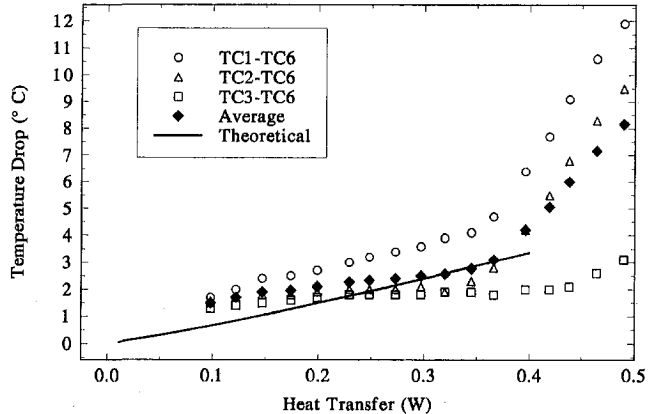


Fig. 8(c)

Fig. 8 Temperature variation along the micro heat pipe at the operating temperature of (a) 40°C; (b) 50°C; and (c) 60°C

During heat pipe operation, the temperature of the thermocouples in the adiabatic section and condenser, i.e., TC4, TC5, and TC6 remained fairly constant and experienced only small temperature increases with corresponding increases in input power. Because the temperature drops from the evaporator to the condenser predicted by the current model were based on the average value in the evaporator, the average values of TC1, TC2, and TC3 were taken and plotted as the solid scattered diamonds. As shown, these are in good agreement with the predicted values. In addition, the current model can predict the capillary heat transport capability in the micro heat pipe and also demonstrates good agreement with the experimental data shown in Fig. 9.

The total heat transfer and the maximum heat flux level for the micro heat pipe evaluated here was less than 1.6 W/cm^2 resulting in the temperature drops shown in Figs. 8(a) through 8(c). However, when the heat flux continues to increase and reaches a very high level, the capillary pumping ability increases significantly and does not present a limitation to the heat transport capability. In order to find the temperature drop as a function of this high heat flux, the following assumptions must be made to avoid the capillary heat transport limitation: (a) the heat pipe has the same geometric shape shown in Fig. 1; (b) the meniscus radius of the liquid film in the evaporator is assumed to be constant and equal to 0.00035 m ; (c) the nonevaporating film thickness was assumed to be constant and equal to 10^{-8} m since as the heat flux increases, the temperature difference between the wall temperature and vapor temperature increases which results in an unconverged solution of Eq. (1) if the nonevaporating film thickness was obtained using Eq. (8); (d) other boundary conditions are the same as previously stated. Using the current model, the temperature drop can be found and plotted in Fig. 10. As indicated in Fig. 10, the temperature drops are very high, even with a relatively low heat flux level, and the temperature drops occurring in the evaporator are larger than those in the condenser. It can be concluded that the micro heat pipe investigated in this paper cannot transfer high heat flux with low temperature drops, i.e., this kind micro heat pipe cannot obtain low effective conductivity. In order to increase the total heat transfer capability in a micro heat pipe, new designs must be developed which maximize the thin film region.

Conclusions

A detailed mathematical model for predicting the temperature drops as a function of heat transfer and the heat transport capability in a micro heat pipe has been developed. This model includes an equation that governs the fluid flow and heat transfer in the evaporating thin film region; the analytical solution for the two-dimensional heat conduction equation governing the macro evaporating film region; the effects of the vapor flow on the liquid flow in the micro heat pipe; the flow and condensation of the thin film caused by the surface tension in the condenser; and the capillary flow along the axial direction of the micro heat pipe. In this investigation, the evaporating film variation was effectively connected by Eq. (1) governing the micro thin film region where the disjoining pressure plays a very important part and Eq. (10) governing the macro film region due to the triangular groove limitation and surface tension.

The results obtained from this model indicate that the temperature drop occurring in the evaporator is considerably larger than those occurring in the condenser, and with increases in the input power, both temperature drops increase. In order to verify the model presented here, an experimental investigation to predict the

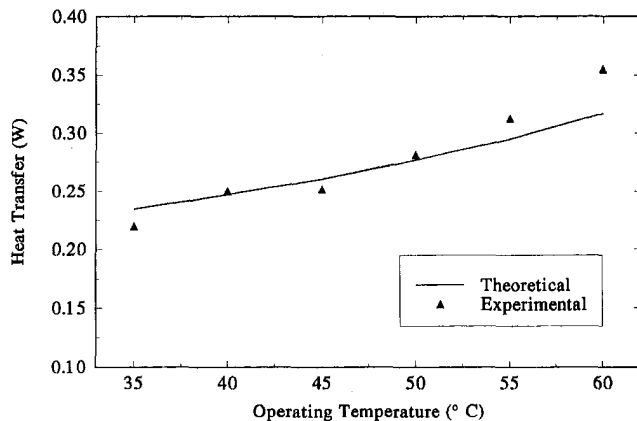


Fig. 9 Heat transport as a function of operating temperature

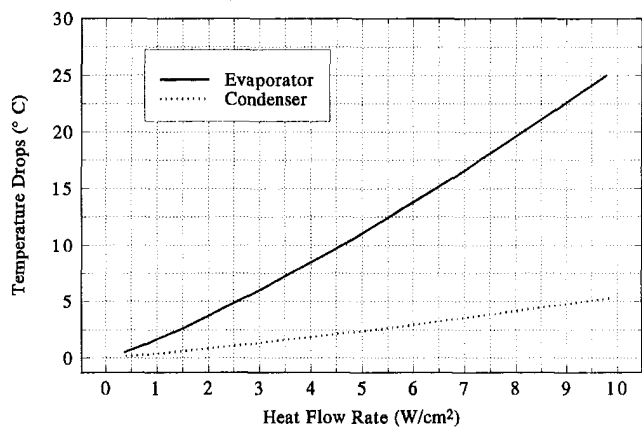


Fig. 10 Temperature drops in the evaporator and the condenser

temperature variation as a function of the heat transfer was conducted, and good agreement was obtained. Using this model, it is clear that as the heat transfer level increases, the temperature drop between the condenser and the evaporator increases significantly. As a result, it can be concluded that the micro heat pipe investigated here cannot transfer high levels of heat flux. This work will lead to a better understanding of the heat transfer capability and temperature variation occurring in micro heat pipes.

Acknowledgments

The authors would like to acknowledge the partial support of the National Science Foundation under Grant No. CTS-9632685.

References

- Babin, B. R., Peterson, G. P., and Wu, D., 1990, "Steady-State Modeling and Testing of a Micro Heat Pipe," *ASME JOURNAL OF HEAT TRANSFER*, Vol. 112, pp. 595–601.
- Cotter, T. P., 1984, "Principle and Prospects of Micro Heat Pipes," *Proc. 5th Int. Heat Pipe Conf.*, Tsukuba, Japan, pp. 328–335.
- Holm, F. W., and Goplen, S. P., 1979, "Heat Transfer in the Meniscus Thin film Transition Region," *ASME JOURNAL OF HEAT TRANSFER*, Vol. 101, pp. 543–547.
- Khrustalev, D., and Faghri, A., 1994, "Thermal Analysis of A Micro Heat Pipe," *ASME JOURNAL OF HEAT TRANSFER*, Vol. 116, pp. 189–198.
- Khrustalev, D., and Faghri, A., 1995, "Heat Transfer during Evaporation on Capillary-Grooved Structures of Heat Pipes," *ASME JOURNAL OF HEAT TRANSFER*, Vol. 117, pp. 740–747.
- Longtin, J. P., Badran, B., and Gerner, F. M., 1994, "A One-Dimensional Model of Micro Heat Pipe During Steady-State Operation," *ASME JOURNAL OF HEAT TRANSFER*, Vol. 116, pp. 709–715.
- Ma, H. B., and Peterson, G. P., 1998, "The Minimum Meniscus Radius and Capillary Heat Transport Limit in Micro Heat Pipes," *ASME JOURNAL OF HEAT TRANSFER*, Vol. 120, pp. 227–233.
- Ma, H. B., and Peterson, G. P., 1997a, "The Friction Factor for Laminar Flow in Micro scale Ducts of Irregular Cross-section," *Micro scale Thermophysical Engineering*, Vol. 1, No. 3, pp. 253–265.
- Ma, H. B., and Peterson, G. P., 1997b, "Temperature Variation and Heat Transfer in Triangular Grooves with an Evaporating Film," *AIAA Journal of Thermophysics and Heat Transfer*, Vol. 11, No. 1, pp. 90–97.
- Peterson, G. P., and Ma, H. B., 1996a, "The Theoretical Analysis of the Maximum Heat Transport in Triangular Grooves—A Study of Idealized Micro Heat Pipes," *ASME JOURNAL OF HEAT TRANSFER*, Vol. 118, pp. 731–739.
- Peterson, G. P., and Ma, H. B., 1996b, "Analysis of Countercurrent Liquid-Vapor Interactions and the Effect on the Liquid Friction Factor," *International Journal of Experimental Thermal and Fluid Science*, Vol. 12, No. 1, pp. 13–24.
- Stephan, P. C., and Busse, C. A., 1992, "Analysis of the Heat Transfer Coefficient of Grooved Heat Pipe Evaporator Walls," *Int. J. Heat Mass Transfer*, Vol. 35, No. 2, pp. 383–391.
- Szeto, M. D., 1992, "Design and Fabrication of an Experiment for Testing the Transient Operation of a Micro Heat Pipe in Microgravity," Master's thesis, Texas A&M University, College Station, TX.
- Wayner, P. C., 1994, "Thermal and Mechanical Effects in the Spreading of a Liquid Film due to a Change in the Apparent Finite Contact Angle," *ASME JOURNAL OF HEAT TRANSFER*, Vol. 117, pp. 938–945.
- Wu, D., and Peterson, G. P., 1991, "Investigation of the Transient Characteristics of Micro Heat Pipes," *AIAA Journal of Thermophysics and Heat Transfer*, Vol. 5, No. 2, pp. 129–134.

Heat Transfer of Sprays of Large Water Drops Impacting on High Temperature Surfaces

T. L. Cox

Senior Engineer,
Alcoa Technical Center,
100 Technical Drive,
Alcoa Center, PA 15069
Mem. ASME

S. C. Yao

Professor,
Department of Mechanical Engineering,
Carnegie Mellon University,
Pittsburgh, PA 15213-3890
Fellow ASME

Experiments were performed to evaluate the heat transfer of monodisperse sprays of large droplet diameters, ranging from 3 to 25 mm, on high temperature surfaces. This range of drop sizes has not previously been studied, and it was of interest to determine their heat transfer characteristics and how they relate to sprays of smaller drops. Parametric tests showed that the spray heat flux depends on mass flux with a power-law relationship, and that spray effectiveness, which relates the actual spray heat transfer to the maximum heat transfer potential, varies with $d^{-1/2}$. There was no discernible relationship between the heat transfer and droplet velocity. These results agreed favorably with published results for smaller droplets. The current data was compared to previous tests with smaller droplets using the droplet Reynolds and Weber numbers. This analysis showed some grouping, with a marked separation at $We = 80$, where the dynamic behavior of droplets has been shown to change for nonwetting impaction.

Introduction

Liquid spray cooling is used extensively in industrial processes. In applications involving stationary, slow moving, or vertical surfaces, disperse sprays, arrays of scattered liquid droplets, are favored for their high heat transfer rates and low water consumption. Industrial sprays are typically polydisperse, producing a spectrum of droplet sizes. On horizontal moving surfaces with downward impingement, high surface velocities and a water or vapor layer prohibit the use of such finely atomized sprays. The droplets do not possess enough momentum to penetrate the existing surface layer. Circular or planar water jets are often used in these situations because they have high momentum which can penetrate the surface water or vapor layer. However, the effectiveness of jets—the amount of cooling per amount of water—is small compared to disperse sprays.

One possible alternative to jets is the use of disperse sprays of very large droplet diameters, greater than 5 mm. Larger drops may provide the momentum necessary to penetrate the water or vapor layer while retaining much of the efficiency of a disperse spray.

There is evidence in the literature that increasing the droplet diameter may increase heat transfer for the range of droplets diameters studied (Shoji et al., 1984; Yao and Choi, 1987). However, there is no information for sprays of droplets greater than 3 mm in diameter. This is because currently available commercial nozzles cannot produce such large droplet sizes, and also because droplets greater than 5 mm in diameter are hydrodynamically unstable (Gunn and Kinzer, 1948).

The purpose of the current tests are to determine the heat transfer characteristics of sprays of large droplets of diameters ranging from 3 to 25 mm. In addition to evaluating the heat transfer characteristics of these large droplets, it is of interest to compare the results obtained to those previously published for smaller droplets to determine if existing relationships can be extrapolated for much larger droplets sizes.

Background

Heat transfer from an upward-facing horizontal surface to a subcooled impinging drop or spray has been widely studied for small droplet sizes. However, there is no heat transfer data for droplet diameters greater than 3 mm.

For small droplets, the heat transfer effectiveness has been predicted by Bolle and Moreau (1982), Labeish (1994), and Inada and Yang (1994) to vary as the inverse of the square root of droplet diameter. Bernardin and Mudawar (1997) predict that the effectiveness varies as $d^{-0.062}$ for dilute sprays. It is of interest to clarify this relationship for very large droplet diameters.

Additionally, the mass flux has been shown by Mizikar (1970), Bolle and Moureau (1982), and Choi and Yao (1987) to have a strong relationship to the heat transfer. They suggest that the heat flux varies as G^n , with values of n ranging from 0.556 to 1.0. Bernardin and Mudawar (1997) show an inverse effect, with spray effectiveness varying as $G^{-0.736}$.

There is also disagreement in the literature as to the effect of droplet velocity on the heat transfer effectiveness. Pederson (1970) noticed an increase in effectiveness with velocity for tests on single droplets for velocities up to 10 m/s and Weber numbers up to 550. Labiesh (1994) predicted that the heat transfer should decrease with increased velocity for $We > 100$. Bernardin and Mudawar (1997) also showed a decrease in effectiveness for single droplet streams of Weber numbers between 3.4 and 124. Shi et al. (1993) observed mixed velocity effects, noting an increase in effectiveness with velocity below 350°C, but detecting a decrease above the wetting temperature. The velocity for their tests ranged between 0.5 and 2 m/s, corresponding to Weber numbers of 13 to 200.

Other parameters such as test specimen material and surface roughness have also been shown to influence spray heat transfer (Labeish, 1994; Bernardin et al., 1997). However, the effects are secondary in nature, and the primary focus of these experiments are to determine the effects of spray parameters on the heat transfer.

Lacking from the literature is the presentation of data with dimensionless parameters such as Reynolds or Weber numbers. Also, there has not been a set of parameters presented that correlates the data of several authors and a wide range of spray parameters.

Contributed by the Heat Transfer Division for publication in the JOURNAL OF HEAT TRANSFER and presented at the ASME Thermal Physics Conference, NM. Manuscript received by the Heat Transfer Division, Mar. 2, 1998; revision received, Dec. 21, 1998. Keywords: Droplet, Heat Transfer, High Temperature, Thermophysical, Two-Phase. Associate Technical Editor: J.-C. Han.

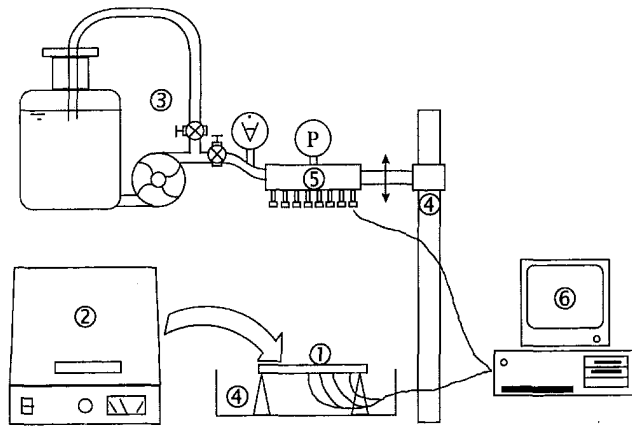


Fig. 1 Schematic of the experimental apparatus

Experimental Apparatus and Procedure

A transient testing method was used to measure the heat transfer of the sprays. This test procedure consisted of heating a test specimen to a desired temperature away from the influence of the spray. After achieving the desired temperature, the heat source is removed from the test specimen and the specimen is exposed to the liquid spray. The temperature of the test specimen is recorded as it cools. Heat flux information is then calculated from the time-temperature data.

For these tests, the water spray was placed above the hot test surface and the spray impacted vertically downward against the specimen. The experimental equipment, shown in Fig. 1, consisted of a test specimen (1), a furnace for heating the specimen (2), a water supply system (3), a test stand (4), various spray nozzles (5), and a data acquisition system (6). This experimental arrangement allowed the independent variation of droplet diameter, velocity, and mass flux.

The test specimen was a circular copper disk 190 mm in diameter plated with a 0.075 mm layer of chrome to reduce surface oxidation and emissivity. The disk center was elevated 0.25 mm and tapered smoothly toward the edges to reduce pooling of the water. The bottom was notched near the outer radius to facilitate the detachment of water running down the sides. Holes for thermocouples were located at the center, $\frac{1}{4}r$, $\frac{1}{2}r$, and $\frac{3}{4}r$ positions to detect radial temperature variations.

An electric muffle furnace was used to heat the test disk. Once removed from the furnace, the heated disk was supported by three small refractory cones to reduce contact losses. A reservoir below the disk collected the spent spray water, which was discharged continuously by a small pump. The nozzles were mounted above the test stand on an adjustable platform, and the droplet velocity was varied by changing the height of the platform above the test disk.

The droplet diameters produced from each of the three different nozzles ranged between 3 and 25 mm. This was measured by capturing a known number of drops in a container, measuring the

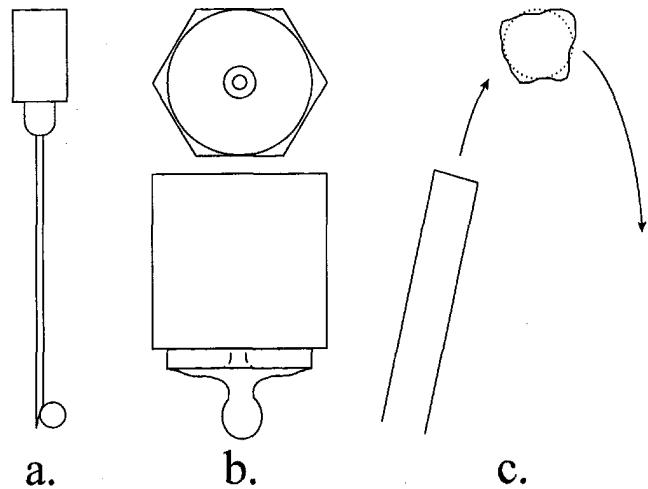


Fig. 2 Nozzles used to generate droplets of various diameters

total volume, and converting that value to an average droplet diameter. This method was accurate to within five percent, and the droplet diameter was also verified photographically.

To produce the large range of droplet sizes for the experiments, three different types of nozzles were used. A minimum droplet size of 3 mm was chosen in order to overlap existing data. These droplets were produced with an array of inverted 18-gauge hypodermic needles with an outside diameter of 1.24 mm (Fig. 2(a)). The nozzles were staggered from row to row and were spaced 16 mm apart. The needles produced consistent drop sizes which varied with flow rate between 2 and 3 mm in diameter, with the larger drops being produced at the lower flow rates.

Intermediate drop sizes of 7 to 9 mm were generated using surface tension effect nozzles (Fig. 2(b)). Water collected on downward facing circular surface, and droplets were formed from the surface tension of the liquid. Data from Harkins and Brown (1919) indicated that the maximum drop size that could be produced by this method was around 9 mm in diameter using a 25-mm diameter surface. The nozzle surface was roughened using 20-grit sandpaper to increase the surface tension. Tests indicated that these nozzles produced uniform droplet diameters consistently individually and between nozzles. Drop sizes for these nozzles also varied with the flow rate from 7.7 mm to 9.7 mm, with the diameter decreasing with increasing flow rate.

A pulsing technique was used to generate drops from 12 to 25 mm in diameter. Pressurized water (5–40 psig) was supplied to a solenoid valve, which was pulsed open using a frequency generator and electronic relay. As the solenoid opened, a volume of water discharged upwards at a small angle (<15 deg) to the vertical (Fig. 2(c)). The water pressure, pulse duration, and frequency were varied to adjust the flow rate and droplet diameter. The pulse duration was 10 ms for all tests and the frequency varied between 0.5 and 1.5 Hz. Because of the high volume of each of these large drops, the number of nozzles was small. For the 12 mm

Nomenclature

c_p = specific heat (J/kg/K)
 d = droplet diameter (m)
 G = liquid mass flux (kg/m²/s)
 h = height of nozzle above test disk (m)
 Δh_v = latent heat of vaporization (J/kg)
 q = heat transfer rate (W)
 q'' = heat flux (W/m²)
 P = liquid pressure (psig)

Re = droplet Reynolds number ($\rho v d / \mu$)
 T = Temperature (K)
 v = droplet velocity (m/s)
 \dot{V} = volumetric flow rate (m³/s)
 We = droplet Weber number ($\rho v^2 d / \sigma$)

Greek

ϵ = heat transfer effectiveness
 μ = dynamic viscosity (kg/m/s)

ρ = density (kg/m³)
 σ = surface tension (N/m)

Subscripts

l = property of liquid phase
 L = characteristic length
 sat = liquid saturation properties
 v = property of vapor phase
 w = conditions at target surface

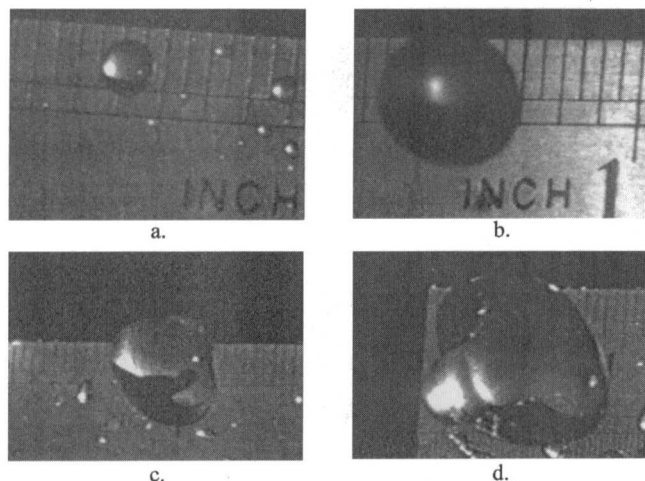


Fig. 3 Droplets produced by the various nozzles, $v = 3$ m/s, (a) nozzle: Fig. 2(a), $d = 3$ mm, (b) nozzle: Fig. 2(b), $d = 8$ mm, (c) nozzle: Fig. 2(c), tube dia. = $\frac{3}{8}$ in., $d = 13$ mm, (d) nozzle: Fig. 2(c), tube dia. = $\frac{1}{2}$ in., $d = 18$ mm (scale divisions in photo are $\frac{1}{80}$ in.)

drops, two $\frac{3}{8}$ in. tubes were used, and a single $\frac{1}{2}$ in. tube produced the 20 and 25 mm drops.

Figure 3 shows photographs of droplets generated by the various nozzle configurations. It can be seen in Fig. 3(a, b) that the 3 mm and 8-mm droplets are nearly spherical. However, the 12 and 20-mm drops (Fig. 3(c, d)) formed a slug of fluid that varied in shape during their flight, with a few small drops trailing the large one (the ancillary droplets observed in the photographs are liquid on the scale).

The stability of the pulsed drops varied with pulse duration and frequency, water pressure, and nozzle angle. A 5 to 10-deg angle from vertical, longer pulse duration, high frequency, and moderate water pressure (~ 20 psig) produced the most coherent drops.

The large droplets displayed similar impaction behavior as smaller droplets. For surface temperatures above the Leidenfrost point and very low Weber numbers (< 80), the 3-mm and 8-mm diameter droplets would impact the disk, rebound, and float on the surface until they forced off by other impacting droplets. Weber numbers less than 80 were not achievable for the larger droplet diameters. Above Weber number of 100, the droplets would break up upon impact. The resulting smaller droplets would scatter along the surface, with some collisions between secondary droplets.

The disk temperature was measured at four points along its radius using 1-mm diameter stainless steel sheathed type K thermocouples. Temperature measurements were recorded on a personal computer equipped with a data acquisition card coupled to a thermocouple input board at a rate of 2 Hz. The surface temperature for the tests was between 400°C and 700°C to insure non-wetting conditions.

The velocity of the drops was varied by changing the height of the nozzle above the test surface, and allowing the droplets to free fall to the target. The height of the nozzle was varied between 2 cm and 2.75 m producing velocities between 0.6 and 7.3 m/s. Droplet Weber numbers between 15 and 11,000, and droplet Reynolds numbers between 2000 and 150,000.

The velocity was calculated as the free fall velocity, which is accurate to within three percent for the large droplet diameters and low velocities used. Accuracy of the height measurement was proportional to the height. Small velocities (< 1 m/s) are accurate within 15 percent, while higher velocities are accurate to five percent.

Flow rates for the tests ranged from 240 ml/min to 940 ml/min ± 5 percent of the indicated value, corresponding to mass fluxes of 0.137 through $0.53 \text{ kg/m}^2/\text{s}$. The upper surface area of the test disk was used to calculate the mass flux.

Parametric studies to determine the effects of mass flux, droplet

velocity, and droplet diameter used a polished chrome plated disk and tap water. For these tests, a base case of $h = 1.37$ m ($v = 5.2$ m/s), flow rate = 650 ml/min ($G = 0.37 \text{ kg/m}^2/\text{s}$), and $d = 8$ mm was used.

A second series of tests was performed to increase the data base, clarify trends observed in the first tests, and to confirm the accuracy of the original data. For these tests, the mass flux was held constant at $0.37 \text{ kg/m}^2/\text{s}$ and only the droplet diameter and velocity were varied. A high purity, hard chrome plated disk and distilled water was used in this series of tests. The distilled water was supplied by a pump and reservoir system that could supply 1.5 liters per minute at up to 40 psig. For both systems, the water temperature was a constant 23°C .

Data Analysis

The temperature at each thermocouple location was assumed to be constant through the thickness of the disk. A one-dimensional analysis showed that there is only a 2.5°C (or one percent) temperature difference through the disk for the range of heat fluxes encountered. Radial variations in temperature in the disk were converted to an average temperature of the disk by area weighting the individual thermocouple readings. The radial temperature difference across the disk was within three percent of the average disk temperature for all but the largest drop size.

Thermocouple errors were minimized by inserting grounded thermocouples into the test disk from the surface opposite the spray, and by press-fitting the thermocouples into the holes to a depth of 1.5 mm below the impingement surface. Because of the reduced heat flux in the film boiling temperature regime for the spray, the temperature error for this configuration is expected to be within five percent of the local value.

Total temperature error is estimated by taking the square root of the sum of the squares of the individual errors. This provides an overall temperature error estimate of six percent in the film boiling regime.

The averaged temperature data was smoothed in time using a ten point moving average filter. The heat content of the disk was computed for each time step, and this value was numerically differentiated using a four point, fourth-order accurate differentiation scheme to obtain the total heat transfer rate.

To determine the heat transfer due to the spray alone, the contribution of radiation and natural convection was subtracted from the measured heat flow. Calibration tests with no spray applied were performed periodically to evaluate the influence of radiation and free convection. For these tests, natural convection was determined for both the upper and lower surfaces. When the spray was applied to the top surface, only the contribution due to the lower surface was included in the correction. Because the disk was thin, convection from the sides was neglected.

Radiation heat loss was approximated as gray body radiation emanating from the entire surface area of the disk. Bolle and Moureau (1982) indicated that the decrease in participating surface area due to the presence of the spray is negligible. Emissivity was used as the variable for calibration, and the contribution from free convection was assumed to follow the results of Fuji and Imura (1972). Because this correction was calibrated experimentally on a daily basis, it is predicted to be within five percent of the actual value for the test date. Combining the uncertainty for temperature with that of the heat flux correction, a total expected error in the heat flux measurement is predicted to be eight percent.

The polished chrome disk had an initial emissivity of 0.2. However, as testing proceeded, the emissivity increased to 0.4 due to oxidation of the surface. Aging effects were also observed with the high alloy chrome-plated disk, with its emissivity increasing from 0.4 to 0.66. Each set of spray data was corrected using the emissivity measurement for the test date.

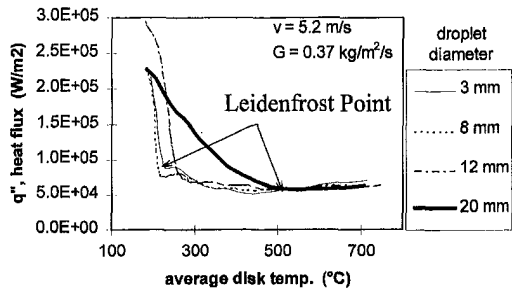


Fig. 4 Typical cooling curves for heat transfer tests

Parametric Results

Figure 4 shows cooling histories of typical spray tests. At high surface temperatures, where film boiling is dominant, the heat flux decreases only slightly with decreasing temperature. Just before wetting, the heat flux experiences a minimum at the Leidenfrost point. As the surface begins to wet, there is a sharp increase in the heat flux which reaches a maximum, and the surface quenches rapidly. Interestingly, the quenching of the surface occurs at a slightly higher temperature for the 20 mm drops than for the smaller diameters, and has a more gradual transition.

The variation of heat transfer with mass flux for constant droplet velocity and diameter is shown in Fig. 5, which shows that the heat flux increases with increasing mass flux. Many authors have noted a similar correlation between the heat flux and the mass flux for smaller droplets. Mizikar (1970) observed a linear relationship between q'' and G for polydisperse sprays of 0.86-mm diameter. Bolle and Moureau (1982) and Choi and Yao (1987) suggest that q'' varies as G^n ($n < 1$), with values of n ranging from 0.556 to 0.95 for droplets between 0.11 mm to 0.56 mm. Figure 5 suggests that for 8-mm drops at 5.2 m/s, $n \cong 0.75$, which falls within the range of published values of n . A single fit of the data from 400°C to 600°C provides a prediction accurate to ± 10 percent of the data, which is within the range of uncertainty for the data.

The spray heat transfer effectiveness is given by Eq. (1):

$$\epsilon = \frac{q''}{G[\Delta h_v + c_{p,l}(T_{sat} - T_{spray}) + c_{p,v}(T_w - T_{sat})]} \quad (1)$$

This parameter relates the amount of heat removed by the spray to the total heat removal capacity of the liquid. The advantage of this form of presentation is that it removes some ambiguity as to the appropriate area to use when presenting area dependent quantities such as heat or mass flux. It is seen in Fig. 5 that the heat transfer effectiveness decreases with increasing mass flux. Based on the uncertainty of heat flux, mass flux, and surface temperature, it is predicted that the values of effectiveness are within 12 percent of actual values.

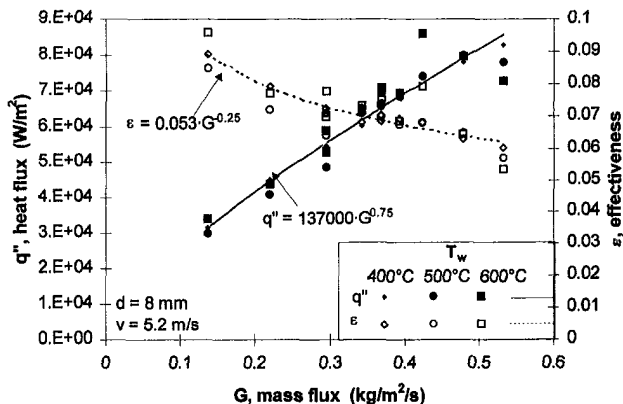


Fig. 5 Variation of heat flux and spray effectiveness with mass flux

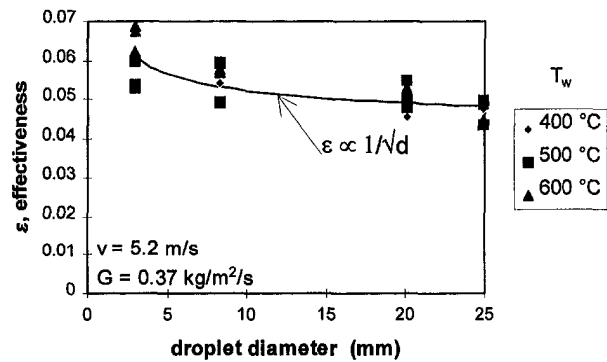


Fig. 6 Effect of droplet diameter on effectiveness

Data on the influence of droplet diameter on effectiveness (Fig. 6) showed a decrease in effectiveness for increasing the droplet diameter. This is in agreement with the predictions of the aforementioned authors who suggested that for smaller droplets the effectiveness decreases with droplet diameter as $\epsilon \propto 1/\sqrt{d}$.

Figure 7 indicates the variation in effectiveness due to droplet velocity. The slight variation in effectiveness with droplet velocity is less than the range of experimental error. Hence, no accurate interpretation of the data is possible.

Because the parametric tests indicated that the larger drops behaved similarly to previously studied small drops, it was of interest to see if results from the large droplets tests could be directly correlated to those from small droplet studies. For this, data was collected from various authors (Yao and Choi, 1987, Choi and Yao, 1987, Ito et al., 1991, Shoji et al., 1984) covering a wide range of test conditions, including single droplet streams, monodisperse sprays, and polydisperse sprays. The range of spray parameters included mass fluxes of 0.016 to 2.05 kg/m²/s, droplet velocities of 0.6 to 7.3 m/s, and droplet diameters of 0.13 to 1.33 mm.

To promote comparability, all heat transfer data was taken at 400°C. Additionally, the data of Shoji et al. (1984) was corrected using the results of Deb and Yao (1989) to account for the geometry of their test which eliminated the effects of secondary droplet impaction.

When the liquid and surface temperatures are constant, the two most significant nondimensional parameters are the droplet Weber number and Reynolds number. The Weber number relates the importance of surface tension effects to heat transfer behavior through the spreading dynamics of the droplet on the surface. The droplet Weber number has been shown (Wachters and Westerling, 1966) to play a large role in the dynamic behavior of droplets impacting high-temperature surfaces. It is of interest to determine if the Weber number also influences the heat transfer characteristics of the spray.

Figure 8 indicates the relationship between droplet Weber num-

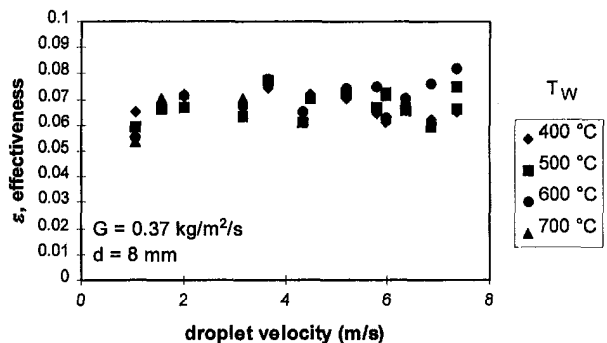


Fig. 7 Influence of droplet velocity on effectiveness

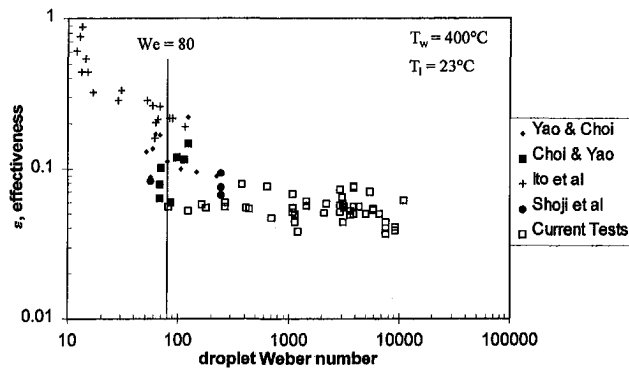


Fig. 8 Comparison between effectiveness and droplet Weber number

ber and heat transfer effectiveness. In general, the effectiveness decreases with increasing We , with a jump at around $We = 80$. This is the same Weber number value that Wachters and Westerling relate to a change in the dynamic behavior of a droplet as it impacts a nonwetting surface. This phenomenon may be caused by the repeated strikes of rebounding droplets at low We and the breakup and dispersal of drops with a higher Weber numbers. It may also be due to the increased liquid/surface contact time resulting from lower droplet velocity.

The large scatter of the current data at lower We is characteristic of the larger uncertainty present at lower velocities. Uncertainty in the Weber number for $We < 100$ is near 25 percent, while it is only nine percent at higher We .

The droplet impaction behavior has also been shown to be influenced by the liquid viscous forces (Scheller and Bousfield, 1995). The droplet Reynolds number (defined using the liquid viscosity) is representative of the importance of viscous effects in the droplet impaction.

The comparison between droplet Reynolds number and spray effectiveness in Fig. 9 depicts a similar trend to the Weber number results in Fig. 8. The data is somewhat ordered on either side of a Reynolds number of about 1100. It is expected that this graph should be similar to the graph of We because, for a given liquid and subcooling, both parameters are dependent only on the droplet diameter and velocity.

Conclusions

Tests were performed to evaluate the heat transfer characteristics for a range of large drop sizes not previously analyzed in the literature. Droplets sizes ranging from 3 to 25 mm were studied, and a method of producing droplets of very large diameter, up to 25 mm, was demonstrated.

Parametric tests showed that the heat transfer for sprays of large

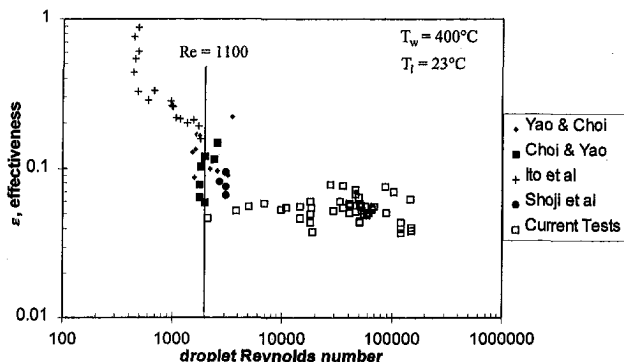


Fig. 9 Comparison between effectiveness and droplet Reynolds number

droplets is most dependent on spray mass flux. This power-law dependence agrees with the results in published literature for smaller droplets, and the exponent is expected to vary with droplet diameter, velocity, subcooling, and surface temperature.

It was also observed that spray heat transfer effectiveness for large droplets varies with $d^{-1/2}$. This, too, matches published results for smaller drops.

The effects of droplet velocity were also investigated. However, there was no distinct correlation deducible from the results. Similarly, mixed results have been published for smaller droplets.

The parametric behavior of the sprays of large drops in this study is similar to previously published results for sprays of small drops. Therefore, it can be concluded that although the large drops may not be spherical and constant in shape, the heat transfer characteristics of droplets greater than 3 mm in diameter are similar to those of smaller, hydrodynamically stable droplets.

A direct comparison between the current tests of large droplets and the results previously published for sprays of smaller drops using the droplet Reynolds and Weber numbers showed some correlation, with a marked separation at the point $We = 80$. This Weber number corresponds to the one where the dynamic behavior of the drops has been shown to change for nonwetting impaction, suggesting that the multiple impaction of rebounding droplets and longer contact time between the droplet and the surface at low Weber numbers increases the efficiency of the spray.

Acknowledgments

Partial funding for this project was provided by the Weirton Steel Corporation. The authors would also like to thank Danieli Wean, Inc. for their cooperation and support in the completion of this work.

References

- Bernardin, J. D., and Mudawar, I., 1997, "Film Boiling Heat Transfer of Droplet Streams and Sprays," *Int. J. of Heat and Mass Transfer*, Vol. 40, No. 11, pp. 2579–2593.
- Bernardin, J. D., Stebbins, C. J., and Mudawar, I., 1997, "Effects of Surface Roughness on Water Droplet Impact History and Heat Transfer Regimes," *Int. J. of Heat and Mass Transfer*, Vol. 40, pp. 73–88.
- Bolle, L., and Moureau, J. C., 1982, "Spray Cooling of Hot Surfaces," *Multiphase Science and Technology*, Hemisphere, Washington, DC.
- Choi, K. J., and Yao, S. C., 1987, "Mechanisms of Film Boiling Heat Transfer of Normally Impinging Spray," *Int. J. Heat and Mass Transfer*, Vol. 30, No. 2, pp. 311–318.
- Deb, S., and Yao, S.-C., 1989, "Analysis on Film Boiling Heat Transfer of Impinging Sprays," *Int. J. Heat and Mass Transfer*, Vol. 32, No. 11, pp. 2099–2112.
- Fujii, T., and Imura, H., 1972, "Natural Convection Heat Transfer from a Plate with Arbitrary Inclination," *Int. J. Heat and Mass Transfer*, Vol. 15, pp. 755–767.
- Gunn, R., and Kinzer, G. D., 1948, "The Terminal Velocity of Fall for Water Droplets in Stagnant Air," *Journal of Meteorology*, Vol. 6, pp. 243–248.
- Harkins, W., and Brown, F., 1919, "Determination of surface tension (free surface energy) and the weight of falling drops: The surface tension of water and benzene by the capillary height method," *J. of the Am. Chem. Soc.*, Vol. 41, p. 499.
- Inada, S., and Yang, W.-J., 1994, "Film Boiling Heat Transfer for Saturated Drops Impinging on a Heated Surface," *Int. J. Heat and Mass Transfer*, Vol. 37, No. 16, pp. 2588–2591.
- Ito, T., Takata, Y., Mousa, M. M. M., and Yoshikai, H., 1991, "Studies on the Water Cooling of Hot Surfaces (Experiment of Spray Cooling)," *Memoirs of the Faculty of Engineering Kyushu University*, Vol. 51, No. 2.
- Labeish, V. G., 1994, "Thermohydrodynamic Study of a Drop Impact against a Heated Surface," *Exp. Thermal and Fluid Science*, Vol. 8, pp. 181–194.
- Mizikar, E. A., 1970, "Spray Cooling Investigation for Continuous Casting of Billets and Blooms," *Iron and Steel Engineer*, June, pp. 53–60.
- Pederson, C. O., 1970, "An Experimental Study of the Dynamic Behavior and Heat Transfer Characteristics of Water Drops Impinging upon a Heated Surface," *Int. J. Heat and Mass Transfer*, Vol. 13, pp. 369–381.
- Scheller, B. L., and Bousfield, D. W., 1995, "Newtonian Drop Impact with a Solid Surface," *AIChE Journal*, Vol. 41, No. 6, pp. 1357–1367.
- Shi, M. H., Bai, T. C., and Yu, J., 1993, "Dynamic Behavior and Heat Transfer of a Liquid Droplet Impinging on a Solid Surface," *Experimental Thermal and Fluid Science*, Vol. 6, pp. 202–207.
- Shoji, M., Wakunaga, T., and Kodama, K., 1984, "Heat Transfer from a Heated Surface to an Impinging Subcooled Droplet (Heat Transfer Characteristics in the Non-wetting Regime)."
 - Wachters, L. H. J., and Westerling, N. A. J., 1966, "The Heat Transfer from a Hot Wall to Impinging Water Drops in the Spheroidal State," *Chem. Eng. Science*, Vol. 21, pp. 1047–1056.
 - Yao, S. C., and Choi, K. J., 1987, "Heat Transfer Experiments of Mono-dispersed Vertically Impinging Sprays," *Int. J. Multiphase Flow*, Vol. 13, No. 5, pp. 639–648.

Mass, Momentum, and Energy Transport in a Molten Pool When Welding Dissimilar Metals

F. K. Chung
Graduate Student

P. S. Wei
Professor,
e-mail: pswei@mail.nsysu.edu.tw
Mem. ASME

Department of Mechanical Engineering,
National Sun Yat-Sen University,
Kaohsiung, Taiwan, R.O.C.

Velocity and temperature fields, and shapes of the fusion zone in welding dissimilar metals are systematically investigated. Fluid flow in the molten pool is driven by the Marangoni force in different directions and magnitudes on the flat free surface. To interpret clearly without loss of generality, the three-dimensional quasi-steady welding is simulated by an unsteady two-dimensional process. Transport process on the maximum cross section of the molten region (or a cross section of the fusion zone) therefore is predicted. Interfaces between immiscible dissimilar metals and solid and liquid are, respectively, calculated by the volume of fluid and enthalpy methods. The computed results show different flow and thermal fields and molten regions of dissimilar metals as functions of dimensionless surface tension coefficients, viscosities, melting temperatures, and thermal conductivities of dissimilar metals and distinct phases, and beam power, welding speed, and the energy distribution parameter. The predicted shapes of fusion zones in welding pure irons, and aluminum to iron, agree with the experimental results.

Introduction

Weldments are often made from dissimilar metals in order to satisfy different requirements for working. A successful weld between dissimilar metals possesses sufficient tensile strength and ductility so that the joint will not fail. Such joints can be accomplished in a variety of different metals and by many of the welding processes (Sun and Moio, 1994). An investigation of transport processes and fusion zone shapes by accounting for different working parameters and properties between dissimilar metals therefore becomes the objective of this study.

Practically speaking, if there is mutual solubility of the two metals, the dissimilar joint can be made successfully (Cary, 1989). In some cases, it is necessary to use a third metal that is soluble with each other to produce a successful joint. An example is the attempt to weld copper to steel, which are not mutually soluble. A soluble nickel with both of them therefore is required. If thermal expansion coefficients of dissimilar metals are widely different, there will be internal stresses set up in the intermetallic zone during any temperature change of the weldment. Failure may soon occur for an intermetallic zone of extremely brittle. Provided that melting temperatures or thermal conductivities of the two metals are different, the joint becomes complex. This is because one metal will be molten before the other.

A systematic investigation of welding requires a study of heat transfer and fluid flow in the molten pool. Transport processes in welding the same metals or alloys in arc, low-power-density electron (or laser) beam welding have been very well understood (Giedt et al., 1984; Kou and Wang, 1986; Zacharia et al., 1989). The driving force is Marangoni or thermocapillary force, which is a surface tension gradient force resulting from the variations in temperature or solute. Surface tension of pure liquid metals is increased by decreasing temperature. In view of a decrease in temperature surface flow accompanied with energy transport is directed from the center to edge of the pool. The molten pool is shallow and wide. On the other hand, a positive surface tension

coefficient results in a surface flow from the edge to the center and in a narrow and deep molten pool.

In welding dissimilar metals such as titanium and nickel a frozen convection swirling from the poorly mixed liquids of different composition in the pool was observed by Seretsky and Ryba (1976). The flow pattern was similar to those obtained by Unger (1941) and by Nippes et al. (1950) in their studies of spot resistance welding of Cor-Ten to 18-8 stainless steel and monel to steel. In a typical welding the time for completing the welding is around 0.1 s based on a welding speed of 0.01 m/s and a length of fusion zone 0.001 m. Since solute diffusivities of liquid metals are around 10^{-9} m²/s, the distance for solute diffusion is 10^{-5} m, which is only a hundredth of the length of the pool. Dissimilar molten metals therefore can be considered as immiscible fluids.

Tinkler et al. (1983) observed that when both steels have the same sulfur levels either good penetration (90 ppm) or poor penetration (30 ppm) was obtained. Good penetration is referred to a fusion zone with a greater depth-to-width ratio. However, when samples with different penetration characteristics were welded together, the weld pool was displaced toward the material with the lower sulfur content. Since sulfur is a surface active element, an increase of sulfur content in iron results in a decrease of surface tension and an increase of surface tension coefficient from negative to positive values at a concentration of 70 ppm (Belton, 1976; Sahoo et al., 1988; Mills and Keene, 1990). Heiple and Roper (1982) first found that the existence of a minor surface active element can change the direction of surface flow and the shape of the fusion zone. Mills and Keene (1990) therefore interpreted that all of these flows operated in the direction from high sulfur to low sulfur. This resulted in the transport of hot metal to the low sulfur side. The meltback will occur preferentially in the low sulfur steel and an asymmetric weld will be produced. The predominance of Marangoni flow in the weld pool was also confirmed. Marangoni forces can be in different directions and magnitudes in welding dissimilar metals. In view of the complexity of the process, a systematic investigation of heat transfer and fluid flow in the molten pool when welding dissimilar metals is still lacking.

In this study, velocity and temperature fields and shapes of the fusion zone in welding dissimilar metals are predicted. The flat free surface is imposed by thermal and solutal Marangoni forces in

Contributed by the Heat Transfer Division for publication in the JOURNAL OF HEAT TRANSFER. Manuscript received by the Heat Transfer Division, Mar. 11, 1998; revision received, Nov. 1, 1998. Keywords: Heat Transfer, Manufacturing, Phase Change, Thermocapillary. Associate Technical Editor: D. Zumbrennen.

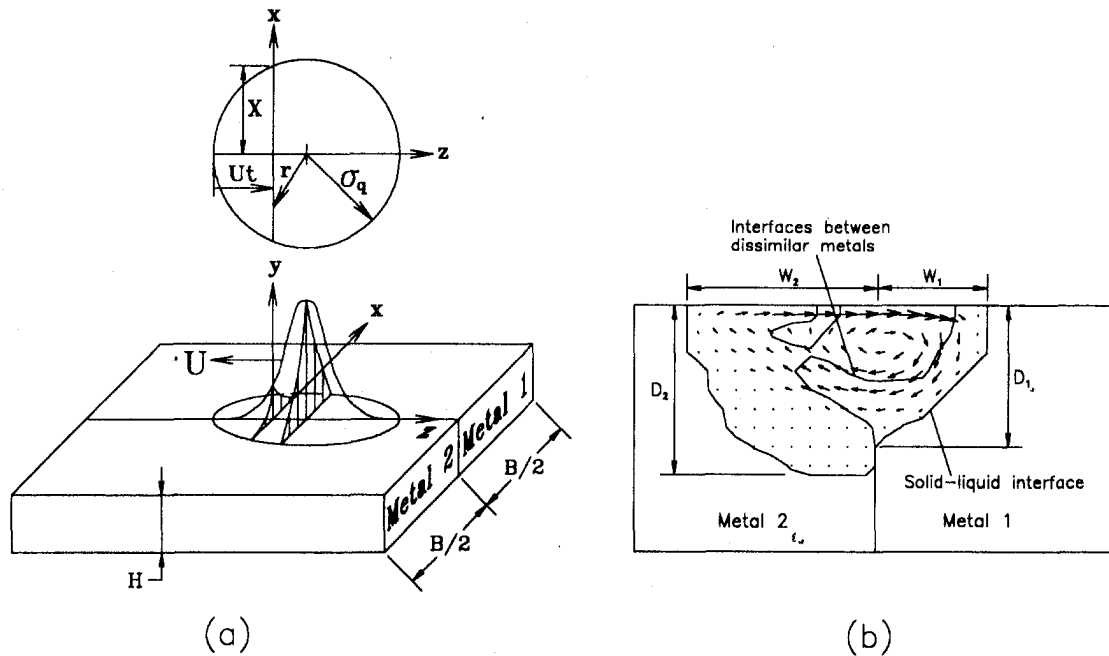


Fig. 1 Schematic sketch for (a) system model and coordinates, (b) cross section of the fusion zone

different directions and magnitudes. The unknown interfaces between solid and liquid and immiscible dissimilar metals are coupled with velocity fields and distinct thermal, physical, and transport properties. The result gives a systematic insight into transport phenomena in welding dissimilar metals.

System Model and Analysis

Welding dissimilar metals by an incident flux from a low-power-density electron or laser beam is illustrated in Fig. 1 (a). Hence, no cavity is formed in the molten pool (Elmer et al., 1990; Wei and Kuo, 1998). A Cartesian coordinate system is fixed on

metals. The incident flux moves with a constant speed U in the negative z -direction. This work extends the unsteady two-dimensional mode proposed by Paul and DebRoy (1988) by further including the effects of welding speed, distinct properties between phases, and dissimilar metals. Temperature at a given location $z = 0$ increases and reaches the melting point when the beam is approached. After the beam is passed by temperature decreases. Unsteady heat transfer and fluid flow at this location therefore are determined by considering the incident flux as a function of time, the energy distribution parameter, and welding speed. Fluid flow in the molten pool is driven by Marangoni force

Nomenclature

A = absorptivity
 B = total metal width, $B^* = B/H$, as illustrated in Fig. 1 (b)
 Bi = Biot number = hH/k_{1l}
 c = specific heat
 c_σ = surface tension coefficient, $c_\sigma^* = c_\sigma H / (T_{m1} - T_\infty) / (\mu_1 \alpha_{1l})$
 D = maximum depth of pool, as illustrated in Fig. 1 (b)
 f = volumetric fraction of liquid to solid
 F = volumetric fraction of metals 1 to 2
 g = gravitational acceleration
 $G = H^3 g / \alpha_{1l}^2$
 h = heat transfer coefficient
 h_{sl} = latent heat
 $h_{sl}^* = h_{sl} / h_{sl1}$
 H = metal thickness, as illustrated in Fig. 1 (a)
 I = sensible heat, $I^* = I / [c_{1s}(T_{m1} - T_\infty)]$
 k = thermal conductivity, $k^* = k / k_{1l}$
 p = pressure, $p^* = p H^2 / (\rho_1 \alpha_{1l}^2)$

Pr = Prandtl number = $\mu_1 c_{1l} / k_{1l}$
 Q = beam power, $Q^* = Q / [H k_{1l} (T_{m1} - T_\infty)]$
 r = radial coordinate, $r^* = r / H$
 St = Stefan number = $[c_{1s}(T_{m1} - T_\infty)] / h_{sl1}$
 t = time, $t^* = t \alpha_{1l} / H^2$
 T = temperature, $T^* = (T - T_\infty) / (T_{m1} - T_\infty)$
 u = velocity component in x direction, $u^* = u H / \alpha_{1l}$
 U = welding speed
 v = velocity component in y direction, $v^* = v H / \alpha_{1l}$
 W = surface width of pool, $W^* = W / H$, as illustrated in Fig. 1 (b)
 x, y, z = Cartesian coordinate, $(x^*, y^*, z^*) = (x, y, z) / H$, as illustrated in Fig. 1 (a)

Greek letters

α_{1l} = thermal diffusivity = $k_{1l} / (\rho_1 c_{1l})$

β = expansion coefficient, $\beta^* = \beta / \beta_1$
 μ = viscosity, $\mu^* = \mu / \mu_1$
 ρ = density, $\rho^* = \rho / \rho_1$
 σ = surface tension = $\sigma_m + c_\sigma (T - T_m)$
 σ_q = energy distribution parameter, $\sigma_q^* = \sigma_q / H$

Superscript

* = dimensionless quantity

Subscript

b = boiling
 l = liquid
 m = melting
 s = solid
 0 = initial
 $1, 2$ = dissimilar metals, as illustrated in Fig. 1 (a)
 ∞ = ambient

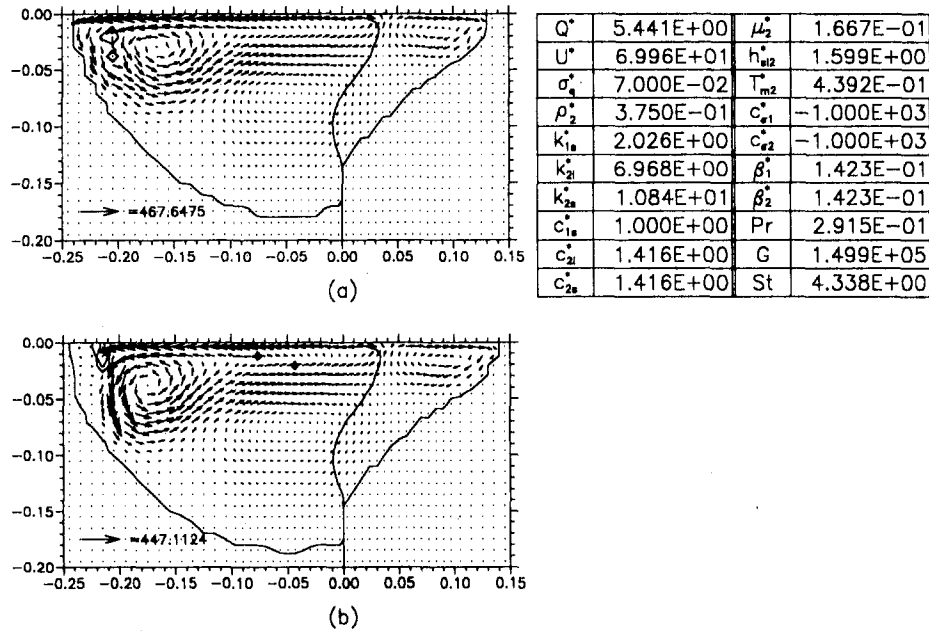


Fig. 2 Dimensionless velocity and temperature fields affected by temperature at downstream

on the free surface, as illustrated in Fig. 1 (b). Widths on the surface and maximum depths of molten regions 1 and 2 designating on the right and left-hand sides are denoted by W_1 and D_1 , and W_2 and D_2 , respectively. The major assumptions made are the following:

1 Incident flux absorbed by the top surface is of a Gaussian distribution.

2 Unsteady heat transfer and fluid flow vary primarily in the x - y planes. Since velocity and temperature fields are calculated on the maximum cross section, gradients of transport variables in the z -direction are neglected. Although a three-dimensional description can be extended from this work, the two-dimensional model is used for a clearer interpretation without loss of generality. Ignorance of the temperature field in the z -direction can be examined by varying temperatures at a downstream location, as will be shown later.

3 The free surface of the pool is flat. This is confirmed by a small capillary number ($\equiv c_s \Delta T / \sigma_m$) (Sen and Davis, 1982). In welding, typical metals $c_s \sim 10^{-4}$ N/m-K, $T_m - T_\infty \sim 500$ K, $\sigma_m \sim 1$ N/m. The capillary number yields 0.05.

4 Evaporation rates are neglected due to experimental data provided by DebRoy et al. (1991).

5 Physical and thermal properties of distinct phases and dissimilar metals are, respectively, averaged within the temperature range considered.

With the above assumptions, dimensionless continuity, momentum, and energy equations, respectively, reduce to

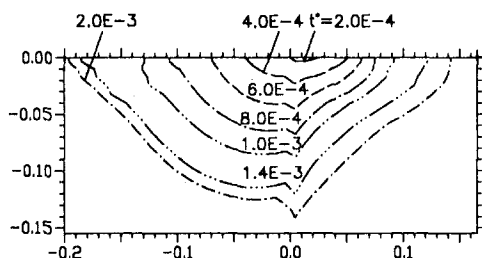


Fig. 3 Development of dimensionless temperature $T^* = 1$ during heating

$$\frac{\partial u^*}{\partial x^*} + \frac{\partial v^*}{\partial y^*} = 0 \quad (1)$$

$$\frac{\partial \rho^* u^*}{\partial t^*} + \frac{\partial}{\partial y^*} \left(\rho^* u^* v^* - 2 \text{Pr} \mu^* \frac{\partial u^*}{\partial x^*} \right) + \frac{\partial}{\partial y^*} \left[\rho^* u^* v^* - \text{Pr} \mu^* \left(\frac{\partial u^*}{\partial y^*} + \frac{\partial v^*}{\partial x^*} \right) \right] = - \frac{\partial p^*}{\partial x^*} \quad (2)$$

$$\frac{\partial \rho^* v^*}{\partial t^*} + \frac{\partial}{\partial y^*} \left[\rho^* u^* v^* - \text{Pr} \mu^* \left(\frac{\partial u^*}{\partial y^*} + \frac{\partial v^*}{\partial x^*} \right) \right] + \frac{\partial}{\partial y^*} \left(\rho^* v^* v^* - 2 \text{Pr} \mu^* \frac{\partial v^*}{\partial y^*} \right) = - \frac{\partial p^*}{\partial y^*} - \rho^* G [1 - \beta^* (T^* - 1)] \quad (3)$$

$$\frac{\partial \rho^* I^*}{\partial t^*} + \frac{\partial}{\partial x^*} \left(\rho^* u^* I^* - \frac{k^*}{c^*} \frac{\partial I^*}{\partial x^*} \right) + \frac{\partial}{\partial y^*} \left(\rho^* v^* I^* - \frac{k^*}{c^*} \frac{\partial I^*}{\partial y^*} \right) = - \frac{1}{\text{St}} \rho^* h_{sl}^* \frac{\partial f}{\partial t^*} \quad (4)$$

Energy Eq. (4) is expressed in terms of the sensible heat defined as

$$I^* = I_0^* + \int_{T_0^*}^{T^*} c^* dT^* \quad (5)$$

Since function f denotes the volumetric fraction of liquid, the term on the right-hand side of Eq. (4) becomes a heat sink for a melting solid, and vice versa. Dimensionless density, viscosity, thermal expansion coefficient, and latent heat in Eqs. (1)–(4) are, respectively, defined as

$$\begin{Bmatrix} \rho^* \\ \mu^* \\ \beta^* \\ h_{sl}^* \end{Bmatrix} = F + (1 - F) \begin{Bmatrix} \rho_2^* \\ \mu_2^* \\ \beta_2^* \\ h_{sl2}^* \end{Bmatrix} \quad (6)$$

where function F denotes the volumetric fraction of metal 1 to metal 2. For function $F = 0$ and 1 in a numerical cell, Eq. (6)

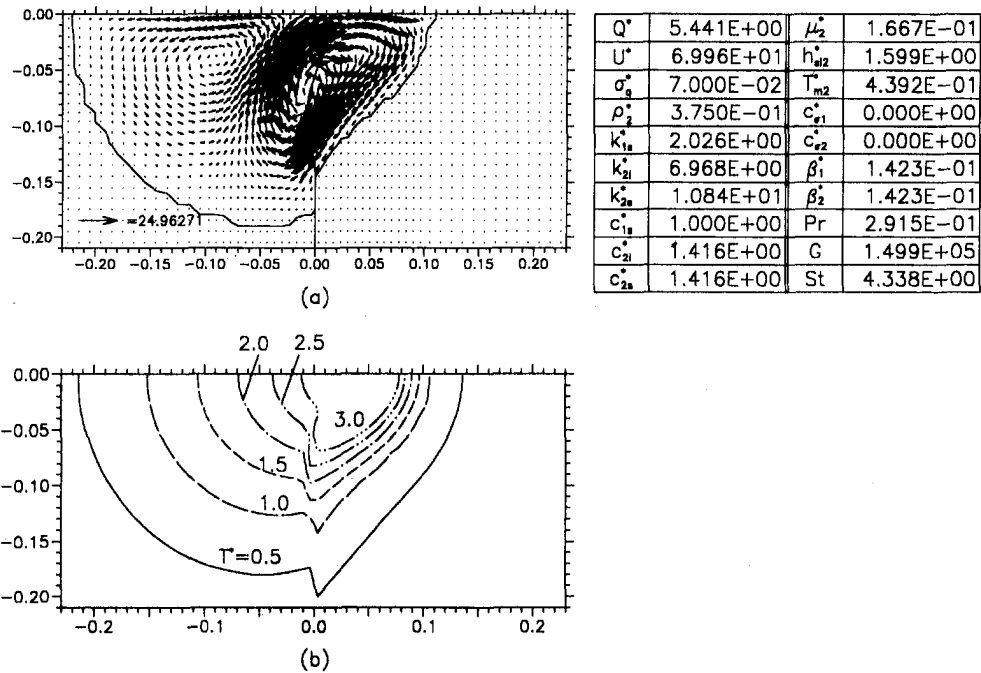


Fig. 4 Buoyancy effects on dimensionless velocity, temperature fields, and shapes of molten metals 1 and 2

represents density, viscosity, the expansion coefficient and latent heat of metals 2 and 1, respectively. Provided that $0 < F < 1$, properties are weighted by two metals coexisting in the cell. Thermal conductivity and specific heat in Eq. (4) are defined as

$$\begin{Bmatrix} k^* \\ c^* \end{Bmatrix} = F \begin{Bmatrix} k_1^* \\ c_1^* \end{Bmatrix} + (1 - F) \begin{Bmatrix} k_2^* \\ c_2^* \end{Bmatrix} \quad (7)$$

where thermal conductivities and specific heats of metals 1 and 2 are averaged between solid and liquid

$$\begin{Bmatrix} k_1^* \\ k_2^* \\ c_1^* \\ c_2^* \end{Bmatrix} = f \begin{Bmatrix} 1 \\ k_{2l}^* \\ 1 \\ c_{2l}^* \end{Bmatrix} + (1 - f) \begin{Bmatrix} k_{1s}^* \\ k_{2s}^* \\ c_{1s}^* \\ c_{2s}^* \end{Bmatrix} \quad (8)$$

It can be seen that Eqs. (1)–(4) reduces to conservation equations of liquid, solid, metal 1 or metal 2 for $f = 1, 0$ and $F = 1$ or 0 , respectively. Function f can be determined from a weighting of latent heat (Brent et al., 1988) while volumetric fraction F is calculated by

$$\frac{\partial F}{\partial t^*} + \frac{\partial u^* F}{\partial x^*} + \frac{\partial v^* F}{\partial y^*} = 0 \quad (9)$$

which is derived by substituting continuity Eq. (1) into zero material derivative of F . Equation (9) is used to determine domains of molten metals 1 and 2. The Marangoni force balanced by viscous stress at the free surface $y^* = 0$ yields

$$\mu^* \frac{\partial u^*}{\partial y^*} = c_\sigma^* \frac{\partial T^*}{\partial x^*} \quad (10)$$

where the surface tension coefficient is weighted between molten metals 1 and 2,

$$c_\sigma^* = F c_{\sigma 1}^* + (1 - F) c_{\sigma 2}^* \quad (11)$$

No evaporation or condensation leads to

$$v^* = 0 \quad (12)$$

Incident energy is balanced by conduction heat

$$k^* \frac{\partial T^*}{\partial y^*} = \frac{3Q^*}{\pi \sigma_q^{*2}} \exp\left(-\frac{3r^{*2}}{\sigma_q^{*2}}\right) \quad \text{for } |x^*| \leq X^*(t^*), \quad 0 \leq t^* \leq \frac{2\sigma_q^*}{U^*} \quad (13)$$

where the radial coordinate and the boundary of the beam are described by (see Fig. 1 (a))

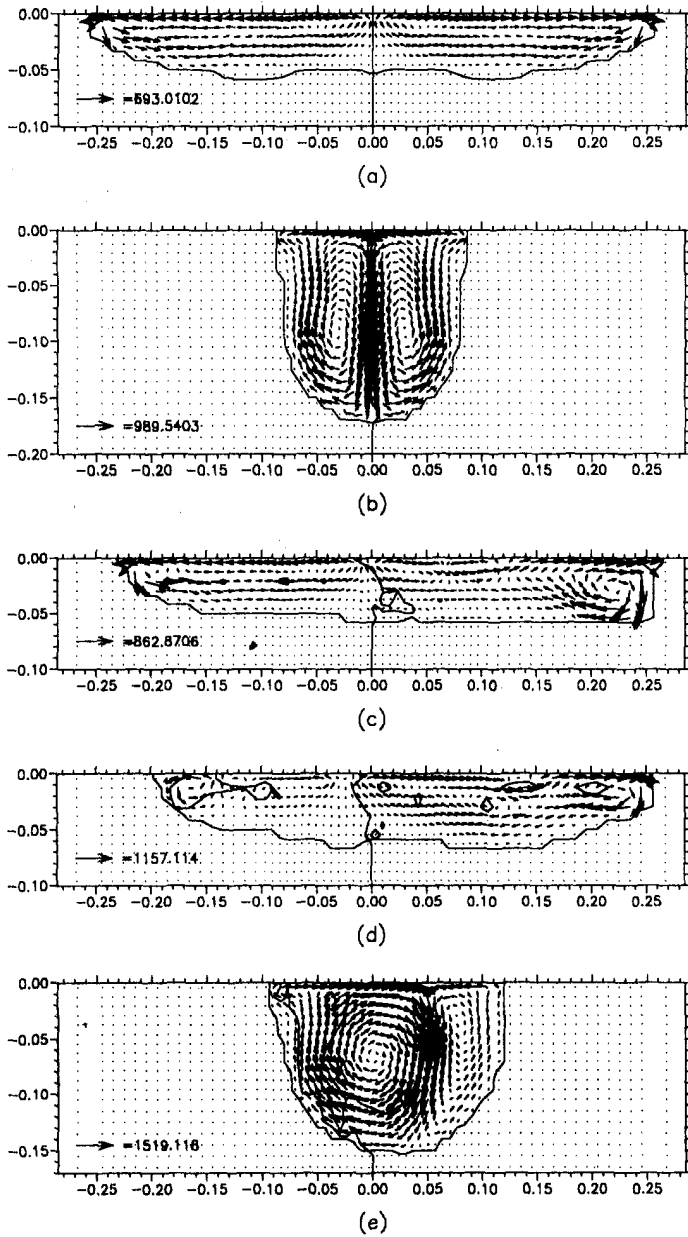
$$\begin{aligned} r^*(t^*) &\equiv \sqrt{x^{*2} + (\sigma_q^* - U^* t^*)^2}, \\ X^*(t^*) &\equiv \sqrt{\sigma_q^{*2} - (\sigma_q^* - U^* t^*)^2}. \end{aligned} \quad (14)$$

Otherwise, the energy balance is given by

$$k^* \frac{\partial T^*}{\partial y^*} = -\text{Bi} T^* \quad (15)$$

In the time interval $0 \leq t^* \leq 2\sigma_q^*/U^*$ and physical domain $|x^*| \leq [\sigma_q^{*2} - (\sigma_q^* - U^* t^*)^2]^{1/2}$, the top surface of the cross section is irradiated by the incident flux from Eq. (13). Outside these ranges conduction is removed by convection as governed by Eq. (15). Other conditions are zero velocities and conduction balanced by convection on the right, left, and bottom surfaces. Initial conditions are $T^* = T_0^*$, $u^* = v^* = 0$, and $F = 1$ for $x^* > 0$ and $F = 0$ for $x^* < 0$.

Numerical Procedure. Equations (1)–(4) were discretized by a control-volume formulation, fully implicit, staggered finite difference method (Patankar, 1980). Discretized cells were finer near the origin and coarser in the outward directions. Different mesh systems, 95×48 , 85×43 , 73×37 , and 61×31 were used for comparison. Although mesh systems increase from 61×31 to 95×48 , the minimum grid sizes reduce from 0.01 to 0.005 in the molten region. The former two systems led to nearly the same flow pattern and fusion zone shape, and the maximum velocity within a relative error of 0.5 percent. Root mean squares of the deviations for velocity and temperature on the free surface, were, respectively, 0.696 and 0.0342, which are less than three percent of the maximum speed of 28.65 and temperature 1.25. Using the mesh system of 85×43 for computation, relative errors of velocity and pressure became smaller than 10^{-4} . The maximum



Q^*	5.441E+00	μ_2^*	1.000E+00
U^*	6.996E+01	h_{m2}^*	1.000E+00
σ_1^*	7.000E-02	T_{m2}	1.000E+00
ρ_2^*	1.000E+00	c_{v1}^*	
k_{1a}^*	2.026E+00	c_{v2}^*	
k_{2l}^*	1.000E+00	β_1^*	1.423E-01
k_{2a}^*	2.026E+00	β_2^*	1.423E-01
c_{1a}^*	1.000E+00	Pr	2.915E-01
c_{2l}^*	1.000E+00	G	1.499E+05
c_{2a}^*	1.000E+00	St	4.338E+00

Fig. 5 Dimensionless velocity fields and shapes of molten metals 1 and 2 for different surface tension coefficients; (a) $c_{v1}^* = c_{v2}^* = -4.148 \times 10^4$, (b) $c_{v1}^* = c_{v2}^* = 4.148 \times 10^4$, (c) $c_{v1}^* = -2.074 \times 10^5$, $c_{v2}^* = -4.148 \times 10^4$, (d) $c_{v1}^* = -2.074 \times 10^5$, $c_{v2}^* = 4.148 \times 10^4$, (e) $c_{v1}^* = 4.148 \times 10^4$, $c_{v2}^* = 1.0 \times 10^5$

dilatation of continuity equation was 10^{-5} . The relative error for sensible heat and fraction of liquid were, respectively, less than 10^{-3} and 10^{-4} . At least 120 uniform time steps for the energy equation were used to investigate the heating process. Viscosity and thermal conductivity on the face between discretized cells were calculated from the concept of interfacial conductivity (Patankar, 1980). For cells containing both metals, properties were calculated from the concept of a mixture. To determine the interface of solid and liquid function $f = 0.5$ was chosen while the interface between metals 1 and 2 was defined by function $F = 0.5$. Sensitivity for choosing these values to determine the shape of the interface was reduced by using finer meshes. The solution procedure is described as follows:

- 1 specify initial conditions;
- 2 solve energy Eq. (4) by a line-by-line scheme and tridiagonal matrix algorithm (TDMA);
- 3 repeat steps 2 and 3 until solid becomes molten;

4 determine function f as melting starts. Energy Eq. (4) and the relationship between internal energy I^* and temperature T^* are used;

5 solve continuity and momentum equations from the SIMPLE procedure (Patankar, 1980);

6 calculate function F from advection Eq. (9) with converged velocities by using a donor-acceptor scheme proposed by Hirt and Nichols (1981); and

7 go to step 4 for the next time.

The use of Hirt-Nichols's donor-acceptor scheme is due to its simplicity and easy generalization to three-dimensional problems. Within the time limitation of stability, a two-dimensional cell exchanges mass with not only the neighboring four cells but also with the four cells at the corners. Accurate reconstruction of the interface and volume of fluid advection therefore account for nine cells. In a more elaborate scheme, for example, FLAIR (Flux Line-Segment Model for Advection and Interface Reconstruction)

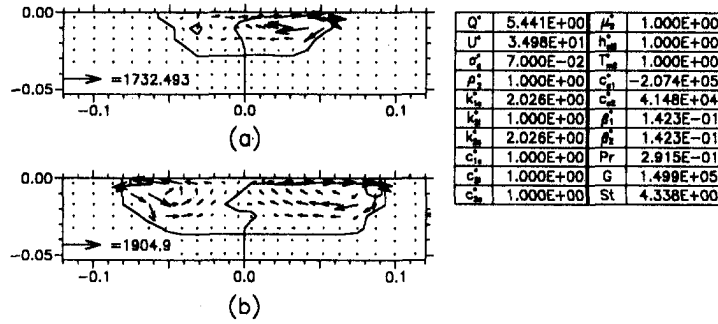


Fig. 6 Development of dimensionless velocity fields and shapes of molten metals 1 and 2 for given dimensionless surface tension coefficients of $c_{s1}^* = -2.074 \times 10^5$ and $c_{s2}^* = 4.148 \times 10^4$ at dimensionless times of (a) $t^* = 8.0 \times 10^{-4}$, (b) $t^* = 1.1 \times 10^{-3}$

(Ashgriz and Poo, 1991), the interface is approximated by a set of line segments fitted at the boundary of every two neighboring cells. Alternate-direction sweeps are used. Fluid fluxes in the x -direction are calculated and a new F field is generated. The new F field is then used for the y -sweep. This procedure is sufficiently accurate for uniform flows but induces errors when vortex exists. In this work, since velocities obtained from a numerical computation are not exactly satisfied by continuity Eq. (1), function F suffers errors. For clarity it is better to rewrite advection Eq. (9) in the form as proposed by Kothe and Mjolsness (1992):

$$\frac{\partial F}{\partial t^*} = F \left(\frac{\partial u^*}{\partial x^*} + \frac{\partial v^*}{\partial y^*} \right) - \frac{\partial u^* F}{\partial x^*} - \frac{\partial v^* F}{\partial y^*} \quad (16)$$

where the parenthesis on the right-hand side is trivial from continuity Eq. (1). A finite difference of Eq. (16) yields

$$\begin{aligned} (F_{i,j}^{n+1} - F_{i,j}^n) \delta x^* \delta y^* &= F_{i,j}^n [(u_{i+1/2,j}^* - u_{i-1/2,j}^*) \delta y^* + (v_{i,j+1/2}^* - v_{i,j-1/2}^*) \delta x^*] \delta t^* \\ &\quad - [(F_{i+1/2,j}^n u_{i+1/2,j}^* - F_{i-1/2,j}^n u_{i-1/2,j}^*) \delta y^* \\ &\quad + (F_{i,j+1/2}^n v_{i,j+1/2}^* - F_{i,j-1/2}^n v_{i,j-1/2}^*) \delta x^*] \delta t^* \end{aligned} \quad (17)$$

where fluxes across the surface between cells are calculated by a donor-acceptor scheme. Provided that a cell and its neighboring cells are filled with material labeled by $F^n = 1$, Eq. (17) becomes

$$\begin{aligned} (F_{i,j}^{n+1} - 1) \delta x^* \delta y^* &= [(u_{i+1/2,j}^* - u_{i-1/2,j}^*) \delta y^* \\ &\quad + (v_{i,j+1/2}^* - v_{i,j-1/2}^*) \delta x^*] \delta t^* - [(u_{i+1/2,j}^* - u_{i-1/2,j}^*) \delta y^* \\ &\quad + (v_{i,j+1/2}^* - v_{i,j-1/2}^*) \delta x^*] \delta t^* \end{aligned} \quad (18)$$

which automatically gives $F_{i,j}^{n+1} = 1$ even though the parenthesis on the right-hand side of Eq. (16) is not zero. However, a finite difference in Eq. (9) yields

$$\begin{aligned} (F_{i,j}^{n+1} - 1) \delta x^* \delta y^* &= -[(u_{i+1/2,j}^* - u_{i-1/2,j}^*) \delta y^* \\ &\quad + (v_{i,j+1/2}^* - v_{i,j-1/2}^*) \delta x^*] \delta t^*. \end{aligned} \quad (19)$$

An error of continuity Eq. (1) leads to $F_{i,j}^{n+1} \neq 1$. In the donor-acceptor scheme, material cannot move through more than one cell in one time step because finite difference equations only consider flux between adjacent cells. Therefore, the increment of time for mass and momentum transport is satisfied by the inequality

$$\Delta t^* < \min \left(\frac{\Delta x_i^*}{|u_{i,j}^*|}, \frac{\Delta y_j^*}{|v_{i,j}^*|} \right). \quad (20)$$

The increment of time for energy transport is chosen several times greater than that from Eq. (20).

Results and Discussion

In this study, the primary independent parameters controlling the joint between dissimilar metals are dimensionless surface tension coefficients, viscosities, melting temperatures, thermal conductivities of dissimilar metals and solid and liquid phases, beam power, welding speed (or Peclet number), and the energy distribution parameter. The values were estimated between aluminum or copper to iron, and nickel to titanium.

Since the transport process on the maximum cross section is investigated, the gradients of transport variables in the z -direction vanish. The validity can be approximately examined by changing temperature at a downstream location. Figure 2 shows that deviations of velocity fields and shapes of the molten region are small for dimensionless downstream temperatures of 0 and 0.2, which correspond to dimensional temperatures of 300 and 600 K, respectively, by choosing metal 1 as iron.

The variations in an isothermal line of dimensionless temperature $T^* = 1$ at different times during heating are shown in Fig. 3. On the top surface the area within the radius around the energy distribution parameter of 0.07 is irradiated by incident flux. This is revealed from a significant temperature gradient in the y -direction. The isothermal line expands with time until it reaches 2×10^{-3} , which corresponds to a dimensional time of around 0.017 s for iron with thermal diffusivity of $2.86 \times 10^{-6} \text{ m}^2/\text{s}$ and thickness of $5 \times 10^{-3} \text{ m}$. The solutions are referred to transport variables on the maximum molten region.

The velocity field induced by thermal buoyancy and gravitational force on the cross section of the fusion zone is shown in Fig. 4. Since temperatures in the pool are higher than those near the solid-liquid interface, buoyancy induces circulation in clockwise and counterclockwise directions on the sides of metals 1 and 2, respectively. The maximum dimensionless velocity is 24.96, which corresponds to 0.014 m/s for metal 1 as iron. Since surface flow is primarily toward metal 1, the interface between molten metals 1 and 2 near the top surface is deflected to the side of metal 1. Isothermal lines far from the center of the top surface are nearly circles. Owing to distinct thermal properties isothermal lines exhibit jumps at the joint plane.

The effects of surface tension coefficients of molten metals 1 and 2 on velocity field and fusion zone shape can be seen from Fig. 5. In welding the same metals with the negative surface tension coefficient the induced surface flow is outwards and symmetric to the joint plane as shown in Fig. 5 (a). The maximum dimensionless speed is 693, which corresponds to the dimensional speed of 0.4 m/s. In this case, the maximum speed produced by Marangoni force is 30 times larger than that induced by gravitational force and buoyancy, as shown previously. A symmetric velocity field for the same metals having a positive surface tension coefficient is seen in Fig. 5 (b). Surface flow, however, is radially inwards. Referring to Fig. 5 (a) and (b) it is evidently seen that the fusion zone is more shallow and wider for a negative surface tension coefficient. The

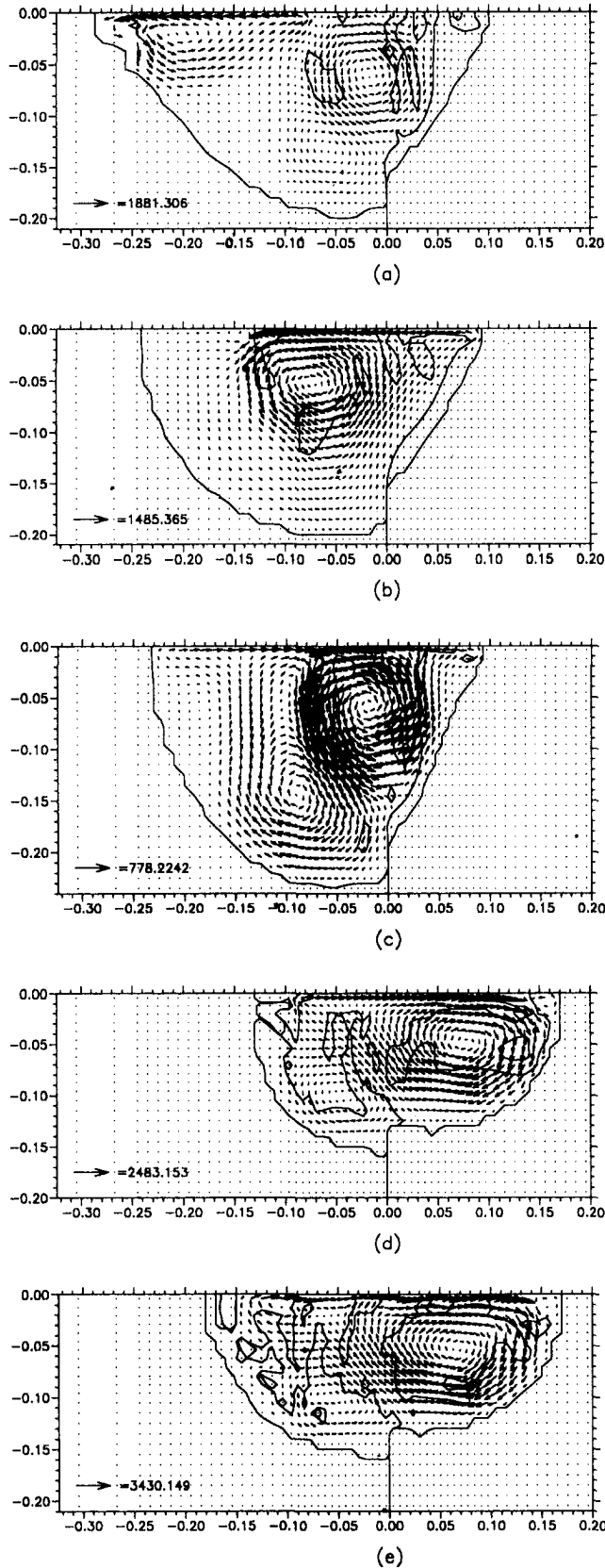


Fig. 7 Dimensionless velocity fields and shapes of molten metals 1 and 2 for a given dimensionless surface tension coefficient $c_{\sigma 1}^* = 4.148 \times 10^4$ and different dimensionless surface tension coefficients of metal 2; (a) $c_{\sigma 2}^* = -4.148 \times 10^4$, (b) $c_{\sigma 2}^* = 0$, (c) $c_{\sigma 2}^* = 4.148 \times 10^3$, (d) $c_{\sigma 2}^* = 2.074 \times 10^5$, (e) $c_{\sigma 2}^* = 4.148 \times 10^5$

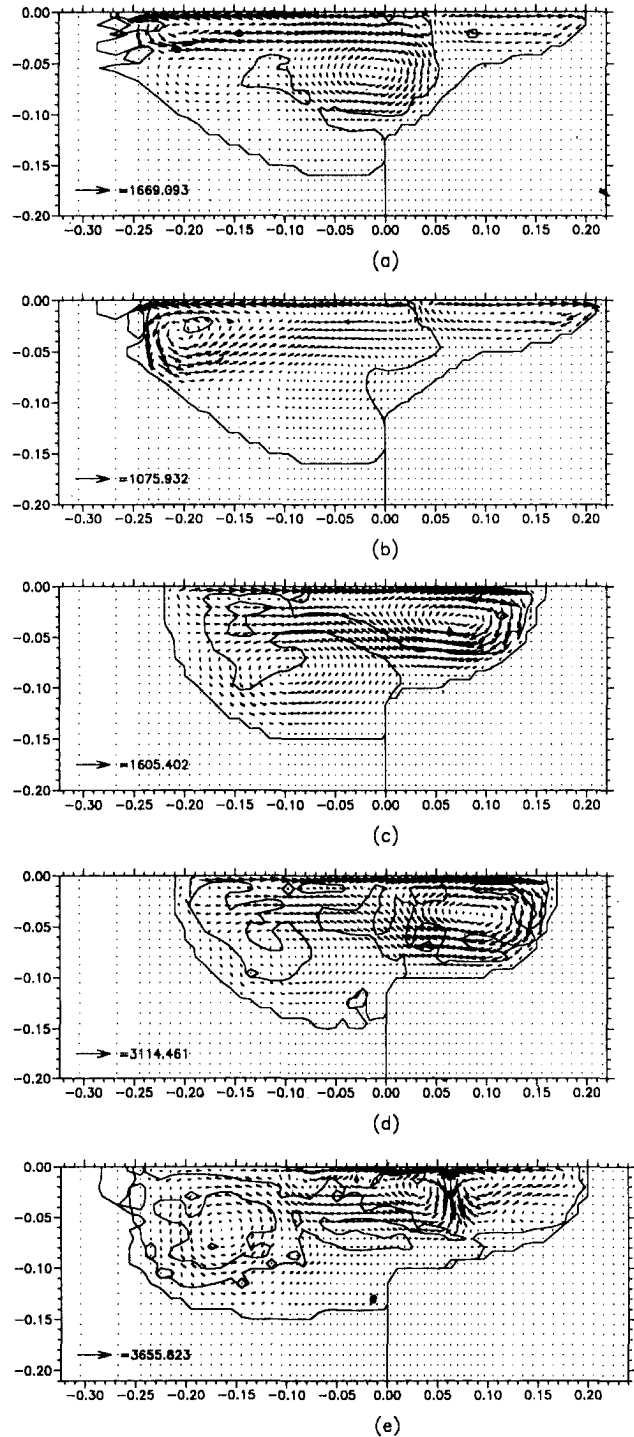
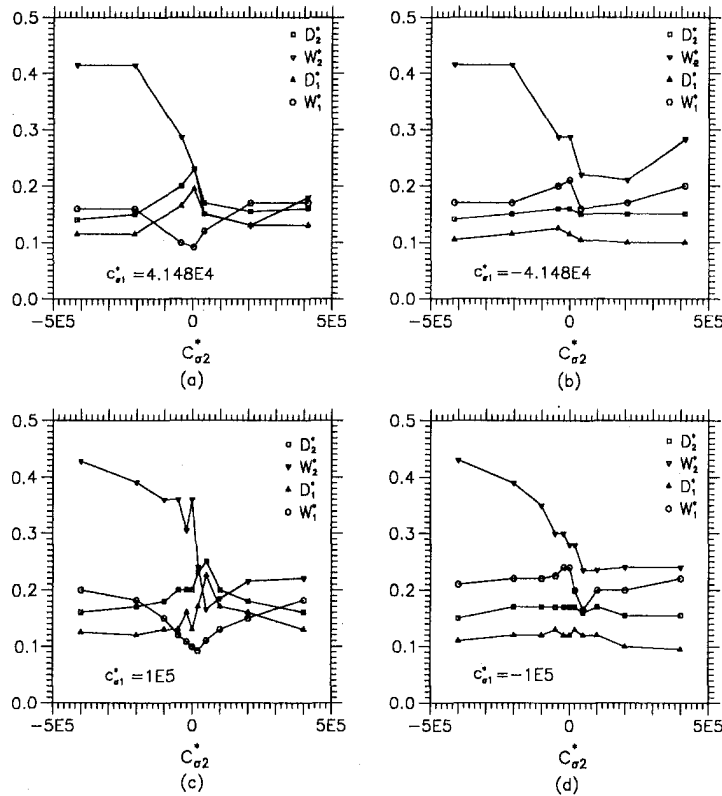


Fig. 8 Dimensionless velocity fields and shapes of molten metals 1 and 2 for a given dimensionless surface tension coefficient $c_{\sigma 1}^* = -4.148 \times 10^4$ and different dimensionless surface tension coefficients of metal 2; (a) $c_{\sigma 2}^* = -4.148 \times 10^4$, (b) $c_{\sigma 2}^* = 0$, (c) $c_{\sigma 2}^* = 4.148 \times 10^4$, (d) $c_{\sigma 2}^* = 2.074 \times 10^5$, (e) 4.148×10^5

result agrees with the theoretical prediction (Kou and Wang, 1986) and experimental observation (Heiple and Roper, 1982).

Figure 5 (c) shows that a change of the surface tension coefficient of molten metal 1 from -4.148×10^4 (see Fig. 5 (a)) to -2.074×10^5 results in a wider fusion zone in metal 1. In this case, surface tension gradients of molten metals 1 and 2 are in opposite directions. A stronger cell takes place near the edge of molten metal 1. The interface between molten metals 1 and 2 is close to the joint plane. This is because fluid flow is upward near



Q^*	5.441E+00	μ_2^*	1.667E-01
U^*	6.996E+01	h_{m2}^*	1.599E+00
σ_2^*	7.000E-02	T_{m2}^*	4.392E-01
ρ_2^*	3.750E-01	$c_{\sigma 1}^*$	
k_{1s}^*	2.026E+00	$c_{\sigma 2}^*$	
k_{2s}^*	6.968E+00	β_1^*	1.423E-01
k_{2a}^*	1.084E+01	β_2^*	1.423E-01
c_{1s}^*	1.000E+00	Pr	2.915E-01
c_{21}^*	1.416E+00	G	1.499E+05
c_{2s}^*	1.416E+00	St	4.338E+00

Fig. 9 Dimensionless depths and surface widths of molten metals 1 and 2 versus dimensionless surface tension coefficient of metal 2 for (a) $c_{\sigma 1}^* = 4.148 \times 10^4$, (b) $c_{\sigma 1}^* = -4.148 \times 10^4$, (c) $c_{\sigma 1}^* = 10^5$, (d) $c_{\sigma 1}^* = -10^5$

the interface and the velocity component normal to the interface is small. By changing the sign of molten metal 2 (see Fig. 5 (c)), Fig. 5 (d) showed that molten metal 2 is trapped and dispersed into molten metal 1. On the other hand, a drop of molten metal 1 is seen in molten pool 2. Dispersed droplets can be due to inherent errors from computation. In reality, dispersed grains, however, were also observed (Seretsky and Ryba, 1976). Molten metals 1 and 2, respectively, circulate in a clockwise and counterclockwise directions. A detailed description of the flow pattern and shapes of the molten region will be shown later. There are tiny dispersed phases which, unfortunately, cannot be drawn in the figure. It is seen that interfaces move dynamically. Figure 5 (e) shows that an increase in the surface tension coefficient of molten metal 2 from 4.148×10^4 to 10^5 (see Fig. 5 (b)) causes the cell in molten metal 2 to move toward the side of metal 1. In view of a greater product of surface tension coefficient-to-dynamic viscosity ratio with temperature gradient (namely the Marangoni number) of molten metal 2 (see Eq. (10)), the interface near the free surface is deflected to the side of metal 1. Interestingly, depths of the pool in metals 1 and 2 are nearly the same even though surface tension coefficients are of different magnitudes. This is attributed to identical thermal properties such as thermal conductivity and melting temperature, as can be seen later. Referring to Figs. 5 (b) and (e) shows that the maximum depth of the molten region is greatest as products of the surface tension coefficient-to-dynamic viscosity ratio with temper-

ature gradient are identical. This is because the maximum heat transfer rate is along the joint plane and toward the bottom.

A more clear insight into the transient behavior of Fig. 5 (d) can be seen from Fig. 6. At a lower welding speed Fig. 6 (a) shows that convection induced by negative and positive surface tension coefficients of molten metals 1 and 2, respectively, is towards the edge of molten metal 1 at a dimensionless time of 8.0×10^{-4} . Molten metals 2 in a thin layer therefore develop along the free surface. To satisfy mass conservation of molten metal 1 the interface near the joint plane is bulged. Flow in molten metal 1 directs toward metal 2 while surface flow in molten metal 2 is towards metal 1. Flow pattern at a later time of 1.1×10^{-3} is shown in Fig. 6 (b). After reaching the edge the thin layer is trapped into molten metal 1 while the bulge is separated into an isolated drop in molten metal 2. Surface flow on the side of metal 2 is changed to a counterclockwise direction induced by an existence of molten metal 1 on the free surface (see Fig. 5 (d)).

The effects of the surface tension coefficient of molten metal 2 on velocity field and fusion zone shape for a given positive dimensionless surface tension coefficient $c_{\sigma 1}^* = 4.148 \times 10^4$ are shown in Fig. 7. In view of a negative surface tension coefficient a cell in a counterclockwise direction occurs near the edge of molten metal 2, as presented in Fig. 7 (a). Molten metal 1 is separated into two parts, a thin layer adjacent to base metal 1 and drops in molten metal 2. In Fig. 7 (b) it can be seen that for the zero

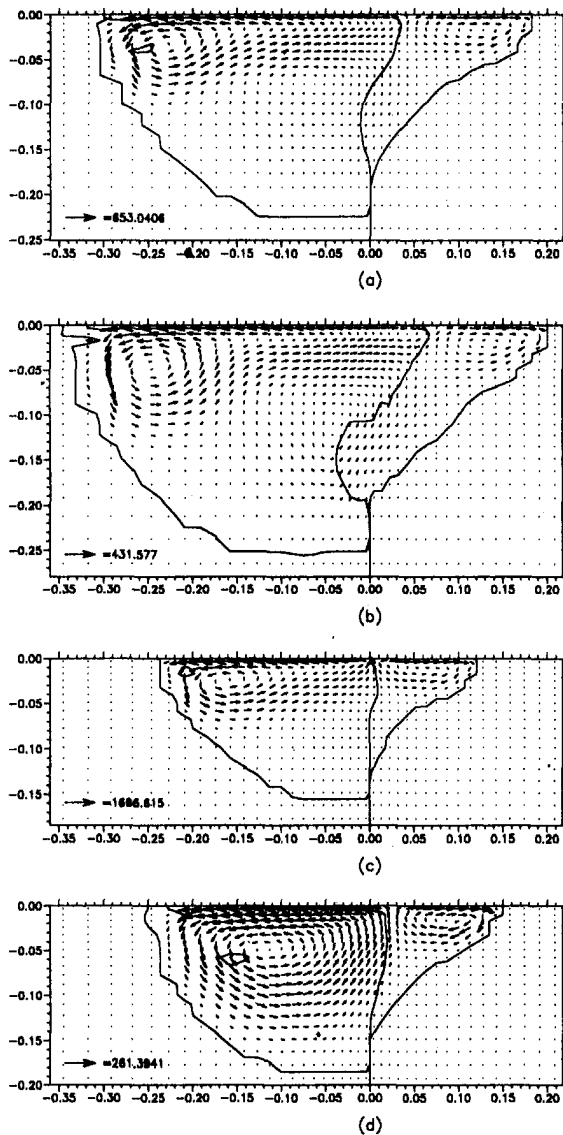


Fig. 10 The effects of dimensionless parameters on dimensionless velocity field and shape of molten metals 1 and 2 for (a) $Q^* = 9.068$, (b) $U^* = 34.98$, (c) $\sigma_1^* = 0.02$, (d) $\mu_2^* = 2.0$, (e) $k_{1s}^* = 4.0$, (f) $k_{2i}^* = 3.0$, (g) $k_{2s}^* = 6.968$, (h) $T_{m2}^* = 1.5$

surface tension coefficient of molten metal 2 the cell circulates in a counterclockwise direction in molten metal 2. This is attributed to the free surface covered by a minor concentration of metal 1 and high temperature displaced to the side of metal 2 (Wei and Chung, 1998). Strong convection is due to a low viscosity along the free surface. Even though concentration of metal 1 is low and surface tension coefficient of metal 2 is zero, surface flow in molten metal 2 is related to the ratio between the decreased surface tension coefficient and viscosity along the free surface. Flow pattern caused by a positive surface tension coefficient of molten metal 2 is shown in Fig. 7 (c). A cell in a clockwise direction grows near the edge of molten metal 2 and opposes the right big cell in the counterclockwise direction. Further increases in surface tension coefficient of molten metal 2 the left cell override the right cell, as can be seen in Figs. 7 (d) and (e).

Velocity field and fusion zone shape affected by surface tension coefficient of molten metal 2 for a given negative dimensionless surface tension coefficient $c_{\sigma 1}^* = -4.148 \times 10^4$ are shown in Fig. 8. Flow pattern and the interface for dissimilar molten metals having negative surface tension coefficients are comparatively regular as shown in Fig. 8 (a). Similarly, flow in molten metal 2 is

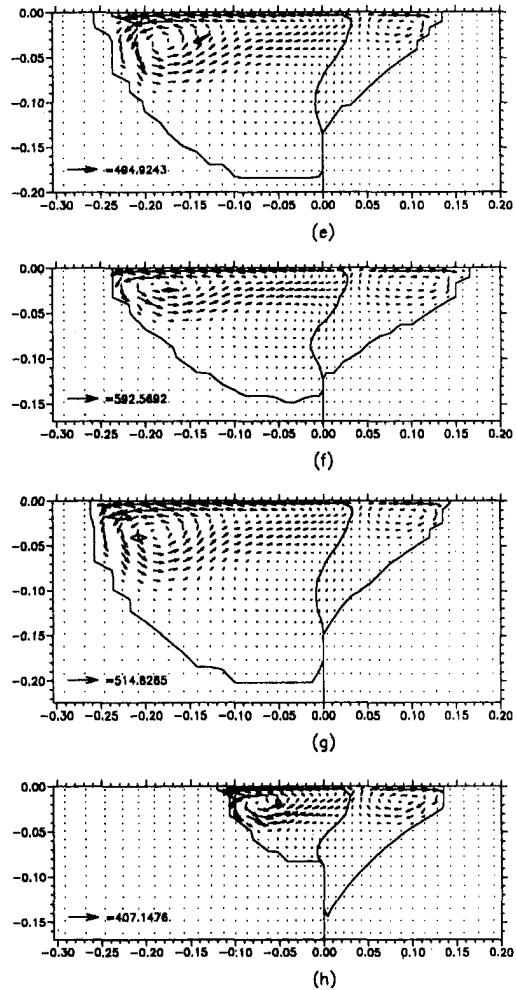
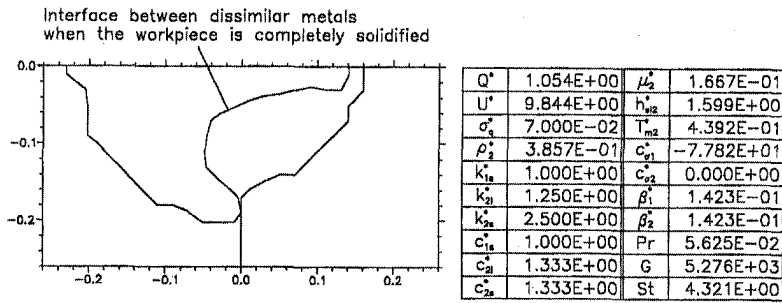


Fig. 10 (con't)

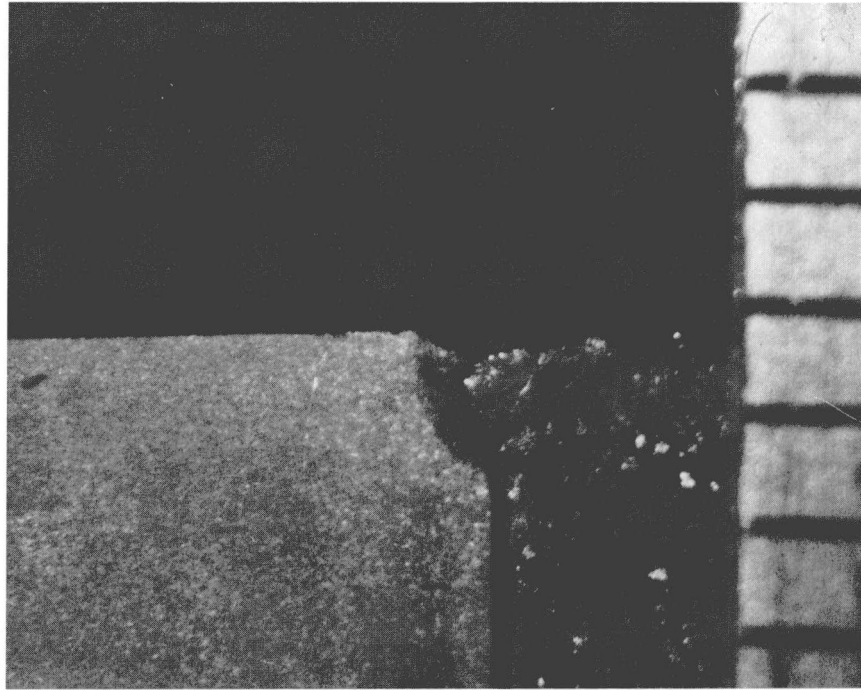
induced by the existence of molten metal 1 on the free surface for zero Marangoni force of molten metal 2 as presented in Fig. 8 (b). High speed in molten metal 2 is a result of a low viscosity. Irrespective of surface tension coefficient of molten metal 1 flow patterns in Figs. 8 (c) and (d) are similar to Figs. 7 (d) and (e) due to the large Marangoni force of molten metal 2.

The effects of surface tension coefficients of molten metals 1 and 2 on the shapes of fusion zone in metals 1 and 2 are shown in Fig. 9. For a given dimensionless surface tension coefficient $c_{\sigma 1}^* = 4.148 \times 10^4$, Fig. 9 (a) shows that surface widths of molten metals 1 and 2 decrease with increasing negative surface tension coefficient of metal 2. This is because the Marangoni convection to the side of metal 2 increase and decrease, respectively (see Fig. 7). A positive surface tension coefficient of metal 2 increases convection towards metal 1. Surface width in metal 2 therefore decreases and that in metal 1 increases (see Figs. 7 (c) and (d)). Interestingly, a further increase in a positive surface tension coefficient of molten metal 2 increases surface width in metal 2 due to strong circulation and mixing of the flow (see Fig. 7 (e)). For inward Marangoni convection with approximately identical products of surface tension coefficient-to-dynamic viscosity ratio with temperature gradient (see Fig. 7 (c)) depths of dissimilar molten regions are at maximum, which corresponds to the minimum surface width on the side of metal 1.

Figure 9 (b) shows the variations in the shape of fusion zone with surface tension coefficient of metal 2 for a given negative surface tension coefficient $c_{\sigma 1}^* = -4.148 \times 10^4$. Surface width on the side of metal 1 increases with negative surface tension coefficient of molten metal 2 until the sign of surface tension



(a)



(b)

Fig. 11 Comparison between (a) theoretical prediction, and (b) experimental photograph in welding aluminum to iron

coefficient of molten metal 2 changes. The drop of surface width on the side of metal 1 is attributed to the covering of molten metal 2 on the free surface on the side of metal 1 and the associated reduction of convection to the side of metal 1 (see Fig. 8 (c)). A further increase in positive surface tension coefficient of molten metal 2 increases surface width on the side of metal 1. Irrespective of the surface tension coefficient of molten metal 1, the variation in surface width on the side of metal 2 with the surface tension coefficient of metal 2 is similar (see Fig. 9 (a)). Depths of molten metals 1 and 2 remain relatively constant. Since the variations of surface widths are greater than those of depths surface convection to edges of dissimilar molten metals is strong. The effects of an increase in surface tension coefficients of metal 1 are shown in Fig. 9 (c) and (d). Similar trends are found.

Comparing to Fig. 2 (a) the effects of different working parameters such as dimensionless beam power, welding speed or Peclet number, energy distribution parameter, viscosity, thermal conductivities between dissimilar metals and distinct phases, and melting temperature on velocity field and fusion zone shape are shown in Figs. 10 (a)–(h), respectively. The size of the fusion zone increases with decreasing dimensionless welding speed, thermal conductivity of solid and melting temperature and increasing the dimensionless beam power, energy distribution parameter, and liquid thermal conductivity.

The computed result is compared to a photograph for welding aluminum to iron, as shown in Fig. 11. Experiments were conducted for a welding speed of 0.04 m/s, accelerating voltage of 50 kV, and welding current 12 mA. Metals on the right and left-hand sides are, respectively, iron and aluminum. Surface tension coefficients were chosen within relevant ranges by considering two metals containing minor surface active elements such as oxygen and sulfur. It can be seen that predictions of the fusion zone shape and the interface between iron and aluminum agree with the photograph. The deviations between the prediction and experimental observation can be due to the assumption of the two-dimensional model. The sharp interface indicates the immiscibility of dissimilar metals. Welding fails if convective mixing is insufficient.

The computed shape of the fusion zone in welding the same metals of iron was also compared with experimental results obtained by Paul and DebRoy (1988). The input data chosen were $A = 15$ percent, $\sigma_q = 0.127$ mm, $U = 5$ mm/s, $\rho = 7,800$ kg/m³, $\mu = 0.01$ kg/m-s, $k = 26.43$ W/m-K, $c = 837.5$ J/kg-K, $\beta = 10^{-4}$ K⁻¹, $T_m = 1,809$ K, $T_b = 3,135$ K. The predicted depth was 0.048 mm and the full width of the fusion zone 0.23 mm, which agreed with the measured depth and width of 0.043 and 0.24 mm, respectively.

Conclusions

The conclusions drawn are as follows:

1 Transport processes and shapes of molten regions subject to Marangoni forces in different directions and magnitudes in welding dissimilar metals are investigated. The computed results agree with experimental observations of fusion zone shapes in welding the same and dissimilar metals.

2 Unlike joining the same metals, the flow pattern and shape of the fusion zone in the molten pool of dissimilar metals, as denoted by metals 1 and 2 on the right and left-hand side of the joint plane, respectively, is determined by competing the products of surface tension coefficient-to-dynamic viscosity ratio with the temperature gradient (i.e., Marangoni number) at the interface between dissimilar molten metals. Hence, the locations of the interface between dissimilar molten metals and the peak temperature, and distributions of solute on the free surface play important roles. The Marangoni convection on the free surface can be in three directions, which are inwards from the sides to the joint plane, outwards from the joint plane to the sides, and horizontal from one side to the other.

3 The interface between dissimilar molten metals near the free surface is initially deflected to the side (say, metal 1) where the product of the surface tension coefficient-to-dynamic viscosity ratio with the temperature gradient at the joint plane is smaller (accounting for the sign). The interface is then bulged near the lower region to satisfy the mass conservation of molten metal 1. The bulged region can be necked, separated, and immersed into molten metal 2.

4 Surface tension coefficients of opposite signs lead to complicated flow patterns. Considering molten metals 1 and 2 having negative and positive surface tension coefficients, respectively, the solute of molten metal 1 on the free surface on the side of metal 2 opposes the flow of molten metal 2 and enhances convective mixing. Dispersed droplets readily take place.

5 Depths of dissimilar molten regions (D_1 and D_2) are insensitive to the variation in the surface tension coefficient of molten metal 2 for a negative surface tension coefficient of molten metal 1, and vice versa. This is because energy transport is primarily in horizontal directions. If the surface tension coefficients are both positive and the corresponding Marangoni numbers are of the same magnitude, the enhanced heat transfer in the downward direction resulting from the cells near the joint plane gives rise to the maximum depth.

6 For a positive surface tension coefficient of molten metal 1, the surface width on the side of metal 1 (W_1) decreases and increases with increasing the negative and positive surface tension coefficient of molten metal 2, respectively. This is because convection to the sides of metal 2 and metal 1 increases, respectively. Surface width on the side of metal 1 becomes minimal as the depth of fusion zone is maximal. When the surface tension coefficient of molten metal 1 is negative, the surface width on the side of metal 1 increases with the negative surface tension coefficient of molten metal 2 until the sign of surface tension coefficient of molten metal 2 changes. The drop of surface width on the side of metal 1 is attributed to a reduction of convection to the side of metal 1 as a result of molten metal 2 covering on the free surface on the side of metal 1. A further increase in the positive surface tension coefficient of molten metal 2 increases the surface width on the side of metal 1.

7 The variation in surface width on the side of metal 2 (W_2) with the surface tension coefficient of molten metal 2 is similar, irrespective of the surface tension coefficient of molten metal 1. Surface width on the side of metal 2 decreases with increasing the surface tension coefficient of molten metal 2 until the latter is slightly greater than zero. A further increase in the surface tension

coefficient of molten metal 2 increases the surface width on the side of metal 2. This is attributed to strong convective mixing in the molten pool.

8 Depths of molten metals 1 and 2 with identical thermal properties such as thermal conductivity and melting temperature are nearly the same, even though the surface tension coefficients are different.

9 This study also provides a fundamental understanding of the transport process induced by the Marangoni forces in different directions and magnitudes in melting dissimilar metals.

Acknowledgment

Electron beam welding was conducted by Mr. J. S. Koo at the Institute of Materials Science and Engineering, National Sun Yat-Sen University. The photograph was provided by Mr. Y. K. Kuo. The authors acknowledge the financial support from the National Science Council, Taiwan, Republic of China, under grant number NSC 87-2212-E-110-027.

References

- Ashgriz, N., and Poo, J. Y., 1991, "FLAIR: Flux Line-Segment Model for Advection and Interface Reconstruction," *J. Computational Physics*, Vol. 93, pp. 449–468.
- Belton, G. R., 1976, "Langmuir Adsorption, the Gibbs Adsorption Isotherm, and Interfacial Kinetics in Liquid Metal Systems," *Metallurgical Transactions B*, Vol. 7B, pp. 35–42.
- Brent, A. D., Voller, V. R., and Reid, K. J., 1988, "Enthalpy-Porosity Technique for Modeling Convection-Diffusion Phase Change: Application to the Melting of a Pure Metal," *Numerical Heat Transfer*, Vol. 13, pp. 297–318.
- Cary, H. B., 1989, *Modern Welding Technology*, 2nd Ed., Prentice-Hall, Englewood Cliffs, NJ, pp. 555–559.
- DebRoy, T., Basu, S., and Mundra, K., 1991, "Probing Laser Induced Metal Vaporization by Gas Dynamics and Liquid Pool Transport Phenomena," *J. Applied Physics*, Vol. 70, pp. 1313–1319.
- Elmer, J. W., Giedt, W. H., and Eagar, T. W., 1990, "The Transition from Shallow to Deep Penetration during Electron Beam Welding," *Welding J.*, Vol. 69, pp. 167s–176s.
- Giedt, W. H., Wei, X.-C., and Wei, S.-R., 1984, "Effect of Surface Convection on Stationary GTA Weld Zone Temperatures," *Welding J.*, Vol. 63, pp. 376s–383s.
- Heiple, C. R., and Roper, J. R., 1982, "Mechanism for Minor Element Effect on GTA Fusion Zone Geometry," *Welding J.*, Vol. 61, pp. 97s–102s.
- Hirt, C. W., and Nichols, B. D., 1981, "Volume of Fluid (VOF) Method for the Dynamics of Free Boundaries," *J. Computational Physics*, Vol. 39, pp. 201–225.
- Kohe, D. B., and Mjolsness, R. C., 1992, "Ripple: A New Model for Incompressible Flows with Free Surfaces," *AIAA J.*, Vol. 30, pp. 2694–2700.
- Kou, S., and Wang, Y. H., 1986, "Weld Pool Convection and Its Effect," *Welding J.*, Vol. 65, pp. 63s–70s.
- Mills, K. C., and Keene, B. J., 1990, "Factors Affecting Variable Weld Penetration," *International Materials Reviews*, Vol. 35, pp. 185–216.
- Nippes, E. F., Pfluger, A. R., and Slaughter, G. M., 1950, "Seam Welding Monel Metal to Steel," *Welding J.*, Vol. 29, pp. 134s–139s.
- Patankar, S. V., 1980, *Numerical Heat Transfer and Fluid Flow*, Hemisphere, New York, pp. 44–46, Chapter 6.
- Paul, A., and DebRoy, T., 1988, "Free Surface Flow and Heat Transfer in Conduction Mode Laser Welding," *Metallurgical Transactions B*, Vol. 19B, pp. 851–858.
- Sahoo, P., DebRoy, T., and McNallan, M. J., 1988, "Surface Tension of Binary Metal-Surface Active Solute Systems under Conditions Relevant to Welding Metallurgy," *Metallurgical Transactions B*, Vol. 19B, pp. 483–491.
- Sen, A. K., and Davis, S. H., 1982, "Steady Thermocapillary Flows in Two-dimensional Slots," *J. Fluid Mechanics*, Vol. 121, pp. 163–186.
- Seretsky, J., and Ryba, E. R., 1976, "Laser Welding of Dissimilar Metals: Titanium to Nickel," *Welding J.*, Vol. 55, pp. 208s–211s.
- Sun, Z., and Moiso, T., 1994, "Effect of Processing Parameters on Laser Welded Dissimilar Steel Joints," *Welding J.*, Vol. 73, pp. 63–70.
- Tinkler, M. J., Grant, I., Mizuno, G., and Gluck, C., 1983, "The Effects of Residual Impurity and Microalloying Elements on Weldability and Weld Properties," paper 29, Abington, The Welding Institute.
- Unger, A. M., 1941, "Electro-Magnetic Stirring Action in a Spotweld," *Welding J.*, Vol. 20, pp. 42–47.
- Wei, P. S., and Chung, F. K., 1999, "Unsteady Marangoni Flow in Molten Pool When Welding Dissimilar Metals," *Metallurgical and Materials Transactions*, submitted for publication.
- Wei, P. S., and Kuo, Y. K., 1998, "Fusion Zone Shapes in Electron-Beam Welding Dissimilar Metals," *ASME JOURNAL OF HEAT TRANSFER*, submitted for publication.
- Zacharia, T., David, S. A., Vitek, J. M., and DebRoy, T., 1989, "Weld Pool Development during GTA and Laser Beam Welding of Type 304 Stainless Steel, Part I—Theoretical Analysis," *Welding J.*, Vol. 68, pp. 499s–509s.

This section contains shorter technical papers. These shorter papers will be subjected to the same review process as that for full papers.

A Boundary Element Method for the Solution of a Class of Steady-State Problems for Anisotropic Media

D. L. Clements¹ and W. S. Budhi²

1 Introduction

The boundary element method is now well established as an effective technique for the numerical evaluation of the steady-state temperature field for media in which the thermal conductivity is constant (see, for example, Brebbia and Dominguez, 1989).

In the case when the thermal conductivity depends on the spatial variables the implementation of the boundary element method for steady-state problems presents some difficulty. However some progress has been made in this area in recent years. Papers by Clements (1980), Cheng (1984), Rangogni (1987), Shaw (1994), Gipson, Ortiz, and Shaw (1995), and Ang, Kusuma, and Clements (1997) provide techniques which enable the boundary element method to be employed for determining the steady-state temperature field for particular classes of isotropic inhomogeneous media. Also Clements and Rogers (1984) obtained a boundary integral equation which is relevant for a certain class of steady-state two-dimensional problems for inhomogeneous anisotropic media.

The present paper seeks to consider the more general case of an anisotropic material for which the thermal conductivity depends on the temperature and the spatial variables. A suitable transformation is obtained to transform the relevant nonlinear variable coefficients equation to linear equations with constant coefficients. The relevant boundary value problems governed by these linear constant coefficients equations may be readily solved using the boundary element method. Some particular examples are considered to illustrate the application of the method.

2 The Boundary Value Problem

Referred to a Cartesian frame $Ox_1x_2x_3$ the equation governing the steady-state temperature field $\phi(x_1, x_2, x_3)$ in an anisotropic

material occupying a region Ω with boundary $\partial\Omega$ in R^3 may be written in the form

$$\frac{\partial}{\partial x_i} \left[\lambda_{ij}(x_1, x_2, x_3, \phi) \frac{\partial \phi}{\partial x_j} \right] = 0, \quad (1)$$

where the λ_{ij} denotes the thermal conductivity and the repeated suffix summation convention (summing from 1 to 3) is employed.

A solution to Equ. (1) is sought which is valid in the region Ω in R^3 with boundary $\partial\Omega$ which consists of a finite number of piecewise smooth closed surfaces. On $\partial\Omega$ either the temperature ϕ or the heat flux is specified through $P = \lambda_{ij}(\partial\phi/\partial x_j)n_i$ where n denotes the outward pointing normal to Ω .

3 Reduction to a Linear Constant Coefficients Equation

The coefficients λ_{ij} in Eq. (1) are now required to take the form

$$\lambda_{ij}(\mathbf{x}, \phi) = \lambda'_{ij}g(\mathbf{x})G(\phi), \quad (2)$$

where $\mathbf{x} = (x_1, x_2, x_3)$, the λ'_{ij} for $i, j = 1, 2, 3$ are constants, $g(\mathbf{x})$ is a twice differentiable function of the independent variables x_1, x_2, x_3 and $G(\phi)$ a differentiable function of ϕ . Equation (1) thus may be written in the form

$$\lambda'_{ij} \frac{\partial}{\partial x_i} \left[g(\mathbf{x})G(\phi) \frac{\partial \phi}{\partial x_j} \right] = 0. \quad (3)$$

Guided partially by work contained in Bear (1972) and Cheng (1984) and also by the Kirchoff transformation, consider a transformation of the form

$$\psi(\mathbf{x}) = g^{1/2}(\mathbf{x}) \int G(\phi) d\phi. \quad (4)$$

Use of (4) in (3) yields the equation

$$\lambda'_{ij} \frac{\partial^2 \psi}{\partial x_i \partial x_j} - g^{-1/2} \lambda'_{ij} \frac{\partial^2 g^{1/2}}{\partial x_i \partial x_j} \psi = 0. \quad (5)$$

Thus if $g(\mathbf{x})$ is such that

$$\lambda'_{ij} \frac{\partial^2 g^{1/2}}{\partial x_i \partial x_j} = 0, \quad (6)$$

then the transformation (4) transforms the variable coefficients Eq. (3) to the constant coefficients equation

$$\lambda'_{ij} \frac{\partial^2 \psi}{\partial x_i \partial x_j} = 0. \quad (7)$$

Also, if $g(\mathbf{x})$ is such that

¹Department of Applied Mathematics, University of Adelaide, S.A. 5005, Australia. e-mail: dclement@maths.adelaide.edu.au.

²Department of Mathematics, Institut Teknologi Bandung, Indonesia.

Contributed by the Heat Transfer Division for publication in the JOURNAL OF HEAT TRANSFER. Manuscript received by the Heat Transfer Division, Sept. 5, 1997; revision received, Jan. 14, 1999. Keywords: Boundary Element, Composites, Computational, Heat Transfer, Numerical Methods. Associate Technical Editor: A. Lavine.

$$\lambda'_{ij} \frac{\partial^2 g^{1/2}}{\partial x_i \partial x_j} + k g^{1/2} = 0, \quad (8)$$

where k is a constant, then the transformation (4) transforms the variable coefficients Eq. (3) to the constant coefficients equation

$$\lambda'_{ij} \frac{\partial^2 \psi}{\partial x_i \partial x_j} + k \psi = 0. \quad (9)$$

The analysis of this section thus shows that if the function $g(\mathbf{x})$ is chosen such that $g^{1/2}$ satisfies Eq. (6) or Eq. (8) then for an arbitrary differentiable function $G(\phi)$ the transformation (4) transforms Eq. (3) to the linear partial differential equations with constant coefficients (7) or (9).

Once ψ has been determined by solving Eq. (7) or Eq. (9) the flux can be determined from the equation

$$\begin{aligned} P &= \lambda_{ij} \frac{\partial \phi}{\partial x_j} n_i \\ &= -P_g \psi + P_\psi g^{1/2}, \end{aligned} \quad (10)$$

where

$$P_g = \lambda'_{ij} \frac{\partial g^{1/2}}{\partial x_j} n_i \text{ and } P_\psi = \lambda'_{ij} \frac{\partial \psi}{\partial x_j} n_i. \quad (11)$$

4 Particular Classes of Forms for the Thermal Conductivity

The requirement that $g^{1/2}$ satisfies either Eq. (6) or Eq. (8) permits considerable flexibility in the choice of $g(\mathbf{x})$. In particular, g can assume a number of multiparameter forms in which the parameters may be used to fit a particular form to given numerical values for the thermal conductivity.

For example, if g is required to satisfy Eq. (6), a possible multiparameter form for g is given by

$$g(x_1, x_2, x_3) = [(\alpha_0 + \alpha_1 x_1 + \alpha_2 x_2 + \alpha_3 x_3)]^2, \quad (12)$$

where the α_i are constants.

For the case when g is required to satisfy Eq. (8) a number of multiparameter forms for the thermal conductivity exhibiting oscillatory behavior may be employed. A possible multiparameter form is given by

$$g(\mathbf{x}) = [A \cos(\alpha_m x_m)]^2 \text{ with } \lambda_{ij} \alpha_i \alpha_j = k \quad (13)$$

where A and the α_m are constants.

For the nonlinear case the thermal conductivity depends on the temperature $\phi(\mathbf{x})$. In many practical situations this dependence may be taken to be linear (see Sawaf, Özisik, and Jarny, 1995) so that coefficients λ_{ij} take the general form

$$\lambda_{ij} = \lambda'_{ij}(1 + \beta \phi), \quad (14)$$

where β and the λ'_{ij} are constants. Equation (4) now yields

$$\psi(x_1, x_2, x_3) = \phi + \frac{1}{2} \beta \phi^2. \quad (15)$$

This change of dependent variable transforms Eq. (3) to the linear constant coefficients form given by Eq. (7) and the heat flux may be obtained from Eq. (10) which in this case (with $g = 1$ and $P_g = 0$) has the simple form $P = P_\psi$. Since ϕ or P are given at each point on $\partial\Omega$, Eqs. (15) and (10) may be readily used to provide ψ or P_ψ at each point of $\partial\Omega$. Thus for the important case when the λ_{ij} are given by Eq. (14), the nonlinear boundary value problem given in Section 2 is readily transformed to a boundary value problem governed by the linear partial differential equations with constant coefficients Eq. (7).

5 The Boundary Integral Equation

For the two-dimensional case the boundary integral equation for the solution of Eq. (7), valid in Ω with either ψ or $P_\psi = \lambda'_{ij}(\partial\psi/\partial x_j)n_i$, specified on $\partial\Omega$, is given by (see Clements, 1981)

$$\begin{aligned} \eta \psi(a, b) &= -\frac{1}{\lambda'_{11}} \int_{\partial\Omega} [P_\psi(x_1, x_2) \Phi(x_1, x_2; a, b) \\ &\quad - \Gamma(x_1, x_2; a, b) \psi(x_1, x_2)] ds, \end{aligned} \quad (16)$$

where $\eta = 1$ if $(a, b) \in \Omega$ and $\eta = \frac{1}{2}$ if $(a, b) \in \partial\Omega$ and $\partial\Omega$ has a continuously turning tangent at (a, b) . Also

$$\begin{aligned} \Phi(x_1, x_2; a, b) &= \frac{-1}{2\pi i(\tau - \bar{\tau})} \left(\frac{\lambda'_{11}}{\lambda'_{22}} \right) \\ &\quad \times \{ \log(z - z_0) + \log(\bar{z} - \bar{z}_0) \}, \end{aligned} \quad (17)$$

$$\begin{aligned} \Gamma(x_1, x_2; a, b) &= \lambda'_{ij} \frac{\partial \Phi}{\partial x_j} n_i \\ &= \frac{\mathcal{M}}{z - z_0} + \frac{\bar{\mathcal{M}}}{\bar{z} - \bar{z}_0} \end{aligned} \quad (18)$$

with

$$\mathcal{M} = \frac{-1}{2\pi i(\tau - \bar{\tau})} \left(\frac{\lambda'_{11}}{\lambda'_{22}} \right) \{ \lambda'_{11} n_1 + \lambda'_{12} n_2 + (\lambda'_{12} n_1 + \lambda'_{22} n_2) \tau \},$$

where $z = x_1 + \tau x_2$, $z_0 = a + \tau b$ and τ is the root with positive real part of the quadratic

$$\lambda'_{11} + 2\lambda'_{12}\tau + \lambda'_{22}\tau^2 = 0 \quad (19)$$

and the bar denotes the complex conjugate. Now from Eq. (10)

$$P_\psi = g^{-1/2} P + g^{-1/2} P_g \psi. \quad (20)$$

Use of Eq. (20) in Eq. (16) provides

$$\eta \psi(a, b) = -\frac{1}{\lambda'_{11}} \int_{\partial\Omega} [P(g^{-1/2} \Phi) + (g^{-1/2} P_g \Phi - \Gamma) \psi] ds. \quad (21)$$

In the boundary value problem specified in Section 2 either ϕ or $P = \lambda_{ij}(\partial\phi/\partial x_j)n_i$ is given at each point of the boundary $\partial\Omega$. For each point where ϕ is given the corresponding value of ψ may be readily obtained from Eq. (4) for given g and G . Thus Eq. (21) is a boundary integral equation which may be used to first determine numerical values of ψ and P at all points of the boundary $\partial\Omega$. It then yields ψ (and by differentiation P_ψ) at any interior point of Ω . Equation (4) and (20) may then be used to determine ϕ and P at any point of Ω .

To obtain the corresponding boundary integral equation for the three-dimensional case an analogous approach is employed with the appropriate fundamental solution available in Brebbia and Dominguez (1989).

Similarly, for the case when the governing equation is given by Eq. (9), an analogous approach is employed with the fundamental solution available in Clements and Larsson (1993) for the two-dimensional case and Brebbia and Dominguez (1989) for the three-dimensional case.

6 Numerical Results

The analysis of the previous sections was obtained on the basis that the coefficients $\lambda_{ij}(\mathbf{x})$ satisfied certain differentiability conditions in Ω . However, in practice the analysis may readily be used for both the case when the coefficients satisfy these conditions and also as an approximation for the case of a wide class of materials consisting of discrete layers of homogeneous anisotropic media.

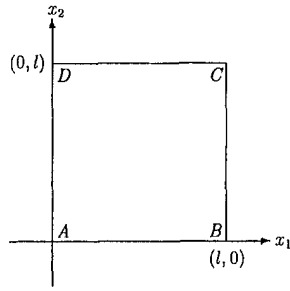


Fig. 1 The geometry for the numerical examples

For such layered materials the integral equation of the previous section will provide an approximate solution. In the case when the material parameters do not vary too greatly from layer to layer, this approximate solution may be used to obtain accurate numerical values for the temperature and flux fields.

In this section the equations of the previous sections are used to calculate the temperature field for some particular boundary value problems. The first two problems to be considered involve determining the two-dimensional temperature field in a layered anisotropic material in the form of a square slab which occupies the region defined by $0 \leq x_1/l \leq 1$ and $0 \leq x_2/l \leq 1$ where l denotes a reference length (Fig. 1). The slab consists of ten homogeneous anisotropic layers which lie in the intervals

$$0.1n \leq x_1/l \leq 0.1(n+1) \text{ for } n = 0, 1, 2, \dots, 9. \quad (22)$$

The constant thermal conductivities in each of these layers are given by

$$\frac{\lambda_{11}}{\lambda_0} = (1 + 0.02n)^2 \text{ for } n = 0, 1, 2, \dots, 9, \quad (23)$$

$$\lambda_{22} = 2\lambda_{11} \text{ and } \lambda_{12} = 0, \quad (24)$$

where λ_0 is a reference thermal conductivity.

The boundary conditions are as follows:

Problem 1.

$$\phi/\phi_0 = 1, \text{ on } DA,$$

$$\phi/\phi_0 = 2, \text{ on } BC,$$

$$P = \lambda_{22} \frac{\partial \phi}{\partial x_2} = 0, \text{ on } CD,$$

$$P = -\lambda_{22} \frac{\partial \phi}{\partial x_2} = 0, \text{ on } AB.$$

Problem 2.

$$\phi/\phi_0 = 2 - x_2/l, \text{ on } DA,$$

$$\phi/\phi_0 = 2, \text{ on } BC,$$

$$P = \lambda_{22} \frac{\partial \phi}{\partial x_2} = 0, \text{ on } CD,$$

$$P = -\lambda_{22} \frac{\partial \phi}{\partial x_2} = 0, \text{ on } AB.$$

Problem 1 may be solved analytically by assuming the temperature ϕ in each homogeneous layer has the form

$$\phi = a_n x_1/l + b_n \text{ for } 0.1n \leq x_1/l \leq 0.1(n+1) \text{ and } n = 0, 1, 2, \dots, 9 \quad (25)$$

Table 1

(x_1, x_2)	$\phi(x_1, x_2)$ (BEM)	$\phi(x_1, x_2)$ (BEM)	$\phi(x_1, x_2)$ (BEM)	$\phi(x_1, x_2)$
	8 segments	20 segments	40 segments	Analytical
(0.1,0.5)	1.1346	1.1170	1.1174	1.1176
(0.3,0.5)	1.3372	1.3391	1.3394	1.3396
(0.5,0.5)	1.5454	1.5455	1.5455	1.5455
(0.7,0.5)	1.7391	1.7374	1.7370	1.7368
(0.9,0.5)	1.9686	1.9156	1.9154	1.9153

where the a_n and b_n for $n = 0, 1, 2, \dots, 9$ are constants. Imposing continuity conditions on the temperature and the flux at each of the interfaces $x_1 = 0.1, 0.2, \dots, 0.9$ together with boundary conditions at the boundaries $AB, BC, CD,$ and DA leads to 20 linear algebraic equations which may be readily solved for the 20 unknowns $a_0, b_0, a_1, b_1, \dots, a_9, b_9$. The Eq. (25) then provide the temperature at all points of the layered slab.

To use the boundary integral method of this paper to solve this boundary value problem, the discrete layered material is approximated by a material with the continuous thermal conductivities

$$\frac{\lambda_{11}}{\lambda_0} = (1 + 0.2x_1/l)^2 \text{ for } 0 \leq x_1/l \leq 1, \quad (26)$$

$$\lambda_{22} = 2\lambda_{11} \text{ and } \lambda_{12} = 0. \quad (27)$$

Some numerical results for Problem 1 are shown in Tables 1 and 2 and results for Problem 2 are shown in Tables 3 and 4. In these tables $P_1 = \lambda_{11} \partial \phi / \partial x_1$ and $P_2 = \lambda_{22} \partial \phi / \partial x_2$. To obtain the numerical values the standard boundary element method was employed using Eqs. (21) (see Clements, 1981). Specifically in (21) the integral was replaced by a sum of integrals over N boundary segments of equal length h . The dependent variable was assumed to be constant over each segment and the integrals were evaluated by employing the trapezoidal rule to yield a system of linear

Table 2

(x_1, x_2)	$P_1(x_1, x_2)$ (BEM)	$P_1(x_1, x_2)$ (BEM)	$P_1(x_1, x_2)$ (BEM)	$P_1(x_1, x_2)$
	8 segments	20 segments	40 segments	Analytical
(0.1,0.5)	0.3313	1.2058	1.1994	1.2
(0.3,0.5)	1.2089	1.2019	1.2008	1.2
(0.5,0.5)	1.2178	1.2039	1.2015	1.2
(0.7,0.5)	1.2111	1.2019	1.2009	1.2
(0.9,0.5)	3.8390	1.1762	1.1994	1.2

Table 3

(x_1, x_2)	$\phi(x_1, x_2)$ (BEM)	$\phi(x_1, x_2)$ (BEM)	$\phi(x_1, x_2)$ (BEM)
	20 segments	40 segments	80 segments
(0.1,0.5)	1.5577	1.5584	1.5586
(0.3,0.5)	1.6685	1.6692	1.6695
(0.5,0.5)	1.7722	1.7725	1.7725
(0.7,0.5)	1.8688	1.8684	1.8683
(0.9,0.5)	1.958	1.9577	1.9576

Table 4

(x_1, x_2)	$P_1(x_1, x_2)$	$P_2(x_1, x_2)$	$P_1(x_1, x_2)$	$P_2(x_1, x_2)$	$P_1(x_1, x_2)$	$P_2(x_1, x_2)$
	BEM 20 segments	BEM 20 segments	BEM 40 segments	BEM 40 segments	BEM 80 segments	BEM 80 segments
(0.1,0.5)	0.9705	-1.4672	0.9763	-1.4858	0.9786	-1.4833
(0.3,0.5)	0.9989	-0.7044	0.9962	-0.7019	0.9954	-0.6981
(0.5,0.5)	1.10186	-0.3068	1.0131	-0.3038	1.0110	-0.3012
(0.7,0.5)	1.0299	-0.1245	1.0271	-0.1227	1.0260	-0.1214
(0.9,0.5)	1.0353	-0.0337	1.0394	-0.0334	1.0402	-0.0327

Table 5

(x_1, x_2)	$\phi(x_1, x_2)$ (BEM)	$\phi(x_1, x_2)$ (BEM)	$\phi(x_1, x_2)$ (BEM)	$\phi(x_1, x_2)$
	8 segments	20 segments	40 segments	Analytical
(0.1,0.5)	1.1283	1.1140	1.1143	1.1145
(0.3,0.5)	1.3297	1.3312	1.3315	1.3317
(0.5,0.5)	1.5355	1.5355	1.5355	1.5355
(0.7,0.5)	1.7300	1.7286	1.7284	1.7283
(0.9,0.5)	1.9516	1.9117	1.9117	1.9115

Table 6

(x_1, x_2)	$P_1(x_1, x_2)$ (BEM)	$P_1(x_1, x_2)$ (BEM)	$P_1(x_1, x_2)$ (BEM)	$P_1(x_1, x_2)$
	8 segments	20 segments	40 segments	Analytical
(0.1,0.5)	0.6896	1.7569	1.7493	1.75
(0.3,0.5)	1.7599	1.7521	1.7509	1.75
(0.5,0.5)	1.7703	1.7544	1.7517	1.75
(0.7,0.5)	1.7628	1.7523	1.7510	1.75
(0.9,0.5)	4.5588	1.7248	1.7494	1.75

algebraic equations for the unknown values of ψ or P on each of the boundary segments. The error involved in these approximations is of order h^2 for each segment. Further, the segment length is given by $h = 4l/N$ where N is the number of segments around the boundary. Each of the calculated values in the Tables 1–4 involves a sum of N integrals and hence the error in each of these values is order $16l^2/N$. Thus doubling the number of segments could be expected to halve the error. In broad terms this expectation is reflected in the results in Tables 1 and 2 and in the convergence properties of the solution in Tables 3 and 4. Some discrepancy in this expectation is observed for the points near the boundary (at (0.1, 0.5) and (0.9, 0.5)), particularly in Tables 1 and 2 for the case of eight segments (two segments per side). With such a large segment size these poor results near to the boundary are not unexpected, but it is worth noting that even with eight segments, reasonably accurate results are obtained for points away from the boundary.

Now consider the same two boundary value problems with the

Table 7

(x_1, x_2)	$\phi(x_1, x_2)$ (BEM)	$\phi(x_1, x_2)$ (BEM)	$\phi(x_1, x_2)$ (BEM)
	20 segments	40 segments	80 segments
(0.1,0.5)	1.3513	1.3519	1.3521
(0.3,0.5)	1.5022	1.5029	1.5031
(0.5,0.5)	1.6513	1.6514	1.6515
(0.7,0.5)	1.7952	1.7948	1.7947
(0.9,0.5)	1.9332	1.9329	1.9328

Table 8

(x_1, x_2)	$P_1(x_1, x_2)$	$P_2(x_1, x_2)$	$P_1(x_1, x_2)$	$P_2(x_1, x_2)$	$P_1(x_1, x_2)$	$P_2(x_1, x_2)$
	BEM 20	BEM 20	BEM 40	BEM 40	BEM 80	BEM 80
	segments	segments	segments	segments	segments	segments
(0.1,0.5)	1.2473	-1.0796	1.2518	-1.0925	1.2640	-1.0906
(0.3,0.5)	1.3224	-0.4987	1.3193	-0.4967	1.3185	-0.4940
(0.5,0.5)	1.3388	-0.2092	1.3337	-0.2072	1.3318	-0.2053
(0.7,0.5)	1.3372	-0.0820	1.3349	-0.0808	1.3338	-0.0799
(0.9,0.5)	1.3372	-0.0215	1.3325	-0.0209	1.3335	-0.0208

layered material replaced by a homogeneous material. The thermal conductivity is taken in the form

$$\frac{\lambda_{11}}{\lambda_0} = \frac{\lambda_{22}}{2\lambda_0} = \left(1 + \beta' \frac{\phi}{\phi_0}\right), \quad \frac{\lambda_{12}}{\lambda_0} = 0 \quad (28)$$

where β' is a nondimensional parameter.

Numerical values for Problem 1 and Problem 2 with the thermal conductivities given by (28) with $\beta' = 0.5$ are given, respectively, in Tables 5 and 6 and Tables 7 and 8. Also in Tables 5 and 6 numerical values obtained from the analytical solution

$$\frac{\phi}{\phi_0} = \frac{-1 + [1 + \beta'(2 + 3\beta')x + \beta'(2 + \beta')]^{1/2}}{\beta'} \quad (29)$$

are included for comparison.

The numerical procedure used to obtain the values in Tables 5–8 was identical to that used for Tables 1–4. As for the results in Tables 1–4 the numerical values in Tables 5–8 exhibit accuracy and convergence behaviour which is consistent with the accuracy of the numerical procedure.

7 Summary

A boundary element method has been obtained which may be used to determine the steady-state temperature and flux fields for a wide class of problems for which the thermal conductivity depends on the temperature and the spatial coordinates. The numerical results obtained for some sample problems indicate that the method will readily yield accurate numerical solutions for many steady-state boundary value problems for anisotropic inhomogeneous materials.

Acknowledgments

The authors acknowledge support under Hibah Tim Grant 012/HTPP-II/URGE/1996.

References

- Ang, W. T., Kusuma, J., and Clements, D. L., 1997, "A boundary element method for a second order elliptic partial differential equation with variable coefficients," *Engineering Analysis with Boundary Elements*, Vol. 18, pp. 311–316.
- Bear, J., 1972, *Dynamics of Fluids in Porous Media*, Elsevier, New York, pp. 198–199.
- Brebbia, C. A., and Dominguez, J., 1989, *Boundary Elements An Introductory Course*, 2nd Ed., McGraw-Hill, New York, pp. 123–125.
- Carslaw, H. S., and Jaeger, J. C., 1947, *Conduction of Heat in Solids*, Clarendon Press, Oxford, pp. 28–31.
- Cheng, A. H. D., 1984, "Darcy's flow with variable permeability: A boundary integral solution," *Water Resources Research*, Vol. 20, pp. 980–984.
- Clements, D. L., 1980, "A boundary integral equation method for the numerical solution of a second order elliptic equation with variable coefficients," *Journal of the Australian Mathematical Society*, Vol. 22 (Series B), pp. 218–228.
- Clements, D. L., 1981, *Boundary Value Problems Governed by Second Order Elliptic Systems*, Pitman, London, pp. 135–155.
- Clements, D. L., and Larsson, A., 1993, "A boundary element method for the solution of a class of time dependent problems for inhomogeneous media," *Communications in Numerical Methods in Engineering*, Vol. 9, pp. 111–119.
- Clements, D. L., and Rogers, C., 1984, "A boundary integral equation for the solution of a class of problems in anisotropic inhomogeneous thermostatics and elastostatics," *Quarterly of Applied Mathematics*, Vol. 41, pp. 99–105.
- Rangogni, R., 1987, "A solution of Darcy's flow with variable permeability by means of B.E.M and perturbation techniques," *Boundary Elements IX*, Vol. 3, C. A. Brebbia ed., Springer-Verlag, Berlin, pp. 359–368.
- Sawaf, B., Özisik, M. N., and Jarny, Y., 1995, "An inverse analysis to estimate linearly dependent thermal conductivity components and heat capacity of an orthotropic medium," *International Journal of Heat and Mass Transfer*, Vol. 38, pp. 3005–3010.
- Shaw, R. P., 1994, "Green's functions for heterogeneous media potential problems," *Engineering Analysis with Boundary Elements*, Vol. 13, pp. 219–221.

The Effective Thermal Conductivity of High Porosity Fibrous Metal Foams

V. V. Calmidi¹ and R. L. Mahajan²

Nomenclature

- A_m = area of cross section of metal foam samples (m²)
 b = half-thickness of bump (Fig. 5)
 k = thermal conductivity (W/m-K)
 L = half-length of fiber (Fig. 5)
 L_m = height of metal foam sample (m)
 q = heat input to the patch heaters (W)
 r = area ratio (Eq. 11)
 t = half-thickness of fiber (Fig. 5)
 T = temperature
 ΔT = temperature difference across metal foam sample (°C)
 V = volume
 w = width of fiber perpendicular to plane of paper (Fig. 5)
 z = direction of macroscopic heat flow

Subscripts

- 1, 2, 3 = refers to different layers (Fig. 5)
 e = effective
 f = fluid
 s = solid

Greek Symbols

- ε = Porosity

Introduction

Starting with the pioneering work of Maxwell (1891), heat conduction in fully saturated porous matrices (e.g., sand, packed beds of cylinders and spheres, fibrous insulations, etc.) has been studied in detail over the past several decades. Kaviany (1995) has provided an extensive review of the available literature on the subject along with a number of correlations and their range of applicability.

Under simplified one-dimensional conduction conditions, two extremes can be considered. One in which the thermal resistances offered by the solid and fluid phases are in series (lower bound) and the other in which they are in parallel (upper bound). The upper bound, given by Eq. (1),

$$k_e = (1 - \varepsilon)k_s + \varepsilon k_f \quad (1)$$

has been successfully used in the past for packed bed studies where the solid and fluid phases have similar conductivities. However, the error in the prediction of k_e using Eq. (1) can be considerable as the difference in the conductivities of the phases increases. There have been several studies that attempt to predict the thermal conductivities of packed beds by invoking the structure of the medium, apart from its porosity. Some of these two and one-dimensional studies are reviewed below. Many of them are related to packed beds of spheres and granular materials.

Nozad et al. (1985) solved the two-dimensional heat conduction equation in a spatially periodic two-phase system of touching

spheres. Under the assumption of local thermal equilibrium (Carbonell and Whitaker, 1984), they derived a set of closure equations for the spatial deviation component of the volume-averaged temperature field in the two constitutive phases. These closure equations were solved analytically and numerically to obtain the effective thermal conductivity. Their numerical results correlated well with the experimental data for a touching parameter, $c/a = 0.02$ (c/a is the ratio of the touching length scale to the length scale of the particle size). Based on a similar two-dimensional study, Sahrui and Kaviany (1993) found a value of $c/a = 0.002$ to be more appropriate. Hsu et al. (1995) demonstrated that a one-dimensional conduction model based on in-line touching cubes ($c/a = 0.13$) was sufficient. It showed good agreement with the experimental data of a packed sphere bed.

Hsu et al. (1994) based their study on the earlier work of Zehner and Schlunder (1970). They proposed two models—the area contact model for packed beds of spheres and the phase symmetry model for sponge-like materials (fibrous media). They showed that for packed beds of spheres, their area contact model was able to predict the thermal conductivity better than the Zehner-Schlunder model because it took into account the finite contact area between adjacent particles. They also developed a phase symmetry model for sponge-like porous media (e.g., metal foams). However, they did not validate their phase symmetry model due to lack of experimental data. Bauer (1993) generalized Maxwell's classical theoretical result to pores of any shape and concentration. He further discussed cases in which other phenomena-like radiation can be included into the analysis. Tien and Vafai (1979) derived statistical bounds for the thermal conductivity of microsphere and fibrous insulations based on cell geometries. Their model for fibrous insulations was used by Hunt and Tien (1988) to study forced convection in metal foams. Its validity is discussed later in this paper.

Our survey indicates a lack of experimentally validated studies that attempt to predict the thermal conductivity of metal foams, although they have been the topic of investigation for quite a while (Yokoyama and Mahajan, 1995; DuPlessis et al., 1994; Hunt and Tien, 1988). Further, in order to explore their use as high-performance heat sinks, an accurate estimate of the effective thermal conductivity is necessary.

In this study, we report our measurements of effective thermal conductivity of metal foams ($\varepsilon > 0.9$) made of aluminum. Experiments were performed with air and water as the fluid phase separately. An empirical relation that correlates the experimental data to within an accuracy of 97.5 percent is developed. Taking the foam structure to be hexagonal, an analytical model for the effective thermal conductivity is derived and validated with the experimental data.

Medium

Figure 1 shows a picture of the metal foam medium. It has an open-celled structure composed of dodecahedron-like cells which have 12–14 pentagonal or hexagonal faces. The edges of these cells are composed of the fibers and, typically, there is a lumping of material (intersection) at points where the fibers intersect. The fibrous matrix is made of aluminum alloy T-6201 which has a thermal conductivity of 218 W/m-K. The matrix is brazed to aluminum base plates on two sides. Two quantities, the porosity and the pore density are used to describe the material. The porosity, ε , is the ratio of the void volume to the total volume of the medium and the pore density is the number of pores present per unit length of the material. The latter is typically expressed in units of pores per inch (ppi), and is roughly constant in the three directions. The first three columns of Table 1 summarize the properties of the metal foam samples which were used in the experimental study. The porosities (provided by the manufacturer) were determined using the weight of the sample with the density of aluminum. Note that the pore density is a nominal quantity used to

¹ IBM Microelectronics, Endicott, NY 13760. e-mail: vara@us.ibm.com.

² Professor of Mechanical Engineering, CAMPmode, Department of Mechanical Engineering, University of Colorado at Boulder, Boulder, CO 80309-0427. e-mail: mahajan@colorado.edu. Fellow ASME.

Contributed by the Heat Transfer Division for publication in the JOURNAL OF HEAT TRANSFER. Manuscript received by the Heat Transfer Division, July 17, 1997; revision received, Nov. 3, 1998. Keywords: Conduction, Porous Media, Thermophysical Properties. Associate Technical Editor: M. Kaviany.

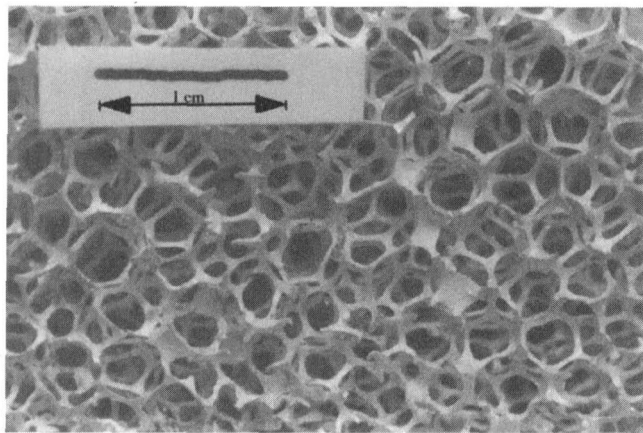


Fig. 1 Photograph of metal foam matrix

classify a particular type of metal foam. In reality, it varies about a mean value from sample to sample.

Experiment

(Metal Foam and Air): A schematic of the experimental setup is shown in Fig. 2. The physical dimensions of the metal foam are 6.3 cm × 6.3 cm × 4.6 cm. The metal foam is brazed at the top and bottom to two aluminum plates (4.7 mm thick). Four T-type thermocouples are attached to each of these two plates at points of varying distance (see Calmidi, 1998, for details). The top plate is heated from above using patch heaters connected to a DC power supply. The surfaces above the heaters and the four sides are insulated using very low conductivity styrofoam. The bottom plate is cooled from below by immersing its bottom surface into a tank which contains cooling water maintained at constant temperature. A silicone-based sealant is used to ensure that the water does not leak out of the tank.

Since the metal foam sample is heated from above, cooled from below and insulated on the rest of the four sides, there is heat conduction in one direction only (as shown in Fig. 2) and buoyancy effects are negligible. Thus, if “ q ” is the net heat input through the top aluminum plate, then

$$q = k_e A_m \Delta T / L_m \quad (2)$$

During a typical experimental run, the power input to the patch heaters was set at a desired value and the temperature difference between the top and bottom plates was monitored till it reached steady state. This took approximately seven to ten minutes depending on the porosity of the sample. The temperature was monitored for five additional minutes to confirm that steady state had indeed been attained. Then, the temperature difference, ΔT between the

Table 1 Metal foam properties and thermal conductivities

No.	Porosity	Pore density (pores/inch)	Conductivity (air + foam) (W/m-K)	Conductivity (water + foam) (W/m-K)
1	0.971	5	2.70	3.70
2	0.946	5	4.60	5.40
3	0.905	5	6.70	7.65
4	0.949	10	4.00	4.95
5	0.909	10	6.70	7.60
6	0.978	20	2.20	3.05
7	0.949	20	3.90	4.80
8	0.906	20	6.90	7.65
9	0.972	40	2.50	3.30
10	0.952	40	3.90	4.75
11	0.937	40	4.50	5.35

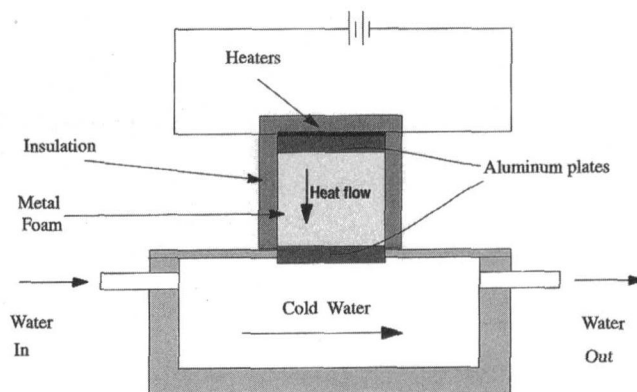


Fig. 2 Schematic of setup used for the metal foam and air experiments

top and bottom plates, was noted. This procedure was repeated for different values of heat input. The maximum heat input to the patch heaters was restricted to about 5–8 W depending on the porosity of the sample being measured. Since the thermal conductivity varies with porosity, the maximum heat input to the heaters was set such that the temperature difference across the plates did not increase beyond $\sim 15^\circ\text{C}$. The variation in temperature across each of the two plates was less than 0.3°C , which is the accuracy of the temperature measurement. At lower temperature differences, the variation was even lower. Thus the two plates were essentially isothermal.

The temperature difference between the hot and cold plates obtained as described above was plotted as a function of the heat input. All data points lied on a straight line passing through the origin. Further, the y-intercept was less than 0.2°C in all cases indicating that the relationship is linear and that buoyancy effects and other nonlinear effects are indeed negligible. From the slope of $\Delta T/q$, the measured value of the thermal conductivity of the sample is

$$k_e = L_m / (A_m (\Delta T/q)_{\text{slope}}) \quad (3)$$

These values are listed in column 4 of Table 1.

Experiment (Metal Foam and Water): Experiments were also performed using water as the fluid phase. An experimental setup similar to the one used for the metal foam and air experiments was used for this purpose (see Calmidi, 1998). The main difference between the two was a thin plexiglass enclosure that was used to contain the water within the void spaces of the metal foam.

The experimental procedure was the same as that for air. The main difference was in the time taken to reach steady state which was around two hours. The measured thermal conductivity values are listed in column 5 of Table 1.

Error Analysis: The main sources of error in the experiment are due to the errors in measurement and those due to conduction losses through the thermocouples and the insulating styrofoam. As noted earlier, buoyancy effects are negligible since the heating is from above. Also, the contact resistance due to the brazing can be neglected because of the high effective conductivity of the brazed layer. The effect of brazing is to introduce an error in the estimation of L_m , the distance between the two aluminum plates. This error is estimated to be one percent of the dimension. The errors in the estimation of q and A_m were 2 percent and 1.6 percent, respectively. The combined error (thermocouple calibration and the resolution of the data acquisition device) in the estimation of ΔT , the temperature difference is 0.3°C . However, the temperature difference was varied up to a maximum of about 15°C . Thus, the percentage error in the estimation of ΔT is 2.0 percent. Based on the conductivity of the styrofoam (0.029 W/m-K), the heat loss through the insulation was estimated to be less than 0.5 percent of

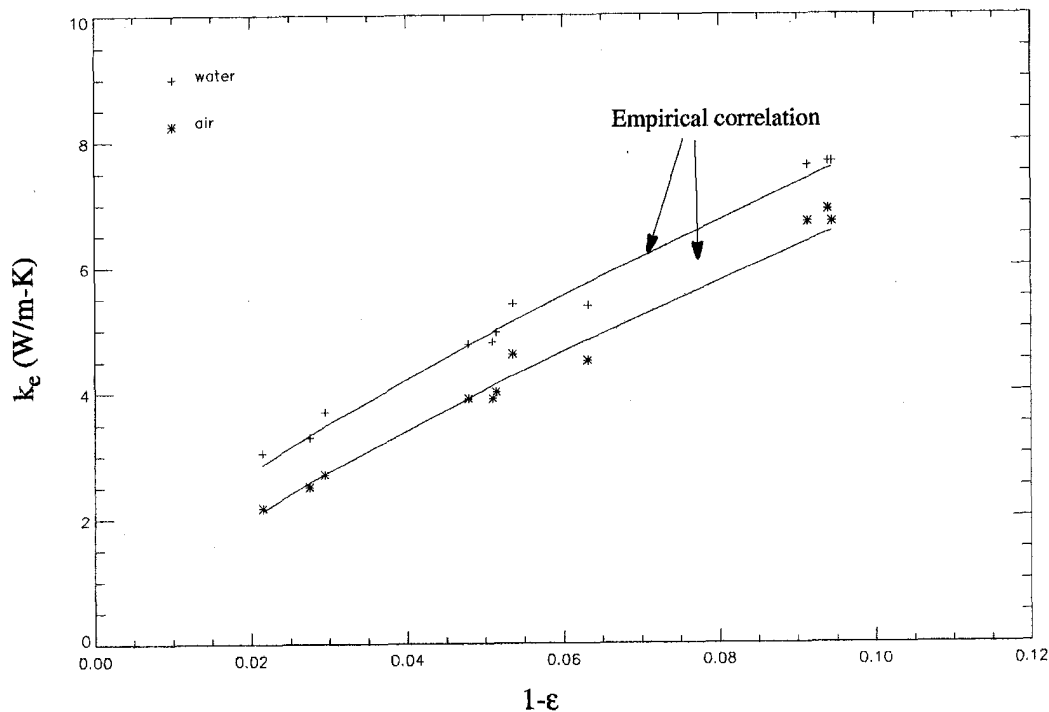


Fig. 3 Experimental data given in Table 1 plotted along with empirical correlation (Eq. (4))

the heat input. The heat conducted away by the thermocouples is insignificant and is neglected. Based on the preceding errors, the total error in the measurement of the thermal conductivity is estimated, using the quadrature sum (Taylor, 1980), to be ± 3.5 percent. For the experiments conducted with water as the fluid phase, there is an additional error introduced due to heat conduction through the plexiglass enclosure. Based on the thermal conductivity and the dimensions of the plexiglass enclosure, the total error in the measurement of the thermal conductivity is increased to ± 3.6 percent.

Empirical Correlation: Based on the experimental data collected, as described above, an empirical correlation was developed. When the heat conducted through the solid and fluid phases is in parallel, the effective thermal conductivity is given by Eq. (1). Based on Eq. (1), the following equation was postulated:

$$\frac{k_e}{k_f} = \varepsilon + A(1 - \varepsilon)^n \frac{k_s}{k_f} \quad (4)$$

The best fit was obtained for $n = 0.763$. However, the value of A was found to be 0.181 for air and 0.195 for water. The maximum and average absolute errors were found to be 6.9 percent and 3.7 percent for air and 7.5 percent and 3.1 percent for water, respectively. The experimental data in Table 1 along with the empirical correlation given in Eq. (4) are shown in Fig. 3.

Analytical Model

In this section, an analytical model is developed based on the structure of the metal foam matrix. First, a periodic structure for the metal foam is postulated and then one-dimensional conduction analysis is performed in the periodic structure to derive the effective thermal conductivity.

Representation of the Metal Foam Structure: In reality, the structure of the metal foam is a complex one and it would be difficult to accurately capture its nuances to every bit of detail. However, there is a fair degree of uniformity associated with the structure which enables it to be treated in a semi-empirical manner.

As mentioned before, the structure of the metal foam consists of dodecahedron-like cells with 12–14 pentagonal or hexagonal faces. The edges of the cells are formed by the individual fibers. We represent this structure by a two-dimensional hexagonal array where the fibers are the edges of the hexagons (Fig. 4). The lumping of material at the points of intersection of the fibers is taken into account in the structure by a square. It is noted here that the area of cross section of the fibers (and of the intersection) is more important than the exact shape itself. Since the structure shown in Fig. 4 is periodic, it is convenient to consider a unit cell (Fig. 5). The conductivity of the unit cell is thus representative of the effective thermal conductivity of the metal foam. This method has been successfully used in the past (Kunii and Smith, 1960; Zehner and Schlunder, 1970; Hsu et al., 1994; Hsu et al., 1995) to determine the effective conductivity of packed beds. In general, one-dimensional heat conduction is assumed in a two (or three) dimensional periodic structure.

Effective Thermal Conductivity: We assume one-dimensional heat conduction in order to derive an analytical expression for the conductivity. The direction of heat flow is as shown in Fig. 5. Note that consistent with the assumption of one-dimensional conduction, the side faces are adiabatic. Although this assumption may not be true

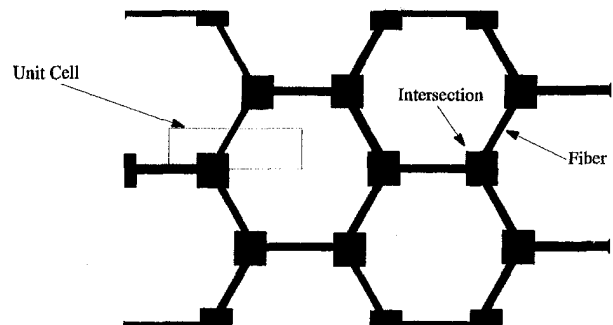


Fig. 4 Hexagonal structure of metal foam matrix

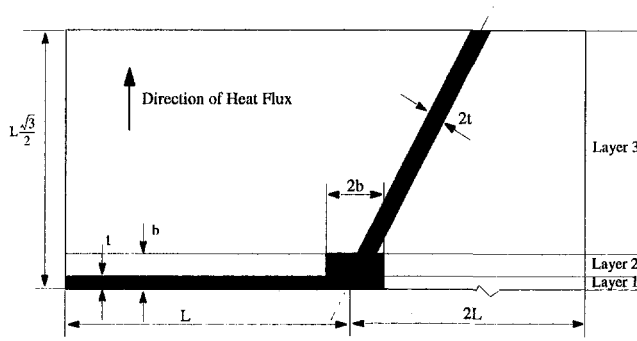


Fig. 5 Unit-cell representation of hexagonal structure

locally, globally the heat transfer is indeed one-dimensional. For determining the effective thermal conductivity, the unit cell in Fig. 5 can be divided into three layers in series. The conductivity of each layer, in turn, is derived separately by applying the parallel law of thermal resistances.

In layer 1, the solid and fluid phases are in parallel. Their respective volumes are given by

$$V_s = t(L + b)w \quad \text{and} \quad (5)$$

$$V_f = t[3L - (L + b)]w. \quad (6)$$

“ w ” in Eqs. (5), (6) is the width in the third direction (perpendicular to the plane of the paper). The conductivity of layer 1 can be written as

$$k_1 = \frac{t(L + b)}{t(3L)} k_s + \frac{t[3L - (L + b)]}{t(3L)} k_f. \quad (7)$$

Equation (7) can be simplified as

$$k_1 = k_f + \frac{(k_s - k_f)}{3} \left(1 + \frac{b}{L}\right). \quad (8)$$

In a similar manner, the conductivities of layers 2 and 3 can be written as

$$k_{II} = k_f + \frac{2}{3}(k_s - k_f) \left(\frac{b}{L}\right) \quad \text{and} \quad (9)$$

$$k_{III} = k_f + \frac{4}{3\sqrt{3}}(k_s - k_f) \left(\frac{t}{L}\right). \quad (10)$$

In Eq. (10), an “area ratio” r is defined as

$$r = \frac{tw}{bw} = \frac{t}{b}. \quad (11)$$

By combining the three layers which are in series, the effective thermal conductivity of the unit cell can be written as

$$\frac{L_1 + L_2 + L_3}{k_e} = \frac{L_1}{k_1} + \frac{L_2}{k_{II}} + \frac{L_3}{k_{III}} \quad (12)$$

where, k_1 , k_{II} , and k_{III} are given by Eqs. (8), (9), and (10), respectively, and L_1 , L_2 , and L_3 are the heights of the three layers in Fig. 5.

The solid volume fraction, $1 - \varepsilon$, is the ratio of solid volume to the volume of the unit cell. For the assumed hexagonal geometry, it can be easily shown to be

$$(1 - \varepsilon) = \frac{t(L + b) + (b - t)2b + \left(L\frac{\sqrt{3}}{2} - b\right) \frac{4t}{\sqrt{3}}}{3L\left(L\frac{\sqrt{3}}{2}\right)}. \quad (13)$$

After substituting for “ r ” from Eq. (11), the resulting quadratic equation in b/L can be solved for b/L as follows:

$$\frac{b}{L} = \frac{-r + \sqrt{r^2 + \frac{2}{\sqrt{3}}(1 - \varepsilon)\left(2 - r\left(1 + \frac{4}{\sqrt{3}}\right)\right)}}{\frac{2}{3}\left(2 - r\left(1 + \frac{4}{\sqrt{3}}\right)\right)} \quad (14)$$

b/L is plotted in Fig. 6 for different values of r . It should be noted that for $r = 0.366$, the fiber extends upto the right edge of the intersection (Fig. 5). Hence, Eq. (14) is not valid for $r > 0.366$. Equation (14) can be used in Eq. (12) to obtain the effective thermal conductivity of the unit cell in terms of the porosity “ ε ” and the area ratio, “ r .” The final expression can be written as

$$k_e = \left(\left(\frac{2}{\sqrt{3}} \right) \left(\frac{r\left(\frac{b}{L}\right)}{k_f + \left(1 + \frac{b}{L}\right)\frac{(k_s - k_f)}{3}} + \frac{(1 - r)\left(\frac{b}{L}\right)}{k_f + \frac{2}{3}\left(\frac{b}{L}\right)(k_s - k_f)} + \frac{\frac{\sqrt{3}}{2} - \frac{b}{L}}{k_f + \frac{4r}{3\sqrt{3}}\left(\frac{b}{L}\right)(k_s - k_f)} \right) \right)^{-1} \quad (15)$$

where b/L is given by Eq. (14).

To assess the validity of this model, we first consider the experimentally measured values for metal foam and air given in column 4 of Table 1. They are plotted in Fig. 7 as a function of $1 - \varepsilon$, the solid fraction. Different symbols have been used for samples of different pore sizes. Clearly, an excellent fit between the experimental data and the predicted values is obtained for $r = 0.09$.

Figure 8 shows the effective thermal conductivity of foamed materials (k_e/k_f) as a function of the porosity for different values of k_s/k_f . Also shown, along with experimental data, are curves for air ($k_s/k_f = 8226$), and water ($k_s/k_f = 357$). As expected, for $k_s/k_f = 1$, $k_e = k_f$ for all porosity values. As k_s/k_f increases, k_e/k_f also increases and all curves converge at $k_e/k_f = 1$.

Discussion

As was seen in the previous section, the area ratio $r = 0.09$ results in excellent agreement with experiment results for both aluminum/air and aluminum/water systems. Due to the two-

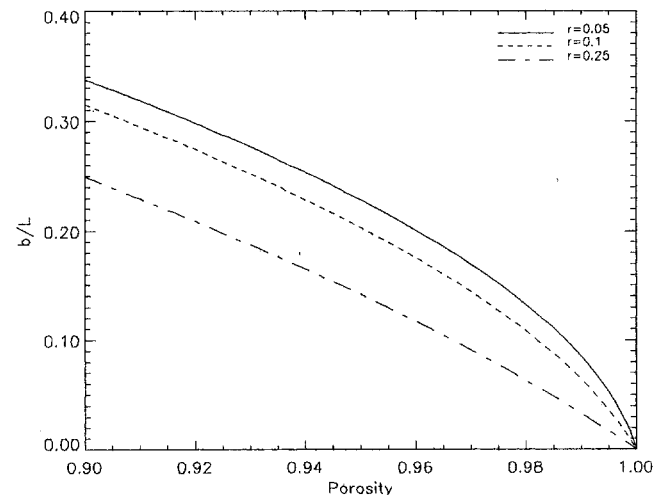


Fig. 6 b/L (Eq. (14)) as a function of ε

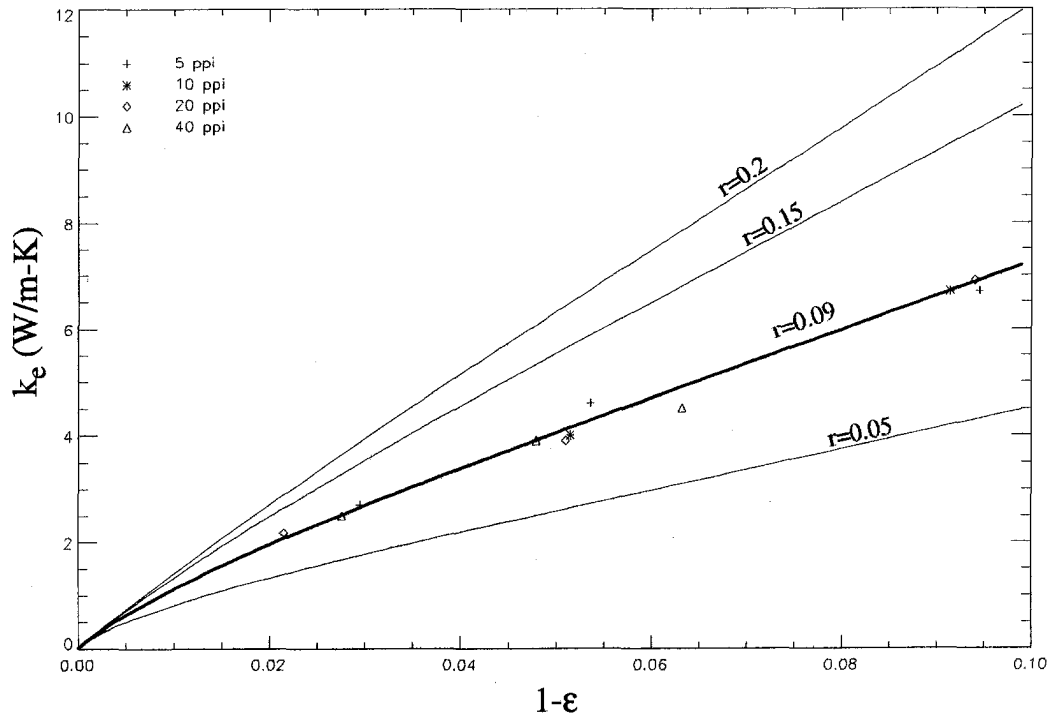


Fig. 7 Comparison of experimental results with model (Eq. (15)) for air ($k_f = 0.0265$ W/m-K)

dimensional nature of the assumed geometry, the ratio of the length scales of the fiber thickness to the intersection size is $r^{1/2} = 0.3$. A close examination of the metal foam structure indicates that r is not unique and it, in fact, varies. However, $r^{1/2} = 0.3$ appears to be a representative value. Due to the one-dimensional conduction analysis, it is expected that the value of r is slightly under-predicted since spreading effects are not included. Nevertheless, these effects are expected to be small due to the high conductivity of aluminum. The experimental data for both air and water suggest

that there is no systematic effect of the pore density variation on the effective thermal conductivity. The implication is that the structure of the metal foam is more or less constant over the range of pore densities considered. This is in sharp contrast to the experimental data for air-saturated polyurethane foams from the Scott Paper Co. reported in the monograph (p. 137) by Kaviany (1995). However, the reported conductivity values are higher than the theoretical maximum given in Eq. (1). It is possible that buoyancy and radiation effects may not have been negligible for

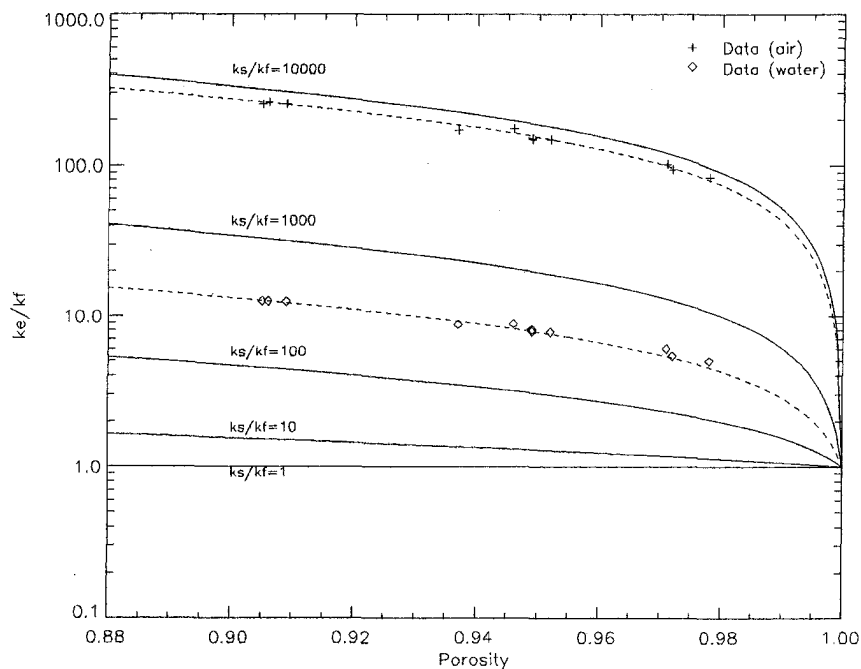


Fig. 8 Effective thermal conductivity of foamed materials using Eq. (15) with $r = 0.09$. Data for aluminum/air and aluminum/water is also shown, with model predictions.

low-conductivity polyurethane foams resulting in higher thermal conductivity values at larger pore densities.

A comparison of the analytical (phase-symmetric) model of Hsu et al. (1994) with our experimental data indicates that their model overpredicts the thermal conductivity for metal foams. Further, the error systematically increases with an increase in the solid fraction, $1-\epsilon$. A possible explanation for this might lie in the extension of the experimentally observed low solid conductivity asymptote result of Zehner and Schlunder (1970) to the low fluid conductivity asymptote by invoking phase symmetry among the solid and fluid phases. Tien and Vafai (1979) have derived statistical upper and lower bounds for the effective thermal conductivity of fibrous insulations. Their three-dimensional model for randomly dispersed fibers was also compared with the experimental data obtained in this study. It was found that, in general, the data were close to the upper bound and orders of magnitude different from the lower bound. However, the recommended value of the cell geometry factor, $G = \frac{1}{6}$, was found unsuitable for accurate predictions of the thermal conductivity over the entire range of porosities considered.

Summary

The effective thermal conductivity of high-porosity fibrous metal foams has been investigated experimentally. Experiments have been conducted using both air and water as the fluid phases. An empirical correlation has been developed based on the experimental data. A theoretical model has also been derived based on the hexagonal structure of the metal foam matrix. The model matches extremely well with the experimental results for both air and water for an area ratio value of 0.09. It is expected that the experimentally validated model for the thermal conductivity will be helpful in the evaluation of metal foams as possible candidates as heat sinks in electronic cooling applications.

Acknowledgments

This work has been funded by CAMPmode, The Center for Advanced Manufacturing, and Packaging of microwave, optical, and digital electronics at the University of Colorado. The help received from Mr. Kyoung-Hwan Ahn for experiments with water is gratefully acknowledged. The authors would like to thank Dr. Yoichi Yokoyama for the many useful discussions and Mr. Bryan Leyda of ERG (Energy Research and Generation), Inc., for providing the samples used in the experimental study and for helpful discussions during the course of this work.

References

- Bauer, T. H., 1993, "A general approach toward the thermal conductivity of porous media," *Int. J. Heat Mass Transfer*, Vol. 36, No. 17, pp. 4181-4191.
- Calmidi, V. V., 1998, "Transport phenomena in high porosity fibrous metal forms," Ph.D. dissertation, University of Colorado, Boulder, CO.
- Carbonell, R. G., and Whitaker, S., 1984, "Heat and mass transfer in porous media," *Fundamentals of Transport Phenomena in Porous Media*, Bear and M. Y. Corapcioglu, eds., Martinus Nijhoff, Dordrecht, The Netherlands, pp. 123-198.
- DuPlessis, P., Montillet, A., Comiti, J., and Legrand, J., 1994, "Pressure Drop Prediction for Flow through High Porosity Metallic Foams," *Chem. Engng. Sci.*, Vol. 49, pp. 3545-3553.
- Hsu, C. T., Cheng, P., and Wong, K. W., 1994, "Modified Zehner-Schlunder models for stagnant thermal conductivity of porous media," *Int. J. Heat Mass Transfer*, Vol. 37, No. 17, pp. 2751-2759.
- Hsu, C. T., Cheng, P., and Wong, K. W., 1995, "A Lumped-Parameter Model for Stagnant Thermal Conductivity of Spatially Periodic Porous Media," *ASME JOURNAL OF HEAT TRANSFER*, Vol. 117, pp. 264-269.
- Hunt, M. L., and Tien, C. L., 1988, "Effects of Thermal Dispersion on Forced Convection in Fibrous Media," *Int. J. Heat Mass Transfer*, Vol. 31, pp. 301-309.
- Lee, Y. C., Zhang, W., Xie, W., and Mahajan, R. L., 1993, "Cooling of a FlipChip package with a 100 Watt, 1 sq. cm chip," *Proceedings of the ASME International Electronic Packaging Conference*, Vol. 1, pp. 419-423.
- Kaviany, M., 1995, *Principles of Heat Transfer in Porous Media*, Springer-Verlag, New York.
- Kunii, D., and Smith, J. M., 1960, "Heat Transfer Characteristics of Porous Rocks," *AIChE J.*, Vol. 6, pp. 71-78.
- Maxwell, J. C., 1891, *A Treatise on Electricity and Magnetism*, Vol. 1, Oxford University Press, reprinted by Dover, New York (1954).
- Nozad, I., Carbonell, R. G., and Whitaker, S., 1985, "Heat conduction in multi-

phase systems I: Theory and Experiments for two-phase systems," *Chem. Engng. Sci.*, Vol. 40, pp. 843-855.

Sahraoui, M., and Kaviany, M., 1993, "Slip and no-slip temperature boundary conditions at interface of porous, plain media: Conduction," *Int. J. Heat Mass Transfer*, Vol. 36, No. 4, pp. 1019-1033.

Taylor, T. R., 1980, *An Introduction to Error Analysis—The study of uncertainties in physical measurements*, University Science Books, Mill Valley, CA.

Tien, C. L., and Vafai, K., 1979, "Statistical Bounds for the Effective Thermal Conductivity of Microsphere and Fibrous Insulation," *AIAA Progress Series*, Vol. 65, pp. 135-148.

Zehner, P., and Schlunder, E. U., 1970, "Thermal conductivity of granular materials at moderate temperatures," *Chemie. Ingr.-Tech.*, Vol. 42, pp. 933-941.

Yokoyama, Y., and Mahajan, R. L., "Non-Darcian Convective Heat Transfer in a Horizontal Duct," *Proceedings of the 30th National Heat Transfer Conference*, Portland, OR, HTD-Vol. 309, ASME, New York, pp. 83-91.

Dimensional Analysis in Heat Transfer

T. M. Dalton¹ and M. R. D. Davies¹

Introduction

The object of dimensional analysis is to reduce the number of parameters in a problem for ease of calculation and experimental economy. It follows that the best analysis will produce the minimum number of nondimensional groups. As these groups have physical significance, the nondimensionalizing technique must always produce the correct scaling groups, and it might also be expected that this method should be applicable to a wide range of problems. The technique must, in short, be concise, correct, and consistent.

The genesis of dimensional analysis is outlined by White (1994) and Ensault-Pelterie (1950), it can be traced back to Fourier (1822) through the work of Rayleigh (1877) and the Pi theorem of Buckingham (1914).

Ehrenfest-Afanassjewa (1916) is attributed with first suggesting the method of expressing the governing equations in nondimensional form to derive the governing nondimensional constants, subsequently named inspectional analysis by Ruark (1935). It is a modification of this method which is the subject of this paper. In inspectional analysis each parameter in the governing equations is nondimensionalized by a reference parameter. It is based on the principle that two systems with identical governing equations and boundary conditions will have identical solutions. This is the condition of similarity. If the equations and boundary conditions are written without dimensions, the principle still holds and great generality is achieved. The method is now widely found in college level texts. In all the published work, the reference parameters include boundary conditions and therefore for each new boundary condition type the process must be repeated. In this analysis, the rescaled groups which arise from the governing equations are separated from those arising from the boundary conditions. This is shown to have a number of advantages over any previously reported techniques: First, if possible, it derives the reference parameters for each variable from the governing equations, thereby avoiding any confusion in their choice; secondly, it represents a straightforward method to produce the minimum number of scaling groups; thirdly, it reduces the effort of inspectional analysis to just nondimensionalizing the boundary conditions; and, finally, it

¹ PEI Technologies, Thermofluids Research Centre, Department of Mechanical and Aeronautical Engineering, University of Limerick, Limerick, Ireland.

Contributed by the Heat Transfer Division for publication in the JOURNAL OF HEAT TRANSFER and presented at '97 NHTC, Baltimore. Manuscript received by the Heat Transfer Division, Mar. 6, 1998; revision received, Jan. 1, 1999. Keywords: Analytical, Heat Transfer, Natural Convection, Scaling. Associate Technical Editor: A. Lavine.

low-conductivity polyurethane foams resulting in higher thermal conductivity values at larger pore densities.

A comparison of the analytical (phase-symmetric) model of Hsu et al. (1994) with our experimental data indicates that their model overpredicts the thermal conductivity for metal foams. Further, the error systematically increases with an increase in the solid fraction, $1-\epsilon$. A possible explanation for this might lie in the extension of the experimentally observed low solid conductivity asymptote result of Zehner and Schlunder (1970) to the low fluid conductivity asymptote by invoking phase symmetry among the solid and fluid phases. Tien and Vafai (1979) have derived statistical upper and lower bounds for the effective thermal conductivity of fibrous insulations. Their three-dimensional model for randomly dispersed fibers was also compared with the experimental data obtained in this study. It was found that, in general, the data were close to the upper bound and orders of magnitude different from the lower bound. However, the recommended value of the cell geometry factor, $G = \frac{1}{6}$, was found unsuitable for accurate predictions of the thermal conductivity over the entire range of porosities considered.

Summary

The effective thermal conductivity of high-porosity fibrous metal foams has been investigated experimentally. Experiments have been conducted using both air and water as the fluid phases. An empirical correlation has been developed based on the experimental data. A theoretical model has also been derived based on the hexagonal structure of the metal foam matrix. The model matches extremely well with the experimental results for both air and water for an area ratio value of 0.09. It is expected that the experimentally validated model for the thermal conductivity will be helpful in the evaluation of metal foams as possible candidates as heat sinks in electronic cooling applications.

Acknowledgments

This work has been funded by CAMPmode, The Center for Advanced Manufacturing, and Packaging of microwave, optical, and digital electronics at the University of Colorado. The help received from Mr. Kyoung-Hwan Ahn for experiments with water is gratefully acknowledged. The authors would like to thank Dr. Yoichi Yokoyama for the many useful discussions and Mr. Bryan Leyda of ERG (Energy Research and Generation), Inc., for providing the samples used in the experimental study and for helpful discussions during the course of this work.

References

- Bauer, T. H., 1993, "A general approach toward the thermal conductivity of porous media," *Int. J. Heat Mass Transfer*, Vol. 36, No. 17, pp. 4181-4191.
- Calmidi, V. V., 1998, "Transport phenomena in high porosity fibrous metal forms," Ph.D. dissertation, University of Colorado, Boulder, CO.
- Carbonell, R. G., and Whitaker, S., 1984, "Heat and mass transfer in porous media," *Fundamentals of Transport Phenomena in Porous Media*, Bear and M. Y. Corapcioglu, eds., Martinus Nijhoff, Dordrecht, The Netherlands, pp. 123-198.
- DuPlessis, P., Montillet, A., Comiti, J., and Legrand, J., 1994, "Pressure Drop Prediction for Flow through High Porosity Metallic Foams," *Chem. Engng. Sci.*, Vol. 49, pp. 3545-3553.
- Hsu, C. T., Cheng, P., and Wong, K. W., 1994, "Modified Zehner-Schlunder models for stagnant thermal conductivity of porous media," *Int. J. Heat Mass Transfer*, Vol. 37, No. 17, pp. 2751-2759.
- Hsu, C. T., Cheng, P., and Wong, K. W., 1995, "A Lumped-Parameter Model for Stagnant Thermal Conductivity of Spatially Periodic Porous Media," *ASME JOURNAL OF HEAT TRANSFER*, Vol. 117, pp. 264-269.
- Hunt, M. L., and Tien, C. L., 1988, "Effects of Thermal Dispersion on Forced Convection in Fibrous Media," *Int. J. Heat Mass Transfer*, Vol. 31, pp. 301-309.
- Lee, Y. C., Zhang, W., Xie, W., and Mahajan, R. L., 1993, "Cooling of a FlipChip package with a 100 Watt, 1 sq. cm chip," *Proceedings of the ASME International Electronic Packaging Conference*, Vol. 1, pp. 419-423.
- Kaviany, M., 1995, *Principles of Heat Transfer in Porous Media*, Springer-Verlag, New York.
- Kunii, D., and Smith, J. M., 1960, "Heat Transfer Characteristics of Porous Rocks," *AIChE J.*, Vol. 6, pp. 71-78.
- Maxwell, J. C., 1891, *A Treatise on Electricity and Magnetism*, Vol. 1, Oxford University Press, reprinted by Dover, New York (1954).
- Nozad, I., Carbonell, R. G., and Whitaker, S., 1985, "Heat conduction in multi-

phase systems I: Theory and Experiments for two-phase systems," *Chem. Engng. Sci.*, Vol. 40, pp. 843-855.

Sahraoui, M., and Kaviany, M., 1993, "Slip and no-slip temperature boundary conditions at interface of porous, plain media: Conduction," *Int. J. Heat Mass Transfer*, Vol. 36, No. 4, pp. 1019-1033.

Taylor, T. R., 1980, *An Introduction to Error Analysis—The study of uncertainties in physical measurements*, University Science Books, Mill Valley, CA.

Tien, C. L., and Vafai, K., 1979, "Statistical Bounds for the Effective Thermal Conductivity of Microsphere and Fibrous Insulation," *AIAA Progress Series*, Vol. 65, pp. 135-148.

Zehner, P., and Schlunder, E. U., 1970, "Thermal conductivity of granular materials at moderate temperatures," *Chemie. Ingr.-Tech.*, Vol. 42, pp. 933-941.

Yokoyama, Y., and Mahajan, R. L., "Non-Darcian Convective Heat Transfer in a Horizontal Duct," *Proceedings of the 30th National Heat Transfer Conference*, Portland, OR, HTD-Vol. 309, ASME, New York, pp. 83-91.

Dimensional Analysis in Heat Transfer

T. M. Dalton¹ and M. R. D. Davies¹

Introduction

The object of dimensional analysis is to reduce the number of parameters in a problem for ease of calculation and experimental economy. It follows that the best analysis will produce the minimum number of nondimensional groups. As these groups have physical significance, the nondimensionalizing technique must always produce the correct scaling groups, and it might also be expected that this method should be applicable to a wide range of problems. The technique must, in short, be concise, correct, and consistent.

The genesis of dimensional analysis is outlined by White (1994) and Ensault-Pelterie (1950), it can be traced back to Fourier (1822) through the work of Rayleigh (1877) and the Pi theorem of Buckingham (1914).

Ehrenfest-Afanassjewa (1916) is attributed with first suggesting the method of expressing the governing equations in nondimensional form to derive the governing nondimensional constants, subsequently named inspectional analysis by Ruark (1935). It is a modification of this method which is the subject of this paper. In inspectional analysis each parameter in the governing equations is nondimensionalized by a reference parameter. It is based on the principle that two systems with identical governing equations and boundary conditions will have identical solutions. This is the condition of similarity. If the equations and boundary conditions are written without dimensions, the principle still holds and great generality is achieved. The method is now widely found in college level texts. In all the published work, the reference parameters include boundary conditions and therefore for each new boundary condition type the process must be repeated. In this analysis, the rescaled groups which arise from the governing equations are separated from those arising from the boundary conditions. This is shown to have a number of advantages over any previously reported techniques: First, if possible, it derives the reference parameters for each variable from the governing equations, thereby avoiding any confusion in their choice; secondly, it represents a straightforward method to produce the minimum number of scaling groups; thirdly, it reduces the effort of inspectional analysis to just nondimensionalizing the boundary conditions; and, finally, it

¹ PEI Technologies, Thermofluids Research Centre, Department of Mechanical and Aeronautical Engineering, University of Limerick, Limerick, Ireland.

Contributed by the Heat Transfer Division for publication in the *JOURNAL OF HEAT TRANSFER* and presented at '97 NHTC, Baltimore. Manuscript received by the Heat Transfer Division, Mar. 6, 1998; revision received, Jan. 1, 1999. Keywords: Analytical, Heat Transfer, Natural Convection, Scaling. Associate Technical Editor: A. Lavine.

provides a systematic way of dealing with a variety of boundary conditions.

Theory

The methodology is as follows. At the greatest level of generality are the family equations which would include all possible fluid phenomena. At the next level are the genus equations which describe different types of flows. In this analysis, the parameters in these equations are written in nondimensional form in order to derive a set of equations with the minimum number of constants. This generates the genus level nondimensional groups and a definition of the nondimensional dependent and independent variables, without reference to any boundary conditions. At the species level are the equations with their boundary conditions; these conditions generate the second set of nondimensional groups and again the aim is to keep these to a minimum. Combined, these form the complete set of nondimensional groups for a particular problem.

In this paper, the method is demonstrated in detail for compressible free convection with three types of boundary conditions and new results are presented. Many more examples of the method are shown in Dalton and Davies (1997).

Compressible Natural Convection. Equations (1a) to (1e) are the closed set of equations for compressible, steady naturally convecting flow in two dimensions which include the gravity force, but internal heat generation, viscous dissipation and compressive work are neglected. Similar terms are omitted.

$$\frac{\partial(\rho u)}{\partial x} + \frac{\partial(\rho v)}{\partial y} = 0, \quad (1a)$$

$$\rho u \frac{\partial u}{\partial x} = -\frac{\partial p}{\partial x} - \rho g + \mu \frac{\partial^2 u}{\partial y^2}, \quad (1b)$$

$$\rho v \frac{\partial v}{\partial y} = -\frac{\partial p}{\partial y} + \mu \frac{\partial^2 v}{\partial x^2}, \quad (1c)$$

$$u c_p \rho \frac{\partial T}{\partial x} = k \frac{\partial^2 T}{\partial y^2}, \quad (1d)$$

$$p = \rho R T. \quad (1e)$$

To nondimensionalize these equations, dimensionless quantities are introduced as follows:

$$\rho^* = \frac{\rho}{A}, \quad u^* = \frac{u}{B}, \quad v^* = \frac{v}{B}, \quad p^* = \frac{p}{C}, \quad x^* = \frac{x}{D}$$

$$y^* = \frac{y}{D}, \quad T^* = \frac{T}{E} \quad (2)$$

where A , B , C , D , and E have the units of density, velocity, pressure, length, and temperature, respectively. In the literature, these reference values are functions of boundary conditions, fluid properties, and a characteristic length. In this analysis, however, generality will be preserved until the boundary conditions of a particular problem are considered. As will be shown, different groups arise from different boundary conditions, but the same equations always give the same groups. Incorporating Eq. (2) into the governing equations and simplifying gives

$$\frac{\partial(\rho^* u^*)}{\partial x^*} + \frac{\partial(\rho^* v^*)}{\partial y^*} = 0, \quad (3a)$$

$$\rho^* u^* \frac{\partial u^*}{\partial x^*} = -\left(\frac{C}{AB^2}\right) \frac{\partial p^*}{\partial x^*}$$

$$+ \left(\frac{Dg}{B^2}\right) \rho^* + \left(\frac{\mu}{DBA}\right) \frac{\partial^2 u^*}{\partial y^{*2}}, \quad (3b)$$

$$\rho^* v^* \frac{\partial v^*}{\partial y^*} = -\left(\frac{C}{AB^2}\right) \frac{\partial p^*}{\partial y^*} + \left(\frac{\mu}{DBA}\right) \frac{\partial^2 v^*}{\partial x^{*2}}, \quad (3c)$$

$$u^* \rho^* \frac{\partial T^*}{\partial x^*} = \left(\frac{k}{ADc_p B}\right) \frac{\partial^2 T^*}{\partial y^{*2}}, \quad (3d)$$

$$p^* = \left(\frac{ARE}{C}\right) \rho^* T^*. \quad (3e)$$

The procedure is to minimize the number of groups and to define the reference parameters A – E . This is achieved by letting all the remaining groups equal unity, except where a group comprises just physical constants: If a group consisting of just physical constants was set equal to unity it would make an incorrect physical statement about the fluid. The result of this reduction is the simplest possible definition of the reference parameters

$$A = \frac{\mu}{D\sqrt{Dg}}, \quad B = \sqrt{Dg}, \quad C = \frac{\mu g}{\sqrt{Dg}}, \quad E = \frac{Dg}{R}, \quad (4)$$

and the nondimensional variables are

$$u^* = \frac{u}{\sqrt{Dg}}, \quad T^* = \frac{TR}{Dg}, \quad p^* = \frac{p}{\mu} \sqrt{\frac{D}{g}}, \quad \rho^* = \frac{\rho D \sqrt{Dg}}{\mu}$$

$$x^* = \frac{x}{D}, \quad y^* = \frac{y}{D}. \quad (5)$$

Including these nondimensional variables, the equations are stated in their most general form: They are independent of the boundary conditions of a specific problem, and they contain only one constant—the Prandtl number.

Application of Nondimensional Boundary Conditions

Each boundary condition has the possibility of introducing a nondimensional group; the aim is therefore to specify the problem with the minimum number of boundary conditions. Each condition must be specified in terms of what is known a priori of a solution.

Consider an infinitely long cylinder of radius R_c , suspended centrally within an isothermal cylindrical enclosure of radius R_e and temperature T_e . A pressure p_i is set in the enclosure prior to the temperature difference between the cylinder and the enclosure being established—this sets the pressure datum. From Eq. (5), with a characteristic length R_e , the nondimensional enclosure conditions are therefore

$$\left(\frac{p_i}{\mu} \sqrt{\frac{R_c}{g}}\right); \quad \text{and at } x^{*2} + y^{*2} = \left(\frac{R_e}{R_c}\right)^2, \quad T^* = \left(\frac{T_e R}{R_c g}\right).$$

Three types of boundary conditions are considered on the surface of the suspended cylinder: case 1, an isothermal surface; case 2 an isoflux surface and, case 3, a trigonometric surface temperature distribution.

$$\text{Case 1: At } x^{*2} + y^{*2} = 1, \quad T^* = \left(\frac{T_s R}{R_c g}\right). \quad (6a)$$

$$\text{Case 2: At } x^{*2} + y^{*2} = 1, \quad q^* = \left(\frac{q_s R}{kg}\right) = \left[\frac{\partial T^*}{\partial r^*}\right]_{r=R_c}. \quad (6b)$$

$$\text{Case 3: At } x^{*2} + y^{*2} = 1, \quad T^* = \left(\frac{T_a R \cos \phi}{R_c g}\right). \quad (6c)$$

Thus the governing dimensionless groups for each case are as follows.

$$\text{Case 1: } \frac{\mu c_p}{k}, \quad \frac{\rho_i R_c^3 g}{\mu^2}, \quad \frac{T_e R}{R_c g}, \quad \frac{T_s R}{R_c g}.$$

Comparative Analysis of Different Models for the Turbulent Prandtl Number

M. C. Silva¹, L. C. De Lima², and R. F. Miranda³

$$\text{Case 2: } \frac{\mu c_p}{k}, \frac{\rho_i^2 R_c^3 g}{\mu^2}, \frac{T_e R}{R_c g}, \frac{q_s R}{k g}$$

$$\text{Case 3: } \frac{\mu c_p}{k}, \frac{\rho_i^2 R_c^3 g}{\mu^2}, \frac{T_e R}{R_c g}, \frac{T_a R \cos \phi}{R_c g}$$

In each case pressure was substituted by the ideal gas law, with the temperature defined at the enclosure wall to define a reference density, so that the groups have a similar format to the Grashof number. The relative ease with which any type of boundary condition may be analyzed is clear.

In case 1, for example, any nondimensional dependent variable, ψ^* , may be written as

$$f(\psi^*, \text{Pr}, \text{Gr}_m, T_e^*, T_s^*, x^*, y^*) = 0, \quad (7)$$

where

$$T_s^* = \frac{T_s R}{R_c g} \quad \text{and} \quad T_e^* = \frac{T_e R}{R_c g},$$

and Gr_m is the modified Grashof number expressed without temperatures, $(\rho_i^2 R_c^3 g / \mu^2)$. Taking a heat balance at the wall of the cylinder,

$$\text{Nu} = \frac{h R_c}{k} = - \frac{1}{(T_s^* - T_e^*)} \left[\frac{\partial T^*}{\partial r^*} \right]_{r=R_c} \quad (8)$$

Assuming that the temperature is the dependent variable in Eq. (7), and, that it can be written as an explicit function, then

$$\text{Nu} = g(\text{Pr}, \text{Gr}_m, T_e^*, T_s^*, \phi). \quad (9)$$

There is a reduction from ten parameters to six nondimensional groups. The surface mean Nusselt number is then

$$\bar{\text{Nu}} = g(\text{Pr}, \text{Gr}_m, T_e^*, T_s^*). \quad (10)$$

This shows that for fully compressible free convection, the Nusselt number is dependent upon the scaled absolute temperatures and the temperature difference, as arises from the Boussinesq approximation. It is known that in air free convection this approximation breaks down at modest temperature differences, approximately 25 K. Greater accuracy in data correlation will therefore be found if the above parameters are used in place of the traditional Grashof and Prandtl description.

This example illustrates the utility of the described method. It is applicable to all systems described by known equations with known boundary conditions. The authors will publish many such examples in the future.

Acknowledgments

The authors would like to thank PEI Technologies for the financial support for this research.

References

- Buckingham, E., 1914, "On Physically Similar Systems: Illustrations on the Use of Dimensional Equations," *Physics Review*, Vol. 8, No. 4, pp. 345-376.
- Dalton, T., and Davies, M. R. D., 1997, "Convection Dimensional Analysis," ASME HTD-Vol. 346, pp. 33-39.
- Ehrenfest-Afanassjewa, T., 1916, "Der Dimensionsbegriff und der Analytische Bau Physikalischer Gleichungen," *Math. Anal.*, Vol. 27, pp. 259-278.
- Esnault-Pelterie, R., 1950, *Dimensional Analysis and Metrology*, F. Rouge & Co. Lausanne.
- Fourier, J., 1822, *Analytical Theory of Heat* (translation by A. Freeman, 1878, Cambridge).
- Rayleigh, Lord, 1877, *Theory of Sound*, 1st Ed., Macmillan and Co., London, p. 280.
- Ruark, A. E., 1935, "Inspectional Analysis: A Method which Supplements Dimensional Analysis," *Journal of the Mitchell Society*, Vol. 51, pp. 127-133.
- Shames, I., 1992, *Mechanics of Fluids*, 3rd Ed., McGraw-Hill, New York, p. 310.
- White, F. M., 1994, *Fluid Mechanics*, 3rd Ed., McGraw-Hill, New York, p. 254.

Nomenclature

- c_p = specific heat at constant pressure
- c_f = friction coefficient, $2\tau_o/(\rho U_\infty^2)$
- k = molecular thermal conductivity
- k_m, k_H = mixing-length constants for momentum and heat, respectively (Eq. 15)
- Pr = Prandtl number (ν/α)
- q_w = wall heat flux
- Re = Reynolds number ($U_\infty x/\nu$)
- St = local Stanton number = $q_w/\rho c_p U_\infty (T_w - T_\infty)$
- T = time-averaged temperature
- T_∞ = temperature of free stream
- T_w = temperature at wall surface
- $\frac{u}{U_\infty}$ = time-averaged velocity in x -direction
- $u'v'$ = turbulent shear stress
- u^+ = mean velocity in wall coordinates (u/u^*)
- U_∞ = velocity at outer edge of boundary layer
- u^* = shear velocity ($\sqrt{\tau_o/\rho}$)
- $\frac{v}{U_\infty}$ = time-averaged velocity in y -direction
- $v'T'$ = turbulent heat flux
- x = distance measured in direction of mean flow
- y = distance measured in direction normal to mean flow
- y^+ = distance from wall in wall coordinates (yu^*/ν)
- α = thermal diffusivity
- δ = velocity boundary layer thickness
- ν = kinematic viscosity coefficient
- ρ = density
- τ_o = wall shear stress

Introduction

The turbulent Prandtl number (Pr_t) is defined as the ratio of eddy diffusivity of momentum (ϵ_M) to eddy diffusivity of heat (ϵ_H). Various assumptions have been made about the turbulent Prandtl number and several expressions have been proposed in attempts to predict the mean temperature profile and the average heat transfer coefficient in the boundary layer (Bagheri et al., 1992). The turbulent Prandtl number was developed by analogy with its molecular counterpart (the Prandtl number, Pr) although it is normally considered to be largely a function of the type of flow rather than the fluid properties (Antonia and Kim, 1991). The simplest one of all attempts and analogies is the Reynolds analogy which implies a turbulent Prandtl number of unity (Bagheri et al., 1992).

Since the 1950s, many researchers have been studying the dependence and behavior of the turbulent Prandtl number, both experimentally and analytically, mainly for the case of wall flows. Despite these past efforts, uncertainty remains. The first to propose

¹ Graduate Student. Currently with UNICAMP-FEM-Campinas SP, Brazil 13081 970.

² Associate Professor of UNIT-Centro Universitario do Triangulo, Uberlandia MD, Brazil 38400 000.

³ Associate Professor of Department of Mechanical Engineering, Universidade Federal de Uberlandia, Uberlandia MG, Brazil 38400 902.

Contributed by the Heat Transfer Division for publication in the JOURNAL OF HEAT TRANSFER. Manuscript received by the Heat Transfer Division, Aug. 6, 1997; revision received, Dec. 1, 1998. Keywords: Boundary Layer, Forced Convection, Heat Transfer, Turbulent. Associate Technical Editor: R. Boyd.

Comparative Analysis of Different Models for the Turbulent Prandtl Number

M. C. Silva¹, L. C. De Lima², and R. F. Miranda³

$$\text{Case 2: } \frac{\mu c_p}{k}, \frac{\rho_i^2 R_c^3 g}{\mu^2}, \frac{T_e R}{R_c g}, \frac{q_s R}{k g}$$

$$\text{Case 3: } \frac{\mu c_p}{k}, \frac{\rho_i^2 R_c^3 g}{\mu^2}, \frac{T_e R}{R_c g}, \frac{T_a R \cos \phi}{R_c g}$$

In each case pressure was substituted by the ideal gas law, with the temperature defined at the enclosure wall to define a reference density, so that the groups have a similar format to the Grashof number. The relative ease with which any type of boundary condition may be analyzed is clear.

In case 1, for example, any nondimensional dependent variable, ψ^* , may be written as

$$f(\psi^*, \text{Pr}, \text{Gr}_m, T_e^*, T_s^*, x^*, y^*) = 0, \quad (7)$$

where

$$T_s^* = \frac{T_s R}{R_c g} \quad \text{and} \quad T_e^* = \frac{T_e R}{R_c g},$$

and Gr_m is the modified Grashof number expressed without temperatures, $(\rho_i^2 R_c^3 g / \mu^2)$. Taking a heat balance at the wall of the cylinder,

$$\text{Nu} = \frac{h R_c}{k} = - \frac{1}{(T_s^* - T_e^*)} \left[\frac{\partial T^*}{\partial r^*} \right]_{r=R_c} \quad (8)$$

Assuming that the temperature is the dependent variable in Eq. (7), and, that it can be written as an explicit function, then

$$\text{Nu} = g(\text{Pr}, \text{Gr}_m, T_e^*, T_s^*, \phi). \quad (9)$$

There is a reduction from ten parameters to six nondimensional groups. The surface mean Nusselt number is then

$$\bar{\text{Nu}} = g(\text{Pr}, \text{Gr}_m, T_e^*, T_s^*). \quad (10)$$

This shows that for fully compressible free convection, the Nusselt number is dependent upon the scaled absolute temperatures and the temperature difference, as arises from the Boussinesq approximation. It is known that in air free convection this approximation breaks down at modest temperature differences, approximately 25 K. Greater accuracy in data correlation will therefore be found if the above parameters are used in place of the traditional Grashof and Prandtl description.

This example illustrates the utility of the described method. It is applicable to all systems described by known equations with known boundary conditions. The authors will publish many such examples in the future.

Acknowledgments

The authors would like to thank PEI Technologies for the financial support for this research.

References

- Buckingham, E., 1914, "On Physically Similar Systems: Illustrations on the Use of Dimensional Equations," *Physics Review*, Vol. 8, No. 4, pp. 345-376.
- Dalton, T., and Davies, M. R. D., 1997, "Convection Dimensional Analysis," ASME HTD-Vol. 346, pp. 33-39.
- Ehrenfest-Afanassjewa, T., 1916, "Der Dimensionsbegriff und der Analytische Bau Physikalischer Gleichungen," *Math. Anal.*, Vol. 27, pp. 259-278.
- Esnault-Pelterie, R., 1950, *Dimensional Analysis and Metrology*, F. Rouge & Co. Lausanne.
- Fourier, J., 1822, *Analytical Theory of Heat* (translation by A. Freeman, 1878, Cambridge).
- Rayleigh, Lord, 1877, *Theory of Sound*, 1st Ed., Macmillan and Co., London, p. 280.
- Ruark, A. E., 1935, "Inspectional Analysis: A Method which Supplements Dimensional Analysis," *Journal of the Mitchell Society*, Vol. 51, pp. 127-133.
- Shames, I., 1992, *Mechanics of Fluids*, 3rd Ed., McGraw-Hill, New York, p. 310.
- White, F. M., 1994, *Fluid Mechanics*, 3rd Ed., McGraw-Hill, New York, p. 254.

Nomenclature

- c_p = specific heat at constant pressure
- c_f = friction coefficient, $2\tau_o/(\rho U_\infty^2)$
- k = molecular thermal conductivity
- k_m, k_H = mixing-length constants for momentum and heat, respectively (Eq. 15)
- Pr = Prandtl number (ν/α)
- q_w = wall heat flux
- Re = Reynolds number ($U_\infty x/\nu$)
- St = local Stanton number = $q_w/\rho c_p U_\infty (T_w - T_\infty)$
- T = time-averaged temperature
- T_∞ = temperature of free stream
- T_w = temperature at wall surface
- $\frac{u}{U_\infty}$ = time-averaged velocity in x -direction
- $u'v'$ = turbulent shear stress
- u^+ = mean velocity in wall coordinates (u/u^*)
- U_∞ = velocity at outer edge of boundary layer
- u^* = shear velocity ($\sqrt{\tau_o/\rho}$)
- $\frac{v}{U_\infty}$ = time-averaged velocity in y -direction
- $v'T'$ = turbulent heat flux
- x = distance measured in direction of mean flow
- y = distance measured in direction normal to mean flow
- y^+ = distance from wall in wall coordinates (yu^*/ν)
- α = thermal diffusivity
- δ = velocity boundary layer thickness
- ν = kinematic viscosity coefficient
- ρ = density
- τ_o = wall shear stress

Introduction

The turbulent Prandtl number (Pr_t) is defined as the ratio of eddy diffusivity of momentum (ϵ_M) to eddy diffusivity of heat (ϵ_H). Various assumptions have been made about the turbulent Prandtl number and several expressions have been proposed in attempts to predict the mean temperature profile and the average heat transfer coefficient in the boundary layer (Bagheri et al., 1992). The turbulent Prandtl number was developed by analogy with its molecular counterpart (the Prandtl number, Pr) although it is normally considered to be largely a function of the type of flow rather than the fluid properties (Antonia and Kim, 1991). The simplest one of all attempts and analogies is the Reynolds analogy which implies a turbulent Prandtl number of unity (Bagheri et al., 1992).

Since the 1950s, many researchers have been studying the dependence and behavior of the turbulent Prandtl number, both experimentally and analytically, mainly for the case of wall flows. Despite these past efforts, uncertainty remains. The first to propose

¹ Graduate Student. Currently with UNICAMP-FEM-Campinas SP, Brazil 13081 970.

² Associate Professor of UNIT-Centro Universitario do Triangulo, Uberlandia MD, Brazil 38400 000.

³ Associate Professor of Department of Mechanical Engineering, Universidade Federal de Uberlandia, Uberlandia MG, Brazil 38400 902.

Contributed by the Heat Transfer Division for publication in the JOURNAL OF HEAT TRANSFER. Manuscript received by the Heat Transfer Division, Aug. 6, 1997; revision received, Dec. 1, 1998. Keywords: Boundary Layer, Forced Convection, Heat Transfer, Turbulent. Associate Technical Editor: R. Boyd.

a modification of the Reynolds analogy was Jenkins (Cebeci, 1973) who considered the motion of a spherical element of fluid across a flow. During the time of flight, it would lose heat by simple conduction and its surface temperature would vary linearly with the time of motion. Using the formula for the average temperature of a sphere, Jenkins obtained an expression for ϵ_H , combined it with an expression of ϵ_M and used it to model Pr_t . Because the predictions of Jenkins were too high in comparison with experiments, various researchers modified his model but in principle maintained the basic idea. Some of them were Deissler and Sleicher and Tribus (Reynolds, 1975).

As highlighted by Antonia and Kim (1991) there was still significant confusion about the manner in which Pr_t varied across a turbulent boundary layer. However, the review of Reynolds (1975) on different analytical ways of predicting Pr_t , the measurements by Blom (1970), Fulachier et al. (cited by Hammond, 1985), Blackwell et al. (cited by Kays, 1974), Sniijders et al. (1983), and more recently the survey of Kays (1994) on the available experimental data on Pr_t have helped to clarify even more its behavior.

The objective of this note is to compare with experiment the predictions of different models for Pr_t in a flat-plate zero-pressure gradient air boundary layer.

Governing Equations

For a steady two-dimensional constant property turbulent air boundary layer over a flat plate with negligible body force, negligible viscous dissipation, and no pressure gradient, the governing equations can be expressed as follows:

Continuity Equation.

$$\frac{\partial u}{\partial x} + \frac{\partial v}{\partial y} = 0 \quad (1)$$

Momentum Equation.

$$u \frac{\partial u}{\partial x} + v \frac{\partial u}{\partial y} = \frac{\partial}{\partial y} \left[(\nu + \epsilon_M) \frac{\partial u}{\partial y} \right] \quad (2)$$

Energy Equation.

$$u \frac{\partial T}{\partial x} + v \frac{\partial T}{\partial y} = \frac{\partial}{\partial y} \left[(\alpha + \epsilon_H) \frac{\partial T}{\partial y} \right] \quad (3)$$

and the definition of the turbulent Prandtl number is

$$Pr_t = \frac{\epsilon_M}{\epsilon_H} = \frac{\overline{u'v'(\partial T/\partial y)}}{\overline{v'T'(\partial U/\partial y)}} \quad (4)$$

Substituting for ϵ_H in Eq. (3) and after slightly rearranging, the energy equation becomes

$$u \frac{\partial T}{\partial x} + v \frac{\partial T}{\partial y} = \frac{\partial}{\partial y} \left\{ \nu \left[\frac{1}{Pr} + \frac{\epsilon_M/\nu}{Pr_t} \right] \frac{\partial T}{\partial y} \right\} \quad (5)$$

The conservation of mass and momentum Eqs. (1)–(3) requires specification of the velocity components at the wall and at the free stream. That is,

$$\begin{aligned} y = 0: & \quad u = 0, \quad v = 0 \\ y \rightarrow \infty: & \quad u = U_\infty, \quad v = 0. \end{aligned} \quad (6)$$

Doing the same for the thermal energy equation requires specification of the temperature at the wall and in the free stream:

$$\begin{aligned} y = 0: & \quad T = T_w \\ y \rightarrow \infty: & \quad T = T_\infty. \end{aligned} \quad (7)$$

In order to solve Eqs. (1), (2), and (5) with their corresponding boundary conditions, a turbulence model has to be introduced to

evaluate the eddy quantities ϵ_M and ϵ_H and consequently the turbulent Prandtl number Pr_t .

After Chyou (1991), the theory of turbulent wall shear layers is still in a state of intense study, and new breakthroughs are continually in sight. But the simplest of all the schemes proposed remains the very old Prandtl mixing-length model, and with new information available on the very important behavior of the viscous sublayer, the mixing-layer model provides a remarkably adequate basis for many engineering applications especially for some simple flow patterns. The following calculations were based on this turbulence model:

$$\epsilon_M = \iota^2 |\partial u / \partial y|. \quad (8)$$

To evaluate the mixing length ι , the outer region of the boundary layer and the near wall region must be considered separately. Still, after Chyou (1991) and for flows remote from walls, ι is usually taken as uniform across the layer and proportional to the thickness of the layer. For a boundary layer on a wall, the variation of ι in the outer part is similar to that in free turbulent flows, but ι is proportional to the distance from the wall for the near-wall region. The coefficient of proportionality between the Prandtl mixing-length ι and the thickness of the layer is normally the Von Karman constant $K = 0.41$, that is $\iota = 0.41y$.

However for the region close to the wall and the viscous sublayer, Eq. (8) needs to be modified. The Van Driest's hypothesis was applied to the wall region as

$$\iota = 0.41y[1 - \exp(-y^+/A^+)] \quad (9)$$

where $A^+ = 26$ (the Van Driest's constant) and y^+ a dimensionless distance defined as $y^+ = y(\tau_w/\rho)^{1/2}/\nu$.

The eddy-viscosity expression based on Prandtl's mixing length modified by Van Driest for the inner viscous sublayer will be

$$\epsilon_{Mi} = 0.16y^2[1 - \exp(-y^+/A^+)]^2 |\partial u / \partial y|. \quad (10)$$

For the outer region, the eddy-viscosity expression is given by

$$\epsilon_{Mo} = 0.0168U_\infty \delta^* \gamma \quad (11)$$

where γ is the Klebanoff's intermittence factor under the formula

$$\gamma = [1 + 5.5(y/\delta)^6]^{-1} \quad (12)$$

and δ^* the boundary layer displacement thickness defined as

$$\delta^* = \int_0^\infty \left(1 - \frac{u}{U_\infty} \right) dy. \quad (13)$$

The limit between both regions is determined by the condition where $\epsilon_{Mi} = \epsilon_{Mo}$.

Equations (1), (2), and (5) were numerically discretized and solved by a Tri-Diagonal Matrix Algorithm Method as outlined by Pereira Filho (1974) and De Lima (1992). In the numerical analysis, the velocities u and v and the temperature T are nondimensionalized by (u/U_∞) , (v/U_∞) and $[(T - T_\infty)/(T_w - T_\infty)]$, respectively. x and y are nondimensionalized by $\xi(x) = \int_0^x (U_\infty/\nu) dx$ and $\eta(x, y) = y(U_\infty/\nu(2\xi)^n)$, respectively. The finite difference equations used a variable grid in the η -direction which permits shorter steps close to the wall and longer steps away from the wall (Cebeci, 1970). The grid has the property that the ratio of lengths of any two adjacent intervals is a constant; that is, $\Delta\eta_j = B\Delta\eta_{j-1}$. The distance to the j th grid line is given by the following formula:

$$\eta_j = \eta_1 \frac{K^j - 1}{K - 1} \quad j = 0, 1, 2, 3, \dots, N, \quad (14)$$

where η_1 is the length of the first step, and K the ratio of two successive steps and are chosen as 10^{-5} and 1.03, respectively. The computer program used in this study has a capacity of 300 points

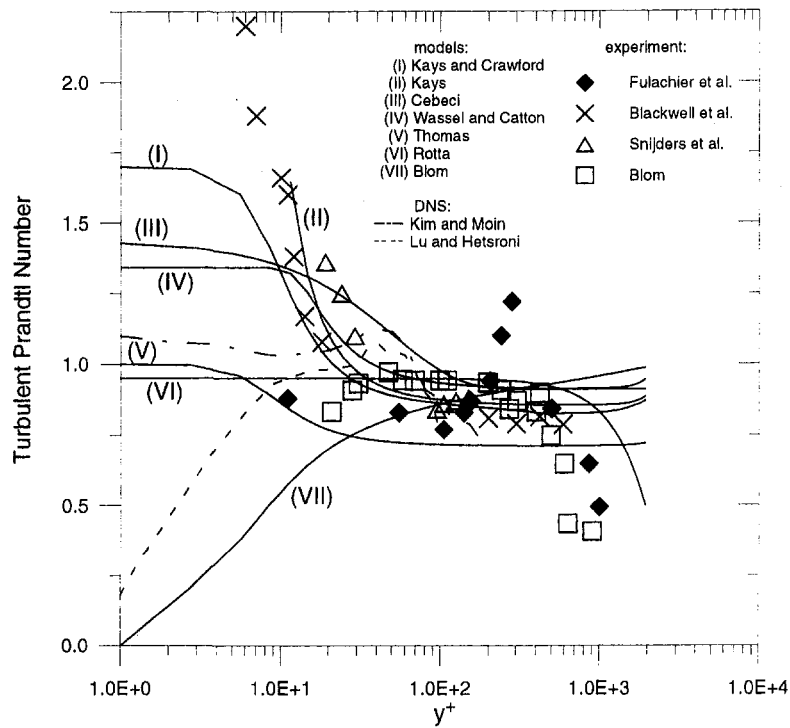


Fig. 1 Experimental and calculated turbulent Prandtl number

in the η -direction. In the ξ -direction, there is no restriction on the number of steps. The numerical procedure is repeated until the maximum relative change of all the variables over the entire fields on iterations satisfies a convergence criterion of 10^{-4} . The computations were performed on a IBM 3090 computer and it took three seconds of CPU time per step in the ξ -direction.

The calculations were started with an initial velocity profile based on the concept of friction velocity and the logarithmic laws of the wall. Since the velocity and temperature profiles are decoupled for nonbuoyant flows, velocity fields were solved first. Thereafter the temperature field was solved with an initial one-seventh profile.

Analyses of Experimental Data and Models for Pr_t

Figure 1 presents a series of experimental data for Pr_t , taken from different authors (Hammond, 1985). All experiments were for air flows over a flat plate. The experimental data of Blackwell et al. show that the turbulent Prandtl number goes to values greater than one when $y^+ < 30$. The region where $y^+ < 30$ is identified as the viscous sublayer region, and it is noticeable that data of Snijders et al. (1983) for that region shows the same behavior as that of Blackwell et al. However, some experimental points of Fulachier and Blom (1970) do not show this same behavior and this could be attributed to experimental uncertainty. It is difficult to obtain reliable measurements of $\overline{u'v'}$ and $\overline{v'T'}$ in the near wall region and this is reflected in the relatively large scatter in published measurements of Pr_t in that region. Notwithstanding, it is possible to observe that the trend of the turbulent Prandtl number in the sublayer region is pointing to a value greater than 1.

In the region $30 < y^+ < 200$, all experimental data show a trend where the average turbulent Prandtl number seems to be around 0.9. This would be the most probable value of Pr_t in the log-law region where the experimentalists' results have the least uncertainty. For example, Snijders et al. (1983) determined that for the region $30 < y^+ < 100$ the value found for Pr_t is 0.9 ± 0.1 ; and in the extended range of $30 < y^+ < 300$, the turbulent Prandtl number would be 0.86. Even considering Pr_t constant and 0.9 in that region, there is an uncertainty estimated by Snijders of

about 11 percent. This emphasizes even more the complex nature of Pr_t , as compared to its values in the log-law region where almost all the experimental data of Pr_t converge to a constant value.

The region $y^+ > 300$ is identified as the wake region; and as can be seen in Fig. 1, the influence of the free-stream conditions is felt and Pr_t differs from its log-law value. As verified in the sublayer region, experimental data in the wake region is somewhat divergent. For example, while data of Snijders et al. point to Pr_t as being greater than 1.0 in that region, other experimental data by Blom, and by Fulachier et al., indicate that Pr_t approaches values smaller than 0.5 for y^+ close to 1000. Chambers et al. (1985) reported that Fiedler investigated a slightly heated two-dimensional shear layer and observed that the transport of heat was primarily due to a large scale vortical motion; and a value of Pr_t of about 0.3 in the almost fully turbulence region of this flow can be inferred. Chambers et al. (1985) affirm also that the wake region can be identified with a large spectral coherence, having a close similarity between spectra of the lateral velocity fluctuation and of temperature and, a small value, typically about 0.4 for Pr_t , can be inferred either from measurements or from calculations based on self-preserving mean velocity and mean temperature distributions. Speculatively they affirm that an inverse relationship may exist between parameters such as Pr_t and the coherence of the flow. Bagheri et al. (1992) measured Pr_t and space-time temperature correlation in an incompressible turbulent boundary layer air flow over a heated flat plate at zero pressure gradient for three different temperature difference cases. For the wake region they concluded that Pr_t gradually decreases to a value of about 0.6 ± 0.05 close the boundary layer edge. This region is characterized by a high intensity of turbulence, high thermal diffusivity, high degree of organization of the mixing layer as in jet flow and in the central part of pipe flow. So it might be reasonable to consider that in the wake region, Pr_t will approach 0.5 when y^+ is close to 1000.

Now, consideration will be given to various analytical models of Pr_t , as depicted in Fig. 1. Cebeci (1973) proposed a model for Pr_t , which is dependent upon the distance of the wall and it is as follows:

$$\text{Pr}_t = \frac{k_m [1 - \exp(-y^+/A^+)]}{k_H [1 - \exp(-y^+/B^+)]} \quad (15)$$

where $k_m = 0.4$, $k_H = 0.44$, $A^+ = 26$ and B^+ is given by the following equation:

$$B^+ = \frac{1}{\sqrt{\text{Pr}}} \sum_{i=1}^5 C_i (\log_{10} \text{Pr})^{i-1}, \quad (16)$$

being $C_1 = 34.96$, $C_2 = 28.79$, $C_3 = 33.95$, $C_4 = 6.33$, and $C_5 = -1.186$, as suggested by Na and Habib (Cebeci, 1973).

Cebeci's model indicates that close to the wall Pr_t increases as the wall is approached and remains constant (≈ 1.4) within the viscous sublayer. In the range when $y^+ > 100$, Pr_t calculated by Cebeci's model fall to about 0.9 until $y^+ = 1000$.

Based on experimental data, Kays and Crawford (Kays, 1994) suggested the following expression for the turbulent Prandtl number:

$$\text{Pr}_t = \left\{ 0.5882 + 0.228(\epsilon_M/\nu) - 0.0441(\epsilon_M/\nu)^2 \left[1 - \exp\left(\frac{-5.165}{(\epsilon_M/\nu)}\right) \right] \right\}^{-1} \quad (17)$$

At the wall, Eq. (17) gives a value of about 1.7 and having a sharp decrease where $y^+ = 6$. For $y^+ > 30$ and extending to the edge of the boundary layer, Eq. (17) gives a value of Pr_t close to 0.85. As can be seen in that equation, the model of Kays and Crawford depends exclusively on ϵ_M/ν . This model follows closely the experimental data in the log-law region. However, it does not follow the trend of the experimental data in the "wake" region. In the viscous sublayer the model of Kays and Crawford follow data of Blackwell et al. mainly when $y^+ > 10$.

Wassel and Catton (1973) have proposed an expression for Pr_t which is also dependent on ϵ_M/ν . Their expression is

$$\text{Pr}_t = \frac{C_3 \left[1 - \exp\left(\frac{-C_4}{(\epsilon_M/\nu)}\right) \right]}{C_1 \text{Pr} \left[1 - \exp\left(\frac{-C_2}{\text{Pr}(\epsilon_M/\nu)}\right) \right]} \quad (18)$$

where $C_1 = 0.21$; $C_2 = 5.25$; $C_3 = 0.20$ and $C_4 = 5.0$. Their model shows constancy of Pr_t (≈ 1.3) within the viscous sublayer ($y^+ < 10$) as can be seen in Fig. 1. In the range $10 < y^+ < 30$, their expression sharply falls to about 1.0. When $y^+ > 30$, Eq. (18) maintains $\text{Pr}_t = 0.9$ until the edge of the boundary layer.

Blom (1970) presented an expression for Pr_t which is dependent on the "wall" velocity u^+ , under the following form:

$$\text{Pr}_t = 1 - \frac{x^4/24}{e^x - 1 - x - x^2/2 - x^3/6} \quad (19)$$

where $x = 0.4u^+$.

The expression of Blom, as depicted in Fig. 1, shows that Pr_t increases with y^+ . There is a sharp rise until $y^+ = 30$ and an attenuated rise when $y^+ > 30$. It is interesting to observe that the model of Blom does not show the same trend as his experimental data on Pr_t does; i.e., in his model there is no presence of constant Pr_t on the log-law region which is basically common to all analytical models and experimental data dealt with in this study.

A very simple model was proposed by Kays (1994) and it is shown in the Fig. 1. The expression for his model is

$$\text{Pr}_t = 0.7/[\text{Pr}(\epsilon_M/\nu)] + 0.85. \quad (20)$$

As can be verified in Fig. 1, the model proposed by Kays follows closely the experimental data of Blackwell et al. in the range $10 < y^+ < 300$ and in the "wake" region ($y^+ > 300$). It maintains a value around 0.9 until the edge of the boundary layer.

Thomas (cited by Reynolds, 1975) proposed a model for Pr_t which is dependent of Pr , ϵ_M/ν , y^+ , and c_f (friction coefficient). His model is given by

$$\text{Pr}_t = \frac{\text{Pr} + (\nu/\epsilon_M) \cdot \exp\left[-\left(\text{Pr} \frac{1}{2} c_f\right)^2 y^+\right]}{1 + (\nu + \epsilon_M) \exp\left[-\left(\frac{1}{2} c_f\right)^2 y^+\right]} \quad (21)$$

where $c_f = \tau_w/(\rho U_\tau^2/2)$. As plotted in Fig. 1, the model of Thomas gives a value of one to Pr_t for $y^+ < 5$, thus applying Reynolds analogy near the wall. In the range $5 < y^+ < 30$, his model leads Pr_t to the value of 0.7 and maintain that value until the edge of the boundary layer. It is interesting to observe that the model of Thomas was the only one which diverged from the well-recognized mean value (0.9) of Pr_t in log-law region.

Rotta (cited by Wassel and Catton, 1973) suggested an expression for Pr_t as a function exclusively of the coordinate y and the boundary layer thickness δ . The model of Rotta is given by

$$\text{Pr}_t = 0.95 - 0.45(y/\delta)^2. \quad (22)$$

Although the model of Rotta was suggested for the outer region ($y/\delta > 0.1$), many authors extended his model to the wall. As can be seen in Fig. 1, the model of Rotta gives a value of 0.95 to Pr_t until the beginning of the wake region ($y^+ = 300$); and in the wake region, Pr_t decreases to 0.5 when $y^+ \approx 2000$. The model of Rotta is the only one which followed the trend of the experimental data of decreasing to 0.5 at the edge of the boundary layer ($y^+ \approx 1000$) although phased to $y^+ = 2000$.

Lu and Hetsroni (1995) performed direct numerical simulation (DNS) in a turbulent open-channel flow with passive heat transfer, and their results are shown in Fig. 1. It is known in the literature that DNS simulation demands supercomputers, grid with fine resolution and long time of computation when compared to conventional finite difference methods. Results of Lu and Hetsroni for Pr_t are restricted to $y^+ < 100$. They demonstrated that the turbulent Prandtl number close to the wall is smaller than one, being 0.2 at the wall; and in the range $10 < y^+ < 100$, their results follow other DNS investigations as, for example, results of Antonia and Kim (1991) and Kim and Moin (1989). To our knowledge, the only model for Pr_t which show such behavior is that of Blom. Even more interesting to observe is that most of the published experimental data on Pr_t , for the sublayer region, point to values greater than one. The results of DNS simulation performed by Kim and Moin and results by Lu and Hetsroni show a peak of Pr_t around $y^+ = 40$. Such a peak was not observed in any experimental data studied in this note.

There is a common understanding (Kays, 1994) that DNS calculations are probably more accurate in the region near the wall than the experimental data. In fact, Antonia and Kim (1991), performing direct numerical simulations of a slightly heated fully developed turbulent channel flow, indicated that Pr_t approaches a constant (≈ 1) at the wall, independently of Pr . They affirmed that the maintenance of this value over most of the wall region (at least for $\text{Pr} = 0.71$) suggests a very close similarity between momentum and heat transfer mechanisms in the wall region. With exception of the calculations of Lu and Hetsroni, all available DNS data reveal the same behavior of Pr_t , as observed by Antonia and Kim and thus indicates the very simple behavior of Pr_t near the wall. This observation could lead us to the conclusion that close to wall, i.e. in the viscous sublayer the application of the Reynolds analogy would not be so far from the true behavior of the turbulent Prandtl number.

The same argument would not be valid for the log-law region. Experimental data for that region converge to the constant value of 0.9 while DNS calculations converge to a smaller value than 0.9. The trend of experimental data for that is more plausible, then in the range $30 < y^+ < 200$ there is the smallest uncertainty of measurement.

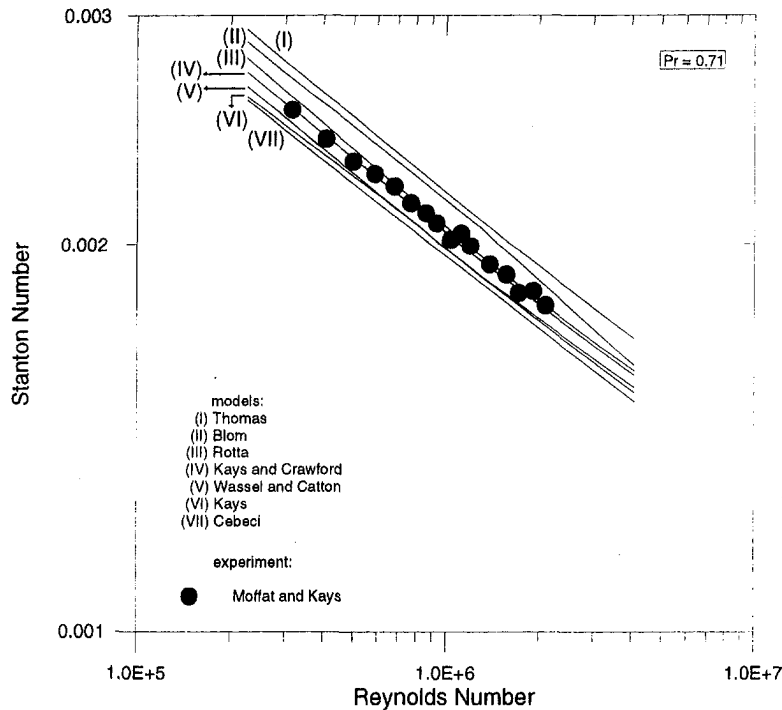


Fig. 2 Experimental and calculated Stanton number

In order to make a comparative analysis of the different models for Pr , presented in the present note, the local Stanton number was calculated for the simple case of zero pressure gradient turbulent air flow over a flat plate.

Figure 2 compares calculated local Stanton numbers with experimental data as a function of the local Reynolds number for every Pr , model studied. The experimental data of Moffat and Kays were used.

As can be seen in Fig. 2, Kays' and Crawford's model, and Rottas's model gave results coincident with the experimental data. Models by Kays and Wassel and Catton presented practically the same deviation (-6 percent) of the calculated local Stanton number. Deviation of the Cebeci's model was about seven percent lower than experimental points. On the other hand, the Blom's model and the Thomas' model presented deviation of seven percent and eight percent, respectively, above than the experimental data.

Conclusions

In the present technical note, different models for the turbulent Prandtl number were studied and compared with experimental data of a flat-plate zero-pressure-gradient air boundary layer. It was verified that despite discrepancies in Pr , shown by almost all models and experimental data at mainly to the near wall region and in the "wake" region of the boundary layer, predictions of the local Stanton number were within the uncertainty envelope of experimental data.

Acknowledgments

The authors thank the reviewers for creative suggestions and Ms. Maria das Graças Daud for manuscript preparation.

References

Antonia, R. A., and Kim, J., 1991, "Heat Transport in Near-Wall Region," *4th International Symposium on Transport Phenomena*, Sydney, Australia, July 14–19, pp. 1001–1009.

Bagheri, N., Stratiridakis, C. J., and White, B. R., 1992, "Measurements of Turbulent Boundary Layer Prandtl Number and Space-Time Temperature Correlations," *AIAA Journal*, Vol. 30, No. 1, pp. 35–42.

Blom, J., 1970, "Experimental Determination of the Turbulent Prandtl Number in a Developing Temperature Boundary Layer," *Proc. Fourth International Heat Transfer Conference*, Vol. II, Elsevier, Amsterdam, Paper FCC 2.2.

Cebeci, T., 1970, "Laminar and Turbulent Incompressible Boundary Layer on Slender Bodies of Revolution in Axial Flow," *ASME Journal of Basic Eng.*, Vol. 92, pp. 545–554.

Cebeci, T., 1973, "A Model for Eddy Conductivity and Turbulent Prandtl Number," *ASME JOURNAL OF HEAT TRANSFER*, Vol. 95C, pp. 227–234.

Chambers, A. J., Antonia, R. A., and Fulachier, L., 1985, "Turbulent Prandtl Number and Spectral Characteristics of a Turbulent Mixing Layer," *International Journal of Heat and Mass Transfer*, Vol. 28, No. 8, pp. 1461–1468.

Chyou, Y. P., 1991, "The Effect of a Short Unheated Length and a Concentrated Heat Source on the Heat Transfer Through a Turbulent Boundary Layer," *International Journal of Heat and Mass Transfer*, Vol. 34, No. 8, pp. 1917–1928.

De Lima, L. C., 1992, "Calculation of Turbulent Boundary Layer over a Flat Plate with Heat Transfer" (in Portuguese), *Ciência & Engenharia*, Vol. 1/2, pp. 7–25.

Hammond, G. P., 1985, "Turbulent Prandtl Number Within a Near-Wall Flow," *AIAA Journal*, Vol. 23, No. 11, pp. 1668–1669.

Kays, W. M., 1994, "Turbulent Prandtl Number—Where Are We?," *ASME JOURNAL OF HEAT TRANSFER*, Vol. 116, pp. 284–295.

Lu, D. M., and Hetsroni, G., 1995, "Direct Numerical Simulation of a Turbulent Open Channel Flow with Passive Heat Transfer," *International Journal of Heat and Mass Transfer*, Vol. 38, pp. 3241–3251.

Pereira Filho, H. V., 1974, "A four-equation Model for Numerical Solution of the Turbulent Boundary-Layer," Ph.D. dissertation, University of Houston, Houston, TX.

Reynolds, A. J., 1975, "The Prediction of Turbulent Prandtl and Schmidt Numbers," *International Journal of Heat and Mass Transfer*, Vol. 18, pp. 1055–1069.

Snijders, A. L., Koppius, A. M., and Nieuwvelt, C., 1983, "An Experimental Determination of the Turbulent Prandtl Number in the Inner Boundary Layer for Air Flow over a Flat Plate," *International Journal of Heat and Mass Transfer*, Vol. 26, No. 3, pp. 425–431.

Wassel, A. T., and Catton, I., 1973, "Calculation of Turbulent Boundary Layer Over Flat Plates with Different Phenomenological Theories of Turbulence and Variable Turbulent Prandtl Number," *International Journal of Heat and Mass Transfer*, Vol. 16, pp. 1547–1563.

Transient Thermal Analysis of a Translucent Thermal Barrier Coating on a Metal Wall

R. Siegel¹

Nomenclature

- a_c = absorption coefficient of coating in translucent spectral band, m^{-1}
 c_c, c_m = specific heats of translucent coating and metal, J/kg K
 C_{mc} = the property ratio, $\rho_m c_m / \rho_c c_c$
 D_c, D_m = thicknesses of translucent coating and metal, m
 $F(T)$ = fraction of blackbody radiation at T in the interval from $\lambda = 0$ to λ_{cu}
 g = Green's function for radiative heat source in translucent spectral band
 G = flux quantity in the two-flux method, W/m^2 ; $\tilde{G} = G/\sigma T_i^4$
 h_1, h_2 = convective heat transfer coefficients at $x_c = 0$ and $x_m = D_m$ (Fig. 1), W/m^2K
 H = dimensionless parameter, $h/\sigma T_i^3$
 k_c, k_m = thermal conductivities of coating and metal, $W/m K$
 n = refractive index of translucent coating
 N_c, N_m = conduction-radiation parameters (based on D_c), $k_c/4\sigma T_i^3 D_c, k_m/4\sigma T_i^3 D_c$
 P_i, P_m = the quantities, $2Ri/3\kappa_D, 2Rm/3\kappa_D$
 q_r = radiative flux in the x -direction, W/m^2 ; $\tilde{q}_r = q_r/\sigma T_i^4$
 q_{r1}, q_{r2} = external radiation fluxes σT_{s1}^4 and σT_{s2}^4 incident at $x_c = 0$ and $x_m = D_m$, W/m^2
 $\tilde{q}_{r1}, \tilde{q}_{r2}$ = dimensionless radiation fluxes, $q_{r1}/\sigma T_i^4$ and $q_{r2}/\sigma T_i^4$
 Ri, Ro = the quantities, $(1 + \rho^i)/(1 - \rho^i), (1 - \rho^o)/(1 - \rho^i)$
 Rm = the quantity, $(2 - \epsilon_{mi})/\epsilon_{mi}$
 T = absolute temperature, K
 t = dimensionless temperature, T/T_i
 T_c, T_m = temperatures in coating and substrate, K; $t_c = T_c/T_i, t_m = T_m/T_i$
 T_{g1}, T_{g2} = gas temperatures for convection at boundaries (Fig. 1), K
 t_{g1}, t_{g2} = dimensionless gas temperatures, T_{g1}/T_i and T_{g2}/T_i
 T_i = initial uniform temperature (used as a reference temperature), K
 T_{s1}, T_{s2} = temperatures of blackbody radiative surroundings at $x_c = 0$ and $x_m = D_m$, K
 x_c, x_m = coordinates in coating and substrate (Fig. 1), m ; $X_c = x_c/D_c, X_m = x_m/D_c$

Greek Symbols

- $\epsilon_{mi}, \epsilon_{mo}$ = emissivities of metal at inner and outer surfaces, Fig. 1
 θ = time, s
 κ_D = optical thickness of coating in translucent band, $(a_c + \sigma_{sc})D_c$
 λ, λ_{cu} = wavelength and cutoff wavelength, μm
 ρ_c, ρ_m = densities of translucent coating and metal, kg/m^3

- ρ^o, ρ^i = external and internal reflectivities at a translucent boundary
 σ = Stefan-Boltzmann constant, W/m^2K^4
 σ_{sc} = scattering coefficient in translucent coating, m^{-1}
 τ = dimensionless time, $(4\sigma T_i^3/\rho_c c_c D_c)\theta$
 Ω = scattering albedo of coating material, $\sigma_{sc}/(a_c + \sigma_{sc})$

Subscripts

- c = translucent coating
 g = gas
 j, k = grid points in coating and metal, $j = 0 \dots J, k = 0 \dots K$
 m = metal wall
 n = time increment

Introduction

A common ceramic used for thermal barrier coatings is zirconia, and it is partially transparent for radiative energy at wavelengths up to approximately $5 \mu m$ (Siegel and Spuckler, 1998). Hence, at elevated temperatures such as in a turbine engine combustor, the temperature distribution in a coating can be affected by absorption of incident radiation, by internal emission, and by scattering which is large for zirconia. Transient temperatures are needed for evaluating thermal stresses, and for translucent materials numerical procedures can be used to solve the transient energy equation coupled with radiative transfer relations. For radiation, both exact and approximate equations have been used. With general external conditions of convection and radiation for a translucent layer with diffuse surfaces, it was demonstrated in Siegel (1996) that the two-flux method compares well with more exact methods for predicting transient temperature distributions and heat fluxes, including large scattering as needed in a material such as zirconia. The two-flux differential equation for the internal radiative source is solved here with a Green's function as in Siegel (1997), including two-band spectral property variations for zirconia. Finite difference relations are developed for transient temperatures in a translucent coating on a metal substrate. Illustrative results for heating a coated wall in a turbine engine combustor demonstrate transient heating behavior with translucent effects as compared with an opaque coating.

Analysis

A translucent thermal barrier coating on an opaque wall is in Fig. 1; the coating is an absorbing dielectric that is heat conducting, has a refractive index larger than one, and is assumed isotropically scattering with diffuse boundaries. To begin a transient, each external boundary is exposed to radiative surroundings and to convection by a transparent gas. Transient temperature distributions are obtained using properties for zirconia, and results at steady-state are compared with independent calculations using the method in Siegel (1997). Zirconia has large scattering, and as discussed in Matthews, Viskanta, and Incropera (1985) it is forward scattering with about 75 percent of the scattered energy going in forward directions. This can be important if zirconia is subjected to a directed beam of radiation, but its effect is diminished by internal emission and internal reflections that tend to make the radiation isotropic. Since the properties of zirconia are not known to high accuracy, the effects of anisotropic scattering are not included here.

Energy Equation and Two-Flux Relations for Coating on Wall. The dimensionless energy equations for transient temperatures in the coating and opaque substrate for constant properties are, from Siegel and Howell (1992),

$$\frac{\partial t_c}{\partial \tau} = N_c \frac{\partial^2 t_c}{\partial X_c^2} - \frac{1}{4} \frac{\partial \tilde{q}_r}{\partial X_c}; \quad \frac{\partial t_m}{\partial \tau} = \frac{N_m}{C_{mc}} \frac{\partial^2 t_m}{\partial X_m^2} \quad (1a, b)$$

¹Research and Technology Directorate, NASA Lewis Research Center, 21000 Brookpark Road, Cleveland, OH 44135. e-mail: robert.siegel@lerc.nasa.gov. Life Fellow ASME.

Contributed by the Heat Transfer Division for publication in the JOURNAL OF HEAT TRANSFER. Manuscript received by the Heat Transfer Division, Aug. 8, 1998; revision received, Jan. 4, 1999. Keywords: Coatings, Heat Transfer, Radiation, Transient. Associate Technical Editor: M. P. Menguc.

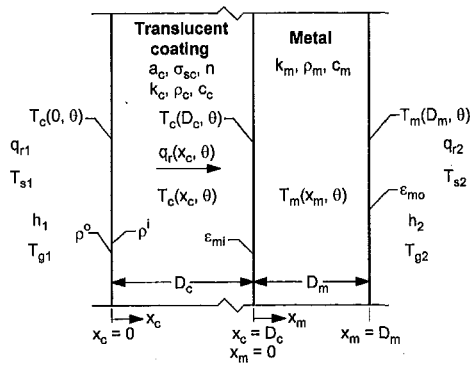


Fig. 1 Geometry and nomenclature for transient radiation and conduction in a translucent thermal barrier coating on an opaque metal wall with boundaries subjected to radiation and convection

The $-\left(\frac{1}{4}\right)\partial\bar{q}_r(X_c, \tau)/\partial X_c$ is the local heat source from radiation, and is obtained from two-flux relations in terms of $t_c(X_c, \tau)$ and surrounding radiative conditions. The two-flux equations are (Siegel, 1996)

$$\frac{\partial\bar{q}_r(X_c, \tau)}{\partial X_c} = \kappa_D(1 - \Omega)\{4n^2t_c^4(X_c, \tau)F[t_c(X_c, \tau)] - \tilde{G}(X_c, \tau)\} \quad (2a)$$

$$\frac{\partial\tilde{G}(X_c, \tau)}{\partial X_c} = -3\kappa_D\bar{q}_r(X_c, \tau). \quad (2b)$$

Boundary and Initial Conditions. For a two-band spectral model with one band opaque, the coating has internal radiant effects for $\lambda = 0$ to λ_{cu} , and has only surface reflection and emission for $\lambda > \lambda_{cu}$. Conduction, convection, and radiation at the exposed boundaries are then related by

$$-4N_c \left. \frac{\partial t_c}{\partial X_c} \right|_{X_c=0} = H_1[t_{g1} - t_c(0, \tau)] + (1 - \rho^o) \times \{t_{s1}^4[1 - F(t_{s1})] - t_c^4(0, \tau)[1 - F(t_c(0, \tau))]\} \quad (3a)$$

$$-4N_m \left. \frac{\partial t_m}{\partial X_m} \right|_{X_m=D_m/D_c} = H_2[t_m(D_m/D_c, \tau) - t_{g2}] + \epsilon_{mo}[t_m^4(D_m/D_c, \tau) - t_{s2}^4]. \quad (3b)$$

Considering incident and reflected fluxes at an interface and emission by the metal, radiative boundary relations were developed in Siegel (1997) for a translucent coating on an opaque substrate,

$$\tilde{G}(0, \tau) - \left. \frac{2Ri}{3\kappa_D} \frac{\partial\tilde{G}}{\partial X_c} \right|_{X_c=0} = 4Ro\bar{q}_r F(t_{s1}) \quad (4a)$$

$$\tilde{G}(1, \tau) + \left. \frac{2Rm}{3\kappa_D} \frac{\partial\tilde{G}}{\partial X_c} \right|_{X_c=1} = 4n^2t_c^4(1, \tau)F[t_c(1, \tau)]. \quad (4b)$$

The initial condition for the present results is a uniform temperature $T_c(x_c, 0) = T_m(x_m, 0) = T_i$.

Green's Function for $\partial\bar{q}_r(X, \tau)/\partial X$. By combining Eqs. (2a) and (2b), and defining $m = \kappa_D[3(1 - \Omega)]^{1/2}$, there is obtained

$$\frac{d^2\tilde{G}}{dX^2} - m^2\tilde{G}(X_c, \tau) = -4m^2n^2t_c^4(X_c, \tau)F[t_c(X_c, \tau)]. \quad (5)$$

In Siegel (1997) a Green's function was developed for Eq. (5) with the conditions in Eqs. (4),

$$g(X_c, \xi) = \begin{cases} \left[\frac{\sinh m(1 - \xi) + P_m m \cosh m(1 - \xi)}{(P_i + P_m)m \cosh m + (1 + P_i P_m m^2) \sinh m} \right] \times [\sinh mX_c + P_i m \cosh mX_c] & 0 \leq X_c < \xi \\ \left[\frac{\sinh m\xi + P_i m \cosh m\xi}{(P_i + P_m)m \cosh m + (1 + P_i P_m m^2) \sinh m} \right] \times [\sinh m(1 - X_c) + P_m m \cosh m(1 - X_c)] & \xi < X_c \leq 1. \end{cases} \quad (6)$$

The $g(X_c, \xi)$ accounts for the nonhomogeneous term in Eq. (5) for $\tilde{G}(X_c, \tau)$ at each time, and for the complete solution the homogeneous portion is (Siegel, 1997)

$$\tilde{G}h(X_c, \tau) = A(\tau) \cosh mX_c + B(\tau) \sinh mX_c \quad (7)$$

$$A(\tau) = \frac{4}{(P_i + P_m)m \cosh m + (1 + P_i P_m m^2) \sinh m} \times \{Ro[\sinh m + P_m m \cosh m]\bar{q}_r F(t_{s1}) + P_i m n^2 t_c^4(1, \tau)F[t_c(1, \tau)]\}$$

$$B(\tau) = \frac{A(\tau) - 4Ro\bar{q}_r F(t_{s1})}{P_i m}$$

The general solution of Eq. (5) at each time is then

$$\tilde{G}(X_c, \tau) = \tilde{G}h(X_c, \tau) + 4mn^2 \int_0^1 g(X_c, \xi) t_c^4(\xi, \tau) F[t_c(\xi, \tau)] d\xi. \quad (8)$$

Finite Difference Relations and Numerical Evaluation. Using the specified initial temperature, the radiative heat source in Eq. (1a) is found from Eq. (2a) by evaluating \tilde{G} from Eq. (8). Temperatures are then advanced $\Delta\tau$ with explicit finite difference relations. For interior points

$$t_{j,n+1} = t_{j,n} + \frac{N_c \Delta\tau}{\Delta X_c^2} (t_{j+1,n} - 2t_{j,n} + t_{j-1,n}) - \frac{\Delta\tau}{4} \left. \frac{\partial\bar{q}_r}{\partial X_c} \right|_{j,n} \quad (9a)$$

$$t_{k,n+1} = t_{k,n} + \frac{N_m \Delta\tau}{C_{mc} \Delta X_m^2} (t_{k+1,n} - 2t_{k,n} + t_{k-1,n}). \quad (9b)$$

These relations are applied at the external boundaries, and the conditions in Eqs. (3a, b) are used to eliminate the unknown external temperature on each side. At $X_c = 0$ where $j = 0$,

$$t_{j=0,n+1} = t_{j=0,n} + \frac{N_c \Delta\tau}{\Delta X_c^2} (t_{j=1,n} - 2t_{j=0,n} + t_{j=-1,n}) - \frac{\Delta\tau}{4} \left. \frac{\partial\bar{q}_r}{\partial X_c} \right|_{j=0,n} \quad (10a)$$

where $t_{j=-1,n}$ is found from the boundary condition Eq. (3a) as

$$t_{j=-1,n} = t_{j=1,n} + \frac{\Delta X_c}{2N_c} [H_1(t_{g1} - t_{j=0,n}) + (1 - \rho^o) \times \{t_{s1}^4[1 - F(t_{s1})] - t_{j=0,n}^4[1 - F(t_{j=0,n})]\}]. \quad (10b)$$

Similarly at $X_m = D_m/D_c$,

$$t_{K,n+1} = t_{K,n} + \frac{N_m \Delta\tau}{C_{mc} \Delta X_m^2} (t_{K+1,n} - 2t_{K,n} + t_{K-1,n}) \quad (10c)$$

where $t_{K+1,n}$ is found from

$$t_{K+1,n} = t_{K-1,n} - \frac{\Delta X_m}{2N_m} [H_2(t_{K,n} - t_{g2}) + \epsilon_{mo}(t_{K,n}^4 - t_{s2}^4)]. \quad (10d)$$

At the internal interface, where the coating and metal temperatures are equal, the relation includes heat conduction, radiative absorption, and emission at the metal surface as in Eq. (4b), and the volumetric radiative heat source in the coating half increment adjacent to the boundary,

$$t_{J,n+1} = t_{J,n} + \frac{2\Delta\tau}{\Delta X_c + C_{mc}\Delta X_m} \left\{ -\frac{N_c}{\Delta X_c} (t_{J,n} - t_{J-1,n}) + \frac{N_m}{\Delta X_m} (t_{k=1,n} - t_{k=0,n}) + \frac{1}{2Rm} \left[\frac{G_{J,n}}{4} - n^2 t_{J,n}^4 F(t_{J,n}) \right] - \frac{\Delta X_c}{32} \left[\frac{\partial \bar{q}_r}{\partial X_c} \right]_{J-1,n} + 3 \frac{\partial \bar{q}_r}{\partial X_c} \right\}. \quad (10e)$$

For stability an explicit method requires small time increments such as $\Delta\tau \approx 10^{-5}$ as estimated from the standard criterion for the heat conduction equation. With small $\Delta\tau$, the heat capacity caused the temperature changes to be small over an interval of several $\Delta\tau$; hence, to decrease computing time, very little accuracy was lost by reevaluating the radiative source after several time increments rather than at each time. Temperature gradients in the coating were larger than in the metal that has high conductivity. It was found that 20 spatial increments in the coating and five in the metal gave good accuracy as tested by reducing the increment size to one-half and the time-step size to one-quarter. If large gradients in temperature or radiative flux are found, a variable grid size can be used, but small grid sizes require a reduction in time increment to maintain stability in an explicit method. An overall heat balance was made at each time step to compare radiation and convection to the composite, with radiation from the composite and the change in its internal energy; the balance was within a few tenths of one percent using the finite difference relations given here.

Results and Discussion

An analytical and numerical procedure was developed to obtain the transient thermal response of a translucent protective coating on a metal wall, including large scattering in the coating as is characteristic of zirconia; the scattering was assumed isotropic. Radiative heating by absorption, emission, and scattering in the coating in the translucent spectral regions, was evaluated by solving a two-flux equation with a Green's function that incorporates the radiative boundary conditions. Explicit finite difference relations for the transient energy equation were derived to include radiative effects at the coating-metal interface, and at the external boundaries in the opaque spectral regions.

Temperatures in Fig. 2 show the transient response of a zirconia-coated metal wall to heating in a turbine engine combustor. Starting at 300 K, the wall was exposed to a 2000 K environment on the coated side, with the cooled side of the metal in 800 K surroundings. The combustion gases and soot were assumed to radiate with a blackbody spectrum, and two spectral bands were used, with zirconia translucent for wavelengths up to $5 \mu\text{m}$. The figure is in two parts to show detailed results, and the parameters are in the caption. The solid lines for a translucent coating are compared with dashed lines for an opaque coating that has internal heat conduction and radiation at its boundaries. Translucence reduces temperature gradients in the coating, and high thermal conductivity provides small gradients in the metal.

During the first few seconds, radiant penetration in the coating causes the metal to heat more rapidly, but the temperature of the

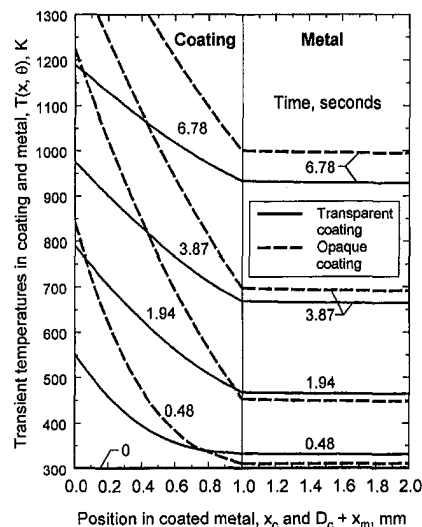


Fig. 2(a) Results for times, $\theta = 0$ to 6.78 s

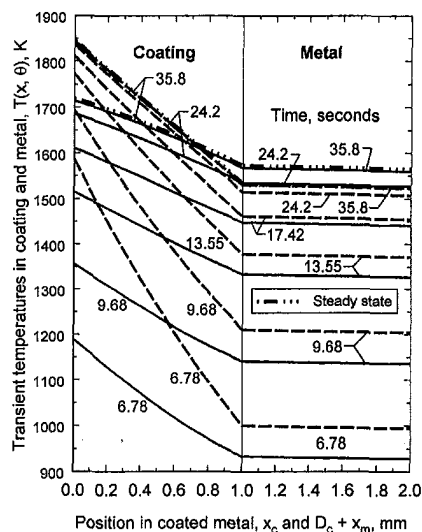


Fig. 2(b) Results for times, $\theta = 6.78$ s to steady state

Fig. 2 Transient temperatures in a zirconia thermal barrier coating on a metal wall following sudden heating in a combustor. Parameters (units are in the Nomenclature): $D_c = D_m = 1 \text{ mm}$, $k_c = 0.8$, $k_m = 33$, $c_c = 570$, $c_m = 460$, $\rho_c = 5200$, $\rho_m = 7800$, $n = 2$ ($\rho^l = 0.79015$, $\rho^o = 0.16060$), $\lambda_{cv} = 5$, $a_c = 30$, $\sigma_{sc} = 10000$, $\epsilon_{ml} = 0.6$ (bond coat), $\epsilon_{mo} = 0.6$ (oxidized), $h_1 = 250$, $h_2 = 110$, $T_1 = 300$, $T_{s1} = T_{g1} = 2000$, $T_{s2} = T_{g2} = 800$.

translucent external surface of the coating is lower than for an opaque coating where all energy absorption is at the surface. Scattering from within the coating shields against combustor radiation, and for the next 20 seconds the transient metal temperatures are below those for an opaque coating. As steady state is approached after about 30 seconds, the metal temperatures rise above those with an opaque coating, as translucence has degraded the steady-state insulating ability of the coating. Steady state is approached a little more slowly when the coating is translucent, and the final results agree with steady-state calculations using the method in Siegel (1997).

Conclusions

A method was developed combining a Green's function solution and finite differences to provide a transient thermal analysis of a translucent thermal barrier coating on a metal wall including isotropic scattering in the coating. For radiative heat-

ing in the coating, the two-flux equation was solved with a Green's function, and finite differences were used for the transient energy equation. The Green's function analytically incorporates the radiative reflective boundary conditions for the translucent spectral regions. Finite difference relations for the transient energy equation were derived to include radiative effects at the coating-metal interface, and at the external boundaries in the opaque spectral regions.

For heating by radiation and convection, transient temperatures for a translucent coating are compared with a coating without internal radiation effects, but with surface absorption and reflection. Translucence decreases the coating surface temperature and its temperature gradients, and thus reduces possible thermal stresses in the coating. Except for very early in the transient and near steady-state, the transient metal temperatures are lower when the coating is translucent; this is attributed to scattering away of incident radiation by the zirconia coating that has a high scattering albedo. At steady-state, translucence degrades the coating insulating ability and produces higher metal temperatures.

References

- Matthews, L. K., Viskanta, R., and Incropera, F. P., 1985, "Combined Conduction and Radiation Heat Transfer in Porous Materials Heated by Intense Solar Radiation," *ASME Journal of Solar Energy Engineering*, Vol. 107, pp. 29-34.
- Siegel, R., 1996, "Two-Flux and Green's Function Method for Transient Radiative Transfer in a Semitransparent Layer," Proceedings of the 1st International Symposium on Radiative Transfer, Kuşadasi, Turkey, *Radiative Transfer I*, Begell House, New York, pp. 473-487.
- Siegel, R., 1997, "Green's Function to Determine Temperature Distribution in a Semitransparent Thermal Barrier Coating," *Journal of Thermophysics and Heat Transfer*, Vol. 11, No. 4, pp. 315-318.
- Siegel, R., and Howell, J. R., 1992, *Thermal Radiation Heat Transfer*, 3rd Ed., Hemisphere, Washington, DC, pp. 691-695.
- Siegel, R., and Spuckler, C. M., 1998, "Analysis of Thermal Radiation Effects on Temperatures in Turbine Engine Thermal Barrier Coatings," *Materials Science and Engineering*, Vol. A245, pp. 150-159.

Inverse Analysis of Radiative Heat Transfer Systems

M. R. Jones¹

The design of heat transfer systems in which radiation is the dominant heat transfer mode is an important industrial problem. Compared to the conventional forward approach, the inverse approach allows a more thorough analysis of a potential design. This note demonstrates that inverse methods can be powerful tools in the analysis of radiative heat transfer systems.

Nomenclature

- d = diameter of the heating element
 F = view factor
 h = distance from the oven centerline to the first edge of the strips
 J = radiosity

¹ Assistant Professor, Department of Aerospace and Mechanical Engineering, The University of Arizona, P. O. Box 210119, Tucson, AZ 85721. e-mail: jones@ame.arizona.edu. Assoc. Mem. ASME.

Contributed by the Heat Transfer Division for publication in the JOURNAL OF HEAT TRANSFER and presented at '97 NHTC, Baltimore. Manuscript received by the Heat Transfer Division, Dec. 8, 1997; revision received Dec. 1, 1998. Keywords: Heat Transfer, Inverse, Radiation. Associate Technical Editor: P. Menguc.

- l = distance between the metallic strips and the heating element
 L = length of the oven walls
 N = total number of surfaces
 q'' = heat flux
 T = temperature
 w = width of the metallic strips

Greek Symbols

- ε = emissivity
 σ = Stefan-Boltzmann constant

Subscripts

- d = design
 h = heating element
 s = metallic strip
 w = wall

Introduction

Optimizing the design of radiative heat transfer systems is a significant problem in many manufacturing and materials processing applications (Bergman and Viskanta, 1996). In general, the design objective is to develop a system that will produce a specified heat flux or temperature distribution on the material processing surface. Traditionally, engineers have employed a forward or direct approach in the analysis and optimization of potential designs. In the forward approach, a designer seeks to determine the result based on knowledge of the cause. That is, the designer posits a model in which the properties, boundary conditions, and source terms are all known. Based on these assumptions, the designer calculates the temperature and/or heat flux distributions on the material processing surface and refines the design in an iterative manner until the desired result is achieved. However, the design objective is often the determination of one or more of the system's properties, boundary conditions or source terms, so these parameters are generally not all known a priori. Design engineers usually know the desired result and are seeking the optimal design to achieve that result, so the steps required by the forward approach proceed in the opposite direction as the natural design process.

A more logical and powerful method is to use an inverse approach. In the inverse approach, the designer seeks to determine the cause based on observable results. The following analysis of a simplified oven design problem illustrates the utility of an inverse approach by comparing it to the forward approach. The results of this simple analysis demonstrate that inverse methods can be powerful tools in the analysis of radiant heat transfer systems.

Forward Analysis

To facilitate the comparison between a forward analysis and an inverse analysis, consider the following problem. The design of an oven that will be used to cure the coatings on long metallic strips by heating the strips to the design temperature T_d is to be developed. The basic design of the oven is shown in Fig. 1, and the overall dimensions of the oven, the diameter of the heating element, and the width of the metallic strips are specified. The operating temperature and power output of the cylindrical heating element are known, and the walls are well insulated everywhere except for the openings through which the metallic strips are placed in the oven. The oven surfaces are assumed to be diffuse and gray, and the radiative surface properties of the heating element and the metallic strips are also assumed to be known. The designer is required to determine ld and hd such that the steady-state temperature of the metallic strips will be the design temperature.

Using a conventional forward approach, the designer would proceed in the following manner. Neglecting heat transfer modes other than radiation, the insulated oven walls can be modeled as a reradiating surface and the steady-state heat rate passing through the metallic strips is equal to the power output of the heating

ing in the coating, the two-flux equation was solved with a Green's function, and finite differences were used for the transient energy equation. The Green's function analytically incorporates the radiative reflective boundary conditions for the translucent spectral regions. Finite difference relations for the transient energy equation were derived to include radiative effects at the coating-metal interface, and at the external boundaries in the opaque spectral regions.

For heating by radiation and convection, transient temperatures for a translucent coating are compared with a coating without internal radiation effects, but with surface absorption and reflection. Translucence decreases the coating surface temperature and its temperature gradients, and thus reduces possible thermal stresses in the coating. Except for very early in the transient and near steady-state, the transient metal temperatures are lower when the coating is translucent; this is attributed to scattering away of incident radiation by the zirconia coating that has a high scattering albedo. At steady-state, translucence degrades the coating insulating ability and produces higher metal temperatures.

References

- Matthews, L. K., Viskanta, R., and Incropera, F. P., 1985, "Combined Conduction and Radiation Heat Transfer in Porous Materials Heated by Intense Solar Radiation," *ASME Journal of Solar Energy Engineering*, Vol. 107, pp. 29-34.
- Siegel, R., 1996, "Two-Flux and Green's Function Method for Transient Radiative Transfer in a Semitransparent Layer," Proceedings of the 1st International Symposium on Radiative Transfer, Kuşadasi, Turkey, *Radiative Transfer I*, Begell House, New York, pp. 473-487.
- Siegel, R., 1997, "Green's Function to Determine Temperature Distribution in a Semitransparent Thermal Barrier Coating," *Journal of Thermophysics and Heat Transfer*, Vol. 11, No. 4, pp. 315-318.
- Siegel, R., and Howell, J. R., 1992, *Thermal Radiation Heat Transfer*, 3rd Ed., Hemisphere, Washington, DC, pp. 691-695.
- Siegel, R., and Spuckler, C. M., 1998, "Analysis of Thermal Radiation Effects on Temperatures in Turbine Engine Thermal Barrier Coatings," *Materials Science and Engineering*, Vol. A245, pp. 150-159.

Inverse Analysis of Radiative Heat Transfer Systems

M. R. Jones¹

The design of heat transfer systems in which radiation is the dominant heat transfer mode is an important industrial problem. Compared to the conventional forward approach, the inverse approach allows a more thorough analysis of a potential design. This note demonstrates that inverse methods can be powerful tools in the analysis of radiative heat transfer systems.

Nomenclature

- d = diameter of the heating element
 F = view factor
 h = distance from the oven centerline to the first edge of the strips
 J = radiosity

¹ Assistant Professor, Department of Aerospace and Mechanical Engineering, The University of Arizona, P. O. Box 210119, Tucson, AZ 85721. e-mail: jones@ame.arizona.edu. Assoc. Mem. ASME.

Contributed by the Heat Transfer Division for publication in the JOURNAL OF HEAT TRANSFER and presented at '97 NHTC, Baltimore. Manuscript received by the Heat Transfer Division, Dec. 8, 1997; revision received Dec. 1, 1998. Keywords: Heat Transfer, Inverse, Radiation. Associate Technical Editor: P. Menguc.

- l = distance between the metallic strips and the heating element
 L = length of the oven walls
 N = total number of surfaces
 q'' = heat flux
 T = temperature
 w = width of the metallic strips

Greek Symbols

- ε = emissivity
 σ = Stefan-Boltzmann constant

Subscripts

- d = design
 h = heating element
 s = metallic strip
 w = wall

Introduction

Optimizing the design of radiative heat transfer systems is a significant problem in many manufacturing and materials processing applications (Bergman and Viskanta, 1996). In general, the design objective is to develop a system that will produce a specified heat flux or temperature distribution on the material processing surface. Traditionally, engineers have employed a forward or direct approach in the analysis and optimization of potential designs. In the forward approach, a designer seeks to determine the result based on knowledge of the cause. That is, the designer posits a model in which the properties, boundary conditions, and source terms are all known. Based on these assumptions, the designer calculates the temperature and/or heat flux distributions on the material processing surface and refines the design in an iterative manner until the desired result is achieved. However, the design objective is often the determination of one or more of the system's properties, boundary conditions or source terms, so these parameters are generally not all known a priori. Design engineers usually know the desired result and are seeking the optimal design to achieve that result, so the steps required by the forward approach proceed in the opposite direction as the natural design process.

A more logical and powerful method is to use an inverse approach. In the inverse approach, the designer seeks to determine the cause based on observable results. The following analysis of a simplified oven design problem illustrates the utility of an inverse approach by comparing it to the forward approach. The results of this simple analysis demonstrate that inverse methods can be powerful tools in the analysis of radiant heat transfer systems.

Forward Analysis

To facilitate the comparison between a forward analysis and an inverse analysis, consider the following problem. The design of an oven that will be used to cure the coatings on long metallic strips by heating the strips to the design temperature T_d is to be developed. The basic design of the oven is shown in Fig. 1, and the overall dimensions of the oven, the diameter of the heating element, and the width of the metallic strips are specified. The operating temperature and power output of the cylindrical heating element are known, and the walls are well insulated everywhere except for the openings through which the metallic strips are placed in the oven. The oven surfaces are assumed to be diffuse and gray, and the radiative surface properties of the heating element and the metallic strips are also assumed to be known. The designer is required to determine ld and hd such that the steady-state temperature of the metallic strips will be the design temperature.

Using a conventional forward approach, the designer would proceed in the following manner. Neglecting heat transfer modes other than radiation, the insulated oven walls can be modeled as a reradiating surface and the steady-state heat rate passing through the metallic strips is equal to the power output of the heating

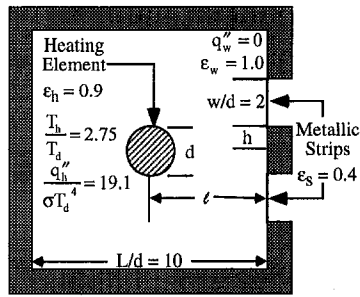


Fig. 1 Proposed oven design. The oven is used to cure coatings on long metallic strips by heating the strips to the design temperature T_d . The designer is required to determine l and h so that the steady-state temperature of the metallic strips will be the design temperature.

element. If each of the three surfaces (the walls, the heating element, and the metallic strips) are isothermal and are characterized by uniform radiosity and irradiation, energy balances on each surface can be used to obtain the following system of equations.

$$\begin{bmatrix} (1 - F_{ww}) & -F_{wh} & -F_{ws} \\ -(1 - \epsilon_h)F_{hw} & 1 & -(1 - \epsilon_h)F_{hs} \\ -F_{sw} & -F_{sh} & (1 - F_{ss}) \end{bmatrix} \begin{bmatrix} J_w \\ J_h \\ J_s \end{bmatrix} = \begin{bmatrix} 0 \\ \epsilon_h \sigma T_h^4 \\ q''_s \end{bmatrix} \quad (1)$$

A complete description of the analysis of radiative exchange in an enclosure formed by an arbitrary number of diffuse gray surfaces is available in most heat transfer texts (e.g., Incropera and DeWitt, 1996).

Equation (1) represents a well-posed model, so the designer can calculate the radiosity of each surface after determining the view factors. Once the radiosities are known, the surface temperature of the metallic strips may be determined. The designer then adjusts the design parameters (l and h) until the desired surface temperature is achieved. Using this approach, the designer would obtain the design curve shown in Fig. 2. According to the model of the radiative heat transfer in the oven, each point on the design curve represents an acceptable design. Therefore, the metallic strips will be heated to the desired steady-state temperature if the designer selects any combination of the design parameters lying on this curve.

While this forward design process is functional, it does not

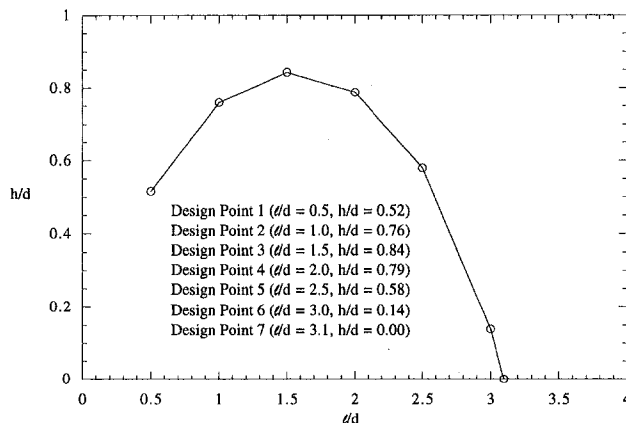


Fig. 2 Design curve. According to the results of the forward analysis, each point on the design curve represents an acceptable design, and metallic strips will be heated to T_d if the designer selects any combination of the design parameters lying on this curve. The seven oven configurations indicated will be analyzed using the Inverse approach.

provide the designer with any means of determining which of the possible design points is optimal. In addition, the forward design process does not allow the designer to investigate some important aspects of the design. For example, the extent to which the temperature distribution is uniform across the metallic strips may be an important factor in determining quality of the coating after it has been cured. The designer may divide the metallic strips into small segments and attempt to calculate the surface temperature of each segment in order to assess the uniformity of the temperature distribution. However, the heat flux passing through each segment is now unknown. Since either the temperature or the heat flux passing through each segment must be specified for the problem to be well-posed, this analysis cannot be completed using the forward approach.

Inverse Analysis

An inverse analysis can be used to assess the uniformity of the temperature distribution over the metallic strips. After dividing the metallic strips into $N-2$ segments, energy balances are again used to derive a system of equations. Harutunian et al. (1995) propose a method in which each surface is categorized as one of four types:

- 1 surfaces on which the temperature is specified,
- 2 surfaces on which the heat flux is specified,
- 3 surfaces on which both the temperature and the heat flux are specified, and
- 4 surfaces on which neither the temperature nor the heat flux are specified.

For each temperature specified surface, the following equation can be written.

$$\epsilon_i \sigma T_i^4 = J_i - (1 - \epsilon_i) \sum_{j=1}^N F_{ij} J_j \quad (2)$$

For each heat flux specified surface, the following equation can be written:

$$q''_i = J_i - \sum_{j=1}^N F_{ij} J_j \quad (3)$$

For surfaces such as the heating element on which both the temperature and the heat flux are specified both Eq. (2) and Eq. (3) can be written. For surfaces on which neither the temperature nor the heat flux are specified such as the metallic strips, Harutunian et al. (1995) recommend that no equation be written. In general, this approach will lead to an underdetermined system of equations since the number of unknowns is greater than the number of equations. A modification to this approach is to include the heat flux for each type 1 and type 4 surface in the set of unknowns and to include Eq. (3) in the system of equations for each of these surfaces. Although this approach increases the number of unknowns, it also allows the addition of the following equation which ensures that energy is conserved globally:

$$0 = \sum_{j=1}^N q''_j A_j \quad (4)$$

Because energy balance equations are not enforced for type 4 surfaces, the approach used by Harutunian et al. (1995) does not explicitly require conservation of energy for the entire system. Explicitly enforcing global energy conservation increases the information content of the system of equations. Therefore, the system of equations obtained when Eq. (4) is included in the formulation is less ill-posed than the system obtained using the method proposed by Harutunian et al. (1995). In this particular oven design problem, the condition number of the system obtained using the method proposed by Harutunian et al. (1995) is more than twice

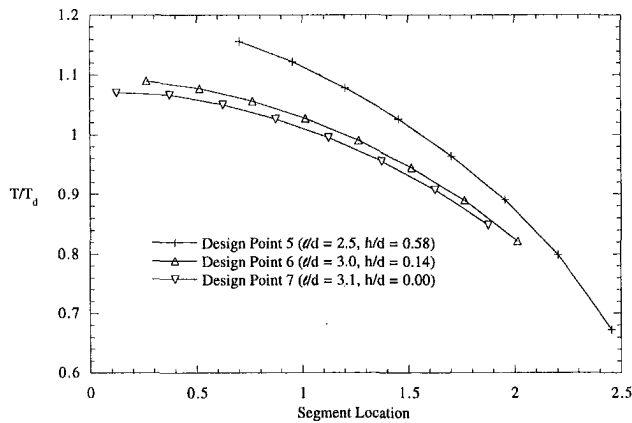


Fig. 3 Temperature distributions for design points 5–7. The metallic strips are divided into eight segments, and each segment is assumed to be isothermal. The location of the segment is defined as the ratio of distance between the center of the segment and the centerline of the oven to the diameter of the heating element. The temperature profiles become more uniform as the distance between the heating element and the metallic strips increases.

the condition number of the system obtained when Eq. (4) is included. Therefore, this modification is advantageous despite the increase in the number of unknowns.

The system of equations represented by Eqs. (2)–(4) is ill-posed, so solutions cannot be obtained using classical matrix inversion techniques. However, a generalized inverse and a regularization method (Beck et al. 1985) can be used to obtain a solution. The solution procedure used in this study has been described previously (Jones 1997).

Results of the Inverse Analysis

Temperature distributions across the metallic strips were determined at seven possible design points using the inverse analysis described in the proceeding section. The values of l/d and h/d for each of these design points are listed in Fig. 2. The temperature distributions for design points 5–7 are plotted in Fig. 3, and it can be seen that the temperature profiles become more uniform as the distance between the heating element and the strips increases. Since only radiative heat transfer is considered, it is reasonable to expect that the most uniform temperature distribution will occur when the irradiation is the most uniform. In the simplified problem considered here, it is fairly intuitive that the irradiation will be more uniform when the heater is located as far from the metallic strips as possible, and the results of the inverse analysis confirm this result. It is important to note that these results are based on the assumption that conduction and convection are negligible.

The results shown in Fig. 3 enable the designer to determine whether or not the temperature distributions are sufficiently uniform. In order to carry out the forward analysis, the designer was required to assume the temperature of strips was uniform, so these results demonstrate the usefulness of an inverse analysis compared to the forward analysis.

Application of the inverse analysis to oven configurations corresponding to design points 1 through 4 were unsuccessful. In each of these cases, the solutions included negative values for one or more of the radiosities. Since such solutions are physically unrealistic, the assumptions made in the development of the radiative heat transfer model were carefully reevaluated. Recall that the model of the radiative transfer is based on the assumption that the irradiation is uniform over each surface. Figure 4 shows the variation in the view factor between the heater and segments of the metallic strips for the seven different oven configurations. The large variation in F_{hs} for design points 1 through 4 indicate that the irradiation on the metallic strips is far from uniform, so the assumptions upon which the model is based are clearly violated for

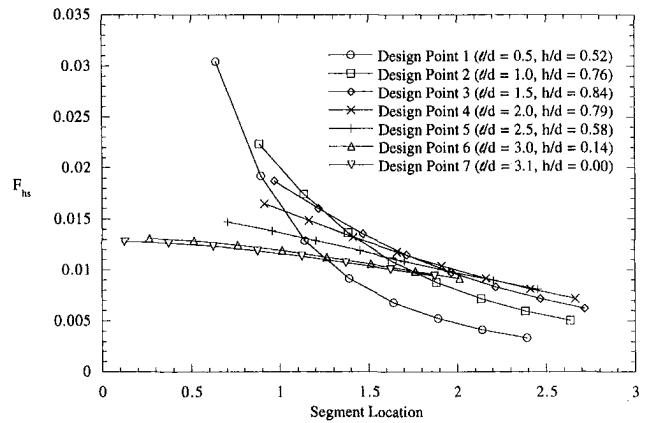


Fig. 4 View factors between the heating element and segments of the metallic strips at several design points. The large variation in F_{hs} for design points 1–4 indicate that the irradiation on the metallic strips is not uniform, so the radiative transfer model is flawed for these oven configurations.

these oven configurations. The fact that the inverse analysis produced physically unrealistic solutions for these configurations is another example of the usefulness of the inverse analysis compared to the forward analysis. The physically unrealistic results serve as a red flag that the model is flawed for these oven configurations. The forward analysis performed for design points 1 through 4 gave no indication that some of the underlying assumptions in the model were invalid.

Finally, temperature distributions with higher resolution can be obtained by increasing the number of segments. However, as the number of segments was increased, the amount of regularization required to obtain a stable solution also increased. Since the accuracy of the solution decreases as the amount of regularization increases, this result illustrates the trade-off between accuracy and resolution that often occurs in inverse problems. This dilemma can be clearly understood by studying the inverse method due to Backus and Gilbert (Press et al., 1992). Figure 5 shows the effect of increasing the number of segments on the temperature distribution at design point 6 ($l/d = 3.0$, $h/d = 0.14$).

Summary

Systems such as ovens, high temperature furnaces, and combustion chambers in which radiation is the dominant heat transfer mode play an important role in many industries. Therefore, the

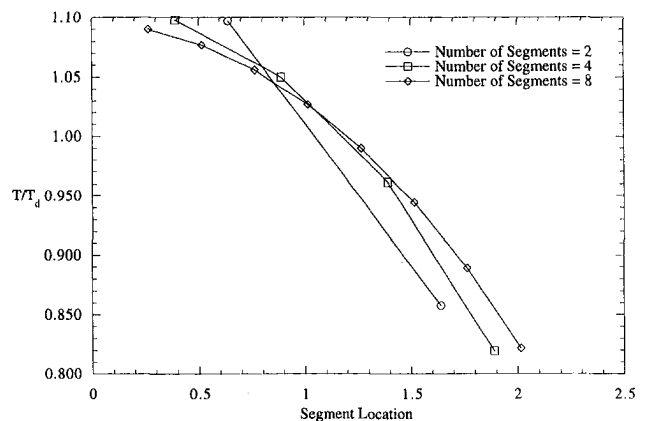


Fig. 5 Effect of increased resolution on the temperature distribution at design point 6 ($l/d = 3.0$, $h/d = 0.14$). The resolution of the temperature distributions can be increased by increasing the number of segments. However, the solution procedure becomes less stable as the number of segments is increased.

development of more efficient methods for designing this type of system would be a significant advancement. This note compares the use of an inverse method in the analysis of a radiative heat transfer system to the use of a forward method. The analysis of a simple oven design was performed using both a forward and an inverse approach to facilitate this comparison. In this particular case, it was found that the inverse approach resulted in physically unrealistic solutions when key assumptions in the radiative heat transfer model were invalid. These unrealistic results are useful in that they serve as a clear indication that the model is flawed, while the forward approach gave no such warning. In addition, the inverse approach allowed the designer to assess the uniformity of the temperature distributions, so the inverse method enabled the designer to perform a more thorough analysis of the potential designs.

References

- Beck, J. V., Blackwell, B., and St. Clair, C. R., Jr., 1985, *Inverse Heat Conduction, Ill-posed Problems*, Wiley-Interscience, New York.
- Bergman, T. L., and Viskanta, R., 1996, "Radiation Heat Transfer in Manufacturing and Materials Processing," *Radiative Transfer-I, Proceedings of the First International Symposium on Radiation Transfer*, M. P. Mengüç, ed., Begell House, New York, pp. 13–39.
- Harutunian, V., Morales, J. C., and Howell, J. R., 1995, "Radiation Exchange within an Enclosure of Diffuse-Gray Surfaces: The Inverse Problem," *Proceedings of the 30th 1995 National Heat Transfer Conference*, Vol. 10, ASME, New York, pp. 133–140.
- Incropera, F. P., and DeWitt, D. P., 1996, *Introduction to Heat Transfer*, 3rd Ed.; John Wiley and Sons, New York.
- Jones, M. R., 1997, "Inverse Analysis of Radiative Exchange in Diffuse Gray Enclosures," *ASME Proceedings of the 32nd National Heat Transfer Conference D*, Kaminski, A. M. Smith, and T. F. Smith, eds., ASME, New York, pp. 59–63.
- Press, W. H., Teukolsky, S. A., Vetterling, W. T., and Flannery, B. P., 1992, *Numerical Recipes in FORTRAN: The Art of Scientific Computing*, Cambridge University Press, New York.

Relative Stability of Boiling on a Flat Plate: Effects of Heater Orientation

W. W. Lin,¹ J. C. Yang,¹ and D. J. Lee^{1,2}

Nomenclatures

- q_c = equilibrium heat flux, W/m^2
 q_F = coexisting film boiling heat flux, W/m^2
 q_N = coexisting nucleate boiling heat flux, W/m^2
 θ = inclination angle, degree
 ω = inclination angle, degree

Introduction

The extent to which heater orientation influences the boiling heat transfer efficiency has attracted increasing attention. El-Genk and Glebov (1995) and Cheung and Haddad (1997) briefly review pertinent literature. The steady and unsteady-state two-mode boiling (nucleate and film boiling) on electrically heated cylindrical tube (Lee, 1998) has been thoroughly examined. According to

previous literature, a unique "equilibrium line" exists on the surface heat flux versus the wall superheat (boiling curve) plot which intersects the boiling curves and separates the nucleate and film boiling curves into *stable* and *metastable* regimes, respectively. A heater under metastable nucleate boiling mode can tolerate a finite-magnitude disturbance (dry patch) to prevent burnout. However, burnout can still occur if the magnitude of disturbance is too large, a phenomenon commonly referred to as "nonhydrodynamic burnout." Therefore, identifying the points which separate stable and metastable regimes on a boiling curve is a relevant task.

Lin and Lee (1997, 1998) examined, for the first time, the relative stability between nucleate and film boiling modes on a conductively heated, flat plane heater under a forced flow condition. To our knowledge, no work has elucidated the relative stability between nucleate and film boiling on an inclined, conductively heated surface, which is the primary focus of this paper.

Experimental

The experimental setup is the same as that employed in Lin et al. (1998) except that the orientation of the heater can be adjusted freely. Where θ is defined as the angle measuring rotation about the horizontal axis that is perpendicular to the flow direction, while angle ω measures the rotation about the horizontal axis that is parallel to the flow direction. Previous works considering orientation effects usually conducted tests at $\omega = 0$ deg. Herein, we study the cases with $\omega = 45$ deg or 90 deg as well, thereby extending the scope of previous works. At $\omega = 90$ deg, changing θ does not produce any difference. All tests were conducted under atmospheric pressure, with saturated methanol flowing at a rate of $20 \text{ kg/m}^2\text{-s}$.

The method of Kline and McClintock (1953) was adopted to estimate the uncertainties of heat flux and surface temperature measurements. The uncertainties thereby existing in the heater surface temperature and the associated heat flux when constructing boiling curves were estimated as ± 7 percent and ± 11 percent, respectively. The mass flowrates exhibited an uncertainty of approximately ± 5 percent, while for fluid temperature measurement, ± 1 K. The error in inclination angles was less than 2 deg.

Results and Discussion

The time evolutions of surface heat flux and superheat at various heater orientations are basically the same as those in Lin and Lee (1997) and, therefore, are not repeated herein. Surface heat fluxes at various positions along the heater can be estimated by solving the transient heat conduction equation with the thermocouple readings as boundary conditions. The heat fluxes corresponding to neutral stability are termed herein as the "coexisting heat fluxes" q_N and q_F .

Figure 1 depicts the (q_N, q_F) sets for $\omega = 0$ deg– 90 deg and $\theta = 0$ – 180 deg. Three points are noteworthy. First, decreasing q_N increases q_F , which is generally expected since the nucleate boiling at a higher surface heat flux is less stable in nature. Second, at a fixed q_N , q_F initially increases with inclination angle θ , after passing a maximum at $\theta = 90$ deg and, then, decreases as θ exceeds 90 deg. Notably, q_F markedly drops between $\theta = 135$ deg and 180 deg. Furthermore, the results for $\theta = 45$ deg are close to those for $\theta = 135$ deg in case of $\omega = 0$ deg. Third, at fixed q_N and θ , increasing ω decreases q_F .

Lin and Lee (1997) demonstrated the feasibility of applying the equal-area criterion to interpret the multimode boiling data. Notably, in cryogenic literature, this criterion is termed as Maddock's criterion (Nishio and Chandratilleke, 1989). With every $(q_N$ and $q_F)$ set in Fig. 1 nucleate and film boiling can coexist steadily on the heating surface. This finding suggests that the equal-area criterion is satisfied. Lin et al. (1998) proposed that the intersection between the (extrapolated) data set in Fig. 1 and the 45 deg-line estimates the corresponding equilibrium heat flux, q_c , where $q_N =$

¹ Department of Chemical Engineering, National Taiwan University, Taipei, Taiwan 106, R.O.C.

² Author to whom correspondence should be addressed. e-mail: djlee@ccms.ntu.edu.tw.

Contributed by the Heat Transfer Division for publication in the JOURNAL OF HEAT TRANSFER. Manuscript received by the Heat Transfer Division, Mar. 5, 1998; revision received, Nov. 2, 1998. Keywords: Boiling, Geometry, Heat Transfer, Stability. Associate Technical Editor: P. Ayyaswamy.

development of more efficient methods for designing this type of system would be a significant advancement. This note compares the use of an inverse method in the analysis of a radiative heat transfer system to the use of a forward method. The analysis of a simple oven design was performed using both a forward and an inverse approach to facilitate this comparison. In this particular case, it was found that the inverse approach resulted in physically unrealistic solutions when key assumptions in the radiative heat transfer model were invalid. These unrealistic results are useful in that they serve as a clear indication that the model is flawed, while the forward approach gave no such warning. In addition, the inverse approach allowed the designer to assess the uniformity of the temperature distributions, so the inverse method enabled the designer to perform a more thorough analysis of the potential designs.

References

- Beck, J. V., Blackwell, B., and St. Clair, C. R., Jr., 1985, *Inverse Heat Conduction, Ill-posed Problems*, Wiley-Interscience, New York.
- Bergman, T. L., and Viskanta, R., 1996, "Radiation Heat Transfer in Manufacturing and Materials Processing," *Radiative Transfer-I, Proceedings of the First International Symposium on Radiation Transfer*, M. P. Mengüç, ed., Begell House, New York, pp. 13–39.
- Harutunian, V., Morales, J. C., and Howell, J. R., 1995, "Radiation Exchange within an Enclosure of Diffuse-Gray Surfaces: The Inverse Problem," *Proceedings of the 30th 1995 National Heat Transfer Conference*, Vol. 10, ASME, New York, pp. 133–140.
- Incropera, F. P., and DeWitt, D. P., 1996, *Introduction to Heat Transfer*, 3rd Ed., John Wiley and Sons, New York.
- Jones, M. R., 1997, "Inverse Analysis of Radiative Exchange in Diffuse Gray Enclosures," *ASME Proceedings of the 32nd National Heat Transfer Conference D*, Kaminski, A. M. Smith, and T. F. Smith, eds., ASME, New York, pp. 59–63.
- Press, W. H., Teukolsky, S. A., Vetterling, W. T., and Flannery, B. P., 1992, *Numerical Recipes in FORTRAN: The Art of Scientific Computing*, Cambridge University Press, New York.

Relative Stability of Boiling on a Flat Plate: Effects of Heater Orientation

W. W. Lin,¹ J. C. Yang,¹ and D. J. Lee^{1,2}

Nomenclatures

- q_c = equilibrium heat flux, W/m^2
 q_F = coexisting film boiling heat flux, W/m^2
 q_N = coexisting nucleate boiling heat flux, W/m^2
 θ = inclination angle, degree
 ω = inclination angle, degree

Introduction

The extent to which heater orientation influences the boiling heat transfer efficiency has attracted increasing attention. El-Genk and Glebov (1995) and Cheung and Haddad (1997) briefly review pertinent literature. The steady and unsteady-state two-mode boiling (nucleate and film boiling) on electrically heated cylindrical tube (Lee, 1998) has been thoroughly examined. According to

¹ Department of Chemical Engineering, National Taiwan University, Taipei, Taiwan 106, R.O.C.

² Author to whom correspondence should be addressed. e-mail: djlee@ccms.ntu.edu.tw.

Contributed by the Heat Transfer Division for publication in the JOURNAL OF HEAT TRANSFER. Manuscript received by the Heat Transfer Division, Mar. 5, 1998; revision received, Nov. 2, 1998. Keywords: Boiling, Geometry, Heat Transfer, Stability. Associate Technical Editor: P. Ayyaswamy.

previous literature, a unique "equilibrium line" exists on the surface heat flux versus the wall superheat (boiling curve) plot which intersects the boiling curves and separates the nucleate and film boiling curves into *stable* and *metastable* regimes, respectively. A heater under metastable nucleate boiling mode can tolerate a finite-magnitude disturbance (dry patch) to prevent burnout. However, burnout can still occur if the magnitude of disturbance is too large, a phenomenon commonly referred to as "nonhydrodynamic burnout." Therefore, identifying the points which separate stable and metastable regimes on a boiling curve is a relevant task.

Lin and Lee (1997, 1998) examined, for the first time, the relative stability between nucleate and film boiling modes on a conductively heated, flat plane heater under a forced flow condition. To our knowledge, no work has elucidated the relative stability between nucleate and film boiling on an inclined, conductively heated surface, which is the primary focus of this paper.

Experimental

The experimental setup is the same as that employed in Lin et al. (1998) except that the orientation of the heater can be adjusted freely. Where θ is defined as the angle measuring rotation about the horizontal axis that is perpendicular to the flow direction, while angle ω measures the rotation about the horizontal axis that is parallel to the flow direction. Previous works considering orientation effects usually conducted tests at $\omega = 0$ deg. Herein, we study the cases with $\omega = 45$ deg or 90 deg as well, thereby extending the scope of previous works. At $\omega = 90$ deg, changing θ does not produce any difference. All tests were conducted under atmospheric pressure, with saturated methanol flowing at a rate of $20 \text{ kg/m}^2\text{-s}$.

The method of Kline and McClintock (1953) was adopted to estimate the uncertainties of heat flux and surface temperature measurements. The uncertainties thereby existing in the heater surface temperature and the associated heat flux when constructing boiling curves were estimated as ± 7 percent and ± 11 percent, respectively. The mass flowrates exhibited an uncertainty of approximately ± 5 percent, while for fluid temperature measurement, ± 1 K. The error in inclination angles was less than 2 deg.

Results and Discussion

The time evolutions of surface heat flux and superheat at various heater orientations are basically the same as those in Lin and Lee (1997) and, therefore, are not repeated herein. Surface heat fluxes at various positions along the heater can be estimated by solving the transient heat conduction equation with the thermocouple readings as boundary conditions. The heat fluxes corresponding to neutral stability are termed herein as the "coexisting heat fluxes" q_N and q_F .

Figure 1 depicts the (q_N, q_F) sets for $\omega = 0$ deg– 90 deg and $\theta = 0$ – 180 deg. Three points are noteworthy. First, decreasing q_N increases q_F , which is generally expected since the nucleate boiling at a higher surface heat flux is less stable in nature. Second, at a fixed q_N , q_F initially increases with inclination angle θ , after passing a maximum at $\theta = 90$ deg and, then, decreases as θ exceeds 90 deg. Notably, q_F markedly drops between $\theta = 135$ deg and 180 deg. Furthermore, the results for $\theta = 45$ deg are close to those for $\theta = 135$ deg in case of $\omega = 0$ deg. Third, at fixed q_N and θ , increasing ω decreases q_F .

Lin and Lee (1997) demonstrated the feasibility of applying the equal-area criterion to interpret the multimode boiling data. Notably, in cryogenic literature, this criterion is termed as Maddock's criterion (Nishio and Chandratilleke, 1989). With every $(q_N$ and $q_F)$ set in Fig. 1 nucleate and film boiling can coexist steadily on the heating surface. This finding suggests that the equal-area criterion is satisfied. Lin et al. (1998) proposed that the intersection between the (extrapolated) data set in Fig. 1 and the 45 deg-line estimates the corresponding equilibrium heat flux, q_c , where $q_N =$

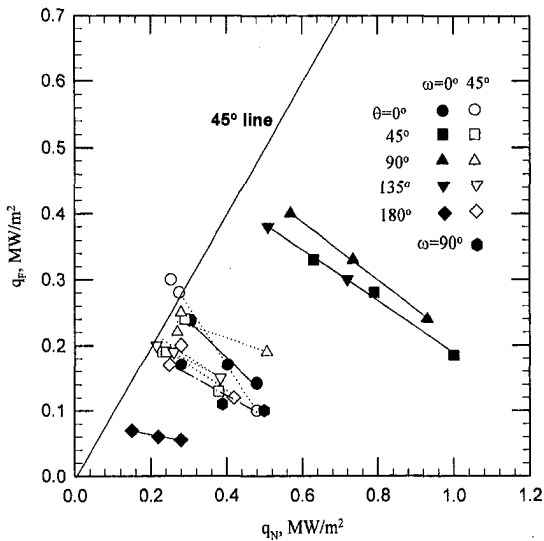


Fig. 1 Coexisting heat fluxes at various inclinations

$q_F = q_C$. The fact that q_C is unique for a given heater/fluid combination (at fixed fluid velocity) accounts for why the relative stability among different boiling configurations can be compared by q_C values. A higher q_C implies a more stable nucleate boiling (and a lesser likelihood of burnout), and vice versa.

Figure 2 displays the q_C versus θ plot with ω as a parameter. Notably, a local maximum occurs at $\theta = 90$ deg. Restated, the nucleate boiling mode exhibits the highest stability relative to the corresponding film boiling mode when the heater is turned vertically at its side. The effect predominates at $\omega = 0$, a horizontal heater. The corresponding q_C at $\theta = 90$ deg is nearly twice that at $\theta = 0$ deg. Therefore, an inclined horizontal surface can markedly enhance the stability of nucleate boiling mode, thereby ensuring the safety of the boiling process. The q_C data for θ ranging from 45 deg to 135 deg are close to each other. The effects of inclination of $\theta = 45$ –135 deg on relative stability of a horizontal heater are secondary.

Notably, increasing ω reduces the q_C , indicating a less stable nucleate boiling mode. At $\omega = 90$ deg, there is no difference in q_C at changing θ , subsequently forming a horizontal line in Fig. 2.

Of particular interest is the cases with $\theta = 180$ deg, i.e., a

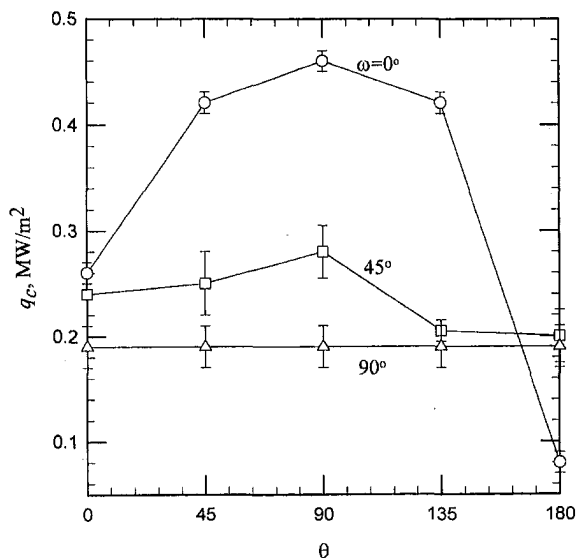


Fig. 2 Equilibrium heat fluxes versus θ plot

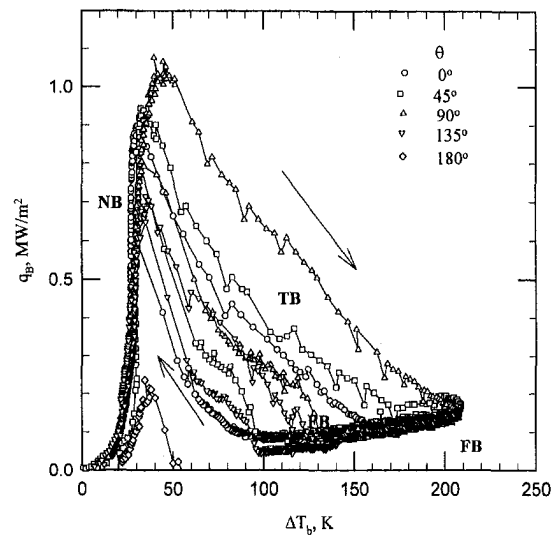


Fig. 3 Boiling curves with $\omega = 0$ deg

downward facing heater. At $\omega = 0$ deg the corresponding q_C is rather low. Therefore, the heater can easily burnout. With a non-zero ω , however, the vapor can more easily escape from the side of the heater, thereby yielding a greater heat transfer rate and ultimately a higher q_C .

According to Nishio and Chandratilleke (1989), the whole boiling curve determines the value of q_C : the nucleate, transition, and film boiling curves as well as the critical points separate these boiling curves (CHF and MHF). This occurrence can be easily accounted for since all of the boiling curves affect the construction of the equal-area criterion. Figure 3 illustrates the boiling curves with $\omega = 0$ deg. According to this figure, the nucleate boiling curve shifts upwards with an increasing θ at a lower heat flux regime, which becomes independent of θ at a high heat flux regime. This finding correlates with the available literature (Nishigawa et al., 1984). An equal-area criterion is constructed on normal-normal scales. The shifts in nucleate boiling curves are insignificant and negligibly influence the resulting q_C .

The film boiling curves shift upwards as θ increases from 0 deg to 90 deg and, then, decreases when θ exceeds 90 deg. The trend in film boiling corresponds to that of Nishigawa et al. (1975) and Nishio and Chandratilleke (1989). However, this trend differs from that of Jung et al. (1987), who found the film boiling monotonically decays with inclination. Nevertheless, the change in film boiling heat flux, except for the case with the heater surface faced downward, is secondary as well.

On the other hand, both CHF and MHF points markedly increase with an inclination for θ ranging from 0–90 deg and, then, decreases rapidly for a further increase in θ . This trend contradicts that of Chang and You (1996), Nishio and Chandratilleke (1989), and Gao and El-Genk (1996); however, it correlates with that of Githinji and Sabersky (1963). Cheung and Haddad (1997) attributed the difference in experimental results to the different heater sizes under investigation. Although the precise location of the transition boiling curve cannot be obtained directly from the present apparatus, it should be located somewhere between CHF and MHF points. Restated, the transition boiling curve should shift greatly as did the CHF and MHF points. According to the construction of equal-area criterion, inasmuch as the changes in nucleate and film boiling curves are secondary, the shift in CHF/MHF/transition boiling curve is primarily responsible for the change in q_C observed in Fig. 3.

The typical boiling curves obtained in test with $\omega = 45$ deg and 90 deg resemble those under the condition $\omega = 0$ deg. However, the dependence on θ of the boiling curves becomes milder, accounting for the milder variation of q_C with θ as observed in Fig. 2.

Conclusions

This work investigates the relative stability between nucleate boiling and film boiling on an inclined surface under a forced flow. According to those results, coexisting heat fluxes are found at various heater's configurations, from which the so-called "equilibrium heat fluxes" are identified. The nucleate boiling mode exhibits the highest stability relative to its corresponding film boiling mode when the heater is placed horizontally with its surface turned vertically at its side. The lowest stability occurs at the downward-facing configuration for a horizontal heater. In addition, equal-area criterion can accurately interpret the effects of heater orientation. Moreover, the shifts in critical heat flux, minimum heat flux, together with the transition boiling curve mainly correspond to the change in relative stability at variable heater orientations.

References

- Barrstar, M. J., and Merte, Jr., H., 1997, "Effect of Heater Surface Orientation on the Critical Heat Flux—I. An Experimental Evaluation of Models for Subcooled Pool Boiling," *Int. J. Heat Mass Transfer*, Vol. 40, pp. 4007–4019.
- Chang, J. Y., and You, S. M., 1996, "Heater Orientation Effects on Pool Boiling of Micro-Porous-Enhanced Surfaces in Saturated FC-72," *ASME JOURNAL OF HEAT TRANSFER*, Vol. 118, pp. 937–943.
- Cheung, F. B., and Haddad, K. H., 1997, "A Hydrodynamic Critical Heat Flux Model for Saturated Pool Boiling on a Downward Facing Curved Heating Surface," *Int. J. Heat Mass Transfer*, Vol. 40, pp. 1291–1302.
- El-Genk, M. S., and Glebov, A. G., 1995, "Transient Boiling from Downward Facing Curved Surfaces," *Int. J. Heat Mass Transfer*, Vol. 38, pp. 2209–2224.
- Githinji, P. M., and Sabersky, R. H., 1963, "Some Effects on the Orientation of the Heating Surface in Nucleate Boiling," *ASME JOURNAL OF HEAT TRANSFER*, Vol. 85, p. 379.
- Jung, D. S., Venart, J. E. S., and Sousa, A. C. M., 1987, "Effects of Enhanced Surfaces and Surface Orientation on Nucleate and Film Boiling Heat Transfer in R-11," *Int. Heat Mass Transfer*, Vol. 30, pp. 2627–2639.
- Kline, S. J., and McClintock, F. A., 1953, "Description of Uncertainties in Single Sample Experiments," *Mech. Engng.*, Vol. 75, Jan., pp. 3–8.
- Lee, D. J., 1998, "Two-mode Boiling on a Horizontal Heating Wire: Effects of Liquid Subcoolings," *Int. J. Heat Mass Transfer*, Vol. 41, pp. 2925–2928.
- Lin, W. W., and Lee, D. J., 1997, "Relative Stability between Nucleate and Film Boiling on a Nonuniformly Heated Flat Surface," *ASME JOURNAL OF HEAT TRANSFER*, Vol. 119, pp. 326–331.
- Lin, W. W., and Lee, D. J., 1998, "Methanol Flow Boiling over a Nonuniformly Heated Flat Plate," *J. Ch. I. Ch. E.*, Vol. 29, pp. 17–23.
- Lin, W. W., Yang, J. C., and Lee, D. J., 1998, "Boiling Stability Characteristics of Methanol Flowing over a Nonuniformly Heated Surface," *Int. J. Heat Mass Transfer*, Vol. 41, pp. 4009–4023.
- Nishikawa, K., Fujita, Y., Uchida, S., and Ohta, H., 1983, "Effects of Heating Surface Orientation on Nucleate Boiling Heat Transfer," *Proc. ASME-JSME Thermal Engineering Joint Conf.*, Vol. 1, Honolulu, HI, pp. 129–136.
- Nisho, S., and Chandratilleke, 1989, "Steady-state Pool Boiling Heat Transfer to Saturated Liquid Helium at Atmospheric Pressure," *JSME Int. J. Ser. B.*, Vol. 32, pp. 639–645.

Pool Evaporation of Decane Into an Enclosed Gas Space Undergoing Thermal Convection

J. P. Burelbach,^{1,2} M. Epstein,^{1,3} and H. K. Fauske¹

Introduction

The present study is motivated by safety concerns during cleanup of certain process waste storage tanks. Prediction of the

¹ Fauske & Associates, Inc., 16W070 West 83rd Street, Burr Ridge, IL 60521

² e-mail: burelbach@fauske.com.

³ Mem. ASME.

Contributed by the Heat Transfer Division for publication in the *JOURNAL OF HEAT TRANSFER*. Manuscript received by the Heat Transfer Division, Oct. 20, 1997; revision received, Dec. 11, 1998. Keywords: Enclosure Flows, Evaporation, Experimental, Heat Transfer, Natural Convection. Associate Technical Editor: P. Ayyaswamy.

evaporation flux off the surfaces of liquid organic pools that rest on top of an aqueous sludge residue in some of the underground storage tanks is critical to characterizing the size of the organic pools and thereby the potential fire hazard associated with these pools. The purpose of the experiments reported here is to investigate the effect of global natural circulation on organic pool evaporation rates. Thus, as in the waste tank application, the "laboratory pool" evaporates into an enclosure (headspace) gas undergoing thermal convection that is driven by the temperature difference between the floor (sludge) and the ceiling (dome).

Experimental Apparatus and Procedure

The apparatus is shown schematically in Fig. 1. The enclosure walls are plexiglass while the floor and ceiling are black painted steel. The free-board height is 1.07 m and the inside walls are 1.14 m wide so the free-board volume is 1.39 m³. Separate circulating water systems maintain uniform and constant temperatures on the floor (T_w) and ceiling (T_c) such that the temperature difference ($\Delta T = T_w - T_c$) is 2°C. AD592 temperature sensors are used to verify that the floor and ceiling boundaries are isothermal and to monitor the gas space temperature. Rigid foam board (polyisocyanurate) is used for thermal insulation, and temperature measurements indicate that sidewall heat losses are less than ten percent of the floor-to-ceiling heat transfer.

Decane ($C_{10}H_{22}$) is used as the test liquid because it is representative of waste tank solvents and because evaporation rates of interest can be obtained at near ambient temperatures (about 22°C). It is contained in a circular pan which is constructed using a 1.2 cm steel band and a sheet of aluminum foil. The weight of the decane holds the pan against the floor. Separate-effects tests indicate that the pool temperature is within 0.1°C of the enclosure floor temperature, confirming that the gap resistance between the pan and the floor is minimal. Pool evaporation is measured by periodically raising the pan and suspending it from a DI-8KD electric balance. The suspension hanger passes through a ½-in. diameter penetration in the ceiling tank. This penetration is sealed when the pan is resting on the heated floor. The balance provides 0.01 g resolution, which allows for accurate measurement of evaporation

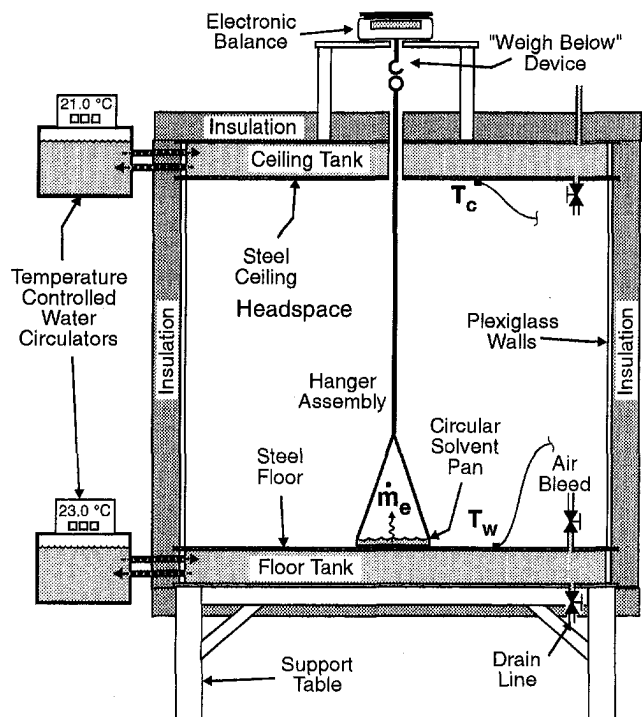


Fig. 1 Schematic illustration of the apparatus

Conclusions

This work investigates the relative stability between nucleate boiling and film boiling on an inclined surface under a forced flow. According to those results, coexisting heat fluxes are found at various heater's configurations, from which the so-called "equilibrium heat fluxes" are identified. The nucleate boiling mode exhibits the highest stability relative to its corresponding film boiling mode when the heater is placed horizontally with its surface turned vertically at its side. The lowest stability occurs at the downward-facing configuration for a horizontal heater. In addition, equal-area criterion can accurately interpret the effects of heater orientation. Moreover, the shifts in critical heat flux, minimum heat flux, together with the transition boiling curve mainly correspond to the change in relative stability at variable heater orientations.

References

- Barrstar, M. J., and Merte, Jr., H., 1997, "Effect of Heater Surface Orientation on the Critical Heat Flux—I. An Experimental Evaluation of Models for Subcooled Pool Boiling," *Int. J. Heat Mass Transfer*, Vol. 40, pp. 4007–4019.
- Chang, J. Y., and You, S. M., 1996, "Heater Orientation Effects on Pool Boiling of Micro-Porous-Enhanced Surfaces in Saturated FC-72," *ASME JOURNAL OF HEAT TRANSFER*, Vol. 118, pp. 937–943.
- Cheung, F. B., and Haddad, K. H., 1997, "A Hydrodynamic Critical Heat Flux Model for Saturated Pool Boiling on a Downward Facing Curved Heating Surface," *Int. J. Heat Mass Transfer*, Vol. 40, pp. 1291–1302.
- El-Genk, M. S., and Glebov, A. G., 1995, "Transient Boiling from Downward Facing Curved Surfaces," *Int. J. Heat Mass Transfer*, Vol. 38, pp. 2209–2224.
- Githinji, P. M., and Sabersky, R. H., 1963, "Some Effects on the Orientation of the Heating Surface in Nucleate Boiling," *ASME JOURNAL OF HEAT TRANSFER*, Vol. 85, p. 379.
- Jung, D. S., Venart, J. E. S., and Sousa, A. C. M., 1987, "Effects of Enhanced Surfaces and Surface Orientation on Nucleate and Film Boiling Heat Transfer in R-11," *Int. Heat Mass Transfer*, Vol. 30, pp. 2627–2639.
- Kline, S. J., and McClintock, F. A., 1953, "Description of Uncertainties in Single Sample Experiments," *Mech. Engng.*, Vol. 75, Jan., pp. 3–8.
- Lee, D. J., 1998, "Two-mode Boiling on a Horizontal Heating Wire: Effects of Liquid Subcoolings," *Int. J. Heat Mass Transfer*, Vol. 41, pp. 2925–2928.
- Lin, W. W., and Lee, D. J., 1997, "Relative Stability between Nucleate and Film Boiling on a Nonuniformly Heated Flat Surface," *ASME JOURNAL OF HEAT TRANSFER*, Vol. 119, pp. 326–331.
- Lin, W. W., and Lee, D. J., 1998, "Methanol Flow Boiling over a Nonuniformly Heated Flat Plate," *J. Ch. I. Ch. E.*, Vol. 29, pp. 17–23.
- Lin, W. W., Yang, J. C., and Lee, D. J., 1998, "Boiling Stability Characteristics of Methanol Flowing over a Nonuniformly Heated Surface," *Int. J. Heat Mass Transfer*, Vol. 41, pp. 4009–4023.
- Nishikawa, K., Fujita, Y., Uchida, S., and Ohta, H., 1983, "Effects of Heating Surface Orientation on Nucleate Boiling Heat Transfer," *Proc. ASME-JSME Thermal Engineering Joint Conf.*, Vol. 1, Honolulu, HI, pp. 129–136.
- Nisho, S., and Chandratilleke, 1989, "Steady-state Pool Boiling Heat Transfer to Saturated Liquid Helium at Atmospheric Pressure," *JSME Int. J. Ser. B.*, Vol. 32, pp. 639–645.

Pool Evaporation of Decane Into an Enclosed Gas Space Undergoing Thermal Convection

J. P. Burelbach,^{1,2} M. Epstein,^{1,3} and H. K. Fauske¹

Introduction

The present study is motivated by safety concerns during cleanup of certain process waste storage tanks. Prediction of the

¹ Fauske & Associates, Inc., 16W070 West 83rd Street, Burr Ridge, IL 60521

² e-mail: burelbach@fauske.com.

³ Mem. ASME.

Contributed by the Heat Transfer Division for publication in the *JOURNAL OF HEAT TRANSFER*. Manuscript received by the Heat Transfer Division, Oct. 20, 1997; revision received, Dec. 11, 1998. Keywords: Enclosure Flows, Evaporation, Experimental, Heat Transfer, Natural Convection. Associate Technical Editor: P. Ayyaswamy.

evaporation flux off the surfaces of liquid organic pools that rest on top of an aqueous sludge residue in some of the underground storage tanks is critical to characterizing the size of the organic pools and thereby the potential fire hazard associated with these pools. The purpose of the experiments reported here is to investigate the effect of global natural circulation on organic pool evaporation rates. Thus, as in the waste tank application, the "laboratory pool" evaporates into an enclosure (headspace) gas undergoing thermal convection that is driven by the temperature difference between the floor (sludge) and the ceiling (dome).

Experimental Apparatus and Procedure

The apparatus is shown schematically in Fig. 1. The enclosure walls are plexiglass while the floor and ceiling are black painted steel. The free-board height is 1.07 m and the inside walls are 1.14 m wide so the free-board volume is 1.39 m³. Separate circulating water systems maintain uniform and constant temperatures on the floor (T_w) and ceiling (T_c) such that the temperature difference ($\Delta t = T_w - T_c$) is 2°C. AD592 temperature sensors are used to verify that the floor and ceiling boundaries are isothermal and to monitor the gas space temperature. Rigid foam board (polyisocyanurate) is used for thermal insulation, and temperature measurements indicate that sidewall heat losses are less than ten percent of the floor-to-ceiling heat transfer.

Decane ($C_{10}H_{22}$) is used as the test liquid because it is representative of waste tank solvents and because evaporation rates of interest can be obtained at near ambient temperatures (about 22°C). It is contained in a circular pan which is constructed using a 1.2 cm steel band and a sheet of aluminum foil. The weight of the decane holds the pan against the floor. Separate-effects tests indicate that the pool temperature is within 0.1°C of the enclosure floor temperature, confirming that the gap resistance between the pan and the floor is minimal. Pool evaporation is measured by periodically raising the pan and suspending it from a DI-8KD electric balance. The suspension hanger passes through a 1/2-in. diameter penetration in the ceiling tank. This penetration is sealed when the pan is resting on the heated floor. The balance provides 0.01 g resolution, which allows for accurate measurement of evaporation

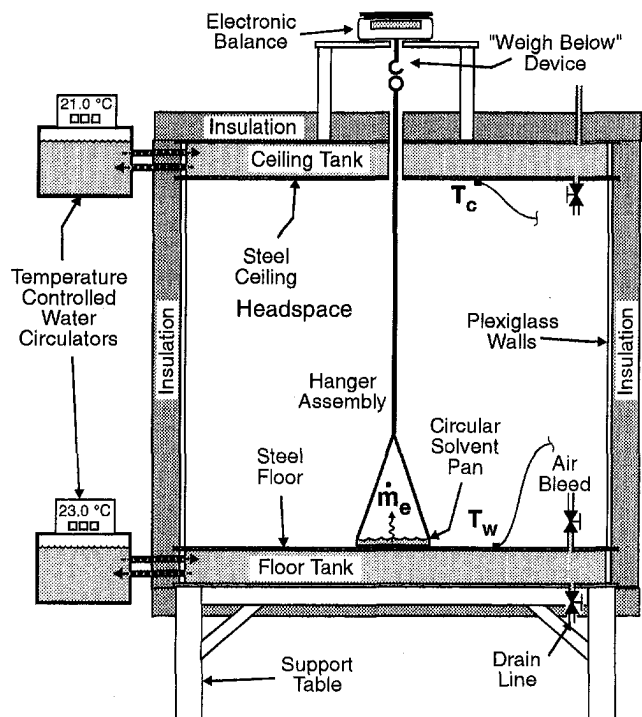


Fig. 1 Schematic illustration of the apparatus

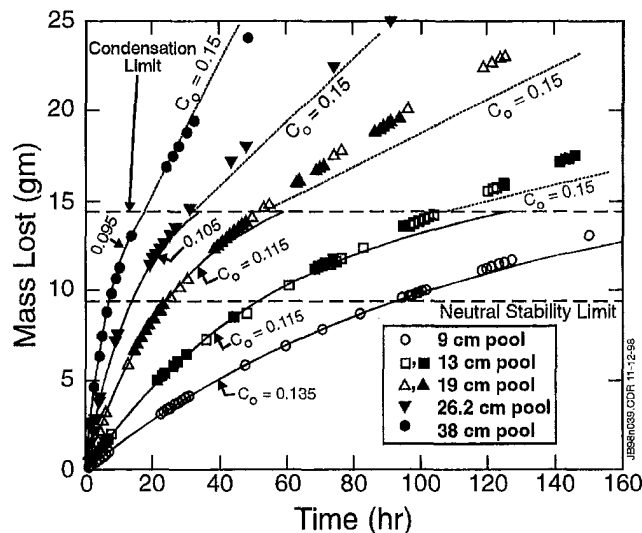


Fig. 2 Mass loss data and comparison to theory. Uncertainty in data is ± 2 percent. Solid curves are given by Eq. (3), while dotted curves ($C_o = 0.15$) are given by Eq. (4).

rates in the range of interest (say from 0.01 to 1.0 g/hr). Mass measurements are reproducible within ± 0.02 g.

We have chosen to run closed-system (no enclosure purge) tests in order to expedite measurement of pool evaporation rates. Thus we assume quasi-steady behavior over a range of evaporation rates, with the maximum rate occurring at the beginning of a test. Enclosure gas composition has not been measured since it may be inferred from the measured evaporation rates.

Experimental Results

Figure 2 illustrates measured evaporation rates for each pool size in terms of mass loss data. For each test the enclosure floor and ceiling temperatures are nominally maintained at 23.0 and 21.0°C, respectively. Pool diameters of 9, 13, 19, 26.2, and 38 cm are investigated so as to double the pool area in successive tests. The surface area of the largest pool covers only 8.7 percent of the 1.3-m² floor area. In each case the decane pool is about 5 mm deep. Two cases are repeated to demonstrate reproducibility.

An uncertainty analysis of the measurements is performed using the root-sum-square method (Kline and McClintock, 1953). Uncertainty in the mass lost, Δm , is within ± 2 percent. The observed ΔT between the average measured T_w and T_c is maintained between 1.90 and 1.95°C. The gas-space sensors indicate that the enclosure bulk gas temperature T_∞ is close to the average of the floor and ceiling temperatures ($\pm 0.2^\circ\text{C}$), from which we infer that the gas space is reasonably well mixed and that $T_\infty \approx (T_w + T_c)/2$. The overall uncertainty in the quantity $T_w - T_\infty$ is estimated to be 25 percent. The nominal value of this driving temperature difference for natural convection is 1°C with an average measured value of 0.96°C.

Discussion of Results

The warm surface of the organic pool is at the same temperature T_w as the uniformly heated metal floor. Far away from the surface of the organic pool the enclosure air has a known uniform temperature T_∞ and, presumably, an instantaneous uniform concentration (mass fraction) of organic vapor Y_∞ . During the course of a run, Y_∞ increases continuously from its initial value $Y_\infty = 0$. In a perfectly sealed enclosure Y_∞ may be inferred from the measurements of the decrease in organic liquid. At the surface of the organic pool the organic vapor concentration is the equilibrium value $Y_{eq}(T_w)$ evaluated at the floor temperature. The organic liquid has a low vapor pressure at the temperatures of interest, so

$Y_{eq}(T_w)$ is small and in this limit the difference between the density of the air/decane mixture at the surface of the decane pool, ρ_w , and the density ρ_∞ of the mixture far from the surface of the pool may be shown to be

$$\frac{\rho_w - \rho_\infty}{\rho_\infty} = \left(1 - \frac{M_g}{M_v}\right) [Y_{eq}(T_w) - Y_\infty] - \frac{T_w - T_\infty}{T_\infty} \quad (1)$$

where M_g and M_v are, respectively, the molecular weights of the air and the organic vapor.

The intrinsic gravitational stability of the gas mixture just above the organic pool depends on whether $(\rho_w - \rho_\infty)/\rho_\infty$ is positive or negative. Examination of Eq. (1) reveals that the vapor pressure exerted by the organic tends to increase the value of this quantity, since $M_v > M_g$, and therefore increase the stability of the gas mixture. For a given floor temperature, T_w and $Y_{eq}(T_w)$ are fixed. Therefore, the sign and magnitude of the ratio $(\rho_w - \rho_\infty)/\rho_\infty$ depends on the bulk concentration Y_∞ of the organic vapor in the enclosure gas. Experiments begin with $Y_\infty = 0$. The relevant temperatures during an experiment are $T_\infty = 22^\circ\text{C}$ and $T_w = 23^\circ\text{C}$ and, for decane, $Y_{eq}(T_w) = 0.01$. Thus during the early stages of an experiment the contributions of organic vapor and temperature to the density ratio $(\rho_w - \rho_\infty)/\rho_\infty$ are $(1 - M_g/M_v)Y_{eq}(T_w) = 7.96 \times 10^{-3}$ and $(T_w - T_\infty)/T_\infty = 3.39 \times 10^{-3}$, respectively. The positive value of $\rho_w - \rho_\infty$ induces a downward flow over the pool as a result of a radial outflow of the dense vapor/gas mixture. However, based on the experimental evidence given below, we feel that the contribution of downflow convection to the pool evaporation rate is probably small relative to the turbulent free-convective structure produced by the floor-to-ceiling temperature difference.

Heat transfer measurements of highly turbulent free convection in horizontal fluid layers, combined with the Chilton-Colburn heat/mass transfer analogy, result in a correlation for the evaporation mass flux \dot{m}'' off the surface of the organic pool of the form

$$\begin{aligned} \dot{m}'' &= h_m [Y_{eq}(T_w) - Y_\infty] \\ &= C_o \rho_\infty D \left[\frac{g(T_w - T_\infty)}{\nu D T_\infty} \right]^{1/3} [Y_{eq}(T_w) - Y_\infty] \end{aligned} \quad (2)$$

where D and ν are the binary diffusion coefficient and kinematic viscosity of the organic vapor/air mixture, respectively, h_m is the coefficient for mass transfer, and g is the gravitational constant. The numerical coefficient C_o has been shown experimentally by Katsaros et al. (1977) to be $C_o = 0.15$, though slightly different values have been suggested by other authors. The thermals that are generated at the ceiling and at the floor just beyond the perimeter of the pool are assumed to affect the motion of the enclosure gas so significantly that turbulent natural convection prevails above the surface of the pool and Eq. (2) represents the evaporation rate reasonably well.

Our simple closed-system (no purge) experimental technique is based on the reasonable expectation that the mass evaporation rate measured during a steady-state experiment with a gas purge and, therefore, with a fixed Y_∞ , is almost identical to the rate measured in our experiment at the instant the bulk enclosure concentration "passes through" Y_∞ . The mass of the organic liquid that has been removed from the pool by evaporation at time t , Δm , is then given by

$$\Delta m = \rho V Y_{eq}(T_w) \left[1 - \exp\left(-\frac{\pi R^2 h_m}{\rho_\infty V} t\right) \right] \quad (3)$$

where R is the pool radius and V is the enclosure volume. Equation (3), with the mass transfer coefficient h_m as defined in Eq. (2), is used to generate the model predictions represented by the solid curves in Fig. 2. Good agreement with early-time data is obtained by allowing the numerical coefficient C_o to vary between 0.1 and 0.15. The decreasing value of C_o with increasing R indicates that

the surrounding thermals become less effective as the pool size increases.

With regard to the downflow mode mentioned previously, it is worth noting that a few isothermal ($T_w = T_c$) evaporation experiments have been performed using 9 and 17-cm diameter pools. During these experiments there was no surrounding thermal convection, and evaporation proceeded by downward flow over the pool and/or by diffusion. The evaporation rate for the 9-cm pool is a factor of two less than that previously measured in the presence of thermal convection. For the 17-cm pool the evaporation rate is a factor of three less than the evaporation rate with thermal convection. If downflow were dominating the evaporation process then evaporation rates in the presence of thermal convection should have been nearly the same as those measured under isothermal conditions. Also the downflow mechanism requires a positive value of $\rho_w - \rho_\infty$. If this mechanism is important, one anticipates a detectable change (reduction) in the slope of the measured mass lost versus time curves as the neutral stability limit is approached (lower dashed line in Fig. 2). On the contrary, the mass lost versus time trend is unchanged as the neutral stability line is crossed. Clearly, the evaporation process is governed mostly by exterior turbulent conditions rather than by the horizontally directed, hydrostatic pressure gradient just above the surface of the pool.

The evaporation history given by Eq. (3) is valid until Δm exceeds the mass of vapor in equilibrium with the ceiling (Δm_{eq}), say at time $t = t_c$. Thereafter evaporation from the pool is balanced by condensation on the ceiling. The (well-mixed) enclosure concentration remains at $Y_\infty = Y_{eq}(T_c)$ and evaporation continues at a constant rate such that

$$\Delta m = \rho V [Y_{eq}(T_c) + \pi R^2 h_m (Y_{eq}(T_w) - Y_{eq}(T_c))(t - t_c)]. \quad (4)$$

Equation (4) is used to extend the model past the point when condensation begins, which is calculated to occur at $\Delta m = \Delta m_{eq}(T_c) = 14.4$ g, or when $Y_\infty = Y_{eq}(21^\circ\text{C}) = 0.00871$ (upper dashed line in Fig. 2).

Note that in the later stages of an experiment the contribution of organic vapor to the density ratio $(\rho_w - \rho_\infty)/\rho_\infty$ is reduced while the thermal contribution is unchanged. By the time condensation begins the vapor contribution becomes $(1 - M_g/M_w)(Y_{eq}(T_w) - Y_{eq}(T_c)) = 1.0 \times 10^{-3}$, and thermal convection is overwhelming. Since the stabilizing influence of the organic vapor is diminished as the enclosure vapor concentration increases, it is reasonable to infer that its apparent impact on the model coefficient C_o is likewise reduced. Thus the appropriate value for C_o is expected to gradually approach 0.15 later in an experiment. In mathematical terms (see Eq. (1)) this transition likely begins at the neutral stability limit where $(\rho_w - \rho_\infty)/\rho_\infty = 0$, which corresponds to $Y_\infty = 0.00568$ or $\Delta m = 9.4$ g (see again Fig. 2). This expectation is supported by the late-time ($t > t_c$) data shown in Fig. 2, which indicate evaporation rates that compare reasonably well with the (steady) rates predicted for $C_o = 0.15$.

Conclusion

The theoretical implications of the comparisons displayed in Fig. 2 are clear: Evaporation from the organic pool is strongly affected by global natural circulation in the enclosure, and the evaporation rate appears to be predictable by a well-established mass transfer correlation. The conventional numerical coefficient for this correlation is $C_o = 0.15$. However, for moderate enclosure vapor concentrations, such that the bulk gas density is less than the gas mixture density just above the organic pool (i.e., $\rho_\infty < \rho_w$), the present data suggest that as the pool size increases above 0.4 m the appropriate coefficient decreases and falls below $C_o \approx 0.1$.

References

Katsaros, K. B., Liu, W. T., Businger, J. A., and Tillman, J. E., 1977, "Heat Transport and Thermal Structure in the Interfacial Boundary Layer Measured in an

Open Tank of Water in Turbulent Free Convection," *J. Fluid Mech.* Vol. 83, pp. 311–335.

Kline, S. J., and McClintock, F. A., 1953, "Describing Uncertainties in Single-Sample Experiments," *Mechanical Engineering*, Jan., pp. 3–8.

Effects of Surface Tension and Binary Diffusion on Pool Boiling of Dilute Solutions: An Experimental Assessment

S. G. Kandlikar^{1,2} and L. Alves¹

Pool boiling heat transfer with dilute binary mixtures introduces two additional effects due to binary diffusion, and due to change in the surface tension. The secondary effects due to changes in contact angle and wetting characteristics may also play a role. The present study focuses on identifying these effects for dilute aqueous solutions of ethylene glycol. Pool boiling experiments are conducted to generate data in the range of one to ten percent mass fraction. It is found that in the low concentration region, the binary diffusion effects are insignificant for aqueous solutions of ethylene glycol, and a slight improvement in heat transfer coefficient is observed over the pure water value. The binary diffusion effects are related to a volatility parameter, V_1 . The heat transfer coefficient does not degrade in the region where $V_1 < 0.03$, and the surface tension does not change appreciably compared to pure water value. This points to the possibility that the changes in contact angle and wetting characteristics play an important role in the pool boiling heat transfer.

Nomenclature

$c_{p,l}$ = liquid specific heat, J/kg°C
 D_{12} = mass diffusivity of 1 in 2, m²/s
 i_{lg} = latent heat, J/kg
 p = pressure, Pa
 R = radius of a bubble, m
 T = temperature, K
 V = volatility parameter, = $(c_{p,l}/i_{lg})(\kappa/D_{12})^{0.5}(x_1 - y_1)dT/dx_1$
 x = liquid mass fraction
 y = vapor mass fraction

Greek

α = heat transfer coefficient, W/m²°C
 κ = thermal diffusivity, m²/s
 λ = thermal conductivity, W/m°C
 σ = surface tension, N/m

Subscripts

1 = component 1, water
 2 = component 2, ethylene glycol
 g = vapor
 l = liquid

¹Mechanical Engineering Department, Rochester Institute of Technology, Rochester, NY 14623.

²e-mail: sgkeme@rit.edu.

Contributed by the Heat Transfer Division for publication in the JOURNAL OF HEAT TRANSFER and submitted for presentation at NHTC, Albuquerque. Manuscript received by the Heat Transfer Division, Oct. 26, 1997; revision received, Jan. 13, 1999. Keywords: Binary, Boiling, Heat Transfers, Surface Tension. Associate Technical Editor: M. Kaviany.

the surrounding thermals become less effective as the pool size increases.

With regard to the downflow mode mentioned previously, it is worth noting that a few isothermal ($T_w = T_c$) evaporation experiments have been performed using 9 and 17-cm diameter pools. During these experiments there was no surrounding thermal convection, and evaporation proceeded by downward flow over the pool and/or by diffusion. The evaporation rate for the 9-cm pool is a factor of two less than that previously measured in the presence of thermal convection. For the 17-cm pool the evaporation rate is a factor of three less than the evaporation rate with thermal convection. If downflow were dominating the evaporation process then evaporation rates in the presence of thermal convection should have been nearly the same as those measured under isothermal conditions. Also the downflow mechanism requires a positive value of $\rho_w - \rho_\infty$. If this mechanism is important, one anticipates a detectable change (reduction) in the slope of the measured mass lost versus time curves as the neutral stability limit is approached (lower dashed line in Fig. 2). On the contrary, the mass lost versus time trend is unchanged as the neutral stability line is crossed. Clearly, the evaporation process is governed mostly by exterior turbulent conditions rather than by the horizontally directed, hydrostatic pressure gradient just above the surface of the pool.

The evaporation history given by Eq. (3) is valid until Δm exceeds the mass of vapor in equilibrium with the ceiling (Δm_{eq}), say at time $t = t_c$. Thereafter evaporation from the pool is balanced by condensation on the ceiling. The (well-mixed) enclosure concentration remains at $Y_\infty = Y_{eq}(T_c)$ and evaporation continues at a constant rate such that

$$\Delta m = \rho V [Y_{eq}(T_c) + \pi R^2 h_m (Y_{eq}(T_w) - Y_{eq}(T_c))(t - t_c)]. \quad (4)$$

Equation (4) is used to extend the model past the point when condensation begins, which is calculated to occur at $\Delta m = \Delta m_{eq}(T_c) = 14.4$ g, or when $Y_\infty = Y_{eq}(21^\circ\text{C}) = 0.00871$ (upper dashed line in Fig. 2).

Note that in the later stages of an experiment the contribution of organic vapor to the density ratio $(\rho_w - \rho_\infty)/\rho_\infty$ is reduced while the thermal contribution is unchanged. By the time condensation begins the vapor contribution becomes $(1 - M_g/M_v)(Y_{eq}(T_w) - Y_{eq}(T_c)) = 1.0 \times 10^{-3}$, and thermal convection is overwhelming. Since the stabilizing influence of the organic vapor is diminished as the enclosure vapor concentration increases, it is reasonable to infer that its apparent impact on the model coefficient C_o is likewise reduced. Thus the appropriate value for C_o is expected to gradually approach 0.15 later in an experiment. In mathematical terms (see Eq. (1)) this transition likely begins at the neutral stability limit where $(\rho_w - \rho_\infty)/\rho_\infty = 0$, which corresponds to $Y_\infty = 0.00568$ or $\Delta m = 9.4$ g (see again Fig. 2). This expectation is supported by the late-time ($t > t_c$) data shown in Fig. 2, which indicate evaporation rates that compare reasonably well with the (steady) rates predicted for $C_o = 0.15$.

Conclusion

The theoretical implications of the comparisons displayed in Fig. 2 are clear: Evaporation from the organic pool is strongly affected by global natural circulation in the enclosure, and the evaporation rate appears to be predictable by a well-established mass transfer correlation. The conventional numerical coefficient for this correlation is $C_o = 0.15$. However, for moderate enclosure vapor concentrations, such that the bulk gas density is less than the gas mixture density just above the organic pool (i.e., $\rho_\infty < \rho_w$), the present data suggest that as the pool size increases above 0.4 m the appropriate coefficient decreases and falls below $C_o \approx 0.1$.

References

Katsaros, K. B., Liu, W. T., Businger, J. A., and Tillman, J. E., 1977, "Heat Transport and Thermal Structure in the Interfacial Boundary Layer Measured in an

Open Tank of Water in Turbulent Free Convection," *J. Fluid Mech.* Vol. 83, pp. 311–335.

Kline, S. J., and McClintock, F. A., 1953, "Describing Uncertainties in Single-Sample Experiments," *Mechanical Engineering*, Jan., pp. 3–8.

Effects of Surface Tension and Binary Diffusion on Pool Boiling of Dilute Solutions: An Experimental Assessment

S. G. Kandlikar^{1,2} and L. Alves¹

Pool boiling heat transfer with dilute binary mixtures introduces two additional effects due to binary diffusion, and due to change in the surface tension. The secondary effects due to changes in contact angle and wetting characteristics may also play a role. The present study focuses on identifying these effects for dilute aqueous solutions of ethylene glycol. Pool boiling experiments are conducted to generate data in the range of one to ten percent mass fraction. It is found that in the low concentration region, the binary diffusion effects are insignificant for aqueous solutions of ethylene glycol, and a slight improvement in heat transfer coefficient is observed over the pure water value. The binary diffusion effects are related to a volatility parameter, V_1 . The heat transfer coefficient does not degrade in the region where $V_1 < 0.03$, and the surface tension does not change appreciably compared to pure water value. This points to the possibility that the changes in contact angle and wetting characteristics play an important role in the pool boiling heat transfer.

Nomenclature

$c_{p,l}$ = liquid specific heat, J/kg°C
 D_{12} = mass diffusivity of 1 in 2, m²/s
 i_{lg} = latent heat, J/kg
 p = pressure, Pa
 R = radius of a bubble, m
 T = temperature, K
 V = volatility parameter, = $(c_{p,l}/i_{lg})(\kappa/D_{12})^{0.5}(x_1 - y_1)dT/dx_1$
 x = liquid mass fraction
 y = vapor mass fraction

Greek

α = heat transfer coefficient, W/m²°C
 κ = thermal diffusivity, m²/s
 λ = thermal conductivity, W/m°C
 σ = surface tension, N/m

Subscripts

1 = component 1, water
 2 = component 2, ethylene glycol
 g = vapor
 l = liquid

¹Mechanical Engineering Department, Rochester Institute of Technology, Rochester, NY 14623.

²e-mail: sgkeme@rit.edu.

Contributed by the Heat Transfer Division for publication in the JOURNAL OF HEAT TRANSFER and submitted for presentation at NHTC, Albuquerque. Manuscript received by the Heat Transfer Division, Oct. 26, 1997; revision received, Jan. 13, 1999. Keywords: Binary, Boiling, Heat Transfers, Surface Tension. Associate Technical Editor: M. Kaviany.

Table 1 Summary of some important studies on surface tension on boiling

Author/Year	Mixtures/Composition	Results	Comments
Lowery and Westwater (1957)	Methanol with additives	Heat transfer increased although the surface tension remained unchanged with additives.	Rate of nucleation on the heating surface was affected by the presence of additives, indicating that other factors may be important besides surface tension.
Jontz and Myers (1960)	Water and Aerosol and Tergitol of different concentrations	Volumetric study with air indicated that dynamic surface tension changed for Trgitol solutions but not for aerosol solutions. Heat transfer increased by 50% with Targitol, and by 400% with Aerosol.	Initiation of nucleation was identified as another parameter being affected by surface tension beside the departure bubble volume.
Dunskus and Westwater (1961)	Isopropanol with additives	Bubble frequency increased with additives, surface viscosity with higher molecular weight additives was identified as a factor.	Changes in contact angle and surface viscosity are believed to affect the heat transfer rates.
Roll and Myers (1964)	Water and five surfactants	Bubble volume at departure and bubble growth rates were obtained experimentally. Bubble volume, growth time and delay time decrease with surface tension, bubble frequency increased by an order of magnitude.	The complex influence of surfactants on heat transfer through bubble growth, departure size and frequency identified.
Frost and Kippenhan (1967)	Water with surface active agent in forced convection boiling	Nucleation, bubble growth and heat transfer for pure water and water containing different amount of surface active agent were compared. With the additive, more sites were nucleated, bubble growth was slower, and heat transfer improved.	Although the results are for forced convection, the observed trends are similar to those for pool boiling by other investigators. The relationship between number of bubbles and their growth rates, and heat transfer is quite complex.
Kochaphakdee and Williams (1970)	Water and polymeric additives	Polymeric additives with long chain molecules improved heat transfer. Although the viscosity was not affected, the heat transfer was improved due to the same factors as those responsible for reducing turbulent drag for these mixtures in pipe flow.	Surface viscosity with high molecular weight additives retards bubble coalescence leading to increase in heat transfer rate.
Shah and Darby (1973)	Water with commercial surfactant	In the falling film experiments, heat transfer improved due to the increased foaming under nucleate boiling conditions.	Foaming results as the bubbles do not coalesce. This behavior is due to the reduction in surface tension.
Yang and Maa (1983)	Water with two different surfactants	As surface tension of the mixture decreased, the heat transfer coefficient increased.	The localized increase in surface tension during the growth of a bubble inhibits coalescence.
Tzan and Yang (1990)	Water with SLS surfactant	Heat transfer improved with addition of surfactant. The bubble density also increased on the heater surface.	The photographs show the increased bubble activity with smaller bubbles as the surface tension decreased.
Wang and Hartnett (1992)	Water with surfactants	Heat transfer with SLS and Tween surfactants in water was same or lower than water though the surface tension was lower.	The results are contradictory to other studies, (for example Tzan and Yang, 1990, Yang and Ma, 1990). The reasons are not clear.
Straub (1993)	Water and refrigerant under regular and micro-gravity	The presence of bubble on a surface induced micro-convection which improved heat transfer with refrigerant, but not for water. Role of surface tension through flow around bubble explained.	Photographic results under saturated conditions should be used with caution as the camera speed was low at 100 fpm. Presence of smaller bubbles improved heat transfer as against the formation of dry spots with large bubbles.
Malyshenko, (1994)	Argon	The experimental values of superheat prior to nucleation are lower than calculated values.	For small bubbles, the curvature effect on surface tension needs to be considered.
Ammerman and You (1996)	Water and FC-72 with SLS surfactant	The heat transfer rate increased with the addition of surfactant. The convection component increased while the latent component decreased.	The system is similar to Wang and Hartnett (1992) for water, but the heat transfer improved with addition of surfactant. Increased nucleation with surfactants caused agitation of liquid.
Wozniak, Wozniak and Bergelt (1996)	Water under regular and micro-gravity	Surface tension driven flow becomes important in the absence of buoyancy circulation caused by gravity.	Role of surface tension becomes more important in micro-gravity.

1 Introduction

Boiling heat transfer is the direct result of nucleation, growth, and subsequent departure or collapse of vapor bubbles. The physical existence of bubbles on a heated surface in a liquid introduces solid-liquid-vapor interfaces whose characteristics play an important role in heat transfer and needs to be included in the analysis. Even the simplistic macroscopic models, such as a mechanical force balance on bubbles growing on a cavity, coupled with transient heat transfer analysis, have provided good engineering estimation of the nucleation criterion and heat transfer to some

extent. Extension of these models to microscale level is certain to raise a number of concerns, some of which may be addressed by the molecular descriptions presented in literature (e.g., Matsumoto et al., 1995). With the focus on microscale heat transfer in many applications, such as high flux cooling, ink-jet printers, or localized cooling on an electronic chip surface, there is a growing need to understand the effects of interface mechanisms. A more challenging task, however, lies ahead in translating the microscopic model into information that provides meaningful solutions to practical engineers. The problem is further complicated in binary and mul-

ticomponent systems, which are often employed in many of the above-mentioned applications.

In the present paper, the heat transfer characteristics of dilute aqueous solutions of ethylene glycol are investigated. The experimental results generated along with the information available in literature are discussed to gain a better understanding of the parameters affecting the boiling heat transfer for such mixtures.

2 Literature Review

Surface tension has been identified as an important property affecting the nucleation behavior of a cavity. The nucleation criteria developed by Bergles and Rohsenow (1964) and Hsu (1962) indicate that as the surface tension is lowered, the excess pressure requirement is lowered, as given by $\Delta p = 2\sigma/R$, where R is the critical radius of the nucleating bubble. Clearly, more nucleation sites would become active at a given superheat if a surface-active agent is added to a pure liquid lowering its surface tension without affecting other properties.

Early investigators recognized the importance of surface tension in improving the boiling heat transfer. Table 1 summarizes some of the important work in this area. It can generally be concluded from these studies that a reduction in surface tension leads to a higher nucleation site density, large number of small bubbles on the heater surface, and generally a higher heat transfer coefficient. However, there may be other factors responsible in improving the heat transfer as indicated by the study of Lowerey and Westwater (1957) where the heat transfer increased while surface tension remained constant.

The effect of surface tension is seen in two ways. First, the range of active nucleation sites increases as the surface tension is reduced. This is clearly observed through the photographic studies listed in Table 1 showing a considerable increase in the bubble population on a heater surface. The other related effect is that the bubbles do not coalesce as readily, causing a large number of bubbles to exist on the heater surface. Departure bubble diameter is also reduced.

Interestingly, it has been reported in literature that the bubble growth rates in binary systems are lower compared to pure fluids. Roll and Myers (1966) attribute this to early nucleation at lower wall superheats. The smaller available temperature difference results in a subsequent slower growth rate. Another influencing factor is that, in the presence of a surface-active agent, bubbles do not coalesce, thereby leaving a larger number of smaller bubbles covering the heater surface. Since the smaller diameter cavities fall in the active range, the surface characteristics become important. This fact could perhaps be responsible for the contradictory results observed by Wang and Hartnett (1994), who observed a decrease in heat transfer with a decrease in surface tension, rather than an increase as reported by other studies reported in Table 1.

The effects of secondary flows, induced by the variation of surface tension around a bubble become important in microgravity applications. The exact dependence is still not clear. As some studies indicate, this phenomenon may not be important with water (Straub, 1993).

The addition of another liquid is expected to change the contact angle and wetting characteristics of the mixture. This effect has been suspected to affect the heat transfer by some investigators (e.g., Dunskus and Westwater, 1961). However, the information available in literature is not enough to draw any conclusions.

An additional mass transfer resistance to evaporation is introduced at the interface in binary systems. This is a direct result of the depletion of the more volatile component during evaporation at the interface. The reduction in the heat transfer depends on the difference between the liquid and vapor phase compositions, and the slope of the bubble point curve. Kandlikar (1998a, b) utilized a volatility parameter, $V_1 = (c_{p,L}/i_{fg})(\kappa/D_{12})^{0.5}(x_1 - y_1)dT/dx_1$, to incorporate the binary effects in pool boiling. The same parameter was utilized in flow boiling, and it was found that the suppression due to mass diffusion effects was negligible for $V_1 < 0.03$, and heat transfer data was well represented by the ideal mixture value (obtained by treating the

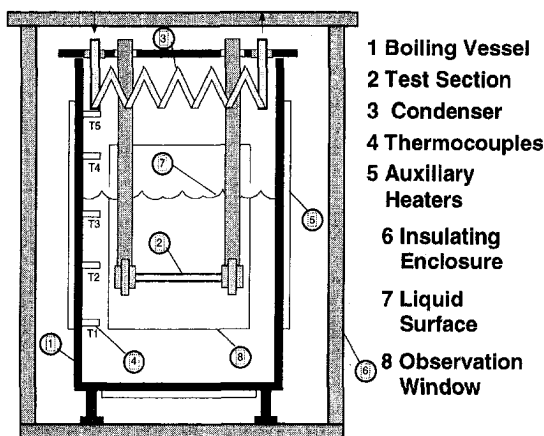


Fig. 1 Experimental setup

mixture as a pseudo-single-component fluid), without any suppression factor (Kandlikar, 1998b). Since the pool boiling data for dilute solution was not available, this limit could not be established in the pool boiling correlation.

The objectives of the present study are to obtain the experimental data for pool boiling of water/ethylene glycol at low concentrations of ethylene glycol, to establish the limits for V_1 in estimating the lower limit of binary diffusion effects. The study is also expected to provide an insight on the effects due to variation in surface tension and mass diffusion on pool boiling, and indicate whether the factors such as contact angle and wettability variation needs to be included in future studies.

3 Experimental Setup

3.1 Experimental Apparatus. The experimental apparatus utilized in this investigation is similar to that employed by Fujita et al. (1996). The apparatus brings a pool of quiescent liquid to its saturation temperature at atmospheric pressure, and allows the data collection while observing the bubble activity on the tubular heating element. A schematic of the pool boiling apparatus is presented in Fig. 1.

The experimental apparatus consists of a boiling vessel, a horizontally mounted seamless stainless steel tubular heating element, and an external insulating vessel or enclosure. The boiling vessel is a rectangular tank made out of $\frac{1}{4}$ -in. 2024-T3 aluminum stock, whose dimensions are 82.16 mm \times 82.16 mm and it is 123.24 mm tall. It provides a glass window for visual observation of the boiling phenomena. A rectangular window 51.35 mm \times 82.16 mm is made out of an amber borosilicate with properties very similar to those of PYREX.

The heating element, or test section, consists of an electrically heated seamless stainless steel tube with 3.08 mm OD, 2.05 mm ID, and 42.4 mm long. It was mounted horizontally 60 mm below the free liquid surface. The circular tube heater geometry was selected because the results obtained by Fujita et al. (1996) for a similar geometry could be used to check the validity of the present experimental setup before conducting experiments in the low concentration region. While previous researchers utilized the test section as a resistance thermometer, in this study the internal wall temperature of the stainless steel tube is measured with a set of four E-type thermocouples. A Teflon tubing was introduced with a slight interference-fit inside the heating tube for positioning and securing the thermocouples against the inner tube wall as shown in Fig. 2. The four thermocouple wires were threaded through the flexible Teflon tube, and the thermocouple beads were manufactured to fit closely inside the tapered hole. The thermocouples were flush with the teflon tube, and measured the inner wall temperature of the stainless steel tube. The thermocouple beads were placed 7 mm and 90 deg apart from its neighbor and were mounted symmetrically from the center of the tube length covering the central

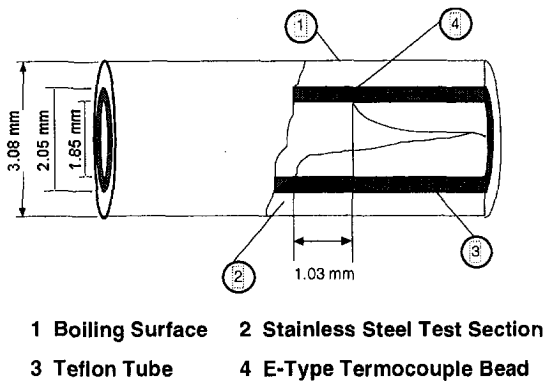


Fig. 2 Details of the test section

25-mm tube length. The resulting geometry yielded an adequate overall coverage of the internal temperature distribution along the inner wall of the heating element. The stainless steel tube was powered by a DC power within a range of 15–60 amps, according to the heat flux specification. The teflon tube was filled with epoxy so that there was no convection inside the stainless steel or teflon tubes. Also, the absence of axial conduction losses in the central region provided accurate estimation of heat flux in the vicinity of the thermocouples.

A second set of thermocouples was deployed vertically in the boiling vessel to measure the bulk liquid and vapor temperatures. Three thermocouples were placed in the liquid, and two in the vapor, and they monitored the saturation state of the mixture. In bringing the liquid to its saturation temperature, four auxiliary sheet heaters were attached on the outside walls of the boiling vessel. The heaters are rated 100 watts at 120 volts. After reaching the saturation state, the power to heaters was reduced to 60–80 percent of the rated output for the duration of the experiments.

In maintaining the original experimental conditions throughout, it was important to maintain the same heating surface characteristics for all runs and to keep the composition of the liquid constant during each run. An ethanol drenched gauze was used to clean the surface prior to each data gathering session followed by thorough rinsing with distilled water. To keep the liquid composition constant during each series of runs, a condenser was provided to condense the vapor generated on the boiling surface.

It should also be noted that to avoid the thermal hysteresis effects, a phenomenon frequently observed in boiling systems, the heat flux was gradually increased to the highest desired value, and the data was collected as the heat flux was reduced in a step-wise fashion.

3.2 Details of the Binary Mixture and Error Estimation.

In the present study the liquid charged to the boiling vessel was made up of distilled water and super-high reagent grade ethylene glycol. The distilled water utilized had been de-gassed. The two pure components were mixed on a volume ratio basis, derived from the desired mass fraction values. The resulting mass fraction was accurate to within ± 0.1 percent. It was decided that data for the entire range of concentration should be gathered first and compared with the published literature to ascertain the accuracy of the experimental setup. After these tests, dilute aqueous solutions of ethylene glycol are tested for the concentrations of one, two, three, five, and ten percent by mass.

The standard fluid properties for each of the components were obtained from the ASHRAE Fundamentals Handbook (1994) for water, and from a Union Carbide (1997) publication for ethylene glycol. Mixture properties were obtained from HYSIM (1996) property routines. The thermocouples were calibrated at steam point and ice point and matched with the actual values within 0.1 C. The error in the surface temperature estimation from the temperature profile equation for a tube with internal heat generation provided a surface temperature estimation within 0.2 K. The heat flux was calculated after measuring the actual voltage applied to

the test section. The heat losses from the sides were minimal and their influence was negligible as only the central 21 mm region of the tube length over the 42 mm heated length was considered for temperature measurement and subsequent data reduction. From this analysis, the overall heat transfer coefficient is estimated following the error analysis procedure outlined by ASME Policy on Error Estimation to be within ± 7.5 percent.

3.3 Experimental Procedure and Data Reduction.

The experimental procedure was initiated with the charging of the binary mixture, at the required concentration, to the boiling vessel. The mixture was then brought up to its saturation temperature, at atmospheric pressure, by the use of four auxiliary heaters. Once the temperature came to within 3 K of the saturation temperature, the auxiliary heater power was cut down to between 60 percent and 80 percent of the maximum power. Direct current, ranging between 15 and 60 amperes, was then supplied to the stainless steel test section, and this was done in the order of decreasing heat flux to avoid boiling hysteresis. The process was allowed to proceed for approximately $\frac{1}{2}$ hour, enough time for degassification of the mixture and for the temperature distribution on the boiling surface to stabilize. The two sets of temperatures inside the vessel and inside the heater tube were then recorded. This procedure was repeated for the entire spectrum of concentrations, and multiple runs verified the validity of the gathered results.

From the measured values of power to the heater, the heat flux was calculated after incorporating the voltage drop in the leads. The average of the four inner wall temperatures was used to estimate the outer wall temperature using the temperature distribution expression for a cylinder with uniform heat generation. The saturation temperature was determined from the atmospheric pressure and the known concentration. HYSIM property routines were employed to determine the saturation properties. Heat transfer coefficient was then calculated on the basis of the outside diameter of the heater tube.

4 Results and Discussion

Experiments were first conducted over the entire range of mass concentration in steps of 0.1 to compare with the available data by Fujita et al. (1996). Figure 3 shows the results for the heat flux value of 100 kW/m^2 . Experiments could not be performed with pure ethylene glycol due to its high boiling point. It can be seen that the agreement between the two sets is excellent. However, the pure water data lies somewhat below Fujita et al.'s data. To confirm this, the pure water runs were repeated three more times over a period of two months. The results were within two percent. Similar agreement was observed at lower heat fluxes as well.

To study the effect of concentration on heat transfer for dilute mixtures, experiments were conducted with one, two, three, five, seven, and ten percent mass fractions of ethylene glycol. Figure 4 shows the results for four different heat fluxes. For one percent concentration, the heat transfer coefficient increased between zero to

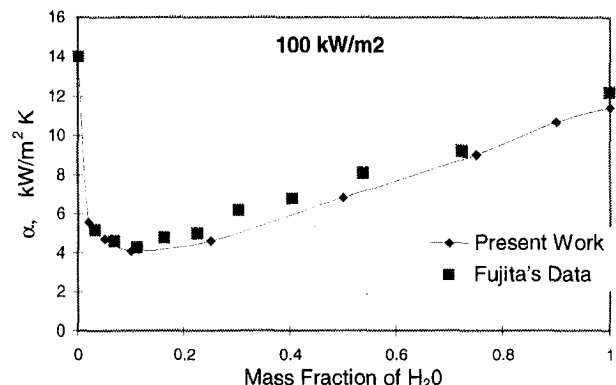


Fig. 3 Comparison of present work with Fujita et al. (1996)

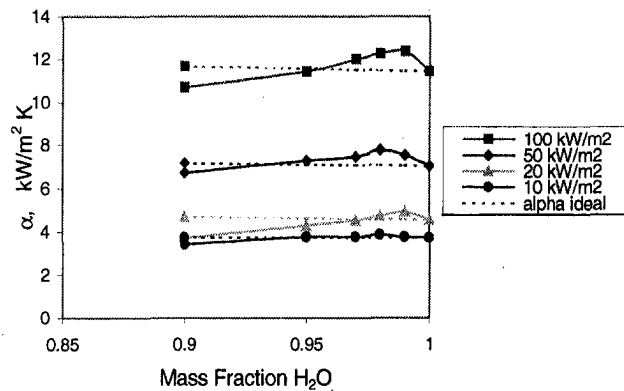


Fig. 4 Experimental data for dilute aqueous solutions of ethylene glycol

five percent above the pure water value, and then it started to decrease with increasing concentration. However, as the heat flux increased, the heat transfer coefficient with two, three, and five percent ethylene glycol concentration was also noted to be above the respective pure water values. There is no data available in literature in this range of composition. To verify the results, the experiments were repeated and found to agree within two to three percent.

The ideal heat transfer coefficient, α_{id} , for the binary solutions are obtained as the reciprocal mass fraction average of the respective pure component value. Fujita et al.'s (1996) values for pure ethylene glycol were used in calculating α_{id} . Variation of α_{id} with concentration is also plotted in Fig. 4.

As noted in the literature survey, the addition of surfactants at low concentration is found to increase the heat transfer coefficient. Figure 5 shows the variation of surface tension with ethylene glycol concentration obtained from the HYSIM property routines. It is seen from this figure that the surface tension remains almost constant with the addition of small quantities of ethylene glycol to water. However, adding water to ethylene glycol increases the surface tension at low concentrations.

In the low concentration region, the surface tension as well as other properties remain essentially constant at the pure water values. The enhancement effect is shifted to higher concentrations (see Fig. 3), in the two to five percent range, as the heat flux is increased from 10 to 100 kW/m².

The most significant factor associated with binary pool boiling heat transfer is the degradation caused by the preferential evaporation of the more volatile component at the bubble interface. The mass transfer resistance in the liquid raises the liquid temperature at the interface with subsequent degradation in heat transfer. In analyzing pool boiling heat transfer, the volatility parameter V_1 is often utilized. The same parameter was utilized by Kandlikar

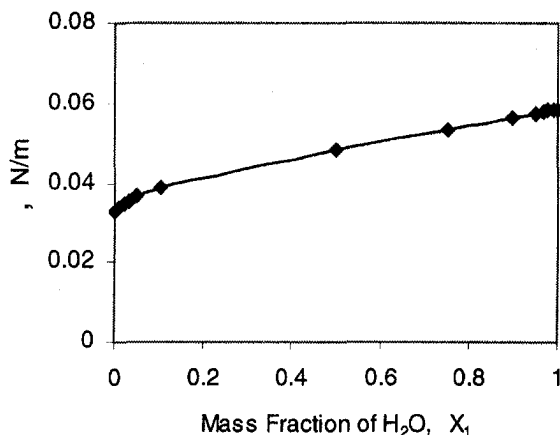


Fig. 5 Surface tension variation with mixture composition

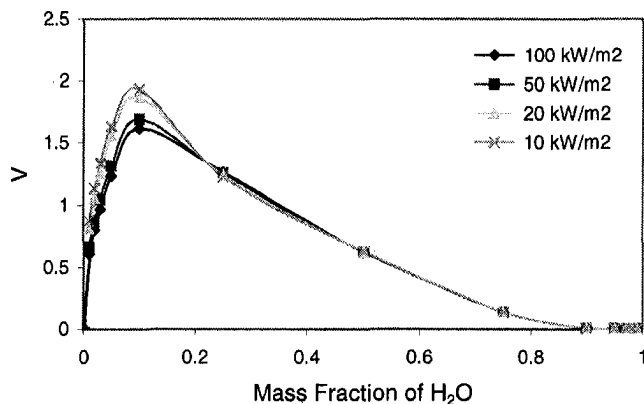


Fig. 6 Variation of the volatility parameter with concentration

(1998b) in correlating the flow boiling data of mixtures. It was noted that for $V_1 < 0.03$, the mixture effects were negligible, and the heat transfer was given by the ideal heat transfer coefficient value. In other words, the mixture behaved like a pure component without any mass diffusion effects.

Figure 6 shows a plot of the volatility parameter, V_1 , plotted against mass concentration for water-ethylene glycol mixture. It can be seen that at low concentrations of ethylene glycol, up to ten percent, the value of V_1 is less than 0.005. In this range, the mass diffusion effects would be negligibly small.

Conversely, the volatility parameter has a very high value near pure ethylene glycol side (Fig. 6). Further, the surface tension increases rapidly with the addition of small amounts of water (Fig. 5). The combined effect of these two factors is a significant deterioration in heat transfer for water-ethylene glycol mixture with small amount of water as seen from Fig. 3.

In the absence of the surface tension changes, or mass diffusion effects, the only explanation for the slight improvement in the heat transfer coefficient seen in the low concentration region could be offered on the basis of the changes in contact angle, or other bubble nucleation and growth related parameters. However, the increase observed is quite small, and it is suggested that similar experiments should be conducted with other binary mixtures to explore the heat transfer characteristics in the low concentration region in the absence of significant mass diffusion effects.

5 Conclusions

The literature survey indicates that addition of a small amount of surface-tension reducing agent enhances the pool boiling heat transfer. An experimental study was performed to determine the effects of binary diffusion and surface tension on pool boiling heat transfer of dilute aqueous solutions of ethylene glycol. The experimental results over the 10 to 98 percent range are in excellent agreement with the experimental data of Fujita et al. (1996). Following conclusions related to the low concentration region are drawn based on the present study.

1 Heat transfer coefficient was seen to increase slightly with the addition of small amount of ethylene glycol to water. Surface tension of the mixture was essentially constant in this range, and is not believed to be the cause for this increase.

2 The binary diffusion effects are insignificant for dilute aqueous solutions of ethylene glycol. The volatility parameter V_1 is seen to represent this effect. For $V_1 < 0.03$, the mixture may be treated like a pure component from a heat transfer viewpoint. The heat transfer coefficient can be estimated as the pool boiling heat transfer coefficient for the ideal mixture. Additional correction for surface tension may be introduced in this term.

3 Since the surface tension and the mass diffusion effects are found to be insignificant for the aqueous solutions of ethylene glycol at low concentrations, the changes in contact angle or other

related parameter are suspected to be responsible for this increase. Further experimentation with different binary combinations is recommended along with accurate measurements of contact angle changes in this region.

Acknowledgments

The author is thankful to Dr. Vijay Srinivasan of Praxair, Inc., Tonawanda, NY, for his help in mixture property evaluation using HYSIM property routines.

References

- Ammerman, C. N., and You, S. M., 1996, "Determination of the Boiling Enhancement Mechanism Caused by Surfactant Addition to Water," *ASME JOURNAL OF HEAT TRANSFER*, Vol. 118, pp. 429–435.
- Bergles, A. E., and Rohsenow, W. M., 1964, "The Determination of Forced-Convection Surface-Boiling Heat Transfer," *ASME JOURNAL OF HEAT TRANSFER*, Vol. 86, pp. 365–372.
- Dunskus, T., and Westwater, J. W., 1961, "The Effect of Trace Additives on the Heat Transfer to Boiling Isopropanol," *Chem. Engng. Prog. Symp.*, Ser. No. 32, Vol. 57, AIChE, New York, pp. 173–181.
- Fujita, Y., Bai, Q., Tsutsui, M., 1996, "Heat Transfer of Binary Mixtures in Nucleate Pool Boiling," *2nd European Thermal Sciences and 14th IIT National Heat Transfer Conference*, G. P. Celata, Di Marco, and A. Mariani, eds., Edizioni ETS, Pisa, Italy, pp. 1639–1646.
- Hsu, Y. Y., 1962, "On the Size Range of Active Nucleation Cavities on a Heating Surface," *ASME JOURNAL OF HEAT TRANSFER*, Vol. 84, pp. 207–216.
- HYSIM, Version 6, 1996, Hyprotech Ltd., Calgary, Alberta, Canada.
- Jontz, P. D., and Myers, J. E., 1960, "The Effect of Dynamic Surface Tension on Nucleate Boiling Coefficients," *AIChE J.*, Vol. 6, No. 1, pp. 34–38.
- Kandlikar, S. G., 1998a, "Boiling Heat Transfer in Binary Systems: Part I—Pool Boiling," *ASME JOURNAL OF HEAT TRANSFER*, Vol. 120, pp. 380–387.
- Kandlikar, S. G., 1998b, "Boiling Heat Transfer in Binary Systems: Part II—Flow Boiling," *ASME JOURNAL OF HEAT TRANSFER*, Vol. 120, pp. 388–394.
- Kochapakdee, P., and Williams, M. C., 1970, "Enhancement of Nucleate Pool Boiling with Polymeric Additives," *Int. J. Heat and Mass Transfer*, Vol. 13, pp. 835–848.
- Lowery, A. J., and Westwater, J. W., 1957, "Heat Transfer to Boiling Methanol—Effect of Added Agents," *Ind. and Eng. Chem.*, Vol. 49, pp. 1445–1448.
- Malyshenko, S. P., 1994, "Effect of a Curved Phase Boundary on Surface Tension and Kinetics of Nucleation in Liquids," *High Temperature*, Vol. 32, No. 5, pp. 671–678.
- Matsumoto, S., Maruyama, S., and Saruwatari, H., 1995, "A Molecular Dynamics Simulation of a Liquid Droplet on a Solid Surface," *Proceedings of ASME-JSME Thermal Engineering Joint Conference*, Miami, Vol. 2, pp. 557–562.
- Roll, J. B., and Myers, J. M., 1964, "The Effect of Surface Tension on Factors in Boiling Heat Transfer," *AIChE J.*, Vol. 10, No. 4, pp. 530–534.
- Shah, B. T., and Darby, R., 1973, "The Effect of Surfactant on Evaporative Heat Transfer in Vertical Film Flow," *Int. J. Heat and Mass Transfer*, Vol. 16, pp. 1889–1903.
- Straub, J., 1993, "The Role of Surface Tension for Two-Phase Heat and Mass Transfer in the Absence of Gravity," *Experimental Heat Transfer, Fluid Mechanics and Thermodynamics 1993*, M. D. Kelleher, ed., Elsevier, New York.
- Tzan, Y. L., and Yang, Y. M., 1990, "Experimental Study of Surfactant Effects on Pool Boiling Heat Transfer," *ASME JOURNAL OF HEAT TRANSFER*, Vol. 112, pp. 207–212.
- Yang, Y. M., and Maa, J. R., 1983, "Pool Boiling of Dilute Surfactant Solutions," *ASME JOURNAL OF HEAT TRANSFER*, Vol. 105, pp. 190–192.
- Wang and Hartnett, 1994, "Pool Boiling of Heat Transfer from a Horizontal Wire to Aqueous Surfactant Solutions," *Heat transfer 1994: Proceedings of 10th International Heat Transfer Conference*, Brighton, Institute of Chemical Engineers/Institute of Mechanical Engineers, pp. 177–182.
- Wozniak, G., Wozniak, K., and Berglet, H., 1996, "On the Influence of Buoyancy on the Surface Tension Driven Flow Around a Bubble on a Heater Wall," *Experiments in Fluids*, Vol. 21, pp. 181–186.

Heat Transfer Studies During Solidification of PCM Inside an Internally Finned Tube

R. Velraj¹ and R. V. Seeniraj¹

Nomenclature

- Bi = Biot number, hr_0/k_p
 c = specific heat, $\text{J kg}^{-1} \text{K}^{-1}$
 H = enthalpy, J kg^{-1}
 h = convective heat transfer coefficient, $\text{W m}^{-2} \text{K}^{-1}$
 k = thermal conductivity, $\text{W m}^{-1} \text{K}^{-1}$
 N = number of nodes
 n = number of fins
 R = nondimensional radial coordinate, r/r_0
 r = radial coordinate, m
 Ste = Stefan number
 T = temperature, K
 t = time
 w = thickness, m

Greek Symbols

- α = thermal diffusivity ($=k/\rho c$), $\text{m}^2 \text{s}^{-1}$
 β = half the angle between two fins
 ε = half of the phase-change temperature range, K
 ϕ = nondimensional temperature

- λ = latent heat, J kg^{-1}
 θ = angular coordinate
 ρ = density, kg m^{-3}
 τ = nondimensional time, $\alpha_p t/r_0^2$
 ω = nondimensional angular coordinate, θ/β
 ψ = nondimensional enthalpy

Subscripts

- b = boundary
 c = junction node
 f = fin
 i, j = node designation
 $init$ = initial
 p = phase-change material
 s = saturated condition
 ∞ = surrounding coolant

1 Introduction

Latent heat thermal storage units have received greater attention in the recent years due to their advantages of modular construction, reliability, isothermal behavior of energy source, and pollution-free operation. However, such units suffer from the disadvantage that the heat transfer rate decreases as the interface moves away from the heat transfer surface, due to the increasing thermal resistance offered by the solidified phase-change material. This calls for the usage of proper heat transfer enhancement methodologies.

The use of finned tubes with different configurations to enhance heat transfer has been reported by various researchers. Studies on external annular fins were made by Lacroix (1993), Padmanabhan and Krishnamurthy (1986a, b), and Sparrow et al. (1981). Griffin and Smith (1980) and Smith and Koch (1982) have done a theoretical study of solidification adjacent to a flat-finned surface. Velraj et al. (1997) have presented experimental results of a thermal storage unit consisting of a vertical cylindrical tube containing the phase-change material with internal longitudinal fins. Among the various methods employed for modeling the phase-change problems, the enthalpy formulation is widely used. Sham-

¹ Department of Mechanical Engineering, Anna University, Chennai 600025, India

Contributed by the Heat Transfer Division for publication in the *JOURNAL OF HEAT TRANSFER*. Manuscript received by the Heat Transfer Division, Jan. 22, 1998; revision received Oct. 14, 1998. Keywords: Finite Difference, Finned Surfaces, Heat Transfer, Phase Change, Solidification, Storage. Associate Technical Editor: M. Kaviany.

related parameter are suspected to be responsible for this increase. Further experimentation with different binary combinations is recommended along with accurate measurements of contact angle changes in this region.

Acknowledgments

The author is thankful to Dr. Vijay Srinivasan of Praxair, Inc., Tonawanda, NY, for his help in mixture property evaluation using HYSIM property routines.

References

- Ammerman, C. N., and You, S. M., 1996, "Determination of the Boiling Enhancement Mechanism Caused by Surfactant Addition to Water," *ASME JOURNAL OF HEAT TRANSFER*, Vol. 118, pp. 429–435.
- Bergles, A. E., and Rohsenow, W. M., 1964, "The Determination of Forced-Convection Surface-Boiling Heat Transfer," *ASME JOURNAL OF HEAT TRANSFER*, Vol. 86, pp. 365–372.
- Dunskus, T., and Westwater, J. W., 1961, "The Effect of Trace Additives on the Heat Transfer to Boiling Isopropanol," *Chem. Engng. Prog. Symp.*, Ser. No. 32, Vol. 57, AIChE, New York, pp. 173–181.
- Fujita, Y., Bai, Q., Tsutsui, M., 1996, "Heat Transfer of Binary Mixtures in Nucleate Pool Boiling," *2nd European Thermal Sciences and 14th IIT National Heat Transfer Conference*, G. P. Celata, Di Marco, and A. Mariani, eds., Edizioni ETS, Pisa, Italy, pp. 1639–1646.
- Hsu, Y. Y., 1962, "On the Size Range of Active Nucleation Cavities on a Heating Surface," *ASME JOURNAL OF HEAT TRANSFER*, Vol. 84, pp. 207–216.
- HYSIM, Version 6, 1996, Hyprotech Ltd., Calgary, Alberta, Canada.
- Jontz, P. D., and Myers, J. E., 1960, "The Effect of Dynamic Surface Tension on Nucleate Boiling Coefficients," *AIChE J.*, Vol. 6, No. 1, pp. 34–38.
- Kandlikar, S. G., 1998a, "Boiling Heat Transfer in Binary Systems: Part I—Pool Boiling," *ASME JOURNAL OF HEAT TRANSFER*, Vol. 120, pp. 380–387.
- Kandlikar, S. G., 1998b, "Boiling Heat Transfer in Binary Systems: Part II—Flow Boiling," *ASME JOURNAL OF HEAT TRANSFER*, Vol. 120, pp. 388–394.
- Kochaphakdee, P., and Williams, M. C., 1970, "Enhancement of Nucleate Pool Boiling with Polymeric Additives," *Int. J. Heat and Mass Transfer*, Vol. 13, pp. 835–848.
- Lowery, A. J., and Westwater, J. W., 1957, "Heat Transfer to Boiling Methanol—Effect of Added Agents," *Ind. and Eng. Chem.*, Vol. 49, pp. 1445–1448.
- Malyshenko, S. P., 1994, "Effect of a Curved Phase Boundary on Surface Tension and Kinetics of Nucleation in Liquids," *High Temperature*, Vol. 32, No. 5, pp. 671–678.
- Matsumoto, S., Maruyama, S., and Saruwatari, H., 1995, "A Molecular Dynamics Simulation of a Liquid Droplet on a Solid Surface," *Proceedings of ASME-JSME Thermal Engineering Joint Conference*, Miami, Vol. 2, pp. 557–562.
- Roll, J. B., and Myers, J. M., 1964, "The Effect of Surface Tension on Factors in Boiling Heat Transfer," *AIChE J.*, Vol. 10, No. 4, pp. 530–534.
- Shah, B. T., and Darby, R., 1973, "The Effect of Surfactant on Evaporative Heat Transfer in Vertical Film Flow," *Int. J. Heat and Mass Transfer*, Vol. 16, pp. 1889–1903.
- Straub, J., 1993, "The Role of Surface Tension for Two-Phase Heat and Mass Transfer in the Absence of Gravity," *Experimental Heat Transfer, Fluid Mechanics and Thermodynamics 1993*, M. D. Kelleher, ed., Elsevier, New York.
- Tzan, Y. L., and Yang, Y. M., 1990, "Experimental Study of Surfactant Effects on Pool Boiling Heat Transfer," *ASME JOURNAL OF HEAT TRANSFER*, Vol. 112, pp. 207–212.
- Yang, Y. M., and Maa, J. R., 1983, "Pool Boiling of Dilute Surfactant Solutions," *ASME JOURNAL OF HEAT TRANSFER*, Vol. 105, pp. 190–192.
- Wang and Hartnett, 1994, "Pool Boiling of Heat Transfer from a Horizontal Wire to Aqueous Surfactant Solutions," *Heat transfer 1994: Proceedings of 10th International Heat Transfer Conference*, Brighton, Institute of Chemical Engineers/Institute of Mechanical Engineers, pp. 177–182.
- Wozniak, G., Wozniak, K., and Berglet, H., 1996, "On the Influence of Buoyancy on the Surface Tension Driven Flow Around a Bubble on a Heater Wall," *Experiments in Fluids*, Vol. 21, pp. 181–186.

Heat Transfer Studies During Solidification of PCM Inside an Internally Finned Tube

R. Velraj¹ and R. V. Seeniraj¹

Nomenclature

- Bi = Biot number, hr_0/k_p
 c = specific heat, $\text{J kg}^{-1} \text{K}^{-1}$
 H = enthalpy, J kg^{-1}
 h = convective heat transfer coefficient, $\text{W m}^{-2} \text{K}^{-1}$
 k = thermal conductivity, $\text{W m}^{-1} \text{K}^{-1}$
 N = number of nodes
 n = number of fins
 R = nondimensional radial coordinate, r/r_0
 r = radial coordinate, m
Ste = Stefan number
 T = temperature, K
 t = time
 w = thickness, m

Greek Symbols

- α = thermal diffusivity ($=k/\rho c$), $\text{m}^2 \text{s}^{-1}$
 β = half the angle between two fins
 ε = half of the phase-change temperature range, K
 ϕ = nondimensional temperature

- λ = latent heat, J kg^{-1}
 θ = angular coordinate
 ρ = density, kg m^{-3}
 τ = nondimensional time, $\alpha_p t/r_0^2$
 ω = nondimensional angular coordinate, θ/β
 ψ = nondimensional enthalpy

Subscripts

- b = boundary
 c = junction node
 f = fin
 i, j = node designation
init = initial
 p = phase-change material
 s = saturated condition
 ∞ = surrounding coolant

1 Introduction

Latent heat thermal storage units have received greater attention in the recent years due to their advantages of modular construction, reliability, isothermal behavior of energy source, and pollution-free operation. However, such units suffer from the disadvantage that the heat transfer rate decreases as the interface moves away from the heat transfer surface, due to the increasing thermal resistance offered by the solidified phase-change material. This calls for the usage of proper heat transfer enhancement methodologies.

The use of finned tubes with different configurations to enhance heat transfer has been reported by various researchers. Studies on external annular fins were made by Lacroix (1993), Padmanabhan and Krishnamurthy (1986a, b), and Sparrow et al. (1981). Griffin and Smith (1980) and Smith and Koch (1982) have done a theoretical study of solidification adjacent to a flat-finned surface. Velraj et al. (1997) have presented experimental results of a thermal storage unit consisting of a vertical cylindrical tube containing the phase-change material with internal longitudinal fins. Among the various methods employed for modeling the phase-change problems, the enthalpy formulation is widely used. Sham-

¹ Department of Mechanical Engineering, Anna University, Chennai 600025, India

Contributed by the Heat Transfer Division for publication in the *JOURNAL OF HEAT TRANSFER*. Manuscript received by the Heat Transfer Division, Jan. 22, 1998; revision received Oct. 14, 1998. Keywords: Finite Difference, Finned Surfaces, Heat Transfer, Phase Change, Solidification, Storage. Associate Technical Editor: M. Kaviany.

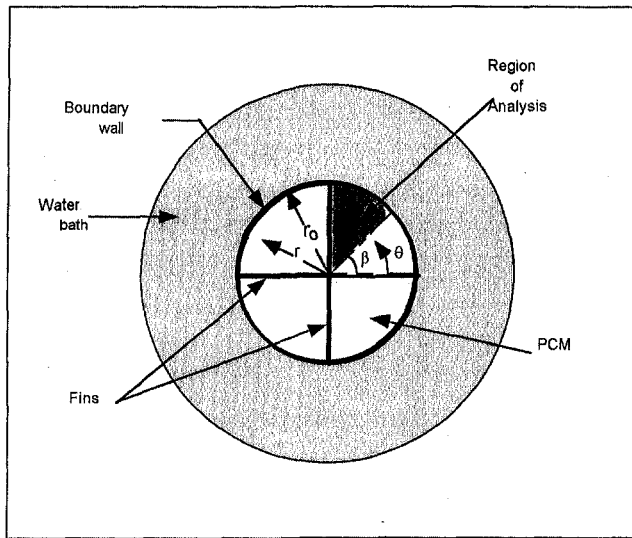


Fig. 1 Cross section of a typical tube-fin arrangement of the latent heat thermal storage system

sunder and Sparrow (1975), Voller (1990), and Lacroix (1993) have used enthalpy formulation for modeling phase-change problems and solved the system of equations through different approaches. Date (1991) generalized the enthalpy temperature relationships in such a way that no "bookkeeping" is required to identify the phase change and the single-phase nodes. Subsequently Velraj et al. (1997) have modified this relationship to accommodate materials having either constant or a range of phase-change temperatures.

The heat transfer analysis during the inward solidification of a phase-change material kept inside a longitudinal internally finned vertical tube is discussed in this paper. As to the authors' review there does not seem to be any theoretical study on this type of fin-tube configuration for latent heat thermal storage units. A unique feature in this formulation is that the heat flow in the circumferential direction along the tube wall is taken into account and its importance is discussed for a practical range of Biot numbers. The combined effect of Biot and Stefan number is discussed. The temperature distribution along the radial direction in the fin and along the circumferential direction in the boundary wall, the interface location in the phase-change material region, the surface heat flux, and the fraction solidified are shown and discussed for a practical range of parameters.

2 Statement of the Problem

The phase-change material filled vertical tube with "n" number of longitudinal fins internally attached, parallel to the axis of the tube and evenly placed along the circumference is kept in a container. The finned tube-container assembly is initially at a uniform temperature which is equal to or slightly greater than the phase-change temperature. The temperature of the circulating coolant in the container is suddenly lowered to a value less than the phase-change temperature and the tube assembly is subjected to a convective environment and subsequently the solidification proceeds towards the center of the tube. The cross section of the physical model considered is shown schematically in Fig. 1. Since symmetry prevails along the center line between two successive fins, only one-half of the region between two fins is chosen for the analysis and this included angle is denoted as β .

Governing Equations. The assumptions made are as follows:

The thermophysical properties of the liquid and the solid phases of the phase-change material are the same except for the density. They remain constant with respect to temperature. The buoyancy force from volume change due to phase change is neglected. The

heat conduction in the fin and the wall is one-dimensional—radial in the fin and circumferential in the wall. There is no temperature variation in the axial direction inside the paraffin tube since the circulating fluid is maintained at a constant temperature. In the case of a phase-change material which changes phase over a range of temperature, the enthalpy temperature relationship during phase change is assumed to be linear.

In accord with these assumptions, the energy conservation equations governing the process are expressed in nondimensional form using the following nondimensional variables:

$$\phi = c_p(T - T_m + \varepsilon)/\lambda; \psi = H - H_s/\lambda \text{ where, } H_s = c_p(T_m - \varepsilon); \tau = \alpha_p t/r_0^2; R = r/r_0; \omega = \theta/\beta; \Delta R = \Delta r/r_0; \Delta \omega = \Delta \theta/\beta; w_{f0} = w_f/r_0; w_{b0} = w_b/r_0; \rho^* = \rho_p/\rho_{ps}; \alpha_{pb} = \alpha_p/\alpha_b; \alpha_{pf} = \alpha_p/\alpha_f; k_{pf} = k_p/k_f; k_{bf} = k_b/k_f; Bi = hr_0/k_p; Ste = c_p(T_m - \varepsilon - T_\infty)/\lambda$$

$$\text{For the PCM: } (0 \leq R \leq 1 \text{ \& } 0 \leq \omega \leq 1)$$

$$\rho^* \frac{\partial \psi}{\partial \tau} = \frac{1}{R} \frac{\partial}{\partial R} \left(R \frac{\partial \phi}{\partial R} \right) + \frac{1}{\beta^2} \frac{1}{R^2} \frac{\partial \phi}{\partial \omega} \quad (1)$$

The nondimensional enthalpy-temperature ($\phi - \psi$) relations for the three regions are

$$\phi = \psi; \psi \leq 0 \quad (\text{Solid})$$

$$\phi = \frac{2\varepsilon c_p}{\lambda + 2\varepsilon c_p} \psi; \quad 0 \leq \psi \leq 1 + \frac{2\varepsilon c_p}{\lambda} \quad (\text{Interface})$$

$$\phi = \psi - 1; \quad \psi \geq 1 + \frac{2\varepsilon c_p}{\lambda} \quad (\text{Liquid}). \quad (2)$$

For the Fin:

$$\alpha_{pf} \frac{\partial \phi_f}{\partial \tau} = \frac{\partial^2 \phi_f}{\partial R^2} + \frac{2k_{pf}}{R\beta w_{f0}} \frac{\partial \phi_f}{\partial \omega} \quad (3)$$

For the Boundary Wall:

$$\alpha_{pb} \frac{\partial \phi_b}{\partial \tau} = \frac{1}{\beta^2} \frac{\partial^2 \phi_b}{\partial \omega^2} - \frac{k_{pb}}{w_{b0}} \frac{\partial \phi_b}{\partial R} \Big|_{R=1} - \frac{Bi k_{pb}}{w_{b0}} (Ste + \phi_b). \quad (4)$$

For the Junction Node:

$$\alpha_{pb} \frac{\partial \phi_c}{\partial \tau} = \frac{2}{\beta w_{f0}} \frac{\partial \phi_b}{\partial \omega} - \frac{1}{k_{bf} w_{b0}} \frac{\partial \phi_f}{\partial R} \Big|_{R=1} - \frac{Bi k_{pb}}{w_{b0}} (Ste + \phi_b). \quad (5)$$

Generalized Enthalpy Temperature Relationship. The enthalpy-temperature relations are now generalized as

$$\phi = \psi + \psi' \quad (6)$$

where

$$\psi' = 0.5(|1 + a - \psi| - |\psi| - 1 - a)/(1 + a),$$

$$\text{with } a = 2\varepsilon c_p/\lambda. \quad (7)$$

It can be seen that $\psi' = 0$ corresponds to solid phase, $\psi' = -1$ for liquid phase and during phase change $\psi' = -\psi/(1 + a)$. Since $\psi/(1 + a)$ represents the liquid fraction of the node, $1 + \psi' = 1 - (\psi/(1 + a))$ represents the solid fraction. For materials having a constant phase-change temperature ($\varepsilon = 0$) Eq. (7) reduces to exactly the same expression as given by Date (1991).

The initial conditions are

$$\tau = 0: \phi_p = \phi_{init}, \phi_f = \phi_b = \phi_{init} \quad (8)$$

and the equations of continuity of temperature and (heat flux) at the fin-pcm and the pcm-wall contact faces, respectively, are

$$\phi_f = \phi_p \text{ at } \omega = 0, 0 \leq R \leq 1$$

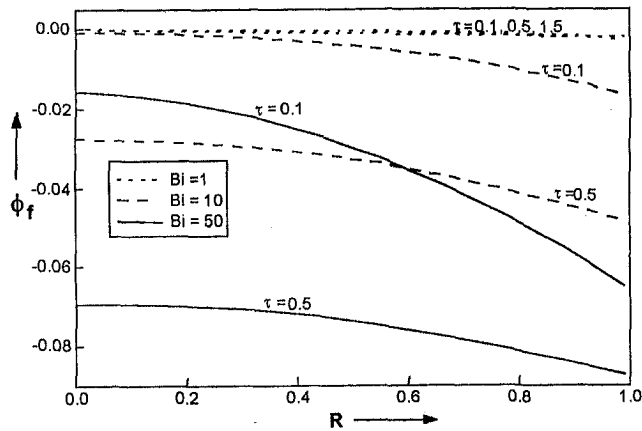


Fig. 2 Temperature variation of the fin along the radial direction with Biot number as parameter at different times ($Ste = 0.1$)

$$\phi_b = \phi_p \text{ at } R = 1, 0 \leq \omega \leq 1. \quad (9)$$

It is seen from the formulation, that all the energy equations are coupled and are to be solved simultaneously.

3 Computational Procedure

The coupled governing equations are written in discretized implicit form and are solved using Gauss-Siedel iterative method. Grid size was varied between 0.1 to 0.04 to study the effect of grid size on accuracy and computation time. While increasing the grid resolution further, convergence could be obtained only if $\Delta\tau$ is also reduced correspondingly. This increased the overall computation time. However, since sufficient accuracy was obtained with a grid size of 0.1 (10×10 matrix), these results were used for further analysis.

In order to check the accuracy of the numerical scheme, the fin thickness was made equal to zero (no fin configuration) and the results obtained were compared with the exact solution for inward solidification with convection boundary condition (London and Seben, 1943). The results were found to be in close agreement (\pm one percent).

The cumulative fraction solidified in the given interval of time can now be obtained as

fraction solidified

$$= 2 \sum_{i,j=1}^N (\Delta R^2 \Delta \omega) (i - \frac{1}{2}) (1 + \psi') \nabla \psi(i, j) < 0. \quad (10)$$

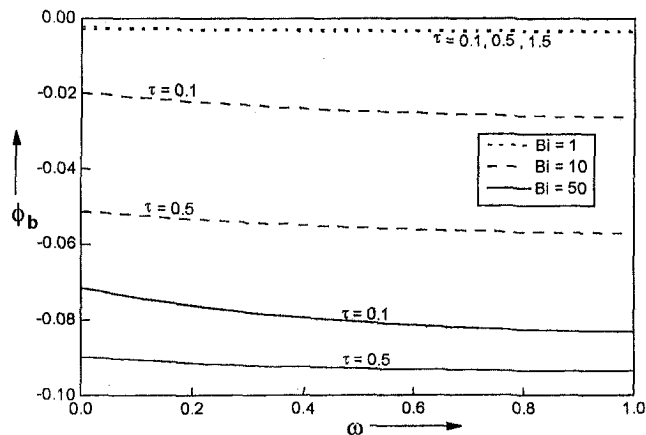


Fig. 3 Temperature variation of the boundary wall along the circumferential direction with Biot number as parameter at different times ($Ste = 0.1$)

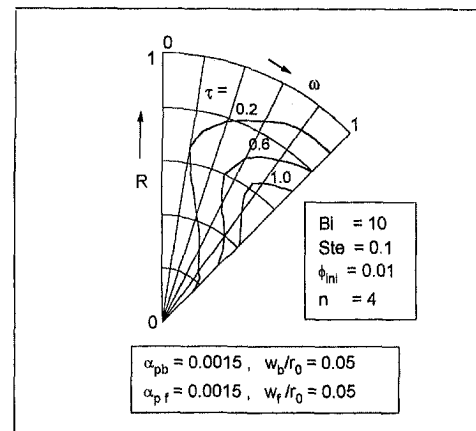


Fig. 4 Interface locations at various times

While calculating the fraction solidified, it should be recalled that $1 + \psi'$ gives the solid fraction for each node.

The area averaged instantaneous surface heat flux, " I ," is normalized with respect to its initial value which is the maximum value (I_{max}) and is given by the expression

$$SHF = \frac{I}{I_{max}} = \frac{\sum_{j=1}^N [\Delta \omega \beta (\phi_j + Ste)] + \frac{w_{f0}}{2} (\phi_c + Ste)}{\left(\beta + \frac{w_{f0}}{2} \right) (\phi_{init} + Ste)}$$

where

$$\beta = \frac{\pi}{n} - \frac{w_{f0}}{2}. \quad (11)$$

4 Results and Discussion

The computed results presented here show the effect of important nondimensional parameters on the temperature distribution along the fin and the tube wall, the interface location, the fraction solidified, and the instantaneous heat flux. It is observed from the formulation and the results that the performance of the model depends on the parameters shown below. The specific values of the parameters mentioned below are applicable for all the graphs unless otherwise specified.

$$\alpha_{pb} = 0.0025; \quad k_{pf} = 0.005; \quad w_{b0} = 0.05;$$

$$Bi = 10; \quad \rho^* = 1; \quad n = 4$$

$$\alpha_{pf} = 0.0025; \quad k_{bf} = 1; \quad w_{f0} = 0.05;$$

$$Ste = 0.1; \quad \phi_{init} = 0.01$$

Temperature Distribution. The temperature variation along the fin and the boundary wall are shown in Fig. 2 and Fig. 3, respectively, for Biot number as parameter at different times. In the above-mentioned figures, $\phi = 0$ for the fin and boundary wall corresponds to the case that they are at the beginning of the phase-change process ($T_m - \varepsilon$) whereas $\phi > 0$ implies that the fin and boundary temperatures are higher than ($T_m - \varepsilon$). Figures 2 and 3 show that there is an appreciable variation in temperature of the fin, ϕ_f , along its length and in the boundary wall, ϕ_b , along its circumferential direction for small times (especially nearer to the fin tip). However, as the solidification progresses, the variation of ϕ_f and ϕ_b becomes smaller.

It is seen from Fig. 2, for $Bi = 1$, ϕ_f curves are relatively flat at all times and this shows that the heat flow from the phase-change material through the fin is very small. For such low values of Biot

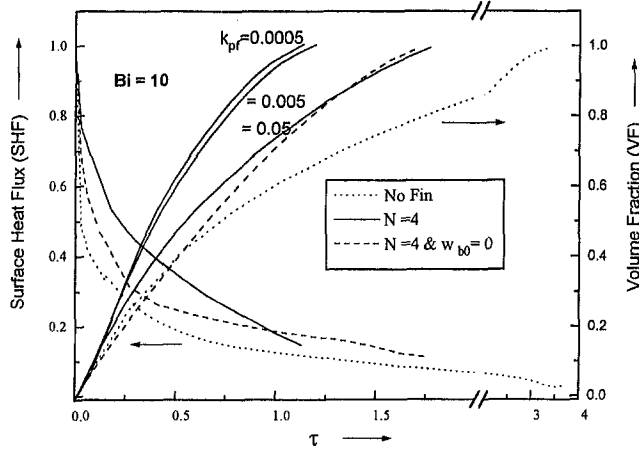


Fig. 5 Variation of normalized surface integrated heat flux and of frozen volume fraction, $Bi = 10$

number the addition of internal fins to the phase-change material does not enhance the rate of solidification. The fin-tip temperature drop at small times for a higher Biot number shows that a larger amount of heat is extracted through the fin. Figure 3 shows the temperature variation along the boundary wall. As a large quantity of heat flows from the phase-change material through the fin to the junction node at small times, the surface area of the tube in contact with the fin tip is not sufficient to pass all the heat. This results in a larger variation in the boundary wall temperature near the junction node, resulting in heat flow in the circumferential direction, especially for a higher Biot number as shown in Fig. 3.

Interface Location. The interface locations plotted in Fig. 4 shows the propagation of the phase front at different rates from the wall and the fin. Due to the presence of the fin, the phase change starts from the fin surface and the center of the tube as well as from the tube wall simultaneously. Since the mass of the phase-change material enclosed between the fins at the center of the tube is less, the rate of interface movement near the center of the tube is faster compared to that at the boundary side. This is due to the faster rate of abstraction of heat through the fins. The conductivity of the fin is nearly 500–2000 times higher than that of the phase-change material depending on the fin material. This causes more heat to pass from the phase-change material at the center region through

the fin compared to that portion of the heat that comes from the phase-change material at the middle and near the wall during the beginning of solidification.

In the unfinned latent heat thermal storage system, the phase-change material away from the tube surface faces maximum thermal resistance. This drawback is overcome by the present fin configuration that forms a V-shaped enclosure and the fin gives uniformly increasing thermal contact with the phase-change material farther away from outer radius. Padmanabhan and Krishnamurthy (1986) have presented the results for a longitudinal externally finned tube configuration, and reported that the interface moves only in the radial direction whereas, from the present results it is seen that the fin has substantial influence on the phase-change material especially nearer to its surface at the center of the pipe.

Frozen Fraction and Surface Heat Flux. The performance of latent heat thermal storage units are closely related to the variation in frozen volume fraction and the surface heat flux which in turn depend upon the parameters listed in the beginning. The variation of surface heat flux and volume fraction with time is shown in Fig. 5 for no fin and fin configuration with k_{pf} as the parameter. Curves are also drawn with $w_{b0} = 0$. Keeping $w_{b0} = 0$ implies the absence of circumferential heat flow. The effect of circumferential heat flow will be maximum when k_{pf} is the least. Hence, for the case with $w_{b0} = 0$, surface heat flux is drawn for the smallest value of k_{pf} (0.0005). From the figure it is seen that for the case with $w_{b0} = 0$, there is a noticeable difference in the volume fraction and surface heat flux curves. Hence, while modeling such storage units with fin configuration, it is necessary to include the effect of circumferential heat flow through the tube wall for higher values of Biot numbers in order to correctly predict the heat transfer behavior.

Numerical results are obtained for $Bi = 1$ to 50 at different intervals, and due to space limitations it is shown only for $Bi = 10$. Figure 5 shows the variation of surface heat flux and volume fraction for $Bi = 10$. The surface heat flux continuously decreases with time and its value at the end of the process is about 0.10 to 0.15 for the fin configuration whereas for no fin this value is about 0.02. There is about 75 percent to 175 percent gain in solidification time for the four-fin configuration over no-fin configuration for different k_{pf} values. Lower values of k_{pf} have appreciable influence on the volume fraction. However, for $k_{pf} < 0.005$ there is no appreciable change in volume fraction.

It is observed from the studies the surface heat flux remains constant for lower Biot number ($Bi \approx 1$) and the gain in solidifi-

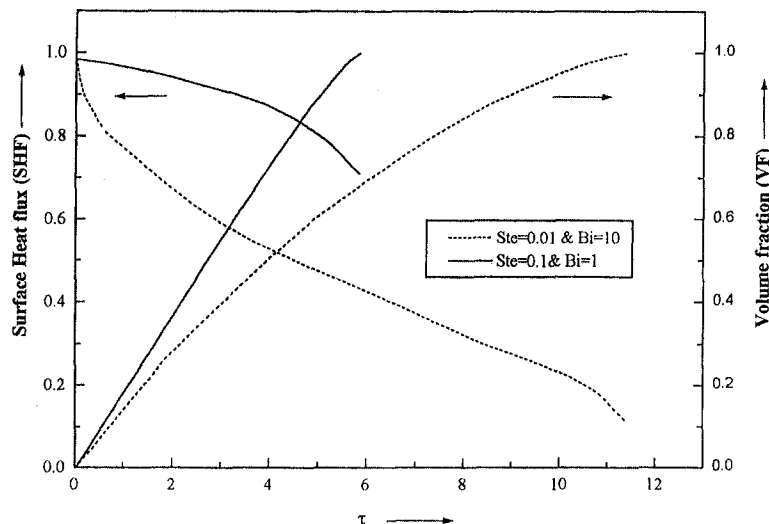


Fig. 6 Combined effect of Stefan number and Biot number on surface heat flux and frozen volume fraction

cation time with fins is marginal. Whereas for $Bi = 50$ the gain in solidification time is about three to fourfold for the four-fin configuration over no-fin configuration. The addition of fins has different advantages for different Biot numbers. For lower Biot numbers though there is not much gain in the solidification time, the fin is very useful in achieving a uniform surface heat flux with time. For a higher Biot number, the gain in solidification time is high but the surface heat flux, though not uniform, is higher for fin configuration. Hence, depending on the application, a suitable Biot number is to be selected.

Figure 6 shows the combined effect of Stefan and Biot numbers on the surface heat flux and volume fraction. Two different values of h and $(T_m - T_\infty)$ are so chosen to yield the same value of the product, $Ste \times Bi$ to study the effect of Biot and Stefan numbers. The product so selected is useful to study the combined variation of h and $(T_m - T_\infty)$ on the process keeping the rest of the variables in the product as constants. The initial surface heat flux [$h \times (T_b - T_\infty)$] is the same for both the cases due to the fact that T_m and T_b are the same at the beginning of solidification (the phase-change material is in liquid-saturated condition). Since all the other physical and geometric properties are kept constant, the total quantity of heat extracted is also the same for both cases. It is seen that the variation of surface heat flux is more uniform throughout the process for a lower Biot number and higher Stefan number. This shows that the selection of combination of Stefan and Biot numbers plays an important role in the design of the latent heat thermal storage unit.

For a given tube radius, any increase in w_{b0} and w_{f0} results in higher values of the boundary wall thickness and the fin width, respectively. It was numerically observed that the curves for $w_{b0} = 0.01$ and $w_{b0} = 0.05$ are very close indicating that there is not much gain in the solidification rate with increase in the boundary wall thickness above $w_{b0} = 0.01$. Hence, it is not required to increase the boundary wall thickness beyond a minimum value required for mechanical stability. However, it was observed that there is a moderate variation in the solidification rate with increasing w_{f0} . Beyond a value of w_{f0} of about 0.01 to 0.02, the increase in fin effect is not proportionate to the increase in volume of the fin material. The above set of values of w_{b0} and w_{f0} would be appropriate for most of the applications.

5 Conclusion

Among the various fin configurations, the present configuration gives maximum benefit of the fin to the phase-change material farther away from the convectively cooled surface. It is necessary to include the effect of circumferential heat flow through the tube wall for higher values of Biot numbers in order to correctly predict the heat transfer behavior. For lower Biot numbers, addition of fins makes the surface heat flux more uniform, whereas for higher Biot number the addition of fins will improve the magnitude of the surface heat flux and appreciably reduce the time for solidification. For a given quantity of heat to be extracted, a combination of lower Biot number and higher Stefan number (within the practical range) is recommended for the uniform extraction of heat. The present heat transfer studies will be very useful for the design of latent heat thermal storage units.

Acknowledgment

This work was initiated with an experimental study at Solar Institut Juelich (SIJ), Fachhochschule Aachen, Juelich, Germany. The authors are thankful to Prof. K. Schwarzer and his colleagues at SIJ for their cooperation and assistance.

References

- Date, A. W., 1991, "A strong enthalpy formulation for the Stefan problem," *Int. J. Heat Mass Transfer*, Vol. 34, No. 9, pp. 2231-2235.
- Griffin, F. P., and Smith, R. N., 1980, "Approximate solution for freezing adjacent to an extended surfaces," *Proc. Joint ASME/AIChE National Heat Transfer Conference*, Orlando, FL, pp. 1-13.

Lacorex, M., 1993, "Study of the heat transfer behavior of a latent heat thermal energy storage unit with a finned tube," *Int. J. Heat. Mass. Transfer*, Vol. 36, No. 8, pp. 2083-2092.

London, A. L., and Seban, R. A., 1943, "Rate of Ice Formation," *ASME JOURNAL OF HEAT TRANSFER*, Vol. 65, pp. 771-778.

Padmanabhan, P. V., and Krishnamurthy, M. V., 1986a, "Outward phase change in a cylindrical annulus with axial fins on the inner tube," *Int. J. Heat Mass Transfer*, Vol. 29, No. 12, pp. 1855-1868.

Padmanabhan, P. V., and Krishnamurthy, M. V., 1986b, "Outward phase change in a cylindrical annulus with circumferential fins," *Proc. 8th International Heat Transfer Conference*, San Francisco, CA, pp. 1773-1779.

Shamsundar, N., and Sparrow, E. M., 1975, "Analysis of Multidimensional Conduction Phase Change via the Enthalpy Model," *ASME JOURNAL OF HEAT TRANSFER*, Vol. 97, pp. 333-340.

Smith, R. N., and Koch, J. D., 1982, "Numerical Solution for freezing adjacent to a finned surface," *Proceedings of Seventh International Heat Transfer Conference*, U. Grigull, et al., eds., Munchen, Germany, pp. 69-74.

Sparrow, E. M., et al., 1981, "Freezing on a finned tube for either conduction controlled or natural convection controlled heat transfer," *Int. J. Heat. Mass. Transfer*, Vol. 24, pp. 273-284.

Velraj, R., et al., 1997, "Experimental Analysis and Numerical Modeling of Inward Solidification on a Finned Vertical Tube for a Latent Heat Storage Unit," *Solar Energy*, Vol. 60, No. 5, pp. 281-290.

Voller, V. R., 1990, "Fast implicit Finite-Difference Method for the Analysis of Phase Change Problems," *Numerical Heat Transfer*, Part-B, Vol. 17, pp. 155-169.

Heat Conduction From Spheroids

R. S. Alassar¹

Introduction

The solution of the problem of heat conduction from a sphere is available in the literature (Ha and Yavuzkurt, 1993). The sphere, however, is a special case of the generalized spheroidal geometries. These spheroids are of two types, namely oblate and prolate. The analytical solutions of the problem of conduction heat transfer from oblate and prolate spheroids are obtained here. Two special cases can be obtained from the general solutions, namely the sphere and the flat circular disk. The present work has relevance in, for example, heat transfer in stationary packed beds. The results can be of use to a wide range of applications where Biot and Rayleigh numbers are small and fluid heat conduction dominates the thermal resistance. Such conditions can be found at small length scales.

Solution

Consider a hot spheroid (oblate or prolate) of major and minor axes $2a$ and $2b$, respectively. The spheroid is at temperature T_s , which is hotter than the fluid around it whose temperature is T_∞ as shown in Fig. 1 (Alassar, 1997). When the fluid surrounding the spheroid is stagnant, heat is transferred only by conduction. Using the oblate spheroidal coordinates (Arfken, 1970), the steady heat conduction process is governed by the following equation:

$$\frac{1}{\cosh \xi} \frac{\partial}{\partial \xi} \left[\cosh \xi \frac{\partial \varphi}{\partial \xi} \right] + \frac{1}{\sin \eta} \frac{\partial}{\partial \eta} \left[\sin \eta \frac{\partial \varphi}{\partial \eta} \right] = 0 \quad (1)$$

and the corresponding equation (in prolate spheroidal coordinates) for prolate spheroid is

¹Department of Mathematical Sciences, KFUPM Box No. 1620, Dhahran 31261, Saudi Arabia.

Contributed by the Heat Transfer Division for publication in the *JOURNAL OF HEAT TRANSFER*. Manuscript received by the Heat Transfer Division, May 4, 1998; revision received, Dec. 16, 1998. Keywords: Conduction, Heat Transfer, Nusselt Number, Spheroids. Associate Technical Editor: P. Ayyaswamy.

cation time with fins is marginal. Whereas for $Bi = 50$ the gain in solidification time is about three to fourfold for the four-fin configuration over no-fin configuration. The addition of fins has different advantages for different Biot numbers. For lower Biot numbers though there is not much gain in the solidification time, the fin is very useful in achieving a uniform surface heat flux with time. For a higher Biot number, the gain in solidification time is high but the surface heat flux, though not uniform, is higher for fin configuration. Hence, depending on the application, a suitable Biot number is to be selected.

Figure 6 shows the combined effect of Stefan and Biot numbers on the surface heat flux and volume fraction. Two different values of h and $(T_m - T_\infty)$ are so chosen to yield the same value of the product, $Ste \times Bi$ to study the effect of Biot and Stefan numbers. The product so selected is useful to study the combined variation of h and $(T_m - T_\infty)$ on the process keeping the rest of the variables in the product as constants. The initial surface heat flux [$h \times (T_b - T_\infty)$] is the same for both the cases due to the fact that T_m and T_b are the same at the beginning of solidification (the phase-change material is in liquid-saturated condition). Since all the other physical and geometric properties are kept constant, the total quantity of heat extracted is also the same for both cases. It is seen that the variation of surface heat flux is more uniform throughout the process for a lower Biot number and higher Stefan number. This shows that the selection of combination of Stefan and Biot numbers plays an important role in the design of the latent heat thermal storage unit.

For a given tube radius, any increase in w_{b0} and w_{f0} results in higher values of the boundary wall thickness and the fin width, respectively. It was numerically observed that the curves for $w_{b0} = 0.01$ and $w_{b0} = 0.05$ are very close indicating that there is not much gain in the solidification rate with increase in the boundary wall thickness above $w_{b0} = 0.01$. Hence, it is not required to increase the boundary wall thickness beyond a minimum value required for mechanical stability. However, it was observed that there is a moderate variation in the solidification rate with increasing w_{f0} . Beyond a value of w_{f0} of about 0.01 to 0.02, the increase in fin effect is not proportionate to the increase in volume of the fin material. The above set of values of w_{b0} and w_{f0} would be appropriate for most of the applications.

5 Conclusion

Among the various fin configurations, the present configuration gives maximum benefit of the fin to the phase-change material farther away from the convectively cooled surface. It is necessary to include the effect of circumferential heat flow through the tube wall for higher values of Biot numbers in order to correctly predict the heat transfer behavior. For lower Biot numbers, addition of fins makes the surface heat flux more uniform, whereas for higher Biot number the addition of fins will improve the magnitude of the surface heat flux and appreciably reduce the time for solidification. For a given quantity of heat to be extracted, a combination of lower Biot number and higher Stefan number (within the practical range) is recommended for the uniform extraction of heat. The present heat transfer studies will be very useful for the design of latent heat thermal storage units.

Acknowledgment

This work was initiated with an experimental study at Solar Institut Juelich (SIJ), Fachhochschule Aachen, Juelich, Germany. The authors are thankful to Prof. K. Schwarzer and his colleagues at SIJ for their cooperation and assistance.

References

- Date, A. W., 1991, "A strong enthalpy formulation for the Stefan problem," *Int. J. Heat Mass Transfer*, Vol. 34, No. 9, pp. 2231–2235.
Griffin, F. P., and Smith, R. N., 1980, "Approximate solution for freezing adjacent to an extended surfaces," *Proc. Joint ASME/AIChE National Heat Transfer Conference*, Orlando, FL, pp. 1–13.

Lacorex, M., 1993, "Study of the heat transfer behavior of a latent heat thermal energy storage unit with a finned tube," *Int. J. Heat. Mass. Transfer*, Vol. 36, No. 8, pp. 2083–2092.

London, A. L., and Seban, R. A., 1943, "Rate of Ice Formation," *ASME JOURNAL OF HEAT TRANSFER*, Vol. 65, pp. 771–778.

Padmanabhan, P. V., and Krishnamurthy, M. V., 1986a, "Outward phase change in a cylindrical annulus with axial fins on the inner tube," *Int. J. Heat Mass Transfer*, Vol. 29, No. 12, pp. 1855–1868.

Padmanabhan, P. V., and Krishnamurthy, M. V., 1986b, "Outward phase change in a cylindrical annulus with circumferential fins," *Proc. 8th International Heat Transfer Conference*, San Francisco, CA, pp. 1773–1779.

Shamsundar, N., and Sparrow, E. M., 1975, "Analysis of Multidimensional Conduction Phase Change via the Enthalpy Model," *ASME JOURNAL OF HEAT TRANSFER*, Vol. 97, pp. 333–340.

Smith, R. N., and Koch, J. D., 1982, "Numerical Solution for freezing adjacent to a finned surface," *Proceedings of Seventh International Heat Transfer Conference*, U. Grigull, et al., eds., Munchen, Germany, pp. 69–74.

Sparrow, E. M., et al., 1981, "Freezing on a finned tube for either conduction controlled or natural convection controlled heat transfer," *Int. J. Heat. Mass. Transfer*, Vol. 24, pp. 273–284.

Velraj, R., et al., 1997, "Experimental Analysis and Numerical Modeling of Inward Solidification on a Finned Vertical Tube for a Latent Heat Storage Unit," *Solar Energy*, Vol. 60, No. 5, pp. 281–290.

Voller, V. R., 1990, "Fast implicit Finite-Difference Method for the Analysis of Phase Change Problems," *Numerical Heat Transfer*, Part-B, Vol. 17, pp. 155–169.

Heat Conduction From Spheroids

R. S. Alassar¹

Introduction

The solution of the problem of heat conduction from a sphere is available in the literature (Ha and Yavuzkurt, 1993). The sphere, however, is a special case of the generalized spheroidal geometries. These spheroids are of two types, namely oblate and prolate. The analytical solutions of the problem of conduction heat transfer from oblate and prolate spheroids are obtained here. Two special cases can be obtained from the general solutions, namely the sphere and the flat circular disk. The present work has relevance in, for example, heat transfer in stationary packed beds. The results can be of use to a wide range of applications where Biot and Rayleigh numbers are small and fluid heat conduction dominates the thermal resistance. Such conditions can be found at small length scales.

Solution

Consider a hot spheroid (oblate or prolate) of major and minor axes $2a$ and $2b$, respectively. The spheroid is at temperature T_s , which is hotter than the fluid around it whose temperature is T_∞ as shown in Fig. 1 (Alassar, 1997). When the fluid surrounding the spheroid is stagnant, heat is transferred only by conduction. Using the oblate spheroidal coordinates (Arfken, 1970), the steady heat conduction process is governed by the following equation:

$$\frac{1}{\cosh \xi} \frac{\partial}{\partial \xi} \left[\cosh \xi \frac{\partial \varphi}{\partial \xi} \right] + \frac{1}{\sin \eta} \frac{\partial}{\partial \eta} \left[\sin \eta \frac{\partial \varphi}{\partial \eta} \right] = 0 \quad (1)$$

and the corresponding equation (in prolate spheroidal coordinates) for prolate spheroid is

¹Department of Mathematical Sciences, KFUPM Box No. 1620, Dhahran 31261, Saudi Arabia.

Contributed by the Heat Transfer Division for publication in the *JOURNAL OF HEAT TRANSFER*. Manuscript received by the Heat Transfer Division, May 4, 1998; revision received, Dec. 16, 1998. Keywords: Conduction, Heat Transfer, Nusselt Number, Spheroids. Associate Technical Editor: P. Ayyaswamy.

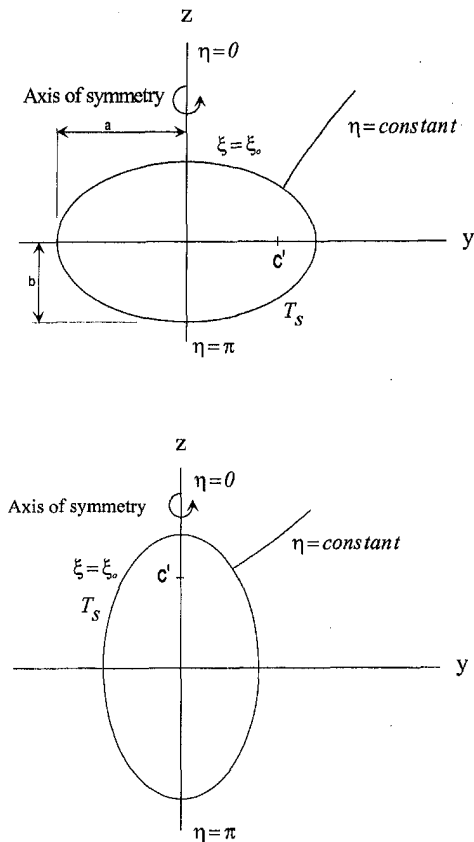


Fig. 1 The oblate and prolate spheroids

$$\frac{1}{\sinh \xi} \frac{\partial}{\partial \xi} \left[\sinh \xi \frac{\partial \varphi}{\partial \xi} \right] + \frac{1}{\sin \eta} \frac{\partial}{\partial \eta} \left[\sin \eta \frac{\partial \varphi}{\partial \eta} \right] = 0 \quad (2)$$

where $\varphi = (T - T_\infty)/(T_s - T_\infty)$ is the dimensionless temperature. The boundary conditions to be satisfied are the scaled thermal conditions on the surface of the spheroid defined by $\xi = \xi_0 = \tanh^{-1}(b/a)$ and the far-field conditions. These can be expressed as

$$\varphi = 1 \quad \text{at} \quad \xi = \xi_0 \quad (3)$$

$$\varphi \rightarrow 0 \quad \text{as} \quad \xi \rightarrow \infty. \quad (4)$$

The local amount of heat transferred from the spheroid is

$$q(\eta) = -\frac{\kappa}{l_1} \left(\frac{\partial \varphi}{\partial \xi} \right)_{\xi=\xi_0} \quad (5)$$

where κ is the thermal conductivity of the fluid. The quantity l_1 is a scale factor of the relevant coordinate system and is given by $l_1 = c' \sqrt{\sinh^2 \xi + \cos^2 \eta}$ in case of an oblate spheroid and by $l_1 = c' \sqrt{\sinh^2 \xi + \sin^2 \eta}$ for a prolate spheroid with c' being the focal distance.

The local Nusselt number (N_u) is defined as

$$N_u(\eta) = \frac{2aq(\eta)}{\kappa}. \quad (6)$$

The steady amount of heat transferred by conduction can be obtained by solving Eqs. (1) and (2) and then using the solutions in Eqs. (5) and (6). The solutions of Eqs. (1) and (2) can be obtained by geometrically observing that the dimensionless temperature φ is independent of η ; a mathematical proof is also possible which results in a direct integration of the equations subject to the boundary conditions (3) and (4). It can be easily

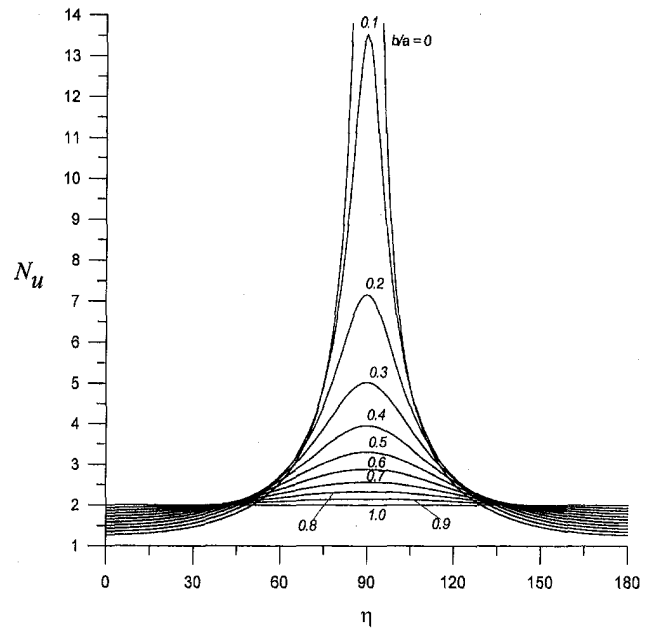


Fig. 2 Local Nusselt number (oblate)

shown that the local Nusselt number associated with conduction from an oblate spheroid is given by

$$N_u(\eta) = -\frac{2}{(2 \tan^{-1} e^{\xi_0} - \pi) \sqrt{\sinh^2 \xi_0 + \cos^2 \eta}} \quad (7)$$

In the limit $\xi_0 \rightarrow \infty$, the oblate spheroid becomes a sphere. One can show that

$$\lim_{\xi_0 \rightarrow \infty} N_u(\eta) = 2 \quad (8)$$

which is, as expected, independent of η . On the other hand, when $\xi_0 \rightarrow 0$, the oblate spheroid becomes a flat circular disk. The following result for the local Nusselt number in the case of a circular disk can be obtained,

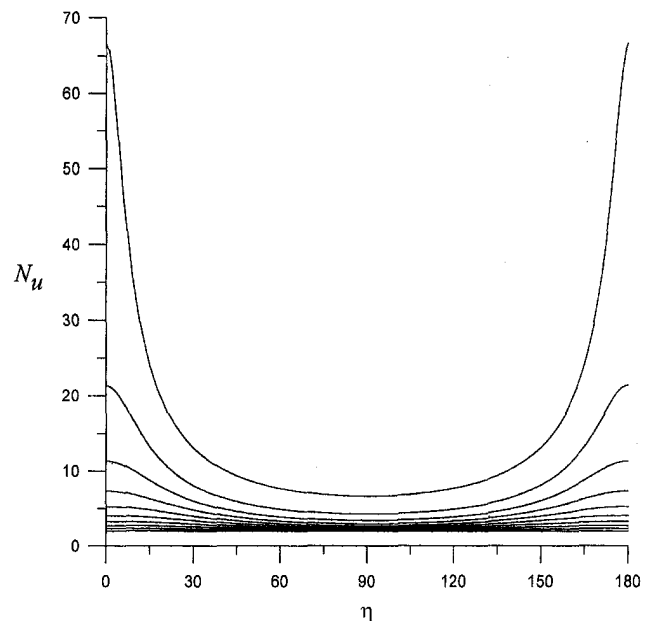


Fig. 3 Local Nusselt number (prolate). Curves from top to bottom are for $b/a = 0.1, 0.2, \dots, 1.0$.

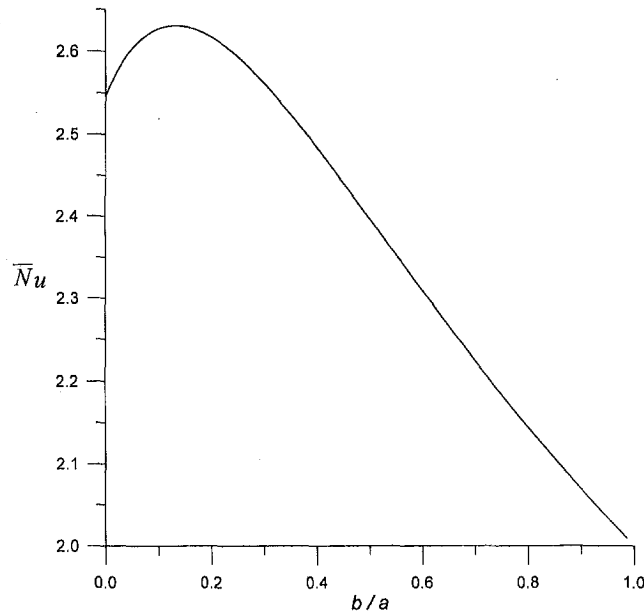


Fig. 4 Averaged Nusselt number (oblate)

$$\lim_{\xi_o \rightarrow 0} N_u(\eta) = \frac{4}{\pi |\cos \eta|} \quad (9)$$

Averaging the Nusselt number over the surface of the oblate spheroid gives the averaged Nusselt number, \bar{N}_u , as

$$\bar{N}_u = \frac{4}{\cosh \xi_o [2 \tan^{-1} e^{\xi_o} - \pi] \left[1 + \sinh \xi_o \tanh \xi_o \ln \left(\coth \frac{\xi_o}{2} \right) \right]} \quad (10)$$

One can also show that

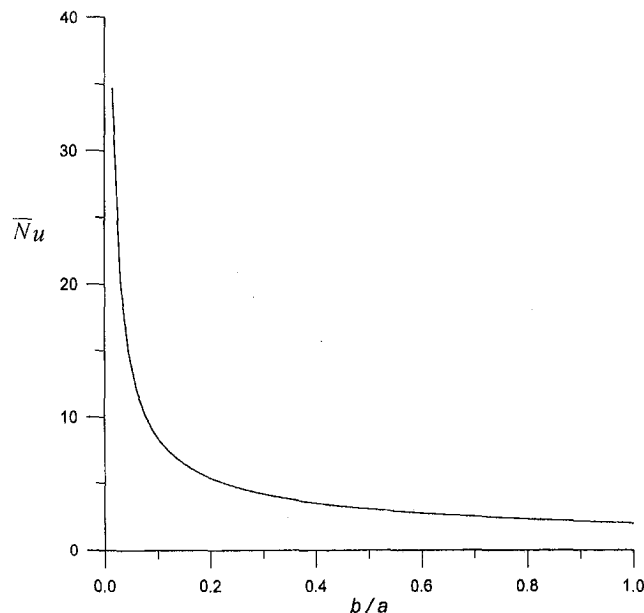


Fig. 5 Averaged Nusselt number (prolate)

$$\lim_{\xi_o \rightarrow \infty} \bar{N}_u = 2 \quad (11)$$

and

$$\lim_{\xi_o \rightarrow 0} \bar{N}_u = \frac{8}{\pi} \quad (12)$$

The result obtained in Eq. (11) is identical to that obtained from the analysis of heat transfer from a sphere. By similar analysis, one can show that the local Nusselt number associated with conduction heat transfer from a prolate spheroid is given by

$$N_u(\eta) = - \frac{2 \coth \xi_o}{\ln \left(\frac{e^{\xi_o} - 1}{e^{\xi_o} + 1} \right) \sqrt{\sinh^2 \xi_o + \sin^2 \eta}} \quad (13)$$

In the limit $\xi_o \rightarrow \infty$, the prolate spheroid also approaches a sphere. The following limiting case is analogous to the one given in Eq. (8),

$$\lim_{\xi_o \rightarrow \infty} N_u(\eta) = 2, \quad (14)$$

and when $\xi_o \rightarrow 0$, the prolate spheroid becomes a thin needle and the Nusselt number is unbounded.

The averaged Nusselt number for prolate spheroid takes the following form:

$$\bar{N}_u = - \frac{4 \cosh \xi_o}{\sinh^2 \xi_o \ln \left(\frac{e^{\xi_o} - 1}{e^{\xi_o} + 1} \right) [1 + \coth \xi_o \cosh \xi_o \tan^{-1}(\operatorname{csch} \xi_o)]} \quad (15)$$

and once more

$$\lim_{\xi_o \rightarrow \infty} \bar{N}_u = 2. \quad (16)$$

Graphical representations of the local Nusselt number for oblate and prolate spheroids for different axis ratios, including the limiting cases, are shown in Figs. 2 and 3, respectively. The averaged Nusselt number for oblate and prolate spheroids is shown in Figs. 4 and 5. An interesting feature of Fig. 4 is that the heat transfer rate reaches a maximum value at $b/a \approx 0.132$. This phenomenon may be explained by observing that the local Nusselt number, Fig. 2, increases with the decrease of b/a near $\eta = 90$. The opposite is true near $\eta = 0$ and $\eta = 180$. Since the averaged Nusselt number is related to the area under the local Nusselt number curve, these two opposing trends compete to build the maximum value of the averaged Nusselt number at $b/a \approx 0.132$.

Acknowledgment

The author wishes to acknowledge the support of King Fahd University of Petroleum and Minerals.

References

- Alassar, R. S., 1997, "Unsteady Hydrodynamic Forces on Spheroidal Bodies," Ph.D. thesis, KFUPM, Dhahran, Saudi Arabia.
- Arfken, G., 1970, *Mathematical Methods for Physicists*, Academic Press, London.
- Ha, M. Y., and Yavuzkurt, S., 1993, "A Theoretical Investigation of Acoustic Enhancement of Heat and Mass Transfer—1. Pure Oscillating Flow," *Int. J. Heat Mass Transfer*, Vol. 36, No. 8, pp. 2183–2192.

A Theoretical Study, With Experimental Verification, of the Temperature-Dependent Viscosity Effect on the Forced Convection Through a Porous Medium Channel

D. A. Nield,¹ D. C. Porneala,² and J. L. Lage³

Introduction

The problem of forced convective flow in a channel is a topic of fundamental importance, and one which features prominently in textbooks on convective heat transfer such as Bejan (1984/1995) and in articles in handbooks such as those by Kays and Harnett (1973) or Shah and Bhatti (1987). However, it appears that there is little accessible information available on the practically important but complex case where the effect of the dependence of the viscosity on temperature is included. In this case, the velocity profile depends on the temperature field and the latter also depends on the former, so in general a system of coupled differential equations must be solved.

Considering specifically the case of flow through a porous medium, an analytical treatment of convection by a temperature-dependent fluid was presented recently by Ling and Dybbs (1992). However, their model is restricted to convection through a porous medium adjacent to an isothermal flat plate.

Our purpose is to present a theory, based on a perturbation approach, which permits the determination of the effect of viscosity variation (with temperature) on the pressure drop of a convectively cooled, porous medium channel. The need for such a theory is not only fundamental but also practical. New designs of microporous enhanced cold plates for cooling airborne microelectronics rely on brazed metallic porous inserts for improved thermal efficiency (Lage et al., 1996; Antohe et al., 1996; Antohe et al., 1997). These devices are to be cooled with PolyAlphaOlefin (PAO), a very common synthetic oil used for cooling military avionics. This oil has viscosity strongly dependent on temperature,

$$\mu(T) = 0.1628 T^{-1.0868}, \quad 5^\circ\text{C} \leq T \leq 170^\circ\text{C}, \quad (1)$$

where T is the temperature in $^\circ\text{C}$, and μ is the dynamic viscosity in kg/ms (Chevron, 1981). The prediction of the thermohydraulic behavior of these devices, particularly the pressure drop increase imposed by the porous insert, is critical for design optimization.

Our theoretical analysis provides a detailed explanation of the way in which the temperature effect comes into play. The validity of the model prediction is checked against experimental data obtained from tests of PAO flowing through a typical microporous cold plate. Obviously, our theory is not limited to PAO, but to any coolant presenting temperature-dependent viscosity (with other properties being much less affected by temperature). PAO was chosen as our test fluid because it presents immediate application interest to the avionics industry.

¹ Associate Professor, Department of Engineering Science, University of Auckland, Private Bag 92019, Auckland, New Zealand.

² Ph.D. Student, Mechanical Engineering Department, Southern Methodist University, Dallas, TX 75275-0337.

³ Associate Professor, Mechanical Engineering Department, Southern Methodist University, Dallas, TX 75275-0337. e-mail: JLL@SEAS.SMU.EDU. Mem. ASME.

Contributed by the Heat Transfer Division for publication in the JOURNAL OF HEAT TRANSFER. Manuscript received by the Heat Transfer Division, July 7, 1998; revision received, Dec. 28, 1998. Keywords: Analytical, Experimental, Forced Convection, Heat Transfer, Porous Media, Viscous. Associate Technical Editor: C. Beckermann.

Theoretical Model and Discussion

We consider the flow of an incompressible fluid in a channel between plane parallel plates at $y = \pm H$ (i.e., H is the half-spacing of the channel, y being a Cartesian coordinate transverse to the plates). The thermal boundary conditions are symmetrical ones of uniform heat flux. The Péclet number is assumed to be sufficiently high for the axial thermal conduction to be neglected. Fluid properties other than the viscosity μ are assumed to be constant (a good approximation for most fluids, including PAO). The energy equation in this case is

$$\frac{u}{\alpha} \frac{\partial T}{\partial x} = \frac{\partial^2 T}{\partial y^2} \quad (2)$$

where α is the thermal diffusivity, x is the longitudinal coordinate, and u is the longitudinal fluid speed. Equation (2) is valid when the fluid velocity is uniform in y (slug flow), which is appropriate to a porous medium when the Darcy's Law is valid, i.e., when

$$u = \frac{K}{\mu} G \quad (3)$$

where K is the permeability of the medium and G is the applied pressure gradient. Even though the slug flow model is also appropriate for the hydrodynamically undeveloped flow of a low Prandtl number fluid, in the following analysis just the porous medium situation is considered, in line with our practical application.

For the present case (uniform wall heat flux) the variables x and y of Eq. (2) can be separated in an additive fashion (compare Eqs. (3.56) and (3.59) of Bejan (1984/1995)) and the First Law of Thermodynamics leads to

$$\frac{\partial T}{\partial x} = \frac{dT_m}{dx} = \frac{\alpha q''}{kHu_m} \quad (4)$$

where u_m is the bulk (mean) longitudinal speed, q'' is the boundary heat flux, k is the thermal conductivity, and T_m is the bulk temperature defined generally as

$$T_m = \frac{1}{u_m H} \int_0^H u T dy. \quad (5)$$

From Eq. (4) it follows that the order of magnitude of the ratio of $\partial T/\partial x$ and $\partial T/\partial y$ is equal to the reciprocal of the Péclet number, and so this ratio is small under an assumption already made. Hence, variations of the viscosity with x are neglected in this analysis. It follows that one can also assume that the speed u is independent of x .

Using Eq. (4), Eq. (2) gives

$$\frac{\partial^2 T}{\partial y^2} = \frac{q'' u}{kHu_m}. \quad (6)$$

The boundary conditions can be rewritten using the wall temperature T_w , as

$$\partial T/\partial y = 0 \quad \text{at } y = 0, \quad T = T_w(x) \quad \text{at } y = H. \quad (7)$$

A linear approximation (based on a truncated Taylor series expansion) for the variation with temperature of the reciprocal of the viscosity is made:

$$\frac{1}{\mu} = \frac{1}{\mu_0} \left\{ 1 - \frac{1}{\mu_0} \left(\frac{d\mu}{dT} \right)_0 (T - T_0) \right\} \quad (8)$$

where the suffix 0 indicates evaluation at the reference temperature T_0 . A "viscosity variation number," N , is now defined as

$$N = \frac{q'' H}{k} \frac{1}{\mu_0} \left(\frac{d\mu}{dT} \right)_0 \quad (9)$$

The following perturbation analysis is made on the assumption that N is a small parameter. A process involving successive approximations is carried out. (A more formal procedure, which leads to the same results, is to expand the dependent variables and the viscosity in powers of N , substitute in the equations, equate the various expressions involving the same power N^i of N , and proceed to solve in turn the system of equations for $i = 0, 1, 2, \dots$. In fact, here the process is stopped at $i = 1$.)

The zeroth-order solution is the familiar one corresponding to constant viscosity, $N = 0$. For this case, $u = u_m$. One readily finds from Eqs. (5), (6), and (7)

$$T = T_w + \frac{q''}{2kH} (y^2 - H^2) \quad (10)$$

$$T_m = T_w - \frac{q''H}{3k} \quad (11)$$

$$\text{Nu} = \frac{2Hq''}{k(T_w - T_m)} = 6 \quad (12)$$

where Nu is the Nusselt number. Proceeding to the next approximation, one returns to Eqs. (3) and (8) with T given approximately by Eq. (10), and with the reference temperature identified with T_w . (Since T_w is taken to be a slowly varying function of x , there is no harm done in doing this. To determine the precise value of N from Eq. (9) one has to specify some particular value of x .) This gives

$$u = \left(\frac{K}{\mu_0} G \right) \left[1 + \frac{1}{2} N \left(1 - \frac{y^2}{H^2} \right) \right] \quad (13)$$

$$u_m = \left(\frac{K}{\mu_0} G \right) \left[1 + \frac{N}{3} \right] \quad (14)$$

With these expressions for u and u_m , one returns to Eqs. (6) and (7). Working to first order in N , one gets in turn, after some algebraic manipulation,

$$\frac{\partial^2 T}{\partial y^2} = \left(\frac{q''}{kH} \right) \left[1 + N \left(\frac{1}{6} - \frac{1}{2} \frac{y^2}{H^2} \right) \right] \quad (15)$$

$$T - T_w = \left(\frac{Hq''}{2k} \right) \times \left\{ \frac{y^2}{H^2} - 1 + N \left[\frac{1}{12} \left(1 - \frac{y^4}{H^4} \right) - \frac{1}{6} \left(1 - \frac{y^2}{H^2} \right) \right] \right\} \quad (16)$$

$$T_m - T_w = - \left(\frac{Hq''}{k} \right) \left[\frac{1}{3} + \frac{2}{45} N \right] \quad (17)$$

$$\text{Nu} = 6 \left(1 - \frac{2}{15} N \right) \quad (18)$$

The conclusion is that the effect of variation of viscosity with temperature is to the Nusselt number being multiplied by a factor of approximately $(1 - 2N/15)$, where N , defined by Eq. (9), represents the proportional change of viscosity, across the half-channel-spacing H , corresponding to that hypothetical linear conduction temperature gradient in the cross-channel (y -) direction which would produce a heat flux q'' . Looking at Eqs. (13), (15), and (17), we see that the change in the value of Nu is a result of changes to the velocity profile, the curvature of the temperature profile, and the difference between T_m and T_w , in turn.

For the case of a fluid whose viscosity decreases with increase of temperature, N is negative. In moving from the case of zero N to that of nonzero negative N , the velocity near the walls is increased relative to that in the center of the channel. As a result, the curvature of the temperature profile is increased near the walls and decreased in the middle of the channel (which has the net effect of flattening the overall profile), and this leads to a decrease

in the magnitude of $T_w - T_m$, which in turn leads to an increase in the magnitude of the Nusselt number Nu.

The previous analysis has been carried out for just the isoflux case. The isothermal case could be treated similarly, but the algebraic manipulation would be messier because then trigonometric functions, as well as polynomials, would be involved. We leave this extension to another opportunity, and now we concentrate on the experimental verification of the model.

Experimental Hydraulic Verification

For testing the theory a microporous cold plate was manufactured. Electric heaters generating a heat flux $q'' = 0.59 \text{ V}^2$, in W/m^2 , where V is the supply voltage in Volts, were used to heat the 0.001 m apart channel plates. The total PAO pressure drop across the cold plate, $\Delta p_e = p_i - p_o$, was calculated from the inlet p_i and outlet p_o pressure measurements. Details on the experimental apparatus and procedure are found in Porneala (1998).

Using Eq. (14) we can define an expression for the theoretical pressure drop Δp across the porous insert when the cold plate is heated as

$$\Delta p = \left(1 + \frac{N}{3} \right) \Delta p_{e0} \quad (19)$$

where Δp_{e0} is the pressure drop across the cold plate when the heaters are off and the coolant flows at a reference temperature T_0 (taken as the coolant bath temperature, in $^\circ\text{C}$). Using q'' , H , Eq. (1), and $k_{\text{PAO}} = 0.1454 \text{ W/m}^2\text{C}$, we can simplify Eq. (9) to: $N = -2.2 \times 10^{-3} \text{ V}^2/T_0$.

The verification of Eq. (19) involves measuring Δp_{e0} with the heaters off and the coolant flowing at a certain reference (bath) temperature, and then using it for comparing the Δp value predicted by Eq. (19) against the Δp_e measured experimentally under different heating conditions.

The uncertainties of the PAO flow rate Q and of the experimental pressure drop Δp_e are estimated following the recommendations of Kim et al. (1993). A conservative estimate for the uncertainty of the experimental volumetric flow rate reported in this work, U_Q/Q , is to five percent.

Because both precision pressure gages are calibrated by the manufacturer using the same equipment and procedure, the resulting bias limit of the pressure difference is zero. Therefore, the uncertainty of the pressure drop across the cold plate becomes equal to the precision limit $P_{\Delta p_e}$. This precision limit is estimated as being equal to twice the standard deviation of several measurements, or approximately three percent.

Results

Figure 1 presents a comparison between the pressure drop predicted by Eq. (19) and the pressure drop measured experimentally, versus the coolant volumetric flow rate, for a reference coolant temperature $T_0 = 21^\circ\text{C}$, and $V = 46.9 \text{ V}$ ($q'' = 1.3 \text{ kW/m}^2$). In this case, $N = -0.23$. It can be seen that the analytical estimate obtained from Eq. (19) compares very well against the experimental measurements when the flow rate is small, deviating to slightly smaller values when the flow rate increases beyond $3 \times 10^{-5} \text{ m}^3/\text{s}$.

As indicated previously, Eq. (19) is expected to be precise for $N \ll 1$ only. To test this limitation, we have performed additional hydraulic tests increasing the voltage to $V = 114.9 \text{ V}$ ($q'' = 7.8 \text{ kW/m}^2$). In this case, $N = -1.383$. The pressure drop predicted by Eq. (19) and the experimental pressure drop values are shown in Fig. 2. Observe that the agreement between the prediction from Eq. (19) and the measured pressure drop Δp_e deteriorates rapidly as the volumetric flow rate increases.

Also plotted in Fig. 2 is the pressure drop measured without heating the cold plate, Δp_{e0} . Observe how the measured pressure drop, when heating the cold plate, Δp_e tends to the pressure drop with no-heating, Δp_{e0} as the coolant volumetric flow rate in-

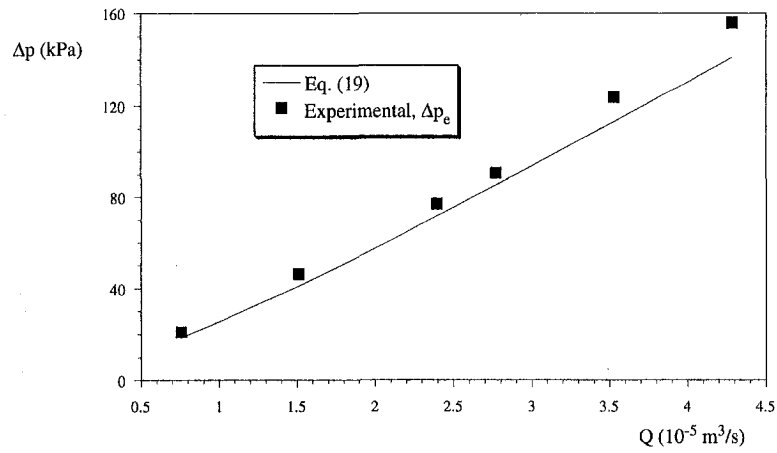


Fig. 1 Pressure drop versus volumetric coolant flow rate for $T_0 = 21^\circ\text{C}$ and $V = 46.9\text{ V}$. (Uncertainties: $U_{\Delta p_e}/\Delta p_e = 3$ percent, $U_Q/Q = 5$ percent).

creases. This is explained by the departure of the flow from a linear velocity regime (the Darcy regime) dominated by viscous drag, to a quadratic velocity regime dominated by the form drag. Recall that the form drag is independent of the fluid viscosity. This means that when the fluid velocity (or the volumetric flow rate) is increased, the temperature effect on the viscosity of the coolant will affect less and less the pressure drop across the cold plate. Because Eq. (19) was derived under the assumption of zero form drag, the analytical pressure drop estimate of Eq. (19) is limited to linear (viscous drag dominated) flow regimes. One can expect the analytical estimate to deteriorate when the flow rate increases, i.e., when the form drag becomes increasingly important.

For the case shown in Fig. 2, it is relatively easy to determine the effective permeability K , and the form coefficient C of the porous insert, in m^{-1} , by fitting the experimental no-heating results with a function of the type

$$\Delta p_0 = \frac{L\mu_0}{K} \frac{Q}{A_f} + L\rho C \left(\frac{Q}{A_f}\right)^2 \quad (20)$$

where L is the cold plate length equal to 0.076 m , A_f is the flow cross-section area equal to $5.08 \times 10^{-4}\text{ m}^2$, and μ_0 and ρ are the PAO viscosity and density at 21°C , respectively, $5.95 \times 10^{-3}\text{ kg/ms}$ and 789.2 kg/m^3 . The values obtained by curve fitting the results of Fig. 2 are $K = 3.28 \times 10^{-10}\text{ m}^2$ and $C = 89.2 \times 10^3\text{ m}^{-1}$. As indicated by Lage (1998), the ratio between the form drag D_c (responsible for the quadratic flow rate term of Eq. (20)) and

the viscous drag D_μ (responsible for the linear flow rate term of Eq. (20)) can be estimated using

$$\frac{D_c}{D_\mu} = \frac{\rho CK}{\left(1 + \frac{N}{3}\right)\mu_0} \frac{Q}{A_f} \quad (21)$$

where the denominator of the RHS term represents the first-order approximation (see Eq. (14)) of the temperature effect on the fluid viscosity.

After substituting the proper values in Eq. (21), one obtains $D_c/D_\mu = 1.42 \times 10^4 Q$. So, when $Q \sim 7 \times 10^{-5}\text{ m}^3/\text{s}$ then $D_c \sim D_\mu$. This criterion indicates that the results of Figs. 1 and 2 are in the range of the transition regime. This is why the analytical results deviate from the experimental results as Q increases.

One of the reviewers has asked for a justification of the high-Péclet number assumption invoked when writing Eq. (2). For the present experimental tests, we can write $\text{Pe} = QL/A_f\alpha$. Using the values listed previously and $\alpha_{\text{PAO}} = 8.68 \times 10^{-5}\text{ m}^2/\text{s}$ we obtain a minimum Pe equal to 8,617 establishing that all results satisfy the high-Pe assumption.

Conclusions

A theory for the thermohydraulic prediction of the single-phase convective cooling of a porous medium enhanced enclosure using a temperature-dependent viscous fluid is presented. The theory

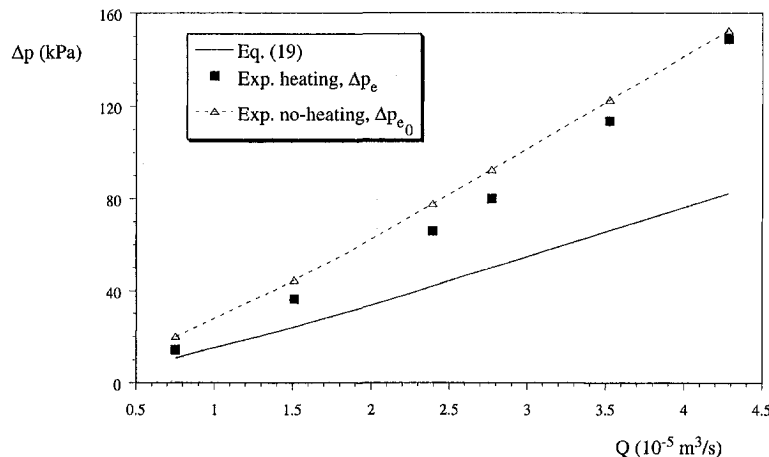


Fig. 2 Pressure drop versus volumetric coolant flow rate for $T_0 = 21^\circ\text{C}$ and $V = 114.9\text{ V}$. (Uncertainties: $U_{\Delta p_e}/\Delta p_e = 3$ percent, $U_Q/Q = 5$ percent).

considers the first-order effect of viscosity variation on the Darcy flow regime valid for low fluid speed.

When applied to the prediction of the pressure drop across a microporous enhanced cold plate, the theory anticipates quite well the experimental results as long as the viscosity variation number is small compared with unity and the flow regime, under heating conditions, is linear in velocity, i.e., when the form drag effect is negligible.

Comparisons with experimental results when N is not small compared with unity, and the form drag effect becomes comparable to the viscous drag effect, indicates a consistent departure of the theoretically predicted pressure drop values from the experimental values. Obviously, when the form drag predominates, the pressure drop can be estimated analytically by neglecting the viscous drag, and thus neglecting the heating effect on the fluid viscosity.

Acknowledgments

The first author is grateful to Dr. X. D. Chen, of the Department of Chemicals and Materials Engineering, University of Auckland, for pointing out to him the need for a theoretical investigation of this type. This work was supported by the Defense Systems and Electronics Group of Texas Instruments, now Raytheon Systems.

References

- Antohe, B. V., Lage, J. L., Price, D. C., and Weber, R. M., 1996, "Numerical Characterization of Micro Heat Exchangers using Experimentally Tested Porous Aluminum Layers," *Int. J. Heat Fluid Flow*, Vol. 17, pp. 594–603.
- Antohe, B. V., Lage, J. L., Price, D. C., and Weber, R. M., 1997, "Experimental Determination of Permeability and Inertia Coefficients of Mechanically Compressed Aluminum Porous Matrices," *ASME Journal of Fluids Engineering*, Vol. 119, pp. 404–412.
- Bejan, A., 1984, *Convective Heat Transfer*, 1st Ed. John Wiley and Sons, New York, pp. 82–94 (2nd Ed. 1995, pp. 107–121).
- Chevron, 1981, Synfluid Synthetic Fluids, Physical Property Data.
- Kays, W. M., and Harnett, J. P., 1973, "Forced Convection, Internal Flow in Ducts," *Handbook of Heat Transfer*, W. M. Rohsenow and J. P. Harnett, eds., McGraw-Hill, New York, Section 7.
- Kim, J. H., Simon, T. W., and Viskanta, R., 1993, "Journal of Heat Transfer Policy on Reporting Uncertainties in Experimental Measurements and Results," *ASME JOURNAL OF HEAT TRANSFER*, Vol. 115, pp. 5–6.
- Lage, J. L., 1998, "The Fundamental Theory of Flow through Permeable Media from Darcy to Turbulence," *Transport Phenomena in Porous Media*, D. B. Ingham and I. Pop, eds., Pergamon, New York, pp. 1–30.
- Lage, J. L., Weinert, A. K., Price, D. C., and Weber, R. M., 1996, "Numerical Study of a Low Permeability Microporous Heat Sink for Cooling Phased-Array Radar Systems," *Int. J. Heat Mass Transfer*, Vol. 39, pp. 3633–3647.
- Ling, J. X., and Dybbs, A., 1992, "The Effect of Variable Viscosity on Forced Convection over a Flat Plate Submersed in a Porous Medium," *ASME JOURNAL OF HEAT TRANSFER*, Vol. 114, pp. 1063–1065.
- Porneala, D. C., 1998, "Experimental Tests of Microporous Enhanced Cold Plates for Cooling High Frequency Microwave Antennas," dissertation, SMU, Dallas, TX.
- Shah, R. K., and Bhatti, M. S., 1987, "Laminar Heat Convective Heat Transfer in Ducts," *Handbook of Single-Phase Convective Heat Transfer*, Eds. S. Kakaç et al., eds., John Wiley and Sons, New York, Chapter 3.